INAUGURAL - DISSERTATION

zur
Erlangung der Doktorwürde
der
Gesamtfakultät für Mathematik,
Ingenieur- und Naturwissenschaften
der
Ruprecht-Karls-Universität
Heidelberg

Vorgelegt von
Roman Graebner
aus Chemnitz

Tag der mündlichen Prüfung: 31.10.2025

Design and Synthesis of Molecular Structural Stabilizers for the ALS-relevant SOD1 Protein

1. Gutachterin: Prof. Dr. Franziska Thomas
2. Gutachter: Prof. Dr. Christian Klein

NATURWISSENSCHAFTLICH-MATHEMATISCHE
GESAMTFAKULTÄT

COMBINED FACULTY OF NATURAL SCIENCES AND
MATHEMATICS

Eidesstattliche Versicherung gemäß § 8 der Promotionsordnung für die Naturwissenschaftlich-Mathematische Gesamtfakultät der Universität Heidelberg / Sworn Affidavit according to § 8 of the doctoral degree regulations of the Combined Faculty of Natural Sciences and Mathematics

1. Bei der eingereichten Dissertation zu dem Thema / The thesis I have submitted entitled

   Design and Synthesis of Molecular Structural Stabilizers for the ALS-relevant SOD1 Protein

   handelt es sich um meine eigenständig erbrachte Leistung / is my own work.

2. Ich habe nur die angegebenen Quellen und Hilfsmittel (inkl. KI-basierter Hilfsmittel) benutzt und mich keiner unzulässigen Hilfe Dritter bedient. Insbesondere habe ich wörtlich oder sinngemäß aus anderen Werken übernommene Inhalte als solche kenntlich gemacht. / I have only used the sources indicated (incl. AI-based tools) and have not made unauthorised use of services of a third party. Where the work of others has been quoted or reproduced, the source is always given.

3. Die Arbeit oder Teile davon habe ich ~~wie folgt/~~bislang nicht[1)] an einer Hochschule des In- oder Auslands als Bestandteil einer Prüfungs- oder Qualifikationsleistung vorgelegt. / I have not yet/have already[1)] presented this thesis or parts thereof to a university as part of an examination or degree.

   Titel der Arbeit / Title of the thesis:

   Hochschule und Jahr / University and year:

   Art der Prüfungs- oder Qualifikationsleistung / Type of examination or degree:

4. Die Richtigkeit der vorstehenden Erklärungen bestätige ich. / I confirm that the declarations made above are correct.

5. Die Bedeutung der eidesstattlichen Versicherung und die strafrechtlichen Folgen einer unrichtigen oder unvollständigen eidesstattlichen Versicherung sind mir bekannt. / I am aware of the importance of a sworn affidavit and the criminal prosecution in case of a false or incomplete affidavit

Ich versichere an Eides statt, dass ich nach bestem Wissen die reine Wahrheit erklärt und nichts verschwiegen habe. / I affirm that the above is the absolute truth to the best of my knowledge and that I have not concealed anything.

Ort und Datum / Place and date

……..……
Unterschrift / Signature

[1)] Nicht Zutreffendes streichen. Bei Bejahung sind anzugeben: der Titel der andernorts vorgelegten Arbeit, die Hochschule, das Jahr der Vorlage und die Art der Prüfungs- oder Qualifikationsleistung. / Please cross out what is not applicable. If applicable, please provide: the title of the thesis that was presented elsewhere, the name of the university, the year of presentation and the type of examination or degree.

The German text is legally binding.

Kurzfassung

Amyotrophe Lateralsklerose (ALS) ist eine seltene, schwere und derzeit unheilbare neurodegenerative Erkrankung. Trotz der zahlreicher Anstrengungen der letzten Jahre gibt es noch immer keine allgemein anwendbare, wirksame Behandlung. Bei einer Untergruppe von ALS-Patienten wird die Krankheit durch die Aggregation des mutierten menschlichen Superoxiddismutase (hSOD1)-Proteins verursacht und vorangetrieben. Die Stabilisierung des katalytisch aktiven, nativen Homodimer-Zustands von hSOD1 verhindert die Dissoziation in zu Aggregation neigende und krankheitsrelevante Monomere. Zu diesem Zweck wurde die Entwicklung von dimerstabilisierenden nicht-kovalenten Liganden verfolgt. Es wurden niedermolekulare Liganden entwickelt, die auf die Val148-Kavität der hSOD1-Dimer-Kontaktfläche abgestimmt sind. Die Leitstruktur der Liganden, bestehend aus einer zentralen funktionalisierten Dibenzol-Einheit, an die eine dritte funktionalisierte Benzol-Einheit über einen Amid-Linker angebunden ist, wurde retrosynthetisch in drei Strukturfragmente zerlegt. Diese Fragmente wurden systematisch variiert und *in-silico* kombinatorisch erschöpfend wieder zusammengefügt, wodurch eine Bibliothek von 320 virtuellen Liganden entstand. Mit dem Ziel, sowohl die wichtigsten Fragmente als auch die vielversprechendsten Ligandenstrukturen zu identifizieren, wurde die virtuelle Ligandenbibliothek mittels molekularem Docking untersucht. Ausgehend von der *in-silico*-Einschätzung wurden zwölf niedermolekulare Liganden synthetisiert. Dazu wurde ein zielgerichteter und direkter modularer organischer Syntheseweg mit Amidkopplung und Suzuki–Miyaura-Kopplung als entscheidende Derivatisierungsschritte entwickelt. Um ein *in-vitro*-Modell der hSOD1-ALS-Pathologie zu erlangen, wurde die rekombinante Expression der Proteine hSOD1 und hSOD1 A4V etabliert. Mit dem Ziel, den physiologische Bedingungen möglichst treu zu bleiben, wurde besonderer Wert darauf gelegt, das Vorhandensein der natürlichen Reifungsmodifikationen von SOD1 sicherzustellen. Massenspektrometrie bestätigte die native Metallierung mit Cu^{2+} und Zn^{2+}, sowie die Ausbildung der Disulfidbrücke innerhalb der Untereinheiten. Der Nachweis der enzymatischen Aktivität von hSOD1 und hSOD1 A4V bestätigte sowohl die korrekte Faltung als auch die Dimerassoziation. Insgesamt bestätigte dies, dass die Proteine hSOD1 und hSOD1 A4V in ihrem nativen Zustand vorlagen. Die inhibitorische Wirkung der Liganden auf die Aggregation von hSOD1 A4V wurde in mehreren komplementären *in-vitro*-Assays. Ein Thioflavin-T-basierter Aggregationsassay diente dabei als Musterungsinstrument. Elf synthetisierte Liganden und zwei weitere, literaturbekannte Verbindungen wurden untersucht. Dabei wurden drei Liganden als mutmaßliche Treffer identifiziert. Messungen der Dynamischen Lichtreuung bestätigten diese drei Treffer und ermöglichten darüber hinaus die Einschätzung der Partikelgrößen der in Lösung gebildeten hSOD1-Aggregate. Bei elektronenmikroskopische Untersuchungen konnten die Morphologien der hSOD1 A4V-Aggregate unter den in dieser Arbeit verwendeten Inkubationsbedingungen gezeigt werden. Die Eingangs durchgeführte molekulare Docking-Studie wurde unter Berücksichtigung der experimentellen Beobachtungen bewertet. Dadurch wurde hervorgehoben, dass sie einen wertvollen Beitrag geleistet hatte, da sie zwei der *in-vitro* identifizierten Treffer korrekt vorhergesagt hatte. Darüber hinaus wurden die Bindungsmodi der Liganden durch das molekulare Docking postuliert, wobei zwei der erfolgreichen Liganden einen gemeinsamen Bindungsmodus aufwiesen. Zusammenfassend lässt sich sagen, dass drei der entwickelten hSOD1-stabilisierenden niedermolekularen Liganden nachweislich die Bildung von ALS-relevanten hSOD1 A4V Aggregaten reduzieren. Ihre Wirksamkeit wurde durch zwei komplementäre *in-vitro*-Assays und eine strenge Bewertung der experimentellen Ergebnisse bestätigt. Diese Liganden sind wertvolle Werkzeuge für die Aufklärung der Pathologie, die der hSOD1-ALS-Erkrankung zugrunde liegt und der damit verbundenen Forschung. Insbesondere einer der Liganden wurde als potenter Leitwirkstoff für die Entwicklung einer therapeutischen Behandlung von hSOD1-ALS aufgezeigt.

Abstract

Amyotrophic lateral sclerosis (ALS) is a rare, devastating, currently incurable neurodegenerative disease. Despite numerous efforts in recent years, there is still no widely effective treatment available. In a subset of ALS patients, aggregation of the mutant human superoxide dismutase (hSOD1) protein drives the development and progression of ALS. Stabilization of hSOD1's catalytically active, native homodimer state prevents dissociation into aggregation-prone and disease relevant monomers. To this end, the development of dimer-stabilizing non-covalent ligands was pursued. Small molecule ligands were designed to target the Val148 cavity of the hSOD1 dimer interface. The ligands lead structure, comprised of a central functionalized biphenyl moiety with a third functionalized benzene moiety connected *via* an amide linker, was retrosynthetically disconnected into three structural fragments. These fragments were systematically varied and combinatorially reconnected *in silico*, affording a library of 320 virtual ligands. Aiming to identify both, the most essential fragments, as well as the most promising ligand structures, molecular docking was utilized to screen the virtual ligand library. Based on the *in silico* prediction, twelve small molecule ligands were synthesized. Featuring amide coupling and Suzuki–Miyaura coupling as key derivatization steps, a concise modular organic synthesis route was developed. In order to provide an *in vitro* model of hSOD1-ALS pathology, recombinant expression of the hSOD1 and hSOD1 A4V proteins was established. Aiming to closely mimic physiological conditions, emphasis was placed on ensuring the presence of SOD1's native maturation modifications. Mass spectrometry confirmed native Cu^{2+} and Zn^{2+} metalation and the formation of the intrasubunit disulfide bond. Demonstrating the enzymatic activity of hSOD1 and hSOD1 A4V proved correct folding and dimer-association. Taken together, this verified that hSOD1 and hSOD1 A4V were obtained in their native states. The ligands inhibitory effect on hSOD1 A4V aggregation was investigated in multiple complementary *in vitro* assays. A thioflavin T based aggregation assay served as a screening tool. Eleven ligands and two literature known compounds were assessed and three ligands were identified as putative hits. Dynamic light scattering confirmed these three hits and in addition, provided estimates of the particle sizes of the formed hSOD1 aggregates in solution. Electron microscopy revealed hSOD1 A4V aggregate morphology under the incubation conditions utilized in this work. The initial molecular docking study was evaluated in light of the experimental observations. This highlighted it as a valuable asset, as it had correctly predicted two of the *in vitro* identified hits. Furthermore, ligand binding modes were proposed by molecular docking and two hit ligands shared a proposed binding mode. In conclusion, three of the developed hSOD1 stabilizing small molecule ligands were demonstrated to reduce the formation of ALS-relevant hSOD1 A4V aggregates. Their effectiveness was confirmed by two complementary *in vitro* assays and rigorous evaluation of experimental results. These ligands provide valuable tools for the elucidation of hSOD1-ALS disease pathology and related research. One ligand in particular was highlighted as a potent lead compound for the development of a therapeutic treatment of hSOD1-ALS.

Acknowledgments

Many people have directly or indirectly contributed to this thesis and assisted me along the journey. Inside and outside of the laboratory, these people have made this work possible and I would like to thank them.

First and foremost I want to thank Prof. Franziska Thomas for the opportunity to conduct this research in her group, for her mentorship and the support and encouragement I received. Working on a topic as current as neurodegenerative diseases and getting to experiment with many different methods and devices has been intriguing. I learned a lot in this interdisciplinary work and for that I am thankful.

I want to thank Prof. Klein for the generous access to his laboratory and equipment, allowing me to express and purify my proteins. I want to thank the AK Klein for the accommodating atmosphere and help in their laboratory. I want to thank Dr. Mila Leuthold in particular for help and support with protein expression and purification and sharing her expertise.

I want to thank Prof. Kai Tittmann and his group, especially Dr. Fabian Rabe von Pappenheim for teaching me the expression and purification of SOD1 and the enjoyable time in Göttingen.

I want to thank my students, Tamara Skarke, Janica Wendt, Moritz Huber, Lars Kreutzer and Aron Blaseg, who conducted bachelor theses and internships in contribution to this study. In addition to the synthesis we conducted together, I thank you for the pleasant time.

I want to thank the entire AK Thomas, current and past, for the good times I had with you all over these last years. I want to thank Dr. Truc Lam Pham for the countless discussions and the experience of assisting in the OC practicals together. I want to thank Dr. Vanessa Reusche for her help and support on numerous occasions. I want to thank Thomas Heim for the experience of assisting in the OC practicals together, for his thorough care for the HPLCs, for sharing his wisdom about DLS and conducting the EM measurements.

I want to thank Dr. Jürgen H. Gross for the MS measurements during the metalation study of SOD1 and his help and guidance with these experiments.

I want to thank Prof. Sinning for the generous access to the MST instrument.

I want to thank all staff members of the NMR and MS service departments of the Institute of Organic Chemistry for the numerous measurements of my samples.

I want to thank everyone who proofread this thesis, notably, Dr. Kristina Bayer and Dr. Truc Lam Pham for their time and invaluable insight.

I want to thank Dr. Vanessa Reusche, Marius Werner, Niklas Schwegler, Kiara Keil, Thomas Heim, and everyone else who sporadically joined our AK bouldering events for their good company.

I want to thank my parents and family for their unconditional love and support. I would not be where I am today if it were not for your support and for that I am truly thankful.

I thank my friend for taking my mind of off work and the fun we have together.

Finally, I want to thank Frauke Huth for always believing in me and always being by my side.

Glossary

Aβ	amyloid β-protein
AβO	amyloid beta oligomer
AA	amino acid
AD	Alzheimer's disease
ADT	AutoDockTools
AFM	atomic force microscopy
ALS	amyotrophic lateral sclerosis
ALSFRS-R	amyotrophic lateral sclerosis functional rating scale-revised
APS	ammonium persulfate
ASO	antisense oligonucleotide
ba	boronic acid fragment
brine	saturated aqueous solution of NaCl
C9orf72	chromosome 9 open reading frame 72
ca	carboxylic acid fragment
CD	circular dichroism
CMA	chaperone mediated autophagy
CNS	central nervous system
COSY	correlation spectroscopy
CSF	cerebrospinal fluid
CV	column volume
DEPT 135	distortionless enhancement by polarization transfer with a 135° selection angle parameter
DHB	2,5-dihydroxybenzoic acid
DIPEA	*N*,*N*-diisopropylethylamine
DLS	dynamic light scattering
DME	1,2-dimethoxyethane
DTT	dithiothreitol
EA	ethyl acetate
EDC	3-(ethyliminomethyleneamino)-*N*,*N*-dimethylpropan-1-amine
EDTA	ethylenediaminetetraacetic acid
EI-MS	electron ionization mass spectrometry
EM	Electron Microscopy
EMA	European Medicines Agency
ERAD	ER-associated degradation
ESI	electrospray ionization
ESI-MS	electrospray ionization mass spectrometry
fALS	familial amyotrophic lateral sclerosis
FDA	U.S. Food and Drug Administration
FTD	frontotemporal dementia
FTIR	fourier-transform infrared spectroscopy
FUS/TLS	RNA-binding protein fused in sarcoma/translocated in liposarcoma
Gdn • HCl	guanidine hydrochloride

hCCS	human copper chaperone for SOD1
HD	Huntington's disease
HEPES	4-(2-hydroxyethyl)-1-piperazineethanesulfonic acid
HMBC	heteronuclear multiple-bond correlation spectroscopy
HOBt	1*H*-benzo[*d*][1,2,3]triazol-1-ol
H-PTFE	hydrophilized polytetrafluoroethylene
HRMS	high resolution mass spectrometry
hSOD1	human superoxide dismutase 1
HSQC	heteronuclear single-quantum correlation spectroscopy
IEX	ion exchange chromatography
IgG	immunoglobulin G
IPTG	isopropyl-β-D-thiogalactopyranosid
ITC	isothermal titration calorimetry
LB	lysogeny broth
LMN	lower motor neurons
MADLS	multi-angle dynamic light scattering
MALDI	matrix-assisted laser desorption/ionization
MALS	multiple angle light scattering
MND	motor neurone disease
MNJ	motor neuron junction
mPEG	methoxypolyethylene glycol
mPEG-550	methoxypolyethylene glycol with a statistical average MW of 550
MS	mass spectrometry
MST	MicroScale Thermophoresis
MTPC	Mitsubishi Tanabe Pharma Corporation
NaPB	sodium phenylbutyrate
NBS	*N*-bromosuccinimide
NDD	neurodegenerative disease
NfL	neurofilament light chain
NIs	nuclear inclusions
NMR	nuclear magnetic resonance
OD_{600}	optical density at 600 nm
PD	Parkinson's disease
PDB	Protein Data Base
PE	petroleum ether
PEG	polyethylene glycol
PEG-550	methoxypolyethylene glycol with a statistical average MW of 550
pI	isoelectric point
PMSF	phenylmethylsulfonyl fluoride
PQC	protein quality control
PTFE	polytetrafluoroethylene
PTMs	post-translational modifications
R_f	retention factor
RISC	RNA-induced silencing complex

RNAi	RNA interference
rt	room temperature
sALS	sporadic amyotrophic lateral sclerosis
SDS	sodium dodecyl sulfate
SDS-PAGE	sodium dodecyl sulfate–polyacrylamide gel electrophoresis
SEC	size exclusion chromatography
SEC-MALS	size exclusion chromatography–multiple angle light scattering
SGs	stress granules
siRNA	small interfering RNA
SMC	Suzuki–Miyaura coupling
SOC	super optimal broth with catabolite repression
SOD1	superoxide dismutase 1
ssASO	splice-switching antisense oligonucleotide
t_R	retention time
TCEP	tris(2-carboxyethyl)phosphine
TDP-43	transactive response DNA binding protein 43 kDa
TEMED	tetramethylethylenediamine
TFA	trifluoroacetic acid
ThT	thioflavin T
TLC	thin-layer chromatography
TMAE	trimethylammoniumethyl
Tris	tris(hydroxymethyl)aminomethane
TUDCA	tauroursodeoxycholic acid
UMN	upper motor neurons
UPS	ubiquitin proteasome system
V_0	void volume
WST-1	water soluble tetrazolium 1 sodium 4-[2-(4-iodophenyl)-3-(4-nitrophenyl)-3H-tetraazol-2-ium-5-yl]-1,3-benzenedisulfonate

Contents

1 Introduction

1.1 Amyotrophic Lateral Sclerosis

Amyotrophic lateral sclerosis (ALS) is a currently incurable, fatal, progressive neurodegenerative disease of the central nervous system (CNS).[1] Other common names for ALS are motor neurone disease (MND), Charcot's disease and Lou Gehrig's disease.[2] ALS is a rare disease with an incidence of ~1.68 per 100000 person-years globally and ~1.7–1.89 in Europe and North America,[1] but incidences vary by region and across populations.[3,4] Typical to ALS is the degeneration of upper and lower motor neurons, resulting in progressive weakening of voluntary skeletal muscles, which control limb movement, swallowing, speaking and breathing, eventually ending in paralysis and respiratory failure.[1,5] On average, the disease symptoms start at an age of about 50–60 years[5] and survival is commonly limited to only about 2–5 years.[1,6,7]

Historically, ALS has been described as a disease affecting both upper motor neurons (UMN) and lower motor neurons (LMN), with symptoms limited to a loss of motor function. Recently, the acceptance of phenotypic heterogeneity has lead to the view of ALS as a complex syndrome.[1] A portion of ALS patients also display cognitive impairment and behavioral deficits. Previously, this was explained by the presence of frontotemporal dementia (FTD), a second condition in addition to the patients ALS diagnosis. Today, cognitive impairment and behavioral deficits are recognized as part of the ALS phenotype[1,5] and ALS and FTD are considered to exist as one spectrum disorder.[8,9] ALS represents the one extreme end of the spectrum with symptoms limited to motor impairment caused by UMN and LMN degeneration and FTD represents the other extreme end of the spectrum with symptoms limited to behavioral and cognitive deficits caused by frontotemporal neurodegeneration.[1] ALS motor symptoms initially appear in one region of the body, then spread over the course of the disease with LMN and UMN affected to varying degrees. What is clinically referred to as classical ALS refers to an onset in the limbs which then spreads into the bulbar (speaking, swallowing) region, presenting both LMN and UMN affection. Depending on affected regions and the spectrum of LMN and or UMN degeneration, patients are classified into various clinical presentations.[1]

While clinically indistinguishably,[10,11] ALS cases are differentiated between sporadic ALS (sALS) accounting for about 90–95% of ALS cases and familial (fALS) accounting for about 5–10% of cases.[6,12] The percentage of ALS cases with a familial heritage is likely higher however, as indicated by twin studies of sALS patients[5,13] and by studies where genealogy was actively investigated.[13] Because ALS presents a variety of heterogeneous phenotypes, resulting from a number of genetic factors and disease progression pathways, the development of effective drug treatment has so far largely been unsuccessful.[5] Due to the genetic component of ALS, therapeutic benefits can potentially be gained by personalized treatment. Enabled by advances in sequencing techniques, genome analysis of ALS patients has become more common in recent years[14] and is helping to differentiate ALS cases by underlying genetics rather than clinical presentation.[15]

Today, numerous genes and proteins are associated with ALS. Superoxide dismutase 1 (SOD1),[16] transactive response DNA binding protein 43 kDa (TDP-43)[17–19] chromosome 9 open reading frame 72 (C9orf72)[20–22] and RNA-binding protein fused in sarcoma/translocated in liposarcoma (FUS/TLS)[23] are among the most extensively studied over the last decades. Together, these four proteins account for ~60% familial ALS cases and ~11% of sporadic ALS cases.[12,24,25] Multiple databases such as ALSoD, STRENGTH, MinE and NINDS Repository ALS collections, have been created; listing the ever growing number of ALS-associated genes.[12] Across its various causes and clinical variations, a hallmark of ALS is the presence of cytoplasmic protein inclusions in motor neurons.[26]

In ~97% of all sALS and fALS patients these inclusions were reported to contain TDP-43, while mutations in the corresponding *TARDBP* gene were only found in ~5% fALS and ~1% sALS cases. Notably, TDP-43 was absent in inclusions of ALS patients with mutant SOD1, where instead mutant SOD1 was found, suggesting that TDP-43 and mutant SOD1 represent separate pathologies.[26,27] TDP-43 and SOD1 related ALS are currently considered distinct and mostly non-overlapping.[27,28]

Published in 1993 by Rosen *et al.*, *SOD1* was the first gene, for which mutations were associated with fALS.[16] A meta-analysis from 2019 reported mutations of SOD1 in 14.8% of fALS and 1.2% of sALS cases in European populations and in 30.0% of fALS and 1.5% sALD cases in Asian populations. The authors further highlight differences in occurrence across different countries in these populations.[6] Different geographic distributions of SOD1 related ALS are widely recognized.[12,24] Because SOD1-ALS represents a distinct subtype of ALS, for which genetics have been demonstrated as a reliable predictor, SOD1-ALS might be susceptible to specific treatment.[29] With the approval of tofersen (Section 2.7.3) in 2023, the first SOD1-ALS specific treatment is now available to patients.[29]

1.2 Protein Aggregation in ALS and Neurodegenerative Diseases

Protein inclusions, caused by the aggregation of so called toxic proteins are a hallmark of many neurodegenerative diseases (NDDs) such as ALS, Alzheimer's (AD), Parkinson's (PD), or Huntington's disease (HD) and are typically observed in affected neurons. While each NDD is typically associated with the presence of disease specific characteristic proteins in these inclusion, they share common underlying mechanisms of disease pathology. Patients may develop NDDs sporadically or due to genetic causes and while the ratio between of the two varies across NDDs, the presence of both genetic and non-genetic factors is typical to NDDs.[30]

Proteins that are misfolded or carry aberrant modifications are common and usually quickly removed by the cells protein quality control (PQC) system, consisting of the ubiquitin-proteasome system (UPS), chaperone mediated autophagy (CMA), macroautophagy and ER-associated degradation (ERAD).[30,31] In the case of NDDs, the presence of aberrant proteins is greatly increased, straining these control systems. Inclusions of toxic proteins often contain ubiquitin and chaperones and neurons are observed to be depleted of ubiquitin and these chaperones.[30] Conversely, studies have demonstrated, that ubiquitination might promote aggregation, suggesting that sequestration of toxic proteins by this mechanism could be a protective function, in addition to the regular UPS pathways.[30] Nuclear inclusions (NIs) and stress granules (SGs) may similarly be a cells attempt to protect themselves by sequestering toxic proteins.[30]

Protein aggregation can disturb a number of systems, which affects neurons more than other cells.[30] Neurons are unable to replicate and therefore form a tissue that is unable to regenerate like other cell types.[30] Because of their large size, they rely on axonal transport systems, which can be compromised by aggregates. Unable to transport these aggregates the cell is then unable to degrade them.[30] Mitochondrial dysfunction is often observed in NDDs and neurons have a greater ATP demand, compared to other cell types. It has been reported that proteasome activity is naturally lower in the spinal cord relative to other tissue types and that proteasome activity declines with age.[32,33] Further, inhibition of proteasome activity was reported to induce neuron death in vitro, highlighting its essential function.[32]

Since the report of Elam *et al.* in 2003, that recombinantly expressed mutant SOD1 can be crystallized as amyloid-like fibrils,[34] the formation of SOD1 fibrils under various experimental conditions has been studied at length.[35] While the ability of SOD1 to form amyloid fibrils, among other morphologies is well established, the possible presence of amyloid fibrils in human ALS pathology is a matter of debate.[35,36] There has not yet been a report of SOD1 amyloid structures found in human postmortem ALS tissues[35] and the correlation between aggregates *in vitro* and aggregates *in vivo* remains uncertain.[37] It has further been reported that SOD1 aggregate morphology strongly depends on both the specific SOD1 mutation and the investigated cell line, suggesting that cells specific micro-environments need to be taken into account.[38]

Instead of large aggregates, small soluble oligomers are suspected to be responsible for the toxicity of aggregation prone SOD1 mutants.[35,39] It has been suggested that large aggregates may actually have a protective function against smaller toxic oligomers.[40] Recently, a lot of attention has been directed towards SOD1 trimers,[41] but their pathological relevance has not yet been examined in detail.[35] While the exact nature of SOD1 aggregates and their toxicity in human ALS pathology remains unclear, the presence of SOD1 aggregates in mutant SOD1-ALS cases is unquestionable. Therapeutic agents targeting the aggregation of mutant SOD1 have therefore been pursued as a potential treatment for ALS.[26,35,42]

In addition to its well established role in mutant SOD1 linked ALS, studies have suggested the involvement of misfolded wild type SOD1 in non-SOD1-linked ALS, Parkinson's (PD) and Alzheimer's disease (AD) as well as general aging.[35,39,43]

As NDDs generally correlate with age and the incidence of ALS has consistently been reported to rise with age, there is a growing need for effective pharmacological treatment in an aging society.[30,44]

2 State of the Art

2.1 The Superoxide Dismutase 1 Protein

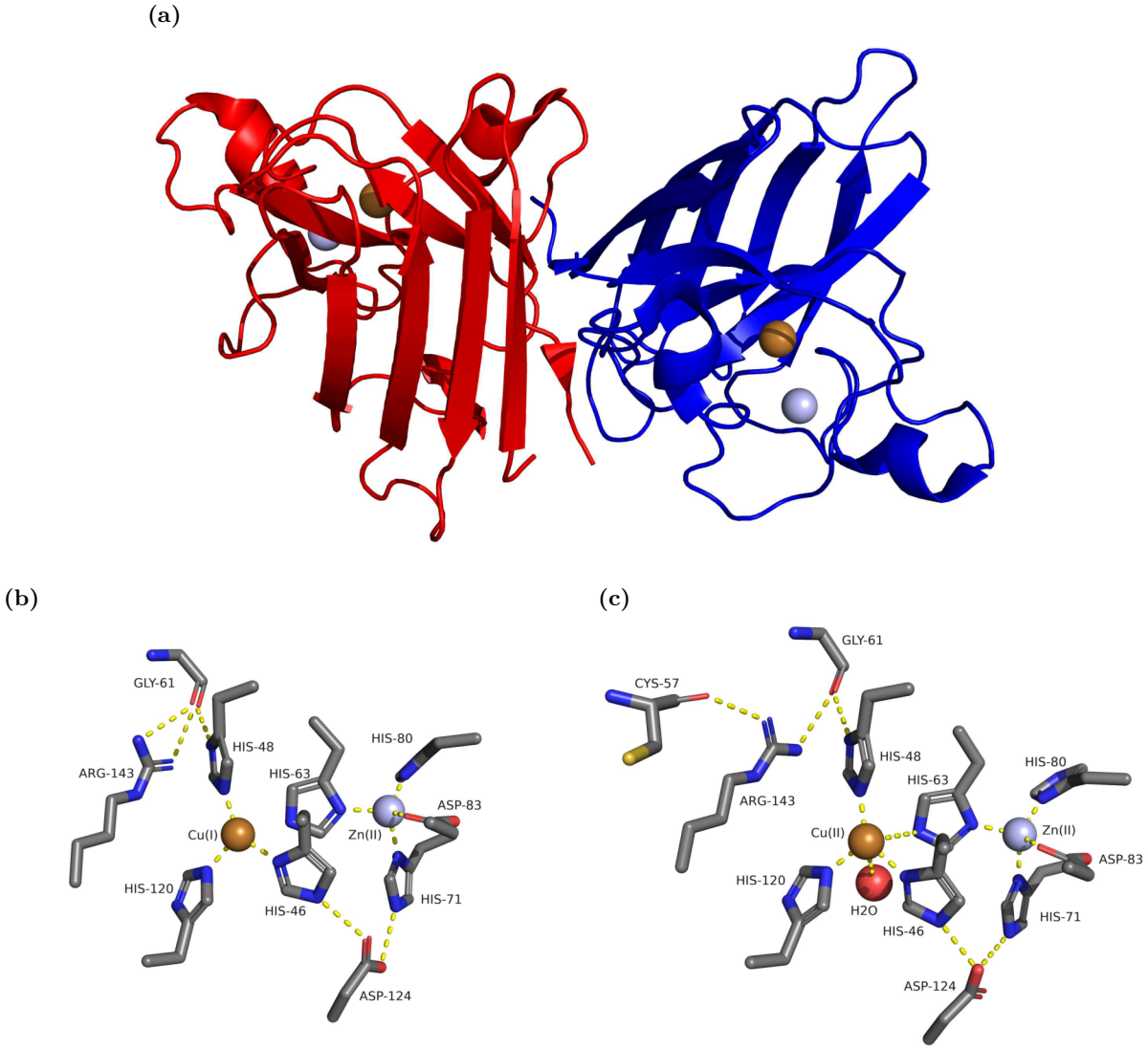

Figure 1: Graphical representation of hSOD1 and close-ups of one of its two active centers in the reduced and in the oxidized state. For clarity, the active site is simplified to the amino acids (AAs) of the first and second coordination sphere of the Cu (orange sphere) and Zn (light blue sphere) ions. Only AA side chains are shown, except for Gly61 and Cys57 where the main chain is also depicted. AA atoms are colored by element (C grey, N blue, O red, S yellow). **(a):** Graphical representations of an X-ray crystal structure (PDB: 2c9u[45]) of wt hSOD1, oriented to show the two metals in close proximity to each other. Monomer A is shown in red and monomer F is shown in blue. **(b):** Reduced state, showing Cu^{+} in almost trigonal planar coordination and Zn^{2+} in almost tetrahedral coordination. An X-ray crystal structure (PDB: 1pu0[46]) of hSOD1 was used. **(c):** Oxidized state, showing Cu^{2+} in distorted square pyramidal coordination and Zn^{2+} in almost tetrahedral coordination. The O-atom of the water molecule coordinated to the Cu^{2+} is shown as a red sphere. An X-ray crystal structure (PDB: 2v0a[47]) of hSOD1 was used. Illustration taken from previous work of the author.[48]

Human SOD1 (UniProt: P00441, EC: 1.15.1.1) is an ubiquitously expressed protein localized primarily in the cytosol, but also present in the mitochondrial intermembrane space and the nucleus.[49] Its enzymatic function is the removal of superoxide radicals ($O_2^{\bullet -}$) by catalyzing the following reaction:

$$2\,O_2^{\bullet -} + 2\,H^{+} \longrightarrow O_2 + H_2O_2$$

The resulting hydrogen peroxide, is then removed by other enzymes.[50] Dismutation of $O_2^{\bullet -}$ proceeds *via* the following two half-reactions, in which the enzymes Cu cycles between the Cu^{2+} and Cu^{+} oxidation states:

$$Cu^{2+}ZnSOD + O_2^{\bullet -} \longrightarrow Cu^{+}ZnSOD + O_2$$
$$Cu^{+}ZnSOD + O_2^{\bullet -} + 2\,H^{+} \longrightarrow Cu^{2+}ZnSOD + H_2O_2$$

The location of the two metals and their coordination are illustrated in Figure 1.

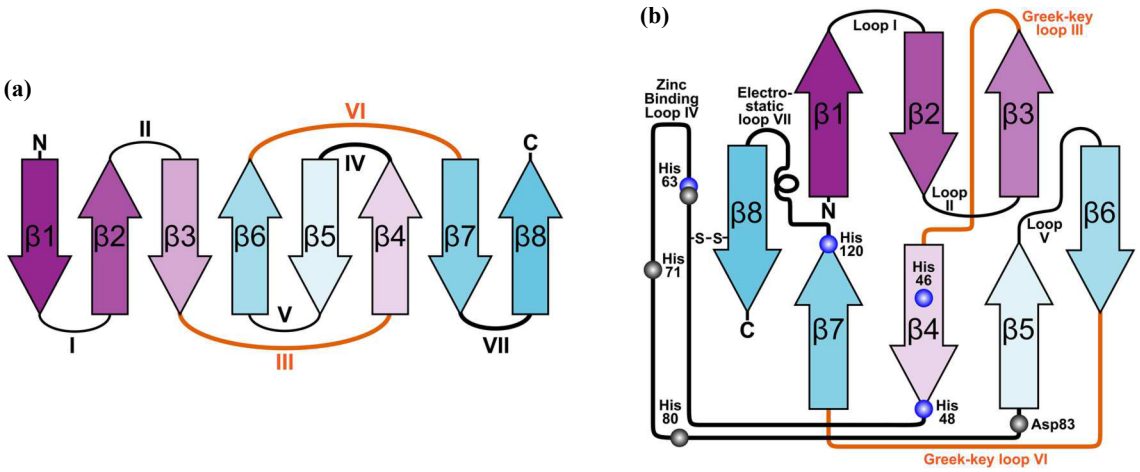

Figure 2: Arrangement and connectivity of loops and β-strands of human monomeric SOD1. **(a):** Order of the eight β-strands of the barrel and the loops connecting them. The pattern that emerges by insertion of β6 and β5 between β3 and β4 is often referred to as a Greek-key arrangement. **(b):** Schematic representation of SOD1 illustrating the position of metal binding amino acids and the intrasubunit disulfide bond. Adapted from Wright *et al.*, Q. Rev. Biophys., 2019, licensed under CC BY 4.0.[35]

Human SOD1 is a homodimeric enzyme with a mass of 16 kDa per monomer or subunit. Due to post-translational cleavage of the start methionine SOD1 has historically been described as a 153 amino acid (AA) protein, with a corresponding amino acid numbering convention.[12] To maintain consistency with past literature, numbering in this work will follow the historic convention. The two conformationally identical subunits are each characterized by an eight-stranded anti-parallel β-barrel. The arrangement of these β-strands in relation to their order in the protein's amino acid sequence is often referred to as a Greek-key arrangement, as highlighted in Figure 2a.[35] Each subunit contains two free cysteines (Cys6 and Cys111), one intramolecular disulfide bond (Cys57-Cys146) and a Zn and a Cu binding-site.[49] The two metals in close proximity and in the oxidized Cu^{2+} state are bridged by the imidazole of His63, as highlighted in Figure 1c. Named after their function, loop IV (residue 49-83) is termed the Zn-binding loop and loop VII (residues 121-142) is termed the electrostatic loop.[49] The Zn-binding loop (IV) contains the four Zn coordinating residues (His63, His71, His80, Asp83). Furthermore, it is of great importance to SOD1's stability, as it also contains Cys146, binding to Cys57 of β-strand 8, copper coordinating His48, Cu-Zn-bridging His63 and Gyl51, which is involved in dimer interface H-bonds, as shown in Figure 4.[35] The electrostatic loop provides a positively charged environment guiding the superoxide substrate into the active site channel and towards the catalytic copper center.[35,50,51] This effect strongly contributes to the enzyme's activity. SOD1 achieves an almost diffusion-limited rate constant of about $2 \cdot 10^9$ $M^{-1}s^{-1}$ and therefore about 10^4 $M^{-1}s^{-1}$ times the rate constant of spontaneous superoxide dismutation.[50,51] While the catalytic reaction takes place at the Cu, it was demonstrated that Zn is similarly essential for catalytic activity, as it influences the coordination and redox potential of the nearby Cu.[52] Similarly, the dimeric state of SOD1 has been demonstrated as an elemental component of its activity.[53]

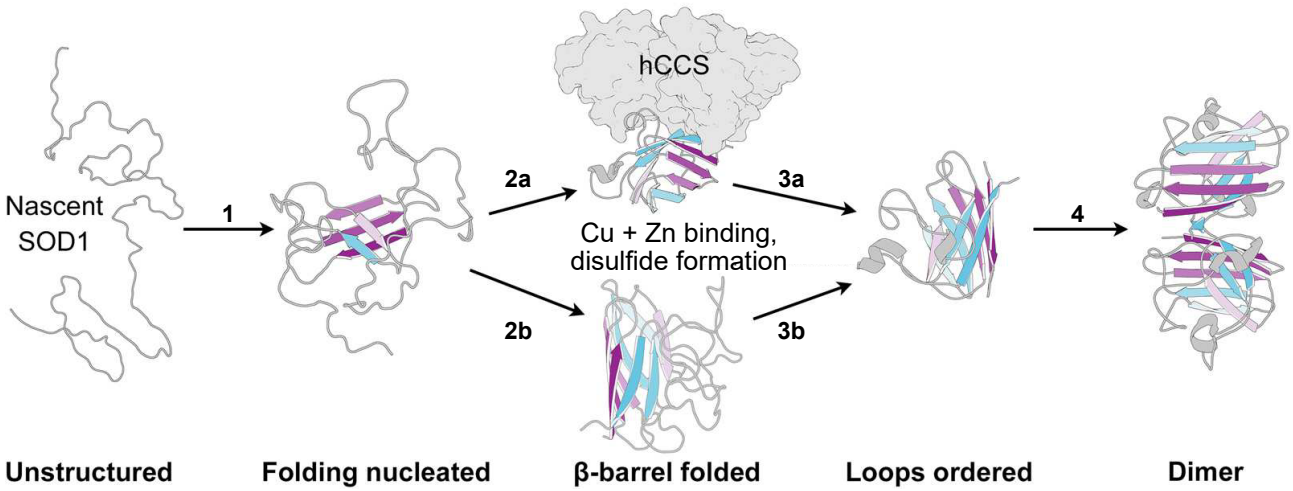

Figure 3: Currently accepted pathway of SOD1 maturation. **1:** Hydrophobic side chain interactions nucleate folding of the β-barrel. **2a, 3a:** Human copper chaperone for SOD1 (hCCS) dependent route. Under assistance of the hCCS, β-barrel folding is completed, Cu is bound and the disulfide bond established, thereby ordering the loops. Zn binding takes place independently before or after interaction of SOD1 and hCCS.[49] **2b, 3b:** hCCS independent route. β-Barrel folding, Zn and Cu binding and disulfide formation can also occur independent of hCCS.[49] **4:** Dimer association. Adapted from Wright *et al.*, Q. Rev. Biophys., 2019, licensed under CC BY 4.0.[35]

Although the entire maturation process of human SOD1 is complex and currently incompletely described,[39] an accepted model of the pathway is illustrated in Figure 3.[35] Following translation, hydrophobic interaction of AAs on β-strands 1, 2, 3, 4 and 7 initiate folding of nascent SOD1. Completion of β-barrel folding then proceeds either mediated by human copper chaperone for SOD1 (hCCS) or by independent pathways, illustrated as 2a, 3a and 2b, 3b in Figure 3.[35] Given that both Cu and Zn concentrations are tightly regulated in cells, Cu and Zn acquisition likely proceed *via* chaperone mediated pathways.[35,39] Since the discovery of the human copper chaperone for SOD1 hCCS, its involvement in Cu binding, Zn binding and disulfide formation have been studied extensively, but hCCS independent pathways have similarly been described.[35,39,49] Metal binding and disulfide bond formation results in an increased conformational order of the loops.[35] While Zn binding and disulfide bond formation are typically considered to add the largest stabilizing effect, Cu binding is also important, as it majorly contributes to the kinetic stability of the protein.[39] Each maturation step, from nascent SOD1 towards the monomeric (Cu|Zn) hSOD1$^{S\text{-}S}$ state subsequently increases its dimer affinity. Dimerization takes place through hydrophobic interactions involving the following regions of both monomers: β-strands 1 and 8, loop VI, parts of loop IV (Zn-binding loop) and the C-terminus. Gly51 and Gly114 of one monomer form hydrogen bonds with Ile151 of the other monomer, as shown in Figure 4. It is important to note, that while Figure 3 shows a likely sequence given the current evidence, these maturation steps don't necessarily have to proceed in this exact order. While less stable than fully mature SOD1, shortcomings in metal binding or disulfide formation, still result in relatively stable SOD1 species. Given the right conditions, these can be converted into fully mature SOD1, even in the absence of hCCS.[35,49,50]

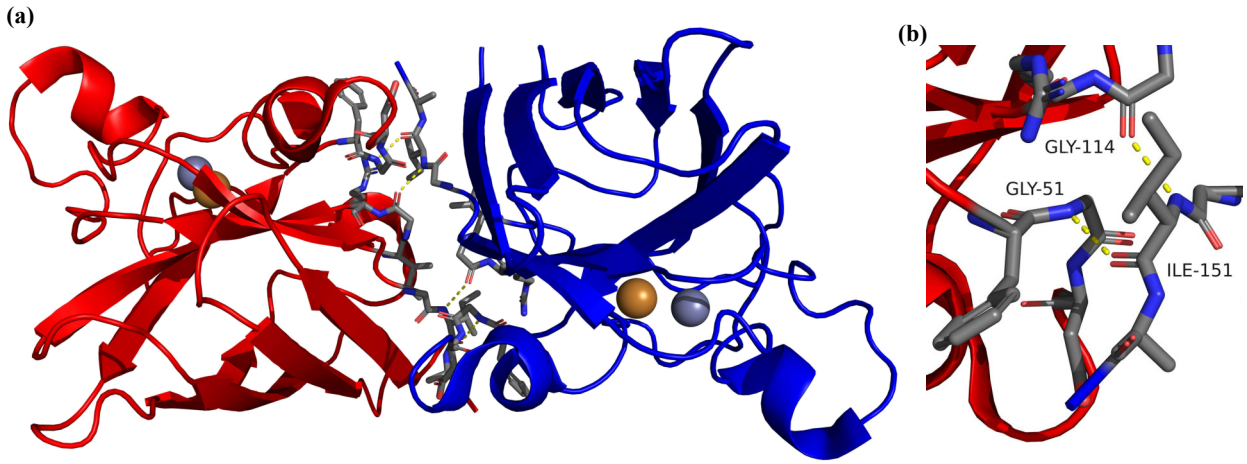

Figure 4: Dimer interface of human SOD1. Monomer A is shown in red and monomer F is shown in blue. **(a):** Dimer interface of human SOD1. Residues 49–51, 113–115 and 150–151 of each subunit are shown as sticks. Hydrogen bonds between Gly51, Gly114 of one monomer and Ile151 of the other monomer are shown as yellow dotted lines. **(b):** Hydrogen bonds between Gly51 and Gly114 of monomer A with Ile151 of monomer F. An X-ray crystal structure (PDB: 2c9u[45]) of wt hSOD1 was used.

Fully matured, dimeric holo (Cu|Zn) $SOD1^{S\text{-}S}$ is incredibly stable. Melting points of 85–95°C have been reported and its enzymatic activity is retained even in the presence of harsh conditions, such as 8 M urea or 4 M guanidine hydrochloride.[39] The existence of a disulfide bond is an uncommon feature for a protein localized in the reducing environment of the cytosol and the demonstrated stability of SOD1 under these conditions highlights its stability.[54] Each of its modifications during maturation, namely disulfide formation, Zn binding, Cu binding and the association into a dimer adds to its stability. While the individual contributions of each modification have been investigated at length, it is their synergistic effect that ultimately affords what is often quoted as one of the most stable proteins we know.[35,39,50]

2.2 Mutations of SOD1 Promote Aggregation

Mutations in SOD1, predominantly single amino acid substitutions, were found in just about every of its domains and while they were shown to decrease the melting temperature of its mature state, the degree of destabilization was often insufficient to explain the resulting ALS pathology. For most mutations the reduction was only moderate and there was generally no clear correlation between melting temperature and disease duration or severity. It indicated that the reduced stability of mature mutant SOD1 would not provide a comprehensive explanation of SOD1-ALS.[35,39] Considering not only the final, mature state, but the maturation process (Figure 3) as a whole, multiple intermediates with reduced stability are observed. Notably, Furukawa and O'Halloran reported that the melting temperature of apo (E|E) wt hSOD1^{2SH} (42.9±0.2°C) lies only a few degrees above physiological temperature (~37°C) and exists primarily in the monomeric state.[55] It is therefore conceivable that introduction of single amino acid substitutions or aberrant post-translational modifications (PTMs) occurring over time may further decrease the stability of certain intermediates, disturbing their maturation, rendering them toxic or aggregation prone.[39]

Numerous mutations of SOD1 in ALS patients were discovered over the years and have traditionally been sorted into groups, depending on the location of their mutation. These groups include: metal binding region, dimer interface, β-barrel or wild type like, among others.[35,39] The underlying assumption was, that disturbance of a certain aspect of the protein's stability or function would result in one of multiple distinct pathological pathways. Similar destabilization effects were often demonstrated within a group, but effects typically associated within one group would often also be found amongst members of other groups, indicating that all of these aspects were connected.[35,39] While specific SOD1 mutations lead to corresponding, rationalizable destabilization of *e.g.* metal binding, disulfide state or the dimer interface interactions to varying degrees, more importantly, they result in a global destabilization of SOD1.[35,39] This makes mutant SOD1 more susceptible to further destabilization by disulfide reduction, dissociation into monomers, unfolding or aberrant modifications, which ultimately contributes to its ALS related aggregation.[35,39] The term "framework destabilization" was coined by DiDonato *et al.* for this effect.[46] ALS related SOD1 mutations therefore directly or indirectly interfere with one or more of its maturation steps or disturb one or more factors related to the stability of its fully mature state.[35] Analogous, to the discussed maturation pathway (Figure 3), destabilization events do not necessarily have to proceed in a specific order. As there is generally an interconversion between different SOD1 states and their modifications, there is most likely not one specific state that provides a therapeutic target.[35,39]

The A4V mutation, represents the most frequently observed ALS SOD1 mutation in north America[13,56] and is currently the only variant associated with a consistently fast disease progression.[29] It was one of the first discovered SOD1 mutations, has been extensively characterized since and is widely established for *in vitro* studies of SOD1 aggregation.[35,39] Notably, mouse models carrying the SOD1 A4V variant only develop ALS if wt SOD1 is also expressed and show a disease onset very late in their lifetime.[57,58] This makes this particular mouse model an unsuitable comparison to humans, as the A4V mutation is characterized by an earlier onset and more rapid disease progression in human patients when compared to other SOD1 variants.[59,60] The widely established G93A mouse model has been found to display a much better resemblance of human ALS disease progression.

2.3 Challenges in the Development of Pharmaceutical Agents for ALS Treatment

The research on ALS drugs in general has been slow and largely unsuccessful. The development of therapeutic agents for ALS has been complicated by the various underlying mechanisms of ALS pathology and the resulting variety of phenotypes.[61] Research on neurodegenerative diseases (NDDs) has traditionally suffered from a lack of suitable disease models, which has caused >90% of clinical trials in NDDs to end unsuccessfully.[62]

While mouse models of mutant SOD1-ALS were first developed in the early 1990s, their validity was questioned, when treatments developed in SOD1 mice failed in clinical trials on human patients.[63] TDP-43 mouse models have only been around since the early 2010s and their development was more challenging, compared to SOD1 mice.[57,64] In recent years it has become apparent, that SOD1-ALS resembles a subtype of ALS and that treatments developed on SOD1 mice may therefore be of limited applicability to non-SOD1-ALS patients.[64] In addition to mouse models, a number of ALS cell models have been developed in recent years, as reviewed by Zhou *et al.*.[65]

The following sections will highlight some therapeutic strategies that have been pursued in the context of small molecules. A number of compounds that recently went through phase II or III clinical trials will be highlighted. ClinicalTrials.gov IDs[66] are provided for discussed clinical trials. A number of extensive reviews on small molecules in recent development for treatment of ALS have been published, which go beyond the examples highlighted here.[37,62,67–70]

2.4 Inhibition of SOD1 Expression as a Therapeutic Strategy

A gain of toxic function, rather than a loss of function is the current consensus for SOD1 related ALS and early ALS mouse models have shown that knock-out of SOD1 does not lead to an ALS pathology.[71,72] A number of SOD1 mutants are associated with reduced activity, but no correlation between SOD1 activity and disease severity was observed.[73] Most SOD1 mutants cause ALS in heterozygous carriers, which provided mutant SOD1 could be knocked out selectively, leaves these patients with one allele of wt SOD1.[35,39] All these factors lead to the proposal that lowering SOD1 expression levels could provide a therapeutic benefit.[73]

2.4.1 Pyrimethamine

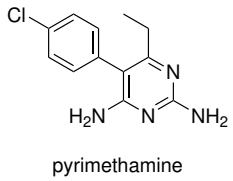

Figure 5: Chemical structure of pyrimethamine.

Pyrimethamine, an FDA approved medication used for the treatment of malaria and toxoplasmosis,[74] has been reported to reduce SOD1 levels in cerebrospinal fluid (CSF) and lymphocytes of ALS patients,[75,76] as well as in hSOD1 G93A transgenic mice.[74] The precise mechanism behind this effect is currently unknown, but pyrimethamine is suspected to act at the post-transcriptional level, since no decrease in SOD1 mRNA has been observed.[76] The effect of pyrimethamine on SOD1 levels has been questioned however.[77] It is important to note, that the two groups that reported theses contradictory findings examined different tissues, cell lines or animal models and used different methodologies in their respective studies, limiting the comparability between their results. Regardless, in order to investigate if pyrimethamine interacts with hSOD1 directly, possibly reducing its aggregation, it was included in biophysical experiments as discussed in Section 5.7.

2.4.2 Antisense Oligonucleotides

Antisense oligonucleotides (ASOs) are short (about 12–25 nucleotides), single- or double-stranded chemically modified oligonucleotides, which are used to sequence specifically target mRNA *via* Watson-Crick base pairing.[78,79] By design, they may target pre-mRNA or mRNA and depending on their mode of action can be used to induce specific subsequent effects. Figure 6 shows the different classes of ASOs and their mode of action.[79]

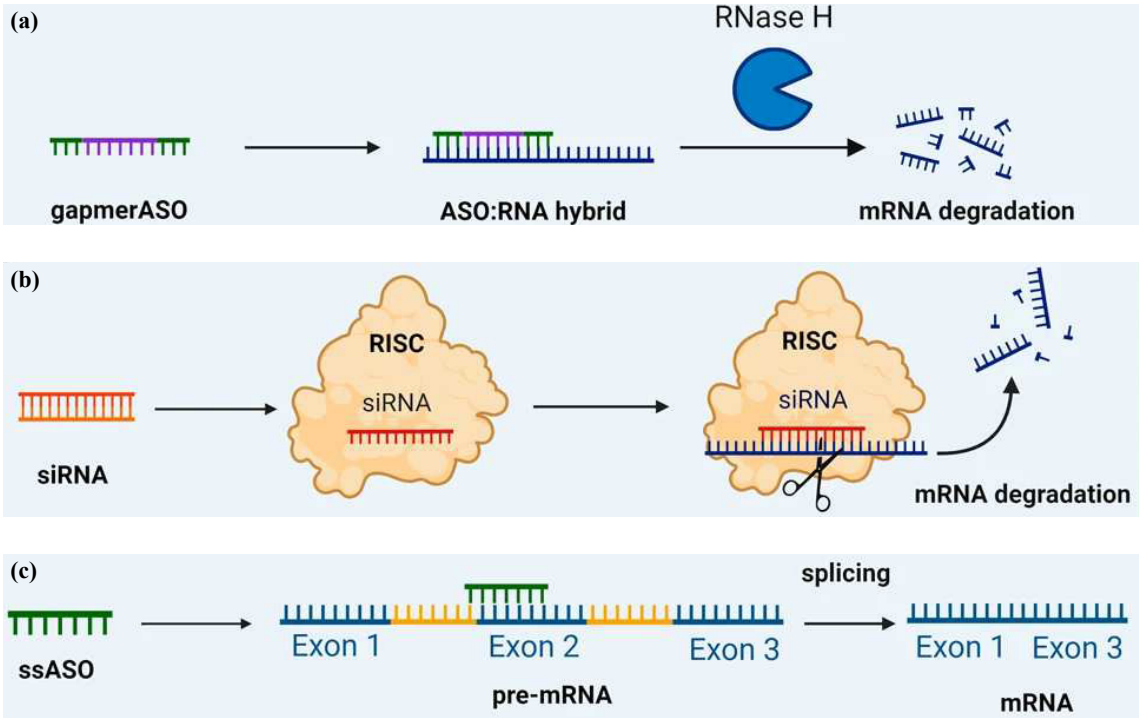

Figure 6: Classes of antisense oligonucleotides (ASOs) and their mode of action. **(a):** gapmerASOs lead to degeneration of target mRNA through recruitment of RNase H. The DNA core of the gapmerASO is shown in purple and the RNA segments are shown in green. **(b):** siRNAs lead to degeneration of target mRNA through incorporation in RISC. **(c):** ssAOSs lead to alternate splicing of target pre-mRNA. In this example ssAOS binding results in skipping of exon 2, effectively removing it from the following mRNA. Exons are shown in blue, introns are shown in yellow. Adapted from Lauffer *et al.*, Commun. Med., 2024, licensed under CC BY 4.0.[79]

GapmerASOs are single-stranded constructs of a DNA center framed with RNA at both ends. They bind to their target mRNA, creating a DNA:RNA hybrid (Figure 6 a). RNase H recognizes these DNA:RNA hybrids and degrades them. GapmerASOs therefore lead to the degradation of their target mRNA. This mode of action is typically used to down regulate the expression of a specific disease related protein.[79] The recently FDA and EMA approved tofersen (Section 2.7.3), used in the treatment of SOD1 related ALS belongs to this class of ASOs.

Small interfering RNAs (siRNAs) are double-stranded RNAs that naturally occur in cells as part of the RNA interference (RNAi) pathway, which regulates gene expression.[80,81] Similarly, siRNA can be rationally designed as a therapeutic agent acting *via* this pathway (Figure 6 b). The two strands of the siRNA are separated by the RNA-induced silencing complex (RISC), the sense strand is degraded while the antisense strand is retained by the complex. RISC then recognizes the complementary target mRNA and degrades it. Therefore, siRNAs can be used to down-regulate the expression of a specific disease related protein.[79]

The choice between gapmerASOs and siRNAs is typically a trade-off between multiple factors. Generally, siRNAs more efficiently down regulate a target protein, but gapmerASOs have a lower mismatch tolerance, making them more target specific and their delivery to the target tissue is generally simpler compared to that of the double-stranded siRNAs.[79]

Splice-switching ASOs (ssASOs) are single-stranded ASOs designed to bind target pre-mRNA, blocking and therefore effectively masking a specific pre-mRNA section from the cells slice apparatus (Figure 6 c). ssASOs can be designed to block splice-regulatory elements, which depending on the nature of the targeted splice-regulatory element result in for example in the skipping or inclusion of a specific exon. Commonly, ssASOs are used to disrupt or restore open reading frames leading to the up or down regulation of a target protein.[79]

Beyond the examples discussed here, ASOs can be used for numerous applications, which have extensively been reviewed elsewhere.[78,79,82] A comprehensive review (as of 2024) about ASOs in development against ALS was published by Van Daele *et al.*.[83]

In summary, ASOs represent a class of pharmaceutical agents, that were only developed in recent decades and are especially relevant to the modern paradigm of personalized medicine. ASOs allow for direct modulation of the cells regulatory mechanisms and the fact that their sequence can be adapted to genetic variations of specific diseases and patients highlights their therapeutic potential.[78,79,82]

2.5 Stabilization of the SOD1 Dimer as a Therapeutic Strategy

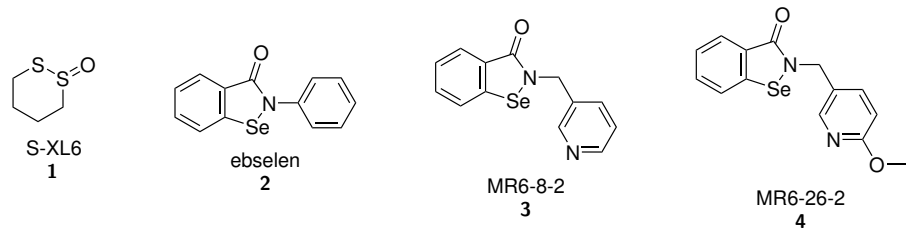

Figure 7: Chemical structures of S-XL6 **1**, ebselen **2** and the ebselen derivatives MR6-8-2 **3** and MR6-26-2 **4**.

Seminal work by Ray *el al.* in 2004 demonstrated that covalently linking the two SOD1 subunits effectively prevented its aggregation. This was achieved through the introduction of a V148C mutation on both subunits and the resulting intersubunit disulfide bond stabilized the aggregation prone A4V mutant.[84] Ray and Lansbury therefore proposed that stabilization of the SOD1 dimer provided a promising therapeutic strategy.[85] Following publications by Ray, Lansbury *et al.* reported that the cavity around Val148 at the dimer interface could provide a binding site for small molecule ligands.[86,87] Later publications by other investigators however demonstrated, that the compounds developed by Ray, Lansbury *et al.* did not bind into the Val148 cavity as had been intended.[69,88,89]

Other studies investigated dimer stabilization by covalently linking SOD1 via small molecule linkers. The two solvent exposed Cys111 residues of both SOD1 subunits provide a target for this approach, as they face each other and are only ~9 Å apart.[90–92] The most recent publication following this approach by Hossain *et al.* in 2024 reported SOD1 dimer stabilization S-XL6 **1**,[92] shown in Figure 7. Covalently linking the subunits was however shown to cause aberrant interactions with the hCCS.[93]

Another strategy still revolved around binding onto Cys111, without covalently linking both subunits. In 2012 Banci *et al.* reported cisplatin to covalently bind the Cys111 residue of mutant SOD1 and stabilize the dimer by non-covalent interaction between the two subunits. While cisplatin could bind onto Cys111 of either subunit, it was observed that the available space between them only allowed one cisplatin molecule in total. Cisplatin was even shown to be able to dissolve preformed insoluble aggregates of mutant SOD1 in a cell model.[94,95] However, cisplatin also disrupted SOD1-hSCC interaction[93] and because of its hepatotoxicity, suggesting off-target binding, may not provide a suitable therapeutic compound.[92]

A different series of publications investigated ebselen **2** and a number of derivatives.[96–99] It was shown that the two Cys111 bind one ebselen each, which then stabilized the dimer by π-π-interactions. Importantly, it did not prevent SOD1 hCCS hetero dimer formation.[96] The most recent publication of this approach was by Watanabe *et al.* in 2024 investigating the ebselen derivatives MR6-8-2 **3** and MR6-26-2 **4**, shown in Figure 7

The recent years have shown a growing research interest in the aim of assisting SOD1 maturation, placing an emphasis on stabilizing immature SOD1 states.[35] However, the stabilization of mature dimeric SOD1 by small molecules is still regarded a valuable asset in the development of therapeutic agents, as highlighted by the recent 2024 publications by Watanabe *et al.* and Hossain *et al.*.[26,92,99]

2.6 Removal of Protein Aggregates as a Therapeutic Strategy

As discussed in Section 1.2 cells natively have the ability to remove protein aggregates. The enhancement of autophagy has therefore been explored for ALS treatment.[42,69,100] A couple of recent literature examples shall be discussed in the following sections.

2.6.1 Trehalose

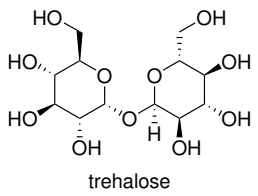

Figure 8: Chemical structure of trehalose.

The disaccharide trehalose is generally regarded to display chaperone-like effects on proteins and its use as a protein stabilizing agent has been documented for a number of protein examples,[101,102] including preparations of yeast SOD1.[103] In the context of ALS, trehalose has been reported to protect against SOD1 related pathology in ALS cell models.[104,105] A reduction of hSOD1 levels and a delaying effect on disease onset and progression has further been reported in transgenic hSOD1 mouse models.[106,107] The precise mode of action in these specific ALS models was reported to be unclear, but a beneficial effect on cell autophagy appeared most likely.[106,107] Its function as an autophagy inducer has been documented in other publications supporting this hypothesis.[108] In order to investigate if trehalose could prevent hSOD1 aggregation by directly interacting with the protein in isolation or if the effects reported *in vivo* are due to a mode of action unspecific to hSOD1, it was included in biophysical experiments, detailed in Section 5.7.

2.6.2 Sodium Phenylbutyrate and Tauroursodeoxycholic Acid

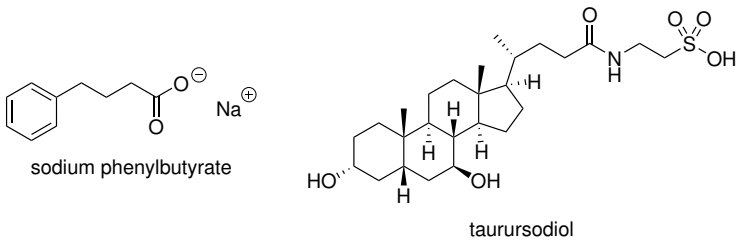

Figure 9: Chemical structure of sodium phenylbutyrate (NaPB) and tauroursodeoxycholic acid (TUDCA) often shortened to taurursodiol. Their fixed combination as under investigation in clinical trials is referred to as AMX0035.

Tauroursodeoxycholic acid (TUDCA) is a bile acid synthesized in the liver, able to cross the blood-brain barrier.[109,110] TUDCA is reported to be a potent inhibitor of apoptosis able to reduce endoplasmic reticulum (ER) stress and to stabilize cells unfolded protein response through interacting with a number of molecular targets.[111] A study on hSOD1 G93A mice with a focus on the sensitivity of motor neurons to ER stress showed that TUDCA had a moderate effect on cell survival, completely restored neurite outgrowth and displayed a moderate but statistically significant increase in motor neuron junction (MNJ) innervation in hSOD1 G93A mice treated with TUDCA compared to vehicle-treated animals.[109] TUDCA and phenylbutyric acid both act as chemical chaperones against unfolded or aggregating proteins.[112,113]

A pilot phase II clinical trial (NCT00877604) reported by Elia *et al.* showed that TUDCA was well tolerated and able to slow down disease progression. This effect was observed to be additional to that of riluzole (Section 2.7.1) treatment.[114] Another phase III trial (NCT03800524) as well as an open-label extension (NCT05753852) were performed by the TUDCA-ALS consortium.[115] However the trial did not meet its primary endpoints and no significant differences were observed across secondary endpoints.[116] The press statement reporting the trials outcome is no longer available online, but was archived by the motor neurone disease association.[116]

A fixed combination of a 2:1 ratio of sodium phenylbutyrate:taurursodiol (3 g of sodium phenylbutyrate and 1 g of taurursodiol) named AMX0035 developed by the American company Amylyx Pharmaceuticals was investigated in multiple clinical trials. The phase II/III CENTAUR trial (NCT03127514) investigated safety, tolerability, efficacy and activity of AMX0035 and while treatment successfully slowed disease progression measured by ALSFRS-R total score over a period of 24 weeks, changes in secondary outcomes as defined in the study were insignificant between placebo and treatment groups.[117] Despite the weak evidence for the drugs effectiveness, it was approved by the FDA in 2022. In contrast, marketing authorisation was refused by the EMA in 2023 (EMEA/H/C/005901). An open label extension study CENTAUR-OLE (NCT05619783) was conducted which supported the findings of the earlier CENTAUR trial.[118–121] Amylyx Pharmaceuticals carried out another trials under the name of PHOENIX (NCT05021536), as well as an accompanying open label extension study (NCT05619783). The PHOENIX trial however did not meet significance in its primary or secondary endpoints and Amylyx voluntarily withdrew AMX0035 from the market in 2024.[122,123]

An in-depth review about the highlighted trials, their results, as well as discrepancies between the trial designs and their reported outcomes between the ClinicalTrials.gov repository and the corresponding scientific publications was published by Lo Giudice *et al.*.[110] Moreover, it remains unclear if addition of sodium phenylbutyrate to a treatment of tauroursodeoxycholic acid has any effect, positive or negative.[110]

2.6.3 Masitinib

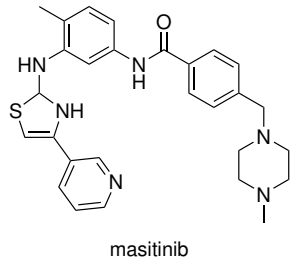

Figure 10: Chemical structure of masitinib.

The tyrosine kinase inhibitor masitinib was shown to have a protective effect when delivered post-paralysis in SOD1 G93A rats prolonging their survival.[124] The French pharmaceutical company AB Science then conducted a phase 2/3 clinical trial (AB10015 / NCT02588677) investigating efficacy and safety of masitinib in combination with riluzole in ALS patients. The trial concluded in 2018 and prolonged survival was reported in a subgroup of patients with mild or moderate disease severity at baseline, indicating that a combination of masitinib and riluzole could be a promising treatment option.[125,126] However, marketing authorisation for masitinib under the trade name Alsitek was refused by the EMA in 2018 (EMA/207380/2018 Rev. 2) and their decision confirmed again in 2024 (EMA/472277/2024), criticizing how the study was conducted, how patients were classified and concluding that the benefits of masitinib could not be convincingly demonstrated. A follow up phase 3 study (AB19001 / NCT03127267) was conducted by AB Science. Consistent with the previous trial, it was reported that for a subgroup of ALS patients with mild or moderate disease severity at baseline, treatment with masitinib as an add-on to riluzole prolonged survival by 25 months, in comparison to treatment with riluzole alone, whereas no long-term survival advantage was observed for the overall masitinib cohort.[127] There has currently not been an application for approval of masitinib by the FDA.

2.6.4 NU-9

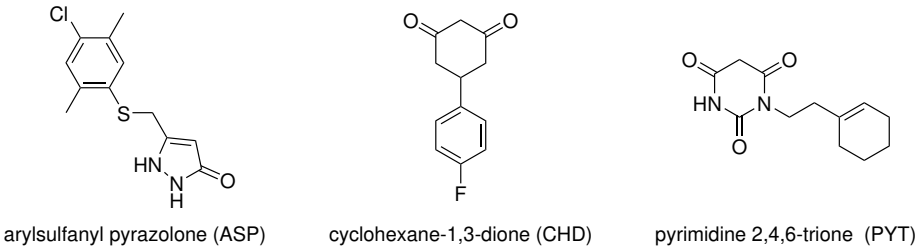

arylsulfanyl pyrazolone (ASP) cyclohexane-1,3-dione (CHD) pyrimidine 2,4,6-trione (PYT)

Figure 11: Representative example for the three lead structures discovered by Benmohamed *et al.*.[128]

In 2010 Benmohamed *et al.*[128] developed a high throughput screening assay based on PC12 cells expressing G93A-SOD1-YFP developed by Matsumoto *et al.*.[129] In their screening assay, Benmohamed *et al.*[128] promoted SOD1 aggregation by addition of the proteasome inhibitor MG132, leading to cell toxicity and observable aggregate formation. In this screening, they discovered three compound classes, shown in Figure 11. These compound classes were further developed in subsequent publications by multiple groups of the Northwestern University (Illinois, USA): arylsulfanyl pyrazolone (ASP),[130–134] cyclohexane-1,3-dione (CHD),[28,135–138] pyrimidine 2,4,6-trione (PYT).[139–141]

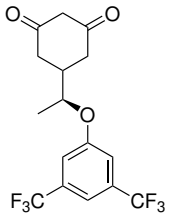

NU-9

Figure 12: Chemical structure of NU-9.[136]

One promising candidate from the cyclohexane-1,3-dione (CHD) compound family is NU-9 shown in Figure 12, first reported in 2012 by Zhang *et al.*[135] as a racemic mixture, denoted as 73 in that publication.[135] The enantiopure form was further investigated in a following publication.[136]

In 2021 Genc *et al.*[137] reported that NU-9 was able to improve the structural integrity of mitochondria and the ER of UMNs in both hSOD1^{G93A}-UCHL1-eGFP mice and prpTDP-43^{A315T}-UCHL1-eGFP mice as well as improve integrity of apical dendrites in both mouse models. The protective effect was limited to UMNs as NU-9 treatment was found to have no effect on the degeneration of lower motor neurons (LMNs). The authors highlight the importance of differentiating between upper and lower MNs as they develop, act and react in very different ways.[137]

In 2022 Genc *et al.*[28] report that NU-9 has a positive effect on upper motor neurons (UMNs). When administered to hSOD1^{G93A}-UCHL1-eGFP mice, UMNs grow longer axons and display enhanced branching and arborization, both parameters to assess cellular response and health of UMNs. Moreover, while riluzole and edaravone also show this effect, it is more pronounced for NU-9 and administration of NU-9 in combination with either riluzole or edaravone was shown to have an additive positive effect.[28]

Importantly, Johnson *et al.*[138] recently reported that in addition to its implication as an ALS treatment, NU-9 prevents the accumulation of amyloid beta oligomers (AβOs) which play a pivotal role in Alzheimer's Disease (AD). They investigated the underlying mode of action in detail and report that rather than interacting with Aβ or AβOs directly, NU-9 acts by a mechanism that is intracellular, and lysosome- and cathepsin B-dependent. The authors hypothesize that NU-9 restores the trafficking of Aβ species to active lysosomes, where formation of cell-binding AβOs can be blocked by cathepsin B. While not fully understood, a number of potential specific mechanisms and targets are presented.[138] They further reason that interaction of NU-9 with the trafficking of Aβ could provide a valuable asset in treating neurodegenerative diseases more generally, as evidence both in cell culture and *in vivo* exists for the internalization to endosomes and subsequent cell–cell spreading of Aβ, tau, α-syneuclein, SOD1, and TDP-43 which supports the possibility of a shared mechanism involving endolysosomal trafficking in both AD and ALS.[142–144]

2.7 Currently Approved Drugs for the Treatment of ALS

In the following sections, currently approved medications for the treatment of ALS will be discussed. The discussions about approval decisions will be limited to the United States Food and Drug Administration (FDA) and the European Union's European Medicines Agency (EMA).

2.7.1 Riluzole

Figure 13: Chemical structure of riluzole.

Riluzole was the first drug for treatment of ALS approved by the FDA in 1995[145] and by the EMA in 1996 (EMEA/H/C/000109). Riluzole was long thought to have an inhibitory effect on glutamate release,[146] but newer evidence suggests that this effect plays a limited role and requires higher concentrations, not achieved in human patients.[61] Instead, the molecular effects of riluzole are highly complex, including effects on the persistent Na^+ current, potentiation of Ca^{2+} dependent K^+ currents and presynaptic reduction of neurotransmitter release. Most of these effects seem to be concentration dependent.[61,147] A detailed review on the mechanism of action of riluzole presenting evidence up until 2011 was published by Bellingham.[147] Original analyses and subsequent meta-analyses of clinical trial data are often quoted, exclaiming that riluzole typically extends survival in ALS patients by 2-–3 months. Conversely, analysis of real world evidence from 10 clinical ALS databases, published by Hinchcliffe and Smith indicated that riluzole may offer significantly longer enhancement of median survival by up to 19 months.[148]

2.7.2 Edaravone

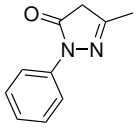

edaravone

Figure 14: Chemical structure of edaravone.

Initially developed under the name MCI-186 for the treatment of stroke by the Japanese Mitsubishi Tanabe Pharma Corporation (MTPC), edaravone was designed as a radical scavenger eliminating lipid peroxide and hydroxyl radicals, reducing oxidative stress and neuroinflammatory response.[42,61] A short history of its development was presented in the review by Watanabe *et al.*.[149] Edaravone, as intravenous infusion under the brand name Radicava was approved for the treatment of ALS by the FDA in 2017.[42,145] However, since multiple previous clinical trials had failed and only a short term benefit, for a subgroup of patients in the early stage of the disease, had been demonstrated, approval was not granted by the EMA.[150] In response MTPC withdrew its application for a marketing authorisation with the EMA in 2019. A detailed account evaluating the previous clinical trials and their evidence was provided by the EMA's withdrawal assessment report (EMA/CHMP/290284/2019). An orally administered suspension of edaravone (brand name Radicava ORS) was approved by the FDA in 2022.[151] A different oral formulation of edaravone under the name FAB122 by the Spanish pharmaceutical company Ferrer was evaluated in the ADORE clinical trial (NCT05178810), which at its completion in 2024 concluded that there was no clinical benefit to patients.[152] The accompanying open-label extension trial ADOREXT (NCT05866926) was thereupon terminated.[152]

2.7.3 Tofersen

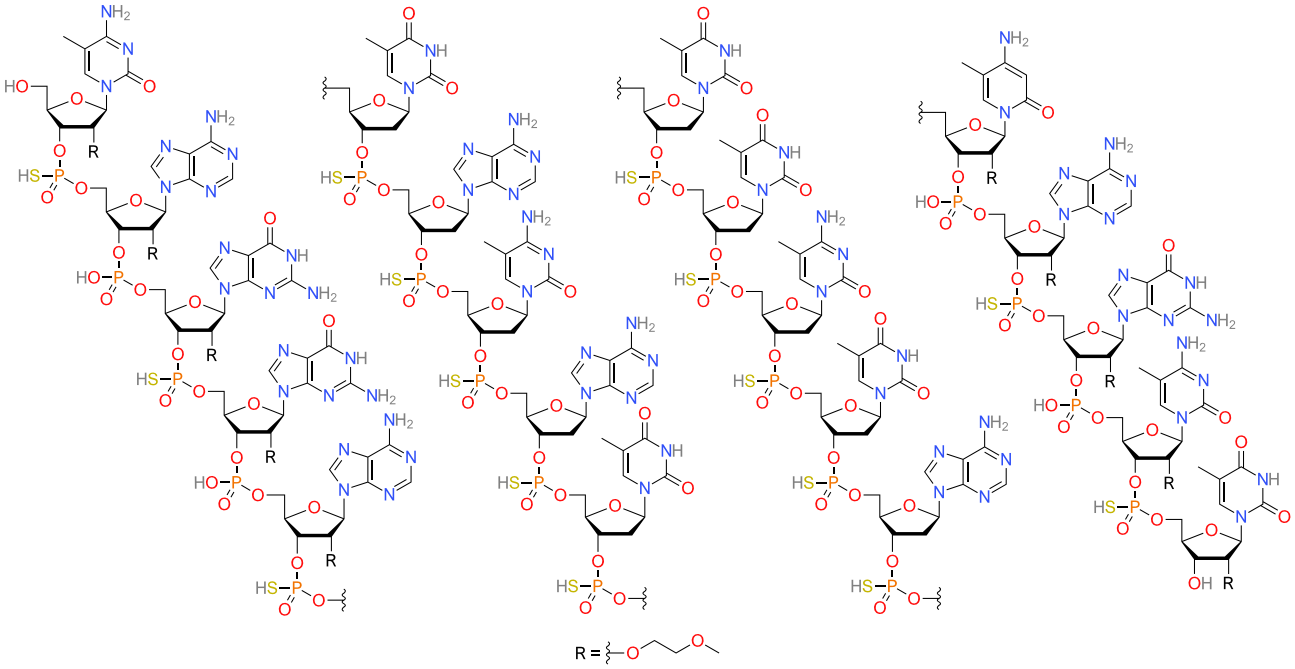

Figure 15: Chemical Structure of tofersen.[153]

Tofersen is an antisense oligonucleotide (ASO) with a length of 20 nucleotides, as shown in Figure 15. As discussed in 2.4.2, tofersen can be categorized as a gapmerASO. Accordingly, its structure contains a central segment of 10 DNAs flanked by 5 RNAs on each side. In regards to ASO typical chemical modifications, its backbone of 19 phosphates bears 15 phosphorothioate modifications, all 10 flanking ribose units bear 2'-*O*-methoxyethyl modifications and its cytosine and uracil bases are methylated at their 5'-positions.[153] In 2006, Smith *et al.* reported that administration of an SOD1 mRNA targeting gapmerASOs in transgenic SOD1 G93A rats successfully extended disease duration after onset, providing a proof of concept of ASOs in ALS.[154] Advancements in the field of ASOs over the following years lead to the development of tofersen, a more potent gapmerASO as reported by McCampbell *el at.* in 2018.[73] Tofersen proceeded into a phase 1-2 clinical trial (NCT02623699, Part A, B) were it was deemed safe.[155] Related to this development, the group determined the half-live of the SOD1 protein in human cerebral spinal fluid CSF to be approximately 25±7 days.[156] Phase 3 of this trial (NCT02623699. Part C) did not meet its primary goal of significantly slowing disease progression, measured by ALSFRS-R score over 28 weeks. The trials secondary goals defined by lowering of SOD1 concentration in CSF and neurofilament light chain (NfL) concentration in plasma, compared to placebo were met over 28 weeks. The subsequent open label extension, which prolonged the treatment to 56 weeks then showed significant therapeutic benefits measured by ALSFRS-R score as published in 2022.[157] Very limited real world data obtained since then, seems to support a therapeutic benefits of tofersen.[158] Nevertheless, tofersen was approved under the accelerated approval pathway by the FDA in 2023[83] and received marketing authorisation under exceptional circumstances by the EMA in 2024 (EMEA/H/C/005493).

2.8 Previous Work by the Thomas Group

Mrđen Debono initially investigated small molecule ligands for the stabilization of the hSOD1 dimer in her PhD thesis.[159] The investigation was thereafter furthered in the author's master's thesis.[48] As these two studies provide the foundation for this work, important developments shall be discussed briefly.

2.8.1 Lead Structure and Molecular Docking Experiments

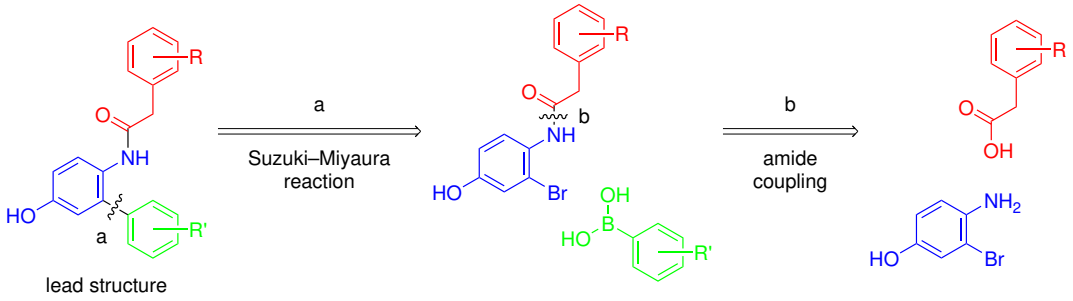

Scheme 1: Retrosynthetic analysis of the ligands lead structure. A number of different carboxylic acid (red) and boronic acid (green) building blocks can be connected to the core scaffold (blue), to afford a diverse library of ligands. Illustration adapted from earlier work of the author.[48]

A lead structure for the hSOD1 ligands, originally proposed by Mrđen Debono[159] had been retrosynthetically disconnected into three structural fragments by the author,[48] as shown in Scheme 1. In theory, the structure of these fragments can be varied independently. A number of possible fragments were proposed and systematically recombined to afford a virtual ligand library, investigated in a molecular docking study by the author.[48] In addition, the initial docking study had demonstrated that the investigated ligands were preferably docked into the Val148 cavity, compared to other possible binding sites.[48] The expansion of the previous *in silico* ligand library, as well as the docking study, are discussed in Section 5.2.

2.8.2 Ligand Synthesis

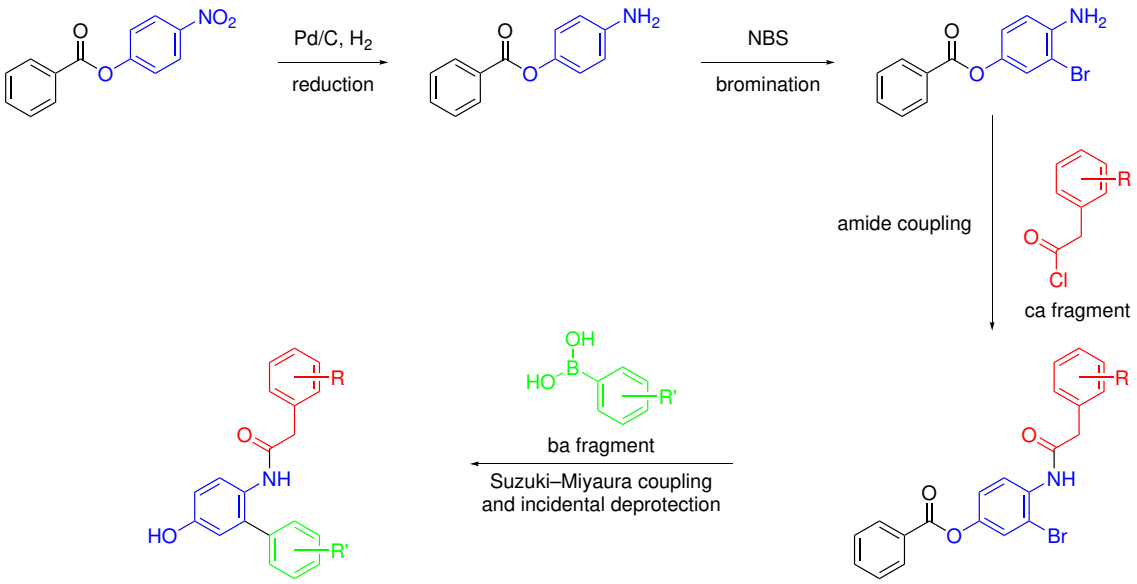

Scheme 2: Outline of the previously refined synthetic sequence.[48] Protecting group steps necessary for certain individual fragments are omitted for clarity. Illustration taken from earlier work of the author.[48]

The initial modular synthesis route for the hSOD1 ligands, reported by Mrđen Debono,[159] with an amide coupling and a Suzuki–Miyaura reaction as its key steps, was since refined by the author.[48] This refined synthesis route is illustrated in Scheme 2. Crucially, the order of reaction steps was revised: Carrying out the amide coupling prior to the Suzuki–Miyaura reaction avoided previously necessary protecting group steps, thereby shortening the reaction sequence. The amide coupling procedure, which previously had utilized EDC • HCl and HOBt as amide coupling reagents, had to be adjusted and carboxylic acid building blocks were instead employed as acid chlorides and coupled with the amine of the core scaffold under basic conditions.[48] The continued development of this modular synthesis is discussed in Section 5.3.

3 Aim

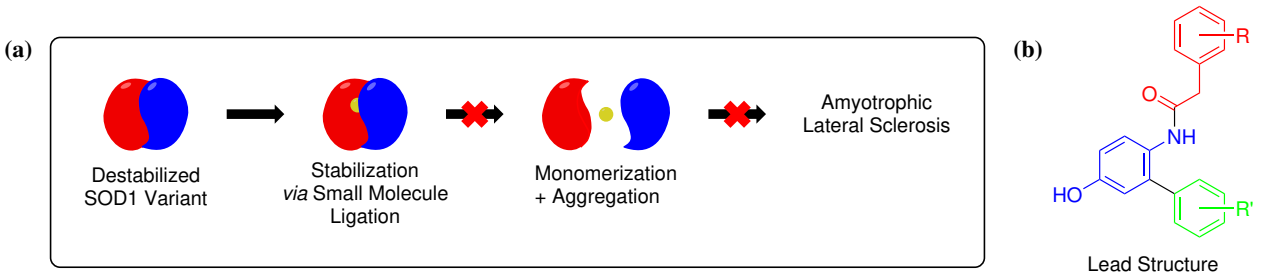

Figure 16: (a): Simplified representation of the envisioned mode of action for small molecule ligands stabilizing mutant human SOD1 in the context of ALS. **(b):** Lead structure of small molecule hSOD1 ligands. Moieties highlighted in red and green will be varied to generate a library of derivatives.

The overarching goal of this work, illustrated in Figure 16a, is the development of small molecule ligands for the stabilization of ALS relevant, aggregation prone hSOD1 mutants. As the cavity around Val148 (Figure 17) had been demonstrated as a suitable non-covalent ligand binding site,[48] it was targeted in the design of native hSOD1 dimer stabilizing ligands. These ligands shall provide novel pharmacological compounds for the research on ALS disease development and progression, and potentially guide the search for a treatment for hSOD1 related ALS.

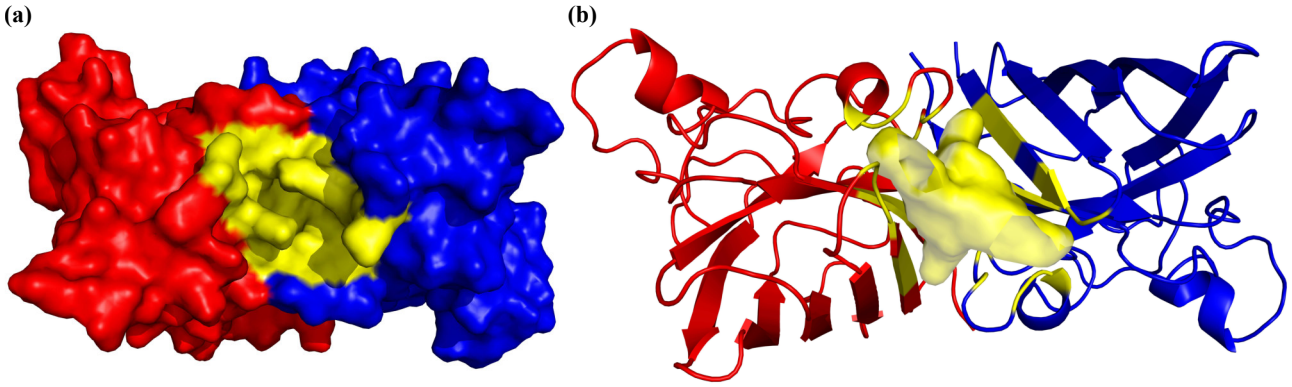

Figure 17: Visualization of the Val148 cavity of hSOD1 (PDB code 2c9u[45]). Monomer A is shown in red, monomer F is shown in blue and AAs of the Val148 cavity and the cavity space are shown in yellow. **(a):** Surface representation of hSOD1 highlighting the Val148 cavity. **(b):** Ribbon representation of hSOD1 highlighting the space within of the Val148 cavity. The cavity space was modeled with PyMOL at 7 Å cavity detection radius and 2 solvent radii cavity detection cutoff.

The ligands in this study will be derived from the common lead structure shown in Figure 16b. Molecular docking of derivatives of this lead structure, generated *in silico* by systematic recombination of a set of precursor fragments, will be used to preselect both for the most essential structural fragments and the most promising ligands. Additionally, molecular docking will provide proposed binding modes of these ligands in the targeted Val148 cavity.

A modular synthesis approach will be utilized to prepare a library of ligands, starting from a comparatively small number of fragment building blocks. The synthetic focus will be on the general applicability of the reaction conditions of each step, rather than optimized yields of individual reactions and building block combinations, in order to facilitate expedience in library preparation.

The hSOD1 protein will be prepared by recombinant expression from *E coli.*. In addition to hSOD1, the ALS associated hSOD1 A4V variant will be prepared to serve as an *in vitro* model of ALS in biophysical assays. As stabilizing effects are generalizable across hSOD1 variants, although not quantitative, the results obtained from investigations stabilizing and reducing aggregation of hSOD1 A4V are transferable to hSOD1-ALS.[26,90,92]

In order to verify that native hSOD1 is obtained by recombinant expression, the presence of hSOD1's native maturation modifications will be assessed. Mass spectrometry will investigate Cu^{2+} and Zn^{2+} metalation and the presence of the native intrasubunit disulfide bond. The hSOD1 specific activity of superoxide conversion will be determined to confirm the correct folding and dimer association of the protein.

The interaction between the synthesized small molecule ligands and the hSOD1 A4V protein will be investigated in multiple biophysical assays. An *in vitro* system is chosen over more complex systems such as hSOD1 expressing cell lines or animal models, to enable the investigation of protein-ligand interactions in isolation of other biochemical processes. The central screening assay will be a thioflavin T (ThT) based aggregation assay, which indicates the ligands influence on disease relevant hSOD1 A4V aggregation. Hit compounds of the ThT assay will then be confirmed through dynamic light scattering (DLS), providing information on the sizes of formed SOD1 aggregates and how the aggregation behavior was influenced in the presence of the stabilizing ligands.

Electron Microscopy (EM) will be used to reveal the morphology of hSOD1 aggregates formed under the incubation conditions utilized in this study.

The experimental results will be compared to the initial molecular docking calculations in order to evaluate the accuracy of this model and its ability to predicting ligand structures that can bind and stabilize hSOD1.

In conclusion, this study aims to develop small molecule ligands, which reduce the aggregation or limit the size of formed aggregates of hSOD1 A4V.

4 Methods

4.1 Ion Exchange Chromatography

Ion Exchange Chromatography (IEX) separates proteins by their charge at a given pH value. The stationary phase consists of a resin with a charged functional group used to bind oppositely charged proteins, which are then sequentially eluted *via* a gradient of aqueous buffer of increasing ionic strength or change in pH value, while uncharged proteins or proteins with the same charge as the resin pass through the column unrestricted. To find an appropriate resin and buffer system, a protein's isoelectric point (pI) is evaluated. The pI refers to the pH value at which a protein exists in a net neutral state. Diverging from this value, the protein exists in either a positive or negative net charged state. As long as the protein is stable at the desired pH value and buffer composition, either an acidic or basic pH value may in principle be used and the choice of an appropriate pH value primarily depends on the separation of the given sample components. Typically, IEX is performed at a buffer pH value at least one unit away from the target protein's pI with the intention to elute the target protein during a buffer gradient of increasing ionic strength or less commonly used a different pH value. An entire IEX run consists of multiple steps typically referred to as equilibration, sample application, wash, elution and regeneration. Their specific purpose and execution can be described as the following: 1) Equilibration: The column is equilibrated with the starting buffer and charged groups on the resin are paired with salt ions present in the buffer. 2) Sample application: The protein sample in starting buffer is injected onto the column and proteins oppositely charged to the resin are bound. Because the protein of interest will remain on the column until the elution step, multiple injections of sample may be performed, provided the columns binding capacity is not exceeded. 3) Wash: The column is flushed with starting buffer and unbound proteins are removed. 4) Elution: A gradient of an elution buffer is used to sequentially elute bound proteins. The elution buffer typically has the same composition as the starting buffer, except for a higher ionic strength (typically a higher concentration of Na^+, $NH_4{}^+$ or Cl^-) or less commonly used a different pH value. Ions in the elution buffer compete with the bound proteins, statistically replacing them at the resins charged groups. Weakly charged proteins therefore elute first followed by more strongly charged ones. Changing the pH value over a gradient similarly weakens the interaction of bound proteins by reducing or inverting their charge. 5) Regeneration: The column is washed with a high ionic strength buffer removing any remaining bound proteins. The column may then again be equilibrated for another run.[160]

4.2 Size Exclusion Chromatography, Desalting and Buffer Exchange

Size Exclusion Chromatography (SEC) separates proteins by their size in solution. The stationary phase consists of a resin made from a porous matrix of spherical particles, designed to not interact with the proteins by any form of attraction. Instead, the pores of the particle's provide additional space through which proteins may travel on their way along the column. Proteins that are too large to fit through these pores will travel a rather straight path only using the space between the particles and elute about as fast as the solvent front. Smaller proteins that can fit into the particle's pores will statistically travel a more divert path because of the space inside the particles accessible to them and move along the column more slowly. The elution speed of different proteins is therefore inversely correlated to their size. The size of a protein hereby approximately depends on its molecular weight and its shape. Buffer composition of the mobile phase does not directly affect separation and the column is equilibrated in the same buffer that is used to isocratically elute the proteins. However since separation is primarily influenced by the type and amount of resin, SEC is most suited for samples with a low number of different components and therefore generally carried out after other chromatography steps have already been performed. The applied flow rate also influences resolution and while a lower flow rate provides more time for proteins to diffuse in and out of the porous resin particles an improvement in resolution is most pronounced in the case of large proteins, while for very small proteins resolution may even be reduced.[161]

Desalting and Buffer Exchange is essentially a specific application of SEC and refers to the separation of metal or salt ions from a protein. It may also be used to simply transfer a protein from one buffer composition to another, effectively exchanging its buffer. The resolution required for this application is generally much lower compared to SEC between multiple proteins and desalting columns are typically optimized for larger sample volumes and higher flow rates.[161]

4.3 hSOD1 Activity Assay

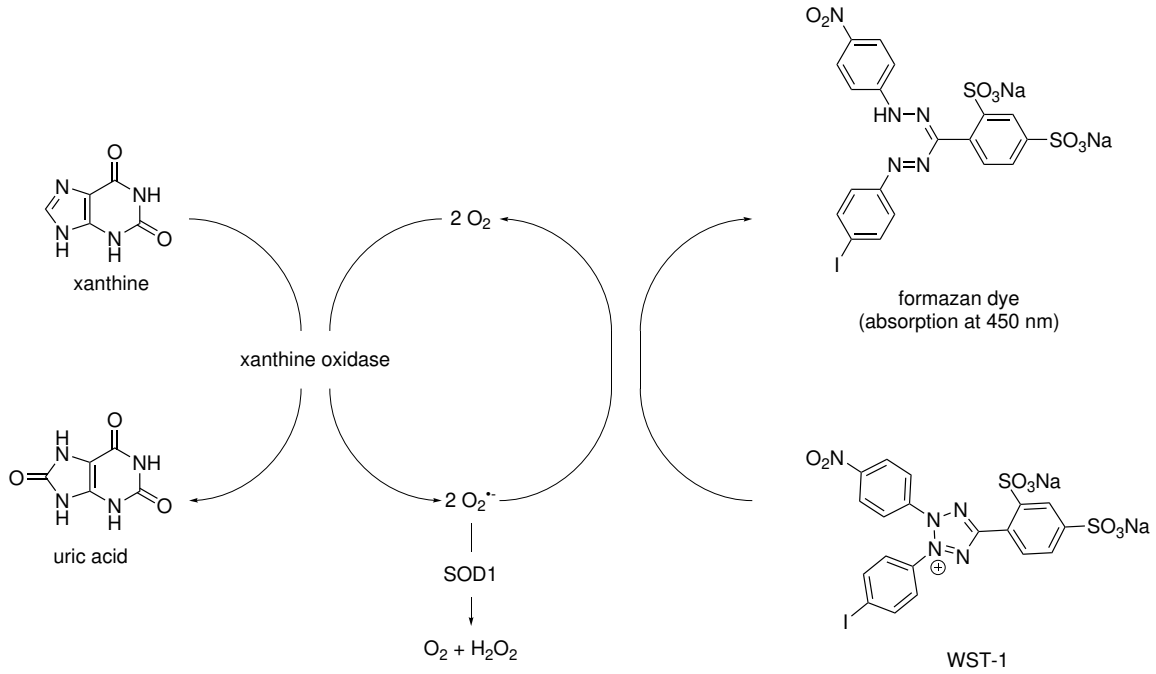

Scheme 3: Simplified representation of the interacting reactions of the hSOD1 activity assay. The protein xanthine oxidase (XO) converts xanthine into uric acid, thereby generating superoxide ($O_2^{\bullet -}$). In the absence of hSOD1, superoxide is consumed in the conversion of WST-1 into its corresponding formazan dye, which is characterized by an absorption maximum at 450 nm. In the presence of hSOD1, superoxide is converted into O_2 and H_2O_2, effectively inhibiting the formation of the formazan dye. Measurements of the absorption at 450 nm may therefore be used to monitor changes in formazan concentration, indirectly reporting on hSOD1's activity to convert generated superoxide. Illustration adapted from the manual of the Superoxide Dismutase (SOD) Activity Assay Kit (CS0009) from Sigma Aldrich.

The activity of expressed hSOD1 and its ALS relevant A4V variant will be determined, in order to verify that expression and reconstitution were successful and that the proteins were obtained in their native states. For this purpose, a commercially available SOD activity assay kit will used. The interacting reactions of the assay are outlined in Scheme 3. This assay is well established in the literature[162–164] and based on the fundamental design developed by McCord and Fridovich.[165–167] Multiple variations have been developed, but the underlying principals remain unchanged. Superoxide ($O_2^{\bullet -}$) is generated electrochemically or *via* an enzymatic reaction and used to convert a precursor into a reporter molecule, whose concentration can be monitored spectroscopically. Inhibition of this conversion through the consumption of superoxide by hSOD1 is then used to indirectly determine hSOD1 activity. Modern iterations of the setup, such as the utilized kit from Sigma Aldrich, use the conversion of xanthine to uric acid by xanthine oxidase to generate superoxide and use WST-1 as a precursor and its corresponding formazan dye as a reporter molecule.[168]

4.4 Thioflavin T based Aggregation Assay

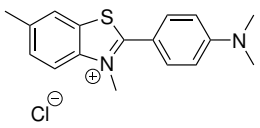

thioflavin T (ThT)

Figure 18: Chemical structure of thioflavin T (ThT), a fluorescent dye widely established for the identification of amyloid fibrils.

Thioflavin T (ThT) is well established as a reporter for amyloid fibrils because of its characteristic shift in excitation (from 385 nm to 450 nm) and emission maxima (from 445 nm to 482 nm) when binding to amyloid fibrils.[169] This shift is caused by reduced rotation about the central C–C bond when binding to amyloid fibrils. Formation of amyloid fibrils can therefore be observed spectroscopically when excitation is performed and emission recorded at these wavelength. The presence of amyloid fibrils or an increase in their concentration over time can then be observed as an increase in ThT fluorescence intensity.[170]

Importantly, while ThT is generally regarded to be specific to amyloid fibrils and considered to not bind to unordered aggregates or oligomers, which are present during amyloid fibril formation, multiple publications highlight important exceptions. ThT fluorescence has been demonstrated for amyloid β-protein (Aβ) protofibrils[171,172] and soluble Aβ oligomers.[172,173] In the context of ALS, ThT fluorescence has been reported for soluble hSOD1 oligomers.[94,174] Therefore, while specific ThT binding sites have been reported for amyloid fibrils, rather than strictly limited to amyloid fibrils, ThT binding and fluorescence is similarly observed for biomolecules, soluble oligomers or any other aggregate morphology that provides a suitable binding site. These are are often hydrophobic, rich in aromatic residues or contain β-sheet regions.[170,172]

When trying to relate ThT fluorescence intensity to the amount of aggregates in solution one needs to be aware that formation of different aggregate species or morphologies with a greater ThT affinity may at least in part also contribute to an increase in fluorescence intensity. This was particularly pointed out by Oztug Durer *et al.* in their systematic study examining the influence of a number of factors on hSOD1 aggregation and fibrillation tendency.[175] More than one ThT binding site or binding mode with different fluorescence intensities has been reported for amyloid fibrils. An increase in ThT fluorescence intensity may therefore not necessarily correspond to an increase in fibril concentration.[176]

Care should further be taken when investigating small molecule agents, as they might interfere with ThT fluorescence by competing with ThT for protein binding sites or quenching of ThT fluorescence.[177] Further, one should keep in mind that a number of experimental factors have been reported to influence ThT fluorescence intensity, such as the presence of cosolvents,[170,178] viscosity,[176] as well as the nature and ionic strength of the employed buffer, especially in regards to NaCl concentration.[179]

ThT assays may be set up in one of two ways, which in the following discussion will be referred to as continuous *in situ* and fixed time point *ex situ*.[176,178,180] Both approaches have situational advantages that shall be highlighted.

In the continuous *in situ* setup ThT is added to the protein prior to its incubation. Protein and ThT are then incubated together and measurements are continuously taken over a period of time, typically by a plate reader, providing a convenient setup and a high number of consistently timed data points. The disadvantages of this step stem from the fact that ThT is present during the incubation. While often disregarded, ThT itself may influence the aggregation or fibrillation process, as highlighted by reported examples.[170,181] Further, it has been shown that ThT already hydroxylates at neutral pH at 37°C reducing the observed fluorescence intensity.[176,182]

In contrast, in the fixed time point *ex situ* setup the protein is incubated without ThT. At fixed time points, aliquots are taken from the incubated sample, ThT is then added and measurements are performed. The setup may be used as an endpoint measurement with only one fixed time point or multiple aliquots are measured over a period of time, providing multiple fixed time points. This setup avoids ThT's potential influence on the aggregation or fibrillation process, but more importantly it avoids degradation of ThT during the incubation. Therefore, when ThT is absent during the incubation, harsher incubation conditions *e.g.* high temperature can be utilized to promote or accelerate aggregation. When performing many fixed time point measurements, this setup is more labor intensive and data points are likely less consistently timed, as compared to the continuous *in situ* setup. In the case of a single endpoint measurement, less overall information is obtained. In a study on hSOD1 aggregation modulators, Malik *et al.*[177] discuss in detail the additional information that can be gained about a ligand's effect on the different stages of the aggregation process, when ThT fluorescence is observed over a period of time. Therefore, end point measurements are also more susceptible to false-positive and false-negative results.[177] The procedure proposed by Mrđen Debono,[159] which will be followed in this study utilized end point measurements, as will be discussed in Section 9.10.8. This provided a qualitative comparison between the investigated ligands to be used for their screening.

Regardless, which ThT assay setup is utilized in a given study, the results should always be verified by additional, complementary, dye-free experiments.[176,178,180]

4.4.1 Conditions determine hSOD1 Aggregate Morphology and ThT Fluorescence

Aggregates of hSOD1 have been reported to form multiple distinct morphologies, including amorphous and fibrous assemblies.[94,174,183–185] While the pathological relevance of these different morphologies is not fully understood, the correlation between experimental conditions and the formed morphologies has been investigated at length, as discussed in Section 1.2. The nature of hSOD1 aggregates can have a noticeable influence on experimental observations. Aside from the readily apparent implications to microscopy observations, the fluorescence intensity of ThT strongly depends on the molecular structure of protein aggregates, as discussed in the previous Section. It is well established, that under suitably conditions hSOD1 can form various types of branched and unbranched fibrils. However, the experimental conditions utilized to obtain them often strongly favor the formation of fibrils and deviate considerably from the physiological conditions inside of ALS-relevant cells and tissues. Factors such as low pH values, the addition of disulfide reducing agents, mechanical agitation or seeding have been demonstrated to facilitate fibril formation specifically.[94,174,183–185] A few very important publications investigating hSOD1 aggregates formed under near physiological conditions and their implications on ThT fluorescence intensity, will be discussed below. Especially, the relevance of disulfide/thiol states are highlighted by these reports.

In 2007, Banci *et al.* investigated the aggregation of apo (E|E) hSOD1 under near physiological conditions and observed that ThT-positive soluble oligomers were formed. These were characterized by an intact intrasubunit Cys57-Cys146 disulfide bond, but required the presence of Cys6 and Cys111 to form disulfide-links between monomers. Moreover, these oligomers displayed an increased percentage of β secondary structure compared to freshly prepared, dimeric apo hSOD1, as observed by CD spectroscopy. The observation that the hydrogen-bond network disruptor Gdn • HCl was able to quench the observed ThT fluorescence, while high molecular weight species were still observed by gel filtration (SEC) demonstrated, that their tertiary structure allowed for ThT binding.[94] The authors extended their investigation to 11 different hSOD1 mutations in a following report, highlighting the generality of their observed aggregation mechanism.[174]

In 2010, Hwang *et al.* showed that holo (Cu|Zn) hSOD1 C6A/C111S incubated at pH 7.8 and 37°C without agitation eventually formed non-amyloid aggregates, after ~5 days. Atomic force microscopy (AFM), revealed that soluble oligomers were formed first, followed by amorphous aggregates and eventually branched and tangled fibrils. ThT binding fluorescence of these aggregates was minimal, highlighting their non-amyloid character.[183] The difference in ThT binding between the studies of Banci et al.[94,174] and Hwang *et al.*[183] highlights that different aggregate morphologies had been observed, most likely due to the exclusion of Cys6 and Cys111 in the hSOD1 variant used by Hwang *et al.*.

In 2017, Khan *et al.* investigated the involvement of hSOD1s cysteine residues (Cys6, Cys57, Cys111, Cys146) in the formation of amyloid fibrils. Specifically, they examined the by design monomeric apo hSOD1 C6A/F50E/G51E/Cys111 and apo hSOD1 C6A/F50E/G51E/Cys57/Cys111/Cys146 variants under near physiological conditions without agitation. The authors reported that reduction or absence of the intrasubunit Cys57-Cys146 disulfide bond was required for fibril formation. Conversely, none of the cysteine residues had to be present for fibril formation to occur, demonstrating that disulfide cross linking is not a requirement for hSOD1 fibril formation.[185] Notably, these fibrils displayed ThT fluorescence and consistent with the reports of Banci *et al.*[94,174] formation of ThT-positive non-

fibrilous aggregates was not observed in the absence of Cys6 and Cys111.[185] Some hSOD1 aggregation studies have utilized mechanical agitation, *e.g.* by teflon beads placed in the plates wells, combined with continuous shaking during their ThT assays to promote aggregation.[175,186,187] This is known however to not simply accelerate fibrillation, but to influence the fibrillation pathway by introducing secondary nucleation processes such as, but not limited to breaking of fibers.[188,189] Even under conditions that facilitate fibril formation, hSOD1 aggregation has been well documented to be a stochastic process, which may lead to either fibrils or amorphous aggregates.[184]

4.5 Dynamic Light Scattering

Dynamic Light Scattering (DLS) is an established method to study protein aggregation, especially in the context of aggregation related diseases. It quantifies the diffusion and thereby estimates the hydrodynamic radius R_H of approximately spherical particles in a sample solution by their light scattering intensity. Because the scattering intensity detected from the sample depends on the particles' radius to the power of six, DLS displays a high sensibility towards the larger particles present and is therefore suitable to study protein aggregation.[181,190]

DLS aims to determine the diffusion coefficient D of particles in the sample, based on the autocorrelation over a delay time τ of intensity of light scattered by the sample. As smaller particles diffuse more quickly than larger particles, the decay in correlation over a delay time τ reflects the mobility of the particles.

To conduct the measurement, the sample solution in a cuvette is exposed to monochromatic polarized light from a laser, which is scattered by the particles in the sample. At a fixed angle θ, a detector is positioned to measure the intensity of the scattered light over time. Experimental time exposures range from ns to µs and this detection method is suitable for sizes between ~1 nm to ~1 µm.[191] Fundamental to DLS analysis is the van Hove autocorrelation function $G_s(\vec{r}, \tau)$ which correlates all points of the sample volume and all time points of measuring time for a given change in location $\vec{r}$ and changes in time delay τ:[192]

$$G_s(\vec{r}, \tau) = \langle n(\vec{r_0}, t_0) \cdot n(\vec{r_0} + \vec{r}, t_0 + \tau) \rangle_{V,T} \tag{1}$$

where $n(\vec{x}, t)$ is the local number density of the particles, a quantity proportional to the local concentration.[192] A constant sample volume V and a constant temperature T are assumed. t_0 as well as $\vec{r_0}$ can be arbitrarily chosen, however $\langle\ \rangle$ indicates that G_s represents the average over all possible choices, eliminating the arbitrary decision.[192] For Brownian motion, an isotropic diffusion process, this autocorrelation function can be specified as:

$$G_s(|\vec{r}|, \tau) = \sqrt{(4\pi D\tau)^3} \cdot e^{-\frac{|\vec{r}|\tau^2}{4\pi D}} \tag{2}$$

which depends on the length of $\vec{r}$, namely $|\vec{r}| = r$, due to the isotropic nature.[192] Fourier transformation of $G_s(r, \tau)$ yields the intermediate scattering function $F(\vec{q}, \tau)$, which is a function of the wavevector $\vec{q}$:

$$F(\vec{q}, \tau) = e^{-Dq^2\tau} \tag{3}$$

Via the Siegert relation,[192,193] the scattering intensity I, *i.e.* the measured signal, relates to the intermediate scattering function as:

$$F(q, \tau) = e^{-Dq^2\tau} = \sqrt{\frac{\langle I(q, t_0) I(q, t_0 + \tau) \rangle}{\langle I(q, t_0)^2 \rangle} - 1} \tag{4}$$

The wavevector $\vec{q}$, for the specific experimental setup can be described as a frequency q:[194]

$$q = \frac{4\pi\nu}{\lambda} \cdot \sin\left(\frac{\theta}{2}\right) \tag{5}$$

where λ is the wavelength of the laser, ν the refractive index of the solution and θ the angle at which the detector is positioned.[192] The relation between the intermediate scattering function and the detected signal is sometimes described as:

$$g_2(q,\tau) = 1 + g_1(q,\tau)^2 \tag{6}$$

with the amplitude autocorrelation function $g_1(q,\tau)$ as:

$$g_1(q,\tau) = F(q,\tau) \tag{7}$$

and the normalized scattered intensity autocorrelation function $g_2(q,\tau)$ as:

$$g_2(q,\tau) = \frac{\langle I(q,t_0)I(q,t_0+\tau)\rangle}{\langle I(q,t_0)^2\rangle} \tag{8}$$

To evaluate a sample, plotting $\log(F(q,\tau))$ over τ and $F(q,\tau)$ over $\log(\tau)$ demonstrates if a sample is poly- or mono-disperse through the resulting curve shape.[192] For a polydisperse sample the scattering intensity I of each contributing particle needs to be considered,[192] as:

$$I \sim nM^2P(q) \tag{9}$$

with n being the number density of that particle and M being its mass and the particle form function P(q) for approximately homogeneous, spherical particles as:

$$P(q) = \frac{9}{(qR_H)^6} \cdot \left(\sin(qR_H) - qR_H\cos(qR_H)\right)^2 \tag{10}$$

These influences are summarized in P(D), a distribution function weighting the individual contributions of the species to the superposition:

$$F(q,\tau) = \int P(D) \cdot e^{-q^2 D\tau} dD \tag{11}$$

Fitting of this relationship allows the determination the diffusion constants of particles in the samples. *Via* the Stokes–Einstein–Sutherland relation, the estimated diffusion coefficient can be mapped to the hydrodynamic radius, which is the radius of a sphere with the same diffusion constant as the, in reality, not quite spherical particle.[192,195] Given that the viscosity η of the sample solution is known, the hydrodynamic radius is calculated as:

$$R_H = \frac{k_B T}{6\pi\eta D} \tag{12}$$

5 Results and Discussions

5.1 Ligand Nomenclature

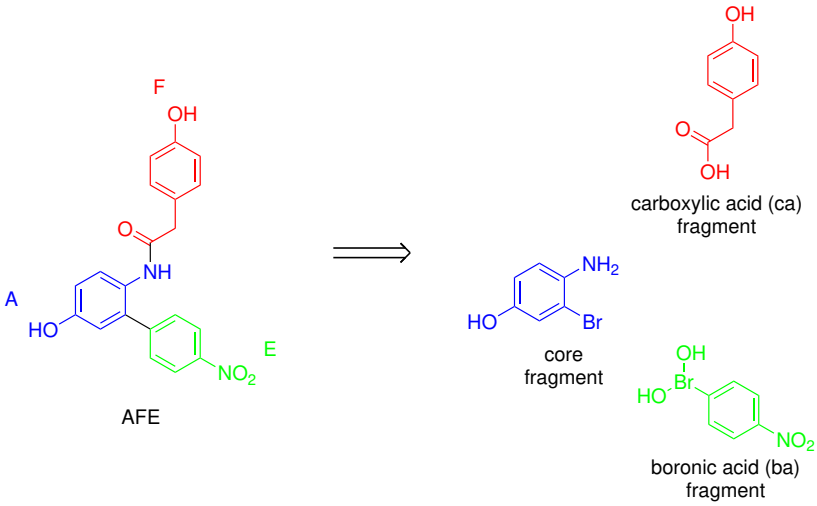

Figure 19: Illustration of the three letter code used to refer to each ligand, on the example of ligand AFE. The first letter corresponds to the core, the second letter corresponds to the carboxylic acid (ca) fragment and the third letter corresponds to the boronic acid (ba) fragment.[48] Illustration taken from earlier work of the author.[48]

A biunique nomenclature for the hSOD1 ligands of this study had previously been established by the author.[48] The nomenclature is based on the retrosynthetic analysis of the underlying lead structure, as illustrated in Figure 19. A ligand's three letter code denotes the three structural fragments that it contains. The fragments themselves are named after their functional group relevant for the synthetic interconnection, being: the core, the carboxylic acid fragments (ca) and the boronic acid (ba) fragment. Fragments were indexed alphabetically by order of accession and refer to distinct chemical structures.

5.2 Molecular Docking of a Virtual hSOD1 Ligand Library

A molecular docking study of a virtual hSOD1 ligand library using AutoDock Vina[196] had been carried out in previous work of the author.[48] The methodology, provided in Section 8, was continued in this work. The virtual ligand library was expanded by the addition of further carboxylic acid (ca) and boronic acid (ba) fragments, from which additional ligands for molecular docking were generated. Indexing of fragments was continued alphabetically in order of accession. A comprehensive list of every ligand docked and every fragment used in the construction of ligands is provided in the appendix (Section 10) of this thesis. For consistency, it needs to be mentioned, that a number of carboxylic acid (ca) and boronic acid (ba) fragments (shown in Figure 20) had been included in the *in silico* generation and docking studies during the authors master's thesis, but were not further used due to limited or costly commercial availability or their unstable chemical nature.[48]

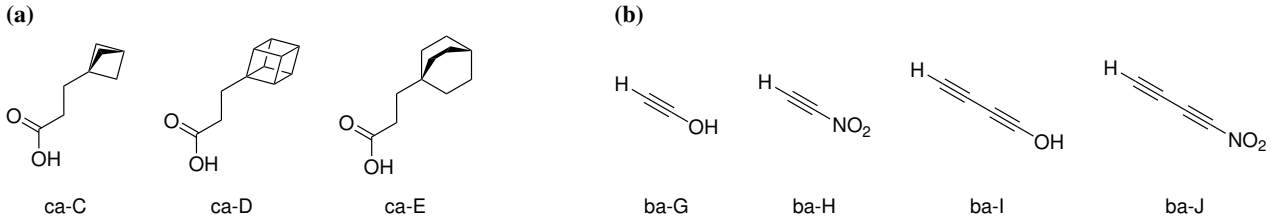

Figure 20: Previously included carboxylic acid (ca) and boronic acid (ba) fragments that were discontinued for *in silico* generation of SOD1 ligands. **(a):** Carboxylic acid fragments bearing aliphatic bioisosteres of benzene. **(b):** Previously also referred to as hypothetical Sonogashira fragments, these building blocks could in theory be coupled to the central core *via* a Sonogashira reaction utilizing the same Br-handle as the boronic acid building blocks coupled *via* a Suzuki–Miyaura reaction. The structures shown however, are reported to be unstable or have not been isolated before.[48]

Previously, only boronic acids bearing 6-membered rings had been investigated.[48] In the internship of Tamara Skarke, as part of this study, it was investigated if the inclusion of boronic acid fragments bearing 5-membered rings could provide promising ligand structures. A selection of commercially available 5-membered heteroaromatic boronic acid fragments shown in Figure 21 was therefore included.

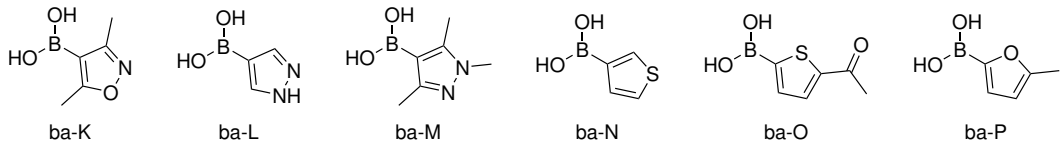

Figure 21: Chemical structures 5-membered heteroaromatic boronic acid fragments featuring a variety of substitution patterns.

In addition to the ligands of this work, pyrimethamine (Section 2.4.1) was investigated as a possible stabilizing ligand for hSOD1. Similar to the underlying lead structure of the proposed ligands, pyrimethamine features a central biphenyl system. Formally derived from its functionalized pyrimidine, ba-Q was included as a boronic acid fragment. Considering that the two ortho substituents of ba-Q may limit rotational freedom about the ligands central biphenyl C–C bond, a less substituted variant was also introduced as ba-S.

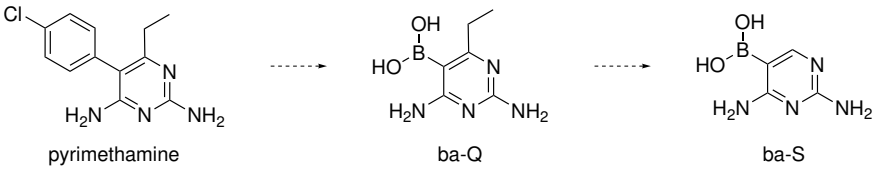

Figure 22: Chemical structure of ba-Q and ba-S as formally derived from pyrimethamine.

Because ba-E (4-nitrophenylboronic acid) **19** previously proved to be a viable Suzuki–Miyaura coupling partner in the ligand synthesis,[48] other 1,4-substituted boronic acids were included. In principle, following construction of the ligand scaffold, the cyano group of ba-T could be converted into other functional groups, further increasing the number of available ligand derivatives. This possibility was however not explored in this study.

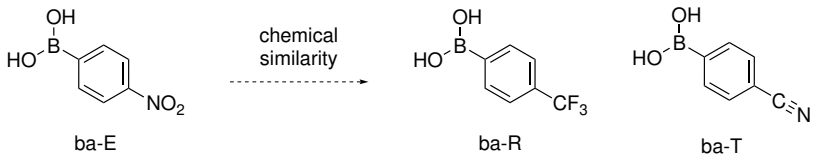

Figure 23: Chemical structure of ba-R and ba-T, included because of their chemical similarity and shared 1,4-substitution pattern compared to ba-E.

Because synthetic work in the bachelor's thesis of Janica Wendt[197] included 2-(3,4-dimethoxyphenyl) acetic acid as a building block, it was included here as ca-V, as shown in Figure 24.

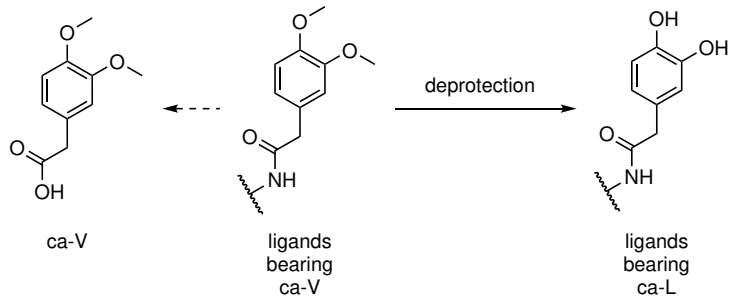

Figure 24: Chemical structure of ca-V and its synthetic relation to ca-L.

Similarly, during synthetic work on the deprotection of aromatic methoxy groups, discussed in Section 5.3.5, access to the 1,4-dihydroxybenzene moiety shown in Figure 25 was obtained. The underlying formal carboxylic acid was therefore also included as ca-W .

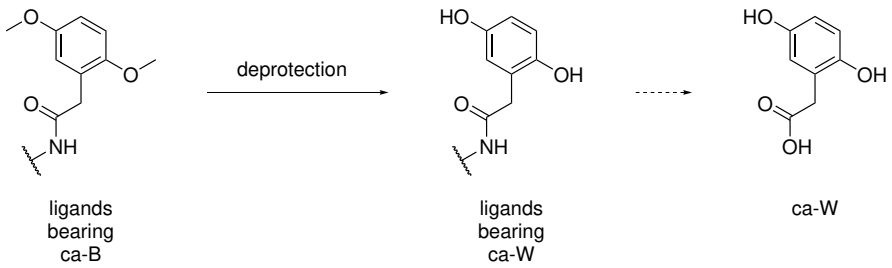

Figure 25: Chemical structure of ca-W introduced by methoxy deprotection of ligands bearing ca-B.

Table 1: Formal structure of the core fragment used in the construction of the virtual ligand library used for molecular docking.

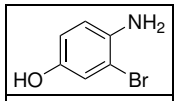	
core-A	

Table 2: Formal structures of carboxylic acid (ca) fragments used in the construction of the virtual ligand library used for molecular docking.

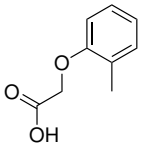	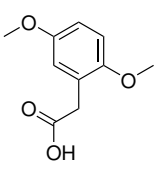	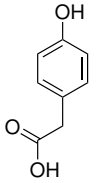	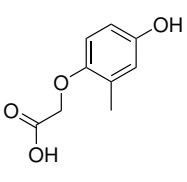	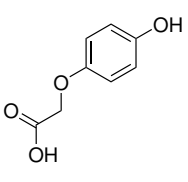	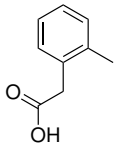	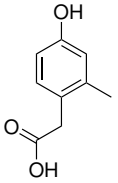
ca-A	ca-B	ca-F	ca-G	ca-H	ca-I	ca-J
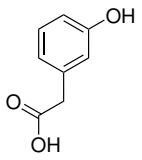	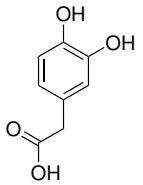	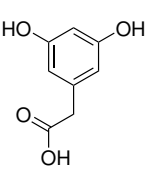	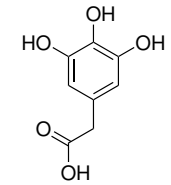	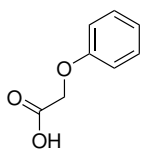	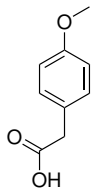	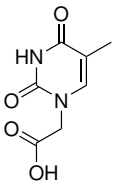
ca-K	ca-L	ca-M	ca-N	ca-O	ca-P	ca-Q
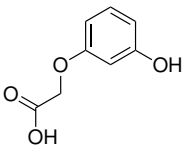	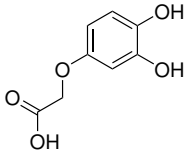	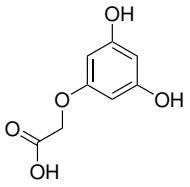	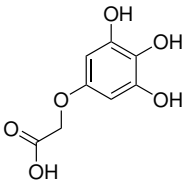	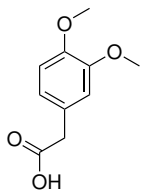	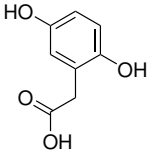	
ca-R	ca-S	ca-T	ca-U	ca-V	ca-W	

Table 3: Formal structures of boronic acid (ba) fragments used in the construction of the virtual ligand library used for molecular docking.

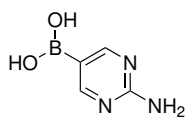	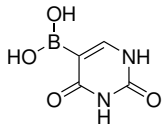	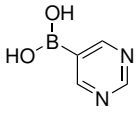	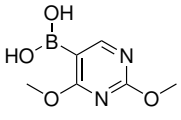	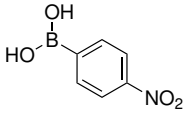	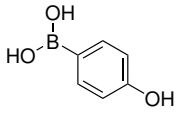
ba-A	ba-B	ba-C	ba-D	ba-E	ba-F
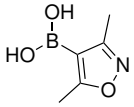	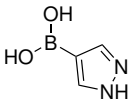	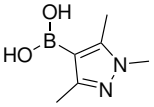	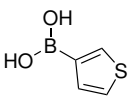	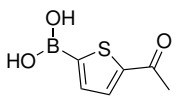	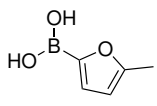
ba-K	ba-L	ba-M	ba-N	ba-O	ba-P
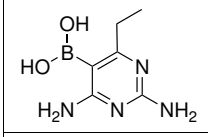	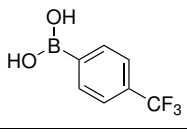	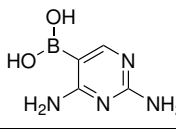	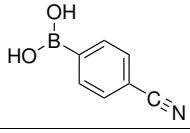		
ba-Q	ba-R	ba-S	ba-T		

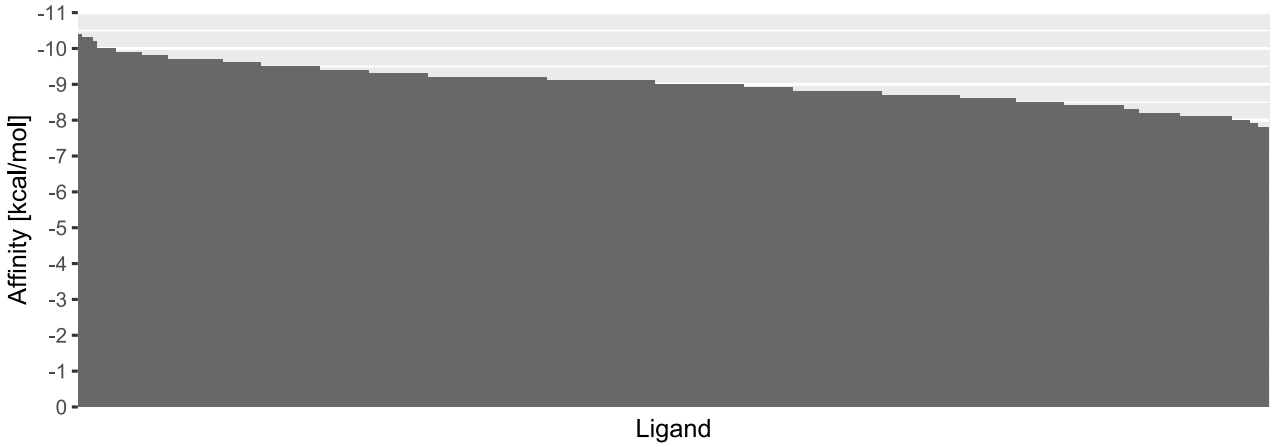

Figure 26: Docking affinities of the 320 generated ligands, ordered by affinity. Ligands are shown as columns. Docking affinities of individual ligands are provided in the appendix (Table 25 in Section 10.2).

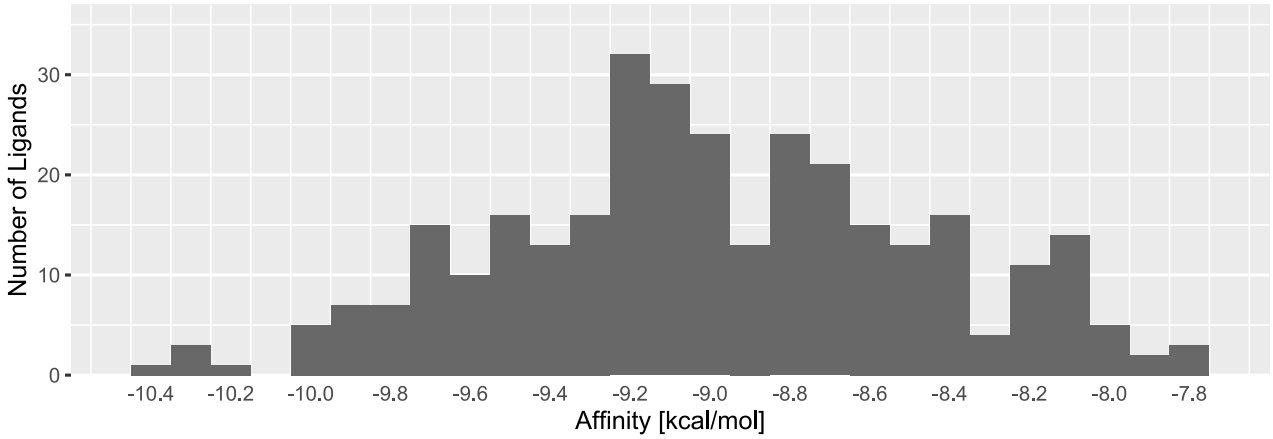

Figure 27: Distribution of docking affinities of the 320 generated ligands, illustrated as a histogram. A bin size of 0.1 kcal/mol was used. The obtained docking affinities had a resolution of up to one decimal place. This resolution was preserved in the binning of the histogram. The data visualized in this figure is provided in the appendix (Section 10.3, Table 26).

From this list of fragments, containing 1 core fragment (Table 1), 20 carboxylic acid fragments (Table 2) and 16 boronic acid fragments (Table 3), a total of 320 ligands were generated and docked to the hSOD1 protein. A detailed description of the preparation of ligands and the hSOD1 protein for molecular docking and the docking procedure are provided in Section 8.

The predicted affinities across all ligands, shown in Figure 26 ranged from -10.4 to -7.8 kcal/mol. As illustrated in Figure 27, the single largest bin of 32 ligands, representing 10% of *in silico* library, displayed an affinity of -9.2 kcal/mol. The chemical structure of the 10 best performing ligands, corresponding to the top four bins in the histogram are highlighted in Table 4. For the docking study, it was assumed, that there is a correlation between a ligand's binding strength, predicted as its docking affinity and its ability to inhibit hSOD1 aggregation. While this may not necessarily be the case and would need to be investigated *in vitro*, it provided a reasonable starting point for the prediction of promising ligands.

Table 4: Chemical structures of the top 10 ligands as determined by docking affinity. The corresponding ligand code and docking affinity are listed below every ligand's chemical structure.

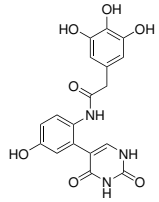	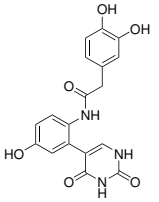	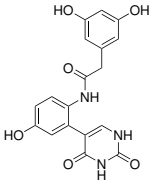	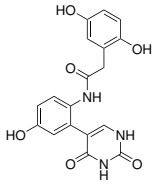	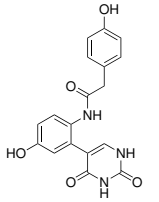
ANB	ALB	AMB	AWB	AFB
-10.4 kcal/mol	-10.3 kcal/mol	-10.3 kcal/mol	-10.3 kcal/mol	-10.2 kcal/mol
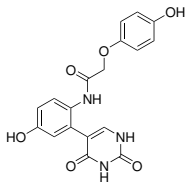	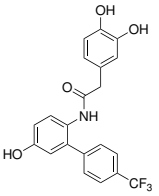	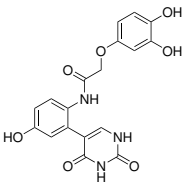	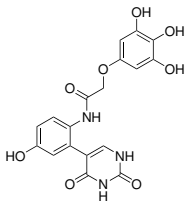	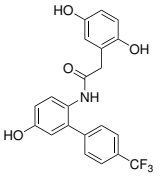
AHB	ALR	ASB	AUB	AWR
-10.0 kcal/mol	-10.0 kcal/mol	-10.0 kcal/mol	-10.0 kcal/mol	-10.0 kcal/mol

Focusing on these 10 ligands for synthesis and testing in assays would be a possible strategy, but it would entirely rely on the accuracy of the docking model's prediction. At this point, the docking model's accuracy has not been evaluated in the context of the investigated protein target. Furthermore, across these 10 ligands 9 different carboxylic and only 2 different boronic acid fragments are represented. In order to better utilize the modularity of the synthesis route, it was intended to combine a variety of both carboxylic and boronic acid fragment building blocks in the synthesis towards a ligand library. Furthermore, it would be beneficial to have ligands of a wider spread in regards to their anticipated effect for assay development. Some assays benefit from qualitative comparison between samples, as hit compounds may be readily identified, if a number of other compounds display none or much less of an effect. Therefore, it was intended to utilize the on average best carboxylic and boronic acid fragments to synthesize ligands from, instead of only relying on the best combinations. In order to evaluate which of the ca fragments and which of the ba fragments generally resulted in favorable ligands, the average docking affinity of all ligands containing a specific ca or ba was calculated, as illustrated in Figure 28 and compared between the ca fragments and the ba fragments, respectively.

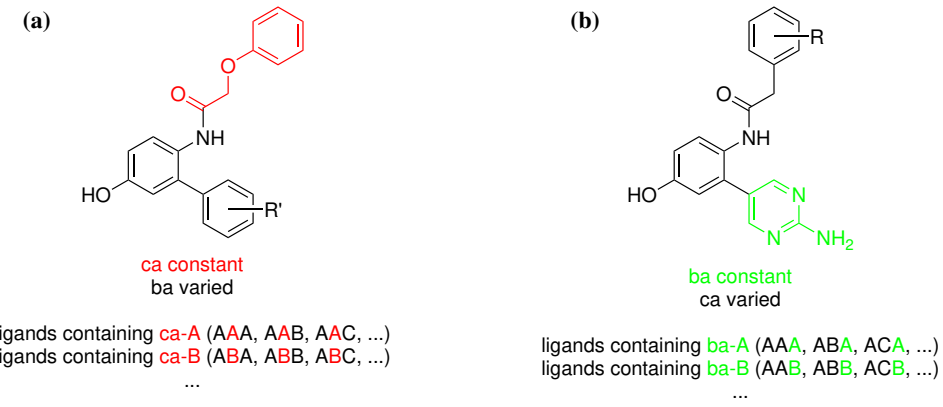

Figure 28: The average docking affinity of each ca and ba was determined across all ligands containing that specific ca or ba fragment. **(a):** Illustration of the average docking affinity for ca fragments. Formal structure of ligands bearing ca-A shown as an example. **(b):** Illustration of the average docking affinity for ba fragments. Formal structure of ligands bearing ba-A shown as an example.

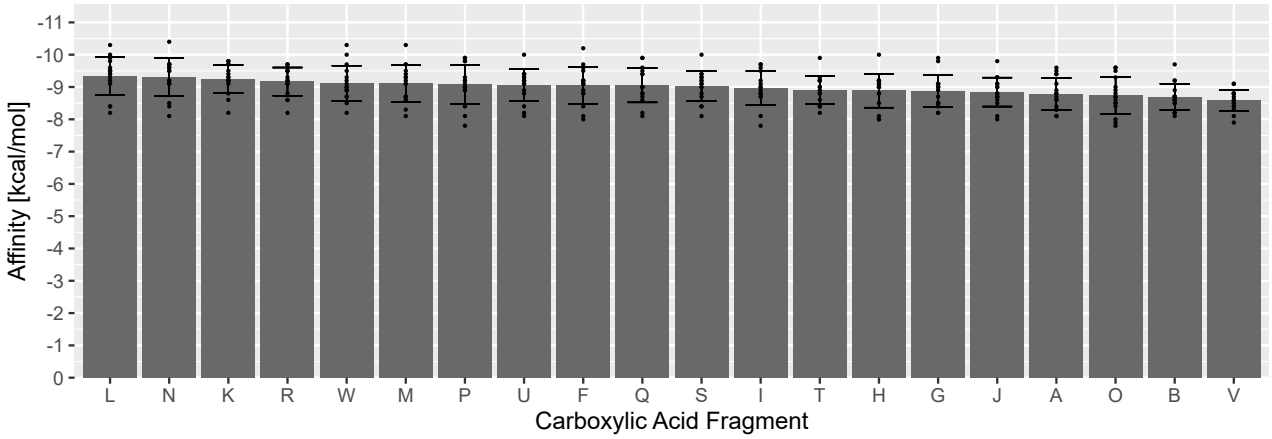

Figure 29: Comparison of average docking affinities of all ligands containing a specific carboxylic acid fragment. Affinities of individual ligands are shown as dots. The data visualized in this figure is provided in the appendix (Section 10.3, Table 27).

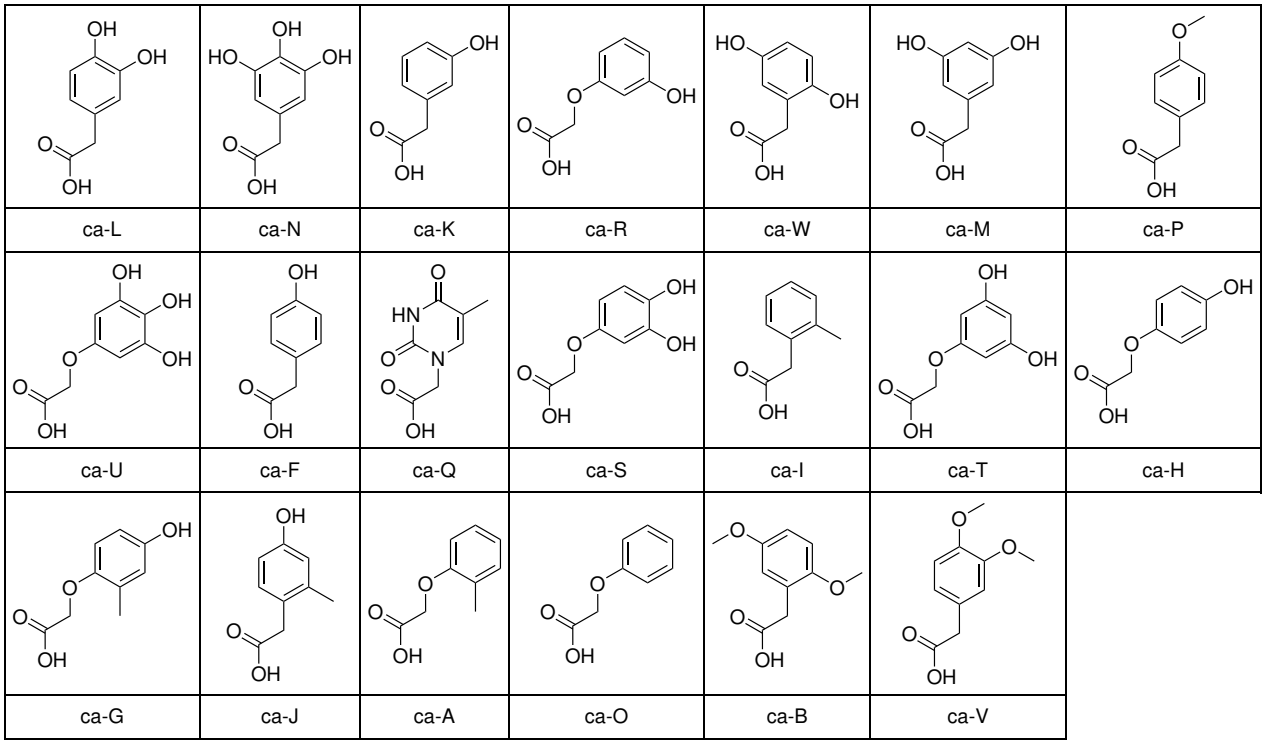

Figure 30: Chemical structures of the carboxylic acid fragments, ordered from left to right, top to bottom by average docking affinity of ligands constructed from them, as shown in Figure 29.

The average docking affinities of all ligands containing a specific carboxylic acid fragment, shown in Figure 30, ranged from -9.34 to -8.59 kcal, a range of 0.75 kcal/mol, as shown in Figure 29. Overall, there is no large difference in average affinity across all ca's. It is observed that ca's bearing methyl or methoxy groups tend to be less favored. While ca-L and N bear 2 and 3 hydroxyl groups, their position on the benzene ring seems to play a greater role than their number alone, as indicated by the ranking of ca-K, R, W, M, U and F. Comparing structures with the same substitution pattern, that differ in linker length, namely the pairs L+S, N+U, K+R, M+T, F+H and I+A the shorter linker seems to be favored. G+J are the exception to this trend, but their difference in average binding is minuscule. In order of average affinity, the following ca's were featured in ligands investigated in biophysical experiments (Section 5.7): L, W, P, F, O, B.

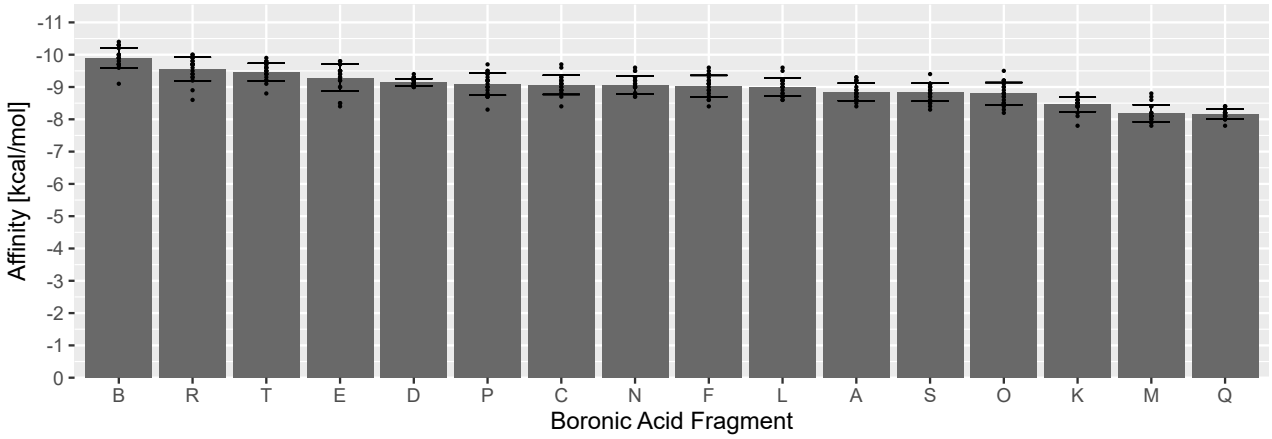

Figure 31: Comparison of average docking affinities of all ligands containing a specific boronic acid fragment. Affinities of individual ligands are shown as dots. The data visualized in this figure is provided in the appendix (Section 10.3, Table 28).

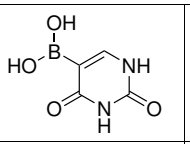	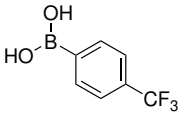	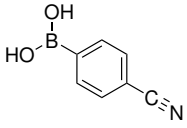	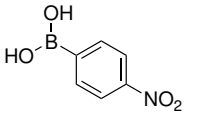	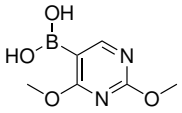	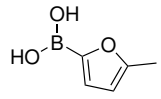
ba-B	ba-R	ba-T	ba-E	ba-D	ba-P
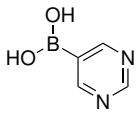	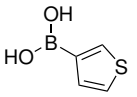	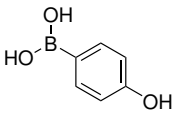	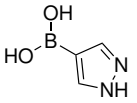	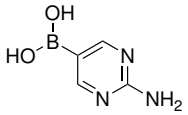	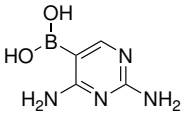
ba-C	ba-N	ba-F	ba-L	ba-A	ba-S
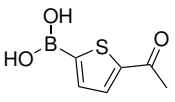	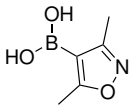	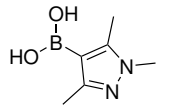	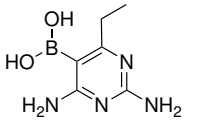		
ba-O	ba-K	ba-M	ba-Q		

Figure 32: Formal chemical structures of the boronic acid fragments, ordered from left to right, top to bottom by average docking affinity of ligands constructed from them, as shown in Figure 31.

The average affinities of all ligands containing a specific boronic acid fragment, shown in Figure 32 ranged from -9.90 to -8.16 kcal/mol, a range of 1.74 kcal/mol as shown in Figure 31 and was therefore much greater than the range observed across the carboxylic acid fragments (Figure 29). This indicates that the boronic acid fragment has a greater influence on a ligands docking affinity. As already suspected from the ligands with the best docking affinity shown in Table 4, ba-B was observed as the most promising boronic acid fragment. Notably, the next three ba's R, T and E all have a linear shape through their 1,4-substitution pattern. Thereafter, ba-D is very similar to ba-B only bearing two additional methyl groups. The ba's bearing 5-membered rings tend to be disfavored, similar to ba's S and Q that were formally derived from pyrimethamine. In order of average affinity, the following ba's were featured in ligands investigated in biophysical experiments (Section 5.7): T, E, D. Synthesis towards ligand containing ba-B were attempted, with limited success as discussed in Section 5.3.4. Similarly, ba-R had been observed by Mrđen Debono[159] to cause issues with ligand solubility and was therefore avoided in this study.

5.3 Modular Chemical Synthesis of the hSOD1 Ligand Library

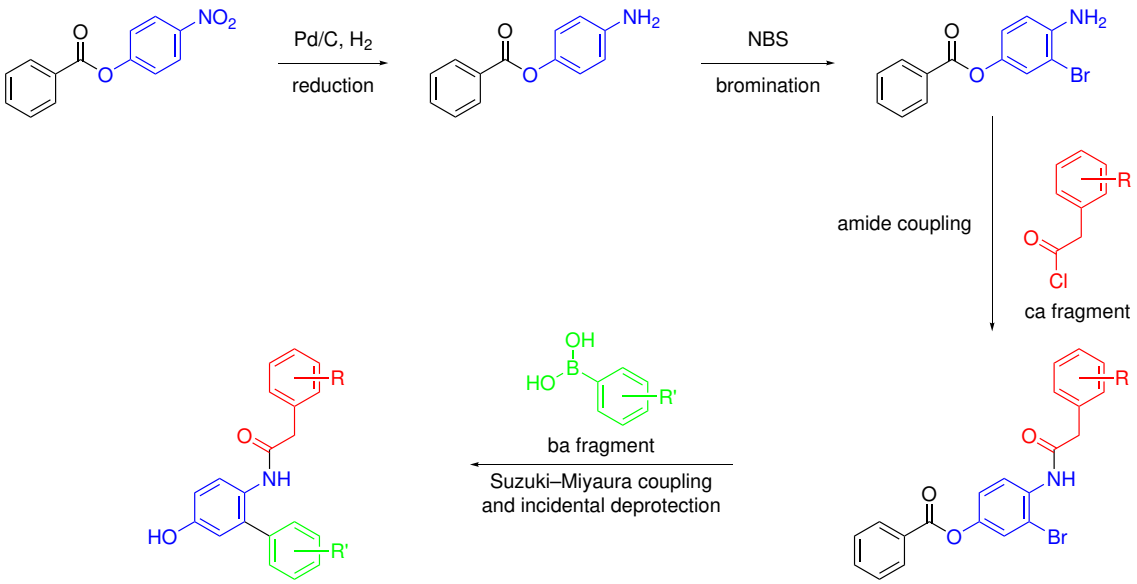

Scheme 4: Outline of the previously established molecular synthesis route.[48] Protecting group steps necessary for certain individual fragments are omitted for clarity. Illustration taken from earlier work of the author.[48]

The modular synthesis approach outlined in Scheme 4 was followed for the synthesis of the ligand library in this study. A brief discussion on the development of this synthetic sequence prior to this work is provided in Section 2.8.2. Both the amide coupling and the Suzuki–Miyaura coupling (SMC) allow for the diversification of the final product through the introduction of functionalized carboxylic acid (ca) or boronic acid (ba) fragments. Originating from one shared starting material, the amide coupling provides a first branching point from which multiple common intermediates for the following SMCs are generated. Each of those common intermediates can then again be branched into multiple products at the SMC step. This way, a great number of combinations can be synthesized from a limited number of building blocks. Amide coupling and Suzuki–Miyaura coupling are both widely established for this type of approach and are among the most used chemical reactions today.[198,199] In 2018, Boström *et al.* even reported them as the first and second most frequently used reactions in drug discovery programs.[199]

5.3.1 Synthesis of the Core Scaffold

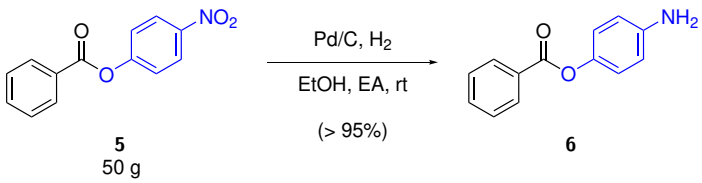

Scheme 5: Hydrogenation of the nitro group of 4-nitrophenyl benzoate **5** using H_2 catalyzed by Pd/C to afford 4-aminophenyl benzoate **6**.

The synthesis started from commercially available 4-nitrophenyl benzoate **5**, which was hydrogenated to an amine using H_2 and Pd/C as catalyst, as illustrated in Scheme 5. Up to a scale of 10 g nitrophenol **5** the reaction was performed at atmospheric pressure using a balloon achieving quantitative yield within a few hours. Scaling up to 50 g nitrophenol **5** the reaction time at atmospheric pressure extended to multiple days, which necessitated the use of an autoclave as the reaction vessel. At 9 bar the reaction was feasibly performed at a scale of 50 g nitrophenol **5**, achieving quantitative yield.

It should be noted, that due to its setup, the autoclave was not used at a constant pressure. Instead, it was filled with H_2 to 9 bar, then the connected gas-bottle was closed off. As the reaction proceeded and H_2 was consumed, the pressure on the autoclave gradually decreased and was manually raised to 9 bar again (every ~15–20 min). This procedure was repeated over the course of 3 days, at night no additional H_2 was added and the reaction stirred at rt. With an autoclave setup that allows for working at a constant pressure, the hydrogenation can likely be performed in a much shorter time frame.

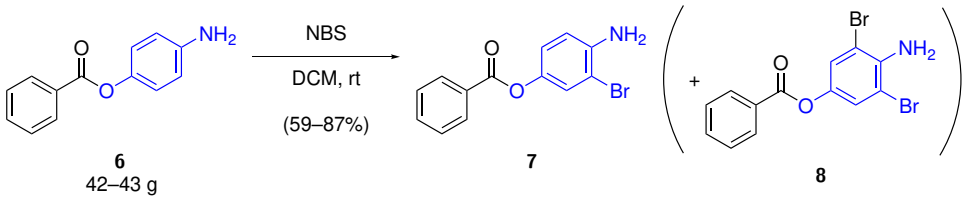

Scheme 6: Bromination of 4-aminophenyl benzoate **6** ortho to the amine group using NBS to afford 4-amino-3-bromophenyl benzoate **7**. Under less optimized reaction conditions formation of dibrominated 4-amino-3,5-dibromophenyl benzoate **8** was also observed.

4-Aminophenyl benzoate **6** was brominated ortho to its amine function using *N*-bromosuccinimide (NBS) under non-radical conditions, as illustrated in Scheme 6. To avoid over-bromination 1.0 eq of NBS was added as a solid in two portions and monitoring by TLC ensured that the first portion of NBS had been consumed before addition of the next one. At a scale of 8.5 g of 4-aminophenyl benzoate **6** a yield of 81% was achieved. Scaling up to 43 g of 4-aminophenyl benzoate **6**, 1.25 eq of NBS were added as a solid in five subsequent portions. This time, dibrominated 4-amino-3,5-dibromophenyl benzoate **8** was observed as a significant side product, which needed to be removed by flash column chromatography decreasing the yield to 59%. Repeating the bromination at 42 g scale of 4-aminophenyl benzoate **6** reaction conditions needed to be adjusted. To minimize formation of side product **8**, 4x 0.25 eq of NBS were dissolved in acetone and each portion was added slowly into the reaction mixture using a dropping funnel. Monitoring by TLC ensured the consumption of NBS before addition of the next portion. With these adaptations, a yield of 87% was achieved.

Together, these two reaction steps allowed to synthesize 4-amino-3-bromophenyl benzoate **7**, as the common precursor for all following ligands on decagram scale starting from 50 g 4-nitrophenyl benzoate **5**, providing a solid foundation for the following library generation.

5.3.2 Synthesis of Protected Carboxylic Acid Building Blocks

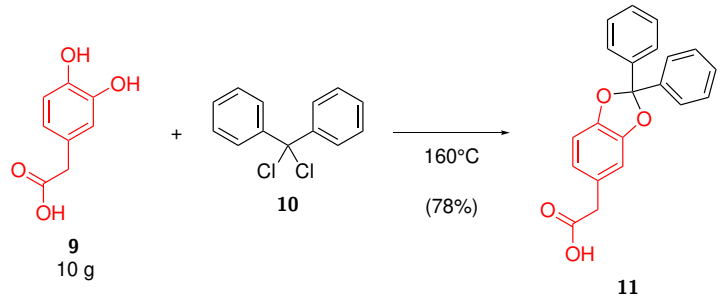

Scheme 7: Protection of 3,4-dihydroroxyphenylacetic acid **9** using dichlorodiphenylmethane **10** carried out on 10 g scale of carboxylic acid **9**.

The carboxylic acid fragment L **9** featured a 1,2-dihydroxybenzene functionality that needed to be protected prior to the amide coupling and the Suzuki–Miyaura coupling. For this purpose, the formation of an acetal, illustrated in Scheme 7 *via* the use of dichlorodiphenylmethane **10**, as reported by Blagg *et al.*[200] had been explored in previous work of the author.[48] Since then, the reaction conditions had been improved. Notably, the reaction was performed without solvent and following consumption of the unprotected carboxylic acid **9**, toluene was added to the reaction mixture, as it was allowed to cool down. Addition of toluene avoided solidification of the reaction mixture into a tar-like film, which otherwise only slowly dissolved. Instead, the reaction mixture remained liquid, simplifying the subsequent workup. Following extraction with NaOH (aq., 2 M), the product was precipitated by acidification with HCl (aq., conc.), which provided 2-(2,2-diphenylbenzo[*d*][1,3]dioxol-5-yl)acetic acid **11** in sufficient purity for further synthesis. Conversely, to obtain compound **11** in high purity, flash column chromatography (PE/EA in various ratios) was performed without issues and addition of 1% acetic acid to the fluent was similarly tolerated. The reaction was performed at a scale of 10 g 3,4-dihydroroxyphenylacetic acid **9** with a yield of 78%. The acetal protecting group would later be removed under acidic conditions.

5.3.3 Amide Couplings

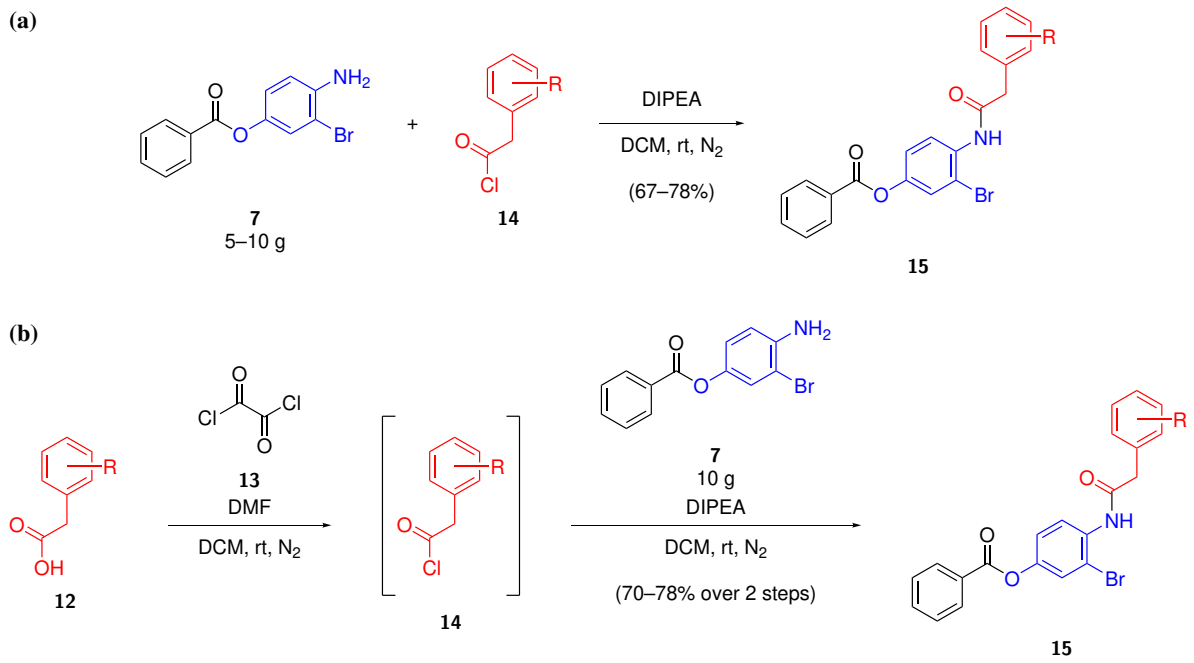

Scheme 8: Amide coupling methods utilized. **Method (a):** Acid chloride **14** was coupled with amine **7** under basic conditions in one step. **Method (b):** Acid chloride **14** was first generated *in situ* from carboxylic acid **12** using oxalyl chloride **13**, then coupled with amine **7** under basic conditions in a second step.

In order to connect the carboxylic acid fragment onto the core scaffold, an amide coupling was performed. As described in Section 2.8, the use of amide coupling reagents such as EDC • HCl and HOBt was found to be unsuccessful. Instead the carboxylic acid building blocks were employed as acid chlorides and coupled with the amide of the core scaffold under basic conditions.[48]

For some building blocks, the acid chloride was commercially available and was used as delivered. In cases where the corresponding acid chloride was not commercially available or to unstable to be stored without decomposition, the respective carboxylic acid was employed and the acid chloride generated *in situ* using oxalyl chloride. Following the reaction, excess oxalyl chloride was removed under reduced pressure. The two described amide coupling methods are shown in Scheme 8. Some of the obtained amides could conveniently be purified by recrystallization. Table 5 provides a summary of the achieved yields for all examined carboxylic acid fragments, as well as which coupling and purification methods had been used.

Table 5: Summary of amide couplings performed, together with their method of coupling and purification found to be viable. **Conditions: Method (a):** 1.0 eq amine **7**, 1.2 eq acid chloride, 1.2 eq DIPEA, DCM, N_2, rt. **Method (b):** 1.2 eq carboxylic acid, 3.0 eq oxalyl chloride **13**, drops of DMF, DCM, N_2, rt, then 1.0 eq amine **7**, 1.5 eq DIPEA, DCM, N_2, rt. Individual deviations from these conditions are specified respectively.

Number	Chemical Structure	Coupling Method	Scale of Amine **7**	Yield	Purification Method	Comment
63	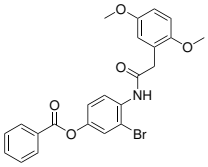	(b)	10 g	70%	recrystallization	4.5 eq oxalyl chloride
65	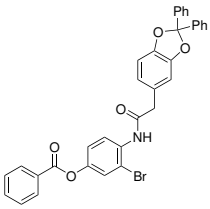	(b)	10 g	78%	flash column chromatography & recrystallization	-
67	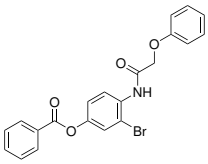	(a)	5 g	67%	recrystallization	-
18	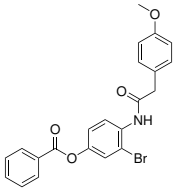	(a)	10 g	78%	recrystallization	1.3 eq DIPEA

5.3.4 Suzuki–Miyaura Couplings

(a)

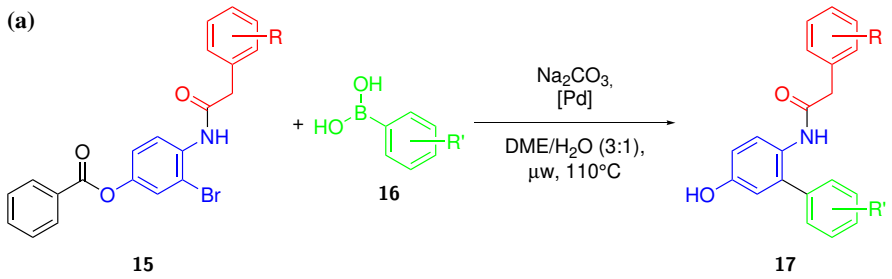

(b)

Yield	Vessel	[Pd]
68–89%	10 ml	PEPPSI-IPr
58–91%	10 ml	$Pd(dppf)Cl_2$
30–37%	35 ml	PEPPSI-IPr

Scheme 9: Suzuki–Miyaura coupling (SMC) reaction between a bromide **15** and a boronic acid **16**. Under the basic conditions and elevated temperature during the microwave reaction the benzoate protecting group is removed in the same reaction step.[48,159] **(a):** Generalized reactions scheme. **(b):** Achieved yields in dependence of the size of the reaction vessel and the utilized Pd catalyst.

To connect the boronic acid fragment and its functionalities onto the core scaffold, a Suzuki–Miyaura coupling (SMC) was performed, shown in Scheme 9. The reactions were carried out under microwave conditions as previously reported.[48,159] The overall aim for the SMCs was to establish general reaction conditions, allowing a number of substrates to be coupled without individual adjustments. The goal was therefore, to focus on simplicity and speed for the generation of the ligand library, rather than achieving the highest possible yield for each individual substrate combination. If among the developed ligands a hit compound would be identified, which warrants extensive follow up experiments, a separate effort to optimize its individual synthesis could still be undertaken.

The initial reaction conditions of Ar^1-Cl (1.0 eq), Ar^2-$B(OH)_2$ (1.1 eq), $Pd(PPh_3)_4$ (5 mol%), Na_2CO_3 (2.0 eq), DME:H_2O (3:1) under microwave irradiation at 110°C for 10 min, were taken from the publication of Blaise *et al.*[159,201] and were adapted by Mrđen Debono[159] and further refined in previous work of the author.[48] Some of these modifications shall be discussed in the following.

It was observed that extension of the reaction time to 30 min or more promoted complete benzoate deprotection next to the SMC itself.[48] The reaction time was therefore generally extended to 1 h under microwave irradiation.

A screening of four common Pd catalysts was performed on the example reaction towards ligand APE **20** as shown in Scheme 10. The aim was to investigate if replacement of $Pd(PPh_3)_4$ with a more modern catalyst such as PEPPSI-IPr[202] or $Pd(dppf)Cl_2$[203] could improve the SMC. The results are summarized in Table 6.

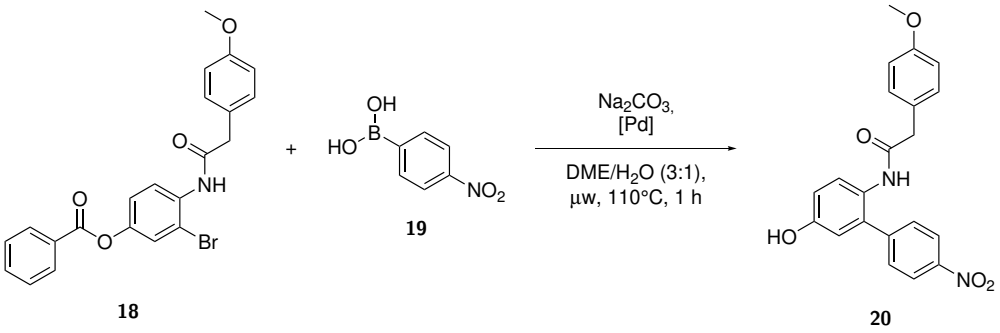

Scheme 10: Test reaction for the screening of Pd-catalysts.

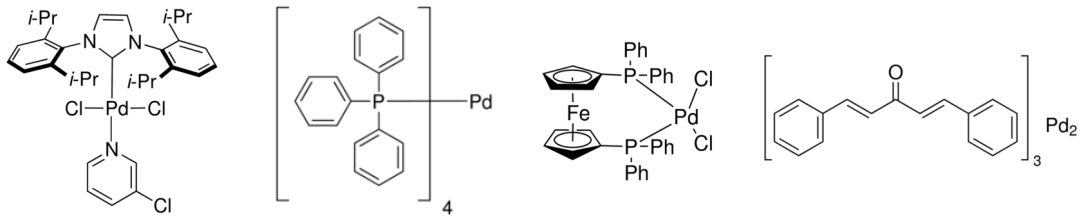

Figure 33: Catalysts screened in the Suzuki–Miyaura test reaction.

Table 6: Summary of the catalyst screening results.

Entry	Catalyst	Catalyst Loading	Yield
1	PEPPSI-IPr	4 mol%	77%
2	$Pd(PPh_3)_4$	1 mol%	64%
3	$Pd(dppf)Cl_2$	1 mol%	48%
4	$Pd_2(dba)_3$	1 mol%	25%

Among the four catalysts tested, PEPPSI-IPr gave the highest yield and it was therefore employed in the following synthesis of the other ligands. A higher catalyst loading was used in entry 1, compared to the other entries. Beyond this catalyst screening, in this study it had been observed, that catalyst loadings of 1–5 mol% afforded about the same yields for the SMCs. The potential influence of a higher catalyst loading in entry 1, compared to the other entries was therefore disregarded. The SMCs of this work typically used 5 mol% PEPPSI-IPr as Pd-catalyst.

In general, this study utilized degassed DME:H_2O 3:1 and 2.0 eq of Na_2CO_3 as solvent and base of the SMCs. 1,2-Dimethoxyethane (DME) can be considered a classical solvent for this reactions. Together with an aqueous solution of a base *e.g.* Na_2CO_3 it provides good solubility for a range of substrates, facilitating homogeneous catalysis.[204] DME can reduce Pd^{II} pre-catalysts such as PEPPSI to the corresponding catalytically active Pd^0-complexes.[205,206] Other solvents may also be used in SMCs and have been reported. DMF and dioxan are common examples, but alcohols such as MeOH, EtOH and iPrOH have also been used with great success in certain examples.[201,202]

Other reaction conditions such as type of base, temperature and equivalents of boronic acid were only varied occasionally. Typically, 1.2 eq of boronic acid were employed.

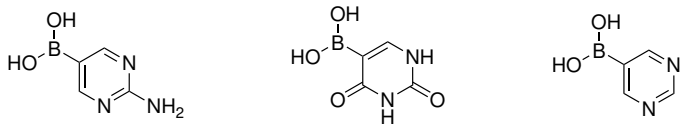

ba-A **21** ba-B **22** ba-C **23**

Figure 34: Examples of boronic acid substrates that were observed to be challenging coupling partners.

It was observed that the nature of the boronic acid had a great influence on the success and yield of the SMC. This was to be expected and especially heteroaromatic boronic acids have been known to be challenging substrates.[207,208] Examples of challenging boronic acids that were attempted to be used are given in Figure 34. For these, yields of around 10% and lower were achieved, typically in single reactions and found to not be reproducible. Substrate ba-A **21** has been reported as a coupling partner in SMCs by Clapham *et al.*[209] and examples for ba-B **22** are reported by Doig *et al.*.[210] Notably, ba-C **23** was reported by Wilson *et al.* as one of the substrates included in their scope and with a yield of 44% was the worst substrate listed.[211]

A potential future remedy for these challenging examples could be to vary the nature of the boron reagent. Instead of employing the building blocks as boronic acids, one could try their derived boronic esters, as they also undergo SMC and under optimized conditions have been shown to react faster and in higher yield as the corresponding boronic acid as exemplified by Kassel *et al.*.[212] Aside from boronic esters, triflouroboronates or MIDA-boronates could also be investigated as reviewed by Lennox and Lloyd-Jones.[213]

One curious detail, which was observed with respect to the microwave reaction setup, was that the choice of 10 or 35 ml reaction vessels had a noticeable influence on the reaction yield. Generally, the 35 ml vessels lead to a drop in yield when scaling up from their 10 ml counterparts. Some examples of this effect are listed in Table 7. Because some of the Suzuki–Miyaura couplings described in this study had only been performed in one size of vessel they are not listed. Similarly, not every single repetition of a given reaction is listed, as for some of them further parameters were varied preventing a reasonable comparison.

Table 7: Comparison of example Suzuki–Miyaura reactions performed with 10 and 35 ml microwave reaction vessel sizes. **Conditions:** 1.0 eq bromide, 1.1 or 1.2 eq boronic acid, 2.0 eq Na_2CO_3, 5 mol% PEPPSI-IPr, degassed DME:H_2O 3:1, microwave irradiation at 110°C for 1 h of reaction time. Individual deviations from these conditions are specified respectively.

Target Compound	Number of Vessels & Solvent per Vessel	Size of Vessels	Yield
ABE **24**	5x 5 ml	10 ml	77%
ABE **24**	1x 10 ml	35 ml	42%
AOD **25**	5x 5 ml	10 ml	71%
AOD **25**	2x 25 ml	35 ml	24%
APE **20**	5x 5 ml	10 ml	68%
APE **20**	1x 23 ml	35 ml	40%

It is well known that microwave reactions are prone to irregularities in heating of the reaction mixture due to the way temperature is typically monitored by the instrument.[214] It is therefore very well possible that the difference in solvent volume and solvent vessel contact area between the two vessel sizes may be the cause of these observed difficulties when scaling up with this particular setup. While more labor intensive, scale up was therefore typically performed by carrying out multiple reactions on 10 ml reaction vessel scale, then combining them for workup and purification. A summary of all SMCs carried out including their yields is provided in Table 8.

Table 8: Summary of the SMCs successfully performed in this study and their yields. **Conditions:** 1.0 eq of bromide, 1.1 or 1.2 eq of boronic acid, 2.0 eq of Na_2CO_3, 5 mol% PEPPSI-IPr, degassed DME:H_2O 3:1, microwave irradiation at 110°C for 1 h of reaction time. Reactions were performed at a scale of 5x 5 ml solvent in 10 ml vials. Individual deviations from these conditions are specified respectively.

Ligand Code & Number	Chemical Structure	Yield	Comments
ABD **26**	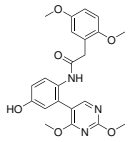	37%	1x 17.5 ml solvent in 35 ml vials
ABE **24**	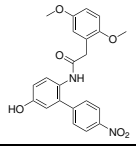	77%	-
ALD (+PG) **27**	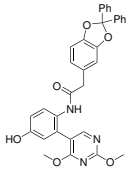	85%	-
ALE (+PG) **28**	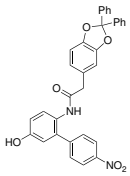	89%	-
AOD **25**	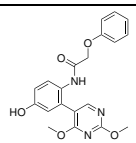	71%	-
AOE **29**	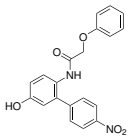	30%	1x 25 ml solvent in 35 ml vials
AOT **30**	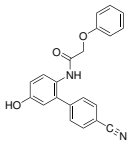	91%	$Pd(dppf)Cl_2$ as catalyst
APD **31**	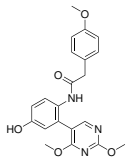	58%	$Pd(dppf)Cl_2$ as catalyst
APE **20**	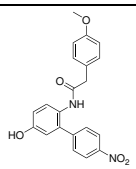	68%	-
APT **32**	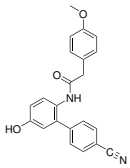	72%	-

5.3.5 Deprotections

(a)

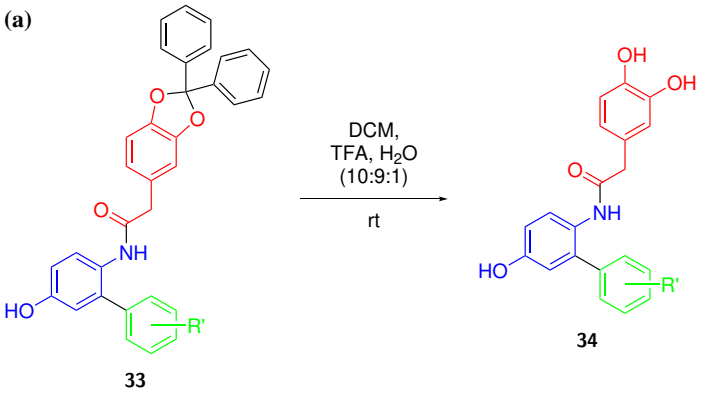

(b)

Product	Scale of Starting Material	Yield
ALD **35**	67 mg	83%
	163 mg	45%
	718 mg	29%
ALE **36**	50 mg	36%
	82 mg	80%
	662 mg	87%

Scheme 11: Removal of the acetal protecting group under acidic conditions affording ligands ALD **35** and ALE **36**. **(a):** Generalized reactions scheme. **(b):** Achieved yields in dependence of reaction scale and the obtained product.

As mentioned in Section 5.3.2 ca-L **9** featured a 1,2-dihydroxybenzene functionality that needed to be protected during the amide coupling and the Suzuki–Miyaura coupling. To this end, an acetal protecting group had been employed as reported by Blagg *et al.*.[200] Therein, the authors reported deprotection by refluxing in AcOH/H_2O (9:1) for 2 h. A simple TLC screening of a test reaction comparing aqueous solutions of acetic acid or trifluoroacetic acid (TFA) with and without DCM as cosolvent revealed that DCM/TFA/H_2O (10:9:1) was sufficient to remove the acetal group at rt over a similar time scale, shown in Scheme 11a. Following the reaction, DCM and TFA were conveniently removed in a stream of N_2, followed by removal of H_2O by lyophilization. The formed benzophenone was then removed by flash column chromatography. It was observed that upon scale-up the yield decreased in the case of ligand ALD **35**, while it improved in the case of ligand ALE **36**, as summarized in Scheme 11b. This was not further investigated, but the purification by flash column chromatography was suspected to be the critical factor, as ALD **35** was observed to be very polar, resulting in tailing during the elution.

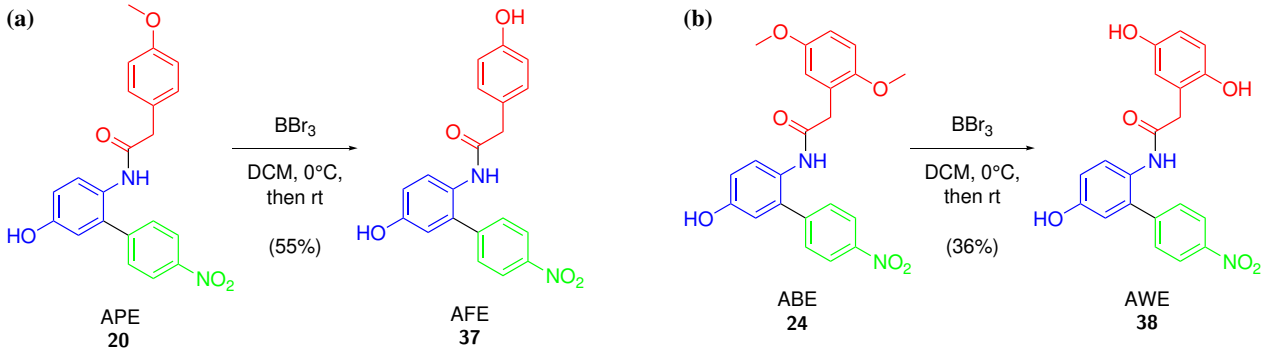

Scheme 12: Transformation of aromatic methoxy groups into aromatic hydroxyl groups using BBr_3. **(a):** Transformation of ligand APE **20** into AFE **37**. **(b):** Transformation of ligand ABE **24** into AWE **38**.

To diversify the ligand library, it was envisioned that transformation of methoxy groups into phenol groups could be employed. On the one hand this provides a protecting group strategy for ligands carrying phenols, on the other hand the corresponding methoxy derivatives were tested as ligands themselves. Therefore, in applicable cases, extension of the synthesis sequence by only one step conveniently provided another ligand for the library to be examined *in vitro*. A classical approach for

this transformation is the use of Lewis acidic BBr_3[215–217] in an inert solvent such as DCM, benzene or pentane at room temperature or lower. While BBr_3 can be considered a harsh reagent, its compatibility with amides has been reported.[218] McOmie *et al.* recommended to use at least 1.0 eq of BBr_3 per methoxy group, as the formed Ar-O-BBr_2 complex is only hydrolyzed upon quenching by addition of H_2O, as well as another 1.0 eq of BBr_3 per functional group present that may coordinate BBr_3.[216] In this study a modified procedure from Roy *et al.*[219] was used, utilizing DCM as solvent and adding BBr_3 as a solution in DCM at 0°C, then stirring the reaction mixture at rt for a few hours or over night followed by quenching with H_2O and MeOH. A yield of 55% for ligand AFE **37** and 36% for ligand AWE **38** was achieved. Both of these reactions were only performed a limited number of times and the reaction conditions, namely eq of BBr_3, temperature during and after addition of BBr_3 and time at each of those temperatures were not systematically investigated. Therefore, yields could potentially be increased by optimizing the reaction conditions.

In the bachelor thesis of Janica Wendt,[197] which was part of this study, the viability of other demethylation reagents, namely 1-dodecanethiol and iodocyclohexane was investigated, but both were found to be unsuccessful for the tested ligands.

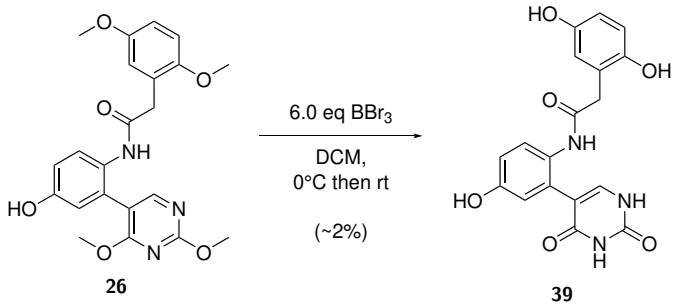

26 **39**

Scheme 13: Single reaction example of multiple simultaneous demethylations by BBr_3 providing access to the functionality of ba-B.

In an attempt to access ba-B, which had previously been shown to be a challenging substrate for SMCs, a transformation of ba-D moiety into ba-B using BBr_3 following the SMC was envisioned. While these attempts were generally unsuccessful, a single reaction (shown in Scheme 13) yielded AWB **39** in ~2% yield, indicating that this transformation is in principle possible. However, due to the low amount of product (1.6 mg) and low quality characterization data that had been obtained, this reaction would need to be repeated, in order to confirm the identity of the product and the viability of this approach.

5.4 HPLC Purifications of hSOD1 Ligands

While purification by flash column chromatography was able to remove most impurities following chemical synthesis, some still remained as evident in the ^{1}H NMR spectra of some of the ligands. An example is shown in Figure 35. Since proteins and biophysical assays can be very sensitive, these impurities needed to be removed to ensure they would not skew the results of the following assays. All small molecule hSOD1 ligands were therefore purified by reversed-phase HPLC. Technical details such as machines, buffers and columns are provided in Section 9.8. Table 9 lists all ligands, gradients and achieved purities. The individual analytical HPLC chromatograms can be found in Section 10.9. Commonly an acid such as 0.1% (v/v) TFA is added to HPLC buffers to prevent deprotonation of weakly acidic analytes, ensuring desired interaction with the unpolar stationary phase and improving separation.[220] However, the use of TFA should be avoided for studies in a pharmacological context. Interactions of residual TFA with proteins or cells, which can negatively effect biological experiments, have been reported in multiple examples.[221] Instead of TFA, 0.1% (v/v) formic acid was therefore used as an additive, which is generally regarded as compatible with *in vitro* studies of proteins.[222] For most ligands the sample loading onto the HPLC column was limited by their solubility in acetonitrile/water mixtures. To alleviate this, DMSO was used as a cosolvent in sample preparation, which only slightly reduced retention times and was itself eluted at the very start of the run. Moreover, samples were dissolved by sequentially adding DMSO, then acetonitrile, then H_2O, which temporarily allowed to dissolve a greater amount of sample. Sample solutions were typically prepared with a H_2O/MeCN ratio matching the A/B ratio at the start of the gradient + 10–20% (v/v) DMSO. With the exception of ligands ABD **26**, ALD **35** and AWE **38** a purity of > 99% was achieved, as determined by analytical HPLC.

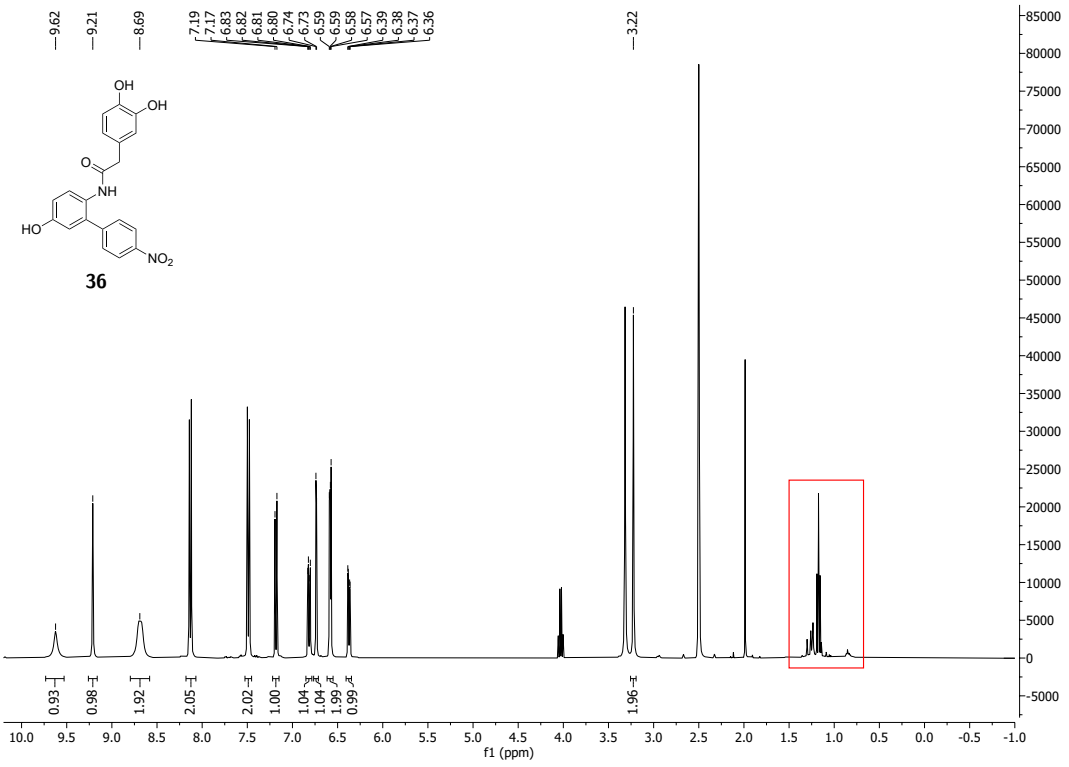

Figure 35: ^{1}H NMR (400 MHz, DMSO−d_6) spectrum of ligand ALE **36** following purification by flash column chromatography. Impurities that needed to be removed by HPLC prior to biophysical assays are highlighted in red. A ^{1}H NMR spectrum of the same compound following HPLC purification is provided on page 236.

Table 9: Summary of the gradients used in the HPLC purification of the ligands and their achieved purities. Achieved Purity refers to the lowest batch purity used in biophysical assays. Buffer A = H_2O + 0.1% HCOOH, Buffer B = MeCN + 0.1% HCOOH.

Ligand Code & Number	Chemical Structure	Gradient used	Achieved Purity
ABD **26**	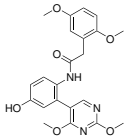	40–60% B in A over 30 min	> 98%
ABE **24**	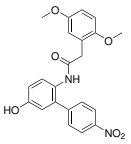	30–80% B in A over 30 min	> 99%
AFE **37**	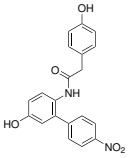	40–60% B in A over 30 min	> 99%
ALD **35**	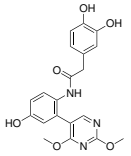	20–40% B in A over 30 min	> 97%
ALE **36**	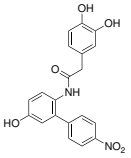	30–60% B in A over 30 min	> 99%
AOD **25**	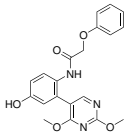	30–80% B in A over 30 min	> 99%
AOE **29**	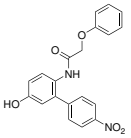	50–70% B in A over 30 min	> 99%
APD **31**	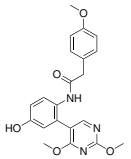	30–80% B in A over 30 min	> 99%
APE **20**	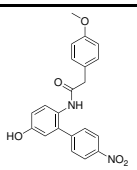	30–80% B in A over 30 min	> 99%
APT **32**	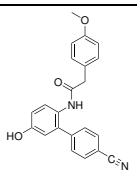	30–80% B in A over 30 min	> 99%
AWE **38**	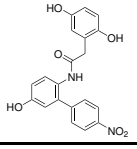	30–50% B in A over 30 min	> 94%

5.5 Ligand Solubility Measurements

Prior to biophysical experiments, solubility of the ligands in the assay buffer system consisting of 80% aqueous buffer (100 mM HEPES, 150 mM NaCl, pH = 7.4) and 20% DMSO cosolvent was determined, as detailed in Section 9.10.4, to ensure that they would not precipitate over the duration of the experiments.

As discussed in Section 2, pyrimethamine **40** (Section 2.4.1) and trehalose **41** (Section 2.6.1) have been investigated as potential therapeutic agents in the context of hSOD1 related ALS research. To examine if pyrimethamine interacts with hSOD1 directly, possibly reducing its aggregation, it was included in the following assays. Similarly, in order to investigate if trehalose could prevent hSOD1 aggregation by directly interacting with the protein in isolation or if the effects reported *in vivo* are due to a mode of action unspecific to hSOD1, it too was included in the following assays. As will be discussed in Section 5.6.4, the building block ca-L **9** was also included in the following assays. Therefore, in addition to the investigated ligands, the solubility of these compounds in the assay buffer system was determined by the same procedure.

While this was a manual process and the thereby determined kinetic solubility is naturally subject to some amount of uncertainty,[223] it provided a safe estimate to prevent problems caused by precipitation of ligands during the following assays. The observed ligand solubilities are summarized in Table 10. In cases where the maximum solubility value of a ligand was observed to be in between two of the prepared incremental concentrations, follow up measurements with more narrowly spaced increments were only carried out if there was a specific need for a more precise quantification.

Table 10: Summary of the ligand's observed maximum solubilities in 80% aqueous buffer (100 mM HEPES, 150 mM NaCl, pH = 7.4) and 20% DMSO.

Ligand Name or Code & Number	Chemical Structure	Maximum Solubility [mM]
ABD **26**	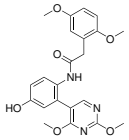	5.0–10.0
ABE **24**	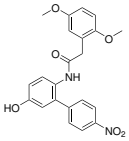	0.5–1.0
AFE **37**	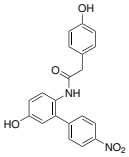	5.0–10.0
ALD **35**	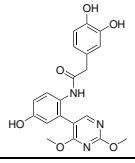	> 20.0

Table 10: *(continued)* Summary of the observed maximum ligand solubilities in 80% aqueous buffer (100 mM HEPES, 150 mM NaCl, pH = 7.4) and 20% DMSO.

Ligand Name or Code & Number	Chemical Structure	Maximum Solubility [mM]
ALE **36**	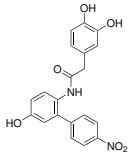	10.0–15.0
AOD **25**	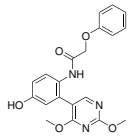	5-0–10.0
AOE **29**	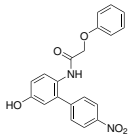	0.2
APD **31**	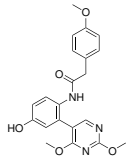	15.0–20.0
APE **20**	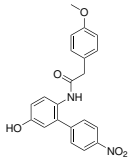	1.0–1.5
APT **32**	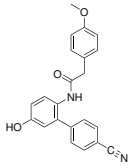	1.0–1.5
AWE **38**	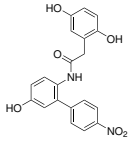	5.0–10.0
pyrimethamine **40**	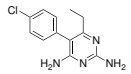	0.5–1.0
trehalose **41**	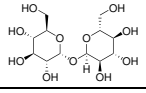	> 20.0
ca-L **9**	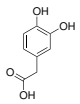	15.0–20.0

5.6 Expression and Characterization of hSOD1

In order to serve as an *in vitro* model of ALS-related mutant hSOD1 aggregation, the hSOD1 protein and its hSOD1 A4V variant were recombinantly expressed and their purification established in the Thomas group. The expression of hSOD1 and hSOD1 ALS related A4V variant in *E. coli.* and their purification by multiple chromatography techniques will be summarized and discussed below. Detailed procedures of each step are provided in the appendix (Section 9.9).

5.6.1 Expression of hSOD1

Plasmids carrying hSOD1 and hSOD1 A4V had been provided for this study, as described in Section 9.9.5. Plasmid preparation was carried out in *E. coli* strain NEB 5-alpha.

For the expression of hSOD1 a modified procedure from Mrđen Debono was used.[159] *E. coli.* strain BL21 (DE3) was transformed with the hSOD1-encoding plasmids *via* heat shock and cultivation was performed in LB medium containing ampicillin (100 µg/ml). The main culture was grown at 37°C while shaking until an OD_{600} of about 0.5 was reached. The culture was then cooled to 22°C and expression induced by addition of isopropyl-β-D-thiogalactopyranosid (IPTG) (0.4 mM final conc.). Expression was carried out at 22°C while shaking over night. Cells were harvested by centrifugation and for a batch of 3 l main culture 4.8 and 5.8 g cells per 1 l medium were obtained for wt hSOD1 in two separate replications and 4.0 g cells per 1 l medium were obtained for hSOD1 A4V in a single replication. The resulting cell pellet was divided into two equally sized aliqouts, flash frozen in liquid N_2 and stored at -80°C.

5.6.2 Purification of hSOD1

For the purification of hSOD1, a modified procedure from Mrđen Debono was used.[159] For one purification-batch, one cell pellet aliqout (about 6–8 g cells) was used. Following cell disruption with a high-pressure homogenizer and lysis, hSOD1 needed to be separated from the other lysate components. Dialysis and centrifugation removed most non-protein contaminants and separation of the obtained protein mixture was achieved by multiple chromatography steps. Since the expressed hSOD1 did not carry an affinity tag, affinity chromatography was not performed.

For hSOD1 an isoelectric point (pI) of 5.70 was predicted using the ProtParam web tool from the Swiss Institute of Bioinformatics.[224] The results of the prediction can be viewed online.[225] Previously, Mrđen Debono[159] had performed IEX at a buffer pH of 8.0, at which hSOD1 is net negatively charged, with a manually packed 50 ml TMAE column filled with Fractogel EMD TMAE 650 (S) from Merck, a resin with a strong cation functional group. As this exact column was not available possible replacements were explored, namely a Mono Q 5/50 GL (CV = 1 ml) and a RESOURCE Q (CV = 6 ml) from Cytiva. Both yielded unsatisfactory separation. The charged functional groups for TMAE ($R-CH_2-CH_2-N^+-(Me)_3$) and Q ($R-CH_2-N^+-(Me)_3$) resins are very similar only differing by one methylene group, but vary in the type of matrix as well as their accompanying particle size and distribution, which can have a secondary effect on resolution. Circling back to the established procedure by Mrđen Debono a MiniChrom Column Fractogel TMAE (S) (CV = 5 ml) from Merck was purchased and IEX repeated. The achieved separation was much better, but the presence of other proteins with a size of around 55 kDa was still observed by SDS-PAGE. In order to remove these, it was decided to perform an additional chromatography step following IEX, based on a different protein property for separation. Further, while the purchased Fractogel TMAE (S) column provided satisfactory purification, its protein binding capacity would be exceeded when attempting to purify the entire protein mixture of one purification batch at once, necessitating a larger column of the same type. Limited by the size of pre-packed, commercially available Fractogel TMAE (S) columns, a 50 ml column was manually packed with Fractogel TMAE (S) resin, which is commercially available in bulk. The packing procedure is detailed in Section 9.9.4.

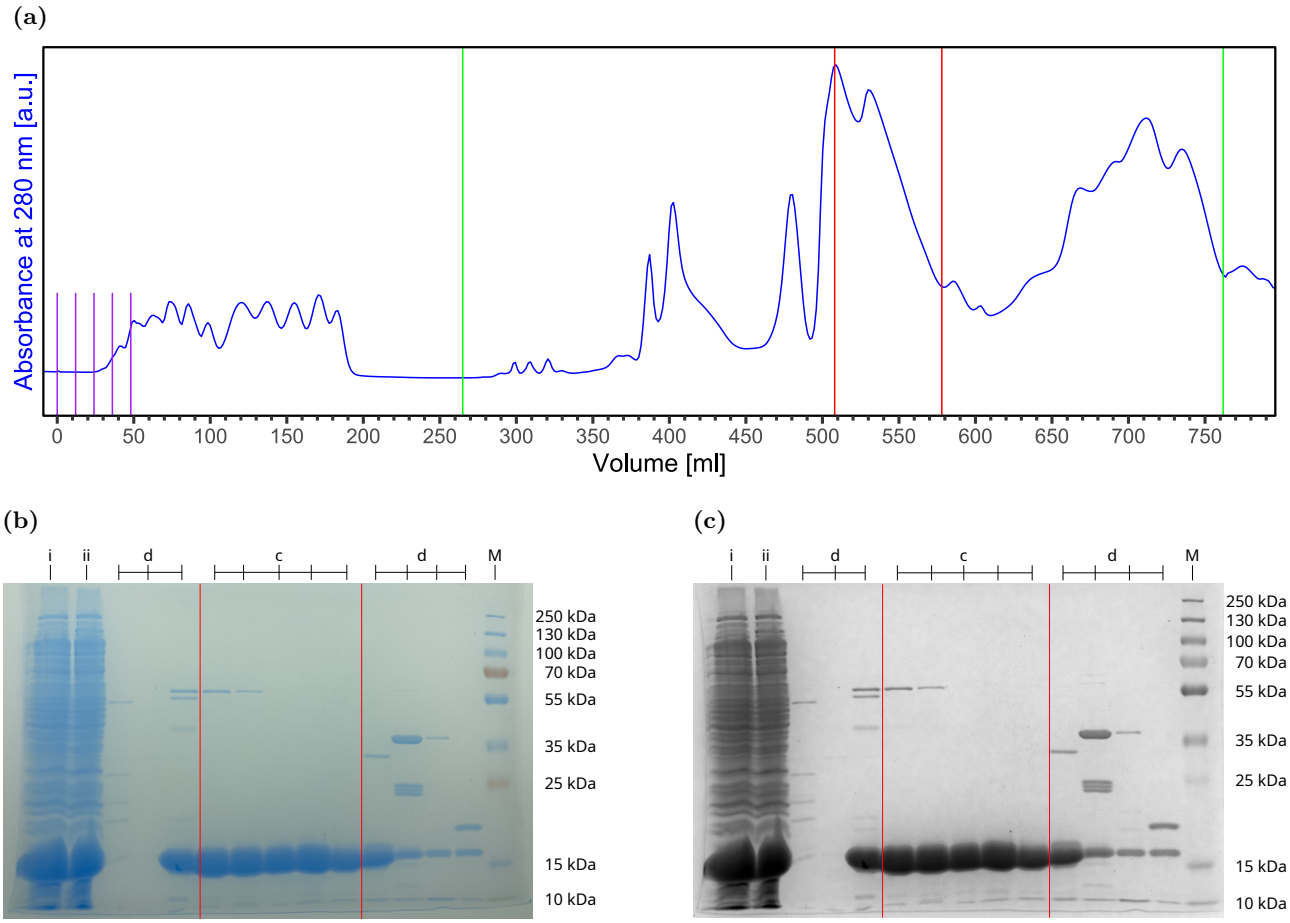

Figure 36: Example of an IEX purification of hSOD1 with the manually packed TMAE column (CV = 50 ml) on an ÄKTA. **(a):** Excerpt of the IEX chromatogram, showing the following steps: Sample application, washing away of unbound proteins and linear gradient elution of bound proteins. The subsequent washing away of any remaining bound proteins and regeneration of the resin are not shown. Injections of sample are shown in purple. The start and end of the gradient from 0–20% Buffer B in Buffer A are shown in green. The start and end of fractions, which contained hSOD1 and were combined for further use are shown in red. **(b, c):** SDS-PAGE gel following IEX, stained with GelCode Blue Safe Protein Stain (b), then imaged with a gel imaging system in greyscale (c). Lanes between the red lines correspond to fractions containing hSOD1 that were combined for further use. i: Supernatent following lysis. ii: Following dialysis in Buffer A, IEX sample solution. c: Collected fractions. d: Discarded fractions. M: Marker. The detailed procedure of this purification is provided in Section 9.9.7.

Ultimately, IEX purification of hSOD1 was performed with this manually packed TMAE column (CV = 50 ml) on an ÄKTA, shown in Figure 36. The obtained protein fractions were analyzed by SDS-PAGE and fractions containing hSOD1 were combined and dialyzed over night. Early in this investigation, IEX repetitions used a 10 ml loop for the ÄKTA, which meant that multiple injections were needed to inject the entire protein mixture sample (about 45 ml) onto the column. As discussed in Section 4.1, this in itself is not an issue, as long as the column's protein binding capacity is not exceeded. Later in this investigation, IEX repetitions utilized a 50 ml Superloop from Cytiva, allowing injection of up to 50 ml sample solution at once without any sample loss, making injection of sample faster and more convenient.

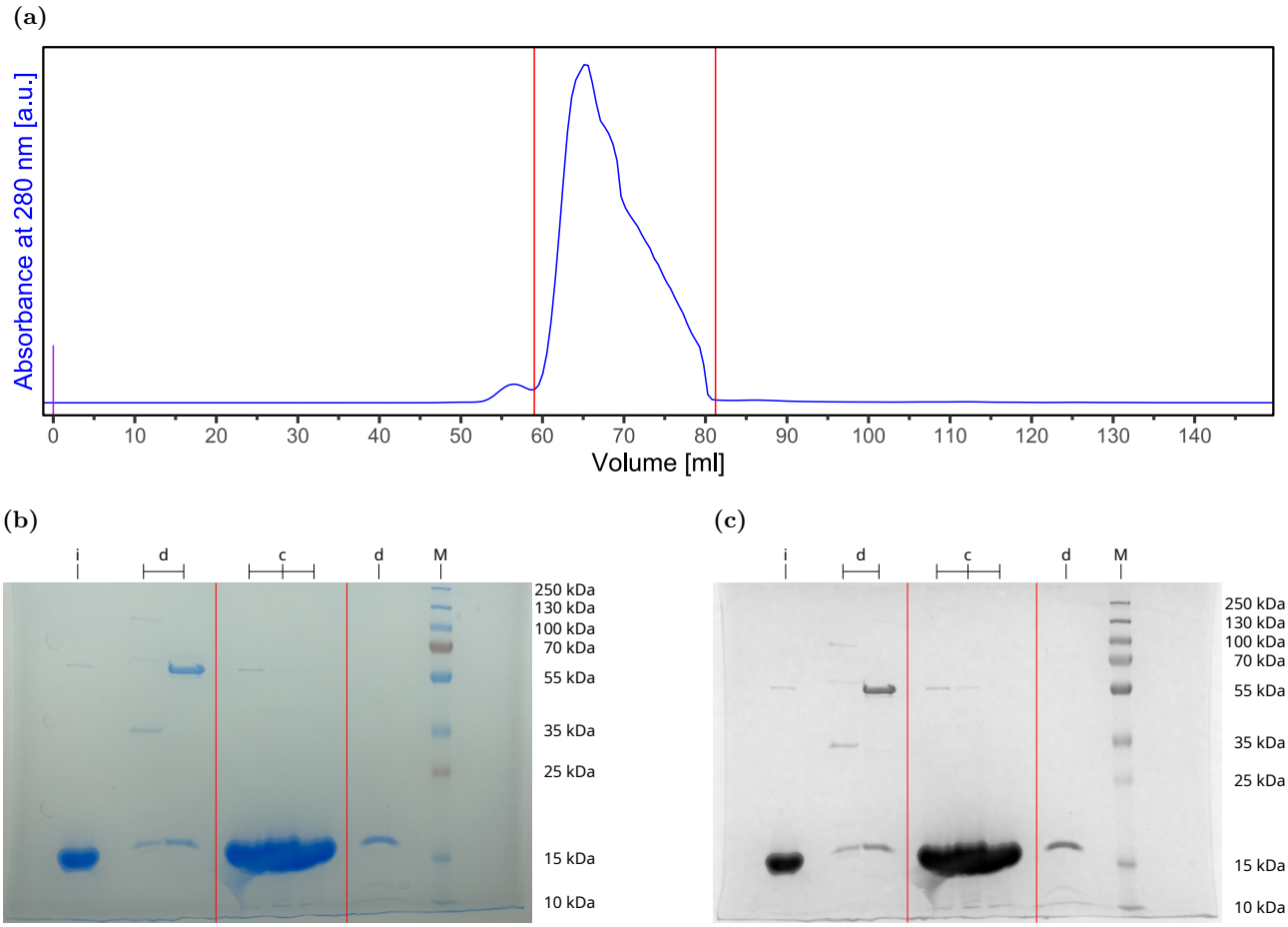

Figure 37: Example of an SEC purification of hSOD1 with a HiLoad 16/600 Superdex 75 pg (CV = 120 ml, V_0 = 40 ml) column on an ÄKTA. **(a):** SEC chromatogram. The injection of sample is shown in purple. The start and end of fractions, which contained hSOD1 and were combined for further use are shown in red. **(b, c):** SDS-PAGE gel following SEC, stained with GelCode Blue Safe Protein Stain (b), then imaged with a gel imaging system in greyscale (c). Lanes between the red lines correspond to fractions containing hSOD1 that were combined for further use. i: Combined IEX fractions following dialysis in Buffer M, SEC sample. c: Collected fractions. d: Discarded fractions. M: Marker. The detailed procedure of this purification is provided in Section 9.9.7.

Following IEX and dialysis over night, the protein mixture was further purified by size exclusion chromatography (SEC), shown in Figure 37. A HiLoad 16/600 Superdex 75 pg (CV = 120 ml, V_0 = 40 ml) column on an ÄKTA was utilized. Obtained protein fractions were analyzed by SDS-PAGE, fractions containing hSOD1 were combined and dialyzed over night.

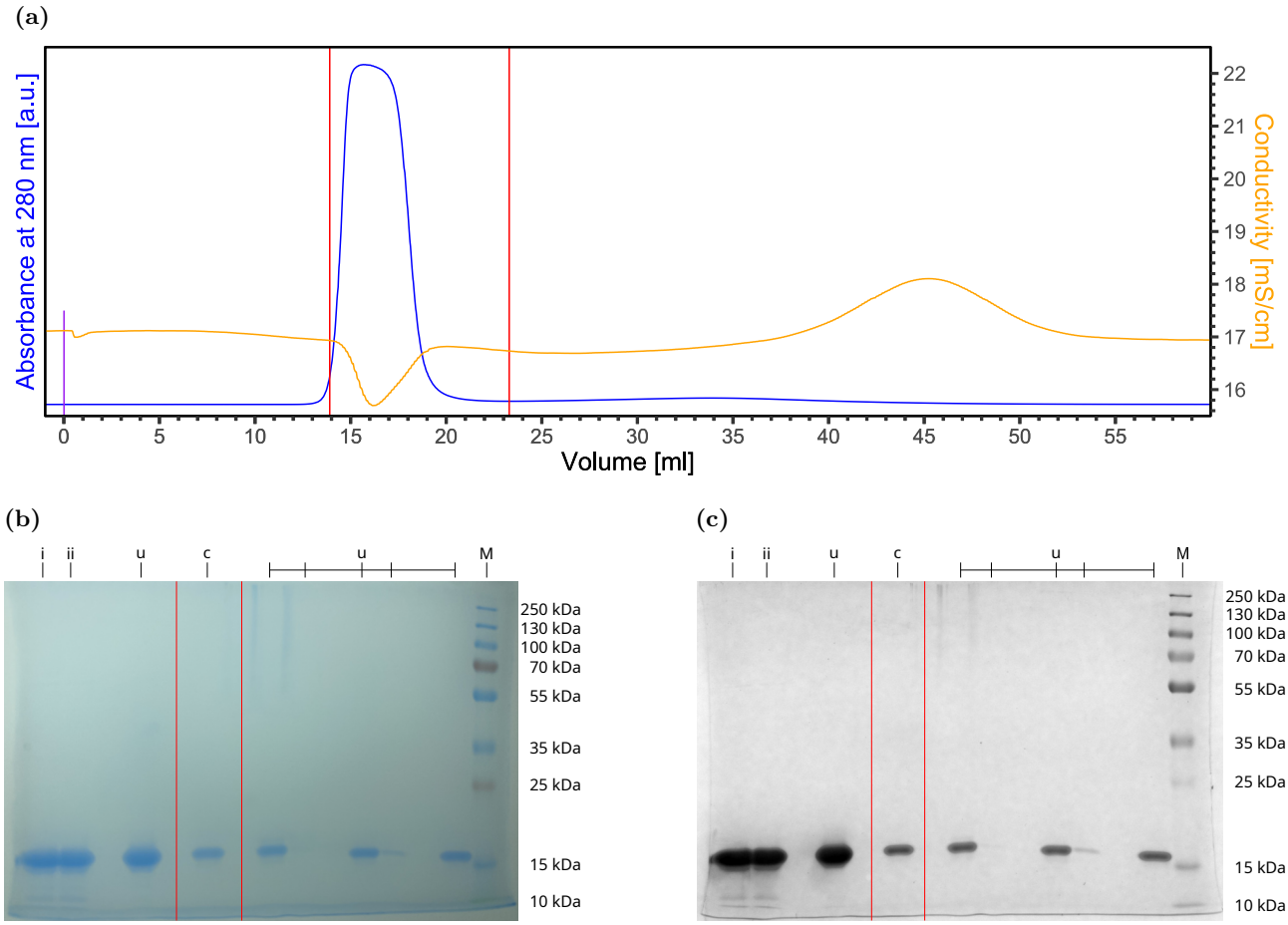

Figure 38: Example of desalting and buffer exchange of apo hSOD1 with a HiPrep 26/10 Desalting (CV = 53 ml, V_0 = 15 ml) on an ÄKTA. **(a):** Desalting and buffer exchange chromatogram. The injection of sample is shown in purple. The start and end of fractions, which contained hSOD1 and were combined for further use are shown in red. **(b, c):** SDS-PAGE gel following desalting and buffer exchange, stained with GelCode Blue Safe Protein Stain (b), then imaged with a gel imaging system in greyscale (c). Lanes between the red lines correspond to fractions containing hSOD1 that were combined for further use. i: Combined SEC fractions following dialysis in Buffer D1. ii: Following Dialysis in Buffer D2, desalting sample. c: Collected fractions. u: Unrelated to this experiment. M: Marker. The detailed procedure of this purification is provided in Section 9.9.7.

To remove any metals bound by hSOD1, the protein solution was dialyzed against an EDTA containing buffer providing demetalated apo (E|E) hSOD1. If the apo state was desired, hSOD1 was desalted as described below. If instead the Cu^{2+} and Zn^{2+} containing holo (Cu|Zn) hSOD1 state was desired, hSOD1 was reconstituted by addition of $CuSO_4$ (10 mM final conc.) and incubation at rt for 15 min, followed by addition of $ZnSO_4$ (10 mM final conc.) and incubation at rt for 15 min. Holo hSOD1 was then likewise desalted as described below.

Desalting and buffer exchange was performed using a HiPrep 26/10 Desalting (CV = 53 ml, V_0 = 15 ml) on an ÄKTA, shown in Figure 38. Obtained protein fractions were analyzed by SDS-PAGE and fractions containing hSOD1 were combined. hSOD1 concentration was determined with a NanoDrop spectrophotometer, then flash frozen in liquid N_2 as 1 ml aliquots and stored at -80°C.

5.6.3 Metalation State of hSOD1

Mass spectrometry (MS) measurements of holo (Cu|Zn) hSOD1 were carried out, in order to verify the reconstitution of hSOD1 with its native Cu^{2+} and Zn^{2+} cofactors. Examples of similar metalation studies employing mass spectrometry have been reported by Yamazaki and Takao,[226] Choi and Tezcan,[227] or Tajiri *et al.*.[228]

Both ESI and MALDI-MS on multiple instruments were explored. Early in the development, it was observed that protein buffer ions needed to be avoided in order to detect the protein itself. For hSOD1 preparations in either Na_2HPO_4, HEPES or sodium citrate containing buffers, only cluster ions formed by the buffer molecules were observed, instead of the ionized protein. Both Tris and NH_4OAc were tolerated at low concentrations, with 2 mM Tris and 20 mM NH_4OAc as the highest concentrations successfully tested. At higher concentrations, both buffers diminished the detection of protein. Later, experiments were therefore carried out with protein solutions in H_2O without additional buffer components. It was observed that lowering the pH value by addition of an acid was required to detect ionized protein species. Early experiments used formic acid (0.5% final conc.) which in later experiments was replaced with the weaker acetic acid (0.5% final conc.), which seemed to have a beneficial effect on the detection of metalated protein species. The best resolution and clearest observation of Cu^{2+} and Zn^{2+} bound hSOD1, was achieved using ESI^+ on a Bruker timsTOFfleX instrument with holo hSOD1 (10.13 µM) in H_2O as a sample, as shown in Figure 39. Acetic acid (0.5% final conc.) was added shortly before the experiment to facilitate ionization of the protein.

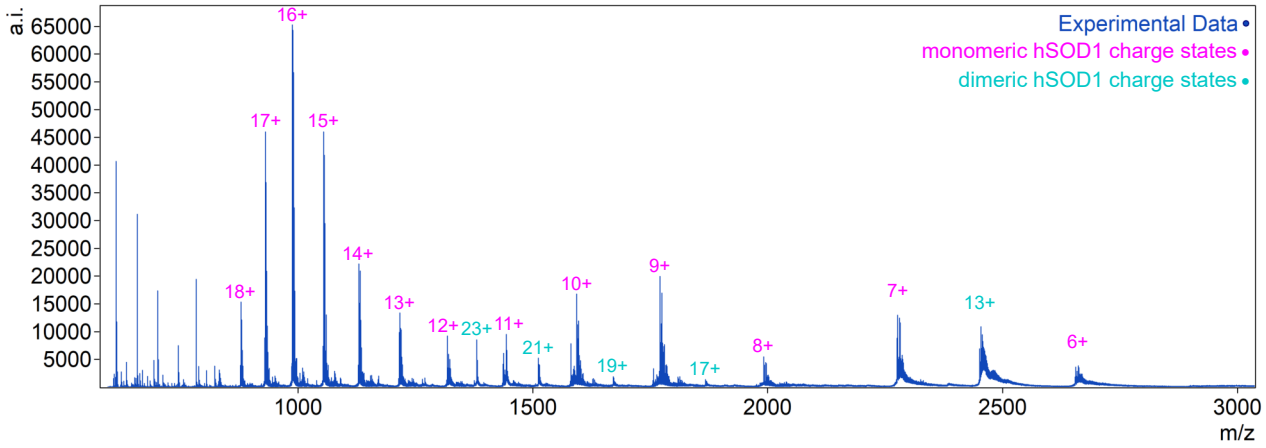

Figure 39: Excerpt of the ESI^+ MS spectrum of holo wt hSOD1 measured on a Bruker timsTOFfleX from 600 to 3000 m/z. A selection of charge states is annotated.

The achieved resolution provided a well resolved isotope pattern. From the amino acid sequence of hSOD1 the chemical formula was calculated using the ProtParam web tool from the Swiss Institute of Bioinformatics.[224] Taking into account that natively matured hSOD1 forms a disulfide bond between Cys57 and Cys146,[45] 2 hydrogen atoms were removed accordingly, which yielded [M] = $C_{679}H_{1083}N_{203}O_{224}S_4$ for monomeric apo $hSOD1^{S\text{-}S}$. Monomeric hSOD1 was detected more intensely compared to its dimeric form. Dissociation of the dimer under the ionization conditions is likely a factor for this observation. Additionally, in order to detect the monomer and the dimer at the same m/z value the dimer needs to be twice as charged, introducing a detection bias in favor of the monomer.

(a) **(b)**

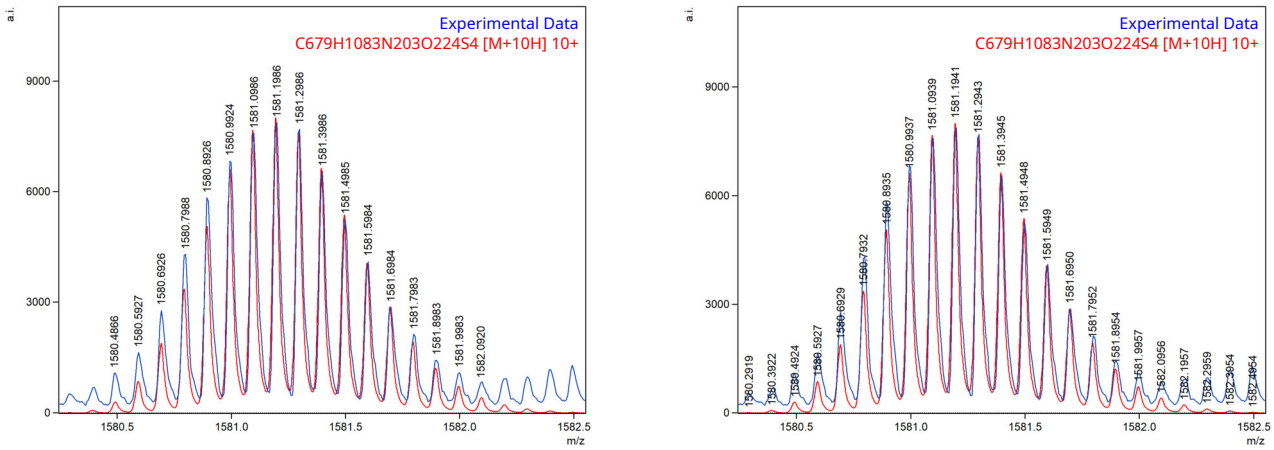

Figure 40: Monomeric $[M+10H]^{10+}$ signal observed in the ESI^+ MS spectrum of holo hSOD1. The experimental data is shown in blue and the simulated isotope pattern is shown in red. **(a):** Annotated with m/z values of the experimental data. **(b):** Annotated with m/z values of the simulated isotope pattern.

The monomeric $[M+nH]^{n+}$ signal is well resolved and observed for all charge states from 8+ to 20+. For states 11+ and 12+, the signal was shifted by -1H. As an example, the $[M+10H]^{10+}$ signal is shown in Figure 40. The dimeric $[2\,M+nH]^{n+}$ signal was not clearly observed. Importantly, the successful formation of the disulfide bond during the expression was confirmed by the detection of $[M+nH]^{n+}$.

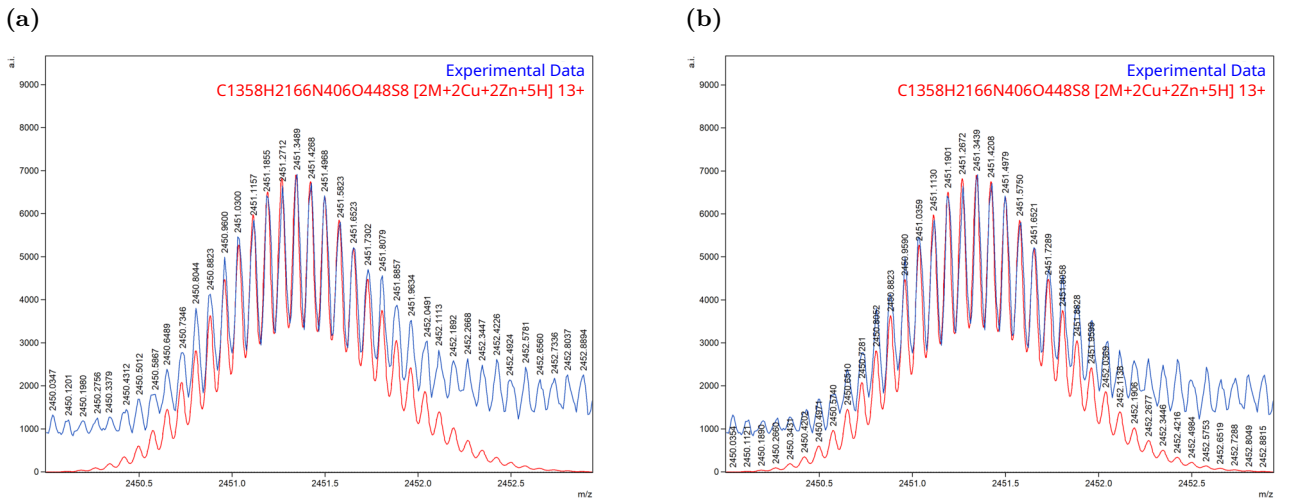

Figure 41: Dimeric $[2M+2Cu+2Zn+5H]^{13+}$ signal observed in the ESI^+ MS spectrum of holo hSOD1. The experimental data is shown in blue and the simulated isotope pattern is shown in red. **(a):** Annotated with m/z values of the experimental data. **(b):** Annotated with m/z values of the simulated isotope pattern.

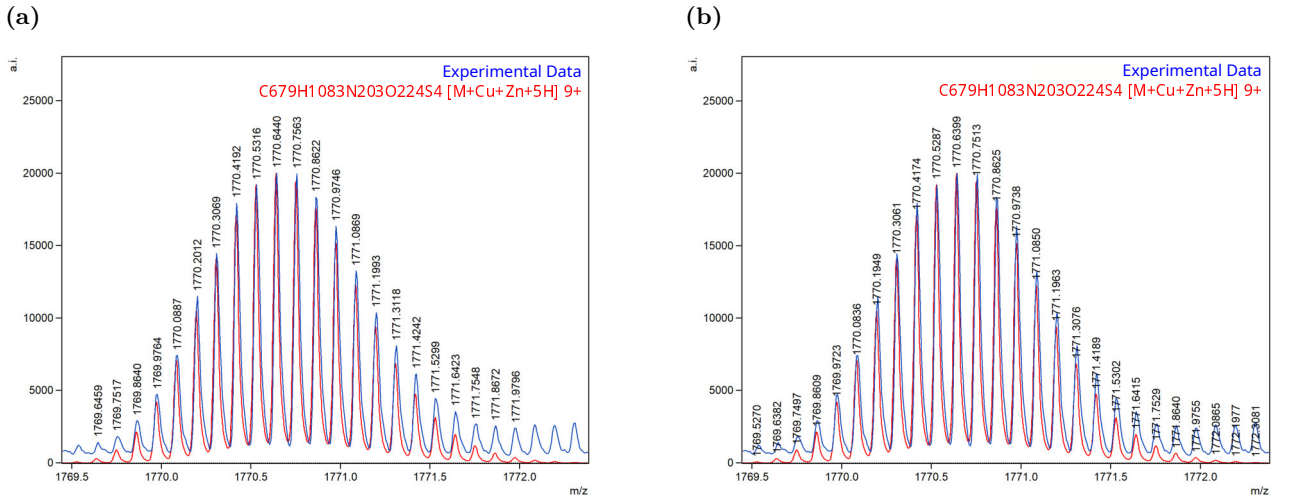

Figure 42: Monomeric $[M+Cu+Zn+5H]^{9+}$ signal observed in the ESI^+ MS spectrum of holo hSOD1. The experimental data is shown in blue and the simulated isotope pattern is shown in red. **(a):** Annotated with m/z values of the experimental data. **(b):** Annotated with m/z values of the simulated isotope pattern.

Natively metalated dimeric hSOD1 was most distinctively observed as $[2\,M+2Cu+2Zn+(n\text{-}8)\,H]^{n+}$ for the 13+ charge state, shown in Figure 41. At states 12+ and 14+, it is likely also present, but overshadowed by the corresponding monomeric signal. Natively metalated monomeric hSOD1 was further observed as $[M+Cu+Zn+(n\text{-}4)\,H]^{n+}$ for the charge states from 6+ to 10+. As an example, the $[M+Cu+Zn+5H]^{9+}$ signal is shown in Figure 42. The observation of these natively metaled species qualitatively confirms that the reconstitution of hSOD1 had been successful.

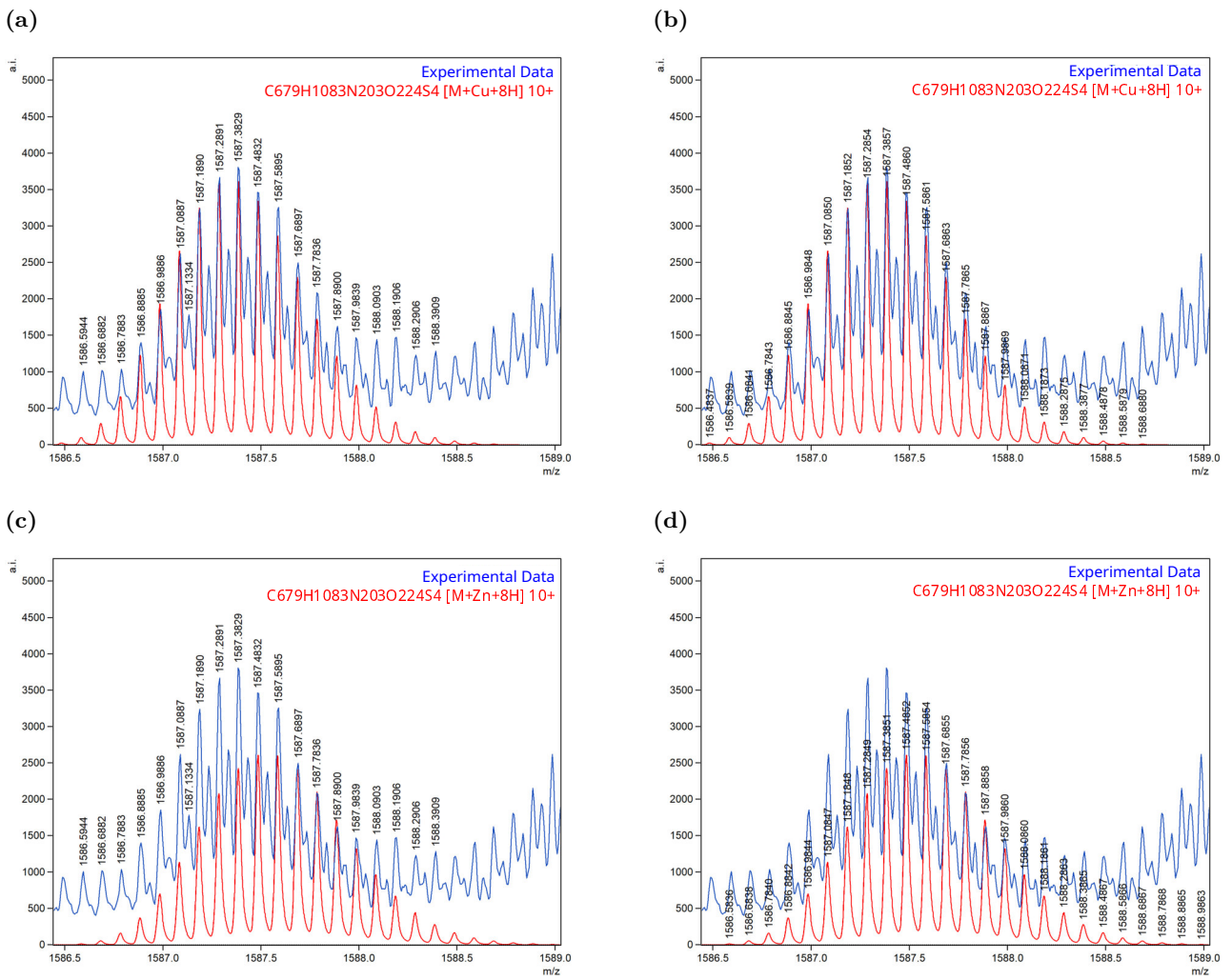

Figure 43: Monomeric $[M+Cu+8H]^{10+}$ and $[M+Zn+8H]^{10+}$ signals observed in the ESI^+ MS spectrum of holo hSOD1. The experimental data is shown in blue and the simulated isotope patterns are shown in red.**(a):** $[M+Cu+8H]^{10+}$, annotated with m/z values of the experimental data. **(b):** $[M+Cu+8H]^{10+}$, annotated with m/z values of the simulated isotope pattern. **(c):** $[M+Zn+8H]^{10+}$, annotated with m/z values of the experimental data. **(d):** $[M+Zn+8H]^{10+}$, annotated with m/z values of the simulated isotope pattern.

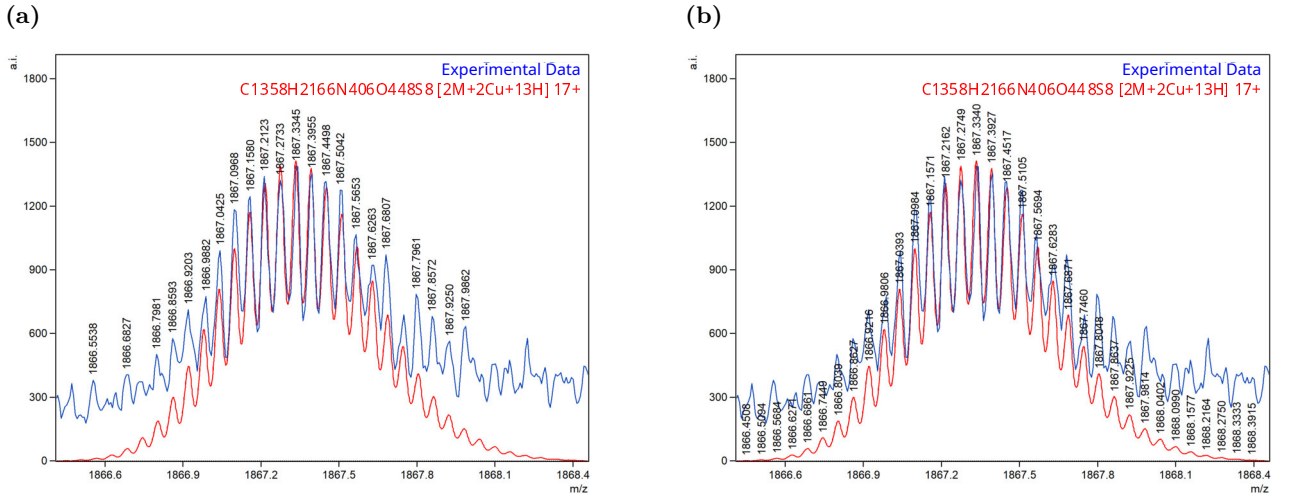

Figure 44: Dimeric $[2M+2Cu+13H]^{17+}$ signal observed in the ESI^+ MS spectrum of holo hSOD1. The experimental data is shown in blue and the simulated isotope pattern is shown in red.**(a):** Annotated with m/z values of the experimental data. **(b):** Annotated with m/z values of the simulated isotope pattern.

Monomeric hSOD1 with only one Cu^{2+} or Zn^{2+} was distinctly observed as $[M+Cu+(n-2)\,H]^{n+}$ and $[M+Zn+(n-2)\,H]^{n+}$ for the charge states 8+ to 10+. At higher charge states the respective monomer signals were observed, with a lower signal intensity, limiting a clear distinction between them. As an example, the $[M+Cu+8H]^{10+}$ and $[M+Zn+8H]^{10+}$ signals are shown in Figure 43. Dimeric hSOD1 with 2 Cu^{2+} was observed as $[2\,M+2Cu+(n-4)\,H]^{n+}$ for charges states 17+ to 25+, as shown in Figure 44.

The following two tendencies were observed across the multiple observed hSOD1 signal: Double metalated species were detected at lower charge states, compared to single metalated species. Species devoid of any metals were still observed at high charge states, where metalated species were no longer observed. Metal binding of proteins is typically reduced the more positively charged the protein is, as occurs at low pH values. More specific to hSOD1, studies by Pantoliano *et al.* have demonstrated that hSOD1 reversibly releases its bound metals at low pH.[229,230] Both tendencies observed in this work are therefore in agreement with previous investigations.

While no quantitative measure of the stoichiometry between protein and metal ions can be provided by ESI-MS, this experiment qualitatively confirmed that hSOD1 was successfully prepared in its native metalation state of 1 Cu^{2+} and 1 Zn^{2+} per subunit. Additionally, the formation of the native intrasubunit disulfide bond was confirmed by this investigation.

5.6.4 Enzymatic Activity of hSOS1

To asses, whether the recombinantly expressed hSOD1 was obtained in a catalytically active conformation and to compare the catalytic capabilities of the two hSOD1 variants, hSOD1 and hSOD1 A4V: The activity of expressed holo hSOD1 and holo hSOD1 A4V was determined *via* a commercially available SOD activity assay kit, with the aim of verifying that expression and reconstitution of hSOD1 was successful and the protein was obtained in its native state. The assay was performed as endpoint measurements and absorbance values were determined on well plates using a plate reader. Relative activity of expressed hSOD1 was then compared to the bovine SOD standard provided with the assay kit. The detailed procedure of these measurements and the data analysis are provided in Section 9.10.6.

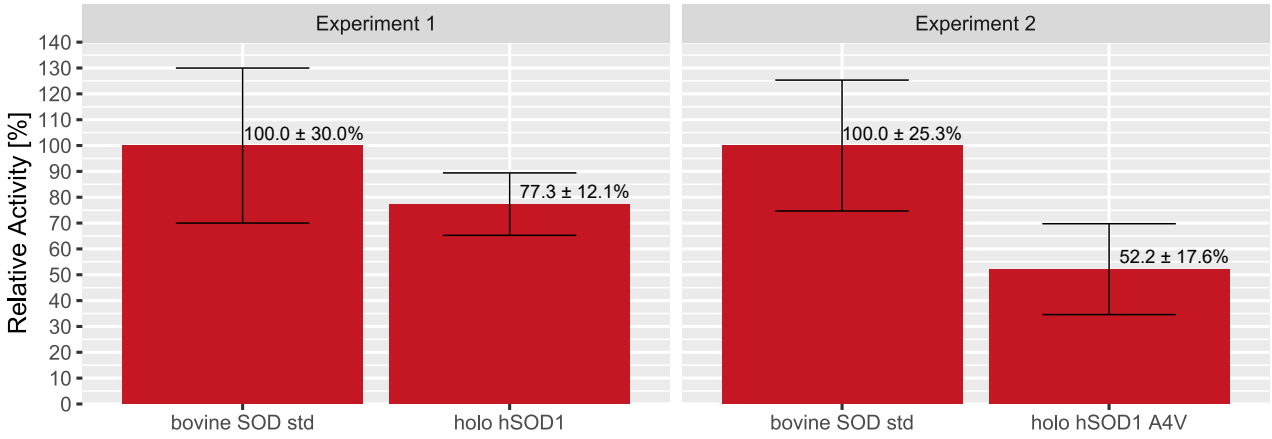

Figure 45: Relative activity of holo hSOD1 and holo hSOD1 A4V in comparison to a bovine SOD standard. The relative activity of the bovine SOD standard was defined as 100% for each individual experiment.

Holo hSOD1 displayed a relative activity of 77.3 ± 12.1%, confirming successful expression and reconstitution, as shown in Figure 45. For monomeric hSOD1, only about 10% of the dimer's activity has been reported.[53] As the dimer state of hSOD1 is essential for its activity, the result of this assay also proved that dimeric hSOD1 was obtained, as intended.[231] For the holo A4V variant, a reduced activity of 52.2 ± 17.6% was observed, which is in line with the literature, consistently reporting about half the activity of hSOD1 for the A4V variant. The reduced activity of holo hSOD1 A4V, has been reported as a result of its reduced metal binding capability.[59,232–234]

The obtained results confirm the as native enzymatic activity of the recombinantly expressed hSOD1 of this study. Together with the observations of the ESI-MS study, the expression of hSOD1 was verified as successful and all native maturation modification had been obtained.

5.7 Ligand Interaction with hSOD1

The small molecule ligands developed in this work are intended to inhibit the ALS-relevant aggregation of mutant hSOD1, by stabilizing the mature hSOD1 dimer state. The experiments conducted in the following sections therefore examined the aggregation behavior of the hSOD1 A4V mutant and the influence exerted by the designed ligands. In order to strengthen the evidence obtained from individual methods, complementary assay systems were utilized. This approach further allowed to verify the results and reveals any false-positive hits of any single assay.

5.7.1 MicroScale Thermophoresis

MicroScale Thermophoresis (MST)[235–237] measurements between holo hSOD1 and the small molecule ligands ALE **36** and ALD **35** were attempted to investigate ligand-protein binding and determine the corresponding dissociation constant K_d. Similar measurements had been performed in preceding work by Mrđen Debono[159] and of the author.[48] However, the obtained data quality only permitted poor fitting in order to provide a K_d with low confidence, in singular examples. Furthermore, MST measurements were observed to be of limited reproducibility. Issues with this method in the given small molecule ligand-hSOD1 context had previously been recognized.[48,159]

While there are reported examples of small molecules binding hSOD1 that have successfully been investigated by MST, such as the ones by the group of Padmanabhan,[238–240] it can be assumed that the interaction between the investigated small molecule ligands and the hSOD1 protein result in structural and electronic changes to the proteins that are to small to be reliably detected by the instrument.[241] Investigations of ligand-protein binding by MST were therefore discontinued.

5.7.2 Thioflavin T Based Aggregation Assay

To investigate how the aggregation of mutant hSOD1 was influenced by the proposed ligands, a thioflavin T (ThT) based aggregation assay was performed. The working principle of this assay is explained in detail in Section 4.4.

Inhibition of hSOD1 aggregation is the intended effect for the ligands of this study. Together with the scalability of a plate reader setup, the aggregation assay provided an appropriate method to screen the prepared ligand library. Compounds that displayed an inhibitory effect on hSOD1 aggregation as identified by this screening resemble promising candidates for further *in vitro* investigation. The experimental protocol the ThT aggregation assay was originally reported by Mrđen Debono[159] and adapted here. Modifications specific of this work are discussed below.

hSOD1 A4V is well known for its destabilized nature[84,242] and removing the Cu and Zn cofactors further decreases its stability, increasing its aggregation tendency.[175,243,244] No additional agents, such as the chaotropic agent guanidine hydrochloride Gdn • HCl[244,245] or the disulfide reducing agents TCEP[177,187] or DTT[246–248] were needed to promote aggregation, as it was demonstrated by Mrđen Debono that apo hSOD1 A4V readily aggregated within 24 h at 50°C.[159] Furthermore, it was intended to limit the number of possible off target interactions between the small molecule ligands and any other non-hSOD1 molecules in the solution.

The aggregation assay was performed as a fixed time point *ex situ* setup, using endpoint measurements (reviewed in Section 4.4). Samples were prepared, incubated at 50°C for 24 h and ThT added shortly before fluorescence measurements with a plate reader were performed.[159] This setup has the advantage, that ThT does not deteriorate under the incubation conditions and that ThT itself does not influence the formation of aggregates, as discussed in Section 4.4. In this work, samples were lightly shaken at 150 rpm during the incubation, to prevent potential demixing of aqueous buffer and cosolvent. These conditions were specifically chosen, to avoid deviating form physiological conditions, unnecessarily. An increased temperature was deemed acceptable, as it allowed aggregation be observed within hours, rather than days or months.[94,183,185]

The assay's buffer system was comprised of 80% aqueous buffer and 20% cosolvent.[159] In the previous work of Mrđen Debono, it had been stated that DMSO influences the aggregation of hSOD1 and would therefore not be suitable as a cosolvent in the ThT based aggregation assay. Instead Mrđen Debono opted to use PEG-550, arguing that its influence on hSOD1 aggregation was much less pronounced.[159] To investigate this claim in more detail, the aggregation of a commercially available standard, as well as holo hSOD1, apo hSOD1, holo hSOD1 A4V and apo hSOD1 A4V were examined by ThT fluorescence, with and without DMSO or PEG-550 as cosolvents, as shown in Figure 46 and Figure 47. The utilized Proteostat standard from Enzo contained partially aggregated immunoglobulin G (IgG) at defined percent ratios. To avoid ambiguity, it should be mentioned that the abbreviation PEG-550 technically refers to a mixture of methoxypolyethylene glycol (mPEG), rather than a mixture of polyethylene glycol (PEG). Both PEG-550 and mPEG-550 are commonly used abbreviations that refer to the same polymer mixture.

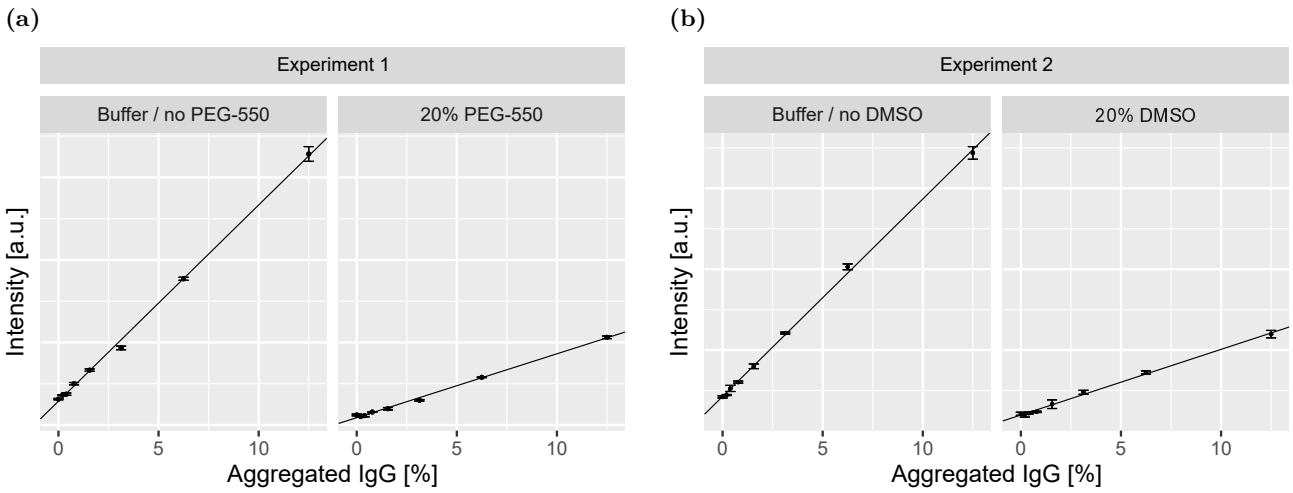

Figure 46: Influence of 20% PEG-550 or 20% DMSO as cosolvent on the Proteostat protein aggregation standards determined in two independent experiments. **(a):** Comparison between buffer with and without 20% PEG-550. A gain of 2200 and a focal height of 5.4 mm was used. **(b):** Comparison between buffer with and without 20% DMSO. A gain of 2100 and a focal height of 5.3 mm was used.

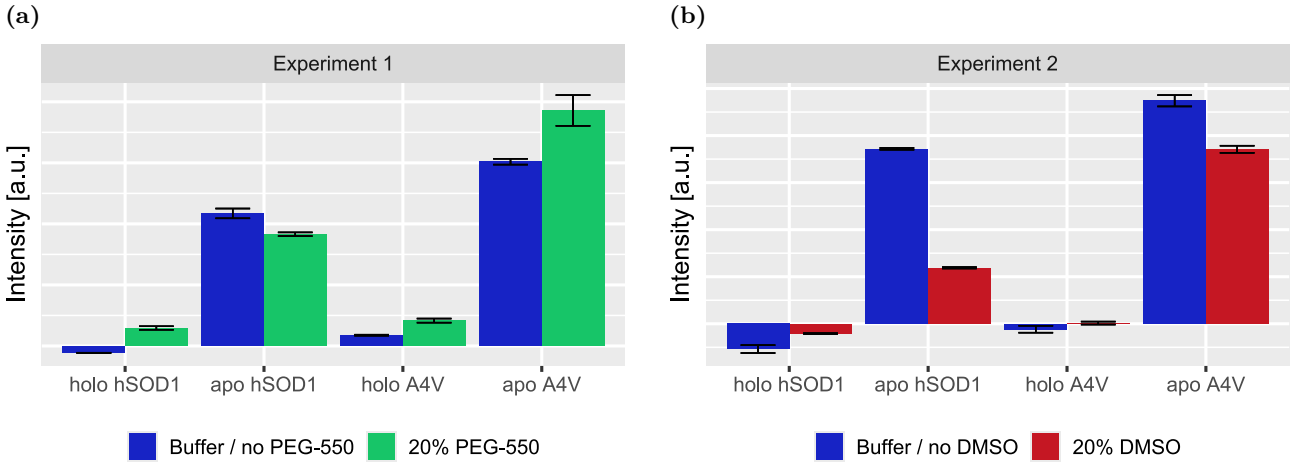

Figure 47: Comparison of the aggregation propensities of wt hSOD1 and hSOD1 A4V in their holo and apo state and the influence of 20% PEG-550 or 20% DMSO as cosolvent determined in two independent experiments. **(a):** Comparison between buffer with and without 20% PEG-550. A gain of 2200 and a focal height of 5.4 mm was used. **(b):** Comparison between buffer with and without 20% DMSO. A gain of 2100 and a focal height of 5.3 mm was used.

Figure 46 shows that while PEG-550 and DMSO both substantially reduce absolute ThT fluorescence values, the expected linear relation between aggregated IgG and intensity remains unchanged, indicating that both cosolvents could viably be used in the ThT aggregation assay.

The influence of PEG-550 or DMSO on the aggregation of different hSOD1 species shown in Figure 47 is not clear. In both experiments, PEG-550 and DMSO containing samples show a deviation from their respective controls in buffer alone. In both experiments, holo hSOD1 and holo hSOD1 A4V indicated none or very limited aggregation, while both apo hSOD1 and apo hSOD1 A4V indicate aggregation, as expected by the reduced stability of the apo hSOD1 state. While both PEG-550 and DMSO show changes in fluorescence intensity, compared to buffer alone for every sample, one can not definitely claim a stabilizing or destabilizing effect of either cosolvent on hSOD1, when taking

the result of the earlier Proteostat experiments into consideration. It is unclear to which extend the cosolvents influence the actual aggregation of the proteins and/or the observed ThT fluorescence. Regardless, the expected order of aggregation tendency of holo hSOD1 ≈ holo A4V < apo hSOD1 < apo A4V holds true for both PEG-550 and DMSO as cosolvent. In conclusion, as there was no indication that suggested one cosolvent to be better suited than the other, either one may be used for the ThT assay. DMSO was utilized in the following experiments, as ligands more readily dissolved in DMSO and highly viscous PEG-550 is more difficult in handling. Additionally, DMSO mixes with water more readily than does PEG-550, providing better sample homogeneity and limiting demixing effects.

The eleven ligands previously synthesized and purified by HPLC (listed in Table 9) were screened. In addition to these ligands, the two literature-known compounds pyrimethamine **40** and trehalose **41** and the carboxylic acid building block ca-L **9** were included in the assay, as explained below. Notably, the analysis procedure was developed independently form the previously reported ThT assay procedure by Mrđen Debono[159] and relies on the evaluation of relative ThT fluorescence intensity, to ensure comparability across multiple well-plates. The detailed procedures of the experiment and its corresponding analysis are provided in Section 9.10.8.

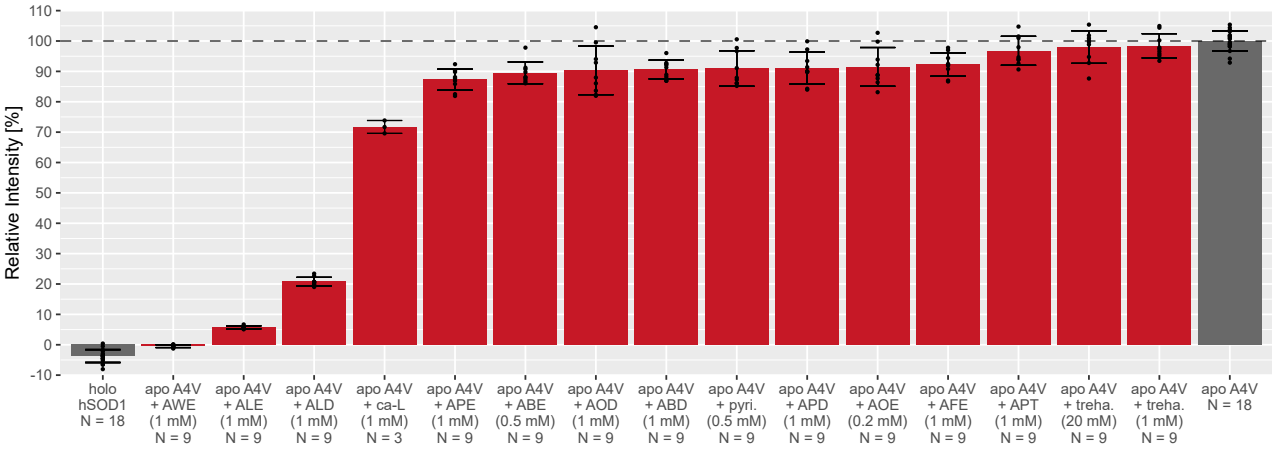

Figure 48: Relative ThT fluorescence intensity as a measure of hSOD1 aggregation. Samples are ordered by relative ThT fluorescence intensity. Protein controls holo hSOD1 and apo hSOD1 A4V are shown in gray. The mean intensity of the apo A4V control of each individual well plate was defined as 100% relative intensity. Relative intensities are shown as mean and standard deviation obtained from multiple independent experiments with multiple replicates each. Relative intensities of each replicate are shown as dots, with the total number of replicates (N) specified. Relative intensities and standard deviations are provided in table from in Section 10.5.

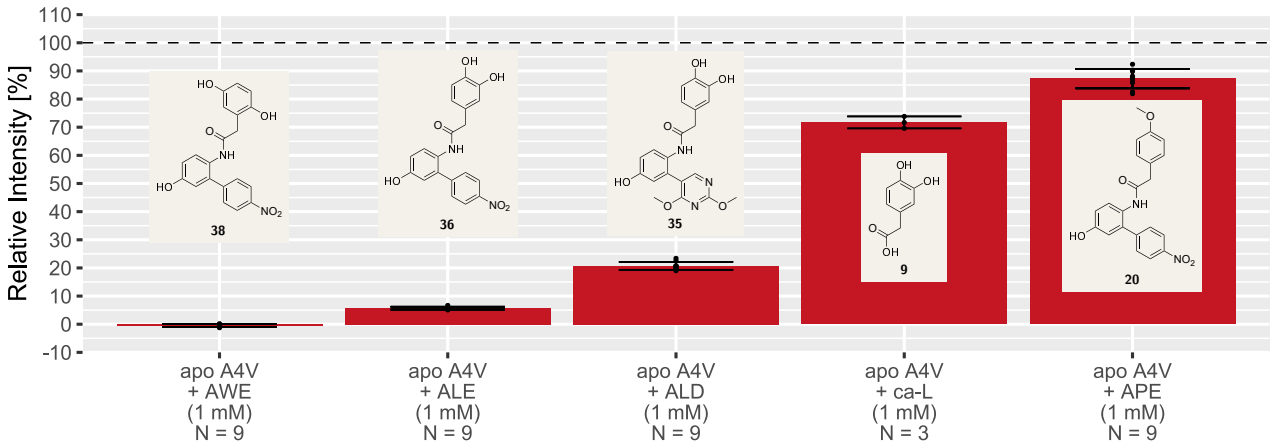

Figure 49: Excerpt of Figure 48, highlighting the five best performing ligands and their chemical structures.

The results, shown in Figure 48, indicate that pyrimethamine **40** did not influence the aggregation of apo hSOD1 A4V. This is consistent with its mode of action reported in ALS cell and animal models, resulting from a reduced expression of hSOD1, as discussed in Section 2.4.1. Similarly, the results of the aggregation assay, indicate that trehalose does not influence the aggregation of apo hSOD1 A4V and that its effects reported for *in vivo* ALS-models are instead due to a more general mechanism of autophagy induction, as discussed in Section 2.6.1.

For most ligands, no appreciable change in ThT fluorescence intensity was observed, compared to the apo hSOD1 A4V control, indicating that they did not influence apo hSOD1 A4V aggregation. The compounds, which most notably reduced ThT fluorescence are highlighted in Figure 49. AWE **38** and ALE **36** and ALD **35** show a substantial decrease in ThT fluorescence intensity, indicating a strongly reduced hSOD1 A4V aggregation in their presence.

As discussed in Section 4.4, it has been reported that interactions between investigated small molecule agents and ThT can cause a reduction in ThT fluorescence intensity. In order to avoid false-positive results due to this common issue, the data obtained by the ThT assay was examined in detail. Going back to the initial steps of the assay's analysis, comparing the absolute intensities of all samples and blanks, a notable effect was observed in the case of ligands AWE **38** and ALE **36**, as shown in Figure 50.

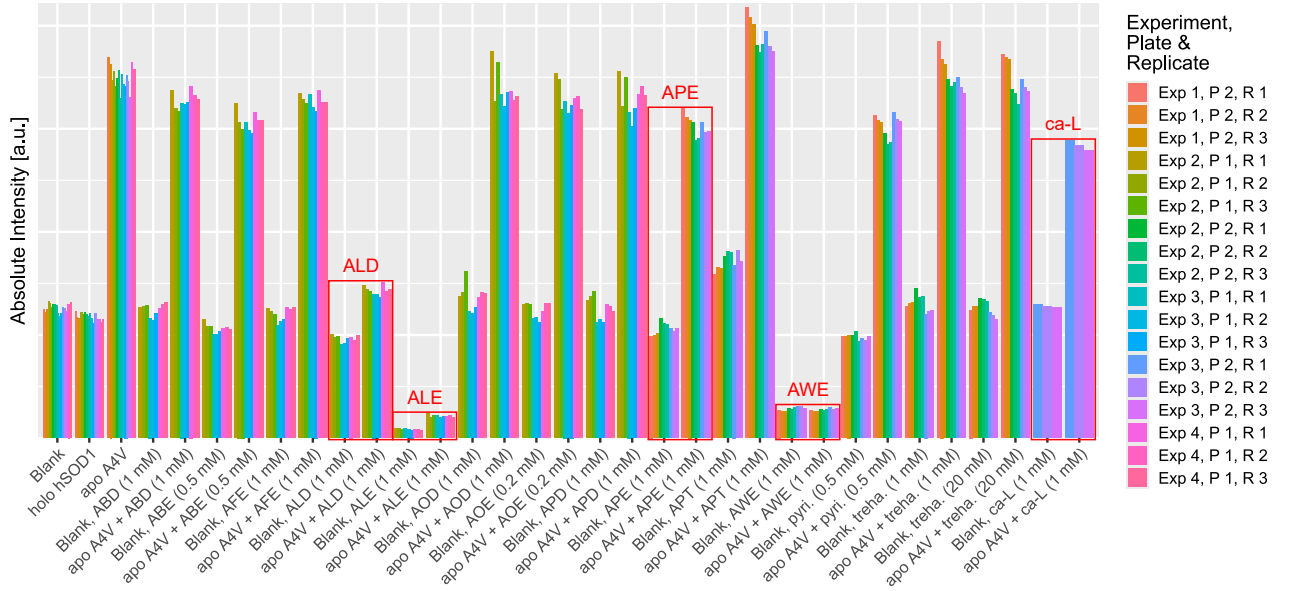

Figure 50: Absolute ThT fluorescence of all samples and their corresponding blanks for every experiment, plate and replicate therein. The five best performing ligands (Figure 49) and their corresponding blanks are highlighted in red.

Ligands AWE **38** and ALE **36** displayed a reduced ThT fluorescence intensity, not only in combination with the hSOD1 A4V protein, but also in their blank control, which only contained ligand and ThT, but no protein. This may indicate an interaction between these specific small molecule ligands and the ThT dye independent of hSOD1. For ALD **35** and APE **20** this does not seem to be the case, as the accompanying blank is in line with the other ligands.

Notably, ligands ALD **35** and ALE **36** share a 1,2-dihydroxybenzene moiety and AWE **38** bears a related 1,4-dihydroxybenzene moiety. In order to examine if this moiety by itself may cause issues by interacting with ThT, the building block ca-L **9**, bearing this 1,2-dihydroxybenzene functionality, was included in one of the ThT experiments. The absolute intensities of ca-L **9** and its blank however, do no not indicate an interaction with ThT.

In order to rule out that AWE **38** and ALE **36**, are false-positives and to confirm the results of the ThT-assay, a complementary assays based on dynamic light scattering (DLS) was conducted. Relying on multiple assays to test a set of compounds is generally an effective way to reveal possible false-positive and false-negative hits of any singular assay.

5.7.3 DLS Assay

Dynamic light scattering (DLS) was carried out in order to confirm or disprove the hits of the previous screening by the aggregation assay. A number of publications have investigated and characterized hSOD1 aggregation by DLS, highlighting it as an established tool in hSOD1-related ALS research.[46,183,184,186,248–252] In the context of this study, DLS was used to examine the previously top performing ligands, AWE **38**, ALE **36** and ALD **35**. Because ALE **36** and ALD **35** share a 1,2-dihydroxybenzene moiety, while AWE **38** bears a related 1,4-dihydroxybenzene moiety, the question was posed if this moiety by itself had any effect. The building block ca-L **9** bearing this 1,2-dihydroxybenzene moiety was therefore included. In order to provide a better ligand comparability, APE **20** was also included.

Samples were prepared as for the previous aggregation assay, without the addition of ThT. To ensure meaningful results, special care was taken in the sample preparation, discussed in the following. It should be noted that for all three DLS experiments, stocks of apo hSOD1 A4V were used that had been subjected to 3–5 freeze-thaw cycles prior to the experiments, as explained in Section 9.10.3. Seeding has been reported as a relevant factor in hSOD1 aggregation[253–256] and freeze-thaw cycles potentially lead to the formation of such seeds. As with all experiments in this study, hSOD1 stocks were centrifuged before their concentration was determined and they were used in experiments. This was done to exclude any precipitates or aggregates that may have formed during storage, as these may seed aggregation. Furthermore, all samples, including the apo hSOD1 A4V control of an individual experiment were prepared from the same apo hSOD1 A4V stock ensuring comparability within the same experiment and allowing to evaluate and compare the ligand's relative effects on hSOD1 A4V aggregation.

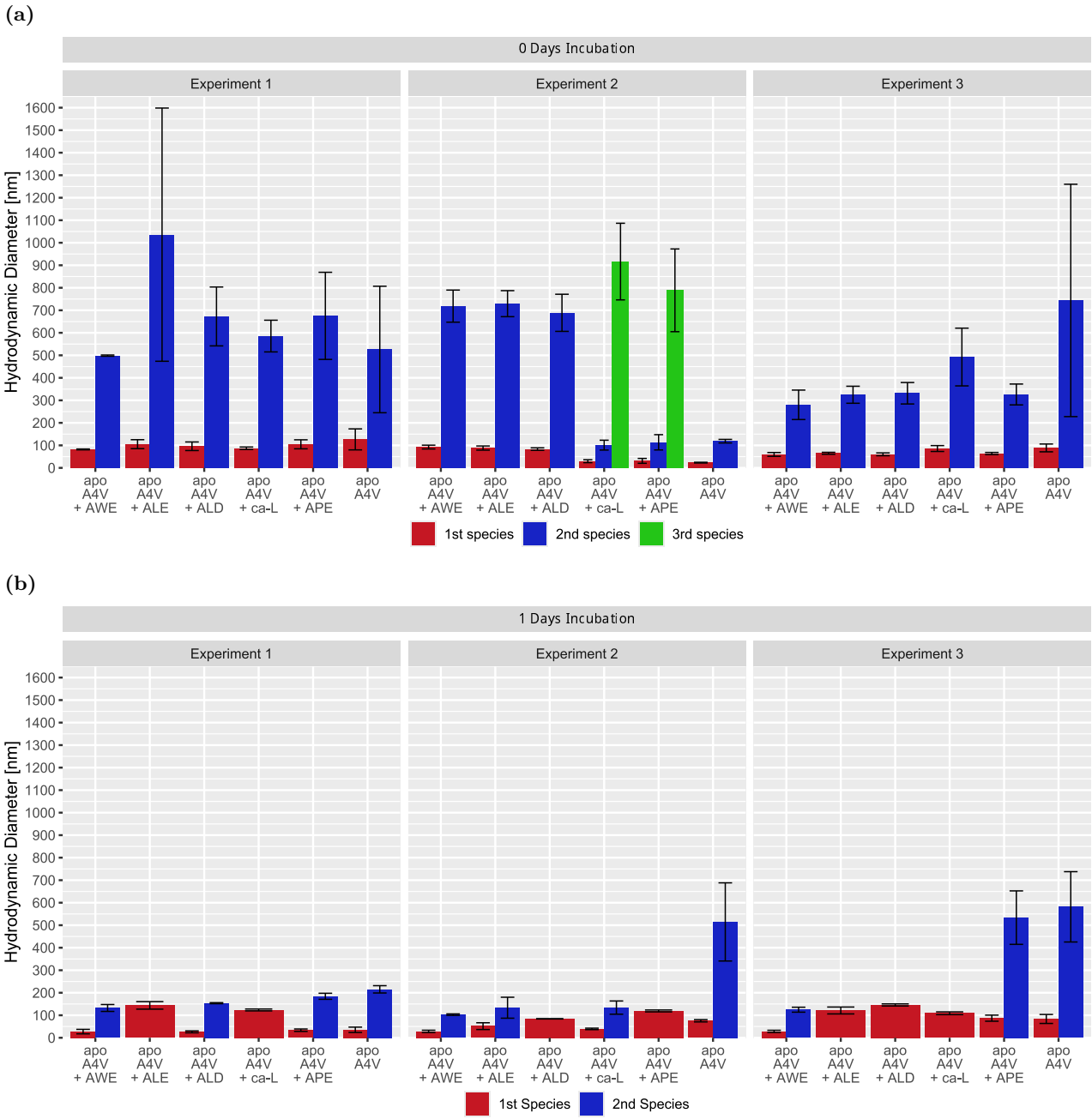

Figure 51: Comparison of measured hydrodynamic diameter d_H of hSOD1 A4V aggregates after 0 days and 1 day of incubation determined by DLS from three independent experiments. Species are numbered from smallest to largest by d_H. Ligands are ordered from left to right based on their performance in the ThT based aggregation assay. The data visualized in this figure is provided in the appendix (Section 10.4, Table 34). **(a):** Without incubation. **(b):** Incubated for 1 day.

Nevertheless, samples of apo A4V alone and in the presence of ligands had also been measured before the incubation, to evaluate the presence of aggregates prior to incubation. A comparison between the obtained results before and after incubation is shown in Figure 51. With only one exception (apo A4V + APE in Experiment 3), for each sample, substantially larger species were detected prior to incubation. Importantly, after incubation, these species were no longer observed in the respective samples. Notably, in Experiment 1 and 2 prior to incubation almost all ligand containing samples displayed a species larger than the ones observed for A4V alone. Following incubation, this trend was no longer observed, as for all three experiments apo hSOD1 A4V displayed the largest aggregate species. Both of these observations demonstrate that the results of the DLS measurements prior to incubation,

taken immediately after sample preparation do not show aggregation of apo hSOD1 A4V. Instead, they display artifacts in the DLS measurement, likely caused by mixing of the freshly prepared sample in the 20% DMSO containing assay buffer.

Samples containing apo hSOD1 A4V alone or in the presence of ligands were measured after 1 day of incubation and the obtained hydrodynamic diameter d_H were used to evaluate and compare the ligands influence on hSOD1 A4V aggregation. The detailed experimental procedures of this assay and the corresponding analysis are provided in Section 9.10.10.

It was observed that DLS displayed a greater variation between individual experiments, compared to the previous ThT-based aggregation assay. It is important to keep in mind that each DLS measurement resembles a snapshot of these presumably ongoing aggregation processes and that the aggregation of hSOD1 is regarded to proceed *via* multiple possible pathways.[183] In addition, a stochastic component as to which aggregation pathway will be followed has been reported.[184] Multiple examined samples therefore may not be expected to display an identical distribution of aggregate species, explaining the observed variation. The three DLS experiments were therefore not averaged and instead evaluated individually, as shown in Figure 52. Depending on the sample, one or more aggregate species were detected and numbered from smallest to largest by d_H. As discussed in Section 4.5, the light scattering intensity of a particle scales with its radius to the power of 6 (Equation 10), resulting in a detection bias towards the larger particles present.[181] Because of this factor, it is generally difficult to asses the relative concentrations between multiple observed species. Consequently, the following comparison between the investigated samples will be limited to their d_H. In order to asses a ligands inhibitory effect on hSOD1 aggregation, the smallest detected species of a sample is therefore especially relevant.

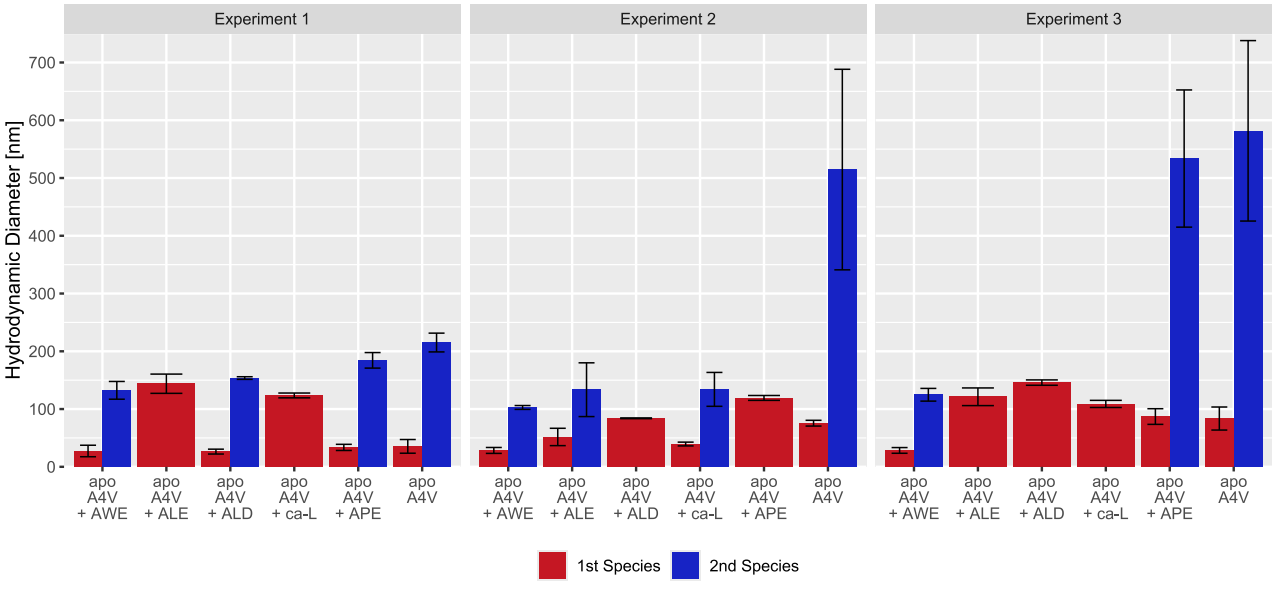

Figure 52: Comparison of measured hydrodynamic diameter d_H of hSOD1 A4V aggregates after 1 day of incubation determined by DLS from three independent experiments. Species are numbered from smallest to largest by d_H. Ligands are ordered from left to right based on their performance in the ThT-based aggregation assay. The data visualized in this figure is provided in the appendix (Section 10.4, Table 34).

In Experiment 1, two species with a d_H of 35 ± 12 and 215 ± 16 nm were detected for apo A4V alone. Ligand APE **20** displays two similarly sized species, suggesting that its effect on hSOD1 A4V aggregation was negligible. In the case of ALE **36** and ca-L **9**, a single species with a size larger than the 1st and smaller than the 2nd species of the apo A4V control was observed. On the one hand, this observation suggested that the formation of a large aggregate species was inhibited. On the other hand, the absence of a small species suggested that aggregation had proceed to a notable degree. Importantly, for AWE **38** and ALD **35** species of ~27 nm are detected, in addition to a reduced size of the 2nd species, compared to the apo A4V control, demonstrating their inhibitory effect on hSOD1 aggregation.

In Experiment 2, both species detected in apo A4V alone are notably larger than in Experiment 1, with a d_H of 76 ± 5 and 515 ± 174 nm. None of the ligands closely resemble the apo A4V control, indicating that all of them inhibited aggregation to some degree. ALD **35** and APE **20** displayed a single species with a size larger than the 1st and smaller than the 2nd species of apo A4V alone, suggesting a weak inhibitory effect. The strongest reduction in aggregate size was observed for AWE **38**, ALE **36** and ca-L **9**, for which a smaller species of ~30–50 nm were detected. Together with a reduced size of the 2nd observed species, compared to the apo A4V control, inhibition of hSOD1 aggregation was demonstrated for these compounds.

In Experiment 3, apo A4V alone displayed aggregates sizes similar to the ones in Experiment 2, with a d_H of 84 ± 20 and 582 ± 156 nm. Also similar to Experiment 1, APE **20** closely resembled the apo A4V control, indicating that it did not effect its aggregation. Notably, only ligands AWE **38** displayed a species smaller than both species observed for the apo A4V control, thereby consistently demonstrating its effect on reducing hSOD1 A4V aggregation. In the case of compounds ALE **36** and ALD **35** and ca-L **9**, a weak inhibitory effect was suggested by the observation of a single species with a size larger than the 1st and smaller than the 2nd species of the apo A4V control.

Control measurements of holo hSOD1 without ligands, as well as samples of ligands without apo hSOD1 A4V had also been included in one of the experiment and DLS was measured before and after incubation. The obtained data (Appendix Section 10.4) indicates that no aggregates were detected in these samples. The absence of detectable particles results in characteristic parameter values and low data quality, explained in the following. The DLS software will always fit the experimental data and return a d_H, necessitating critical evaluation of the measurements by the user.[192,195] The following discrepancies were observed, for these controls: 1) Curve shape of the correlogram. A substantial deviation from a sigmoidal curve shape and notable variation between replicates were observed, indicating inconsistent measurements of a poly-disperse sample. 2) Correlation factor. A maximum correlation factor close to 1 (typically > 0.9) indicates good data quality. For these controls, notably lower maximum correlation factors were observed in almost all cases, compared to the apo hSOD1 A4V containing samples, indicating inconsistent measurements and low data quality. 3) Attenuator index. The attenuator index (Table 29 in Section 10.4) denotes the nominal transmission of laser light into the sample. Transmission can be automatically increased by the instrument to compensate for low scattering intensity of a sample. A high attenuator index and therefore high nominal transmission was observed for these controls, compared to the apo hSOD1 A4V containing samples, indicating the absence of detectable particles.

In conclusion, the effect of ligands AWE **38**, ALE **36** and ALD **35** on reducing hSOD1 A4V aggregation previously observed in the ThT assay was confirmed by DLS. The DLS results indicate that their effectiveness had been overestimated by the ThT assay, as had been suspected. The results for AWE **38**, ALE **36**, ALD **35** and ca-L **9**, both in the ThT and the DLS assay, suggest that there is a merit to a dihydroxybenzene moiety as part of the ligands structure. Among the investigated ligands the effectiveness of AWE **38** was consistently demonstrated across all three DLS experiments. Additionally, it retained a species of $d_H \approx 28$ nm in all three experiments, further highlighting it as the most potent ligand developed in this work. AWE **38** therefore provides a lead compound for the development of a therapeutic treatment of hSOD1-related ALS.

5.7.4 Electron Microscopy

In order to determine the morphology of formed apo hSOD1 A4V aggregates, electron microscopy (EM) was performed. Further, it was investigated if the observed aggregate sizes correlated with the previous DLS experiments and whether the presence of hSOD1 ligands had an influence on the size and type of formed aggregate structures.

Aggregation prone apo hSOD1 A4V (20 µM) alone, and in the presence of ligand ABE **24** (1 mM) or APD **31** (10 mM), was prepared and incubated as for the previous ThT (Section 5.7.2) and DLS assay (Section 5.7.3), with the exception that 20% PEG-550 instead of 20% DMSO had been used as cosolvent. EM samples were prepared and analyzed as described in Section 9.10.9. Both ABE **24** and APD **31** had previously displayed a limited effect on hSOD1 aggregation in the ThT assay (Figure 48) and had not been included in the DLS assay.

EM revealed that apo A4V in the absence of ligands primarily formed amorphous aggregates (Figure 53a), while fibrils were not observed. Figure 53a displays the most frequently observed shape and structure of these aggregates. Less dense assemblies (Figure 53b) and singular smaller aggregates (Figure 53d) were observed less frequently. Predominantly, hSOD1 A4V aggregates had a cloudy appearance (Figure 53b, c). Some aggregates displayed a grainy appearance (Figure 53e), most noticeable at greater magnification (Figure 53f). It is unclear, if these may indicate the presence of limited amounts of ordered structures in addition to the predominantly amorphous aggregates.

The amorphous morphology of the formed apo hSOD1 A4V aggregates under the incubation conditions of this study, as well as their observed increase in ThT fluorescence intensity, is in agreement with previous studies.[94,174,187] These investigations similarly reported increased ThT fluorescence intensity not by the formation of fibrils, but rather by soluble oligomers or amorphous aggregates,[94,174,187] as discussed in Section 4.4.1. Critically, no reducing agent had been added to apo hSOD1 A4V in order to break the intrasubunit Cys57-Cys146 bond, as was reported to be required for fibril formation at pH ~7.[185]

EM images of apo hSOD1 in presence of ligands ABE **24** and APD **31** suggest that these ligands had an influence on the relative abundance of observed hSOD1 aggregate sizes. Conversely, the morphology of hSOD1 A4V aggregates was largely unaffected by these ligands. In the presence of ligands ABE **24** or APD **31**, amorphous aggregates of similar size, compared to hSOD1 A4V alone, were still observed (Figure 54c, Figure 55c, Figure 53a). However, they were much less abundant and only occasionally encountered. Often, they were smaller in size (Figure 54d) and singular aggregates were typically observed in smaller numbers, as compared to hSOD1 A4V alone (Figure 55e, Figure 53d). Characteristic for both ligands was that the background of every images displayed what seemed like crystalline deposits (Figure 54f, Figure 55b). Given that the ligands were used in great excess to the hSOD1 A4V protein (1 and 10 mM ligand to 20 µM protein), these might correspond to precipitation of the ligands themselves during the EM sample preparation. In the case of ligand ABE **24**, dense deposits were observed in a speckled pattern in some areas of the sample. The cloudy appearance of protein aggregates observed for hSOD1 A4V alone (Figure 53b, c) was unchanged in the presence of either ligand (Figure 54e, Figure 55d, f). Proteins aggregate of a grainy appearance, as observed for hSOD1 A4V alone (Figure 53e, f), were not observed in the presence of either ligand.

DLS had detected hSOD1 A4V aggregate species with d_H of ~20–50 nm, ~60–100 nm, ~200–230 nm and ~400–800 nm (Figure 52, Table 34). The two larger species in the several-hundred-nanometer range may correspond to individual aggregates observed in Figure 53b, e and structures observed towards the edges in Figure 53d. The two smaller species were not distinctly observed in EM. It is possible that the EM sample preparation procedure had an influence on their observed absence, as the association of initially dissolved particles during drop casting is a well known phenomenon.[257] A4V aggregates in the multiple-micrometer range, as predominantly observed by EM, lie at the edge or beyond the DLS detection range and were therefore not accounted for in the DLS experiments. The ligand's influence on aggregation size between DLS and EM may only be compared qualitatively, as different ligands had been investigated respectively.

It is unclear whether the presence of 20% PEG-550 had an influence on the morphology of formed A4V aggregates, as observed by EM. Similarly, while it was assumed that in the presence of 20% DMSO similar aggregate morphologies would be formed, the EM investigation does not provide specific information on this, as no control measurements without either cosolvent had been performed.

The previous ThT and DLS assays have provided strong evidence that the aggregation of mutant hSOD1 can be slowed down by the presence of the hSOD1 ligands developed in this work. The EM investigation provides additional preliminary evidence to these observations. The obtained EM images suggest that the relative abundance of different aggregate sizes was influence by ligands ABE **24** and APD **31**, while the morphology of formed A4V aggregates remained largely unchanged by the presence of these ligands.

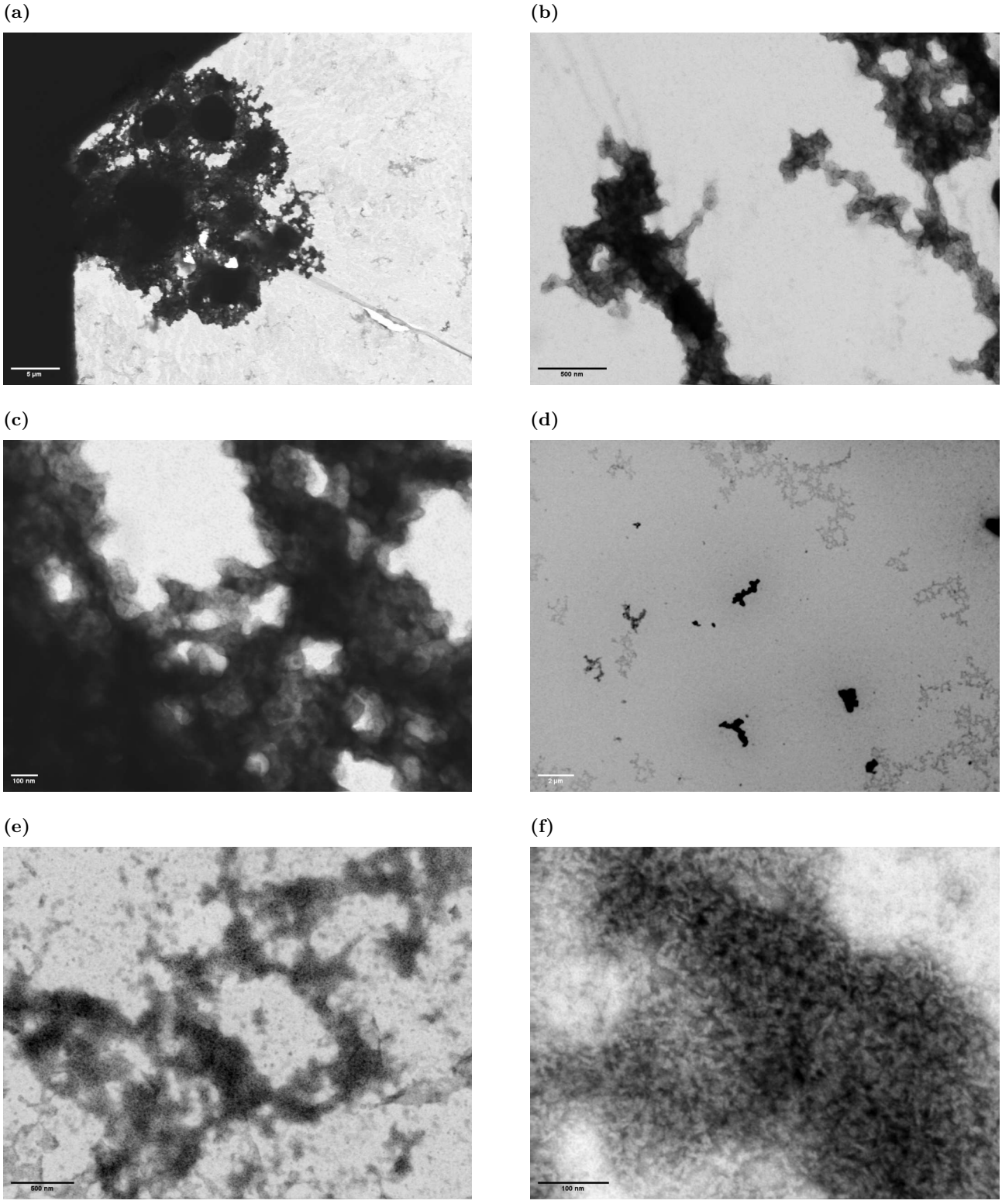

Figure 53: Example electron microscopy images of apo hSOD1 A4V (20 µM) following incubation at aggregation promoting conditions. **(a):** Amorphous aggregate assembly of ~14–16 µm in size. Scale bar = 5 µm. **(b):** Less densely formed aggregates, displaying a cloudy appearance. Scale bar = 500 nm. **(c):** Cloudy appearance of protein aggregates at a greater magnification. Scale bar = 100 nm. **(d):** Scattered deposition of aggregates of ~1–2 µm in size. Scale bar = 2 µm. **(e):** A portion of aggregates display a grainy appearance. Scale bar = 500 nm. **(f):** Grainy appearance of these aggregates at a greater magnification. Scale bar = 100 nm. **Conditions:** The protein's concentration refers to the incubation in a buffer of 80% aqueous buffer (100 mM HEPES, 150 mM NaCl, pH = 7.4) and 20% PEG-550 at 50°C for 24 h, while lightly shaking at 150 rpm. ThT (15 µM final conc.) was added following incubation. EM post-staining was performed with uranyl acetate. A detailed description of the sample preparation and the microscopy procedure is provided in Section 9.10.8.

(a)

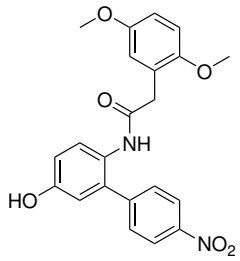

ABE
24

(b)

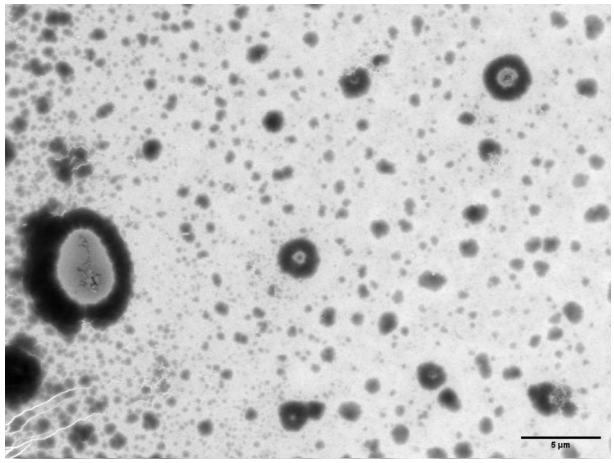

(c)

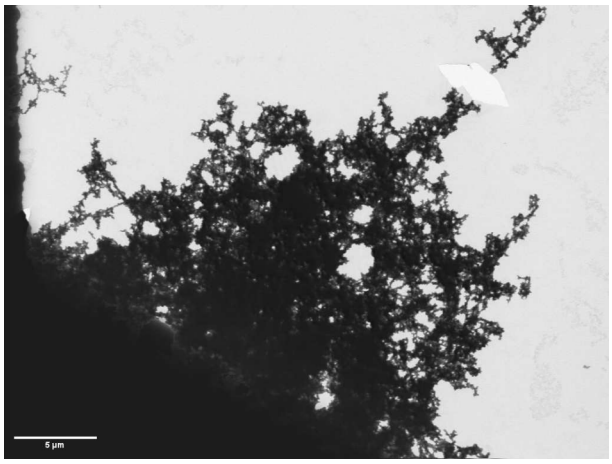

(d)

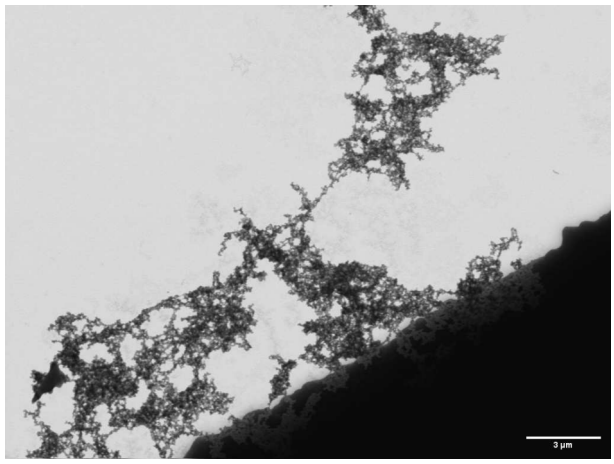

(e)

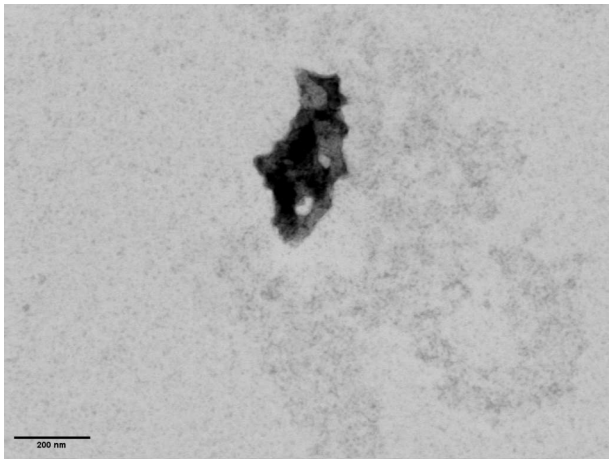

(f)

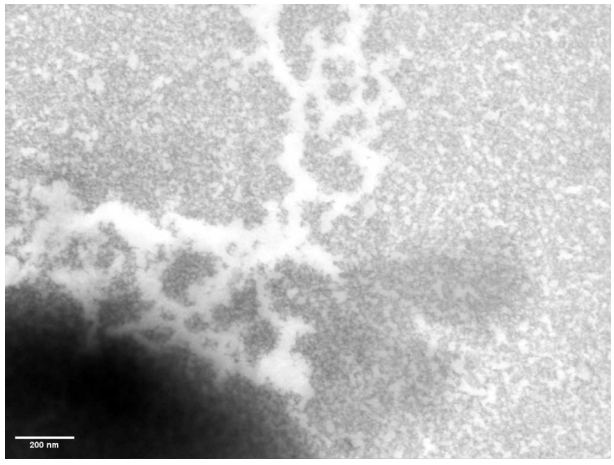

Figure 54: Example electron microscopy images of apo hSOD1 A4V (20 µM) in the presence of ligand ABE **24** (1 mM) following incubation at aggregation promoting conditions. **(a):** Chemical structure of ligand ABE **24**. **(b):** Speckled pattern of dense deposits. Scale bar = 5 µm. **(c):** Amorphous aggregate assembly of ~20–25 µm in size. Scale bar = 5 µm. **(d):** Less dense amorphous aggregate with individual pieces of ~2–8 µm in size. Scale bar = 3 µm. **(e):** Single aggregate of ~250–450 mn in size, amongst seemingly crystalline deposits. Scale bar = 200 nm. **(f):** Seemingly crystalline deposits. Scale bar = 200 nm. **Conditions:** Protein and ligand concentrations refer to the incubation in a buffer of 80% aqueous buffer (100 mM HEPES, 150 mM NaCl, pH = 7.4) and 20% PEG-550 at 50°C for 24 h, while lightly shaking at 150 rpm. ThT (15 µM final conc.) was added following incubation. EM post-staining was performed with uranyl acetate. A detailed description of the sample preparation and the microscopy procedure is provided in Section 9.10.8.

(a)

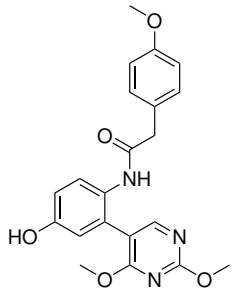

APD
31

(b)

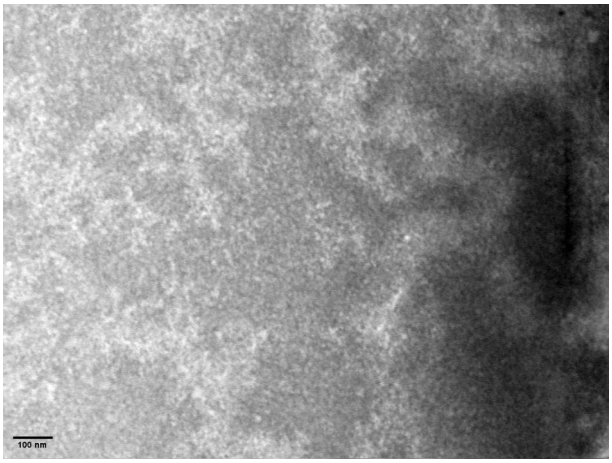

(c)

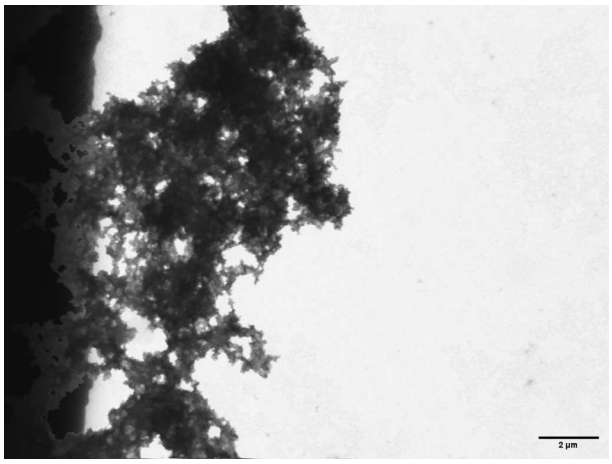

(d)

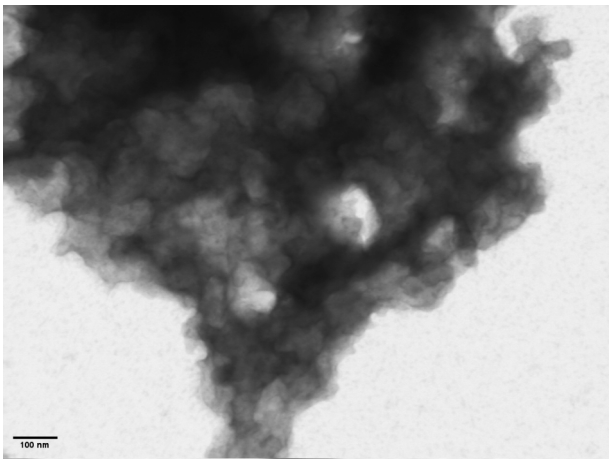

(e)

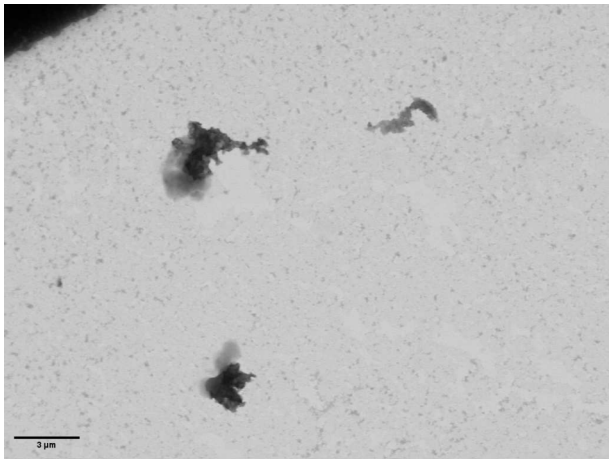

(f)

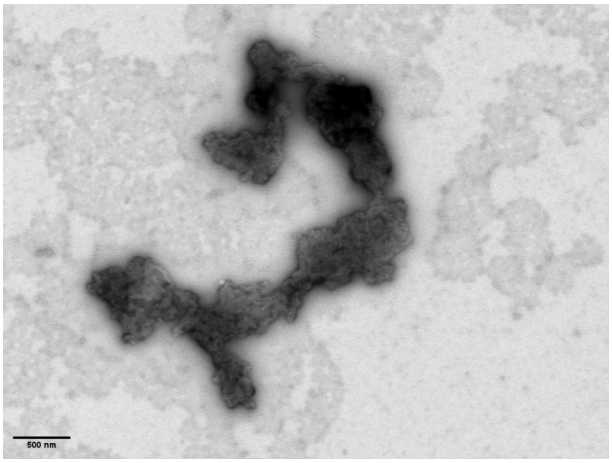

Figure 55: Example electron microscopy images of apo hSOD1 A4V (20 µM) in the presence of ligand APD **31** (10 mM) following incubation at aggregation promoting conditions. **(a):** Chemical structure of ligand APD **31**. **(b):** Seemingly crystalline deposits. Scale bar = 100 nm. **(c):** Amorphous aggregate assembly of ~8–16 µm in size. Scale bar = 2 µm. **(d):** Cloudy appearance of protein aggregates at a greater magnification. Scale bar = 100 nm. **(e):** Singular aggregates of ~2–4 µm in size. Scale bar = 3 µm. **(f):** Singular aggregate at a greater magnification. Scale bar = 500 nm. **Conditions:** Protein and ligand concentrations refer to the incubation in a buffer of 80% aqueous buffer (100 mM HEPES, 150 mM NaCl, pH = 7.4) and 20% PEG-550 at 50°C for 24 h, while lightly shaking at 150 rpm. ThT (15 µM final conc.) was added following incubation. EM post-staining was performed with uranyl acetate. A detailed description of the sample preparation and the microscopy procedure is provided in Section 9.10.8.

5.8 Comparison between Molecular Docking and Experimental Observations

Table 11: Overview of ligands examined in biophysical experiments of this work, ordered by their docking affinity. The corresponding ligand code, number, docking affinity and their position in the top percentage of ligands (Table 26) are listed below every structure.

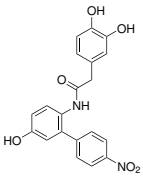	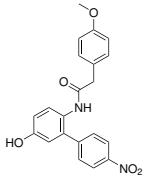	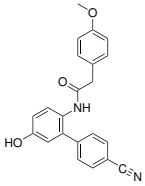	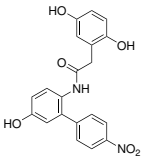	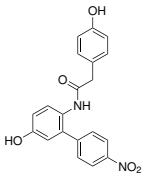	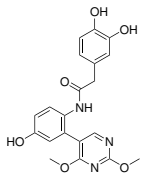
ALE **36**	APE **20**	APT **32**	AWE **38**	AFE **37**	ALD **35**
-9.8 kcal/mol	-9.8 kcal/mol	-9.8 kcal/mol	-9.7 kcal/mol	-9.5 kcal/mol	-9.3 kcal/mol
top 7.5%	top 7.5%	top 7.5%	top 12.2%	top 20.3%	top 29.4%
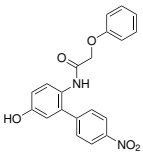	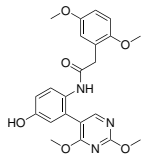	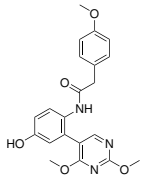	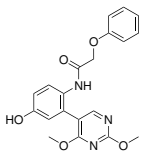	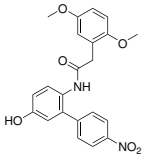	
AOE **29**	ABD **26**	APD **31**	AOD **25**	ABE **24**	
-9.3 kcal/mol	-9.2 kcal/mol	-9.2 kcal/mol	-9.0 kcal/mol	-8.5 kcal/mol	
top 29.4%	top 39.4%	top 39.4%	top 55.9%	top 82.8%	

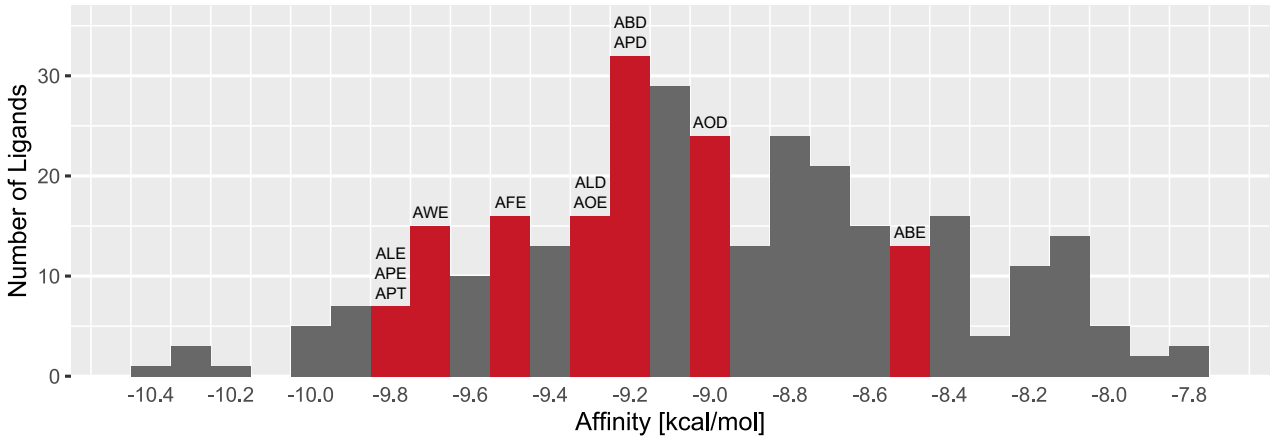

Figure 56: Distribution of docking affinities of all 320 docked ligands shown as a histogram. A bin size of 0.1 kcal/mol was used. The obtained docking affinities had a resolution of up to one decimal place. This resolution was preserved in the binning of the histogram. Bins containing at least one of the examined ligands (listed in Table 11) are shown in red with the corresponding ligands annotated above.

Having collected experimental data for a number of ligands, shown in Table 11, a comparison to the molecular docking experiments (Section 5.2) can be made.

It needs to be repeated, that a correlation between a ligand's ability to stabilize mutant hSOD1 and its binding to hSOD1 as predicted by docking is a simplifying assumption. The *in vitro* binding between ligands and hSOD1 was not quantified in this study. Therefore, while a correlation between a ligands binding strength and its ability to stabilize the protein, thereby preventing its aggregation is a reasonable assumption, it remains to be confirmed.

A visual representation between the docking affinities of the eleven investigated ligands and the entire range of 320 ligands that had been docked, is provided in Figure 56. With the relative position of the ligands visualized, their docking affinity can be compared to their assay performance, to evaluate how well the molecular docking was able to predict their effect *in vitro*. The aggregation assay (Figure 48) provided a suitable base for this comparison, as it had been used to screen all of the investigated ligands. In the case of ligands AWE and ALE which had performed best in the aggregation assay, as well as the DLS assay (Figure 52), the docking had provided an accurate prediction. AWE was predicted in the top 12.2% of ligands based on its affinity and ALE in the top 7.5%. ALD had performed similarly well in these two assays, but with a docking affinity 0.4 and 0.5 kcal/mol lower than AWE and ALE, it was predicted less accurately by the molecular docking and placed in the top 29.4%.

APE which had only shown a modest effect in both assays, was therefore overestimated by the docking prediction. Similarly overestimated by the docking were APT, AFE and AOE as they did not pass the screening stage of the aggregation assay. The remaining ligands ABD, APD, AOD and ABE did not show an effect in the aggregation assay either, but their docking affinities, which placed them in or below the top 39.4%, accurately predicted this *in vitro* observation.

The molecular docking study accurately predicted two of the confirmed hit compounds, in AWE and ALE. As with every *in silico* screen there were false-positive predictions, but those were to be expected. For the development of effective ligands, it is more important that the docking is able to accurately predict true-positives. Highlighted by the identification of AWE and ALE, the docking study proved to be a valuable asset to this investigation.

5.9 Visualization of Predicted Ligand Binding Modes

The proposed binding conformations obtained by the molecular docking simulation allow for analysis and further discussion about the predicted ligand-protein interactions in the form of hydrogen bonds and hydrophobic interactions. However, experimental evidence of the ligand-protein interaction was not obtained within this study. Therefore, it is important to keep in mind, that the proposed binding into the Val148 cavity remains to be confirmed.

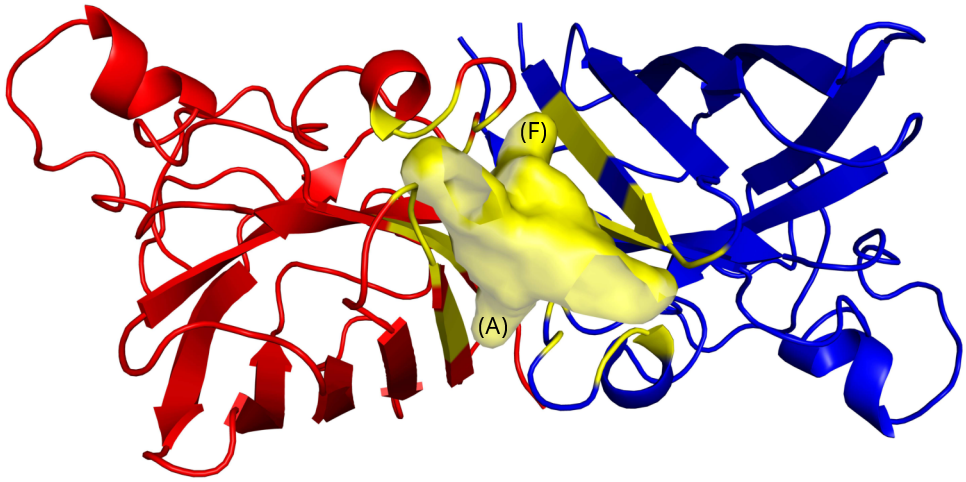

Figure 57: Visualization of the Val148 cavity of hSOD1 (PDB code 2c9u[45]) with its solvent exposed entrance turned towards the viewer and two Channels (A) and (F) of the respective monomers. Monomer A is shown in red, monomer F is shown in blue and AAs of the Val148 cavity and the cavity space are shown in yellow. The cavity space was modeled with PyMOL at 7 Å cavity detection radius and 2 solvent radii cavity detection cutoff.

When overlaying the predicted docking poses of the ligands investigated *in vitro* (Table 11), it could be assumed, that the ones with an overall similar shape and therefore similar space requirements displayed a similar binding mode in the protein's cavity. The compared ligands mostly differ in their boronic acid fragment, while their carboxylic acid fragments are rather similar to each other. The group of ABE, AFE, ALE, AOE, APE, APT, AWE bearing ba-E or ba-T and the group of ALD, AOD, APD and ABD bearing ba-D could therefore be assumed to show similar binding modes, respectively.

(a) **(b)**

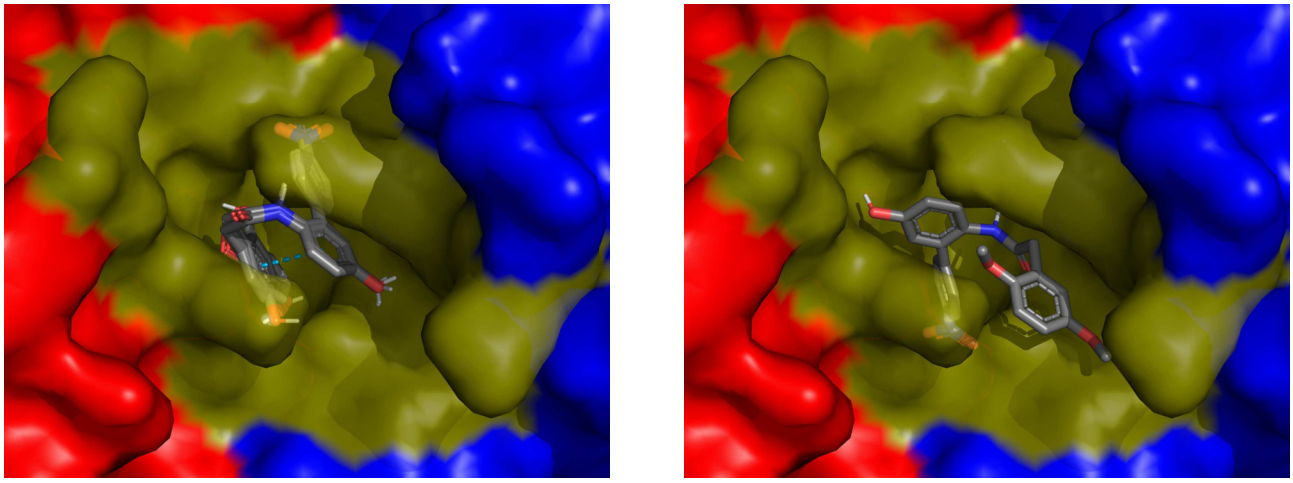

Figure 58: Predicted binding conformations for *in vitro* investigated ligands bearing ba-E or ba-T. Monomer A is shown in red, monomer F is shown in blue, AAs of the Val148 cavity are shown in yellow. **(a):** Ligands AFE, ALE, AOE, APE, APT and AWE overlayed. As as example, the π-π interaction of AFE is shown as a dotted cyan line. **(b):** Ligand ABE.

For the group of ABE, AFE, ALE, AOE, APE, APT, AWE, shown in Figure 58 this was the case, with the exception of ABE. These ligands were positioned with their ca-ring reaching into Channel A and ba-ring reaching into Channel F. Parts of their amide linker and the core were turned towards the outside of the cavity. AOE, which contains a linker elongated by one O compared to the others in its group still adopted the same overall binding mode (Figure 58a). Notably, all but ABE showed a π-π interaction with a distance of 3.8–4.0 Å between the central core-ring and the ca-ring and a distorted amide dihedral angle of 80–95°. It is unclear whether the π-π interaction of these ligands was a relevant factor for the prediction of this conformation or rather a byproduct of this conformation, which predominantly got its shape from the predicted ligand-protein interactions. As shown in Figure 58b, ABE instead adopted a conformation in which its ca-ring was positioned towards the outside of the cavity, likely due to the steric bulk of its two methoxy groups. ABE's ba-ring reached into Channel A and its core occupied the space as the amide linker in the case of ABE, AFE, ALE, AOE, APE, APT, AWE (Figure 58a). While the docking affinities of AFE, ALE, AOE, APE, APT, AWE ranged from -9.8 to -9.3 kcal/mol, ABE was predicted with a much lower affinity of -8.5 kcal/mol.

(a) **(b)**

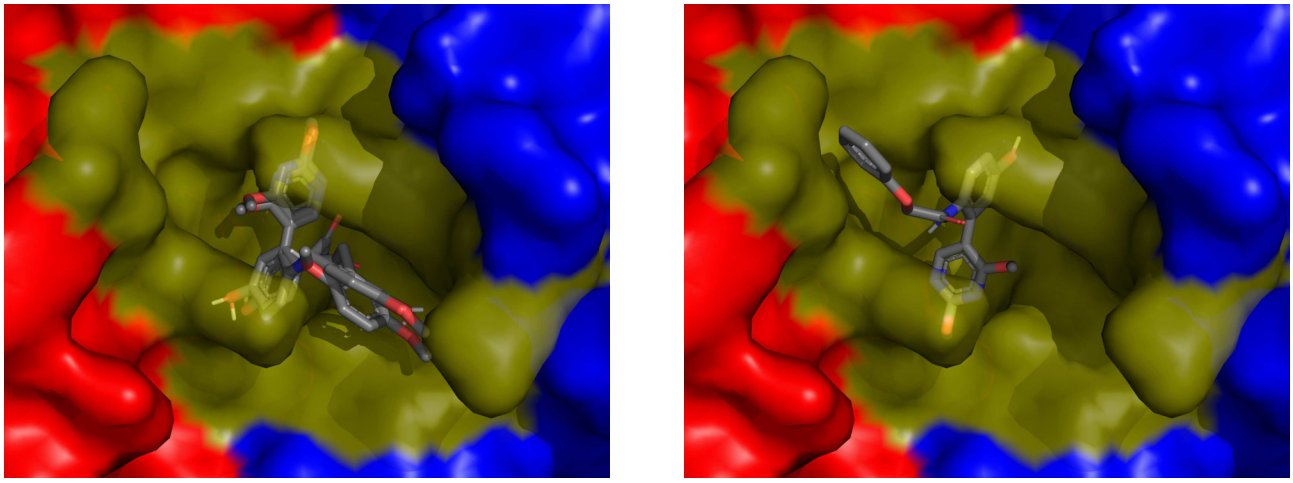

Figure 59: Predicted binding conformations for *in vitro* investigated ligands bearing ba-D. Monomer A is shown in red, monomer F is shown in blue, AAs of the Val148 cavity are shown in yellow. **(a):** Ligands ABD, ALD and APD overlayed. **(b):** Ligand AOD.

The group of ALD, AOD, APD and ABD, shown in Figure 59, with the exception of AOD, all adopted the same conformation, with their ba-ring reaching into Channel F and their core reaching into Channel A, while their ca-ring was positioned towards the outside of the cavity. As shown in Figure 59b, AOD instead had its ba-ring reaching into Channel A and its core reaching into Channel F, with its ca-ring protruding out of the cavity. Similar to the first group (Figure 58), ALD, APD and ABD were predicted with affinities ranging from -9.3 to -9.2 kcal/mol, while AOD was predicted with a lower affinity of -9.0 kcal/mol. This time the difference within the group was less pronounced.

(a) **(b)**

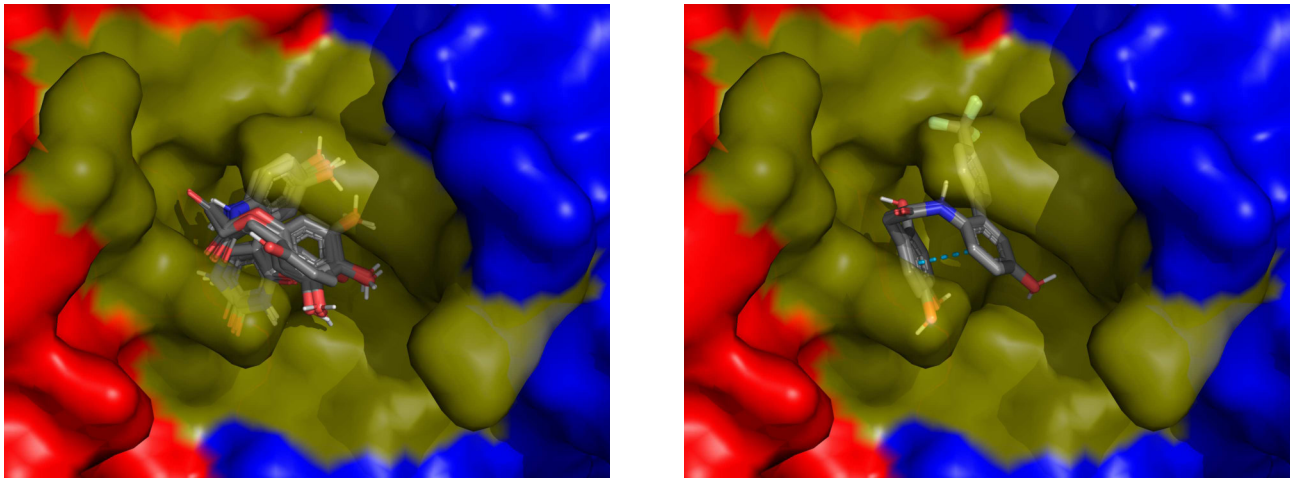

Figure 60: Predicted binding conformations for the best performing ligands of the molecular docking experiments. Monomer A is shown in red, monomer F is shown in blue, AAs of the Val148 cavity are shown in yellow.**(a):** Ligands AWB, ASB, AUB, AMB, ANB, ALB, AHB and AFB overlayed. **(b):** Ligands ALR and AWR overlayed. The π-π interaction of ALR as an example is shown as a dotted cyan line.

Examining the top 10 ligand of the docking (Table 4), as shown in Figure 60 it was observed, that all but ALR and AWR adopted the same docking pose, distinct from the previous ones (Figure 58 and Figure 59), with their ba-ring buried in Channel A and their core pointing into Channel F while their ca-ring was positioned towards the solvent exposed entrance of the cavity. Among them, AWB showed a differently angled ca-ring but adopted the same over all shape (Figure 60a). Ligand AOD, shown in Figure 59b had displayed a similar conformation to the ligands shown in Figure 60a, with its core and ba-ring positioned in the same spaces, only its ca-ring at the entrance of the cavity was turned towards monomer A, instead of F. ALR and AWR, shown in Figure 60b adopted the same binding mode as ligands ABE, AFE, ALE, AOE, APE, APT and AWE (Figure 58a), as could be expected by the shape of their 1,4-substituted ba's. Similarly, ALR and AWR also displayed a π-π interaction with a distance of 3.8–3.9 Å between their core-ring and their ca-ring. AWB, ASB, AUB, AMB, ANB, ALB, AHB and AFB were predicted with affinities ranging from -10.4 to -10.0 kcal/mol, while ALR and AWR were both predicted with an affinity of -10.0 kcal/mol.

Within the presented groups, a trend was observed when taking their docking affinity relative to one another (Figure 56) and their demonstrated *in vitro* effects into consideration. The docking affinity of ALE and AWE, both with confirmed *in vitro* effects, was amongst the highest within their group (Figure 58a). Similarly, ALD, with confirmed *in vitro* effect, had the highest docking affinity within its group (Figure 59a). Notably, ALD had been predicted with a noticeably lower docking affinity, compared to ALE and AWE, as discussed in Section 5.8. The number of investigated ligands is not extensive enough for a definitive statement, but this could suggest that comparison of docking affinity, within a subgroup of ligands sharing a binding mode, could be a better predictor of a ligands *in vitro* performance, than its docking affinity in a global comparison alone.

6 Summary

In this work, the design and synthesis of mutant hSOD1 stabilizing small molecule ligands was pursued. With the identification of AWE **38**, ALE **36** and ALD **35**, three hit compounds were obtained and their *in vitro* effect of reducing hSOD1 A4V aggregation was confirmed by complementary assays.

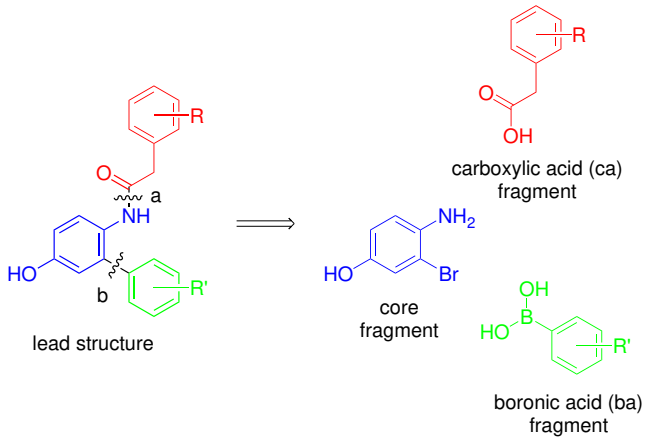

Scheme 14: Retrosynthetic analysis of the ligands lead structure. Disconnection a represents an amide coupling and b represents a Suzuki–Miyaura coupling reaction. Illustration adapted from earlier work by the author.[48]

Prior to this investigation (outlined in Section 2.8), retrosynthetic analysis of the lead structure (Scheme 14) had yielded three structural fragments, which could be independently varied to access a diverse library of potentially mutant hSOD1 stabilizing small molecule ligands.

An *in silico* screening by molecular docking had been explored in previous work by the author,[48] and was substantially expanded in this study, as described in Section 5.2. Molecular docking of 320 lead structure derived ligands to the hSOD1 protein was carried out, in order to reveal the most beneficial fragments and their most promising combinations. In addition to the ligands themselves, emphasis was placed on the evaluation of the underlying fragments, with the aim to identify fragments that generally lead to promising ligands, as opposed to only in limited examples. Fragments that more generally resulted in promising ligands were valuable building blocks for this works modular synthesis. Indeed, it was observed that inclusion of certain fragments, lead to favorable ligand binding *in silico*, while certain other fragments could reasonably be omitted in the chemical synthesis towards a ligand library intended for *in vitro* examination. In addition to these valuable fragments, ligands that displayed strong *in silico* binding were themselves identified as valuable synthetic targets.

Molecular docking was therefore a beneficial asset to this study, as it helped to reduce the synthetic demand, by highlighting which building blocks in general and which ligand structures specifically should be the focus of chemical synthesis.

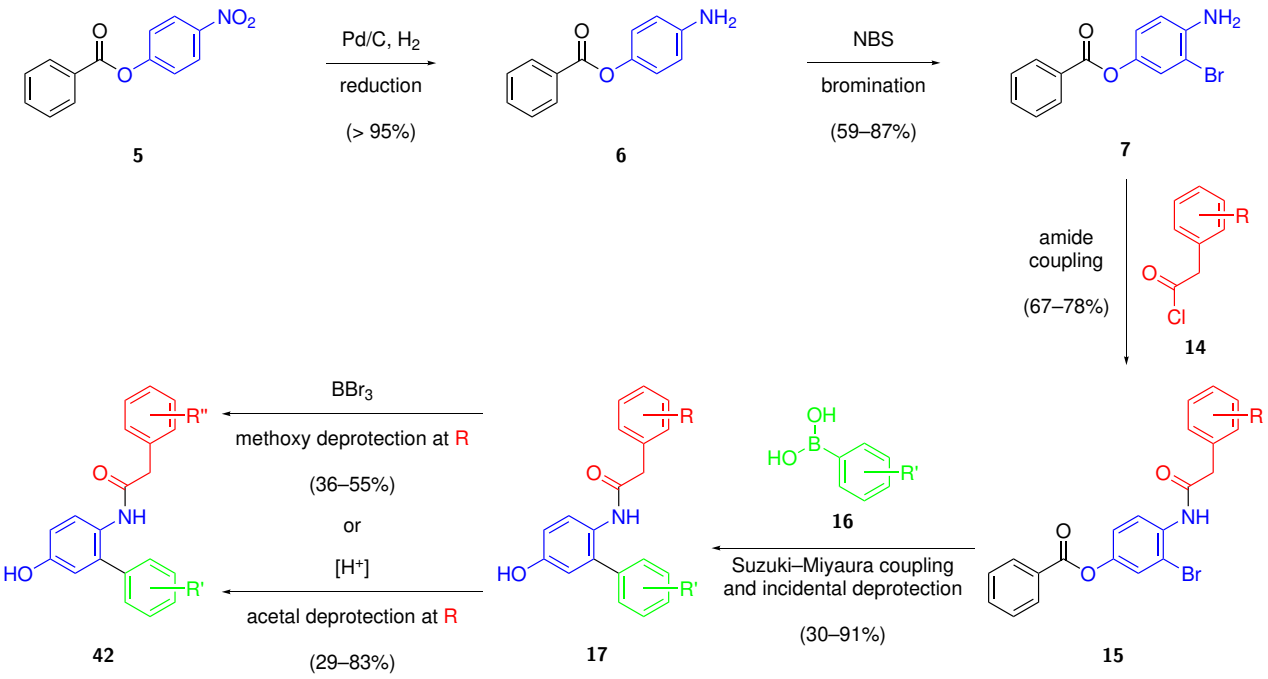

Scheme 15: Generalized scheme of the modular synthesis of this work. The investigated ligands are represented by compound **17** or compound **42**. Protection steps necessary for certain building blocks are omitted for clarity.

The modular synthesis route (Section 5.3), illustrated in Scheme 15, provided the foundation for the ligands chemical synthesis. The individual reaction steps of this route were further adapted and optimized, since prior investigations by Mrđen Debono[159] and subsequently by the author.[48] Two aspects were especially important in this regard and represented points of focus during the synthesis: generality and scalability. The amide coupling and the Suzuki–Miyaura coupling (SMC) both represent branching points for diversification and as such should be as generally applicable as possible, ideally accommodating a wide array of building block combinations. Reaction conditions were therefore investigated with a focus on generality rather than case-specific optimization. Similarly, to best profit from the combinatorial aspect of this modular synthesis approach, compounds that represent shared precursors for following reactions should be accessible at multi- or decagram scale. Scale-up, in particular of early reaction steps, was therefore conducted accordingly. A total of twelve ligands were synthesized, eleven of which were examined *in vitro*, as described in Section 5.7.

The hSOD1 protein and its ALS-relevant hSOD1 A4V variant were successfully expressed from *E. coli.*, as discussed in Section 5.6. The purification of both hSOD1 and hSOD1 A4V was successfully established, providing both protein variants in their natively metalated holo (Cu|Zn), as well as their demetalated apo (E|E) states, for use in biophysical experiments.

Examination of holo hSOD1 by ESI-MS was carried out, as discussed in Section 5.6.3 and provided qualitative evidence that dimeric Cu^{2+} and Zn^{2+} bound hSOD1, containing the native intrasubunit Cys57-Cys146 disulfide bond had successfully been obtained. The activities of holo hSOD1 and holo hSOD1 A4V were determined and demonstrated to be in agreement with the literature, as discussed in Section 5.6.4. The binding of the native Cu^{2+} and Zn^{2+} cofactors, as well as correct folding and dimer association were thereby confirmed.

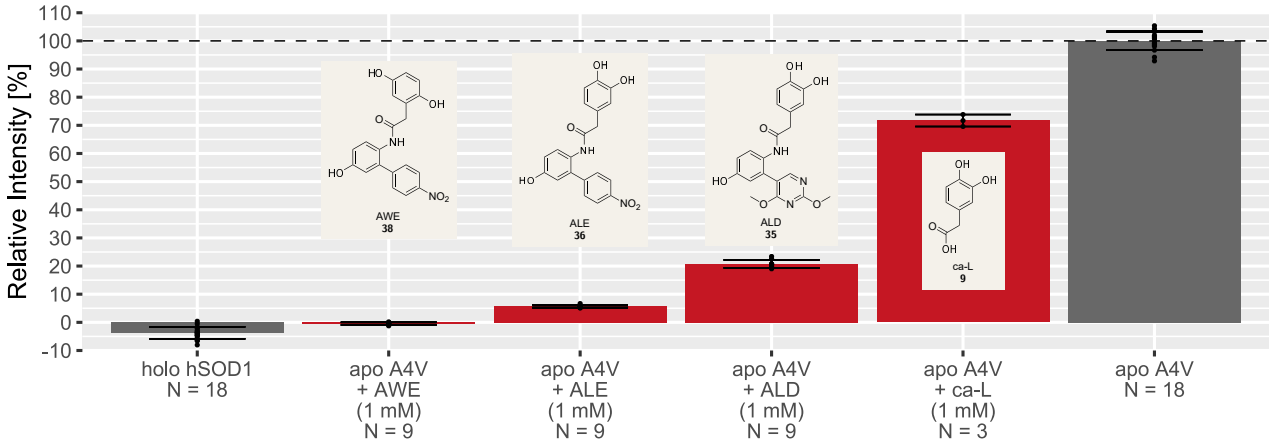

Figure 61: Relative ThT fluorescence intensity as a measure of hSOD1 aggregation. Excerpt of Figure 48, highlighting the best performing ligands and their chemical structures. Samples are ordered by relative intensity. Protein controls holo wt hSOD1 and apo hSOD1 A4V are shown in gray. The mean intensity of the apo A4V control of each individual well plate was defined as 100% relative intensity. Relative intensities are shown as mean and standard deviation obtained from multiple independent experiments with multiple replicates each. The relative intensities of each replicate are shown as dots, with the total number of replicates (N) specified. Relative intensities and standard deviations are provided in table from in Section 10.5

A thioflavin T (ThT)-based aggregation assay formed the screening stage of this works biophysical experiments. As inhibition of ALS-relevant hSOD1 aggregation was the intended function for the investigated ligands, this assay was an appropriate screening tool. While most ligands did not display any appreciable inhibitory effect, the aggregation assay distinctly indicated that ligands AWE **38**, ALE **36** and ALD **35** successfully limited the aggregation of ALS-relevant apo hSOD1 A4V, as shown in Figure 61. Notably, the building block ca-L **9** also displayed an inhibitory effect on hSOD1 A4V aggregation. While its effect was much less pronounced in comparison, this underlined the indication that the dihydroxybenzene moieties of all four of those compounds could be a relevant factor of their effect.

Due to known caveats of the ThT assay, in the context of small molecule agents (Section 4.4), dynamic light scattering (DLS) was chosen as a complementary method to validate the lead structures effect to reduce hSOD1 A4V aggregation.

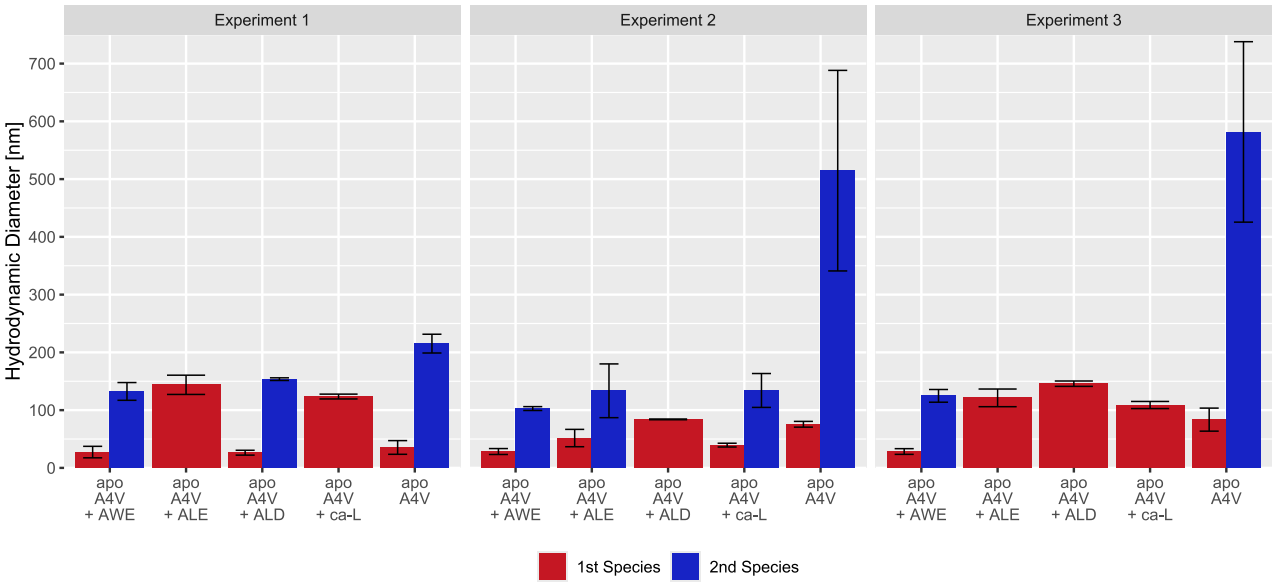

Figure 62: Comparison of hydrodynamic diameter d_H of SOD1 aggregates after 1 day of incubation determined by DLS from three independent experiments. Excerpt of Figure 52, highlighting the best performing compounds of the DLS assay. Species are numbered from smallest to largest by d_H. Ligands are ordered from left to right based on their performance in the ThT based aggregation assay. The data visualized in this figure is provided in the appendix (Section 10.4, Table 34).

In order to validate the results of the ThT assay, hit compounds AWE **38**, ALE **36** and ALD **35**, together with ca-L **9** and ALE **36**, serving as comparisons, were further investigated by DLS. This method provided the hydrodynamic diameter d_H of formed apo hSOD1 A4V aggregates, to examine the aggregation reducing effect of these compounds. Confirming the results of the ThT assay, the observed d_H of aggregate species were smaller in the presence of ligands AWE **38**, ALE **36** and ALD **35**, compared to apo hSOD1 A4V alone (Figure 62). AWE **38** in particular was demonstrated as the most potent among them, consistently retaining the smallest observed aggregate species across all DLS experiments.

However, where the ThT assay had suggested that, specifically in the presence of AWE **38** or ALE **36**, almost no hSOD1 A4V aggregation should be observed, their effectiveness was less pronounced in the DLS assay. This observation was most apparent in the case of Experiment 1, shown in Figure 62. The aggregation reducing effect of the investigated compounds, was therefore difficult to quantify by the ThT and DLS assays.

Similar to the results of the ThT assay, ca-L **9** displayed a reducing effect on hSOD1 A4V aggregation (Figure 62). Notably, the DLS assay indicated that its effectiveness was closer to that of ligands ALE **36** and ALD **35** than the ThT assay had suggested. While the total number of ligands tested was not extensive enough to warrant a definitive statements about the ligands' structure-activity relationship, the results of both the ThT and the DLS assay indicate that a dihydroxybenzene moiety is advantageous to the ligands effect *in vitro*.

Examination of aggregated apo hSOD1 A4V by electron microscopy (EM) revealed that under the incubation conditions of this study, apo hSOD1 A4V predominantly formed aggregates of amorphous morphology, while fibrils were not observed. Importantly, (discussed in Section 4.4.1 and 5.7.4), this observation adds to a body of literature, which had demonstrated that under specific conditions, such as the the ones utilized here, soluble oligomers or amorphous aggregates are formed and ThT fluorescence is readily observed in the absence of amyloid fibrils.[94,174,187]

A comparison between the obtained experimental data of the *in vitro* investigated ligands and their molecular docking demonstrated that the *in vitro* effects of ligands AWE **38** and ALE **36** had been accurately predicted by the docking, as discussed in Section 5.8. The *in vitro* effect of ALD **35** had been predicted less accurately by comparison. The docking had also predicted other ligands, which were revealed as false-positives by the screening of the aggregation assay, as was to be expected. In conclusion, the docking study served its screening purpose and the remaining ligands with high affinity values, in the top percentage of docked ligands, were suggested as synthesis targets for future investigations.

In conclusion, with compounds AWE **38**, ALE **36** and ALD **35** three small molecule ligands, demonstrated to reduce ALS-relevant mutant hSOD1 aggregation, have been developed. Their effectiveness was demonstrated *in vitro* by both the ThT based aggregation assay and the DLS assay. Importantly, the two complementary assays provided orthogonal read outs to monitor the aggregation of apo hSOD1 A4V and the ligands' influence on this process, ruling out potential false-positive observations of either one method.

The overarching goal of this study to design and synthesize molecular structural stabilizers for the ALS-relevant SOD1 protein was successful. These compounds provide valuable assets to research on the development and progression of hSOD1 related ALS. Beyond this, these compounds provide promising scaffolds for the development of therapeutic agents against this fatal, presently incurable disease.

7 Outlook

Valuable building blocks and promising ligands were identified by *in silico* screening of a virtual ligand library, derived from a lead structure, guiding the following synthesis. A library of ligands, to be examined *in vitro*, was prepared *via* a direct modular organic synthesis approach. The hSOD1 and hSOD1 A4V proteins were recombinantly expressed, to serve as an *in vitro* model of ALS. The presence of all their native maturation modifications was confirmed through ESI-MS and assessment of their enzymatic activity. Ligands were screened for their effect on hSOD1 A4V aggregation.
Although this study was comprehensive, it can readily be expanded to identify additional potent ligands, due to the utility of the *in silico* screening and the *in vitro* assay systems. Following the methodology developed in this work, more ligands can be examined. Beyond the ligands that were synthesized so far, the molecular docking (Section 5.2) indicated a number of additional fragments with beneficial moieties and ligands that are promising targets for future synthesis and *in vitro* experiments. The molecular docking study itself can always be extended by the introduction of additional fragments from which new ligands can be combinatorially generated *in silico*.

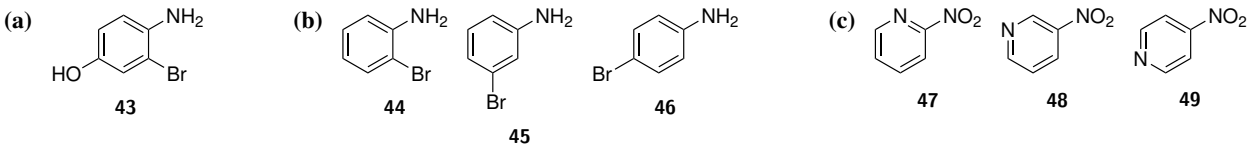

Figure 63: Commercially available building blocks that could provide diversification of the core fragment. **(a):** Currently utilized core fragment. **(b):** Bromoanilines alternatives. **(c):** Nitropyridines alternatives.

Currently, all ligands share the same core fragment in the form of 4-amino-3-bromophenol **43**. A selection of possible alternatives to the current core **43** are shown in Figure 63. Bromoanilines **44**, **45** and **46** can be utilized to investigate, how different angles between the ca and ba moieties affect the ligands docking affinities. While a linear configuration, as in 4-bromoaniline **46** may likely not be ideal, a meta relation between the ca and ba moieties, as in 3-bromoaniline **45** can potentially have a positive effect. Additionally, bromoanilines **44**, **45** and **46** can be readily employed in amide couplings, skipping the first two steps of the reported synthesis route (Scheme 4). Nitropyridines **47**, **48** and **49** can be used to investigate if introduction of a pyridine into the ligand's structure provides benefits *in silico* and *in vitro*. These building blocks only represent a few examples of possible variations of the core fragment that can be investigated in future studies.

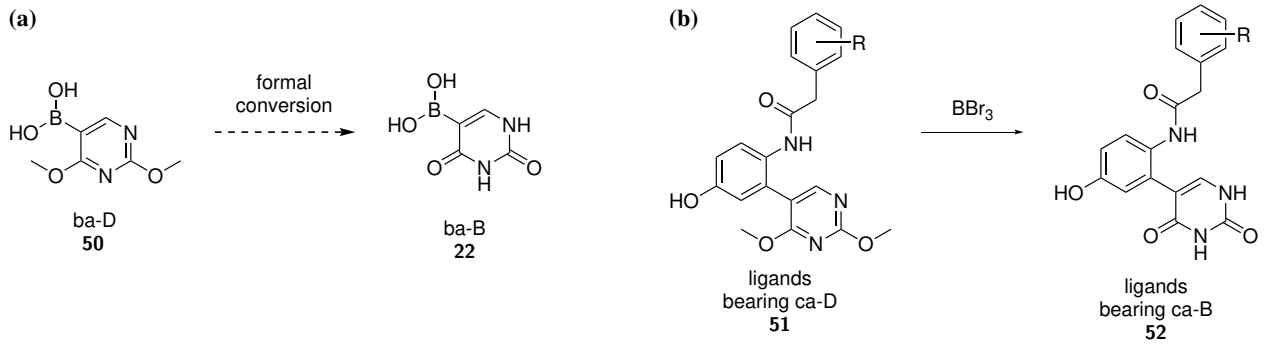

Figure 64: (a): Formal conversion of ba-D **50** into ba-B **22**. **(b):** Potential synthetic conversion of ligands bearing ba-D **51** into ligands bearing ba-B **52**.

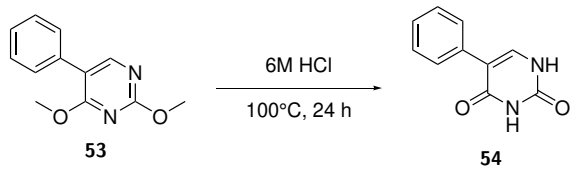

Figure 65: Conversion of 2,4-dimethoxy-5-phenylpyrimidine **53** into 5-phenylpyrimidine-2,4(1*H*,3*H*)-dione **54** as reported by Aronov *et al.*, highlighting another possible way to afford the ba-B functionality.[258]

Further synthetic effort to obtain ligands bearing the uracil boronic acid ba-B **22**, shown in Figure 64a can be undertaken, as the molecular docking study (Section 5.2, in particular Table 4 and Figure 31) strongly suggested these ligands to be promising candidates for *in vitro* examination. Thus far, SMCs of ba-B **22** had not been successful (Section 5.3.4). The coupling of this particular substrate can potentially be enabled by a thorough screening of reaction conditions.

Alternatively, the conversion of ba-D **50** into ba-B **22**, by BBr_3 following SMC as outlined in Figure 64 can be developed further. An example reaction (Scheme 13) indicated that this transformation can be achieved in principle and optimization of the reaction conditions can potentially improve its yield. A similar reaction to afford this moiety, shown in Figure 65 has been reported by Aronov *et al.* and can potentially be applied to access ligands bearing ba-B **22**.[258]

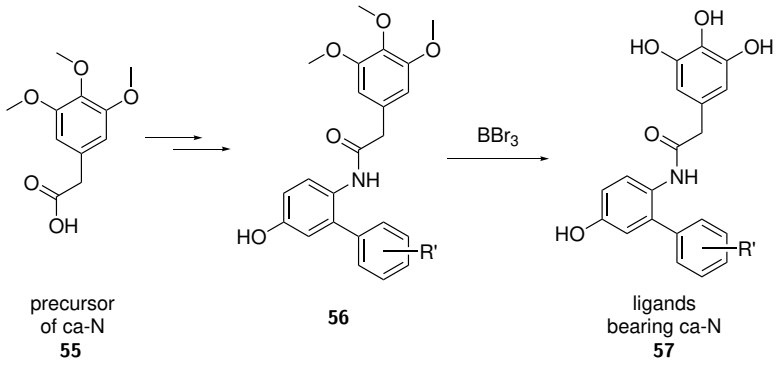

Scheme 16: Simplified representation of an envisioned synthesis towards ligands bearing ca-N **57**, starting from commercially available 2-(3,4,5-trimethoxyphenyl)acetic acid **55**.

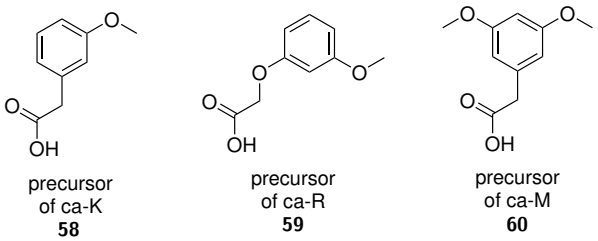

Figure 66: Commercially available building blocks, which could be used to access ligands bearing the functionalities of ca-K, R or M.

Because of the success of Ligand AWE **38**, ALE **36** and ALD **35**, each bearing a dihydroxybenzene moieties, investigation of other (poly)hydroxybenzene ca derived ligands is a valuable endeavor. Further support for this undertaking is provided by the molecular docking study (Section 5.2). Some of the best performing ca fragments and ligands were characterized by multiple aromatic hydroxyl groups, highlighting them as valuable targets for future synthetic efforts.

The synthesis of AWE **38** and AFE **37** (Scheme 12) showed that multiple aromatic hydroxyl groups can be accessed through the deprotection of aromatic methoxy groups by BBr_3. While not compatible with every ba, this method provides a simple protecting group strategy to access these functionalities in a number of ligands. The feasibility of this approach has been demonstrated and the reaction conditions can be optimized to improve it. Carboxylic acids bearing multiple aromatic methoxy groups are readily available from commercial suppliers, highlighting the accessibility to further investigate this strategy. An example of an envisioned synthesis, following this strategy is outlined in Scheme 16 and Figure 66 highlights further building blocks for this approach.

In order to obtain quantitative information on the binding kinetics of the ligands to hSOD1 isothermal titration calorimetry (ITC) can be utilized. An example of small molecule-hSOD1 binding investigated by ITC has been reported by Ip *et al.*.[263] Additionally, preliminary ITC experiments by Mrđen Debono demonstrated that while DMSO as a cosolvent was incompatible with ITC, glycerol was found to be a suitable replacement.[159] As ITC can provide a quantitative evaluation between *in vitro* effective ligands its development is of great interest to future investigations.

In order to ultimately demonstrate ligand binding and its localization, protein NMR or cocrystalization of hSOD1 and bound ligands would provide the strongest evidence. Both methods are therefore of great interest to future studies of the hSOD1 ligands developed in this work.

To identity ligands with an *in vitro* effect of reducing hSOD1 A4V aggregation, the synthesized ligand library was screened by a ThT Assay. Three putative hits (AWE **38**, ALD **35** and ALE **36**) were identified among the ligands and confirmed by a complementary DLS assay. Both assay systems and their results, especially in relation to each other, were critically evaluated, to ensure the validity and consistency of the obtained results. A shared dihydroxybenzene moiety between the three hit ligands, was further assessed by the inclusion of a dihydroxybenzene bearing building block (ca-L **9**) in the assays, which further supported the suggestion that this moiety was a benefit to the ligands' *in vitro* effect. In conclusion, among the eleven ligands that had been investigated *in vitro* three (AWE **38**, ALD **35** and ALE **36**) with confirmed hSOD1 A4V aggregation reducing effects were identified. This demonstrates the utility of the screening and assay systems established in this work.

Generally, it should be investigated if a lower percentage of DMSO cosolvent could be utilized in future investigations. 20% DMSO were used in this study, to ensure that ligands could be used at 1 mM concentration in the aggregation assay, without risking their precipitation during the experiment. This was successful for most, but not all ligands of this study (Table 10). For an initial screening, the use of 20% DMSO was acceptable, but moving forward the hit compound's solubility in buffers containing 10%, 5% or ideally 0% DMSO should be determined. The ligand's water solubility can be improved through the design of their chemical structure, if necessary. There are published indications that DMSO can influence hSOD1's shape and stability, although whether the influence is stabilizing or destabilizing is indicated to depend on the DMSO concentration.[259] It would therefore be desirable to limit this effect on experimental observations.

As discussed in Section 4.4, additional information on the influence of the ligands on hSOD1 aggregation can be obtained by continuous ThT measurements over a period of time.[176,177,181] They can therefore be employed to investigate specific ligands which had displayed an effect in the end point ThT assay. To avoid ThT degradation, the incubation temperature can be lowered to 37°C, which has been demonstrated as sufficient to observe hSOD1 aggregation.[94,174,183] Alternatively, a continuous *ex situ* setup (described in Section 4.4) can be used, to avoid ThT degradation.

A potential concentration dependence for the ligands aggregation inhibition effect can be examined in future studies. Similar to an investigation of their effect over a period of time, this provides additional information to asses the ligand's effectiveness.

Given access to a close-by SEC-device, particles outside of the DLS detection range can be removed prior to measurements, in order to reduce confounding effects. Filtration or degassing of DLS samples may also improve data quality. Alternatively, aggregated hSOD1 samples could be investigated by size exclusion chromatography (SEC) coupled with multiple angle light scattering (MALS) (SEC-MALS). This technique first separates the different components of a sample by their approximate size and then determines their molecular weight, based on their light scattering in dependence of the detection angle.[181,260] Multi-angle dynamic light scattering (MADLS) could also be utilized to characterize

aggregate species of hSOD1 in solution. In very broad terms, in MADLS multiple DLS measurements at various detection angles are combined to obtain a higher resolution, more accurately reporting on a samples particle size distributions.[261,262]

The ability to quaulitatively evaluate the *in vitro* effect of hSOD1 ligands should be a goal of future studies in regards to the optimization and extention of the assay system. Comparability of compounds' effects on hSOD1 aggregation is often limited across publications. The methods used to obtain and characterize aggregated hSOD1 can have a notable effect on the observed effectiveness of the investigated compounds, but are not always consistent across investigations (Section 4.4.1). The most reliable comparison between multiple compounds' effects is provided under identical conditions, usually only provided within the same study. To obtain a meaningful comparison, it would therefore be of interest to evaluate literature-known hSOD1 aggregation inhibitors (Section 2.4), together with the developed hSOD1 ligands, in the assay systems established here.

Similarly, it would be interesting to investigate how the *in vitro* confirmed hSOD1 ligands of this work perform in the hands and assay systems of other research groups, particularly in regards to cell or animal models of ALS. Ligands AWE **38**, ALE **36** and ALD **35** were demonstrated to effectively reduce mutant hSOD1 aggregation *in vitro*, highlighting them as compounds to be examined further in future studies. The next step in their development as potential therapeutic agents would be to investigate their effect in more complex *in vivo* systems.

8 Computational Procedures

The following procedures had been developed in previous work by the author and have been reported therein.[48]

8.1 Molecular Docking employing AutoDock Vina

AutoDock Vina was used for molecular docking calculations.[196] ChemDraw Professional 20, Chem3D 20 and AutoDockTools (ADT) 1.5.7 were used in the preparation of ligands and protein 3D structures in the form of .pdbqt files required by AutoDock Vina. Visualization of ligands and hSOD1 were created with PyMol using an X-ray crystal structure of hSOD1 (PDB: 2c9u) provided by Strange *et al.*. Consistent with Strange *et al.*, monomers of hSOD1 are refereed to as A and F.[45]

8.1.1 Preparation of Ligands

For the preparation of ligand structures the protocol of Forli *et al.*[264] was followed with minor alterations. Two-dimensional ligand structures were drawn in ChemDraw and saved as .cdxml. Acyclic amides, thioamides and ureas were drawn with torsion angles of 180° between O-C-N-H (referred to as trans conformation). The .cdxml files were then opened in Chem3D. The torsion angles between O-C-N-H of amide bonds were set to 180°, because in Chem3D the O-C-N-H torsion angles would sometimes be assumed as 90° instead of the intended 180°. To afford an energetically more realistic conformation of the ligand as a starting point for docking calculations, a MM2 minimization was carried out. Following the MM2 minimization, torsion angles in amide bonds were again set to 180° and ligands saved as .pdb files. The .pdb files were opened in AutoDockTools, the structure set as ligand and rotatable bonds defined. Amide bonds were set as rotatable. In some cases, certain bonds would not be recognized as rotatable by AutoDockTools by default. In such cases they had to manually be defined as rotatable through the softwares Python IDLE shell.[265] The structures were then saved as .pdbqt for use in AutoDock Vina.

8.1.2 Preparation of Protein Receptor

For the preparation of the protein structure, the protocol of Forli *et al.*[264] was followed with minor alterations. The X-ray crystal structure of hSOD1, which was used in the docking studies, was acquired from the Protein Data Base (PDB: 2c9u), provided by Strange *et al.*.[45] The provided X-ray crystal structure had been solved in a 1.24 Å resolution. The .pdb file was opened in ADT, water molecules, Cu, Zn, $SO_4{}^{2-}$ and AcO^- were removed and all hydrogen atoms were added to the structure. The protein was set as macromolecule and saved as .pdbqt for use in AutoDock Vina.

8.1.3 Grid Box Covering the Val148 Cavity

In AutoDock Vina, the molecular docking of a ligand and a protein takes place in a grid box defined by the user. Essentially the grid box acts as a spacial restriction, defining on what region of the protein the docking shall be performed. Generally, increasing the grid box, leads to a greater computational demand. While it has been shown that this is not necessary always the case,[266] it is advised in the AutoDock Vina manual[267] to keep the grid box (referred to as search space in the manual) as small as possible.

To construct a grid box that would cover the Val148 cavity and to include only as much of the remaining protein as necessary, the grid box was first centered on one of the Lys9 sidechain-N. From there, the center was manually adjusted to be centered approximately between the two Lys9 sidechain-N. Then, the grid box' dimensions were chosen in a way as to include the entire surface of the binding site (shown in yellow in Figure 67) in the grid box, while ensuring that the gridbox did not protrude out of the "backside" of the protein.

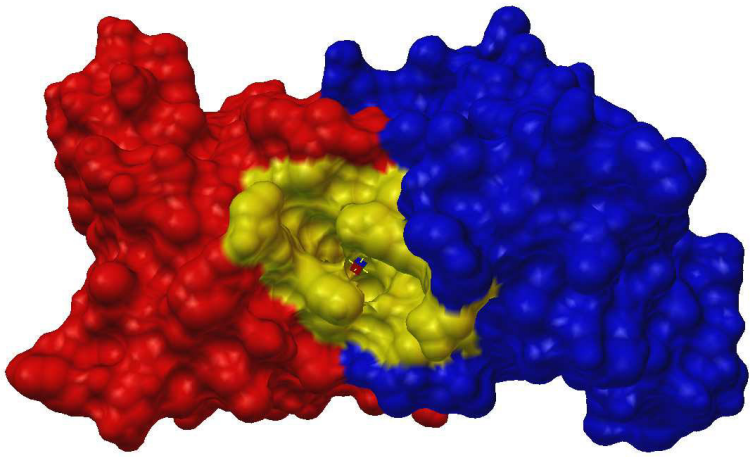

Figure 67: Illustration of the center of the grid box in relation to SOD1. Monomer A is shown in red and monomer F is shown in blue. AA's contributing to the surface of the Val148 cavity (Val5, Cys6, Val7, Lys9, Gly10, Asp11, Gly51, Asn53, Gly56, Cy57, Cys146, Gly147, Val148 of each monomer) are shown in yellow. The sides of the grid box are colored according to the respective dimension (x red, y green, z blue). The sizes of the grid box's are shown as 1 Å in each direction to better visualize its center. The sizes of the grid box's dimensions used in docking experiments are listed in Table 12.

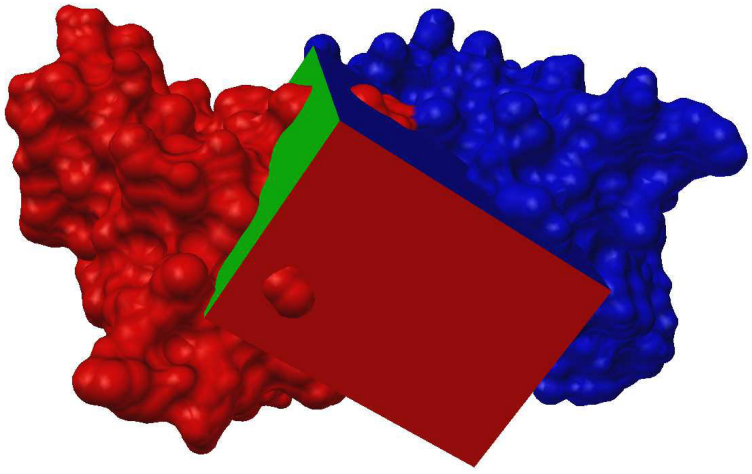

Figure 68: Illustration of the placement and size of the grid box in relation to SOD1. Monomer A is shown in red and monomer F is shown in blue. The sides of the grid box are colored according to the respective dimension (x red, y green, z blue). The sizes of the grid box's dimensions are listed in Table 12.

Table 12: Parameters of the grid box.

center x = 11.000 Å	size x = 25.0 Å
center y = 0.000 Å	size y = 28.0 Å
center z = 12.000 Å	size z = 20.0 Å

9 Experimental

9.1 Data Analysis and Visualization

Unless otherwise stated in the respective section, data analysis was performed in R (Version 4.3.3)[268] with the tidyverse package (Version 2.0.0)[269] or Origin pro. Visualization was performed with the ggplot2 package (Version 3.5.0)[270] in R.

9.2 Chemical Synthesis and Compound Characterization

When stated, reactions were performed under N_2 or Ar and glassware was heated to dryness prior to use. In these cases, glassware was evacuated on a Schlenk-line, then uniformly heated with a heat gun for a couple of minutes, then charged with N_2 and left to cool to rt. This was repeated a total of 3 times. Reactions were then carried out under a positive pressure of N_2 or Ar as specified respectively using standard Schlenk techniques. When stated, anhydrous solvents were used and solvents were degassed. The respective procedure for degassing of solvents is stated respectively. All reagents were purchased at $\geq$ 99% purity at grades ReagentPlus, puriss p.a., or ACS reagent from Sigma Aldrich/Merck if available. If not available from Sigma Aldrich/Merck, the following vendors were consulted: TCI, Across, Carbolution, abcr, Roth or Life Chemicals. Unless stated otherwise reagent were used without further purification. When no reaction temperature is specified, reactions were carried out at room temperature (rt). Microwave reactions were performed with a Microwave Synthesizer Discover SP from CEM using 10 or 35 ml microwave reaction vessels from CEM. Analytical thin layer chromatography (TLC) was carried out on TLC Silica gel 60 F_{254} on Aluminium sheets from Merk. TLC visualization was accomplished using 254 nm UV light or staining solutions of $KMnO_4$ or ninhydrin. Flash column chromatography was performed using Silica gel 60 (0.040-0.063 mm) from Merk. Melting points of solid substances were measured with a Melting Point Meter M5000 from Krüss at a heating rate of 1°C/s. NMR spectra were recorded at rt on a Bruker Avance III 300, 400, 500 or 600 (300.51 MHz, 400.33 MHz, 500.13 MHz, 600.24 MHz respectively), Bruker Avance DRX 300 (300.13 MHz), Bruker Fourier 300 (300.18 MHz) or Bruker Avance Neo 700 (700.13 MHz). With exception of the Avance III 300, instruments were operated by the NMR service department of the Institute of Organic Chemistry, Heidelberg University. NMR solvents were purchased from Deutero or Eurisotop. The residual solvent peak was used as internal reference[271] (^{1}H NMR: $CHCl_3$ (7.26 ppm), DMSO d_6 (2.50 ppm); ^{13}C NMR: $CHCl_3$ (77.16 ppm), DMSO d_6 (39.52 ppm)). NMR spectra were analyzed and visualized with MestReNova 14.1 and multiplets were reported using the abbreviations: singlet = s, doublet = d, triplet = t, doublet of doublets = dd, doublet of triplets = dt, multiplet = m. For some ^{13}C NMR spectra a spike at about 147.5 ppm was observed, an artifact specific to that NMR machine. High-resolution (HR) EI-MS were recorded on a JEOL AccuTOF GCx, and HR ESI-MS were recorded on a Bruker ApexQe. MALDI-MS were recorded on a Bruker Autoflex Speed. For MALDI-MS 1 µl of sample and 1 µl of matrix solution (2,5-dihydroxybenzoic acid (DHB), 20 mg/ml in 3:7 H_2O/MeCN) were mixed, pipetted onto the target plate and air dried. With exception of the Autoflex Speed, instruments were operated by the MS service department of the Organic Chemistry Institute of the University of Heidelberg. Mass spectra were analyzed using mMass.[272] Fourier-transform infrared spectroscopy (FTIR) was carried out on a JASCO FT/IR-4000 spectrometer. Spectra Manager software was used for operating the instrument and analysis of IR data. Substances were measured as solids under ambient atmosphere and at rt. Band frequencies are reported to the nearest 1 cm^{-1}.

9.3 Synthesis of the Core Fragment

9.3.1 Synthesis of 4-Aminophenyl benzoate 6

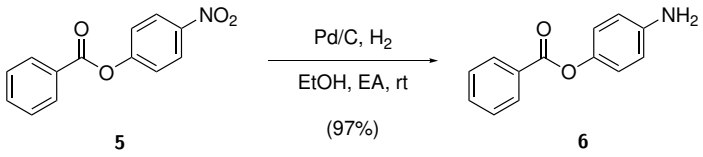

The autoclave was charged with nitrophenol **5** (50.00 g, 205.58 mmol, 1.0 eq) and Pd/C (10% Pd basis, 10.00 g, 20 mol%). EtOH (130 ml) and EA (100 ml) were added. The autoclave was closed and the gas volume of the reaction vessel flushed with H_2. The reaction vessel was pressurized with H_2 (9 bar) and the valve to the gas bottle close off. The reaction mixture was stirred under H_2 at rt and every 15 to 20 min the pressure was monitored and raised to 9 bar again. Conversion of nitrophenol **5** was monitored by TLC. Upon full conversion of starting material **5**, the reaction mixture was filtered through celite and washed with EA. The solvent was removed under reduced pressure and the residue was dried *in vacuo* to afford 4-aminophenyl benzoate **6** (42.41 g, 198.88 mmol, 97% yield) as light brown solid. The title compound **6** was obtained in sufficient purity and used without further purification.

$\mathbf{R_f}$ = 0.28 (PE/EA 2:1).
m.p.: 152.5°C.
^{1}**H NMR** (300 MHz, $CDCl_3$): δ = 8.21–8.18 (m, 2H), 7.65–7.59 (m, 1H), 7.53–7.7.47 (m, 2H), 7.03–6.98 (m, 2H), 6.74–6.69 (m, 2H), 3.67 (s, 2H) ppm.
^{13}**C NMR**: (75 MHz, $CDCl_3$): δ = 165.9, 144.4, 143.2, 133.5, 130.2, 130.0, 128.6, 122.4, 115.8 ppm.
HRMS (EI^+) m/z: $[M]^+$ calculated for $C_{13}H_{11}NO_2{}^+$: 213.0784, found: 213.0765.
Analytical data is consistent with the literature.[273]

9.3.2 Synthesis of 4-Amino-3-bromophenyl benzoate 7

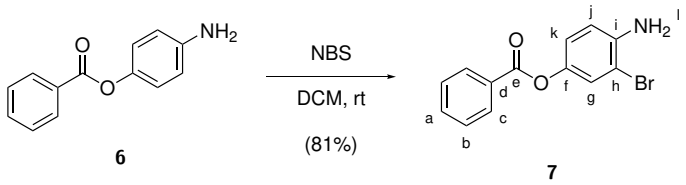

A modified procedure from Aoyama *et al.*[274] was used. Aminophenol **6** (8.474 g, 39.74 mmol, 1.0 eq) was dissolved in DCM (250 ml). NBS (3.555 g, 19.97 mmol, 0.5 eq) was added, the flask wrapped in Al-foil and the reaction mixture stirred at rt. Following the consumption of NBS, which was monitored by TLC after 1 h, a second portion of NBS (3.543 g, 19.90 mmol, 0.5 eq) was added and the reaction mixture was stirred at rt for additional 2.5 h, after which TLC revealed the starting material **6** and NBS to be consumed. The reaction mixture was washed with H_2O (3x 250 ml) and brine (250 ml). The organic phase was separated, dried (Na_2SO_4), filtered and the solvent removed under reduced pressure. The crude product was purified by flash column chromatography (PE:Et_2O, 2:1). A mixed fraction obtained by flash column chromatography was purified again by flash column chromatography (PE:Et_2O, 2:1) The combined purified product was dried *in vacuo* to afford 4-amino-3-bromophenyl benzoate **7** (9.462 g, 32.25 mmol, 81% yield) as a dark red/orange solid.

R_f = 0.30 (PE/Et_2O 2:1)
m.p.: 62.5°C.
^{1}**H NMR** (300 MHz, $CDCl_3$): δ = 8.23–8.13 (m, 2H, H_b), 7.69–7.57 (m, 1H, H_a), 7.56–7.45 (m, 2H, H_c), 7.33 (d, J = 2.6 Hz, 1H, H_g), 7.00 (dd, J = 8.7 Hz, J = 2.6 Hz, 1H, H_k), 6.80 (d, J = 8.6 Hz, 1H, H_j), 4.07 (s, 2H, H_l) ppm.
^{13}**C NMR** (75 MHz, $CDCl_3$): δ = 165.6 (C, C_e), 142.7 (C, C_f), 142.3 (C, C_i), 133.7 (CH, C_a), 130.3 (CH, C_b), 129.5 (C, C_d), 128.7 (CH, C_c), 125.7 (CH, C_g), 121.9 (CH, C_k), 115.7 (CH, C_j), 108.8 (C, C_h) ppm.
IR: $\tilde{\nu}$ = 3447, 3363, 3059, 1726, 1617, 1599, 1584, 1497, 1491, 1455, 1416, 1313, 1267, 1249, 1185, 1178, 1167, 1145, 1086, 1071, 1033, 1022, 1002, 938, 893, 874, 807, 702, 686, 668, 568, 530 cm^{-1}.
HRMS (EI^+) m/z: $[M]^+$ calculated for $C_{13}H_{10}{}^{79}BrNO_2{}^+$: 290.9890, found: 290.9872 and calculated for $C_{13}H_{10}{}^{81}BrNO_2{}^+$: 292.9869, found: 292.9818.

9.4 Synthesis of Carboxylic Acid Fragments

9.4.1 Synthesis of 2-(2,2-Diphenylbenzo[*d*][1,3]dioxol-5-yl)acetic acid 11

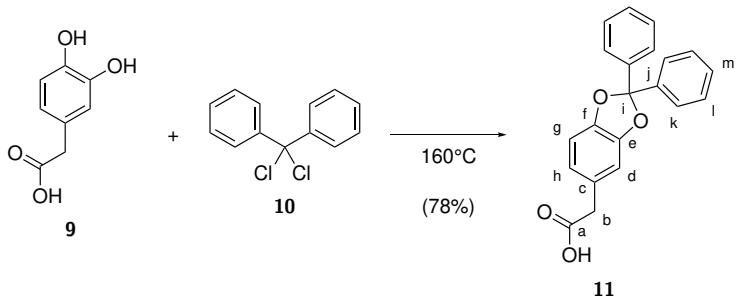

A modified procedure from Blagg *et al.*[200] and Xie *et al.*[275] was used. A flask was charged with acid **9** (10.016 g, 59.57 mmol, 1.0 eq) and Ph_2CCl_2 **10** (17.13 ml, 89.22 mmol, 1.5 eq) was added. The reaction was heated to 160°C while stirring. A stream of N_2 and wash bottles with NaOH (aq., 1 M) were used to drive off and neutralize formed HCl gas. TLC after 1 h revealed starting material **9** to be consumed. Heating was removed and the reaction mixture allowed to cool down. Toluene (40 ml) was added to avoid solidification and the reaction mixture was allowed to cool to rt. The reaction mixture was transferred into a separation funnel, Et_2O (350 ml) and NaOH (aq., 2 M, 200 ml) were added, mixed, phases separated and the organic phase extracted with NaOH (aq., 2 M, 3x 100 ml). The combined aqueous phases were acidified by slow addition of HCl (aq., conc., 100 ml), resulting in precipitation, left to cool to rt then placed at -20°C over night. The suspension was allowed to warm to rt, the yellow/light brown solid was filtered off, then dissolved in DCM (400 ml), washed with brine (250 ml), dried ($MgSO_4$), filtered and the solvent removed under reduced pressure to afford title compound **11** (15.443 g, 46.48 mmol, 78% yield) as off white solid. The title compound **11** was obtained in sufficient purity and used without further purification.

$\mathbf{R_f}$ = 0.26 (PE/Et_2O 2:1 + 1% AcOH).
^{1}**H NMR** (300 MHz, $CDCl_3$): δ = 7.58 (dd, J = 7.3 Hz, J = 2.5 Hz, 4H, H_k), 7.37 (dd, J = 5.1, J = 2.1 Hz, 6H, H_l, H_m), 6.88–6.78 (m, 2H, H_g, H_d), 6.72 (dd, J = 8.0 Hz, J = 1.7 Hz, 1H, H_h), 3.54 (s, 2H, H_b) ppm.
^{13}**C NMR** (75 MHz, $CDCl_3$): δ = 177.7 (C, C_a), 147.5 (C, C_e), 146.7 (C, C_f), 140.4 (C, C_i), 129.2 (CH, C_m), 128.4 (CH, C_l), 126.9 (C, C_c), 126.4 (CH, C_k), 122.7 (CH, C_h), 117.1 (C, C_j), 110.0 (CH, C_d), 108.6 (CH, C_g), 40.8 (CH_2, C_b) ppm.
HRMS (ESI$^-$) m/z: $[M-H]^-$ calculated for $C_{21}H_{15}O_4^-$: 331.0976, found: 331.0967.
Analytical data is consistent with the literature.[200]

9.5 Amide Couplings

9.5.1 Synthesis of 3-Bromo-4-(2-(2,5-dimethoxyphenyl)acetamido)phenyl benzoate 63

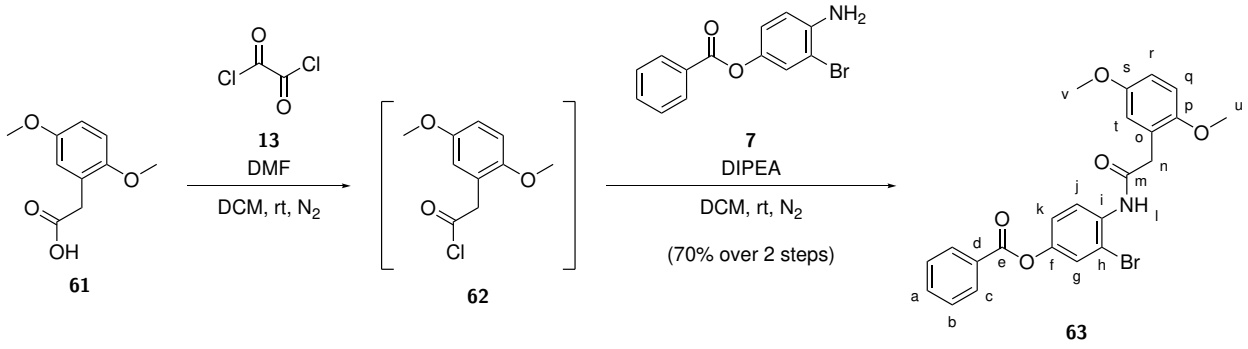

A modified procedure from Higginson *et al.*[276] and Baud *et al.*[277] was used. Carboxylic acid **61** (8.076 g, 41.16 mmol, 1.2 eq) was dissolved in anhydrous DCM (120 ml) under N_2. Oxalyl chloride **13** (13.2 ml, 153.96 mmol, 4.5 eq) was added slowly. A catalytic amount DMF (3 drops) was added and the reaction stirred at rt. TLC after 105 min revealed carboxylic acid **61** to be consumed. Solvent was removed under reduced pressure, the residue dissolved in DMC (30 ml) and the solvent again removed under reduced pressure. This was repeated a total of 3 times, to remove excess oxalyl chloride **13** and obtain crude acid chloride **62**. Amine **7** (10.026 g, 34.32 mmol, 1.0 eq) was dissolved in anhydrous DCM (100 ml) under N_2. DIPEA (9.0 ml, 51.67 mmol, 1.5 eq) was slowly added the solution of amine **7**. Crude acid chloride **62** was dissolved in anhydrous DCM (100 ml) under N_2 and slowly added to the solution of amine **7**. The reaction mixture was stirred at rt. TLC after 1 h revealed amine **7** to be consumed. The reaction mixture was washed with citric acid (aq., 10 %, 2x 200 ml), H_2O (2x 200 ml) and brine (2x 200 ml), then dried (Na_2SO_4), filtered and the solvent removed under reduced pressure. The crude product was dissolved in DCM (5 ml), Et_2O (500 ml) added, then placed at -20°C over night to facilitate crystallization. The resulting solid was filtered off, washed with Et_2O and dried *in vacuo* to afford title compound **63** (11.293 g, 24.01 mmol, 70% yield) as off white solid.

R_f = 0.22 (PE:Et_2O 2:1).

m.p.: 133.5°C.

^{1}H NMR (400 MHz, $CDCl_3$): δ = 8.44 (d, J = 9.0 Hz, 1H, H_j), 8.20 (s, 1H, H_l), 8.16 (dd, J = 8.4 Hz, J = 1.3 Hz, 2H, H_c), 7.63 (t, J = 7.4 Hz, 1H, H_a), 7.50 (t, J = 7.7 Hz, 2H, H_b), 7.41 (d, J = 2.6 Hz, 1H, H_g), 7.16 (dd, J = 9.0 Hz, J = 2.6 Hz, 1H, H_k), 6.94–6.79 (m, 2H, H_q, H_t), 6.85 (dd, J = 8.9 Hz, J = 2.9 Hz, 1H, H_r), 3.89 (s, 3H, H_u), 3.79 (s, 3H, H_v), 3.76 (s, 2H, H_n).

^{13}C NMR (100 MHz, $CDCl_3$): δ = 169.5 (C, C_m), 165.0 (C, C_e), 154.1 (C, C_s), 151.3 (C, C_p), 146.7 (C, C_f), 134.2 (C, C_i), 133.9 (CH, C_a), 130.3 (CH, C_c), 129.2 (C, C_d), 128.8 (CH, C_b), 125.6 (CH, C_g), 123.7 (C, C_o), 122.1 (CH, C_j), 121.7 (CH, C_k), 117.2 (CH, C_t), 114.1 (CH, C_r), 112.7 (C, C_h), 111.9 (CH, C_q), 56.3 (CH_3, C_u), 55.9 (CH_3, C_v), 40.5 (CH_2, C_n) ppm.

IR: $\tilde{\nu}$ = 3248, 3197, 3002, 2924, 2831, 1734, 1670, 1593, 1525, 1505, 1482, 1463, 1451, 1431, 1396, 1348, 1294, 1256, 1246, 1231, 1185, 1178, 1160, 1129, 1078, 1059, 1052, 1042, 1027, 1022, 1002, 972, 938, 921, 892, 878, 809, 801, 747, 717, 707, 691, 668, 622, 589, 567, 552, 540, 533, 528, 521, 509, 502 cm^{-1}.

HRMS (ESI^+) m/z: $[M+Na]^+$ calculated for $C_{23}H_{20}{}^{79}BrNNaO_5{}^+$: 492.0418, found: 492.0417 and calculated for $C_{23}H_{20}{}^{81}BrNNaO_5{}^+$: 494.0397, found: 494.0397.

9.5.2 Synthesis of 3-Bromo-4-(2-(2,2-diphenylbenzo[*d*][1,3]dioxol-5-yl)acetamido)phenyl benzoate 65

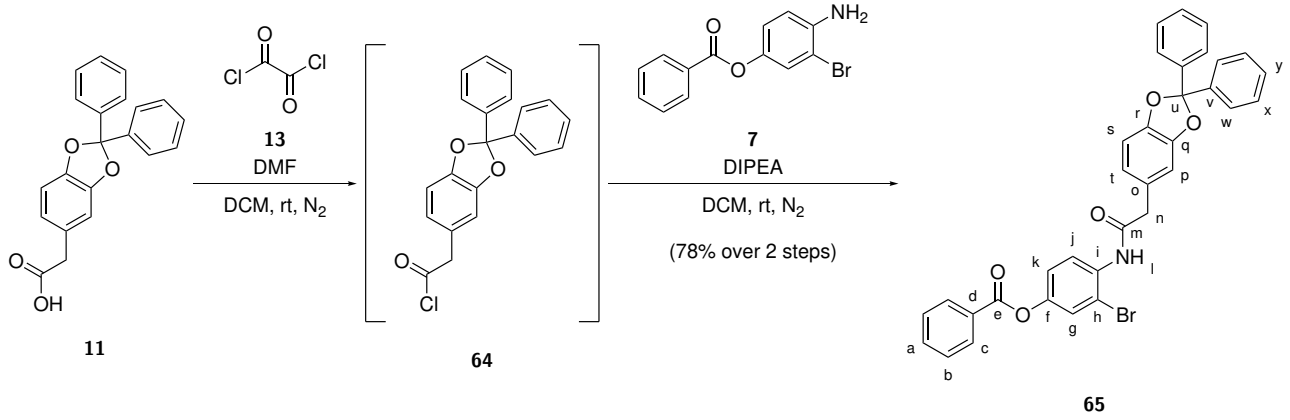

A modified procedure from Higginson *et al.*[276] and Baud *et al.*[277] was used. Carboxylic acid **11** (13.659 g, 41.10 mmol, 1.2 eq) was dissolved in anhydrous DCM (100 ml) under N_2. Oxalyl chloride **13** (8.81 ml, 102.69 mmol, 3.0 eq) was added slowly. A catalytic amount DMF (5 drops) was added and the reaction stirred at rt. TLC after 1 h revealed carboxylic acid **11** to be consumed. Solvent was removed under reduced pressure, the residue dissolved in DMC (20 ml) and the solvent again removed under reduced pressure. This was repeated a total of 3 times, to remove excess oxalyl chloride **13** and obtain crude acid chloride **62**. Amine **7** (10.025 g, 34.32 mmol, 1.0 eq) was dissolved in anhydrous DCM (100 ml) under N_2. DIPEA (9.0 ml, 51.53 mmol, 1.5 eq) was slowly added the solution of amine **7**. Crude acid chloride **62** was dissolved in anhydrous DCM (115 ml) under N_2 and slowly added to the solution of amine **7**. The reaction mixture was stirred at rt. TLC after 30 min revealed amine **7** to be consumed. The reaction mixture was washed with citric acid (aq., 10 %, 2x 200 ml), H_2O (3x 200 ml) and brine (200 ml), then dried ($MgSO_4$), filtered and the solvent removed under reduced pressure. The crude product was recrystallized from EA. Residual crude product form the mother liquor was purified by flash column chromatography (PE:EA, 4:1). Combined product fractions were dried *in vacuo* to afford title compound **65** (16.339 g, 26.94 mmol, 78% yield) as off white solid.

$\mathbf{R_f}$ = 0.33 (PE:EA 4:1).

m.p.: 189.0°C.

^{1}**H NMR** (400 MHz, $CDCl_3$): δ = 8.44 (d, J = 9.0 Hz, 1H, H_j), 8.20–8.12 (m, 2H, H_c), 7.66 (s, 1H, H_l), 7.66–7.61 (m, 1H, H_a), 7.61–7.55 (m, 4H, H_w), 7.50 (dd, J = 8.4 Hz, J = 7.2 Hz, 2H, H_b), 7.43–7.36 (m, 6H, H_x, H_y), 7.36 (d, J = 2.6 Hz, 1H, H_g), 7.16 (dd, J = 9.0 Hz, J = 2.6 Hz, 1H, H_k), 6.94 (d, J = 7.9 Hz, 1H, H_s), 6.91 (d, J = 1.6 Hz, 1H, H_p), 6.83 (dd, J = 7.9 Hz, J = 1.8 Hz, 1H, H_t), 3.70 (s, 2H, H_n) ppm.

^{13}**C NMR** (100 MHz, $CDCl_3$): δ = 169.5 (C, C_m), 165.0 (C, C_e), 148.2 (C, C_q), 147.3 (C, C_r), 146.9 (C, C_f), 140.0 (C, C_v), 133.9 (CH, C_a), 133.6 (C, C_i), 130.3 (CH, C_c), 129.4 (CH, C_y), 129.2 (C, C_d), 128.8 (CH, C_b), 128.5 (CH, C_x), 127.5 (C, C_o), 126.5 (CH, C_w), 125.6 (CH, C_g), 123.5 (CH, C_t), 121.7 (CH, C_k), 121.5 (CH, C_j), 117.5 (C, C_u), 113.0 (C, C_h), 110.4 (CH, C_p), 109.4 (CH, C_s), 44.9 (CH_2, C_n) ppm.

IR: $\tilde{\nu}$ = 3345, 2167, 2159, 2005, 1975, 1731, 1683, 1599, 1586, 1515, 1492, 1446, 1394, 1312, 1303, 1267, 1237, 1214, 1187, 1124, 1074, 1058, 1046, 1017, 964, 948, 936, 917, 885, 811, 778, 752, 694, 642, 585, 554, 521, 517.

HRMS (EI^+) m/z: $[M]^+$ calculated for $C_{34}H_{24}{}^{79}BrNO_5{}^+$: 605.0833, found: 605.0821 and calculated for $C_{34}H_{24}{}^{81}BrNO_5{}^+$: 607.0812, found: 607.0782.

9.5.3 Synthesis of 3-Bromo-4-(2-phenoxyacetamido)phenyl benzoate 67

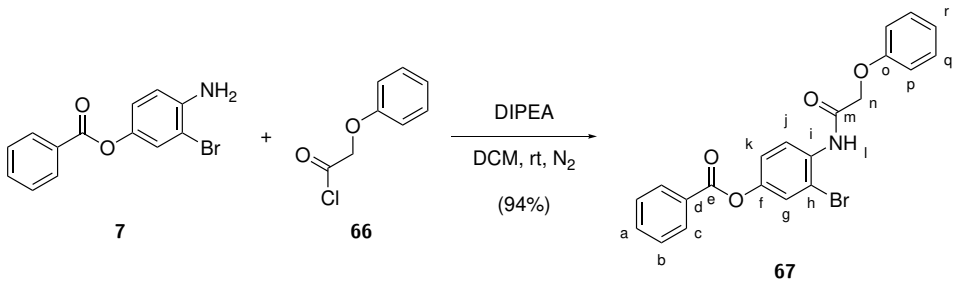

A modified procedure from Baud *et al.*[277] was used. Amine **7** (5.000 g, 17.12 mmol, 1.0 eq) was dissolved in DCM (50 ml) under N_2 and acid chloride **66** (2.90 ml, 21.00 mmol, 1.2 eq) was added slowly. DIPEA (3.60 ml, 20.61 mmol, 1.2 eq) was added dropwise. The reaction was stirred under N_2 at rt. After 4 h TLC revealed amine **7** to be consumed. Et_2O (100 ml) was added and the reaction mixture washed with $NaHCO_3$ (aq., sat., 3x 100 ml). The organic phases were separated, dried (Na_2SO_4), filtered and the solvent removed under reduced pressure. The crude product was purified by recrystallization in Et_2O and dried *in vacuo* to afford 3-bromo-4-(2-phenoxyacetamido)phenyl benzoate **67** (4.900 g, 11.50 mmol, 67%) as white solid.

$\mathbf{R_f}$ = 0.26 (PE:Et_2O 3:1).

m.p.: 133.5°C.

^{1}**H NMR** (400 MHz, $CDCl_3$): δ = 9.05 (s, 1H, H_l), 8.55 (d, J = 9.0 Hz, 1H, H_j), 8.22–8.14 (m, 2H, H_c), 7.70–7.60 (m, 1H, H_a), 7.57–7.47 (m, 3H, H_g, H_b), 7.41–7.30 (m, 2H, H_q), 7.24 (dd, J = 9.0 Hz, J = 2.6 Hz, 1H, H_k), 7.08 (tt, J = 7.4 Hz, J = 1.1 Hz, 1H, H_r), 7.07–6.99 (m, 2H, H_p), 4.68 (s, 2H, H_n) ppm.

^{13}**C NMR** (100 MHz, $CDCl_3$): δ = 166.5 (C, C_n), 165.0 (C, C_e), 157.1 (C, C_o), 147.3 (C, C_f), 134.0 (CH, C_a), 133.1 (C, C_i), 130.4 (CH, C_c), 130.1 (CH, C_q), 129.2 (C, C_d), 128.8 (CH, C_b), 125.9 (CH, C_g) 122.7 (CH, C_r), 121.9 (2CH, C_j, C_k), 115.0 (CH, C_p), 113.5 (C, C_h), 67.7 (CH_2, C_n) ppm.

IR: $\tilde{\nu}$ = 3373, 3103, 3059, 3044, 2906, 2847, 1743, 1731, 1696, 1601, 1585, 1533, 1498, 1480, 1460, 1450, 1437, 1397, 1357, 1314, 1278, 1268, 1234, 1190, 1180, 1155, 1081, 1058, 1040, 1023, 1001, 971, 887, 849, 820, 796, 750, 700, 687, 682, 655, 566, 550 cm^{-1}.

HRMS (EI^+) m/z: $[M]^+$ calculated for $C_{21}H_{16}{}^{79}BrNO_4{}^+$: 425.0258, found: 425.0166 and calculated for $C_{21}H_{16}{}^{81}BrNO_4{}^+$: 427.0237, found: 425.0250.

9.5.4 Synthesis of 3-Bromo-4-(2-(4-methoxyphenyl)acetamido)phenyl benzoate 18

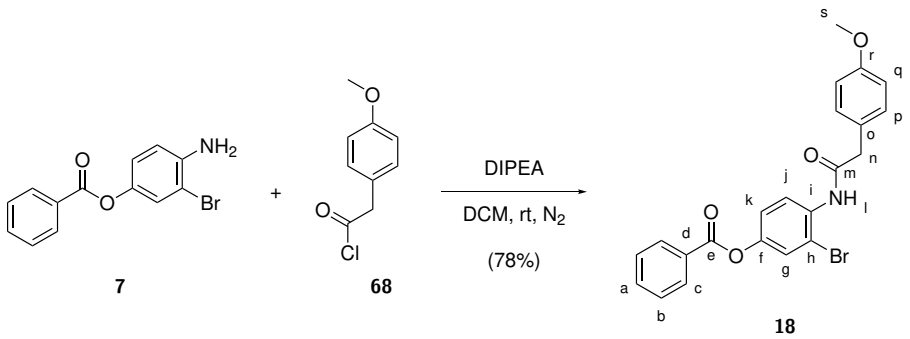

A modified procedure from Baud *et al.*[277] was used. Amine **7** (10.057 g, 34.43 mmol, 1.0 eq) was dissolved in DCM (100 ml) under N_2. DIPEA (7.8 ml, 44.62 mmol, 1.3 eq) was added slowly. Acid chloride **68** (6.3 ml, 40.95 mmol, 1.2 eq) was added slowly. DCM (10 ml) was added and the reaction was stirred under N_2 at rt. After 1 h TLC revealed amine **7** to be consumed. Et_2O (100 ml) and DCM (250 ml) was added and the organic phase washed with citric acid (aq., 10 %, 2x 200 ml), H_2O (2x 200 ml) and brine (300 ml). The organic phase was separated, dried (Na_2SO_4), filtered and the solvent removed under reduced pressure. The crude product was dissolved in DCM (250 ml), Et_2O (900 ml) added, then placed at -20°C over night to facilitate crystallization. The resulting solid was filtered off, washed with Et_2O (150 ml) and dried *in vacuo* to afford title compound **18** (11.538 g, 26.20 mmol, 78%) as white solid.

$\mathbf{R_f}$ = 0.21 (PE:Et_2O 2:1).
m.p.: 156.8°C.
^{1}**H NMR** (400 MHz, $CDCl_3$): δ = 8.45 (d, J = 9.0 Hz, 1H, H_j), 8.20–8.11 (m, 2H, H_c), 7.68 (s, 1H, H_l), 7.66–7.59 (m, 1H, H_a) 7.55–7.45 (m, 2H, H_b), 7.40 (d, J = 2.6 Hz, 1H, H_g), 7.32–7.27 (m, 2H, H_p), 7.18 (dd, J = 9.0 Hz, J = 2.7 Hz, 1H, H_k), 7.00–6.92 (m, 2H, H_q), 3.83 (s, 3H, H_s), 3.74 (s, 2H, H_n) ppm.
^{13}**C NMR** (100 MHz, $CDCl_3$): δ = 169.7 (C, C_m), 165.0 (C, C_e), 159.5 (C, C_r), 146.9 (C, C_f), 133.9 (CH, C_a), 133.7 (C, C_i), 131.1 (CH, C_p), 130.3 (CH, C_c), 129.2 (C, C_d), 128.8 (CH, C_b), 125.9 (C, C_o), 125.6 (CH, C_g), 121.8 (CH, C_j), 121.7 (CH, C_k), 115.0 (CH, C_q), 113.0 (C, C_h), 55.5 (CH_3, C_s), 44.4 (CH_2, C_n) ppm.
IR: $\tilde{\nu}$ = 3273, 1734, 1700, 1678, 1653, 1612, 1587, 1522, 1513, 1449, 1395, 1345, 1267, 1247, 1192, 1176, 1081, 1064, 1036, 1024, 967, 902, 862, 836, 809, 800, 770, 733, 708, 686, 668, 662, 638, 613, 595, 580, 577, 575, 562, 556, 547, 539, 527, 523, 521, 516, 514, 510, 507, 504, 502 cm^{-1}.
HRMS (EI^+) m/z: $[M]^+$ calculated for $C_{22}H_{18}{}^{79}BrNO_4{}^+$: 439.0414, found: 439.0371 and calculated for $C_{22}H_{18}{}^{81}BrNO_4{}^+$: 441.0394, found: 441.0372.

9.6 Suzuki–Miyaura Couplings

9.6.1 Synthesis of 2-(2,5-Dimethoxyphenyl)-*N*-(2-(2,4-dimethoxypyrimidin-5-yl)-4-hydroxyphenyl)acetamide 26

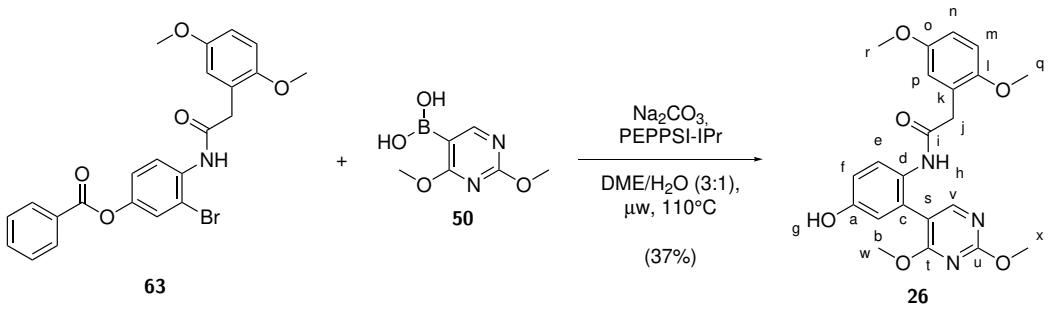

63 + 50 → 26

A 3:1 DME/H_2O mixture was degassed by sparging with N_2 for 30 min. A 35 ml microwave vials was flushed with Ar, then charged with bromide **63** (710 mg, 1.51 mmol, 1.0 eq), boronic acid **50** (300 mg, 1.63 mmol, 1.1 eq), Na_2CO_3 (325 mg, 3.07 mmol, 2.0 eq) and PEPPSI-IPr (24 mg, 0.074 mmol, 5 mol%). The vial was again flushed with Ar, then DME/H_2O (3:1, 17.5 ml) was added, again flushed with Ar, then sealed and subjected to the following microwave reaction conditions:

T = 115°C	Time = 01:00:00	µλ = 150 W	P_{max} = 250 PSI
stirring = high	PreMix = 120 s	Power Max = Off	

The reaction mixtures was allowed to cool to rt, then transferred into a separation funnel. The vial was rinsed with DCM (3x) and H_2O (3x), which was also added to the separation funnel. DCM (100 ml) and H_2O was added and the phases separated. The organic phase was washed with citric acid (aq., 10%, 200 ml), H_2O (3x 200 ml), then dried (Na_2SO_4), filtered and the solvent removed under reduced pressure. The crude product was purified by flash column chromatography (PE:EA 1:1 to PE:EA 1:2 to PE:EA 1:4 to EA) to afford title compound **26** (237 mg, 0.56 mmol, 37% yield) as white solid.

$\mathbf{R_f}$ = 0.29 (PE:EA 1:4).

$\mathbf{t_R}$ = 22.77 min (gradient of 10–80% B in A over 30 min).

m.p.: 151.0°C.

^{1}**H NMR** (400 MHz, DMSO–d_6): δ = 9.45 (s, 1H, H_q), 8.45 (s, 1H, H_h), 8.07 (s, 1H, H_v), 7.40 (d, J = 8.7 Hz, 1H, H_e), 6.82 (d, J = 8.8 Hz, 1H, H_m), 6.78–6.76 (m, 1H, H_n), 6.76–6.73 (m, 1H, H_f), 6.72 (d, J = 3.0 Hz, 1H, H_p), 6.58 (d, J = 2.8 Hz, 1H, H_b), 3.95 (s, 3H, H_w), 3.74 (s, 3H, H_x), 3.68 (s, 3H, H_r), 3.63 (s, 3H, H_q), 3.40 (s, 2H, H_j) ppm.

^{13}**C NMR** (100 MHz, DMSO–d_6): δ = 168.7 (C, C_i), 167.5 (C, C_u), 164.3 (C, C_t), 158.3 (CH, C_v), 154.4 (C, C_a), 152.9 (C, C_o), 151.2 (C, C_l), 128.5 (C, C_c), 127.9 (C, C_d), 126.4 (CH, C_e), 124.9 (C, C_k), 117.1 (CH, C_b), 116.8 (CH, C_p), 115.0 (CH, C_f), 113.1 (C, C_s), 112.2 (CH, C_n), 111.6 (CH, C_m), 55.8 (CH_3, C_q), 55.3 (CH_3, C_r), 54.5 (CH_3, C_w), 53.7 (CH_3, C_x), 37.4 (CH_2, C_j) ppm.

IR: $\tilde{\nu}$ = 3372, 3260, 2939, 1641, 1594, 1559, 1521, 1503, 1487, 1468, 1450, 1397, 1383, 1300, 1277, 1220, 1078, 1055, 1035, 1023, 1011, 957, 893, 875, 844, 823, 800, 733, 713, 695, 645, 620, 578 cm^{-1}.

HRMS (EI^+) m/z: $[M]^+$ calculated for $C_{22}H_{23}N_3O_6^+$: 425.1582, found: 425.1547.

9.6.2 Synthesis of 2-(2,5-Dimethoxyphenyl)-*N*-(5-hydroxy-4'-nitro-[1,1'-biphenyl]-2-yl) acetamide 24

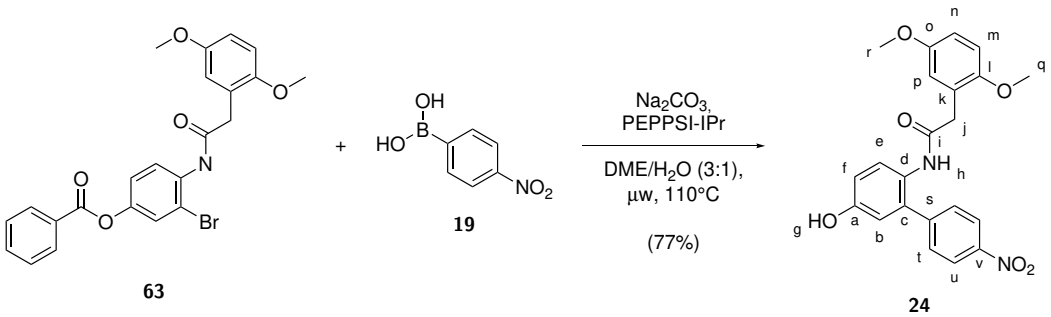

A 3:1 DME/H_2O mixture was degassed by sparging with Ar for 30 min. Five 10 ml microwave vials were each flushed with Ar, then each charged with bromide **63** (151 mg, 0.32 mmol, 1.0 eq), boronic acid **19** (65 mg, 0.38 mmol, 1.2 eq), Na_2CO_3 (68 mg, 0.64 mmol, 2.0 eq) and PEPPSI-IPr (11 mg, 0.016 mmol, 5 mol%). The vials were again flushed with Ar, then DME/H_2O (3:1, 5 ml) was added to each, again flushed with Ar, then sealed and each subjected to the following microwave reaction conditions:

T = 110°C	Time = 01:00:00	µλ = 150 W	P_{max} = 250 PSI
stirring = high	PreMix = 120 s	Power Max = Off	

The reaction mixtures were allowed to cool to rt, then combined into a separation funnel. Each vial was rinsed with DCM (3x) and H_2O (3x), which was also added to the separation funnel. The organic phase was separated and washed with citric acid (aq., 10%, 2x 100 ml), H_2O (3x 100 ml) and brine (1x 100 ml), then dried ($MgSO_4$), filtered and the solvent removed under reduced pressure. The crude product was purified by flash column chromatography (PE:EA 2:1 to PE:EA 1:1 to PE:EA 1:2), then dried *in vacuo* to afford title compound **24** (505 mg, 1.24 mmol, 77% yield) as light yellow solid.

R_f: 0.19 (PE:EA 1:1).

t_R: 21.20 min (gradient of 30–80% B in A over 30 min).

m.p.: 128.6°C.

^{1}H NMR (300 MHz, DMSO–d_6): δ = 9.66 (s, 1H, H_g), 9.12 (s, 1H, H_h), 8.19–8.09 (m, 2H, H_u), 7.57–7.46 (m, 2H, H_t), 7.23 (d, J = 8.6 Hz, 1H, H_e), 6.88–6.78 (m, 2H, H_f, H_m), 6.77–6.67 (m, 2H, H_b, H_n), 6.55 (d, J = 3.1 Hz, 1H, H_p), 3.65 (s, 3H, H_q), 3.62 (s, 3H, H_r), 3.38 (s, 2H, H_j) ppm.

^{13}C NMR (75 MHz, DMSO–d_6): δ = 169.2 (C, C_i), 155.6 (C, C_a), 152.8 (C, C_o), 151.2 (C, C_l), 146.3 (C, C_v), 146.2 (C, C_d), 136.6 (C, C_s), 129.7 (CH, C_t), 128.9 (CH, C_e), 126.2 (C, C_c), 124.9 (C, C_k), 123.2 (CH, C_u), 116.9 (CH, C_p), 116.0 (CH, C_b), 115.7 (CH, C_f), 111.6 (CH, C_n), 111.6 (CH, C_m), 55.9 (CH_3, C_r), 55.1 (CH_3, C_q), 36.8 (CH_2, C_j).

IR: $\tilde{\nu}$ = 3212, 3018, 2925, 2829, 2359, 1647, 1594, 1503, 1454, 1431, 1406, 1345, 1316, 1285, 1235, 1217, 1154, 1128, 1107, 1051, 1023, 985, 942, 922, 903, 874, 859, 851, 820, 802, 756, 731, 714, 695, 665, 639, 600 cm^{-1}.

HRMS (EI^+) m/z: $[M]^+$ calculated for $C_{22}H_{20}N_2O_6^+$: 408.1316, found: 408.1256.

9.6.3 Synthesis of *N*-(2-(2,4-Dimethoxypyrimidin-5-yl)-4-hydroxyphenyl)-2-(2,2-diphenylbenzo[*d*][1,3]dioxol-5-yl)acetamide 27

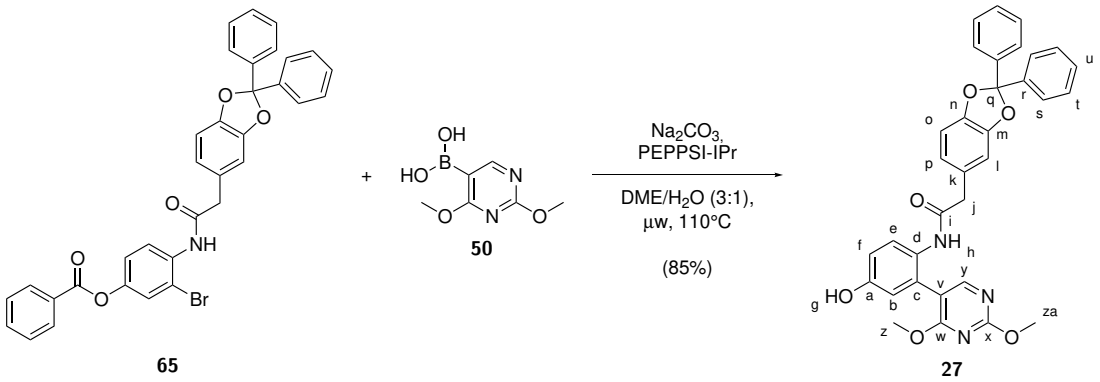

A 3:1 DME/H_2O mixture was degassed by sparging with Ar for 1 h. Five 10 ml microwave vials were each flushed with Ar, then each charged with bromide **65** (195 mg, 0.32 mmol, 1.0 eq), boronic acid **50** (71 mg, 0.39 mmol, 1.2 eq), Na_2CO_3 (69 mg, 0.65 mmol, 2.0 eq) and PEPPSI-IPr (11 mg, 0.016 mmol, 5 mol%). The vials were again flushed with Ar, then DME/H_2O (3:1, 5 ml) was added to each, again flushed with Ar, then sealed and each subjected to the following microwave reaction conditions:

T = 110°C	Time = 01:00:00	µλ = 150 W	P_{max} = 250 PSI
stirring = high	PreMix = 120 s	Power Max = Off	

The reaction mixtures were allowed to cool to rt, then combined into a separation funnel and DCM (50 ml) was added. Each vial was rinsed with DCM (3x) and H_2O (3x), which was also added to the separation funnel. The organic phase was separated and washed with citric acid (aq., 10%, 2x 50 ml), H_2O (2x 50 ml) and brine (1x 100 ml), then dried ($MgSO_4$), filtered and the solvent removed under reduced pressure. The crude product was purified by flash column chromatography (PE:EA 1:1 to PE:EA 1:3), then dried *in vacuo* to afford title compound **27** (768 mg, 1.37 mmol, 85% yield) as light brown solid. While small amounts of impurities and residual EA were observed by NMR analysis, product **27** was obtained in a purity sufficient for synthesis used without further purification.

R_f: 0.11 (PE:EA 1:1).

m.p.: 111.3°C.

^{1}**H NMR** (400 MHz, DMSO–d_6): δ = 9.44 (s, 1H, H_g), 8.93 (s, 1H, H_h), 8.04 (s, 1H, H_y), 7.59–7.39 (m, 6H, H_s), 7.48–7.36 (m, 4H, H_s, H_u), 7.28 (d, J = 8.7 Hz, 1H, H_e), 6.87 (d, J = 8.0 Hz, 1H, H_o), 6.79 (d, J = 1.6 Hz, 1H, H_l), 6.74 (dd, J = 8.7 Hz, J = 2.8 Hz, 1H, H_f), 6.61 (dd, J = 8.0 Hz, J = 2.1 Hz, 2H, H_b, H_p), 3.88 (s, 3H, H_z), 3.67 (s, 3H, H_{az}), 3.34 (s, 2H, H_j) ppm.

^{13}**C NMR** (100 MHz, DMSO–d_6): δ = 169.0 (C, C_i) 167.5 (C, C_x) 164.2 (C, C_w) 158.2 (CH, C_y) 154.6 (C, C_a) 146.3 (C, C_m) 145.0 (C, C_n) 139.9 (C, C_r) 130.1 (C, C_k) 129.4 (C, C_c) 129.2 (CH, C_u) 128.4 (CH, C_t) 127.7 (C, C_d) 127.1 (CH, C_e) 125.8 (CH, C_s) 122.1 (CH, C_p) 117.1 (CH, C_b) 115.9 (C, C_q) 115.0 (CH, C_f) 113.4 (C, C_v) 109.5 (CH, C_l) 108.2 (CH, C_o) 54.4 (CH_3, C_z) 53.5 (CH_3, C_{za}) 41.9 (CH_2, C_j) ppm.

IR: $\tilde{\nu}$ = 3853, 3802, 3743, 3723, 3649, 3596, 3234, 3062, 2954, 2925, 2854, 2363, 2338, 2219, 2182, 2158, 2081, 2062, 1979, 1887, 1733, 1652, 1598, 1557, 1524, 1493, 1471, 1444, 1394, 1382, 1304, 1244, 1205, 1077, 1059, 1043, 1016, 948, 918, 870, 814, 798, 777, 751, 696, 641, 600 cm^{-1}.

HRMS (EI^+) m/z: $[M]^+$ calculated for $C_{33}H_{27}N_3O_6{}^+$: 561.1894, found: 561.1861.

9.6.4 Synthesis of 2-(2,2-Diphenylbenzo[*d*][1,3]dioxol-5-yl)-*N*-(5-hydroxy-4'-nitro-[1,1'-biphenyl]-2-yl)acetamide 28

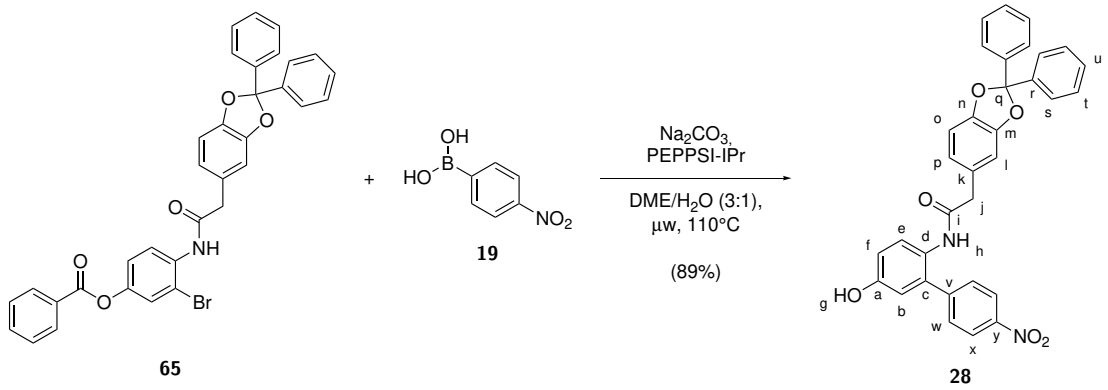

A 3:1 DME/H_2O mixture was degassed by sparging with Ar for 30 min. Five 10 ml microwave vials were each flushed with Ar, then each charged with bromide **65** (195 mg, 0.32 mmol, 1.0 eq), boronic acid **19** (65 mg, 0.39 mmol, 1.2 eq), Na_2CO_3 (69 mg, 0.65 mmol, 2.0 eq) and PEPPSI-IPr (12 mg, 0.017 mmol, 5 mol%). The vials were again flushed with Ar, then DME/H_2O (3:1, 5 ml) was added to each, again flushed with Ar, then sealed and each subjected to the following microwave reaction conditions:

T = 110°C	Time = 01:00:00	µλ = 150 W	P_{max} = 250 PSI
stirring = high	PreMix = 120 s	Power Max = Off	

The reaction mixtures were allowed to cool to rt, then combined into a separation funnel and DCM (50 ml) was added. Each vial was rinsed with DCM (3x) and H_2O (3x), which was also added to the separation funnel. The organic phase was separated and washed with citric acid (aq., 10%, 2x 50 ml), H_2O (2x 50 ml) and brine (1x 100 ml), then dried ($MgSO_4$), filtered and the solvent removed under reduced pressure. The crude product was purified by flash column chromatography (PE:EA 3:2 to PE:EA 1:1), then dried *in vacuo* to afford title compound **28** (777 mg, 1.43 mmol, 89% yield) as yellow brown solid. While small amounts of impurities and residual EA were observed by NMR analysis, product **28** was obtained in a purity sufficient for synthesis used without further purification.

R_f: 0.13 (PE:EA 3:2).

m.p.: 111.3°C.

^{1}H NMR (400 MHz, DMSO–d_6): δ = 9.65 (s, 1H, H_g), 9.37 (s, 1H, H_h), 8.17–8.09 (m, 2H, H_x), 7.61–7.52 (m, 4H, H_s), 7.52–7.46 (m, 2H, H_w), 7.48–7.35 (m, 6H, H_t, H_u), 7.16 (d, J = 8.6 Hz, 1H, H_e), 6.86 (d, J = 8.0 Hz, 1H, H_o), 6.82 (dd, J = 8.6 Hz, J = 2.8 Hz, 1H, H_f), 6.74 (d, J = 2.8 Hz, 1H, H_b), 6.72 (d, J = 1.6 Hz, 1H, H_l), 6.61 (dd, J = 8.0 Hz, J = 1.7 Hz, 1H, H_p), 3.32 (s, 2H, H_j) ppm.

^{13}C NMR (100 MHz, DMSO–d_6): δ = 169.4 (C, C_i), 155.7 (C, C_a), 146.3 (C, C_v or C_m or C_y), 146.2 (C, C_v or C_m or C_y), 146.2 (C, C_v or C_m or C_y), 145.1 (C, C_n), 139.9 (C, C_r), 136.8 (C, C_d), 129.8 (C, C_k), 129.7 (CH, C_w), 129.2 (2x CH, C_u, C_e), 128.4 (CH, C_t), 125.9 (C, C_c), 125.7 (CH, C_s), 123.2 (CH, C_x), 122.4 (CH, C_p), 116.0 (CH, C_b), 115.9 (C, C_q), 115.7 (CH, C_f), 109.5 (CH, C_l), 108.1 (CH, C_o), 41.9 (CH_2, C_j) ppm.
Some NMR signals could not be unambiguously assigned.

IR: $\tilde{\nu}$ = 3854, 3372, 3344, 3060, 2922, 2852, 2210, 2167, 2161, 2151, 2037, 2026, 2002, 1996, 1962, 1732, 1646, 1595, 1517, 1490, 1441, 1412, 1349, 1311, 1304, 1266, 1245, 1211, 1182, 1131, 1074, 1042, 1016, 949, 920, 899, 876, 864, 853, 844, 822, 811, 778, 756, 704, 692, 665, 648, 640, 619, 600, 565, 537, 525, 523, 509, 506 cm^{-1}.

HRMS (EI^+) m/z: $[M]^+$ calculated for $C_{33}H_{24}N_2O_6^+$: 544.1629, found: 544.1537.

9.6.5 Synthesis of *N*-(2-(2,4-Dimethoxypyrimidin-5-yl)-4-hydroxyphenyl)-2-phenoxyacetamide 25

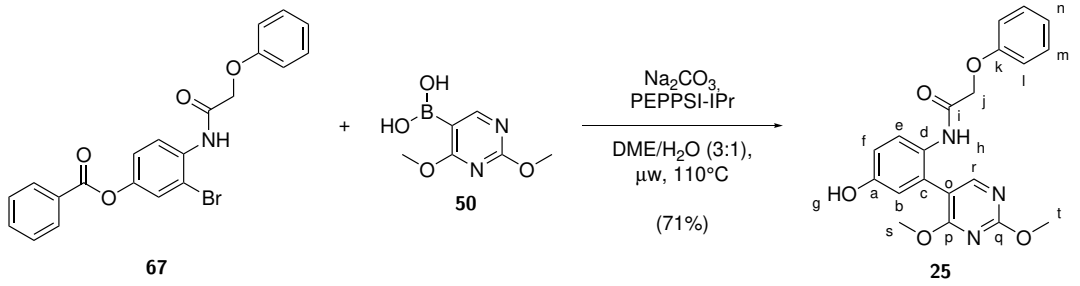

67 + 50 → 25

A 3:1 DME/H_2O mixture was degassed by sparging with Ar for 30 min. Five 10 ml microwave vials were each flushed with Ar, then each charged with bromide **67** (136 mg, 0.32 mmol, 1.0 eq), boronic acid **50** (71 mg, 0.38 mmol, 1.2 eq), Na_2CO_3 (68 mg, 0.64 mmol, 2.0 eq) and PEPPSI-IPr (11 mg, 0.016 mmol, 5 mol%). The vials were again flushed with Ar, then DME/H_2O (3:1, 5 ml) was added to each, again flushed with Ar, then sealed and each subjected to the following microwave reaction conditions:

T = 110°C	Time = 01:00:00	µλ = 150 W	P_{max} = 250 PSI
stirring = high	PreMix = 120 s	Power Max = Off	

The reaction mixtures were allowed to cool to rt, then combined into a separation funnel. Each vial was rinsed with DCM (3x) and H_2O (3x), which was also added to the separation funnel. The organic phase was separated and washed with citric acid (aq., 10%, 2x 100 ml), H_2O (3x 100 ml) and brine (1x 100 ml), then dried ($MgSO_4$), filtered and the solvent removed under reduced pressure. The crude product was purified by flash column chromatography (PE:EA 1:1 to PE:EA 1:2), then dried *in vacuo* to afford title compound **25** (435 mg, 1.14 mmol, 71% yield) as light brown solid.

R_f: 0.20 (PE:EA 1:1).

t_R: 14.73 min (gradient of 30–80% B in A over 30 min).

m.p.: 98.7°C.

^{1}H NMR (300 MHz, DMSO–d_6): δ = 9.54 (s, 1H, H_g), 8.89 (s, 1H, H_h), 8.14 (s, 1H, H_r), 7.43 (d, J = 8.7 Hz, 1H, H_e), 7.33–7.20 (m, 2H, H_m), 7.01–6.90 (m, 1H, H_n), 6.87–6.75 (m, 2H, H_l), 6.80 (d, J = 8.7 Hz, 1H, H_f), 6.65 (d, J = 2.8 Hz, 1H, H_b), 4.49 (s, 2H, H_j), 3.94 (s, 3H, H_s), 3.84 (s, 3H, H_t) ppm.

^{13}C NMR (75 MHz, DMSO–d_6): δ = 167.4 (C, C_q), 166.3 (C, C_i), 164.4 (C, C_p), 158.5 (CH, C_r), 157.4 (C, C_k), 154.9 (C, C_a), 129.5 (CH, C_m), 129.0 (C, C_d), 126.7 (C, C_c), 126.5 (CH, C_e), 121.3 (CH, C_n), 117.2 (CH, C_b), 115.1 (CH, C_f), 114.4 (CH, C_l), 113.0 (C, C_o), 67.0 (CH_2, C_j), 54.5 (CH_3, C_s), 53.9 (CH_3, C_t) ppm.

IR: $\tilde{\nu}$ = 3373, 3164, 1644, 1595, 1533, 1518, 1489, 1469, 1457, 1441, 1412, 1398, 1381, 1350, 1304, 1268, 1245, 1212, 1071, 1041, 1015, 964, 949, 898, 879, 854, 823, 811, 798, 778, 757, 704, 692, 665, 640, 600, 566, 542, 521, 517, 511, 505 cm^{-1}.

HRMS (EI^+) m/z: $[M]^+$ calculated for $C_{20}H_{19}N_3O_5^+$: 381.1319, found: 381.1341.

9.6.6 Synthesis of *N*-(5-Hydroxy-4'-nitro-[1,1'-biphenyl]-2-yl)-2-phenoxyacetamide 29

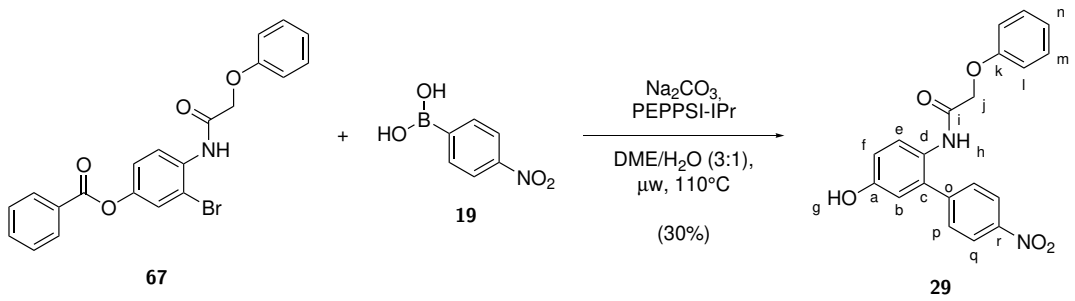

67 + 19 → 29

A 3:1 DME/H_2O mixture was degassed by sparging with N_2 for 30 min. A 35 ml microwave vial was flushed with Ar, charged with bromide **67** (682 mg, 1.60 mmol, 1.0 eq), boronic acid **19** (321 mg, 1.92 mmol, 1.2 eq), Na_2CO_3 (340 mg, 3.20 mmol, 2.0 eq) and PEPPSI-IPr (56 mg, 0.08 mmol, 5 mol%). The vial was again flushed with Ar, then DME/H_2O (3:1, 25 ml) was added, again flushed with Ar, then sealed and subjected to the following microwave reaction conditions:

T = 110°C	Time = 01:00:00	µλ = 150 W	P_{max} = 250 PSI
stirring = high	PreMix = 120 s	Power Max = Off	

The reaction mixture was allowed to cool to rt, Na_2CO_3 (508 mg, 4.80 mmol, 3.0 eq) was added, then subjected to these microwave conditions again. The reaction mixture was allowed to cool to rt, then transferred into a separation funnel. The vial was rinsed with DCM (3x) and H_2O (3x), which was also added to the separation funnel. The organic phase was separated and washed with citric acid (aq., 10%, 2x 100 ml), H_2O (3x 100 ml) and brine (1x 100 ml), then dried (Na_2SO_4), filtered and the solvent removed under reduced pressure. The crude product was purified by flash column chromatography (PE:EA 2:1), then dried *in vacuo* to afford title compound **29** (176 mg, 0.48 mmol, 30% yield) as yellow solid.

R_f: 0.26 (PE:EA 2:1).

t_R: 28.32 min (gradient of 10–80% B in A over 30 min).

m.p.: 215.3°C.

^{1}**H NMR** (400 MHz, DMSO–d_6): δ = 9.74 (s, 1H, H_g), 9.45 (s, 1H, H_h), 8.21–8.13 (m, 2H, H_q), 7.62–7.54 (m, 2H, H_p), 7.29–7.18 (m, 3H, H_e, H_m), 6.98–6.89 (m, 1H, H_n), 6.86 (dd, J = 8.6 Hz, J = 2.8 Hz, 1H, H_f), 6.85–6.77 (m, 2H, H_l), 6.77 (d, J = 2.8 Hz, 1H, H_b), 4.49 (s, 2H, H_j) ppm.

^{13}**C NMR** (100 MHz, DMSO–d_6): δ = 167.3 (C, C_i), 157.6 (C, C_k), 155.9 (C, C_a), 146.4 (C, C_r), 146.0 (C, C_o), 136.9 (C, C_l), 129.8 (CH, C_p), 129.4 (CH, C_m), 129.0 (CH, C_e), 125.3 (C, C_d), 123.4 (CH, C_q), 121.2 (CH, C_n), 116.2 (CH, C_b), 115.8 (CH, C_f), 114.6 (CH, C_l), 66.9 (CH_2, C_j) ppm.

IR: $\tilde{\nu}$ = 3375, 3212, 1680, 1621, 1598, 1539, 1520, 1498, 1484, 1446, 1352, 1302, 1230, 1194, 1178, 1154, 1129, 1082, 1059, 1017, 879, 857, 850, 843, 823, 754, 732, 706, 682, 672, 655, 598, 590, 546, 528, 507 cm^{-1}.

HRMS (EI^+) m/z: $[M]^+$ calculated for $C_{20}H_{16}N_2O_5^+$: 364.1054, found: 364.1053.

9.6.7 Synthesis of *N*-(4'-Cyano-5-hydroxy-[1,1'-biphenyl]-2-yl)-2-phenoxyacetamide 30

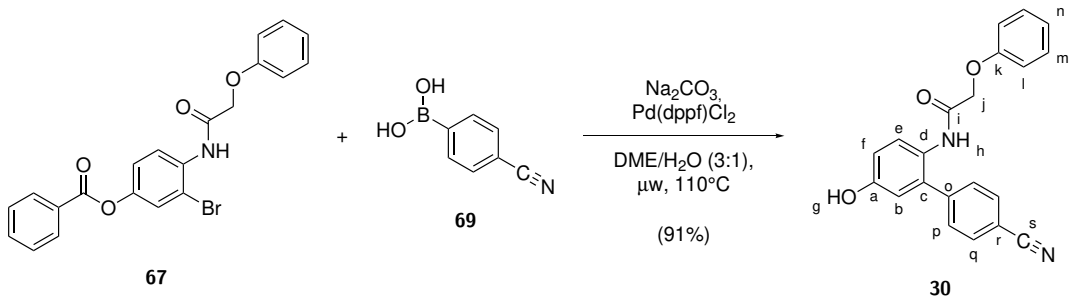

67 + 69 → 30

A 3:1 DME/H_2O mixture was degassed by sparging with N_2 for 30 min. Five 10 ml microwave vials were each flushed with N_2, then each charged with bromide **67** (138 mg, 0.32 mmol, 1.0 eq), boronic acid **69** (57 mg, 0.39 mmol, 1.2 eq), Na_2CO_3 (69 mg, 0.65 mmol, 2.0 eq) and Pd(pddf)Cl_2 (12 mg, 0.016 mmol, 5 mol%). The vials were again flushed with N_2, then DME/H_2O (3:1, 5 ml) was added to each, again flushed with N_2, then sealed and each subjected to the following microwave reaction conditions:

T = 110°C	Time = 01:00:00	µλ = 150 W	P_{max} = 250 PSI
stirring = high	PreMix = 120 s	Power Max = Off	

The reaction mixtures were allowed to cool to rt, then combined into a separation funnel. Each vial was rinsed with DCM (3x) and H_2O (3x), which was also added to the separation funnel. The organic phase was separated and washed with citric acid (aq., 10%, 2x 100 ml), H_2O (2x 100 ml) and brine (1x 100 ml), then dried ($MgSO_4$), filtered and the solvent removed under reduced pressure. The crude product was purified by flash column chromatography (PE:EA 2:1 to PE:EA 1:1), then dried *in vacuo* to afford title compound **30** (508 mg, 1.48 mmol, 91% yield) as white solid.

R_f: 0.15 (PE:EA 2:1).

m.p.: 196.0°C (decomposition).

^{1}H NMR (400 MHz, DMSO–d_6): δ = 9.66 (s, 1H, H_g), 9.35 (s, 1H, H_h), 7.79 (dt, J = 8.3 Hz, J = 1.7 Hz, 2H, H_q), 7.52 (dt, J = 8.3 Hz, J = 1.8 Hz, 2H, H_p), 7.33–7.21 (m, 3H, H_e, H_m), 7.02–6.91 (m, 1H, H_n), 6.88–6.78 (m, 3H, H_f, H_l), 6.74 (d, J = 2.8 Hz, 1H, H_b), 4.48 (s, 2H, H_j) ppm.

^{13}C NMR (100 MHz, DMSO–d_6): δ = 167.1 (C, C_i), 157.6 (C, C_k), 155.8 (C, C_a), 143.9 (C, C_o), 137.2 (C, C_c), 132.1 (CH, C_q), 129.5 (CH, C_p), 129.4 (CH, C_m), 128.7 (CH, C_e), 125.2 (C, C_d), 121.2 (CH, C_n), 118.8 (C, C_s), 116.2 (CH, C_b), 115.6 (CH, C_f), 114.6 (CH, C_l), 109.9 (C, C_r), 66.9 (CH_2, C_j) ppm.

IR: $\tilde{\nu}$ = 3374, 3198, 2923, 2868, 2293, 2232, 1675, 1653, 1621, 1608, 1598, 1584, 1536, 1509, 1496, 1484, 1447, 1402, 1366, 1329, 1297, 1231, 1203, 1188, 1155, 1126, 1081, 1058, 1021, 995, 976, 944, 900, 878, 853, 838, 821, 773, 755, 678, 668, 647, 600, 589, 567, 548, 527, 519, 506 cm^{-1}.

HRMS (EI^+) m/z: $[M]^+$ calculated for $C_{21}H_{16}N_2O_3^+$: 344.1155, found: 344.0979.

9.6.8 Synthesis of *N*-(2-(2,4-Dimethoxypyrimidin-5-yl)-4-hydroxyphenyl)-2-(4-methoxyphenyl)acetamide 31

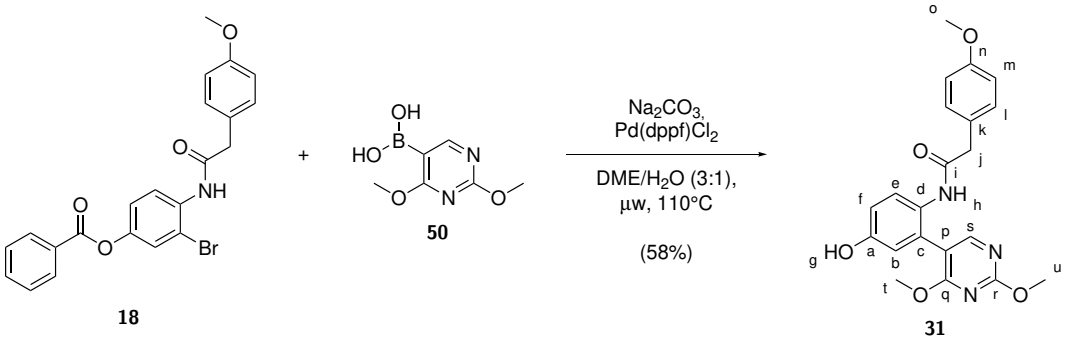

18 + 50 → 31

A 3:1 DME/H_2O mixture was degassed by sparging with N_2 for 30 min. Five 10 ml microwave vials were each flushed with N_2, then each charged with bromide **18** (143 mg, 0.32 mmol, 1.0 eq), boronic acid **50** (72 mg, 0.39 mmol, 1.2 eq), Na_2CO_3 (68 mg, 0.64 mmol, 2.0 eq) and Pd(pddf)Cl_2 (12 mg, 0.016 mmol, 5 mol%). The vials were again flushed with N_2, then DME/H_2O (3:1, 5 ml) was added to each, again flushed with N_2, then sealed and each subjected to the following microwave reaction conditions:

T = 110°C	Time = 01:00:00	µλ = 150 W	P_{max} = 250 PSI
stirring = high	PreMix = 120 s	Power Max = Off	

The reaction mixtures were allowed to cool to rt, then combined into a separation funnel. Each vial was rinsed with DCM (3x) and H_2O (3x), which was also added to the separation funnel. The organic phase was separated and washed with citric acid (aq., 10%, 2x 100 ml), H_2O (2x 100 ml) and brine (1x 100 ml), then dried ($MgSO_4$), filtered and the solvent removed under reduced pressure. The crude product was purified by flash column chromatography (PE:EA 1:2 to EA), then dried *in vacuo* to afford title compound **31** (371 mg, 0.94 mmol, 58% yield) as light yellow brown solid.

R_f: 0.24 (PE:EA 1:2).

t_R: 21.55 min (gradient of 10–80% B in A over 30 min).

m.p.: 146.3°C.

^{1}H NMR (300 MHz, DMSO–d_6): δ = 9.45 (s, 1H, H_g), 8.85 (s, 1H, H_h), 8.01 (s, 1H, H_s), 7.28 (d, J = 8.6 Hz, 1H, H_e), 7.12–6.97 (m, 2H, H_l), 6.85–6.73 (m, 2H, H_m), 6.75 (dd, J = 8.7 Hz, J = 2.8 Hz, 1H, H_f), 6.59 (d, J = 2.8 Hz, 1H, H_b), 3.93 (s, 3H, H_t), 3.74 (s, 3H, H_u), 3.73 (s, 3H, H_o), 3.35 (s, 2H, H_j) ppm.

^{13}C NMR (75 MHz, DMSO–d_6): δ = 169.3 (C, C_i), 167.5 (C, C_r), 164.2 (C, C_q), 158.1 (CH, C_s), 157.8 (C, C_n), 154.7 (C, C_a), 129.8 (CH, C_l), 129.5 (C, C_d), 127.9 (C, C_c or C_k), 127.8 (C, C_c or C_k), 127.0 (CH, C_e), 117.1 (CH, C_b), 115.0 (CH, C_f), 113.6 (CH, C_m), 113.3 (C, C_p), 54.9 (CH_3, C_o), 54.4 (CH_3, C_t), 53.6 (CH_3, C_u), 41.6 (CH_2, C_j) ppm.

Some NMR signals could not be unambiguously assigned.

IR: $\tilde{\nu}$ = 3207, 3004, 2950, 2836, 1700, 1653, 1598, 1563, 1507, 1470, 1446, 1398, 1382, 1329, 1301, 1283, 1241, 1206, 1178, 1141, 1059, 1030, 1024, 1013, 960, 897, 881, 858, 848, 816, 805, 798, 785, 765, 713, 692, 672, 654, 649, 618, 590, 585, 568, 566, 546, 536, 532, 529, 520, 516, 514 cm^{-1}.

HRMS (EI^+) m/z: $[M]^+$ calculated for $C_{21}H_{21}N_3O_5^+$: 395.1476, found: 395.1426.

9.6.9 Synthesis of *N*-(5-Hydroxy-4'-nitro-[1,1'-biphenyl]-2-yl)-2-(4-methoxyphenyl) acetamide 20

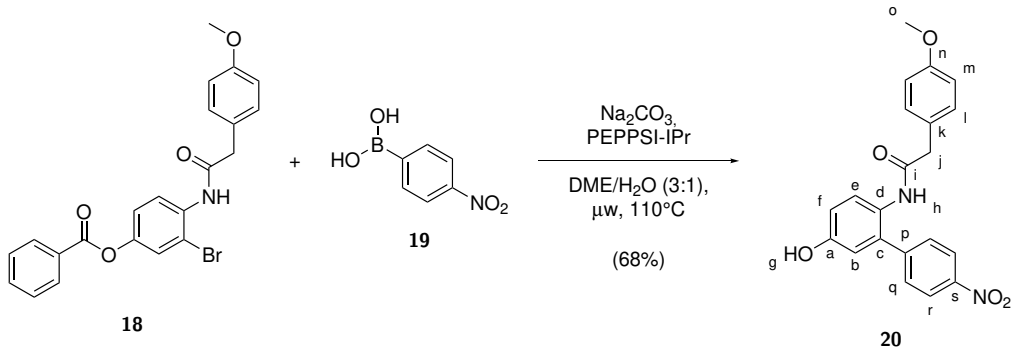

A 3:1 DME/H_2O mixture was degassed by sparging with Ar for 30 min. Five 10 ml microwave vials were each flushed with Ar, then each charged with bromide **18** (142 mg, 0.32 mmol, 1.0 eq), boronic acid **19** (65 mg, 0.39 mmol, 1.2 eq), Na_2CO_3 (69 mg, 0.65 mmol, 2.0 eq) and PEPPSI-IPr (11 mg, 0.016 mmol, 5 mol%). The vials were again flushed with Ar, then DME/H_2O (3:1, 5 ml) was added to each, again flushed with Ar, then sealed and each subjected to the following microwave reaction conditions:

T = 110°C	Time = 01:00:00	µλ = 150 W	P_{max} = 250 PSI
stirring = high	PreMix = 120 s	Power Max = Off	

The reaction mixtures were allowed to cool to rt, then combined into a separation funnel. Each vial was rinsed with DCM (3x) and H_2O (3x), which was also added to the separation funnel. The organic phase was separated and washed with citric acid (aq., 10%, 2x 100 ml), H_2O (3x 100 ml) and brine (1x 100 ml), then dried ($MgSO_4$), filtered and the solvent removed under reduced pressure. The crude product was purified by flash column chromatography (PE:EA 1:1), then dried *in vacuo* to afford title compound **20** (418 mg, 1.10 mmol, 68% yield) as light yellow solid.

R_f: 0.36 (PE:EA 1:1).

t_R: 19.25 min (gradient of 30–80% B in A over 30 min).

m.p.: 214.8°C.

^{1}H NMR (300 MHz, DMSO–d_6): δ = 9.67 (s, 1H, H_g), 9.35 (s, 1H, H_h), 8.09–7.98 (m, 2H, H_r), 7.48–7.37 (m, 2H, H_q), 7.16 (d, J = 8.5 Hz, 1H, H_e), 7.09–6.98 (m, 2H, H_l), 6.82 (dd, J = 8.6 Hz, J = 2.8 Hz, 1H, H_f), 6.83–6.70 (m, 2H, H_m), 6.72 (d, J = 2.7 Hz, 1H, H_b), 3.72 (s, 3H, H_o), 3.32 (s, 2H, H_j) ppm.

^{13}C NMR (75 MHz, DMSO–d_6): δ = 169.7 (C, C_i), 157.9 (C, C_n), 155.8 (C, C_a), 146.1 (C, C_c or C_s), 146.1 (C, C_c or C_s), 137.0 (C, C_p), 130.0 (CH, C_l), 129.6 (CH, C_q), 129.3 (CH, C_e), 127.5 (C, C_k), 126.0 (C, C_d), 123.1 (CH, C_r), 116.0 (CH, C_b), 115.7 (CH, C_f), 113.4 (CH, C_m), 54.9 (CH_3, C_o), 41.7 (CH_2, C_j) ppm.

IR: $\tilde{\nu}$ = 3371, 2921, 2850, 1655, 1639, 1611, 1594, 1543, 1512, 1475, 1441, 1412, 1346, 1304, 1246, 1220, 1175, 1105, 1033, 962, 918, 901, 870, 851, 821, 758, 721, 699, 668, 650, 567, 560, 553, 551, 535, 527, 525, 519, 514, 512, 510, 506, 501 cm^{-1}.

HRMS (EI^+) m/z: $[M]^+$ calculated for $C_{21}H_{18}N_2O_5^+$: 378.1210, found: 378.1173.

9.6.10 Synthesis of *N*-(4'-Cyano-5-hydroxy-[1,1'-biphenyl]-2-yl)-2-(4-methoxyphenyl) acetamide 32

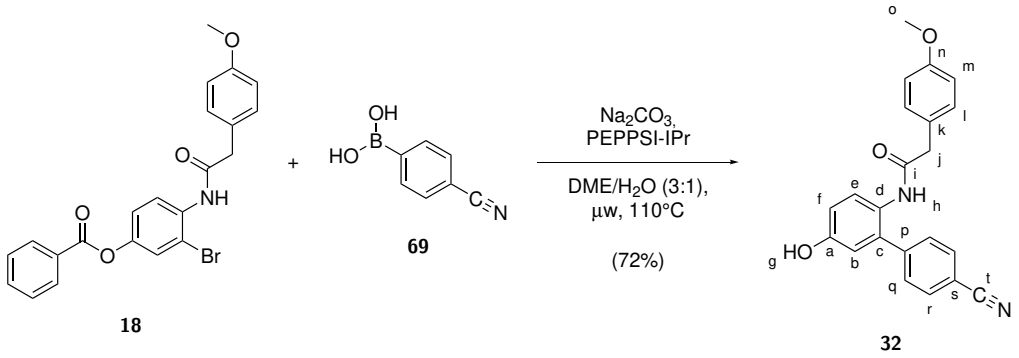

A 3:1 DME/H_2O mixture was degassed by sparging with Ar for 30 min. Five 10 ml microwave vials were each flushed with Ar, then each charged with bromide **18** (142 mg, 0.32 mmol, 1.0 eq), boronic acid **69** (57 mg, 0.39 mmol, 1.2 eq), Na_2CO_3 (69 mg, 0.65 mmol, 2.0 eq) and PEPPSI-IPr (11 mg, 0.016 mmol, 5 mol%). The vials were again flushed with Ar, then DME/H_2O (3:1, 5 ml) was added to each, again flushed with Ar, then sealed and each subjected to the following microwave reaction conditions:

T = 110°C	Time = 01:00:00	µλ = 150 W	P_{max} = 250 PSI
stirring = high	PreMix = 120 s	Power Max = Off	

The reaction mixtures were allowed to cool to rt, then combined into a separation funnel. Each vial was rinsed with DCM (3x) and H_2O (3x), which was also added to the separation funnel. The organic phase was separated and washed with citric acid (aq., 10%, 2x 100 ml), H_2O (3x 100 ml) and brine (1x 100 ml), then dried ($MgSO_4$), filtered and the solvent removed under reduced pressure. The crude product was purified by flash column chromatography (PE:EA 1:1 to PE:EA 1:2), then dried *in vacuo* to afford title compound **32** (416 mg, 1.16 mmol, 72% yield) as light white solid.

R_f: 0.26 (PE:EA 1:1).

t_R: 25.33 min (gradient of 10–80% B in A over 30 min).

m.p.: 179.1°C (decomposition).

^{1}H NMR (400 MHz, DMSO–d_6): δ = 9.64 (s, 1H, H_g), 9.30 (s, 1H, H_h), 7.72–7.65 (m, 2H, H_r), 7.42–7.33 (m, 2H, H_q), 7.15 (d, J = 8.6 Hz, 1H, H_e), 7.07–6.98 (m, 2H, H_l), 6.86–6.81 (m, 2H, H_m), 6.81–6.77 (m, 1H, H_f), 6.69 (d, J = 2.7 Hz, 1H, H_b), 3.75 (s, 3H, H_o), 3.32 (s, 2H, H_j) ppm.

^{13}C NMR (100 MHz, DMSO–d_6): δ = 169.8 (C, C_i), 158.0 (C, C_n), 155.8 (C, C_a), 144.0 (C, C_p), 137.4 (C, C_c), 132.0 (CH, C_r), 130.0 (CH, C_l), 129.4 (CH, C_q), 129.3 (CH, C_e), 127.7 (C, C_k), 126.0 (C, C_d), 118.9 (C, C_t), 116.1 (CH, C_b), 115.5 (CH, C_f), 113.6 (CH, C_m), 109.6 (C, C_s), 55.0 (CH_3, C_o), 41.6 (CH_2, C_j) ppm.

IR: $\tilde{\nu}$ = 3378, 3363, 3121, 2950, 2836, 2220, 1635, 1610, 1604, 1585, 1540, 1513, 1506, 1440, 1412, 1399, 1299, 1249, 1218, 1179, 1115, 1035, 962, 917, 899, 870, 845, 824, 817, 768, 707, 657, 614, 571, 521, 507, 505 cm^{-1}.

HRMS (EI^+) m/z: $[M]^+$ calculated for $C_{22}H_{18}N_2O_3^+$: 358.1312, found: 358.1278.

9.7 Deprotections

9.7.1 Synthesis of *N*-(5-Hydroxy-4'-nitro-[1,1'-biphenyl]-2-yl)-2-(4-hydroxyphenyl) acetamide 37

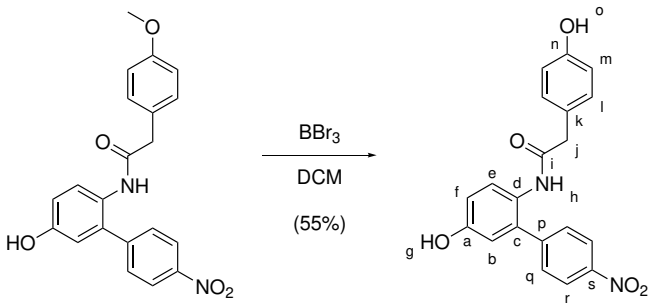

20 **37**

A modified procedure from Roy *et al.*[219] was used. A flask was charged with methyl ether **20** (329 mg, 1.01 mmol, 1.0 eq) under N_2 and anhydrous DMC (20 ml) was added. The suspension was stirred and cooled to 0°C with an ice bath. BBr_3 dissolved in DCM (2.0 ml, 1 M, 2.00 mmol, 2 eq) was slowly added to the reaction mixture. The ice bath was removed and the reaction mixture allowed to warm to rt, then stirred at rt. After 3.5 h TLC revealed starting material **20** to be consumed. The reaction mixture was cooled to 0°C with an ice bath then quenched by careful addition of H_2O (10 ml) and MeOH (5 ml). The reaction mixture was allowed to warm to rt, H_2O (50 ml) and DCM (50 ml) was added and extracted with NaOH (aq., 2 M, 4x 50 ml). The basic aqueous phase was neutralized with HCl (aq., conc., 32 ml) to about pH = 7. The resulting precipitate was filtered off. NaCl was added to the remaining aq. solution until saturated and the resulting precipitate again filtered off. The precipitate was washed with H_2O then dissolved in EA, washed with brine (200 ml), dried ($MgSO_4$), filtered and the solvent removed under reduced pressure. The crude product was purified by flash column chromatography (MeOH:DCM 1:99 to MeOH:DCM 5:95), then dried *in vacuo* to afford title compound **37** (203 mg, 0.56 mmol, 55% yield) as off white light pink solid.

R_f: 0.15 (MeOH:DCM 5:95).

t_R: 21.85 min (gradient of 10–80% B in A over 30 min).

m.p.: 231.8°C.

^{1}H NMR (400 MHz, DMSO–d_6): δ = 9.67 (s, 1H, H_g), 9.31 (s, 1H, H_h), 9.24 (s, 1H, H_o), 8.15–8.07 (m, 2H, H_r), 7.51–7.43 (m, 2H, H_q), 7.16 (d, J = 8.6 Hz, 1H, H_e), 6.95–6.87 (m, 2H, H_l), 6.82 (dd, J = 8.6 Hz, J = 2.8 Hz, 1H, H_f), 6.73 (d, J = 2.8 Hz, 1H, H_b), 6.65–6.57 (m, 2H, H_m), 3.28 (s, 2H, H_j) ppm.

^{13}C NMR (100 MHz, DMSO–d_6): δ = 169.9 (C, C_i), 156.0 (C, C_n), 155.7 (C, C_a), 146.2 (C, C_s), 146.2 (C, C_p), 136.8 (C, C_c), 129.9 (CH, C_l), 129.7 (CH, C_q), 129.2 (CH, C_e), 126.1 (C, C_d), 125.8 (C, C_k), 123.2 (CH, C_r), 116.1 (CH, C_b), 115.8 (CH, C_f), 114.9 (CH, C_m), 41.7 (CH_2, C_j) ppm.

IR: $\tilde{\nu}$ = 3355, 3087, 2919, 2828, 1700, 1653, 1618, 1601, 1581, 1508, 1489, 1463, 1451, 1417, 1385, 1346, 1320, 1309, 1234, 1206, 1107, 931, 906, 891, 853, 820, 790, 758, 722, 699, 667, 624, 605, 565, 538, 534, 518, 516, 514, 506 cm^{-1}.

HRMS (EI^+) m/z: $[M]^+$ calculated for $C_{20}H_{16}N_2O_5^+$: 364.1054, found: 364.1029.

9.7.2 Synthesis of 2-(3,4-Dihydroxyphenyl)-*N*-(2-(2,4-dimethoxypyrimidin-5-yl)-4-hydroxyphenyl)acetamide 35

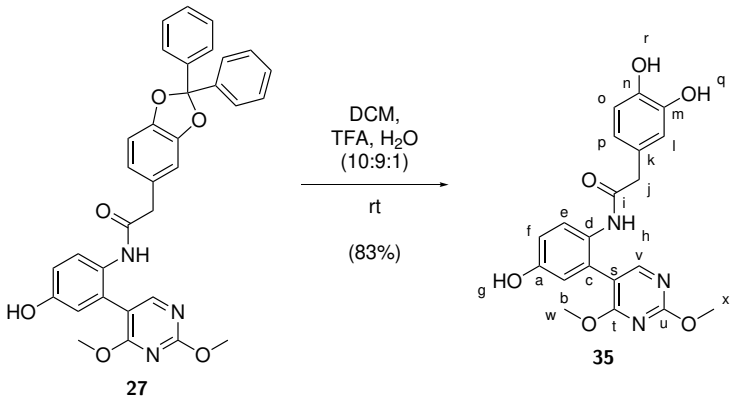

A modified procedure from Blagg *et al.*[200] was used. A flask was charged with acetal **27** (67 mg, 0.12 mmol, 1.0 eq). A solution of DMC, TFA and H_2O (2 ml, 10:9:1) was prepared and slowly added to dissolve acetal **27**. The reaction mixture was stirred at rt. After 2 h TLC revealed starting material **27** to be consumed. The reaction mixture was placed under a stream of N_2 to remove DCM and TFA. The residue was dissolved in MeCN, H_2O added and the solvent removed by lyophilization. The crude product was purified by flash column chromatography (PE:EA 1:4 + 1% HCOOH), then dried *in vacuo* to afford title compound **35** (40 mg, 0.10 mmol, 83% yield) as white solid.

R_f: 0.22 (PE:EA 1:4 +1% HCOOH).
t_R: 14.81 min (gradient of 10–80% B in A over 30 min).
m.p.: 65.3°C (decomposition).
^{1}H NMR (400 MHz, DMSO–d_6): δ = 9.45 (s, 1H, H_g), 8.76 (s, 1H, H_q), 8.75 (s, 1H, H_h), 8.70 (s, 1H, H_r), 8.03 (s, 1H, H_v), 7.31 (d, J = 8.7 Hz, 1H, H_e), 6.74 (dd, J = 8.7 Hz, J = 2.8 Hz, 1H, H_f), 6.61–6.55 (m, 3H, H_b, H_l, H_o), 6.34 (dd, J = 8.0 Hz, J = 2.1 Hz, 1H, H_p), 3.94 (s, 3H, H_w), 3.74 (s, 3H, H_x), 3.23 (s, 2H, H_j) ppm.
^{13}C NMR (100 MHz, DMSO–d_6): δ = 169.5 (C, C_i), 167.6 (C, C_u), 164.3 (C, C_t), 158.2 (CH, C_v), 154.5 (C, C_a), 145.0 (C, C_n), 143.8 (C, C_m), 129.1 (C, C_c), 127.9 (C, C_d), 126.9 (CH, C_e), 126.7 (C, C_k), 119.5 (CH, C_p), 117.1 (CH, C_b), 116.5 (CH, C_l), 115.3 (CH, C_o), 115.0 (CH, C_f), 113.3 (C, C_s), 54.5 (CH_3, C_w), 53.7 (CH_3, C_x), 41.9 (CH_2, C_j) ppm.
IR: $\tilde{\nu}$ = 3886, 3881, 3874, 3854, 3843, 3821, 3819, 3807, 3752, 3749, 3745, 3738, 3691, 3677, 3675, 3649, 3629, 3586, 2920, 2851, 2175, 2159, 2153, 2060, 2031, 2006, 1977, 1700, 1653, 1601, 1560, 1386, 1182, 1131, 1004, 895, 839, 767, 747, 707, 671, 669, 661, 649, 631, 624, 602, 594, 588, 579, 573, 563, 558, 553, 542, 537, 533, 526, 520, 514, 511, 508, 506, 504 cm^{-1}.
HRMS (EI^+) m/z: $[M]^+$ calculated for $C_{20}H_{19}N_3O_6^+$: 397.1268, found: 397.1254.

9.7.3 Synthesis of 2-(3,4-Dihydroxyphenyl)-*N*-(5-hydroxy-4'-nitro-[1,1'-biphenyl]-2-yl) acetamide 36

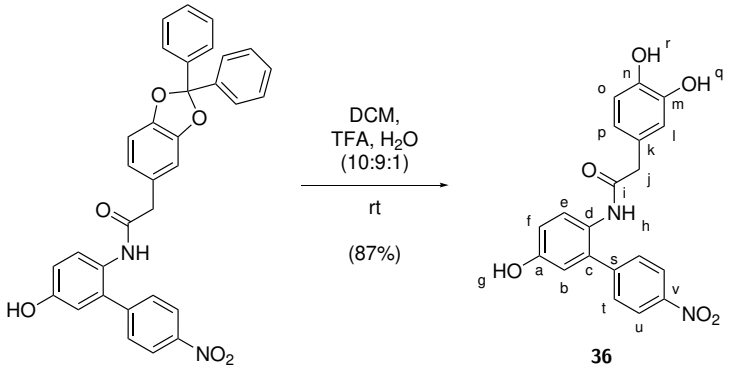

A modified procedure from Blagg *et al.*[200] was used. A flask was charged with acetal **28** (662 mg, 1.22 mmol, 1.0 eq). A solution of DMC, TFA and H_2O (10 ml, 10:9:1) was prepared and slowly added to dissolve acetal **28**. The reaction mixture was stirred at rt. After 2 h TLC revealed starting material **28** to be consumed. The reaction mixture was placed under a stream of N_2 to remove DCM and TFA. The residue was dissolved in MeCN, H_2O added and the solvent removed by lyophilization. The crude product was purified by flash column chromatography (PE:EA 1:1 + 1% HCOOH), then dried *in vacuo* to afford title compound **36** (403 mg, 1.06 mmol, 87% yield) as white solid.

R_f: 0.12 (PE:EA 1:1 + 1% HCOOH).
t_R: 20.11 min (gradient of 10–80% B in A over 30 min).
m.p.: 192.8°C (decomposition).
^{1}H NMR (400 MHz, DMSO–d_6): δ = 9.66 (s, 1H, H_g), 9.26 (s, 1H, H_h), 8.73 (s, 2H, Hq, H_r), 8.17–8.09 (m, 2H, H_u), 7.53–7.44 (m, 2H, H_t), 7.18 (d, J = 8.6 Hz, 1H, H_e), 6.82 (dd, J = 8.6 Hz, J = 2.8 Hz, 1H, H_f), 6.74 (d, J = 2.8 Hz, 1H, H_b), 6.61–6.54 (m, 2H, H_l, H_o), 6.37 (dd, J = 8.0 Hz, J = 2.1 Hz, 1H, H_p), 3.22 (s, 2H, H_j) ppm.
^{13}C NMR (100 MHz, DMSO–d_6): δ = 170.0 (C, C_i), 155.6 (C, C_a), 146.3 (C, C_v), 146.1 (C, C_s), 144.9 (C, C_n), 144.0 (C, C_m), 136.5 (C, C_c), 129.7 (CH, C_t), 129.2 (CH, C_e), 126.4 (C, C_k), 126.2 (C, C_d), 123.3 (CH, C_u), 119.8 (CH, C_p), 116.5 (CH, C_l), 116.1 (CH, C_b), 115.8 (CH, C_f), 115.2 (CH, C_o), 41.9 (CH_2, C_j) ppm.
IR: $\tilde{\nu}$ = 3536, 3347, 2924, 2852, 1704, 1654, 1651, 1594, 1583, 1507, 1484, 1445, 1373, 1343, 1307, 1278, 1254, 1188, 1142, 1112, 1042, 1014, 961, 902, 871, 854, 812, 798, 778, 754, 729, 699, 634, 592, 520, 505 cm^{-1}.
HRMS (EI^+) m/z: $[M]^+$ calculated for $C_{20}H_{16}N_2O_6^+$: 380.1003, found: 380.0979.

9.7.4 Synthesis of 2-(2,5-Dihydroxyphenyl)-*N*-(5-hydroxy-4'-nitro-[1,1'-biphenyl]-2-yl) acetamide 38

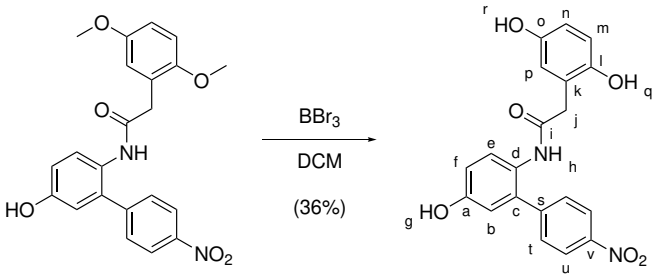

24 **38**

A modified procedure from Roy *et al.*[219] was used. A flask was charged with methyl ether **24** (491 mg, 1.20 mmol, 1.0 eq) under N_2 and anhydrous DMC (20 ml) was added. The suspension was stirred and cooled to 0°C with an ice bath. BBr_3 dissolved in DCM (7.2 ml, 1 M, 7.20 mmol, 6 eq) was slowly added to the reaction mixture. The ice bath was removed and the reaction mixture allowed to warm to rt, then stirred at rt over night. The reaction mixture was cooled to 0°C with an ice bath then quenched by careful addition of H_2O (10 ml) and MeOH (5 ml). The reaction mixture was allowed to warm to rt, DCM (50 ml) and NaOH (aq., 2 M, 50 ml) was added. The organic phase was separated and extracted with NaOH (aq., 2 M, 2x 50 ml). The basic aqueous phase was neutralized with HCl (aq., conc., 35 ml) to about pH = 7 then extracted with EA (3x 200 ml). The combined organic phases were washed with brine (300 ml), dried ($MgSO_4$), filtered and the solvent removed under reduced pressure. The crude product was purified by flash column chromatography (PE:EA 1:1 + 1% HCOOH to PE:EA 1:3 + 1% HCOOH), then dried *in vacuo* to afford title compound **38** (165 mg, 0.43 mmol, 36% yield) as brown solid.

R_f: 0.18 (PE:EA 1:1 + 1% HCOOH).
t_R: 20.00 min (gradient of 10–80% B in A over 30 min).
m.p.: 226.8°C (decomposition).
^{1}H NMR (400 MHz, DMSO–d_6): δ = 9.66 (s, 1H, H_g), 9.14 (s, 1H, H_h), 8.77 (s, 1H, H_q), 8.60 (s, 1H, H_r), 8.19–8.10 (m, 2H, H_u), 7.57–7.48 (m, 2H, H_t), 7.28 (d, J = 8.6 Hz, 1H, H_e), 6.82 (dd, J = 8.6 Hz, J = 2.8 Hz, 1H, H_e), 6.74 (d, J = 2.8 Hz, 1H, H_b), 6.57–6.47 (m, 1H, H_m), 6.48–6.39 (m, 2H, H_n, H_p), 3.31 (s, 2H, H_j) ppm.
^{13}C NMR (100 MHz, DMSO–d_6): δ = 170.1 (C, C_i), 155.5 (C, C_a), 149.7 (C, C_o), 147.6 (C, C_l), 146.4 (C, C_v), 145.8 (C, C_s), 136.0 (C, C_c), 129.8 (CH, C_t), 128.6 (CH, C_e), 126.2 (C, C_d), 123.4 (CH, C_u), 122.5 (C, C_k), 117.2 (CH, C_p), 116.0 (CH, C_b), 115.7 (CH, C_f), 115.5 (CH, C_m), 113.9 (CH, C_n), 37.6 (CH_2, C_j) ppm.
IR: $\tilde{\nu}$ = 3364, 3196, 2922, 2854, 1632, 1620, 1595, 1582, 1524, 1507, 1463, 1345, 1319, 1284, 1254, 1205, 1180, 1152, 1126, 1105, 1012, 981, 960, 906, 888, 849, 815, 770, 757, 720, 697, 585, 523, 512 cm^{-1}.
HRMS (EI^+) m/z: $[M-2H]^+$ calculated for $C_{20}H_{14}N_2O_6^+$: 378.0846, found: 378.0786 and $[M]^+$ calculated for $C_{20}H_{16}N_2O_6^+$: 380.1003, found: 380.0969.

9.8 HPLC Purification and Analysis

Table 13: HPLC machines and components.

Supplier	Scale	Components	Software
Jasco	(semi)preparative	UV-4070 UV/Vis detector, PU-4180 RHPLC pump, CO-4060 column oven, LC-Net II/ADC Interface box	ChromNav
Shimadzu	(semi)preparative	SPD-M40 photo diode array detector, LC-40D solvent delivery module DGU-405 degassing unit, CTO-40S column oven, CBM-40 system controller	LabSolutions
Hitachi	analytical	Primaide System, Primaide 1430 Diode Array Detector, Primaide 1110 Pump, Primaide 1210 Auto Sampler, Primaide 1310 Column Oven	Primaide

Table 14: HPLC Columns.

Supplier	Name	Scale	Specifications
VDS optilab	VDSpher PUR	(semi)preparative	C18-SE, 250 x 20 mm, 100 Å poresize, 5 µm particle diameter
VDS optilab	VDSpher OptiBio PUR	(semi)preparative	C18-SE, 250 x 10 mm, 300 Å poresize, 5 µm particle diameter
VDS optilab	VDSpher PUR	analytical	C18-SE 250 x 4.6 mm, 100 Å poresize, 5 µm particle diameter

Table 15: Buffers used in HPLC.

Name	Scale	Components
Buffer A	(semi)preparative	H_2O + 0.1% (v/v) formic acid
Buffer B	(semi)preparative	acetonitrile + 0.1% (v/v) formic acid
Buffer A	analytical	H_2O + 0.1% (v/v) trifluoroacetic acid
Buffer B	analytical	acetonitrile + 0.1% (v/v) trifluoroacetic acid

Table 16: Materials used in HPLC purification.

Item	Supplier
HPLC grade formic acid 5.43804	Sigma Aldrich
CHROMAFIL Xtra 0.45 µm H-PTFE Syringe filter	Macherey Nagel
CHROMAFIL Xtra 0.2 µm H-PTFE Syringe filter	Macherey Nagel

Buffers for HPLC were prepared from HPLC grade solvents and ultrapure water provided by an Arium Mini from Satorius. HPLC grade formic acid and trifluoroacetic acid were used as additives.

For (semi)preparative HPLC purification of SOD1 ligands a weight out amount of solid sample was first dissolved by vortexing in DMSO (1–2 ml), then acetonitrile (1–9 ml) was added and again vortexed, lastly H_2O (1–9 ml) was added and again vortexed. Samples solutions were typically prepared with a H_2O/MeCN ratio matching the A/B ratio at the start of the gradient + 10–20% (v/v) DMSO. Prior to injection, samples were centrifuged (4000 × g, 5–10 min) and filtered through a 0.2 µm H-PTFE filter. For larger volumes or particularly cloudy samples a 0.45 µm H-PTFE filter, then a 0.2 µm H-PTFE filter were used.

(Semi)preparative HPLC purification of SOD1 ligands was performed on the Jasco HPLC detailed above, with the (semi)preparative 300 Å VDSpher OptiBio PUR column, a flow of 8 ml/min and an oven temperature of 50°C. The absorbance was monitored at 220 and 280 nm. Preliminary exploration of the (semi)preparative HPLC purification conditions of SOD1 ligands was performed on the Shimadzu HPLC detailed above, with the (semi)preparative 100 Å VDSpher PUR column, a flow of 2.5 ml/min and an oven temperature of 25°C. The Absorbance was monitored at 220 and 280 nm.

Following HPLC purification, the obtained product fractions were analyzed by analytical HPLC and MALDI-MS. Analytical HPLC was performed on the Hitachi HPLC detailed above, with the analytical 100 Å VDSpher PUR column, a flow of 1 ml/min and an oven temperature of 50°C. The Absorbance was monitored at 220 and 280 nm. To determine product purity, the integrals of peaks in the analytical HPLC chromatogram and their relative ratios were calculated. HPLC solvent was removed by lyophilization and the obtained solid residues again dried *in vacuo* to remove trace H_2O and acetonitrile. Multiple batches of sufficient purity were combined to prepare assay stocks.

9.9 Molecular Biology

9.9.1 Devices and Materials

Table 17: Devices, materials, enzymes and reagents.

Item	Supplier
Arium Mini Ultrapure Water System	Satorius
LB Medium was made from: LB Broth L3022	Sigma Aldrich
The following was used as SOC Medium: Recovery Medium for Cloning CMR0002	Sigma Aldrich
QIAGEN Plasmid Kits for Plasmid DNA Extraction	QIAGEN
Ultraspec 2100 pro UV/Vis Spectrometer	Amersham Bioscience
NanoDrop Photometer NanoDrop Lite	Thermo Fisher Scientific
NEB 5-alpha Competent *E. coli* Derivative of DH5α	New England Biolabs
BL21 (DE3) Competent *E. coli*	New England Biolabs
DNase1, RNase-free 1000 U/ml EN0521	Thermo Fisher Scientific
Lysozyme from chicken egg white L6876	Sigma Aldrich
High-Pressure Homogenizer One Shot Cell Disruptor	Constant Systems LTD
SnakeSkin Dialysis Tubing 22 mm i.D., 3.5 kDa MWCO 68035	Thermo Fisher Scientific
SnakeSkin Dialysis Tubing Clips 68011	Thermo Fisher Scientific
Mini-PROTEAN Tetra Handcast Systems	Bio-Rad
Mini-PROTEAN Tetra Vertical Electrophoresis Cell	Bio-Rad

Table 17: *(continued)* Devices, materials, enzymes and reagents.

Item	Supplier
4x Laemmli Sample Buffer 1610747	Bio-Rad
GelCode Blue Safe Protein Stain	Thermo Fisher Scientific
PageRuler Plus Prestained Protein Ladder 10 to 250 kDa	Thermo Fisher Scientific
acrylamide / bisacrylamide solution ROTIPHORESE Gel 30 (37.5:1)	Carl Roth
ChemiDoc XRS+ Gel Imaging System Image Lab Software	Bio-Rad
Amicon Ultra-15 Centrifugal Filter Units 10 kDa cut-off	Merck Millipore
Amicon Ultra-50 Centrifugal Filter Units 10 kDa cut-off	Merck Millipore
protein low binding pipet tips	VWR
protein low binding Eppendorf tubes	Eppendorf

Table 18: Äkta, columns and accessories.

Item	Supplier
ÄKTApurifier UNICORN start UNICORN control software	GE Healthcare, now Cytiva
50 ml TMAE column	manually packed as detailed in Section 9.9.4
XK 16/40 Column	Cytiva
Packing Reservoir XK	Cytiva
Fractogel EMD TMAE (S)	Merck Millipore
HiLoad 16/600 Superdex 75 pg CV = 120 ml, V_0 = 40 ml	Cytiva
HiPrep 26/10 Desalting CV = 53 ml, V_0 = 15 ml	Cytiva

9.9.2 SDS-PAGE

Table 19: Components of the separation gel (12%) for 4 SDS-PAGE gels.

Component	Amount
H_2O	10.5 ml
Tris buffer (1.5 M, pH = 8.8)	7.5 ml
Acrylamide	12 ml
10% SDS in H_2O	300 µl
10% APS in H_2O	150 µl
TEMED	15 µl

Table 20: Components of the stacking gel (6%) for 4 SDS-PAGE gels.

Component	Amount
H_2O	6.6 ml
Tris buffer (0.5 M, pH = 6.8)	3.0 ml
Acrylamide	2.4 ml
10% SDS in H_2O	120 µl
10% APS in H_2O	60 µl
TEMED	6 µl

All components except APS and TEMED of the separation and the stacking gel were mixed. Glass plates for gel casting were clamped together in a stand. APS and TEMED were added to the separation gel, mixed, then transferred between the glass plates. Each separation gel was topped off with 1 ml isopropanol to prevent evaporation, then left to polymerize at rt for 45 min. The isopropanol was removed, APS and TEMED were added to the stacking gel, mixed, then transferred on top of the separation gel between the glass plates. A 15-well comb was inserted and the stacking gel left to polymerize at rt for 45 min. Gels were then released from their stand, wrapped in wetted plastic cling film, stored at 4–8°C and used within 14 days.

Protein samples were denatured using sodium dodecyl sulfate (SDS) prior to gel electrophoresis. 100 µl 2-mercaptoethanol as reducing agent was added to 900 µl 4x Laemmli Sample Buffer prior to use. 30 µl protein sample was mixed with 10 µl 4x Laemmli Sample Buffer, the denatured at 95°C for 5 min. Wells in the polyacrylamide gel were typically filled with 12.5 or 10 µl denatured protein sample, less sample volume was used for more concentrated protein samples. 4 µl PageRuler Plus Prestained Protein Ladder 10 to 250 kDa from Thermo Fisher was used as a size reference.

Sodium dodecyl sulfate–polyacrylamide gel electrophoresis (SDS-PAGE) was performed with manually cast gels in a Mini-PROTEAN Tetra vertical electrophoresis cell from Bio-Rad. The electrophoresis chamber was filled to its specified level with SDS-running buffer (25 mM Tris, 190 mM glycerine, 0.1% SDS) and gels were typically run at 120 V for about 1 h 20 min after which they were removed from the glass slides and stained with GelCode Blue Safe Protein Stain from Thermo Fisher. Stained gels were photographed and or imaged with a ChemiDoc XRS+ gel imaging system from Bio-Rad.

9.9.3 Molar Extinction Coefficient of SOD1

hSOD1 concentrations were determined using a NanoDrop spectrophotometer at 280 nm and unless stated otherwise refer to the dimer state. The molar extinction coefficient for dimeric hSOD1 was calculated using the ProtParam web tool from the Swiss Institute of Bioinformatics.[224] The results of the prediction can be viewed online.[225] For monomeric hSOD1 a molar extinction coefficient of 5750 $M^{-1}cm^{-1}$ assuming all pairs of Cys residues form cystines and 5500 $M^{-1}cm^{-1}$ assuming all Cys residues are reduced were predicted. Because hSOD1 contains 4 cystein residues (Cys6, Cys57, Cys111 and Cys146), each of the 2 possible disulfide bonds is therefore estimated by ProtParam to add 125 $M^{-1}cm^{-1}$. Considering that in the native state of hSOD1 Cys57 and Cys146 form a disulfide bond and Cys111 and Cys146 exist as thiols,[45] 5625 $M^{-1}cm^{-1}$ was assumed as molar extinction coefficient for the monomer of SOD1 and 11250 $M^{-1}cm^{-1}$ for the dimer.

For assays employing bovine SOD as control, the procedure to determine its concentrations needed to be adjusted, as bovine SOD does not contain any Trp residues, which are mainly responsible for proteins UV absorption at 280 nm. Instead absorption was determined at 258 mn and the corresponding molar extinction coefficient of 10300 $M^{-1}cm^{-1}$ for dimeric bovine SOD as reported by McCord and Fridovich was used.[166]

9.9.4 Manual Packing of the 50 ml TMAE Column

An empty XK 16/40 Column from Cytiva was packed to a CV of 50 ml with Fractogel EMD TMAE (S) resin from Merck by method of flow compression using a Packing Reservoir XK and an ÄKTA-purifier from GE Healthcare, now Cytiva. 150 mM NaCl in 20% EtOH in H_2O was used as buffer for column packing. Taking into account the slurry concentration of 70% and the recommended compression factor of 1.18 for this resin, 84 ml of slurry was poured into the packing packing reservoir and the resin settled with a flow of 2 ml/min = 60 cm/h. The flow was slowly increased stepwise until a maximum of 4 ml/min = 120 cm/h under which the column was compressed until the bed height did not decrease further. The bed height was then secured with the columns plunger.

To validate the packed columns quality, two different column tests were performed. 1) Using H_2O as running buffer, a sample of 1% acetone in H_2O (0.5 ml = 1% CV) was injected and the symmetry of the resulting peak in the UV signal was evaluated. 3 injections were performed and uniform symmetry and retention time were observed across all 3 peaks. 2) Using 0.4 M NaCl as running buffer, a sample of 0.8 M NaCl (0.5 ml = 1% CV) was injected and the symmetry of the resulting peak in the conductivity signal was evaluated. 3 injections were performed and uniform symmetry and retention time were observed across all 3 peaks.

9.9.5 hSOD1-Plasmids

Plasmid pET303C-hSOD1wt had kindly been provided by Prof. Samar Hasnain (University of Liverpool) to Mrđen Debono.[159] From this, a plasmid for the hSOD1 A4V variant had been derived by site-directed mutagenesis polymerase chain reaction by Mrđen Debono.[159] These plasmids for hSOD1 and the ALS related hSOD1 A4V variant were kindly provided by Mrđen Debono and the group of Prof. Kai Tittmann (University of Göttingen) for this study.

Competent NEB 5-alpha were thawed on ice, plasmids (50 ng for hSOD1 or 30 ng for hSOD1 A4V) added, then incubated on ice for 30 min. Cells were heat-shocked in a 42°C water bath for 30 s, then placed back on ice for 2 min. 600 µl pre-warmed SOC medium was added and cells incubated for 40 min at 37°C while shaking at 200 rpm. Cells were then plated onto LB-agar plates containing ampicillin (100 µg/ml) and placed at 37°C over night. A single colonies was picked and transferred into 200 ml LB medium containing ampicillin (100 µg/ml), then incubated at 37°C while shaking at 120 rpm over night. The plasmids were obtained and purified using a QIAGEN Plasmid Kit, then Sanger sequencing of plasmid DNA was performed by Microsynth Seqlab (Göttingen) with primers AmpStart, AmpStop, T7 and RV4. Purified plasmid solutions were stored at -20°C.

9.9.6 Expression of hSOD1 Variants

For the expression of hSOD1 and hSOD1 A4V a modified procedure from Mrđen Debono was used.[159] Competent BL21 (DE3) were thawed on ice, plasmids (about 500 ng for hSOD1 or about 50 ng for hSOD1 A4V) added, then incubated on ice for 30 min. Cells were heat-shocked in a 42°C water bath for 30 s, then placed back on ice for 2 min. 600 µl pre-warmed SOC medium was added and cells incubated for 40 min at 37°C while shaking at 200 rpm. Cells were then plated onto LB-agar plates containing ampicillin (100 µg/ml) and placed at 37°C over night. A pre-culture was prepared as follows: 1–3 single colonies were picked and transferred into 200 ml LB medium containing ampicillin (100 µg/ml), then incubated at 30°C while shaking at 140 rpm over night. The main culture was prepared as follows: A total of 3 l LB medium containing ampicillin (100 µg/ml) was inoculated with pre-culture (1:50), then incubated at 37°C while shaking at 140 rpm. OD_{600} of the main culture was periodically measured until about $OD_{600} = 0.5$ was reached, typically about 1–2 h after inoculation. The culture was cooled to 22°C, then induction was performed by addition of IPTG (0.4 mM final conc.), $ZnSO_4$ (0.5 mM final conc.) was added and culture incubated at 22°C while shaking at 140 rpm over night. Cells were harvested by centrifugation (3500 × g, 4°C, 20 min), the obtained pellet divided into two equally sized aliquots, flash frozen in liquid N_2 and stored at -80°C. 4.8 and 5.8 g cells per 1 l medium were obtained for hSOD1 in two separate replications and 4.0 g cells per 1 l medium were obtained for hSOD1 A4V in a single replication.

9.9.7 Purification of hSOD1 Variants

Protein purification was performed on an ÄKTApurifier from GE Healthcare, now Cytiva. Buffers were freshly prepared, filtered, degassed, stored at 4–8°C and used within one week. Buffers were placed on ice when connected to the ÄKTA and fractions obtained by chromatography were stored on ice.

Table 21: List of buffers used during protein purification.

Name	Content and pH	Usage
Buffer A	20 mM Tris, pH = 8.0	dialysis, IEX
Buffer B	20 mM Tris, 500 mM NaCl, pH = 8.0	IEX
Regeneration Buffer	20 nM Tris, 2 M NaCl, pH = 8.0	IEX
Buffer D1	100 mM NaOAc, 5 mM EDTA, pH = 3.8	dialysis, cofactor exchange
Buffer D2	100 mM NaOAc, 150 mM NaCl, pH = 3.8	dialysis, cofactor exchange
Buffer M	100 mM HEPES, 150 mM NaCl, pH = 7.4	dialysis, SEC, desalting and buffer exchange

Cell Disruption: For the protein purification of hSOD1 and A4V a modified procedure from Mrđen Debono was used.[159] For one batch of purification one cell pellet (about 6–8 g cells) obtained from the expression was used. Cells were thawed on ice and suspended in Buffer A (about 4 ml buffer per 1 g cells). PMSF (0.5 mM final conc.), lysozyme (spatula tip), DNase1 (10 u/ml final conc.) and $MgCl_2$ (5 mM final conc.) was added to the cells and stirred at 4–8°C for 45 min. Cell disruption was carried out on a high-pressure homogenizer and PMSF (another 0.5 mM final conc.) was again added to the disrupted cells. The suspension was centrifuged (47810 × g, 10°C, 45 min) and the supernatant dialyzed against Buffer A (2 l) at 4–8°C over night.

Ion Exchange Chromatography (IEX): The protein solution was taken out of the dialysis bag and centrifuged (47810 × g, 4°C, 30 min), then filtered through a H-PTFE filter (0.45 µm). A TMAE column (CV = 50 ml) pre-equilibrated with Buffer A was used on an ÄKTA had been equilibrated the previous night. The protein sample was loaded onto the loop of the ÄKTA, then injected onto the column. Unbound proteins were washed off in about 4 CV Buffer A (flow = 3.35 ml/min = 100 cm/h), then SOD1 was eluted over a gradient of 0–20% Buffer B in Buffer A over 10 CV. Remaining bound proteins were washed off with 5 CV Regeneration Buffer. The obtained fractions were analyzed by SDS-PAGE and fractions containing SOD1 were combined, then dialyzed against Buffer M (2 l) at 4–8°C over night.

Size-Exclusion Chromatography (SEC): The protein solution was taken out of the dialysis bag and concentrated by centrifugation (4000 × g, 4°C, 20 min) using Amicon centrifugal filter units (10 kDa cut-off) from Merck Millipore, to a volume of 2–3 ml, then filtered through a H-PTFE filter (0.2 µm). A HiLoad 16/600 Superdex 75 pg (CV = 120 ml, V_0 = 40 ml) on an ÄKTA had been equilibrated with Buffer M the previous night. The protein sample was loaded onto the loop of the ÄKTA, then injected onto the column. SOD1 was eluted with Buffer M (flow = 0.8 ml/min = 24 cm/h) over 1 CV. The obtained fractions were analyzed by SDS-PAGE and fractions containing SOD1 were combined, then dialyzed against Buffer D1 (2 l) at 4–8°C over night.

Cofactor Exchange: The protein solution was dialyzed against Buffer D2 (2 l) at 4–8°C over 4 h, then taken out of the dialysis bag. At this point, the apo (E|E) hSOD1 state was obtained and could be desalted as described below. If instead the holo (Cu|Zn) hSOD1 state was desired, Cu^{2+} and Zn^{2+} cofactors were subsequently introduced. $CuSO_4$ (10 mM final conc.) was added and the protein solution stirred at rt for 15 min, then $ZnSO_4$ (10 mM final conc.) was added and the protein solution stirred at rt for 15 min. The resulting holo hSOD1 could then be desalted as described below.

Desalting and buffer exchange: The protein solution was concentrated by centrifugation (4000 × g, 4°C, 20 min) using Amicon centrifugal filter units (10 kDa cut-off) from Merck Millipore, to a volume of 1–2 ml, then filtered through a H-PTFE filter (0.2 µm). A HiPrep 26/10 Desalting (CV = 53 ml, V_0 = 15 ml) on an ÄKTA had been equilibrated with Buffer M. The protein sample was loaded into the loop of the ÄKTA, then injected onto the column. SOD1 was eluted with Buffer M (flow = 2.5 ml/min = 28 cm/h) over 1 CV. The obtained fractions were analyzed by SDS-PAGE and fractions containing SOD1 were combined. The protein concentration was determined with a NanoDrop spectrophotometer at 280 nm (ε = 11250 $M^{-1}cm^{-1}$ for dimeric SOD1), then divided into 1 ml aliquots, flash frozen in liquid N_2 and stored at -80°C.

9.10 Biophysical Assays

9.10.1 Devices and Materials

Table 22: Devices and materials used in biophysical assays.

Item	Supplier
Arium Mini Ultrapure Water System	Satorius
NanoDrop & UV Spectrometer NanoPhotometer NP80	Implen
DLS Instrument Zetasizer Advance Ultra Red ZS Xplorer Software	Malvern
Superoxide Dismutase (SOD) Activity Assay Kit CS0009	Sigma Aldrich
PROTEOSTAT Protein aggregation standards ENZ-51039	Enzo
CLARIOstar plate reader	BMG Labtech
UV-Cuvette micro center height 15 mm filling volume 70–550 µl	Brand
96-well plates with transparent bottom MICROPLATE, 96 WELL, PS, F-BOTTOM (CHIMNEY WELL), µCLEAR, BLACK, NON-BINDING	Greiner
96-well plates with opaque bottom MICROPLATE, 96 WELL, PS, F-BOTTOM (CHIMNEY WELL), BLACK, NON-BINDING	Greiner
protein low binding pipet tips	VWR
protein low binding Eppendorf tubes	Eppendorf
MST device, Monolith NT.115 with MO.Affinity Analysis v2.3 software	NanoTemper Technologies
Monolith NT.115 Premium Capillaries	NanoTemper Technologies
2^{nd} generation RED NHS dye MO-L011	NanoTemper Technologies
timsTOFfleX mass spectrometer	Bruker
Ultra 55 field-emission scanning electron microscope	Zeiss
FCF300-CU-UA Formvar/Carbon Hexagonal Mesh, Cu 300 Mesh, UA sample holder grids	Science Services
Uranyl Acetate Solution (aq., 1% w/v)	Science Services

9.10.2 Pyrimethamine and Trehalose

Pyrimethamine was purchased from Sigma Aldrich (VETRANAL, analytical standard) and used without further purification. Trehalose was purchased from Sigma Aldrich (≥99% purity by HPLC) and used without further purification.

9.10.3 Handling of Protein and Ligand Stocks

Purified hSOD1 protein stocks were stored as aliquots in aqueous buffer (100 mM HEPES, 150 mM NaCl, pH = 7.4) flash frozen in liquid N_2, then placed at -80°C unless otherwise stated. When used in experiments, one or more aliquots were thawed on ice, then carefully inverted to ensure a homogeneous solution. Protein stocks were never vortexed or shaken to limit precipitation or aggregation by agitation. Stocks were centrifuged (15000 × g, 15 min, 4°C) to separate any precipitates or aggregates that may have formed during storage, before concentration of the individual aliquot was determined with an Implen NanoDrop. A molar extinction coefficient of 11250 $M^{-1}cm^{-1}$ at 280 nm was used for the hSOD1 dimer as detailed in Section 9.9.3.

Thawed protein stock, when not actively used, was placed on ice. Once no longer needed, remaining protein stock was again flash frozen in liquid N_2, then placed at -80°C. Whenever possible, experiments used proteins stocks that had not been thawed before. Preparations of apo hSOD1 A4V protein however were limited in this study, which necessitated to conserve remaining protein stocks, subjecting it to freeze-thaw cycles. For each individual experiment it was documented if and how often a protein stock had been through freeze-thaw cycles to closely monitor any adverse effects on the data quality of individual experiments. Generally, no noticeable adverse effect on the data quality of individual experiments was observed. When an influence on the result of a specific assay could not be exuded with certainty, this is detailed in the corresponding discussion. The number of freeze-thaw cycles apo hSOD1 A4V stocks had been subjected to was: 0–2 for the aggregation assay Section 5.7.2 and 3–5 in case of the DLS assay Section 5.7.3.

Ligands were stored as stocks in DMSO prior to use in biophysical experiments. Ligand stocks were stored in glass vials with a solid lid with a PTFE septum insert to ensure air tight closing. Closed vials were stored at rt in the dark and only opened shortly, when used, to limit deterioration as well as ingress of water from the surrounding air into the hygroscopic DMSO.

9.10.4 Ligand Solubility Measurements

DMSO stocks of the ligands were used to prepare 50 µl solutions at incremental ligand concentrations, typically ranging from 0.1 mM up to 20.0 mM in the assay buffer system, consisting of 80% aqueous buffer (100 mM HEPES, 150 mM NaCl, pH = 7.4) and 20% DMSO cosolvent at rt. Solutions were manually examined for precipitation or crystal formation immediately following their preparation and after 24 h at rt. Hardly visible floating particles were spun down using a benchtop centrifuge and pellet formation was examined.

9.10.5 MicroScale Thermophoresis

Samples of labeled hSOD1 had been prepared and were provided by Mrđen Debono. A 2nd generation RED NHS dye (MO-L011) from NanoTemper Technologies had been used to prepare fluorescently labeled hSOD1 samples with a degree of labeling of 1.18, 2.56 or 3.24.[159] Labeled hSOD1 was stored in phosphate buffer (50 mM Na_2HPO_4, pH = 7.4) at -80°C. Ligands stocks solutions were prepared in DMSO. Before use, labeled hSOD1 was thawed on ice, then centrifuged (14100 × g, 15 min, rt). Phosphate buffer (50 mM Na_2HPO_4, pH = 7.4) was prepared, filtered and degassed. A solution of labeled hSOD1 (50 nM, 25 nM, 12.5 nM or 10 nM) in phosphate buffer and DMSO (80:20) was prepared. A solution of ligand (14.5 mM, 6.0 mM or 2.0 mM) in phosphate buffer and DMSO (80:20) was prepared and a 1:1 dilution series of the ligand in phosphate buffer and DMSO (80:20) was prepared with 16 different concentrations in total. The labeled hSOD1 solution was added to the 16 samples of the ligand dilution series, providing MST samples with a constant final concentrations of labeled hSOD1 (25 nM, 12.5 nM, 7.25 nM or 5 nM) and varying final concentration of ligand (highest final concentration of the dilution series of 7.25 mM, 3.0 mM or 1.0 mM). Using a benchtop centrifuge samples were spun down for 2 min at rt, then incubated at 0°C for 2 h. Following incubation, the samples were loaded into Monolith NT.115 Premium Capillaries from NanoTemper Technologies. Measurements were performed on a Monolith NT.115 from NanoTemper Technologies, access to which was generously provided by Prof. Sinning at the Heidelberg University Biochemistry Center (BZH). MO.Affinity Analysis v2.3 software from NanoTemper Technologies was used for analysis of MST data. The dissociation constant K_d was obtained by fitting in the MO.Affinity Analysis software.

9.10.6 Activity Assay

Activity of expressed holo hSOD1 and holo hSOD1 A4V were determined with the commercially available Superoxide Dismutase (SOD) Activity Assay Kit (CS0009) from Sigma Aldrich. The assay includes bovine SOD at a given concentration in units/ml, which was used as a relative comparison for the determined activities of the expressed SOD1 preparations. The assay was performed as an endpoint measurement on 96-well plates with absorbance values determined on a CLARIOstar plate reader.

The assays included instructions were followed with modifications, as described below. The concentration of bovine SOD standard included in the kit was determined with the Implen NanoDrop at 258 nm each time the assay was performed, using $\varepsilon = 10300\ M^{-1}cm^{-1}$ as described in Section 9.9.3. Holo hSOD1 or holo hSOD1 A4V was thawed on ice and its concentration determined with an Implen NanoDrop at 280 nm using $\varepsilon = 11250\ M^{-1}cm^{-1}$ as described in Section 9.9.3.

Bovine SOD standard was prepared as incremental concentrations from 0.03–0.60 units/ml. Holo hSOD1 was prepared as incremental concentrations from 0.1–10 nM. Because about half the activity of hSOD1 was expected for the A4V variant,[59,232–234] holo hSOD1 A4V was prepared as concentration from 1–20 nM. WST and xanthine oxidase (XO) working solutions were prepared and added as per the assays instructions. Wells that contained buffer, substrate and dye, but no protein (Blank) and wells that contained buffer, substrate, dye, and xanthine oxidase but no SOD1 (No SOD) were included as controls. At least 3 replicates were prepared for each sample, control and blank. Following the addition of xanthine oxidase, plates were incubated at 25°C for 30 min on an orbital shaker. Absorption was measured at 450 nm on a CLARIOstar plate reader.

Starting with the measured absorbance values at 450 nm for each well the following analysis was carried out. Absorbance values of No SOD control wells were averaged across all replicates. Absorbance values of Blank wells were averaged across all replicates. The linearized SOD rate (LSR) of individual standard and sample concentration wells were calculated as follows:

$$\mathrm{LSR} = \frac{\mathrm{A} - \mathrm{B}}{\mathrm{C} - \mathrm{B}} \tag{13}$$

A: Average absorbance value of No SOD control

B: Average absorbance value of Blank

C: Absorbance value of Standard or Sample

The linearized SOD rate (LSR) of the standard was plotted against the standard concentration in units/ml and fitted with a linear regression model. Standard concentrations of 0.06 units/ml and below were excluded, as it was observed that they deviated from the observed linear behavior of the other control concentrations and their inclusion resulted in a skewed fit. It can be assumed that for these concentrations the lower detection limit of the kit was exceeded. The obtained slope and intercept of the linear regression were used to calculate the activity in units/ml of the individual standard and sample concentrations as:

$$\text{activity [units/ml]} = \frac{\text{LSR} - \text{intercept}}{\text{slope}} \tag{14}$$

The micromolar activity of individual standard and sample concentrations was calculated as follows:

$$\text{micromolar activity [units/}\mu\text{mol]} = \frac{\text{activity [units/ml]}}{\text{c [nM]}} \cdot 1000 \tag{15}$$

Sample concentrations of 1 mM and below were excluded, as their micromolar activity was strongly overestimated in comparison to the other concentrations. Again, it can be assumed that the lower detection limit of the kit was exceeded. The obtained micromolar activity values for standard and sample wells were averaged across all remaining concentrations and replicates and the standard deviation determined. Defining the average micromolar activity of the bovine SOD standard of the individual experiment as 100%, relative activities and the corresponding standard deviation were calculated for holo hSOD1 and holo hSOD1 A4V. Relative activities for holo hSOD1, holo hSOD1 A4V and their respective bovine SOD standards were plotted as columns with the standard deviation represented as error bars.

9.10.7 MS Metalation Study

A sample of holo hSOD1 in H_2O (6.31 µM) was prepared as follows: An aliquot of holo hSOD1 in aqueous buffer (100 mM HEPES, 150 mM NaCl, pH = 7.4) was thawed on ice, then filtered through a H-PTFE filter (0.45 µm). A HiPrep 26/10 Desalting column (CV = 53 ml, V_0 = 15 ml) connected to an Äkta had been equilibrated with H_2O. The protein sample was loaded onto the loop of the ÄKTA, then injected onto the column. SOD1 was eluted with H_2O (flow = 2.5 ml/min = 28 cm/h) over 1 CV. The obtained fractions were analyzed by SDS-PAGE and fractions containing SOD1 were combined. The protein concentration was determined with a NanoDrop spectrophotometer at 280 nm (ε = 11250 $M^{-1}cm^{-1}$ for dimeric SOD1).

The Bruker timsTOFfleX mass spectrometer had been calibrated for an m/z range of 600–6000. The SOD1 samples was acidified by addition of acetic acid (0.5% final conc.), then injected into the mass spectrometer. Electrospray ionization (ESI) was used as ionization method and a spectrum with positive ion polarity was recorded. The instrument was operated by Dr. Jürgen H. Gross Head of the Mass Spectrometry Laboratory at the Organic Chemistry Institute of the University of Heidelberg.

Data was analyzed and visualized with mMass.[272] Isotope patterns and m/z values for various SOD1 species were simulated and overlayed with the experimental data to assign MS signals.

9.10.8 Thioflavin T Based Aggregation Assay

Protein stocks of holo hSOD1 and apo hSOD1 A4V were thawed, centrifuged and their concentration determined with an Implen NanoDrop as described in Section 9.10.3. From these protein stocks, protein working solutions (40 µM) were prepared in buffer (100 mM HEPES, 150 mM NaCl, pH = 7.4). Ligand stocks in DMSO were used to prepare ligand working solutions (5.0 mM) in DMSO, with the exception of the following ligands, which had ligand working solutions of a different concentration prepared: ABE (2.5 mM), AOE (1.0 mM), pyrimethamine (2.5 mM), trehalose (both 5.0 mM and 100 mM).

Master mixes were prepared containing apo hSOD1 A4V (20 µM) and each ligand (1 mM) in assay buffer comprised of 80% aqueous buffer (100 mM HEPES, 150 mM NaCl, pH = 7.4) and 20% DMSO, with the exception of the following ligands, which had master mixes of a different concentration prepared: ABE (0.5 mM), AOE (0.2 mM), pyrimethamine (0.5 mM), trehalose (both 1 mM and 20 mM). For each ligand a corresponding blank control master mix was prepared that had the same concentration of ligand but did not contain any apo hSOD1 A4V. Protein control master mixes were prepared that contained holo hSOD1 (20 µM) or apo hSOD1 A4V (20 µM) but did not contain any ligand. For the two protein samples a corresponding blank control master mix was prepared that did not contain any protein or ligand. The master mixes were mixed, then incubated at 50°C for 24 h, while lightly shaking at 150 rpm.

From an aqueous ThT stock a ThT working solution (750 µM) in water was prepared. The incubated master mixes were allowed to cool to rt, ThT working solution was added to each of them (15 µM final conc.) and mixed. From each master mix 3 wells of a well plate (black, with opaque bottom) were filled with 100 µl master mix each. Any unused wells of the plate were filled with 100 µl water to limit evaporation. Well plates were incubated at rt for 15 min in the dark while lightly shaking at 150 rpm.

Fluorescence was measured at a plate reader with the following settings: excitation 445–455 nm, emission 477-487 nm, gain 2200, focal height 5.2 mm, 25°C.

Intensity values of the blank wells were averaged across the 3 replicates. Absolute intensity values for all ligands + protein and protein sample wells had the averaged intensity of their corresponding blanks subtracted. Defining the average intensity of the apo hSOD A4V sample of the individual experiment as 100%, relative intensities and the corresponding standard deviation were calculated for holo hSOD1 and holo hSOD1 A4V. Corrected intensity values for the holo hSOD1 samples were observed to be slightly below 0, therefore an intensity value of 0 instead of the averaged corrected intensity values for the holo hSOD1 samples was chosen as the defined 0% for this relativization. Relative intensities values for all ligand samples were plotted as columns to compare their effectiveness in preventing SOD1 aggregation.

9.10.9 Electron Microscopy

A protein stocks of apo hSOD1 A4V was thawed, centrifuged and its concentration determined with an Implen NanoDrop as described in Section 9.10.3. From this protein stocks, a protein working solutions (40 µM) was prepared in buffer (100 mM HEPES, 150 mM NaCl, pH = 7.4). Ligand stocks in PEG-550 were used to prepare ligand working solutions (5.0 mM ABE or 50 mM APE) in PEG-550.

Master mixes were prepared containing apo hSOD1 A4V (20 µM) and each ligand (1 mM ABE or 10 mM APE) in assay buffer comprised of 80% aqueous buffer (100 mM HEPES, 150 mM NaCl, pH = 7.4) and 20% PEG-550. A protein control master mix was prepared, which contained apo hSOD1 A4V (20 µM) but did not contain any ligand. The master mixes were mixed, then incubated at 50°C for 24 h, while lightly shaking at 150 rpm.

From an aqueous ThT stock a ThT working solution (750 µM) in water was prepared. The incubated master mixes were allowed to cool to rt, ThT working solution was added to each of them (15 µM final conc.) and mixed. From each master mix microscopy samples on copper grids were prepared. Hexagonal copper grids with 300 mesh and a layer of 5-6 nm formvar and 1 nm carbon from Science Services were plasma cleaned for 30 s. Samples were mixed, then 3 µl sample were drop casted on the grid and left to settle for 2 min 30 s under ambient atmosphere. Excess buffer was carefully removed using a filter paper. Samples were washed by drop casting 3 µl ultra purified water onto the grid, then immediately removing it using a filter paper. Samples were stained by drop casting 3 µl uranyl acetate solution (aq., 1% w/v) onto the grid. After 45 s, excess liquid was removed it using a filter paper. The uranyl acetate staining was performed a total of 2 times. Prepared sample grids were stored under ambient atmosphere at rt.

Electron Microscopy was performed a Zeiss Ultra 55 field-emission scanning electron microscope. A STEM module at a primary electron energy of 20 keV and the following segment configurations were used: S1 off, S2 inverted and S3 on.

Obtained microscopy images had their contrast and brightness manually adjusted with ImageJ (Version 1.54).[278,279]

9.10.10 DLS Assay

Protein stocks of holo hSOD1 and apo hSOD1 A4V were thawed, centrifuged and their concentration determined with an Implen NanoDrop as described in Section 9.10.3. From these protein stocks, protein working solutions (40 µM) were prepared in buffer (100 mM HEPES, 150 mM NaCl, pH = 7.4). Ligand stocks in DMSO were used to prepare ligand working solutions (5.0 mM) in DMSO.

Master mixes were prepared containing apo hSOD1 A4V (20 µM) and each ligand (1 mM) in assay buffer comprised of 80% aqueous buffer (100 mM HEPES, 150 mM NaCl, pH = 7.4) and 20% DMSO. For each ligand a corresponding blank control master mix was prepared that had the same concentration of ligand but did not contain any apo hSOD1 A4V. Protein control master mixes were prepared that contained holo hSOD1 (20 µM) or apo hSOD1 A4V (20 µM) in assay buffer comprised of 80% aqueous buffer (100 mM HEPES, 150 mM NaCl, pH = 7.4) and 20% DMSO), without any ligand. For the two protein samples a corresponding blank control master mix was prepared that did not contain any protein or ligand. The master mixes were mixed and 10 µl were used for DLS prior to incubation. Master mixes were then incubated at 50°C for 24 h, while lightly shaking at 150 rpm. Incubated master mixes were allowed to cool to rt, then mixed and 10 µl were used for DLS.

DLS measurements were performed as follows: A cuvette was charged with 90 µl assay buffer comprised of 80% aqueous buffer (100 mM HEPES, 150 mM NaCl, pH = 7.4) and 20% DMSO, then 10 µl master mix were added and carefully mixed. During mixing care was taken to avoid the introduction any air bubbles. Samples were measured at a final concentration of 2 µM (≈ 0.06 mg/ml) protein and 0.1 mM ligand, on a Zetasizer Advance Ultra Red from Malvern, with a 10 mW He-Ne laser (632.8 mm). ZS Xplorer software was used for operation and data analysis. The following settings were used: cell: ZEN0040 (low volume disposable cuvette), material: protein, dispersant: 20% DMSO in H_2O, temperature: 25°C, equalibration time: 60 s, analysis model: general purpose, size display limit mode: automatic, size threshold mode: automatic, auto size average: no, reflective index: 1.33, viscosity: 1.3704 mPa·s, angle of detection: back scatter (173°), positioning method: measure at a fixed position, cell position: 3.00, attenuation: automatic, measurement process: automatic, use pause after sub-runs: no, optical filter: no filter, pause between repeats: 0 s.

The viscosity of 20% DMSO in aqueous buffer at 25°C was assumed as 1.3704 mPa·s based on the model for DMSO:H_2O binary mixtures reported by del Carmen Grande *et al.*.[280] 3–5 replicates were measured per sample.

Correlation coefficient in dependence of time and size distribution of the hydrodynamic diameter d_H of detected particle species were determined by the ZS Xplorer software. The correlation coefficient was plotted against time and intensity was plotted against hydrodynamic diameter d_H. From the size distribution plot, the start and end of individual peaks were manually determined for each replicate. Peaks that extended past the detection range of ~5500 nm were excluded from analysis, as their d_H could not be determined. In cases where peaks partially overlapped or displayed a notable shoulder, it was decided on a case by case basis if they were treated as one single or two separate peaks, based on comparison with the other replicates of the sample. Individual replicated were excluded from analysis, if they substantially deviated from the other replicates of the sample. The d_H of each peak was calculated as the average d_H weighted by intensity across all data points of the peak. The mean and standard deviation of d_H were determined for similarly sized peaks across all replicates. Peaks that appeared only in a single replicate of a sample were disregarded. Detected species were numbered from smallest to largest by d_H. For comparison between samples mean d_H of detected species were plotted as columns with their standard deviation shown as error bars.

10 Appendix

10.1 Fragments Used in the Construction of Ligands for Molecular Docking

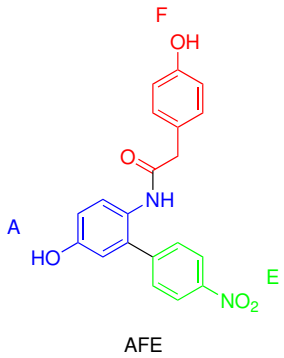

AFE

Figure 69: Illustration of the code used to refer to the ligands generated for molecular docking, on the example of ligand AFE. The first letter corresponds to the core fragment, the second letter corresponds to the carboxylic acid (ca) fragment and the third letter corresponds to the boronic acid (ba) fragment.

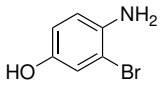

A

Figure 70: Formal structure of the core fragment used in the construction of the virtual ligand library used for molecular docking.

Table 23: Formal structures of all carboxylic acid (ca) fragments used in the construction of the virtual ligand library used for molecular docking. Fragments utilized in previous work by the author[48] but excluded in this study, as explained in Section 5.2 are included in this listing for consistency.

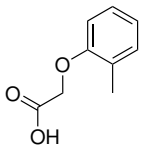	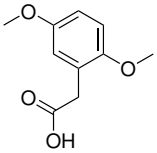	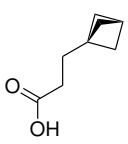	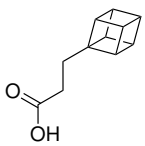	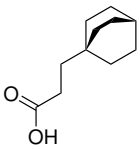	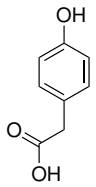
ca-A	ca-B	ca-C	ca-D	ca-E	ca-F
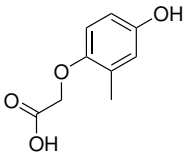	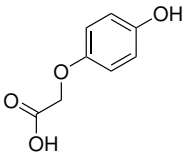	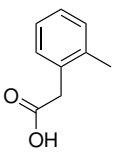	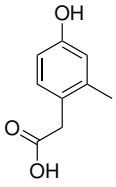	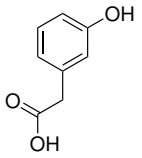	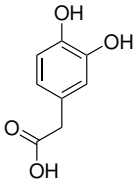
ca-G	ca-H	ca-I	ca-J	ca-K	ca-L
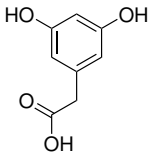	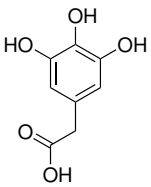	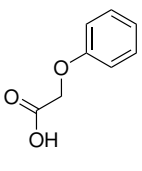	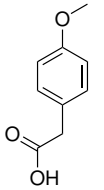	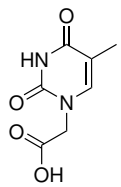	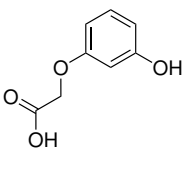
ca-M	ca-N	ca-O	ca-P	ca-Q	ca-R
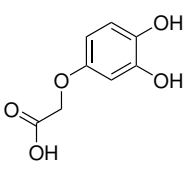	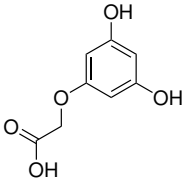	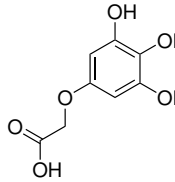	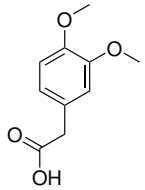	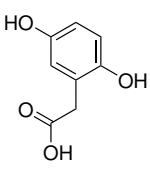	
ca-S	ca-T	ca-U	ca-V	ca-W	

Table 24: Formal structures of all boronic acid (ba) fragments used in the construction of the virtual ligand library used for molecular docking. Fragments utilized in previous work by the author[48] but excluded in this study, as explained in Section 5.2 are included in this listing for consistency.

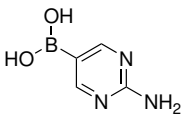	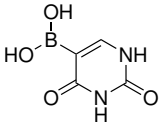	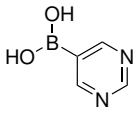	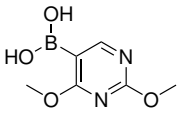	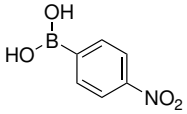
ba-A	ba-B	ba-C	ba-D	ba-E
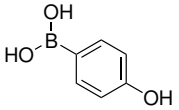	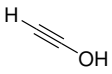	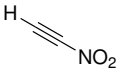	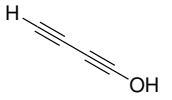	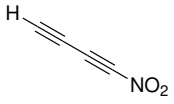
ba-F	ba-G	ba-H	ba-I	ba-J
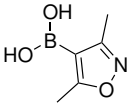	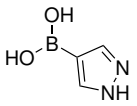	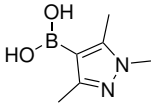	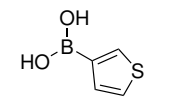	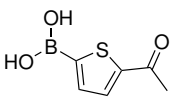
ba-K	ba-L	ba-M	ba-N	ba-O
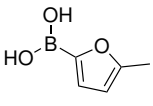	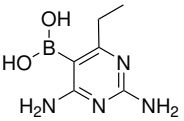	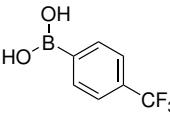	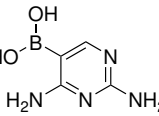	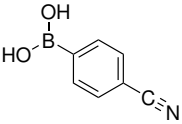
ba-P	ba-Q	ba-R	ba-S	ba-T

10.2 Docking Affinities of Ligands used in Molecular Docking

Table 25: List of every virtual ligand generated and docked, sorted by ligand code. The ligand code and affinity are shown below its chemical structure.

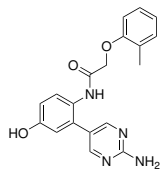	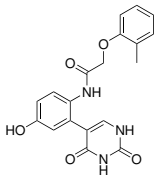	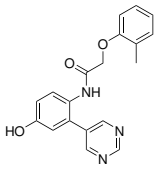	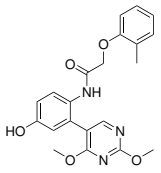	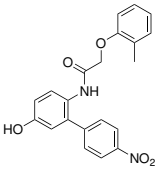
AAA	AAB	AAC	AAD	AAE
-8.6 kcal/mol	-9.6 kcal/mol	-8.9 kcal/mol	-9.1 kcal/mol	-9.4 kcal/mol
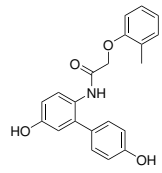	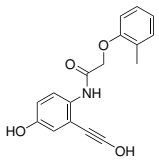	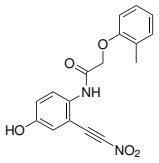	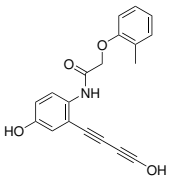	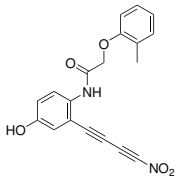
AAF	AAG	AAH	AAI	AAJ
-8.8 kcal/mol	-8.3 kcal/mol	-8.3 kcal/mol	-8.4 kcal/mol	-8.2 kcal/mol
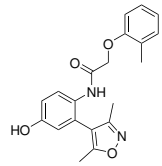	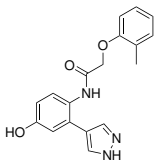	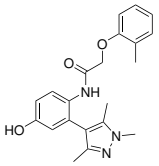	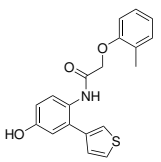	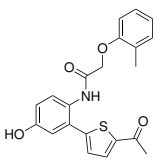
AAK	AAL	AAM	AAN	AAO
-8.6 kcal/mol	-8.7 kcal/mol	-8.1 kcal/mol	-8.8 kcal/mol	-8.4 kcal/mol
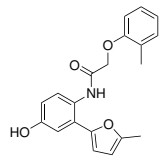	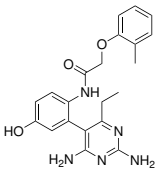	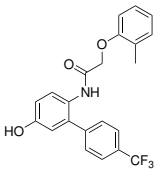	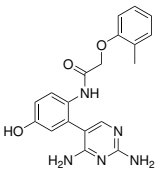	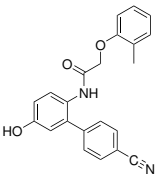
AAP	AAQ	AAR	AAS	AAT
-8.3 kcal/mol	-8.1 kcal/mol	-9.5 kcal/mol	-8.3 kcal/mol	-9.4 kcal/mol
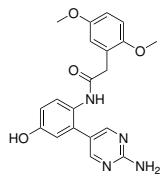	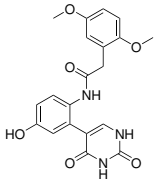	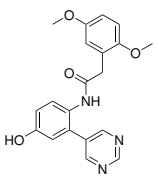	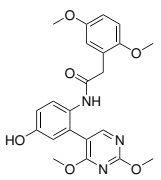	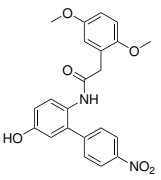
ABA	ABB	ABC	ABD	ABE
-8.6 kcal/mol	-9.7 kcal/mol	-8.7 kcal/mol	-9.2 kcal/mol	-8.5 kcal/mol

Table 25: *(continued)* List of every virtual ligand generated and docked, sorted by ligand code. The ligand code and affinity are shown below its chemical structure.

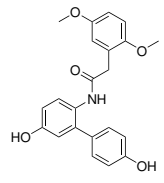	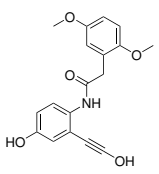	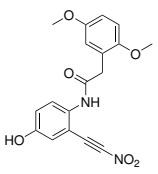	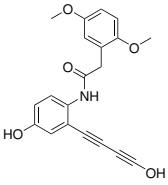	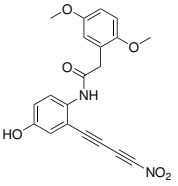
ABF	ABG	ABH	ABI	ABJ
-8.6 kcal/mol	-8.2 kcal/mol	-8.5 kcal/mol	-8.3 kcal/mol	-8.2 kcal/mol
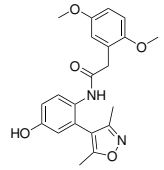	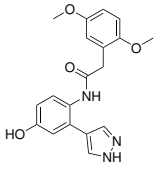	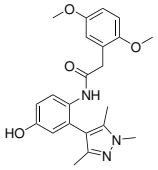	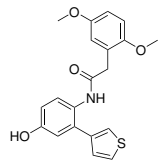	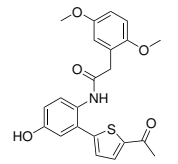
ABK	ABL	ABM	ABN	ABO
-8.5 kcal/mol	-8.6 kcal/mol	-8.1 kcal/mol	-8.7 kcal/mol	-8.2 kcal/mol
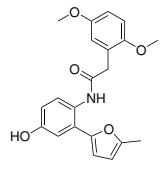	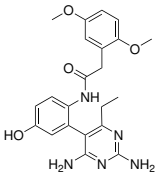	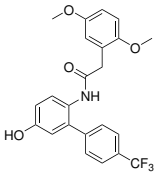	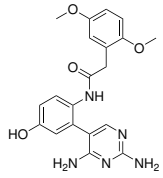	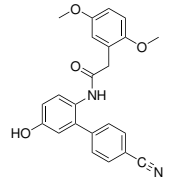
ABP	ABQ	ABR	ABS	ABT
-8.7 kcal/mol	-8.2 kcal/mol	-8.9 kcal/mol	-8.7 kcal/mol	-9.2 kcal/mol
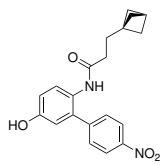	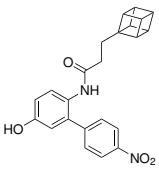	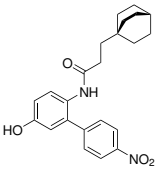	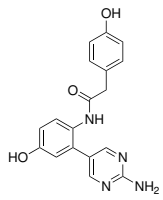	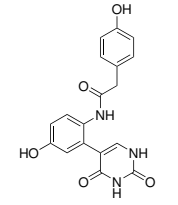
ACE	ADE	AEE	AFA	AFB
-9.1 kcal/mol	-9.1 kcal/mol	-8.6 kcal/mol	-8.8 kcal/mol	-10.2 kcal/mol
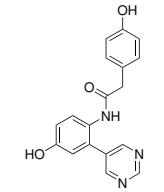	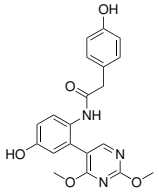	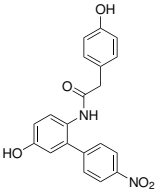	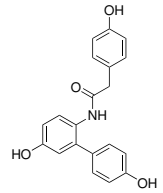	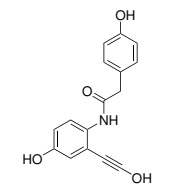
AFC	AFD	AFE	AFF	AFG
-9.2 kcal/mol	-9.1 kcal/mol	-9.5 kcal/mol	-9.1 kcal/mol	-8.7 kcal/mol
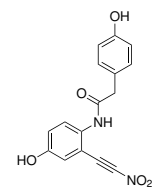	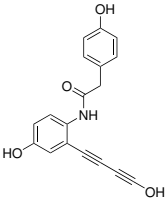	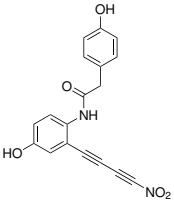	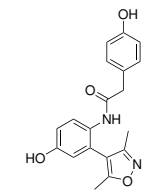	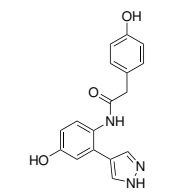
AFH	AFI	AFJ	AFK	AFL
-9.0 kcal/mol	-8.8 kcal/mol	-8.7 kcal/mol	-8.4 kcal/mol	-9.1 kcal/mol

Table 25: *(continued)* List of every virtual ligand generated and docked, sorted by ligand code. The ligand code and affinity are shown below its chemical structure.

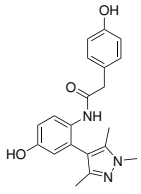	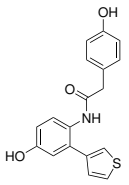	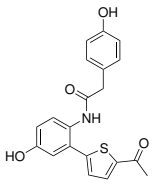	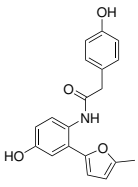	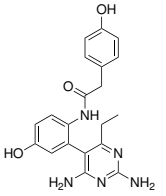
AFM	AFN	AFO	AFP	AFQ
-8.0 kcal/mol	-9.2 kcal/mol	-8.8 kcal/mol	-9.2 kcal/mol	-8.1 kcal/mol
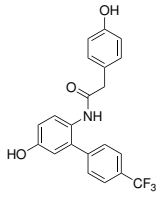	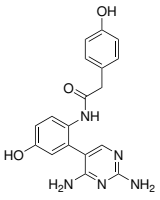	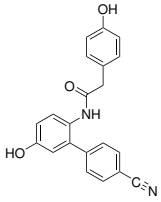	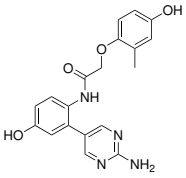	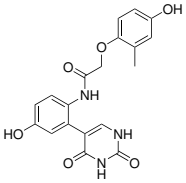
AFR	AFS	AFT	AGA	AGB
-9.7 kcal/mol	-8.9 kcal/mol	-9.6 kcal/mol	-8.7 kcal/mol	-9.9 kcal/mol
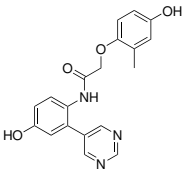	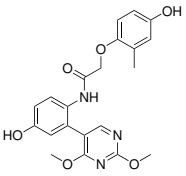	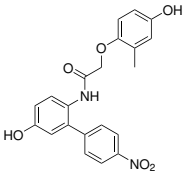	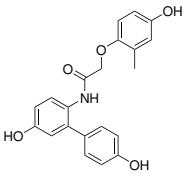	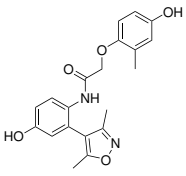
AGC	AGD	AGE	AGF	AGK
-9.1 kcal/mol	-9.1 kcal/mol	-8.5 kcal/mol	-8.9 kcal/mol	-8.5 kcal/mol
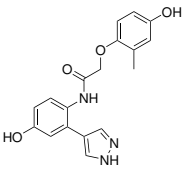	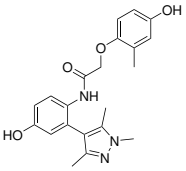	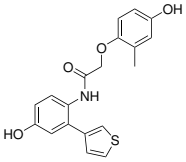	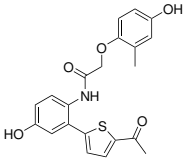	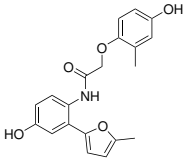
AGL	AGM	AGN	AGO	AGP
-9.0 kcal/mol	-8.2 kcal/mol	-9.0 kcal/mol	-8.5 kcal/mol	-9.0 kcal/mol
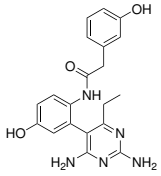	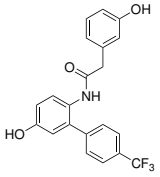	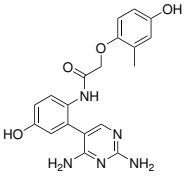	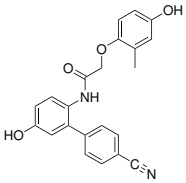	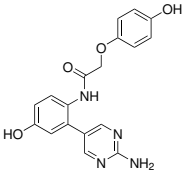
AGQ	AGR	AGS	AGT	AHA
-8.2 kcal/mol	-9.8 kcal/mol	-8.4 kcal/mol	-9.1 kcal/mol	-8.8 kcal/mol
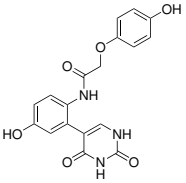	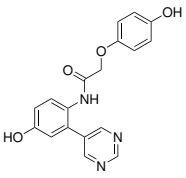	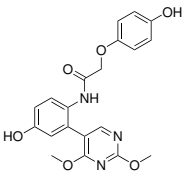	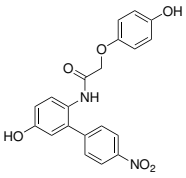	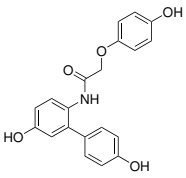
AHB	AHC	AHD	AHE	AHF
-10.0 kcal/mol	-9.1 kcal/mol	-9.0 kcal/mol	-9.0 kcal/mol	-9.0 kcal/mol

Table 25: *(continued)* List of every virtual ligand generated and docked, sorted by ligand code. The ligand code and affinity are shown below its chemical structure.

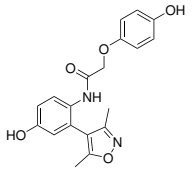	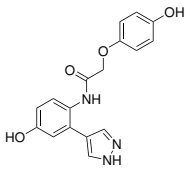	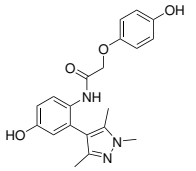	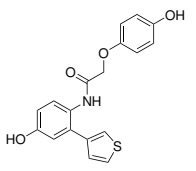	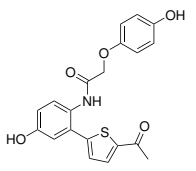
AHK	AHL	AHM	AHN	AHO
-8.1 kcal/mol	-9.2 kcal/mol	-8.0 kcal/mol	-9.1 kcal/mol	-8.5 kcal/mol
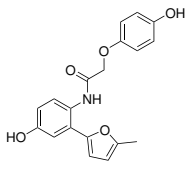	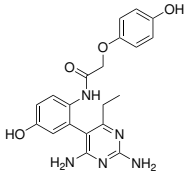	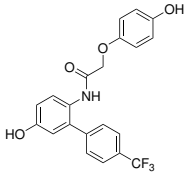	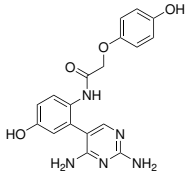	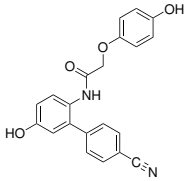
AHP	AHQ	AHR	AHS	AHT
-9.2 kcal/mol	-8.0 kcal/mol	-9.2 kcal/mol	-8.8 kcal/mol	-9.2 kcal/mol
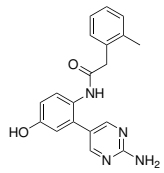	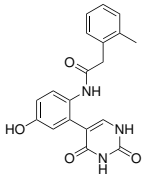	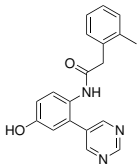	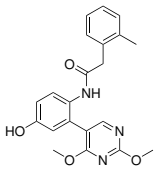	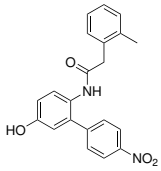
AIA	AIB	AIC	AID	AIE
-9.0 kcal/mol	-9.7 kcal/mol	-8.9 kcal/mol	-9.2 kcal/mol	-9.5 kcal/mol
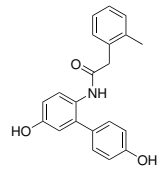	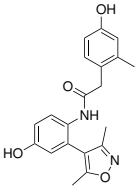	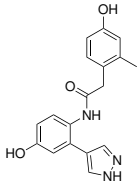	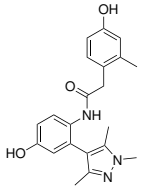	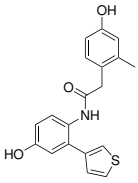
AIF	AIK	AIL	AIM	AIN
-9.1 kcal/mol	-8.7 kcal/mol	-8.8 kcal/mol	-8.1 kcal/mol	-8.8 kcal/mol
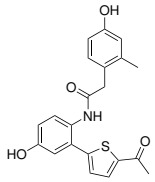	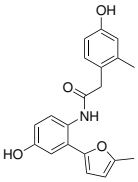	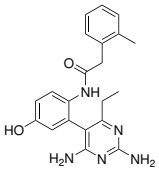	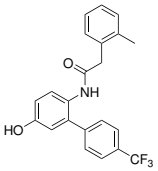	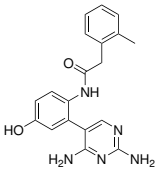
AIO	AIP	AIQ	AIR	AIS
-9.0 kcal/mol	-8.7 kcal/mol	-7.8 kcal/mol	-9.7 kcal/mol	-8.8 kcal/mol
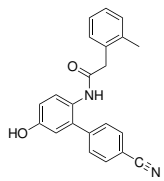	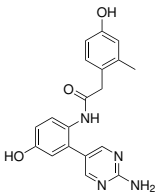	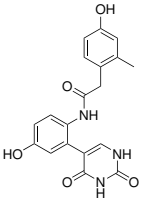	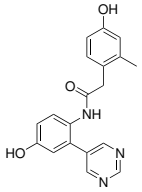	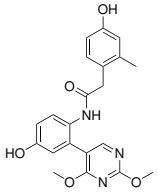
AIT	AJA	AJB	AJC	AJD
-9.6 kcal/mol	-8.6 kcal/mol	-9.8 kcal/mol	-9.1 kcal/mol	-9.1 kcal/mol

Table 25: *(continued)* List of every virtual ligand generated and docked, sorted by ligand code. The ligand code and affinity are shown below its chemical structure.

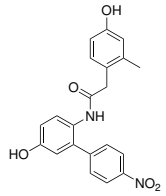	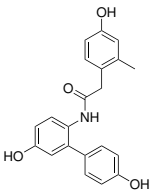	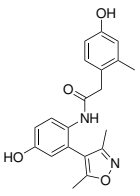	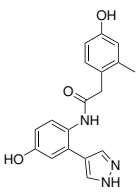	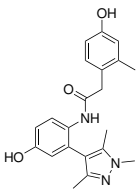
AJE	AJF	AJK	AJL	AJM
-9.0 kcal/mol	-8.7 kcal/mol	-8.7 kcal/mol	-8.8 kcal/mol	-8.1 kcal/mol
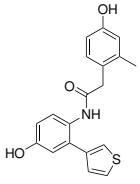	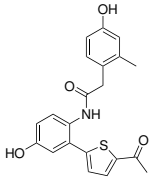	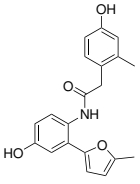	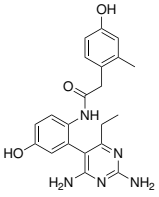	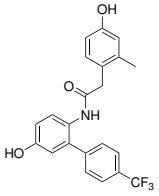
AJN	AJO	AJP	AJQ	AJR
-8.8 kcal/mol	-9.0 kcal/mol	-8.7 kcal/mol	-8.0 kcal/mol	-9.3 kcal/mol
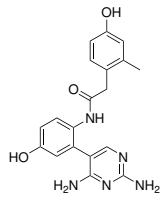	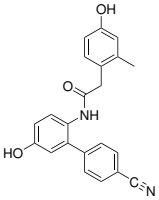	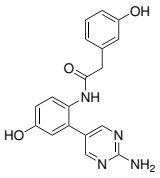	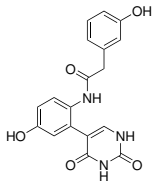	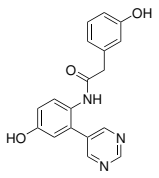
AJS	AJT	AKA	AKB	AKC
-8.5 kcal/mol	-9.3 kcal/mol	-9.3 kcal/mol	-9.7 kcal/mol	-9.2 kcal/mol
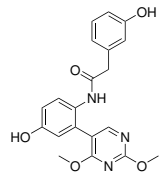	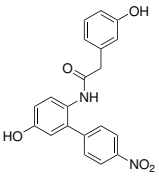	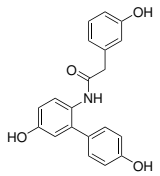	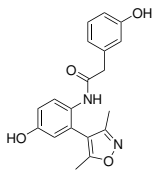	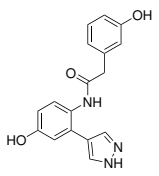
AKD	AKE	AKF	AKK	AKL
-9.3 kcal/mol	-9.7 kcal/mol	-9.4 kcal/mol	-8.6 kcal/mol	-9.2 kcal/mol
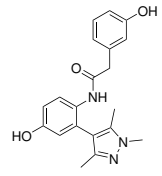	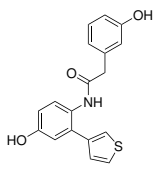	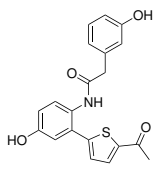	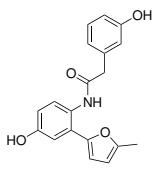	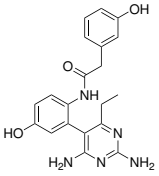
AKM	AKN	AKO	AKP	AKQ
-8.8 kcal/mol	-9.2 kcal/mol	-9.5 kcal/mol	-9.2 kcal/mol	-8.2 kcal/mol
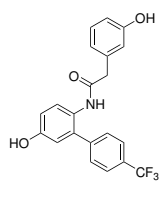	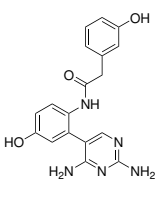	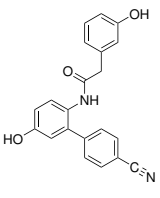	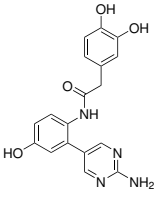	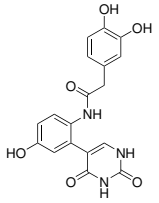
AKR	AKS	AKT	ALA	ALB
-9.8 kcal/mol	-9.1 kcal/mol	-9.8 kcal/mol	-9.2 kcal/mol	-10.3 kcal/mol

Table 25: *(continued)* List of every virtual ligand generated and docked, sorted by ligand code. The ligand code and affinity are shown below its chemical structure.

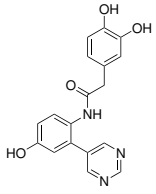	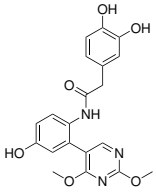	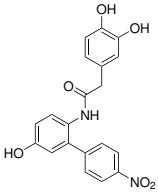	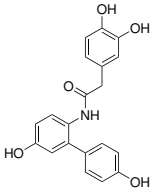	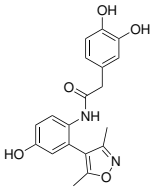
ALC	ALD	ALE	ALF	ALK
-9.6 kcal/mol	-9.3 kcal/mol	-9.8 kcal/mol	-9.4 kcal/mol	-8.2 kcal/mol
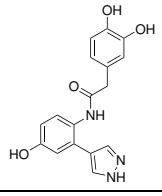	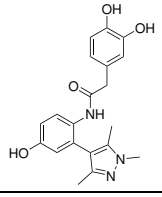	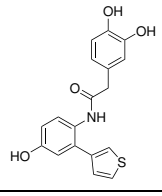	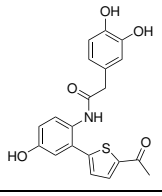	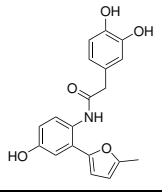
ALL	ALM	ALN	ALO	ALP
-9.5 kcal/mol	-8.4 kcal/mol	-9.5 kcal/mol	-9.1 kcal/mol	-9.5 kcal/mol
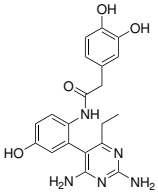	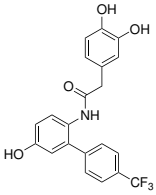	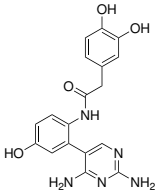	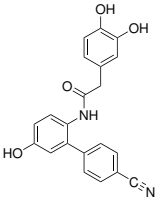	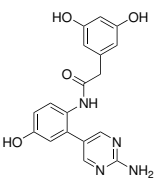
ALQ	ALR	ALS	ALT	AMA
-8.4 kcal/mol	-10.0 kcal/mol	-9.4 kcal/mol	-9.9 kcal/mol	-8.7 kcal/mol
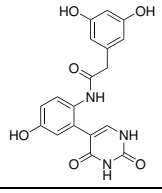	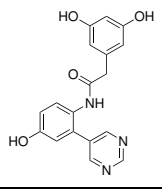	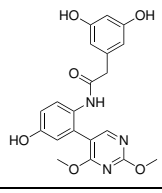	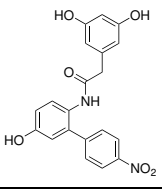	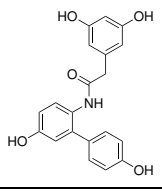
AMB	AMC	AMD	AME	AMF
-10.3 kcal/mol	-9.3 kcal/mol	-9.1 kcal/mol	-9.5 kcal/mol	-9.2 kcal/mol
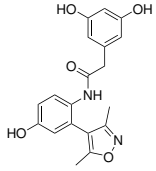	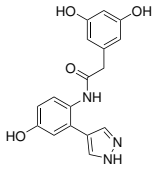	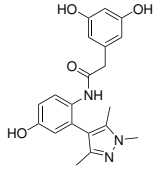	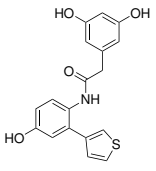	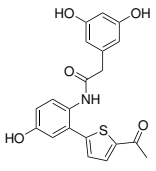
AMK	AML	AMM	AMN	AMO
-8.6 kcal/mol	-9.1 kcal/mol	-8.1 kcal/mol	-9.3 kcal/mol	-8.7 kcal/mol
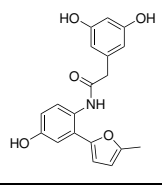	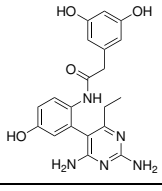	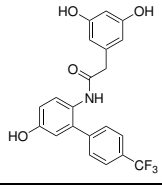	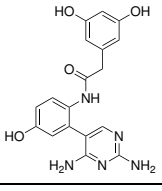	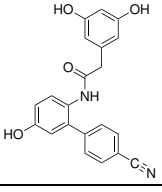
AMP	AMQ	AMR	AMS	AMT
-9.4 kcal/mol	-8.3 kcal/mol	-9.7 kcal/mol	-8.7 kcal/mol	-9.7 kcal/mol

Table 25: *(continued)* List of every virtual ligand generated and docked, sorted by ligand code. The ligand code and affinity are shown below its chemical structure.

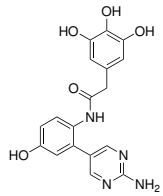	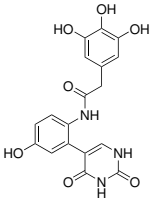	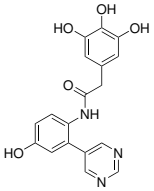	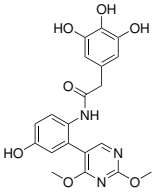	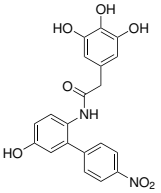
ANA	ANB	ANC	AND	ANE
-9.2 kcal/mol	-10.4 kcal/mol	-9.7 kcal/mol	-9.1 kcal/mol	-9.5 kcal/mol
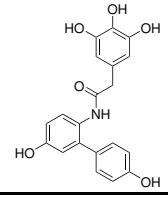	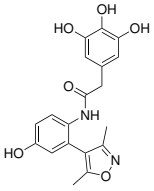	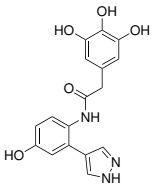	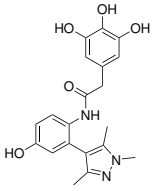	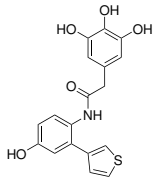
ANF	ANK	ANL	ANM	ANN
-9.5 kcal/mol	-8.5 kcal/mol	-9.6 kcal/mol	-8.1 kcal/mol	-9.6 kcal/mol
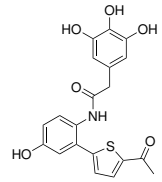	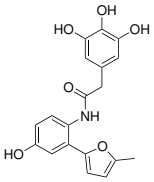	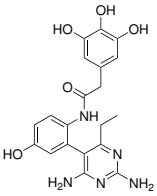	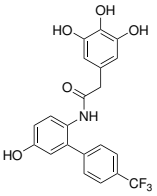	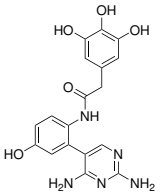
ANO	ANP	ANQ	ANR	ANS
-9.2 kcal/mol	-9.7 kcal/mol	-8.4 kcal/mol	-9.7 kcal/mol	-9.1 kcal/mol
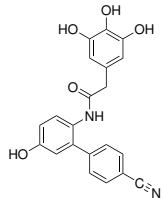	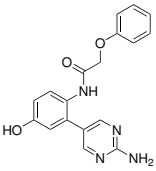	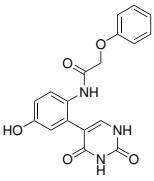	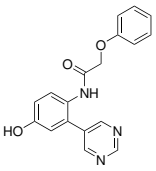	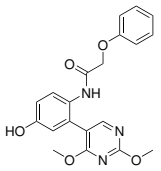
ANT	AOA	AOB	AOC	AOD
-9.7 kcal/mol	-8.5 kcal/mol	-9.6 kcal/mol	-8.8 kcal/mol	-9.0 kcal/mol
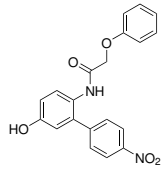	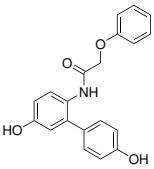	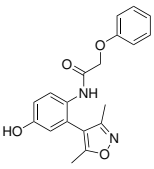	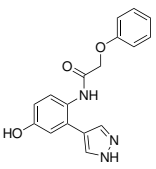	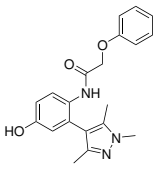
AOE	AOF	AOK	AOL	AOM
-9.3 kcal/mol	-8.4 kcal/mol	-7.8 kcal/mol	-8.7 kcal/mol	-7.9 kcal/mol
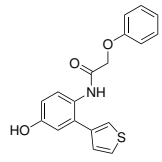	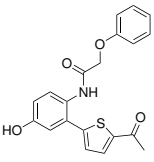	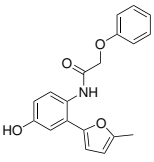	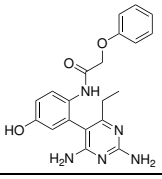	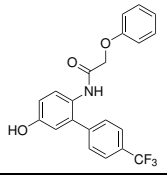
AON	AOO	AOP	AOQ	AOR
-8.7 kcal/mol	-8.5 kcal/mol	-8.9 kcal/mol	-8.0 kcal/mol	-9.6 kcal/mol

Table 25: *(continued)* List of every virtual ligand generated and docked, sorted by ligand code. The ligand code and affinity are shown below its chemical structure.

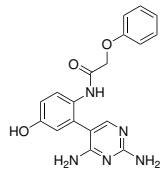	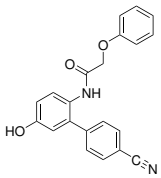	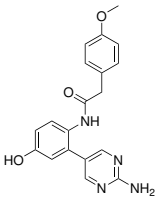	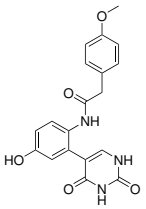	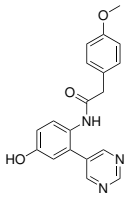
AOS	AOT	APA	APB	APC
-8.6 kcal/mol	-9.5 kcal/mol	-9.2 kcal/mol	-9.9 kcal/mol	-9.0 kcal/mol
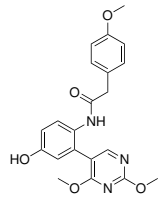	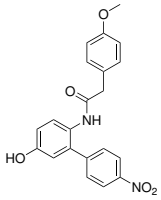	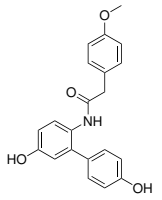	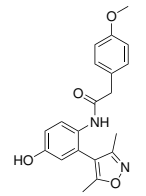	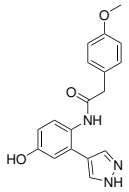
APD	APE	APF	APK	APL
-9.2 kcal/mol	-9.8 kcal/mol	-9.3 kcal/mol	-8.4 kcal/mol	-8.9 kcal/mol
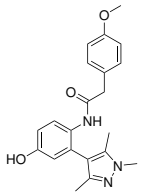	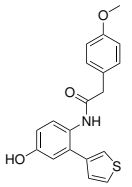	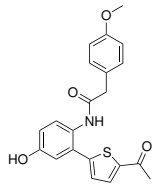	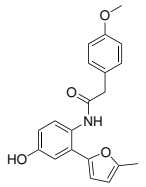	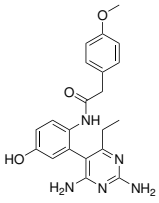
APM	APN	APO	APP	APQ
-7.8 kcal/mol	-9.0 kcal/mol	-8.9 kcal/mol	-9.1 kcal/mol	-8.1 kcal/mol
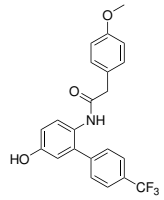	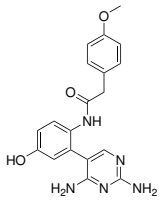	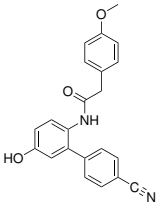	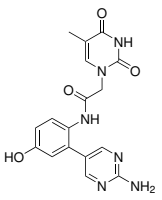	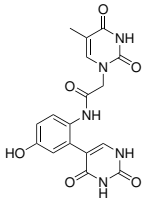
APR	APS	APT	AQA	AQB
-9.9 kcal/mol	-9.0 kcal/mol	-9.8 kcal/mol	-8.7 kcal/mol	-9.9 kcal/mol
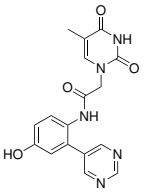	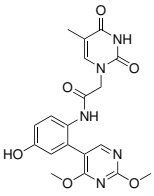	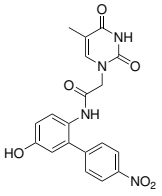	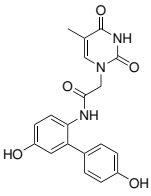	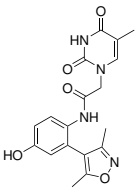
AQC	AQD	AQE	AQF	AQK
-9.0 kcal/mol	-9.4 kcal/mol	-9.4 kcal/mol	-8.6 kcal/mol	-8.8 kcal/mol

Table 25: *(continued)* List of every virtual ligand generated and docked, sorted by ligand code. The ligand code and affinity are shown below its chemical structure.

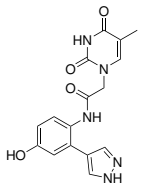	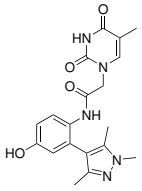	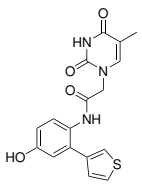	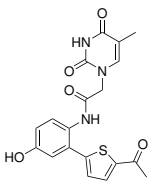	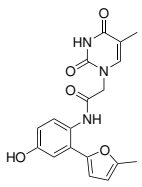
AQL	AQM	AQN	AQO	AQP
-9.0 kcal/mol	-8.1 kcal/mol	-9.5 kcal/mol	-8.8 kcal/mol	-9.0 kcal/mol
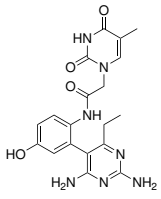	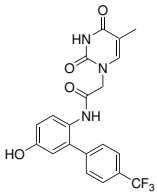	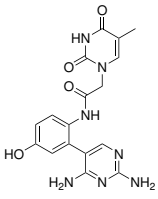	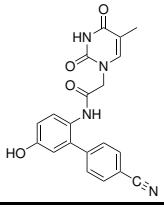	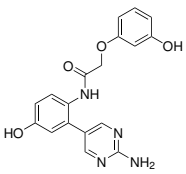
AQQ	AQR	AQS	AQT	ARA
-8.2 kcal/mol	-9.9 kcal/mol	-9.0 kcal/mol	-9.6 kcal/mol	-9.3 kcal/mol
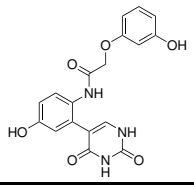	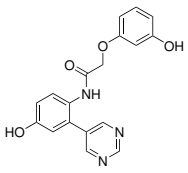	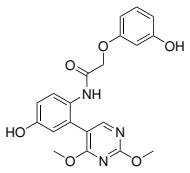	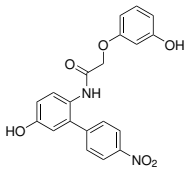	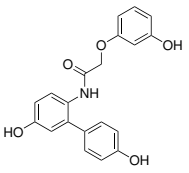
ARB	ARC	ARD	ARE	ARF
-9.7 kcal/mol	-9.1 kcal/mol	-9.1 kcal/mol	-9.5 kcal/mol	-9.6 kcal/mol
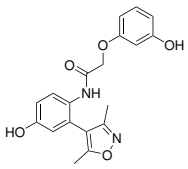	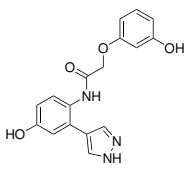	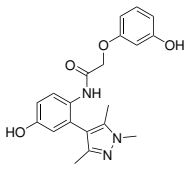	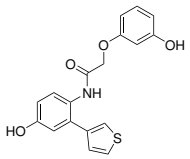	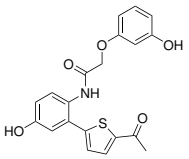
ARK	ARL	ARM	ARN	ARO
-8.6 kcal/mol	-9.2 kcal/mol	-8.6 kcal/mol	-8.8 kcal/mol	-9.2 kcal/mol
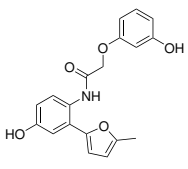	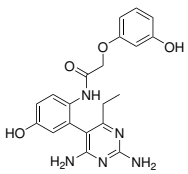	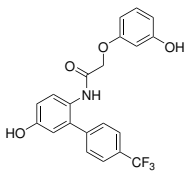	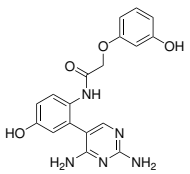	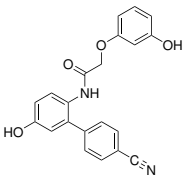
ARP	ARQ	ARR	ARS	ART
-9.5 kcal/mol	-8.2 kcal/mol	-9.7 kcal/mol	-9.1 kcal/mol	-9.5 kcal/mol
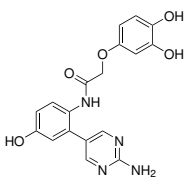	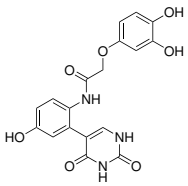	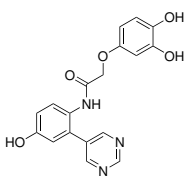	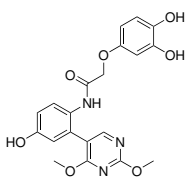	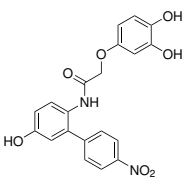
ASA	ASB	ASC	ASD	ASE
-8.8 kcal/mol	-10.0 kcal/mol	-9.2 kcal/mol	-9.0 kcal/mol	-9.3 kcal/mol

Table 25: *(continued)* List of every virtual ligand generated and docked, sorted by ligand code. The ligand code and affinity are shown below its chemical structure.

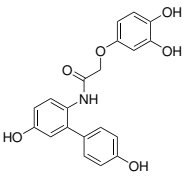	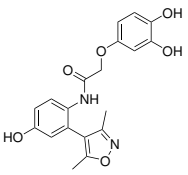	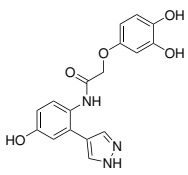	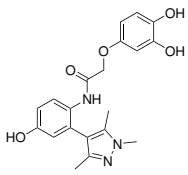	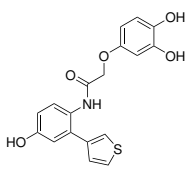
ASF	ASK	ASL	ASM	ASN
-9.1 kcal/mol	-8.4 kcal/mol	-9.2 kcal/mol	-8.4 kcal/mol	-9.1 kcal/mol
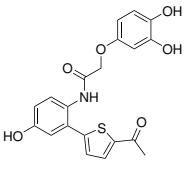	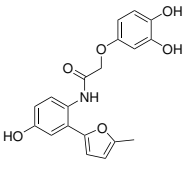	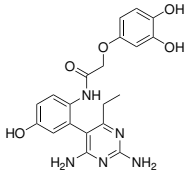	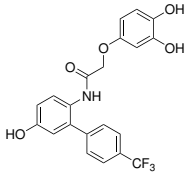	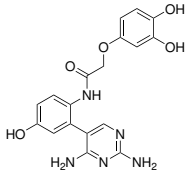
ASO	ASP	ASQ	ASR	ASS
-8.7 kcal/mol	-9.3 kcal/mol	-8.1 kcal/mol	-9.4 kcal/mol	-9.0 kcal/mol
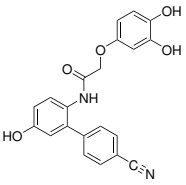	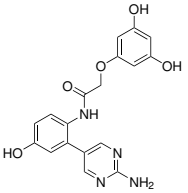	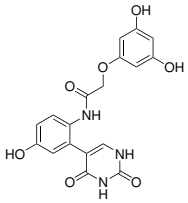	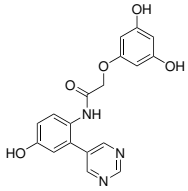	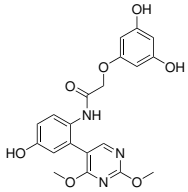
AST	ATA	ATB	ATC	ATD
-9.4 kcal/mol	-8.8 kcal/mol	-9.9 kcal/mol	-8.4 kcal/mol	-9.2 kcal/mol
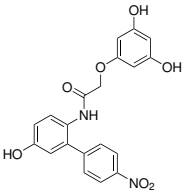	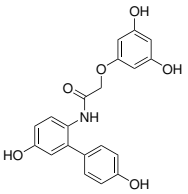	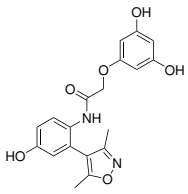	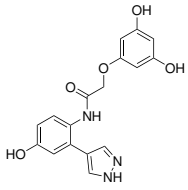	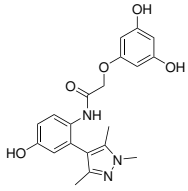
ATE	ATF	ATK	ATL	ATM
-9.2 kcal/mol	-8.9 kcal/mol	-8.4 kcal/mol	-9.0 kcal/mol	-8.2 kcal/mol
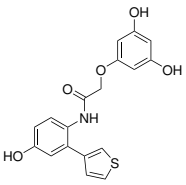	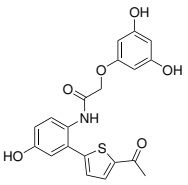	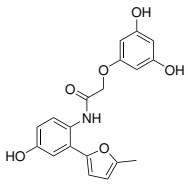	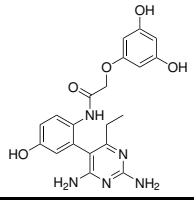	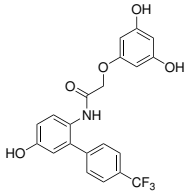
ATN	ATO	ATP	ATQ	ATR
-9.0 kcal/mol	-8.6 kcal/mol	-9.2 kcal/mol	-8.4 kcal/mol	-9.3 kcal/mol
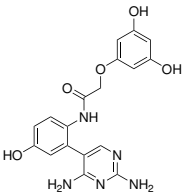	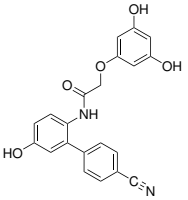	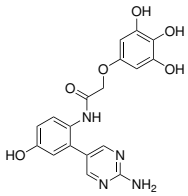	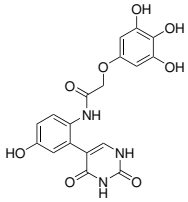	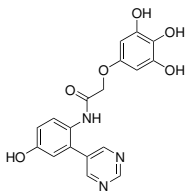
ATS	ATT	AUA	AUB	AUC
-8.8 kcal/mol	-9.2 kcal/mol	-8.9 kcal/mol	-10.0 kcal/mol	-9.3 kcal/mol

Table 25: *(continued)* List of every virtual ligand generated and docked, sorted by ligand code. The ligand code and affinity are shown below its chemical structure.

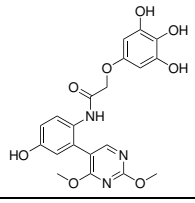	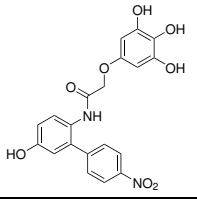	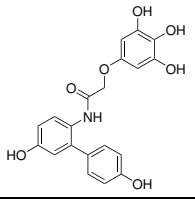	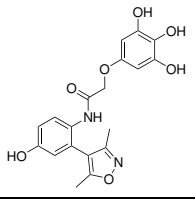	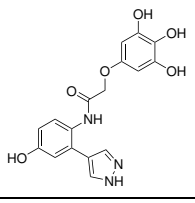
AUD	AUE	AUF	AUK	AUL
-9.1 kcal/mol	-9.2 kcal/mol	-9.2 kcal/mol	-8.4 kcal/mol	-9.2 kcal/mol
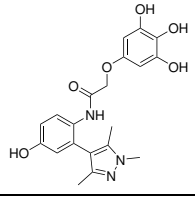	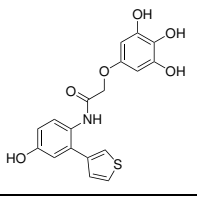	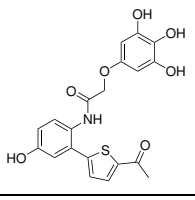	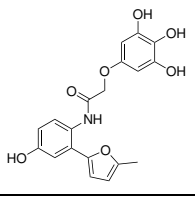	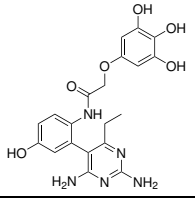
AUM	AUN	AUO	AUP	AUQ
-8.1 kcal/mol	-9.3 kcal/mol	-8.8 kcal/mol	-9.4 kcal/mol	-8.2 kcal/mol
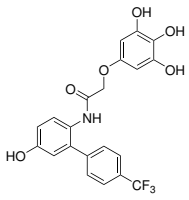	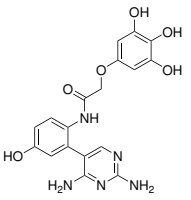	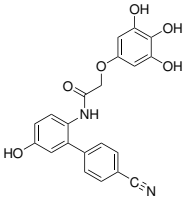	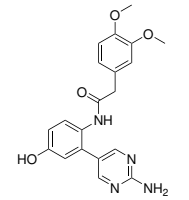	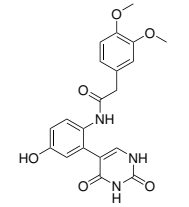
AUR	AUS	AUT	AVA	AVB
-9.4 kcal/mol	-9.1 kcal/mol	-9.4 kcal/mol	-8.4 kcal/mol	-9.1 kcal/mol
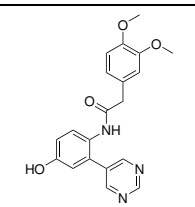	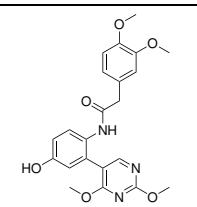	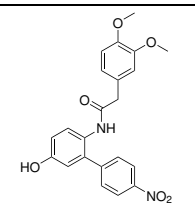	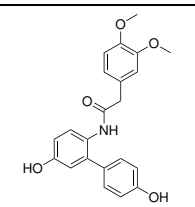	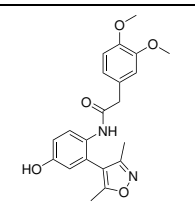
AVC	AVD	AVE	AVF	AVK
-8.8 kcal/mol	-9.1 kcal/mol	-8.4 kcal/mol	-8.7 kcal/mol	-8.5 kcal/mol
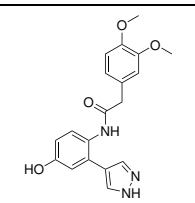	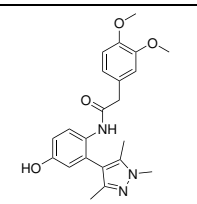	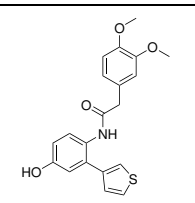	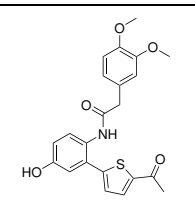	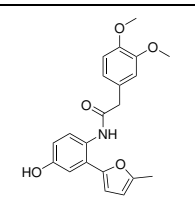
AVL	AVM	AVN	AVO	AVP
-8.6 kcal/mol	-7.9 kcal/mol	-8.8 kcal/mol	-8.3 kcal/mol	-8.8 kcal/mol

Table 25: *(continued)* List of every virtual ligand generated and docked, sorted by ligand code. The ligand code and affinity are shown below its chemical structure.

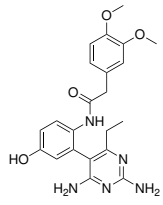	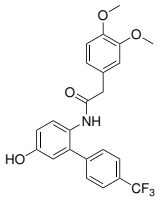	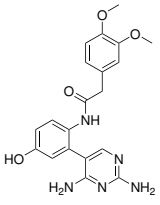	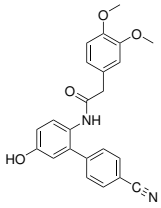	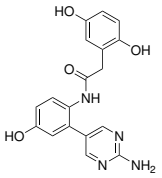
AVQ	AVR	AVS	AVT	AWA
-8.1 kcal/mol	-8.6 kcal/mol	-8.5 kcal/mol	-8.8 kcal/mol	-8.9 kcal/mol
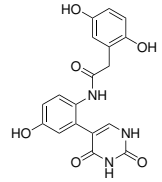	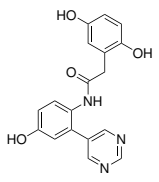	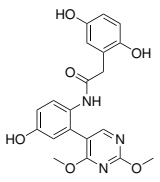	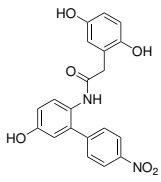	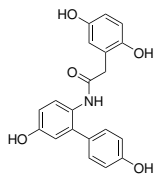
AWB	AWC	AWD	AWE	AWF
-10.3 kcal/mol	-8.9 kcal/mol	-9.3 kcal/mol	-9.7 kcal/mol	-9.1 kcal/mol
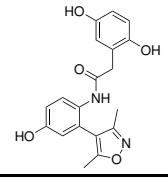	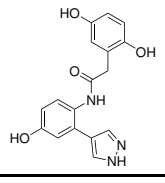	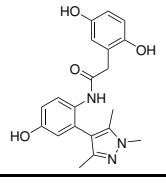	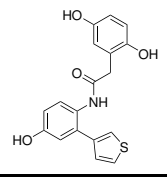	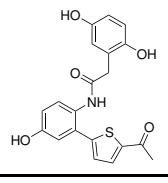
AWK	AWL	AWM	AWN	AWO
-8.5 kcal/mol	-8.7 kcal/mol	-8.7 kcal/mol	-9.0 kcal/mol	-9.2 kcal/mol
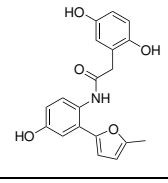	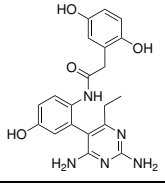	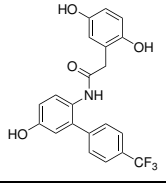	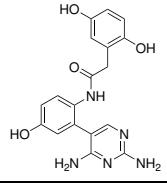	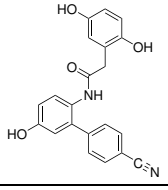
AWP	AWQ	AWR	AWS	AWT
-9.0 kcal/mol	-8.2 kcal/mol	-10.0 kcal/mol	-8.9 kcal/mol	-9.5 kcal/mol

10.3 Molecular Docking

Table 26: Distribution of docking affinities of the 320 generated ligands. N represents the number of ligands with that specific affinity.

Affinity	N	Cumulative Sum of N	Top Percentage
-10.4 kcal/mol	1	1	0.3%
-10.3 kcal/mol	3	4	1.3%
-10.2 kcal/mol	1	5	1.6%
-10.0 kcal/mol	5	10	3.1%
-9.9 kcal/mol	7	17	5.3%
-9.8 kcal/mol	7	24	7.5%
-9.7 kcal/mol	15	39	12.2%
-9.6 kcal/mol	10	49	15.3%
-9.5 kcal/mol	16	65	20.3%
-9.4 kcal/mol	13	78	24.4%
-9.3 kcal/mol	16	94	29.4%
-9.2 kcal/mol	32	126	39.4%
-9.1 kcal/mol	29	155	48.4%
-9.0 kcal/mol	24	179	55.9%
-8.9 kcal/mol	13	192	60.0%
-8.8 kcal/mol	24	216	67.5%
-8.7 kcal/mol	21	237	74.1%
-8.6 kcal/mol	15	252	78.8%
-8.5 kcal/mol	13	265	82.8%
-8.4 kcal/mol	16	281	87.8%
-8.3 kcal/mol	4	285	89.1%
-8.2 kcal/mol	11	296	92.5%
-8.1 kcal/mol	14	310	96.9%
-8.0 kcal/mol	5	315	98.4%
-7.9 kcal/mol	2	317	99.1%
-7.8 kcal/mol	3	320	100.0%

Table 27: Average docking affinities of all ligands containing a specific carboxylic acid fragment.

Carboxylic Acid Fragment	Mean Affinity [kcal/mol]	Standard Deviation [kcal/mol]
L	-9.34	0.59
N	-9.31	0.58
K	-9.25	0.44
R	-9.17	0.43
W	-9.12	0.54
M	-9.11	0.57
P	-9.08	0.61
U	-9.06	0.49
F	-9.06	0.57
Q	-9.06	0.53
S	-9.03	0.47
I	-8.96	0.53
T	-8.91	0.44
H	-8.89	0.52
G	-8.87	0.50
J	-8.84	0.45
A	-8.79	0.50
O	-8.74	0.57
B	-8.69	0.41
V	-8.59	0.33

Table 28: Average docking affinities of all ligands containing a specific boronic acid fragment.

Boronic Acid Fragment	Mean Affinity [kcal/mol]	Standard Deviation [kcal/mol]
B	-9.90	0.31
R	-9.56	0.36
T	-9.46	0.27
E	-9.29	0.42
D	-9.15	0.11
P	-9.09	0.34
C	-9.07	0.30
N	-9.06	0.28
F	-9.03	0.33
L	-9.01	0.28
A	-8.85	0.27
S	-8.84	0.28
O	-8.80	0.34
K	-8.46	0.23
M	-8.19	0.27
Q	-8.16	0.15

10.4 DLS Assay

Table 29: Correlation between the attenuator index and the nominal transmission of laser light that enters the sample cuvette.[195]

Attenuator Index	Transmission (% nominal)
11	100
10	30
9	10
8	3
7	1
6	0.3
5	0.1
4	0.03
3	0.01
2	0.003
1	0.0003

Table 30: Attenuator index and maximum correlation coefficient for DLS control measurements.

Exp	Protein	Ligand	0 Days Incubation		1 Day Incubation	
			Attenuator Index	Maximum Correlation Coefficient	Attenuator Index	Maximum Correlation Coefficient
1	none	none	10	0.785	10	0.696
1	holo hSOD1	none	10	0.778	10	0.700
1	none	ALD	9	0.886	10	0.594
1	none	ALE	10	0.768	9	0.811
1	none	APE	9	0.873	11	0.478
1	none	AWE	9	0.830	10	0.594
1	none	ca-L	9	0.804	11	0.462

Table 31: Attenuator index and maximum correlation coefficient for DLS measurements of Experiment 1.

Exp	Protein	Ligand	0 Days Incubation		1 Day Incubation	
			Attenuator Index	Maximum Correlation Coefficient	Attenuator Index	Maximum Correlation Coefficient
1	apo A4V	none	8	0.952	8	0.955
1	apo A4V	ALD	8	0.961	9	0.875
1	apo A4V	ALE	8	0.981	9	0.957
1	apo A4V	APE	8	0.958	8	0.949
1	apo A4V	AWE	8	0.970	7	0.998
1	apo A4V	ca-L	8	0.997	9	0.896

Table 32: Attenuator index and maximum correlation coefficient for DLS measurements of Experiment 2.

Exp	Protein	Ligand	0 Days Incubation		1 Day Incubation	
			Attenuator Index	Maximum Correlation Coefficient	Attenuator Index	Maximum Correlation Coefficient
2	apo A4V	none	9	0.913	8	0.971
2	apo A4V	ALD	8	0.970	9	0.963
2	apo A4V	ALE	8	0.962	8	0.957
2	apo A4V	APE	8	0.966	8	0.968
2	apo A4V	AWE	8	0.968	7	1.014
2	apo A4V	ca-L	8	0.961	9	0.885

Table 33: Attenuator index and maximum correlation coefficient for DLS measurements of Experiment 3.

Exp	Protein	Ligand	0 Days Incubation		1 Day Incubation	
			Attenuator Index	Maximum Correlation Coefficient	Attenuator Index	Maximum Correlation Coefficient
3	apo A4V	apo	8	0.978	8	0.923
3	apo A4V	ALD	8	0.971	8	0.891
3	apo A4V	ALE	8	0.958	8	0.960
3	apo A4V	APE	8	0.996	8	0.974
3	apo A4V	AWE	8	0.989	7	0.999
3	apo A4V	ca-L	8	0.970	9	0.915

Table 34: Mean hydrodynamic diameter d_H of detected species in DSL Experiments 1,2 and 3.

Exp	Protein	Ligand	0 Days Incubation			1 Day Incubation	
			1st Species mean d_H [nm]	2nd Species mean d_H [nm]	3rd Species mean d_H [nm]	1st Species mean d_H [nm]	2nd Species mean d_H [nm]
1	apo A4V	none	127 ± 47	526 ± 281	-	35 ± 12	215 ± 16
1	apo A4V	ALD	96 ± 19	673 ± 131	-	26 ± 4	154 ± 2
1	apo A4V	ALE	105 ± 20	1036 ± 562	-	144 ± 17	-
1	apo A4V	APE	105 ± 20	675 ± 194	-	34 ± 5	184 ± 13
1	apo A4V	AWE	82 ± 2	499 ± 3	-	27 ± 10	132 ± 15
1	apo A4V	ca-L	87 ± 6	586 ± 70	-	124 ± 4	-
2	apo A4V	none	23 ± 2	119 ± 8	-	76 ± 5	515 ± 174
2	apo A4V	ALD	83 ± 6	689 ± 82	-	84 ± 1	-
2	apo A4V	ALE	88 ± 9	729 ± 58	-	52 ± 15	133 ± 47
2	apo A4V	APE	31 ± 11	114 ± 34	789 ± 184	119 ± 4	-
2	apo A4V	AWE	92 ± 8	718 ± 71	-	28 ± 5	103 ± 3
2	apo A4V	ca-L	30 ± 6	101 ± 22	916 ± 170	39 ± 3	134 ± 29
3	apo A4V	none	89 ± 17	744 ± 516	-	84 ± 20	582 ± 156
3	apo A4V	ALD	60 ± 6	332 ± 48	-	146 ± 5	-
3	apo A4V	ALE	65 ± 4	325 ± 38	-	121 ± 15	-
3	apo A4V	APE	64 ± 5	326 ± 46	-	87 ± 14	534 ± 119
3	apo A4V	AWE	60 ± 9	280 ± 65	-	28 ± 5	125 ± 11
3	apo A4V	ca-L	86 ± 13	492 ± 128	-	109 ± 6	-

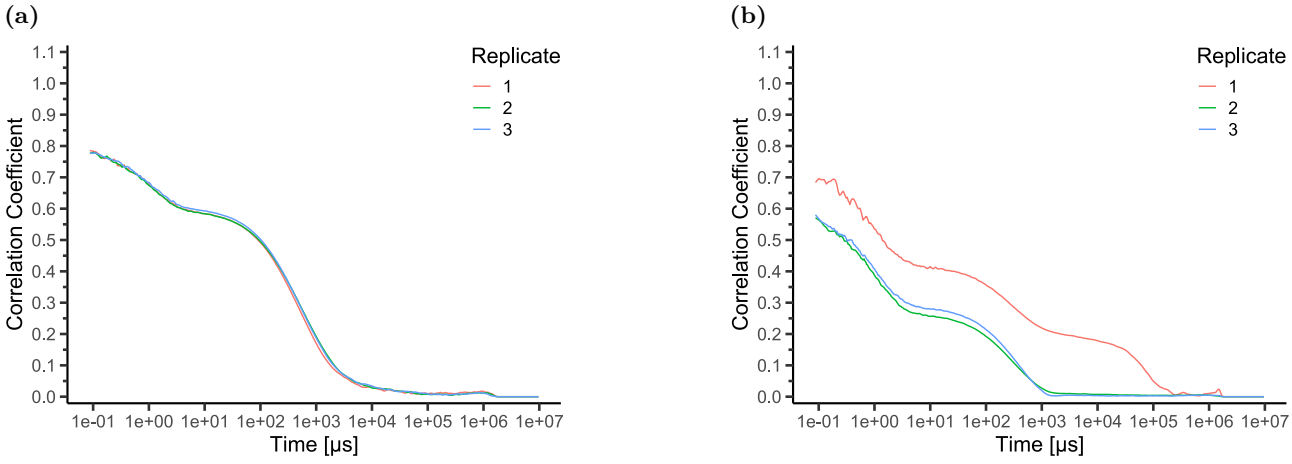

Figure 71: DLS Experiment 1: Correlogram of a sample containing no protein and no ligand.
(a): Without incubation. Attenuator Index = 10, Maximum Correlation Factor = 0.785.
(b): Incubated for 1 day. Attenuator Index = 10, Maximum Correlation Factor = 0.696.

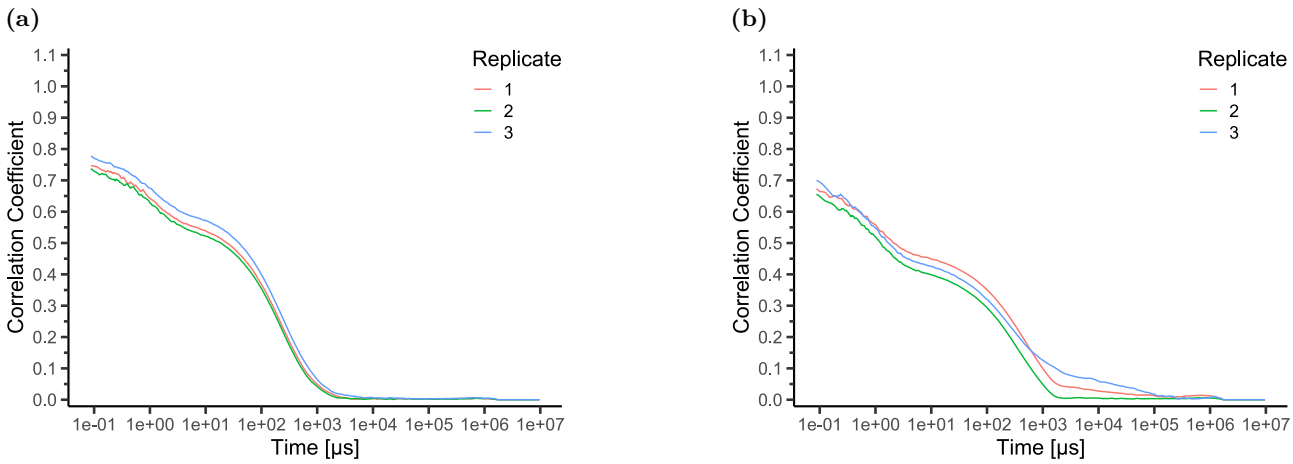

Figure 72: DLS Experiment 1: Correlogram of a sample containing holo hSOD1 and no ligand.
(a): Without incubation. Attenuator Index = 10, Maximum Correlation Factor = 0.778.
(b): Incubated for 1 day. Attenuator Index = 10, Maximum Correlation Factor = 0.700.

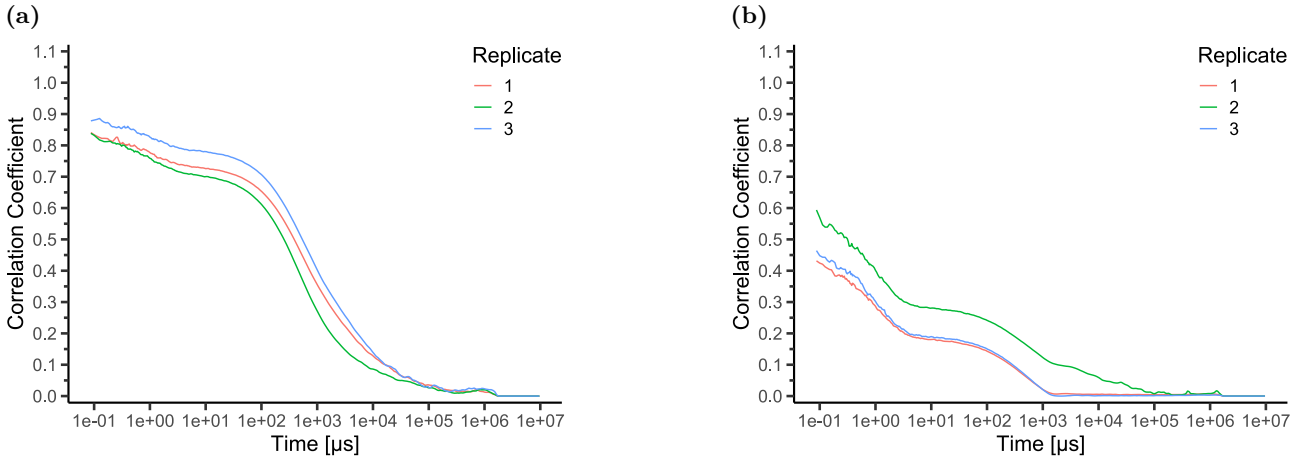

Figure 73: DLS Experiment 1: Correlogram of a sample containing ligand ALD **35** and no protein.
(a): Without incubation. Attenuator Index = 9, Maximum Correlation Factor = 0.886.
(b): Incubated for 1 day. Attenuator Index = 10, Maximum Correlation Factor = 0.594.

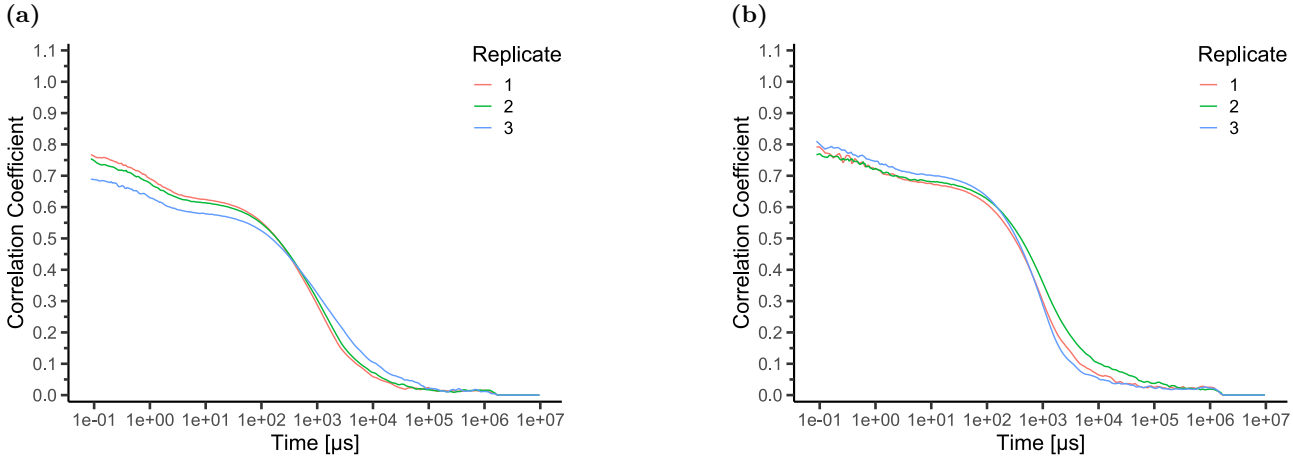

Figure 74: DLS Experiment 1: Correlogram of a sample containing ligand ALE **36** and no protein.
(a): Without incubation. Attenuator Index = 10, Maximum Correlation Factor = 0.768.
(b): Incubated for 1 day. Attenuator Index = 9, Maximum Correlation Factor = 0.811.

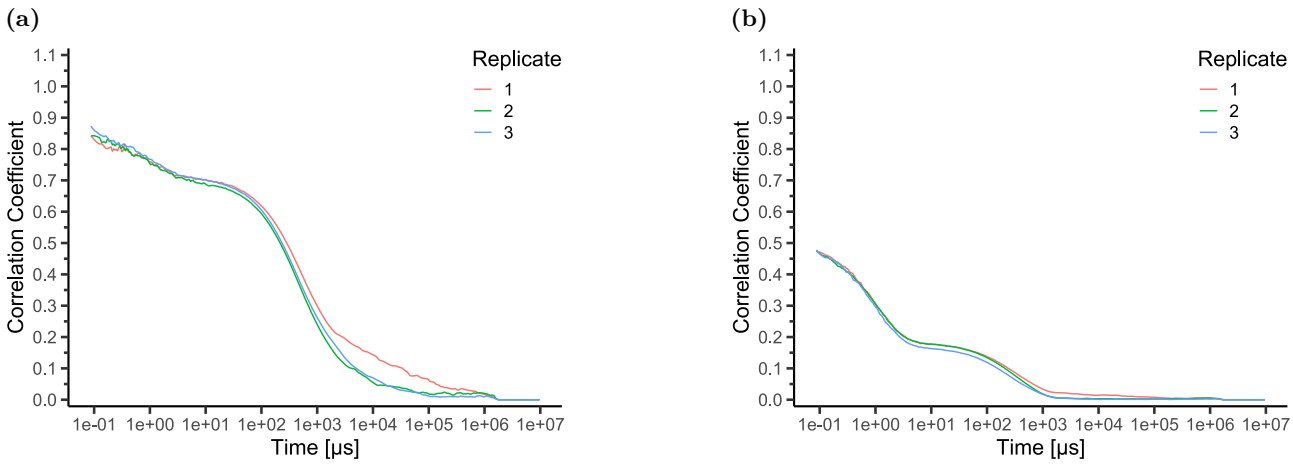

Figure 75: DLS Experiment 1: Correlogram of a sample containing ligand APE **20** and no protein.
(a): Without incubation. Attenuator Index = 9, Maximum Correlation Factor = 0.873.
(b): Incubated for 1 day. Attenuator Index = 11, Maximum Correlation Factor = 0.478.

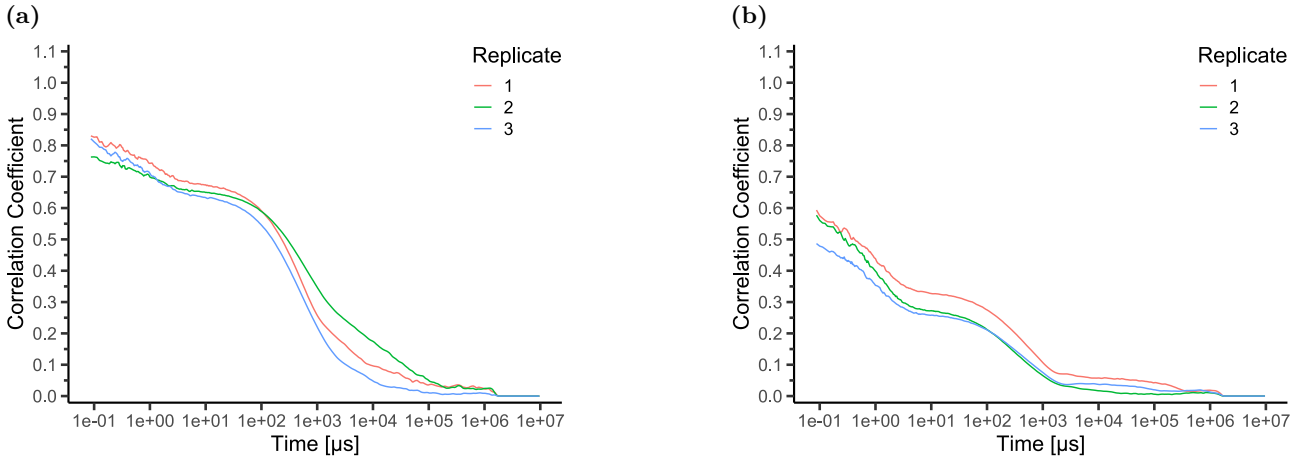

Figure 76: DLS Experiment 1: Correlogram of a sample containing ligand AWE **38** and no protein.
(a): Without incubation. Attenuator Index = 9, Maximum Correlation Factor = 0.830.
(b): Incubated for 1 day. Attenuator Index = 10, Maximum Correlation Factor = 0.594.

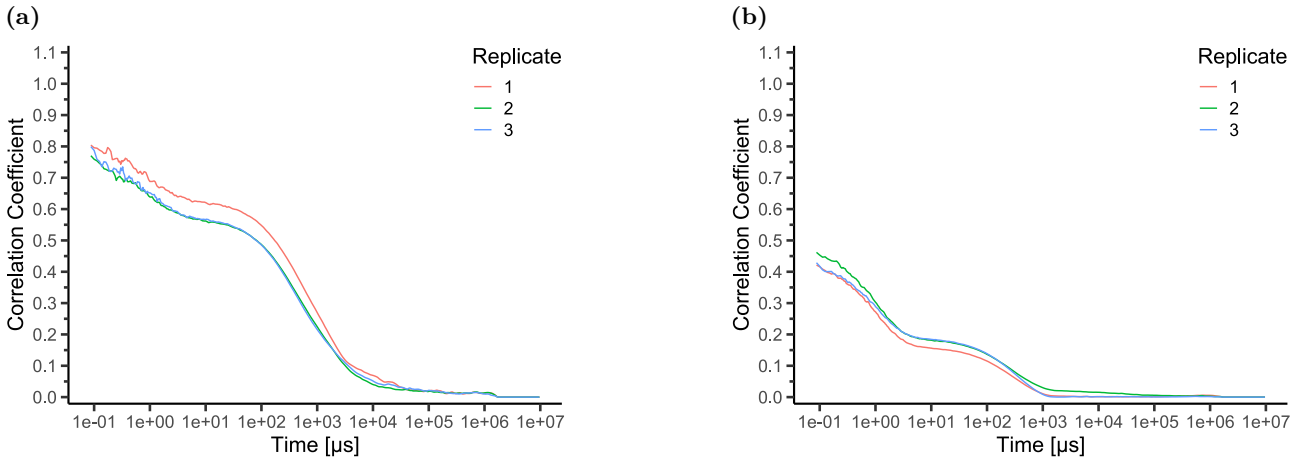

Figure 77: DLS Experiment 1: Correlogram of a sample containing ligand ca-L **9** and no protein.
(a): Without incubation. Attenuator Index = 9, Maximum Correlation Factor = 0.804.
(b): Incubated for 1 day. Attenuator Index = 11, Maximum Correlation Factor = 0.462.

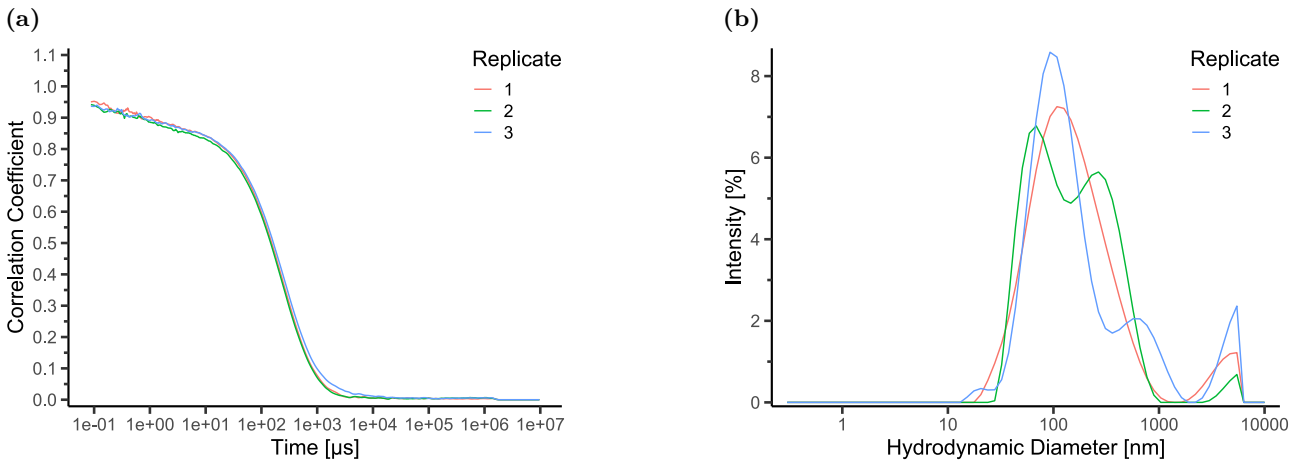

Figure 78: DLS Experiment 1: Measurement of a sample containing apo A4V and no ligand, without incubation. Attenuator Index = 8, Maximum Correlation Factor = 0.952. **(a):** Correlogram. **(b):** Size distriction.

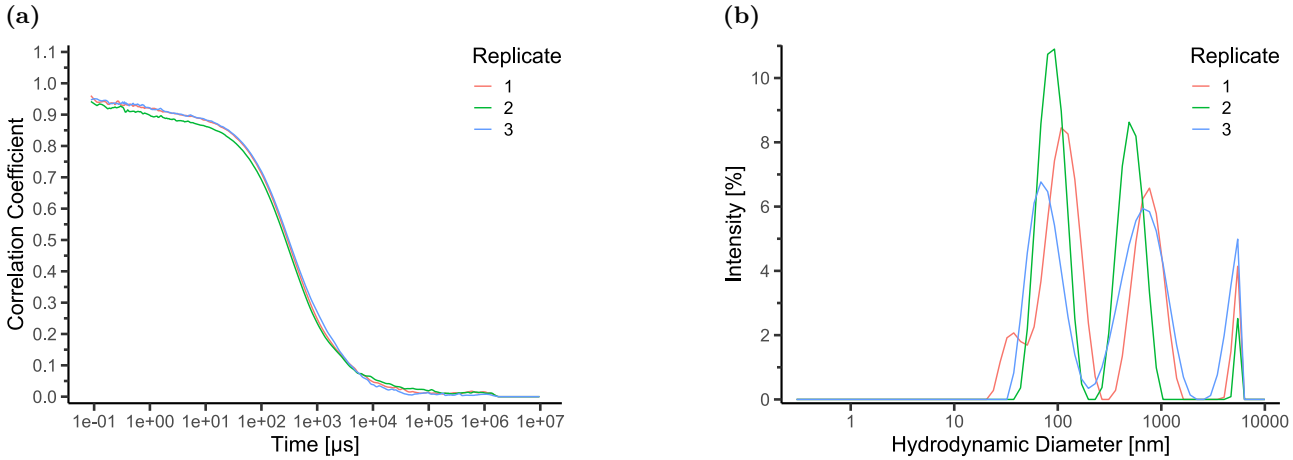

Figure 79: DLS Experiment 1: Measurement of a sample containing apo A4V and ligand ALD **35**, without incubation. Attenuator Index = 8, Maximum Correlation Factor = 0.961. **(a):** Correlogram. **(b):** Size distriction.

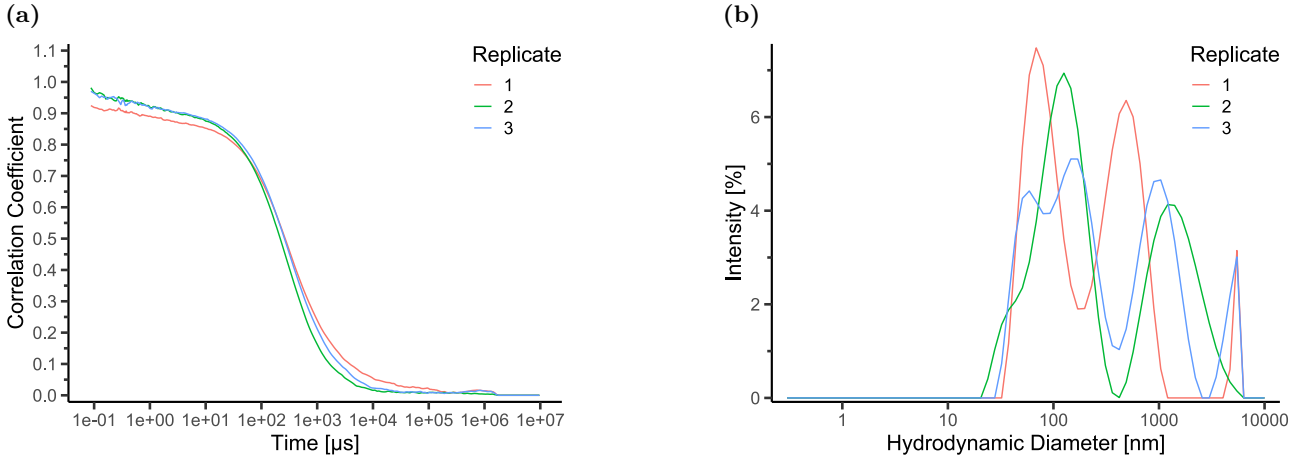

Figure 80: DLS Experiment 1: Measurement of a sample containing apo A4V and ligand ALE **36**, without incubation. Attenuator Index = 8, Maximum Correlation Factor = 0.981. **(a):** Correlogram. **(b):** Size distriction.

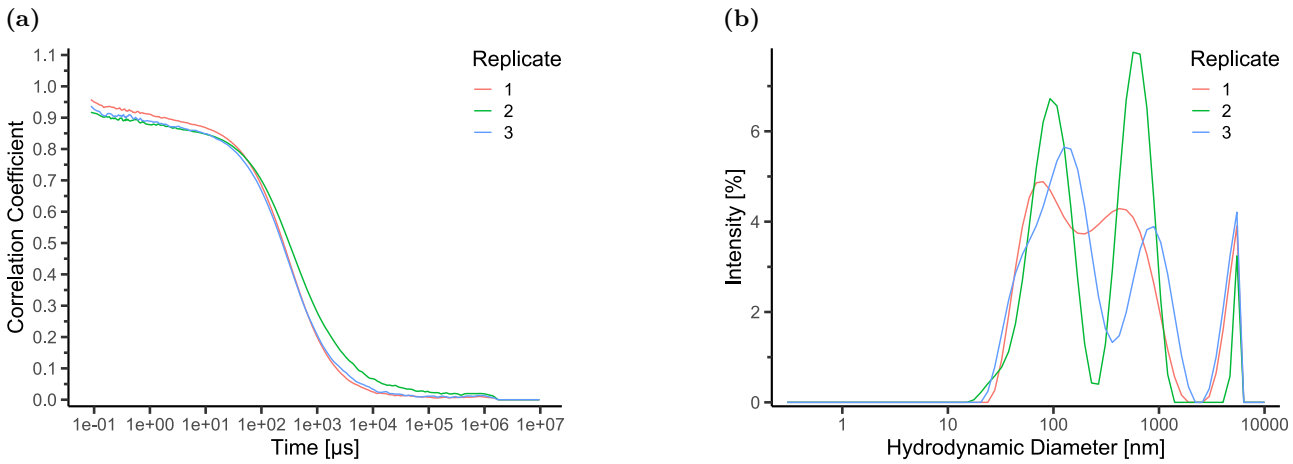

Figure 81: DLS Experiment 1: Measurement of a sample containing apo A4V and ligand APE **20**, without incubation. Attenuator Index = 8, Maximum Correlation Factor = 0.958. **(a):** Correlogram. **(b):** Size districation.

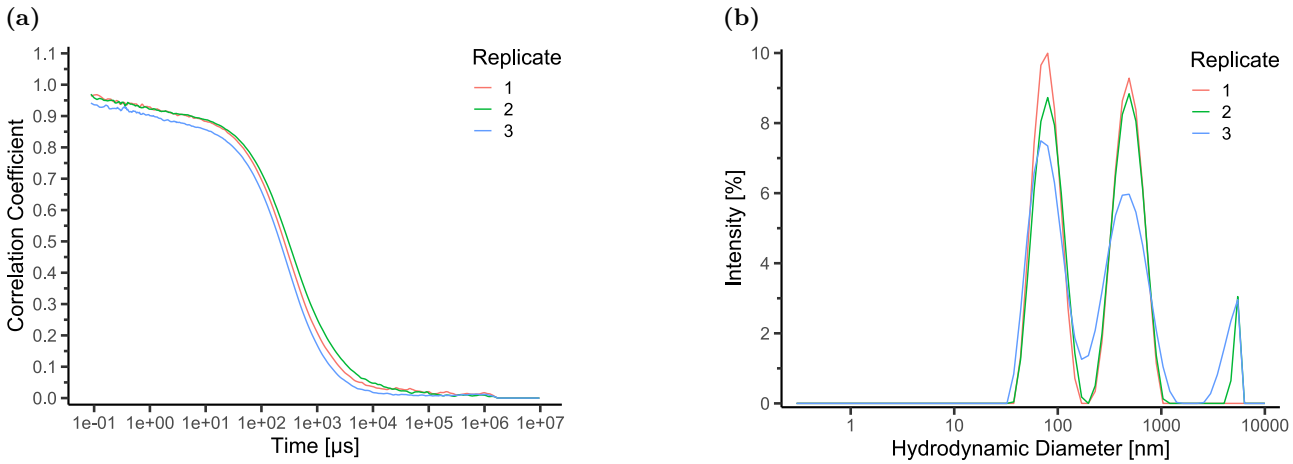

Figure 82: DLS Experiment 1: Measurement of a sample containing apo A4V and ligand AWE **38**, without incubation. Attenuator Index = 8, Maximum Correlation Factor = 0.970. **(a):** Correlogram. **(b):** Size districation.

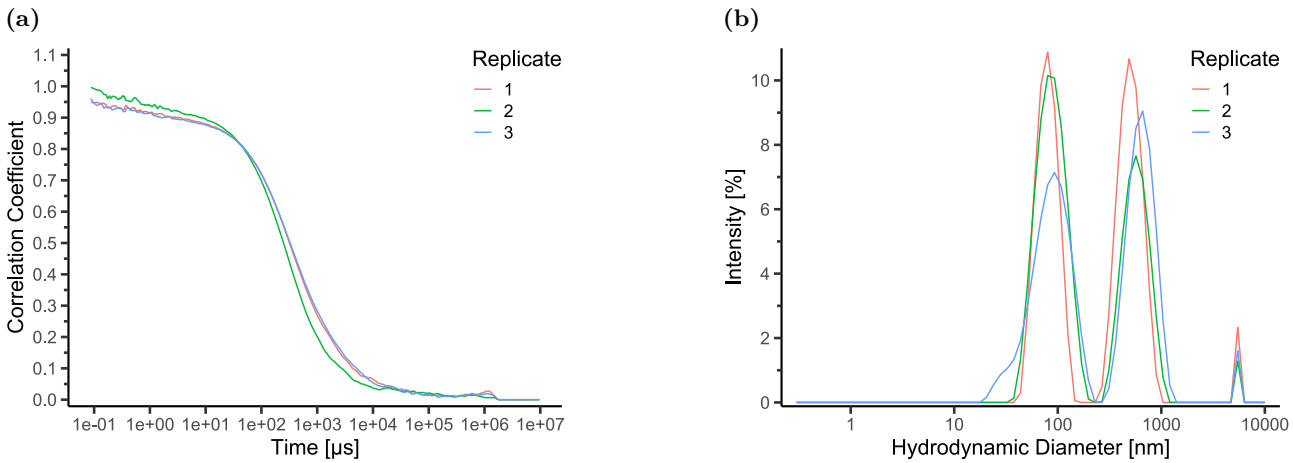

Figure 83: DLS Experiment 1: Measurement of a sample containing apo A4V and ligand ca-L **9**, without incubation. Attenuator Index = 8, Maximum Correlation Factor = 0.997. **(a):** Correlogram. **(b):** Size districation.

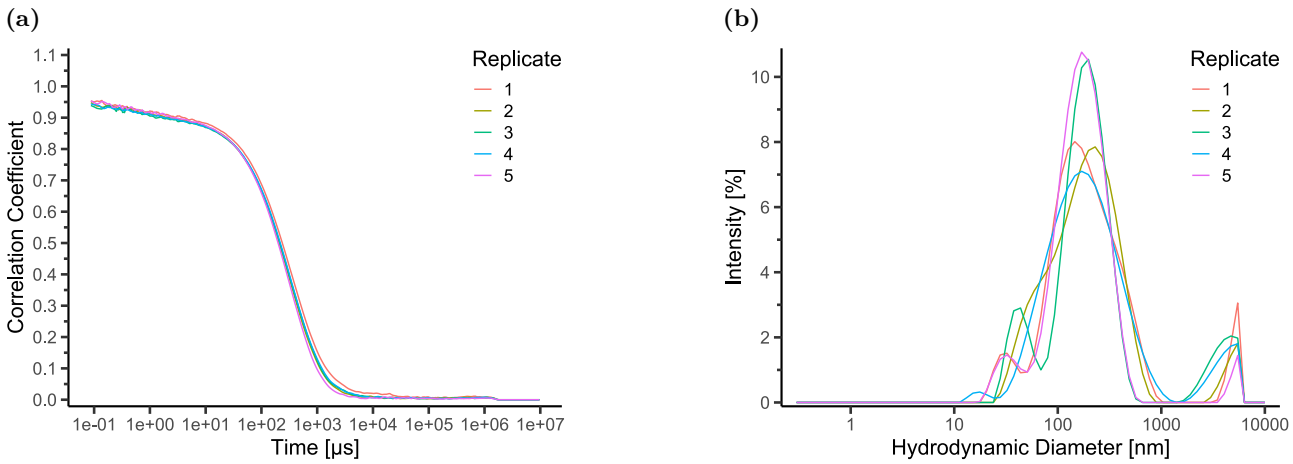

Figure 84: DLS Experiment 1: Measurement of a sample containing apo A4V and no ligand, incubated for 1 day. Attenuator Index = 8, Maximum Correlation Factor = 0.956. **(a):** Correlogram. **(b):** Size districation.

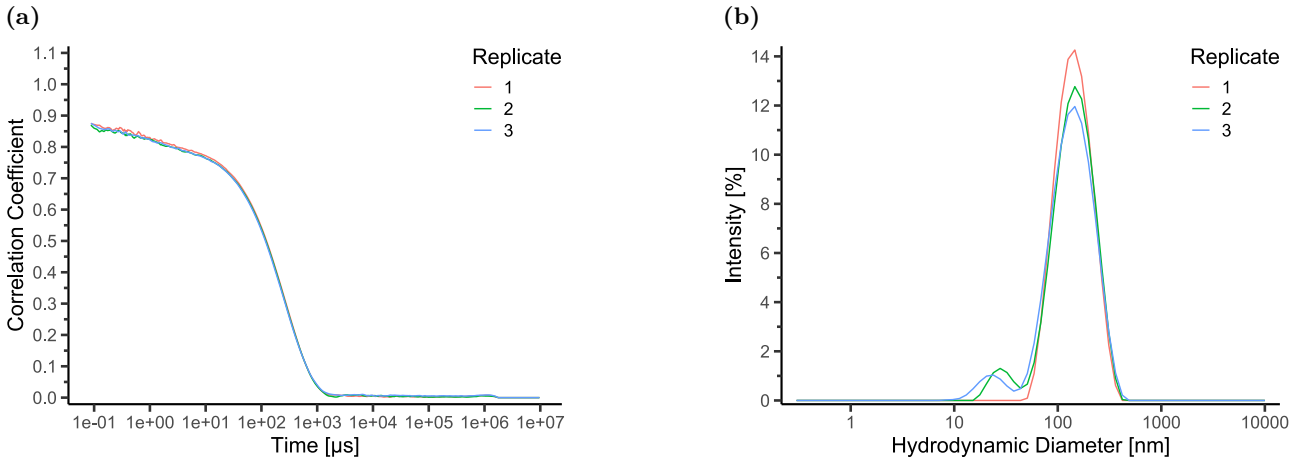

Figure 85: DLS Experiment 1: Measurement of a sample containing apo A4V and ligand ALD **35**, incubated for 1 day. Attenuator Index = 9, Maximum Correlation Factor = 0.875. **(a):** Correlogram. **(b):** Size districation.

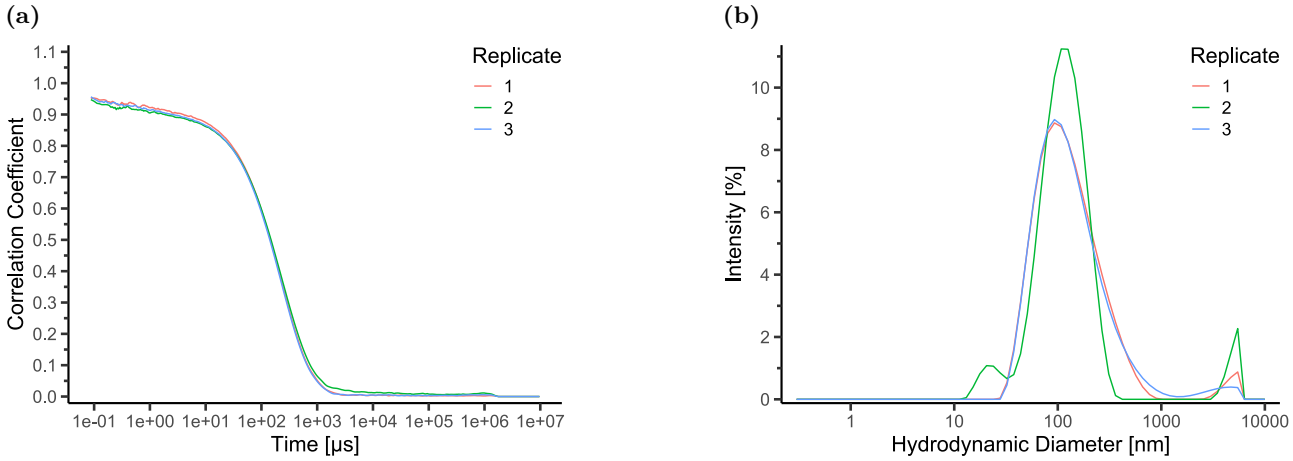

Figure 86: DLS Experiment 1: Measurement of a sample containing apo A4V and ligand ALE **36**, incubated for 1 day. Attenuator Index = 9, Maximum Correlation Factor = 0.957. **(a):** Correlogram. **(b):** Size districation.

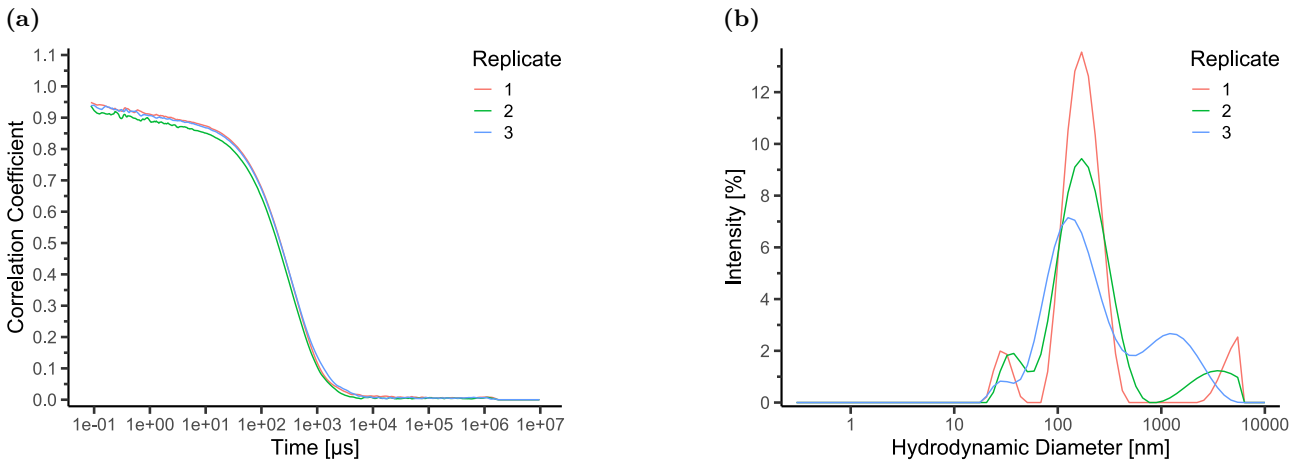

Figure 87: DLS Experiment 1: Measurement of a sample containing apo A4V and ligand APE **20**, incubated for 1 day. Attenuator Index = 8, Maximum Correlation Factor = 0.949. **(a):** Correlogram. **(b):** Size districation.

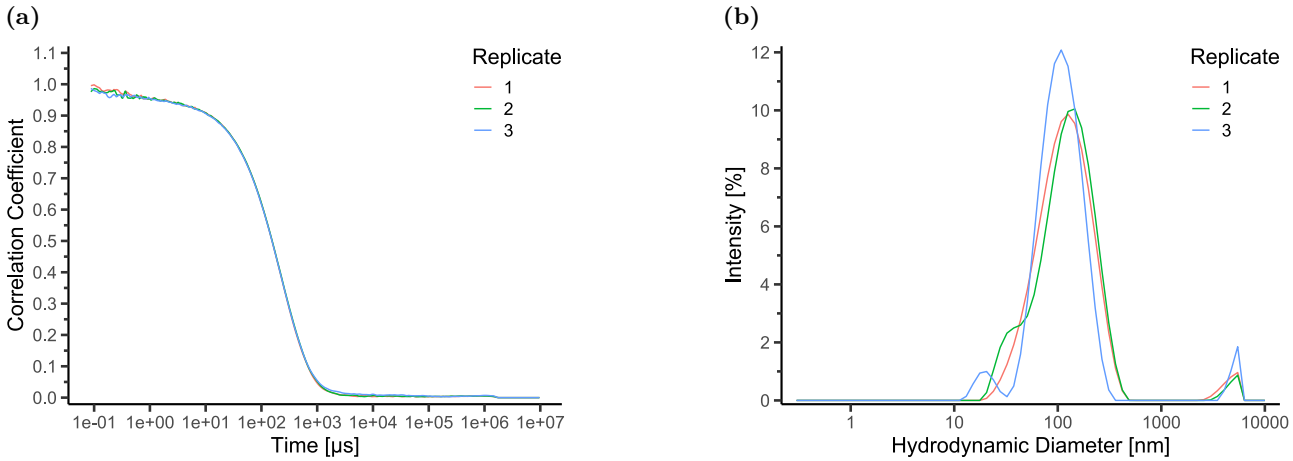

Figure 88: DLS Experiment 1: Measurement of a sample containing apo A4V and ligand AWE **38**, incubated for 1 day. Attenuator Index = 7, Maximum Correlation Factor = 0.998. **(a):** Correlogram. **(b):** Size districation.

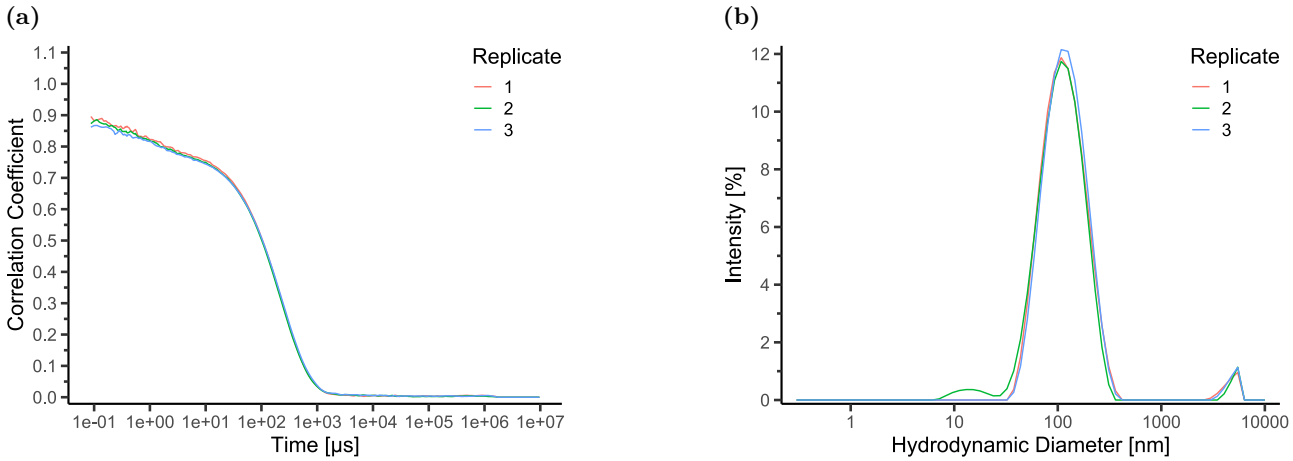

Figure 89: DLS Experiment 1: Measurement of a sample containing apo A4V and ligand ca-L **9**, incubated for 1 day. Attenuator Index = 9, Maximum Correlation Factor = 0.896. **(a):** Correlogram. **(b):** Size districation.

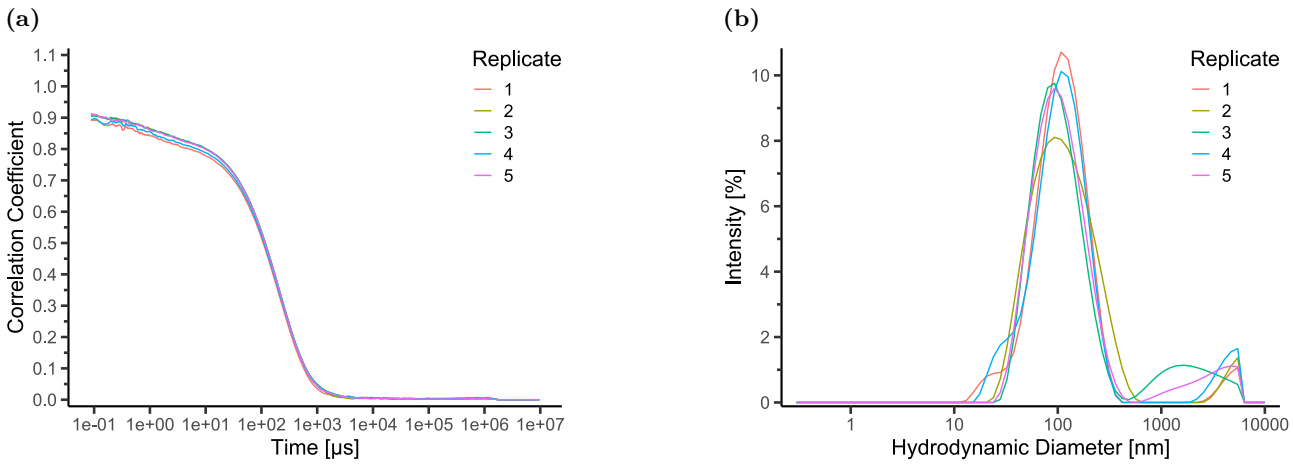

Figure 90: DLS Experiment 2: Measurement of a sample containing apo A4V and no ligand, without incubation. Attenuator Index = 9, Maximum Correlation Factor = 0.913. **(a):** Correlogram. **(b):** Size districation.

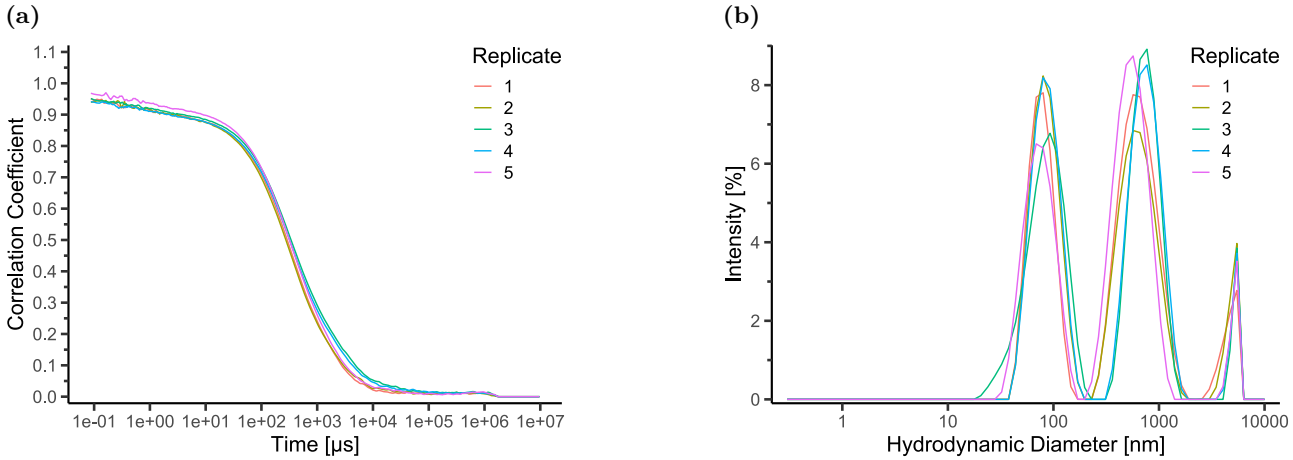

Figure 91: DLS Experiment 2: Measurement of a sample containing apo A4V and ligand ALD **35**, without incubation. Attenuator Index = 8, Maximum Correlation Factor = 0.970. **(a):** Correlogram. **(b):** Size districation.

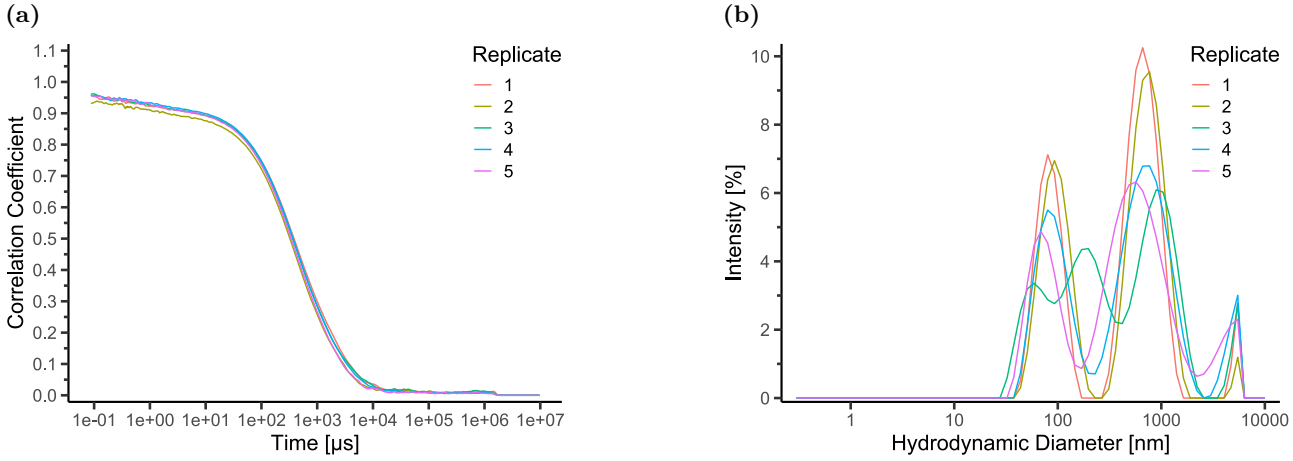

Figure 92: DLS Experiment 2: Measurement of a sample containing apo A4V and ligand ALE **36**, without incubation. Replicate 3 was excluded from analysis. Attenuator Index = 8, Maximum Correlation Factor = 0.962. **(a):** Correlogram. **(b):** Size districation.

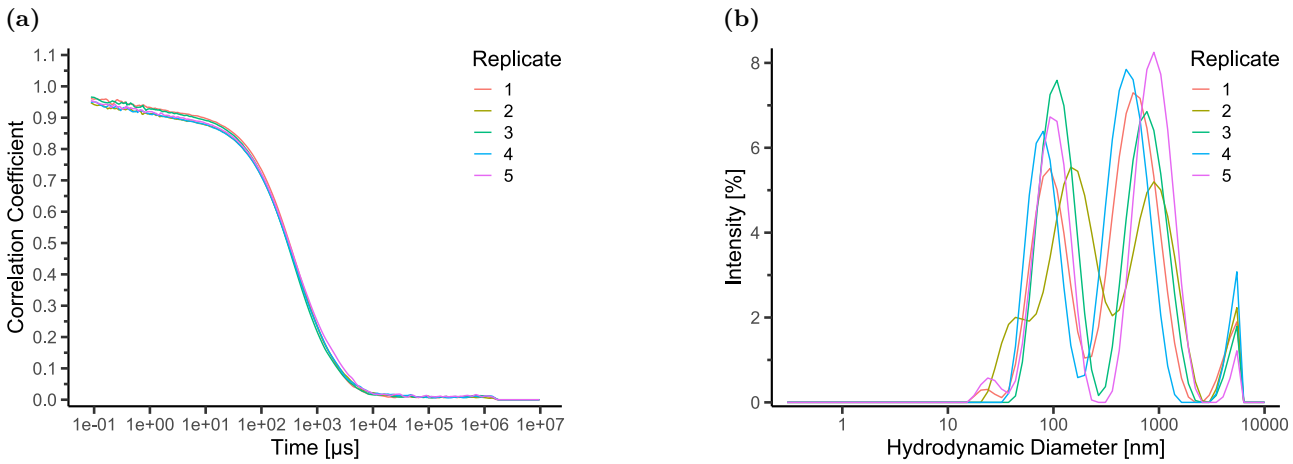

Figure 93: DLS Experiment 2: Measurement of a sample containing apo A4V and ligand APE **20**, without incubation. Attenuator Index = 8, Maximum Correlation Factor = 0.966. **(a):** Correlogram. **(b):** Size districation.

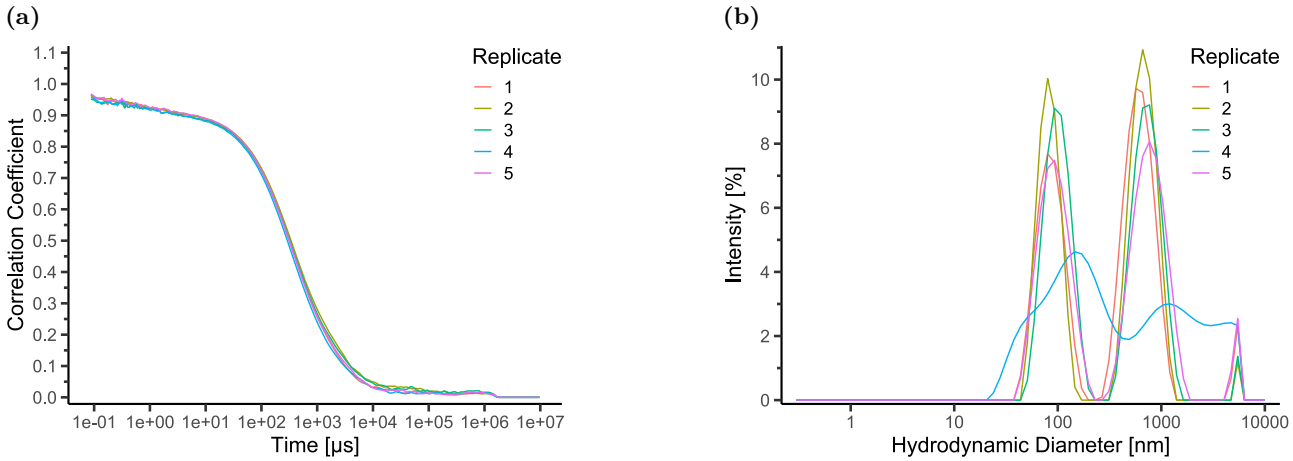

Figure 94: DLS Experiment 2: Measurement of a sample containing apo A4V and ligand AWE **38**, without incubation. Replicate 4 was excluded from analysis. Attenuator Index = 8, Maximum Correlation Factor = 0.968. **(a):** Correlogram. **(b):** Size districation.

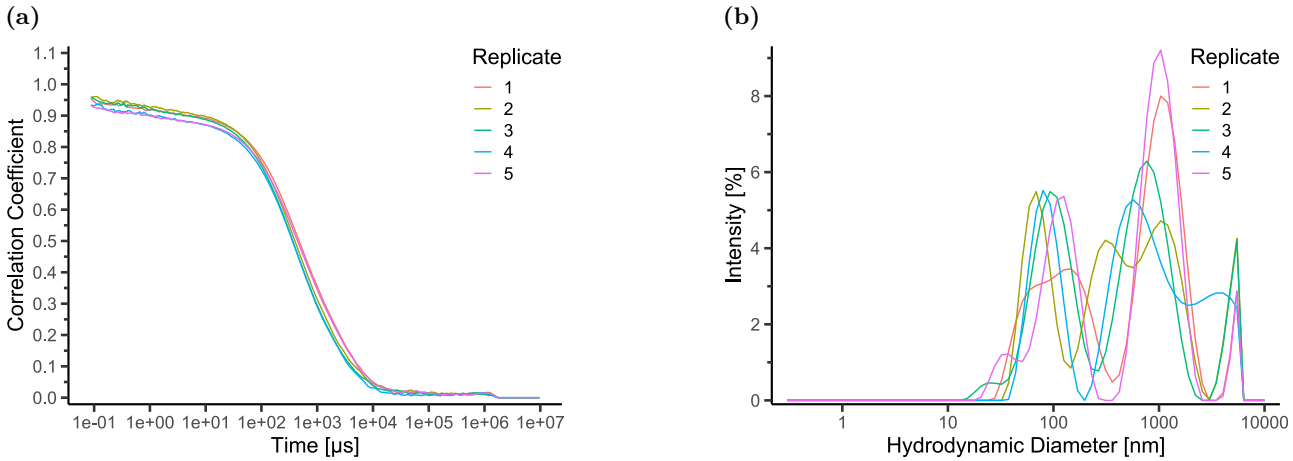

Figure 95: DLS Experiment 2: Measurement of a sample containing apo A4V and ligand ca-L **9**, without incubation. Attenuator Index = 8, Maximum Correlation Factor = 0.961. **(a):** Correlogram. **(b):** Size districation.

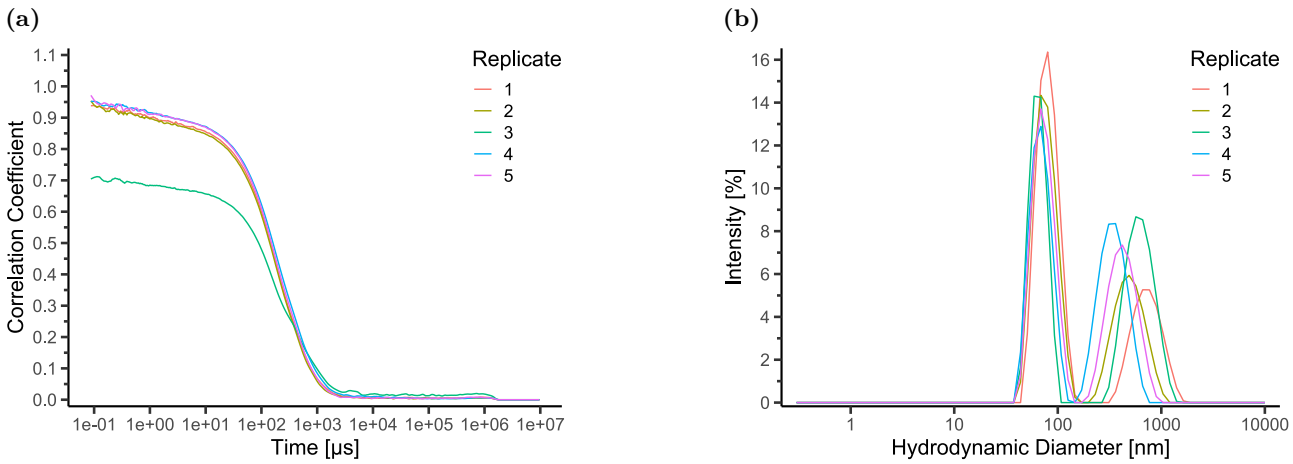

Figure 96: DLS Experiment 2: Measurement of a sample containing apo A4V and no ligand, incubated for 1 day. Replicate 3 was excluded from analysis. Attenuator Index = 8, Maximum Correlation Factor = 0.971. **(a):** Correlogram. **(b):** Size districation.

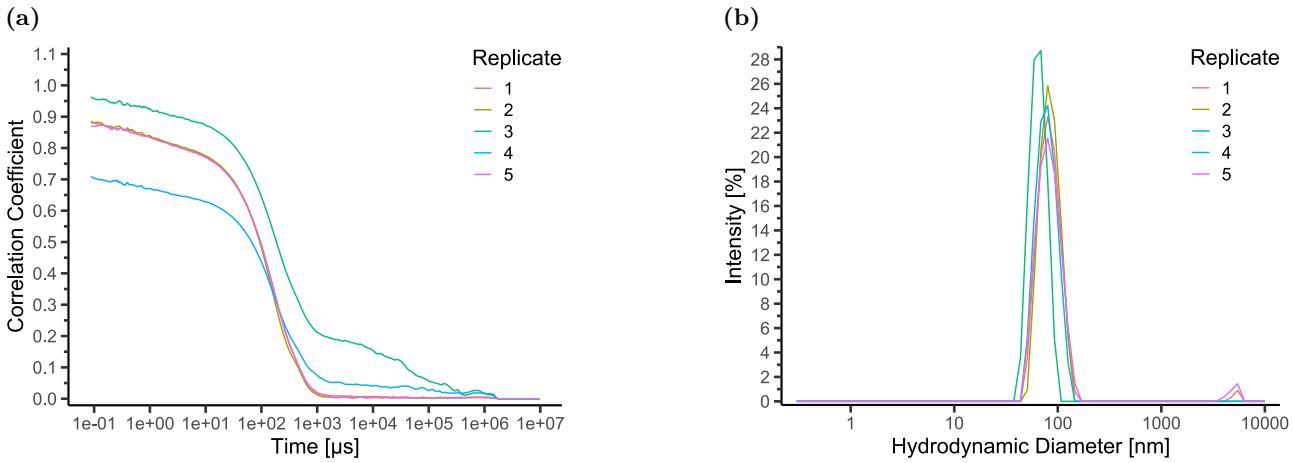

Figure 97: DLS Experiment 2: Measurement of a sample containing apo A4V and ligand ALD **35**, incubated for 1 day. Replicate 3 and 4 were excluded from analysis. Attenuator Index = 9, Maximum Correlation Factor = 0.963. **(a):** Correlogram. **(b):** Size districation.

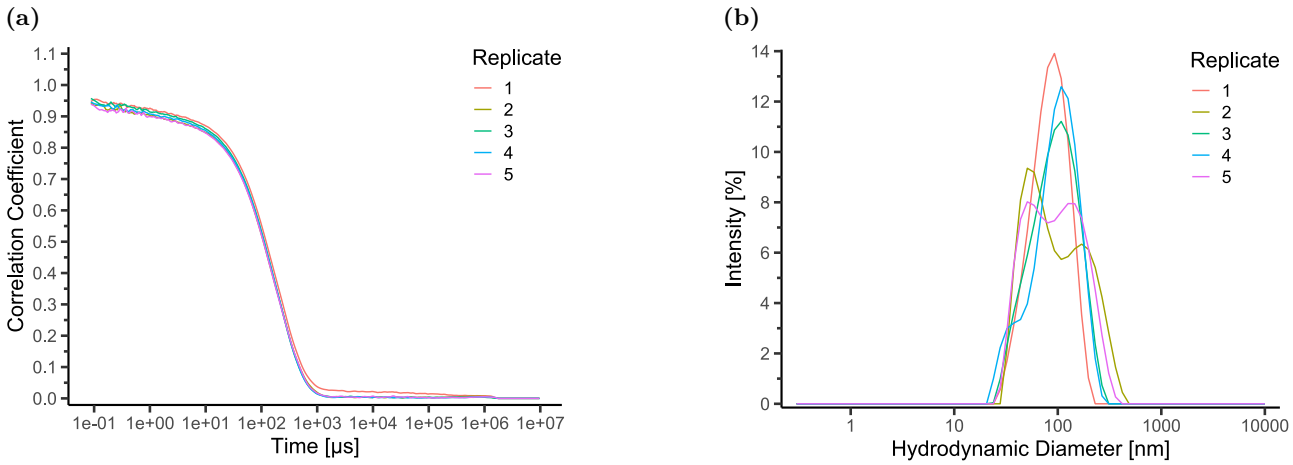

Figure 98: DLS Experiment 2: Measurement of a sample containing apo A4V and ligand ALE **36**, incubated for 1 day. Attenuator Index = 8, Maximum Correlation Factor = 0.957. **(a):** Correlogram. **(b):** Size districation.

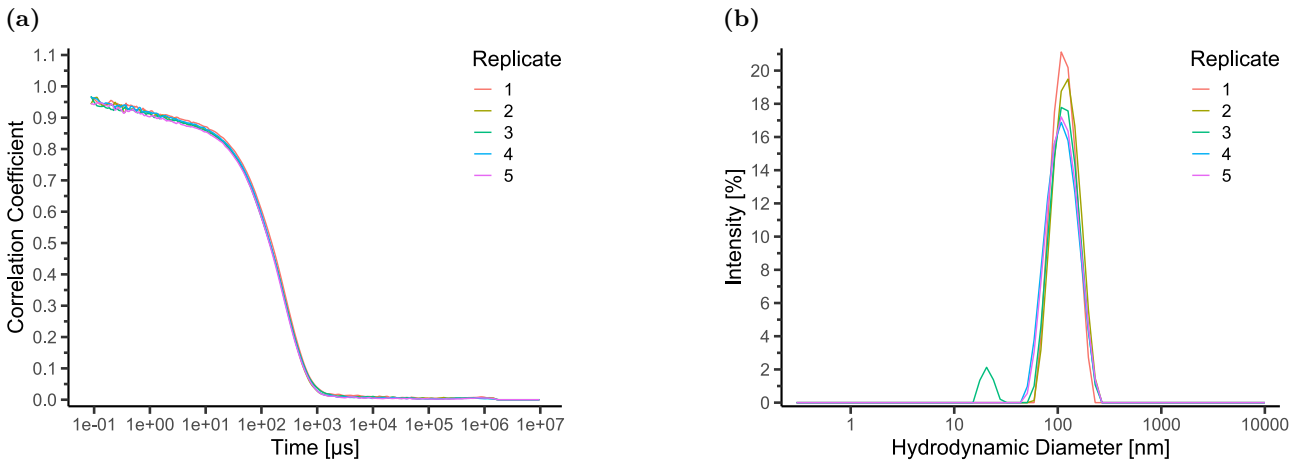

Figure 99: DLS Experiment 2: Measurement of a sample containing apo A4V and ligand APE **20**, incubated for 1 day. Attenuator Index = 8, Maximum Correlation Factor = 0.968. **(a):** Correlogram. **(b):** Size districation.

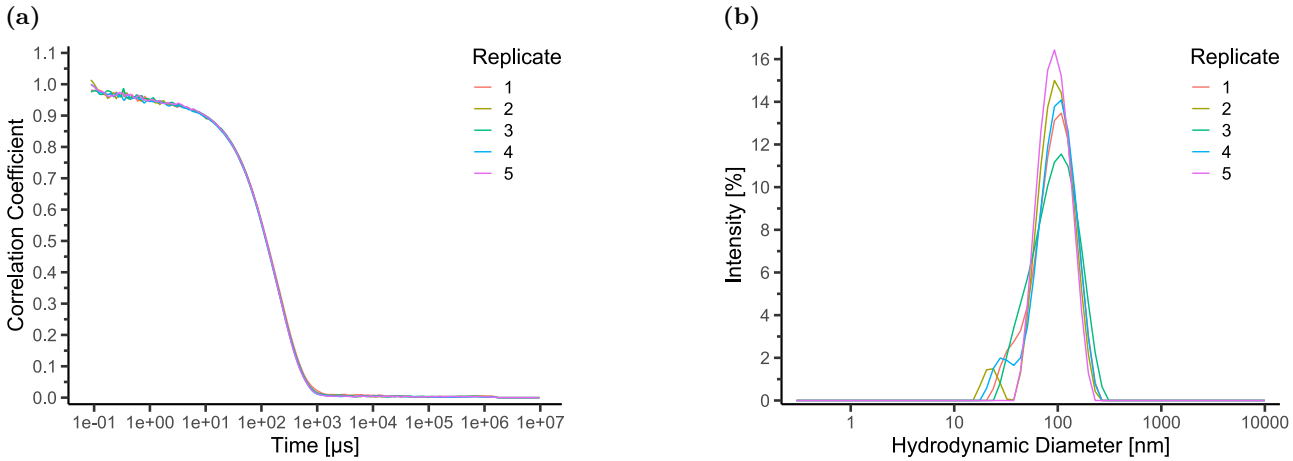

Figure 100: DLS Experiment 2: Measurement of a sample containing apo A4V and ligand AWE **38**, incubated for 1 day. Attenuator Index = 7, Maximum Correlation Factor = 1.014. **(a):** Correlogram. **(b):** Size districation.

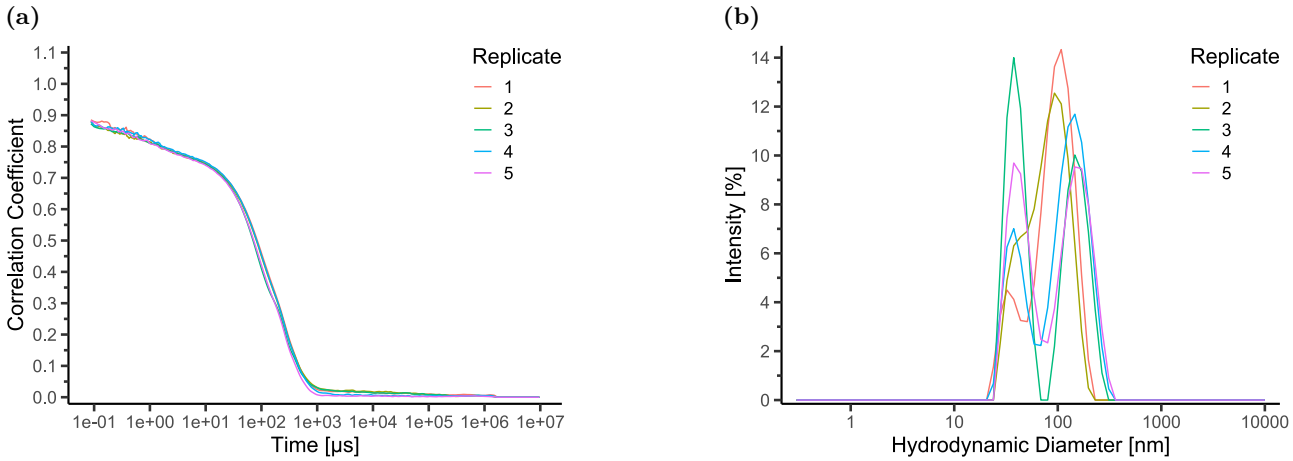

Figure 101: DLS Experiment 2: Measurement of a sample containing apo A4V and ligand ca-L **9**, incubated for 1 day. Attenuator Index = 9, Maximum Correlation Factor = 0.8851. **(a):** Correlogram. **(b):** Size districation.

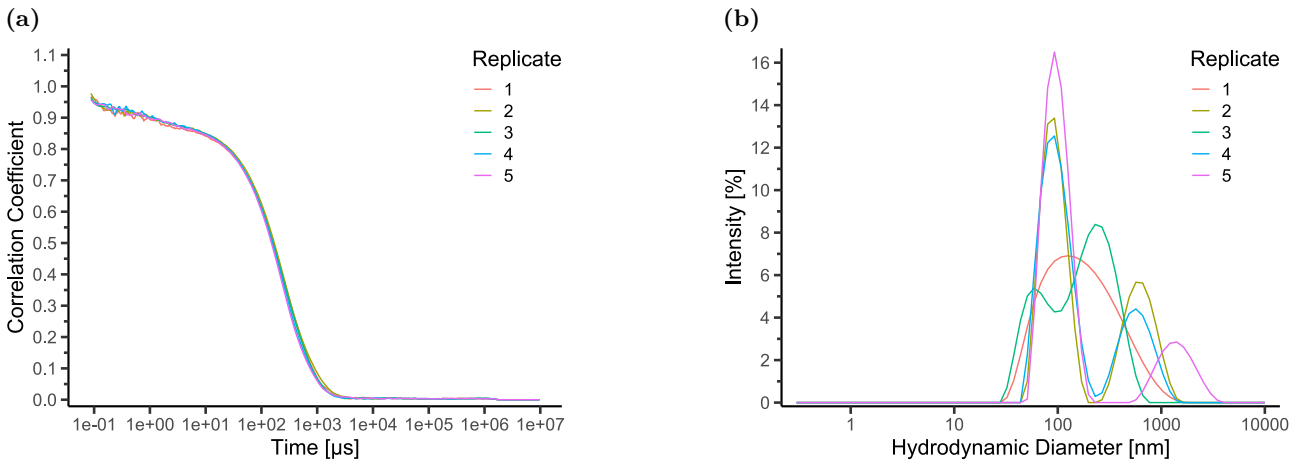

Figure 102: DLS Experiment 3: Measurement of a sample containing apo A4V and no ligand, without incubation. Replicate 1 was excluded from analysis. Attenuator Index = 8, Maximum Correlation Factor = 0.978. **(a):** Correlogram. **(b):** Size districation.

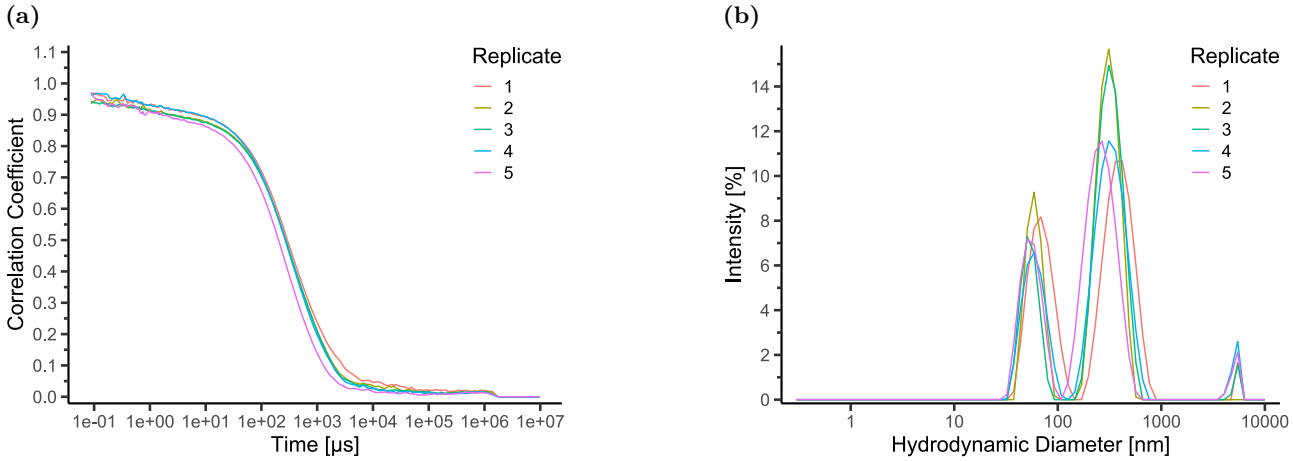

Figure 103: DLS Experiment 3: Measurement of a sample containing apo A4V and ligand ALD **35**, without incubation. Attenuator Index = 8, Maximum Correlation Factor = 0.971. **(a):** Correlogram. **(b):** Size districation.

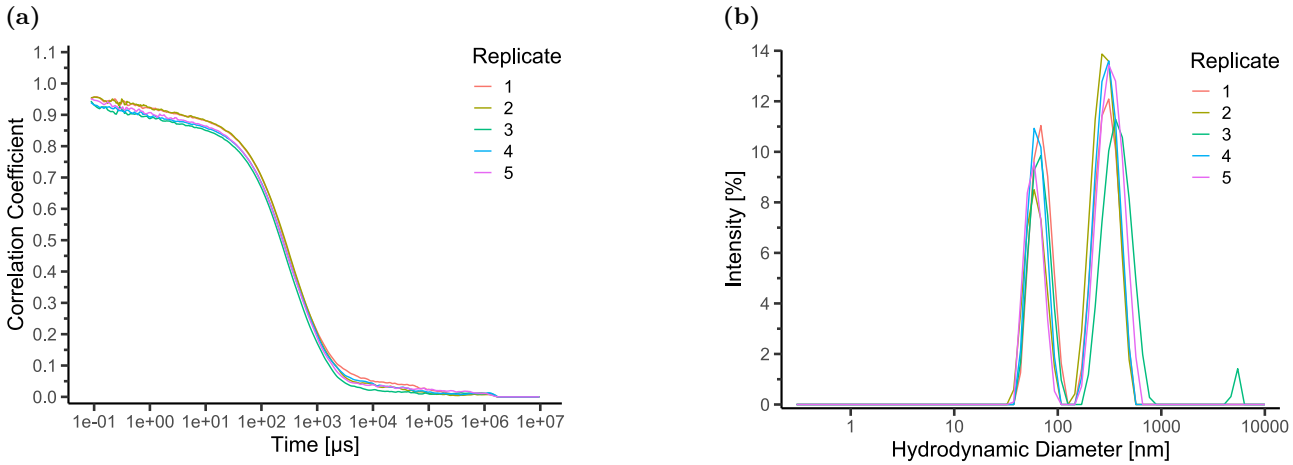

Figure 104: DLS Experiment 3: Measurement of a sample containing apo A4V and ligand ALE **36**, without incubation. Attenuator Index = 8, Maximum Correlation Factor = 0.958. **(a):** Correlogram. **(b):** Size districation.

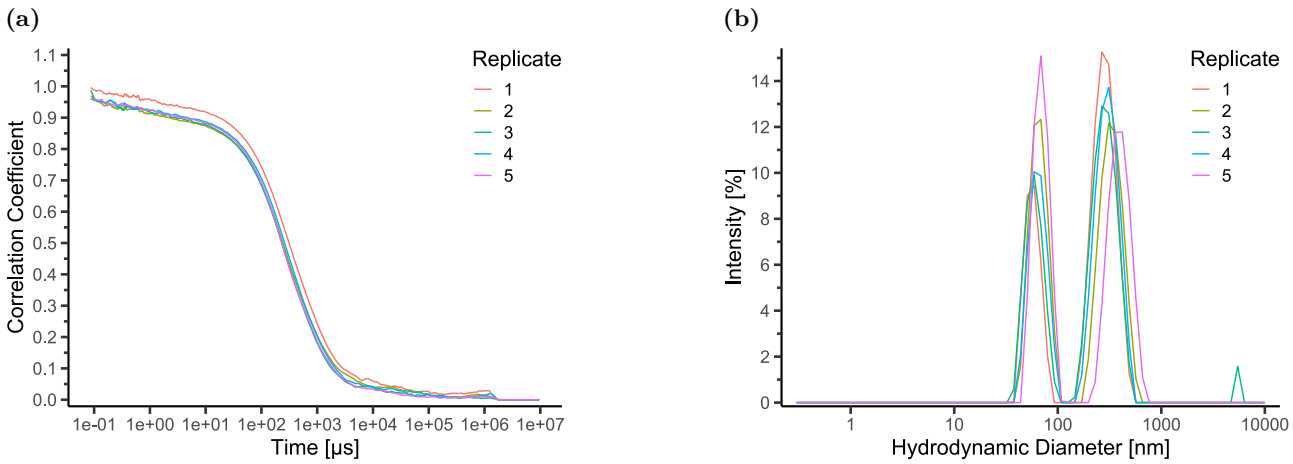

Figure 105: DLS Experiment 3: Measurement of a sample containing apo A4V and ligand APE **20**, without incubation. Attenuator Index = 8, Maximum Correlation Factor = 0.996. **(a):** Correlogram. **(b):** Size districation.

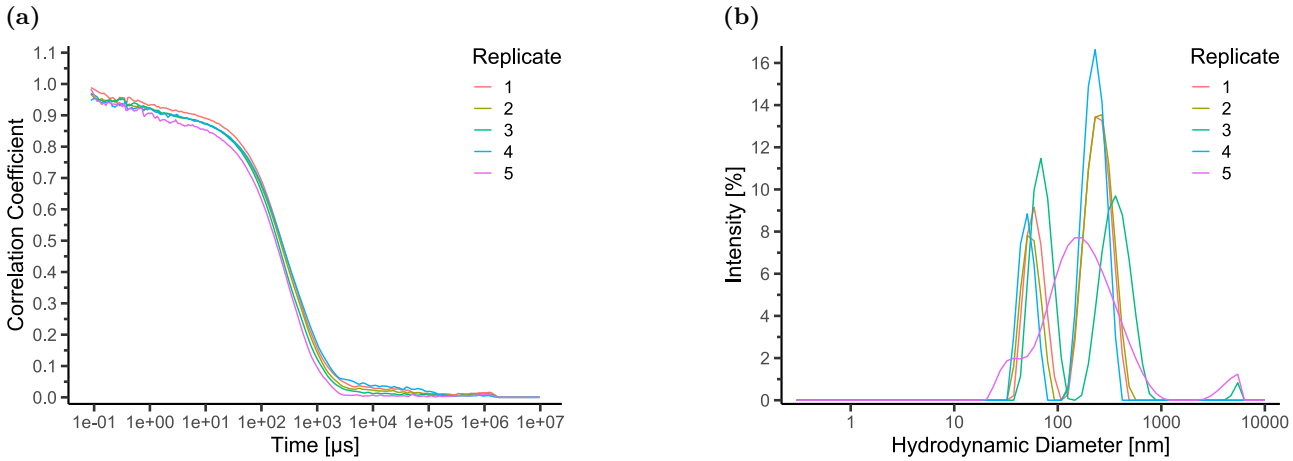

Figure 106: DLS Experiment 3: Measurement of a sample containing apo A4V and ligand AWE **38**, without incubation. Replicate 5 was excluded from analysis. Attenuator Index = 8, Maximum Correlation Factor = 0.989. **(a):** Correlogram. **(b):** Size districation.

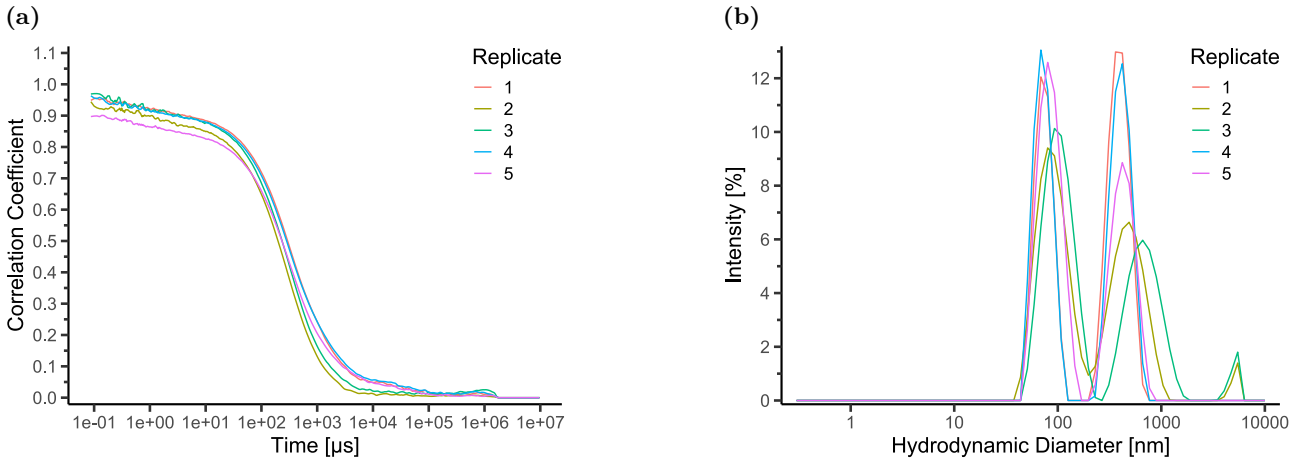

Figure 107: DLS Experiment 3: Measurement of a sample containing apo A4V and ligand ca-L **9**, without incubation. Attenuator Index = 8, Maximum Correlation Factor = 0.9703. **(a):** Correlogram. **(b):** Size districation.

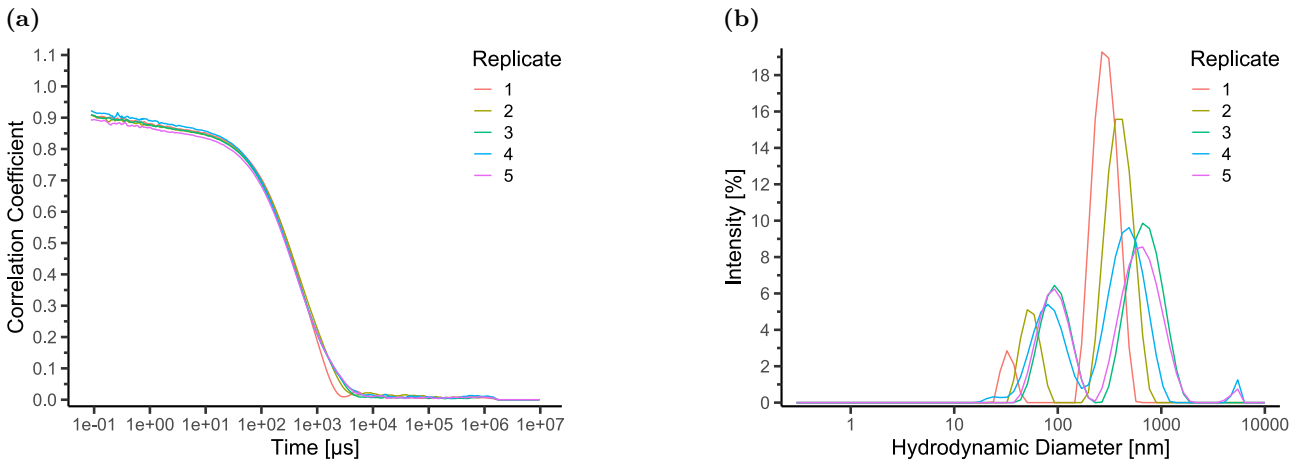

Figure 108: DLS Experiment 3: Measurement of a sample containing apo A4V and no ligand, incubated for 1 day. Replicate 1 was excluded from analysis. Attenuator Index = 8, Maximum Correlation Factor = 0.923. **(a):** Correlogram. **(b):** Size districation.

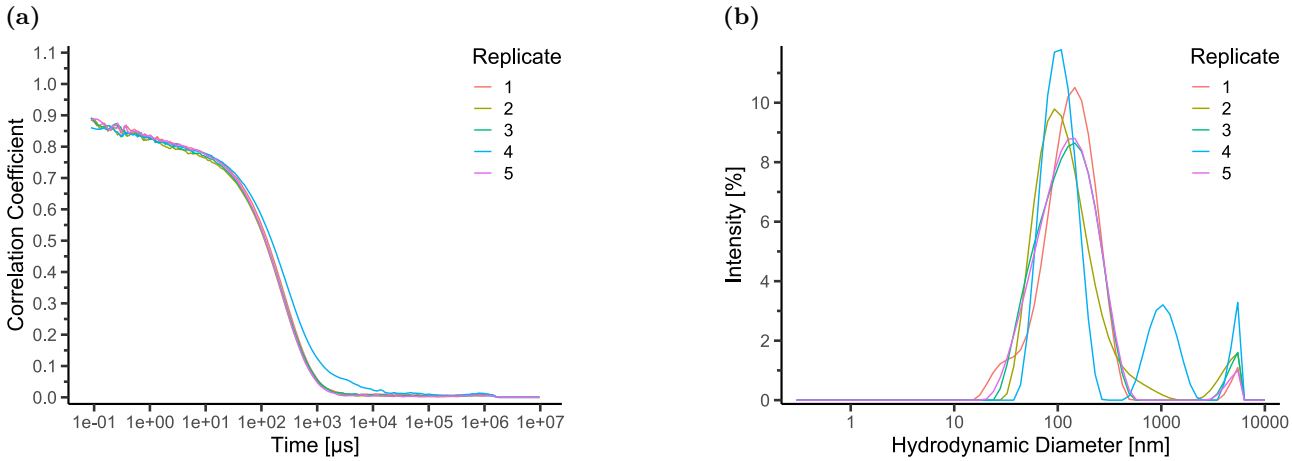

Figure 109: DLS Experiment 3: Measurement of a sample containing apo A4V and ligand ALD **35**, incubated for 1 day. Replicate 4 was excluded from analysis. Attenuator Index = 8, Maximum Correlation Factor = 0.891. **(a):** Correlogram. **(b):** Size districation.

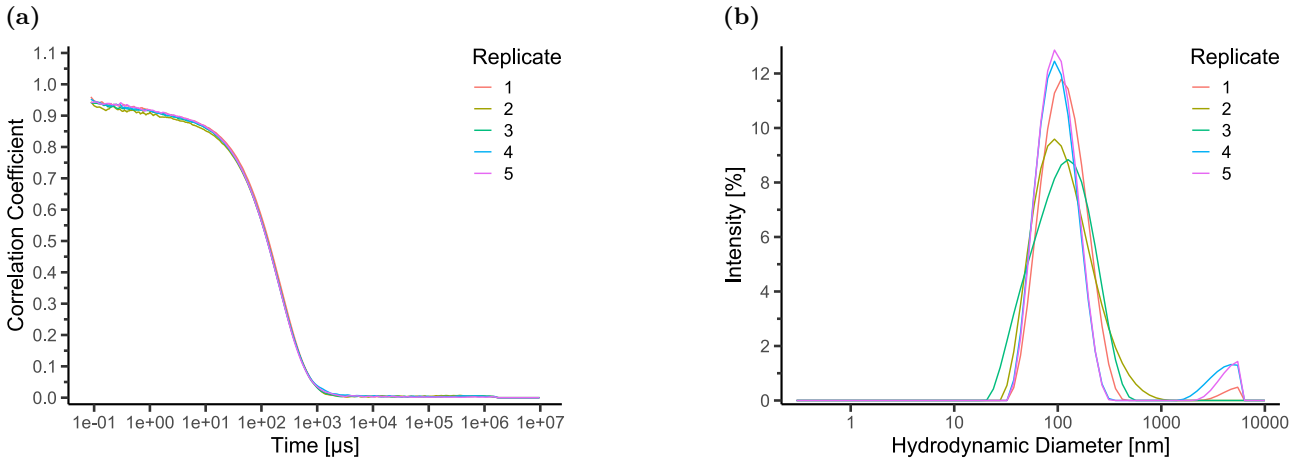

Figure 110: DLS Experiment 3: Measurement of a sample containing apo A4V and ligand ALE **36**, incubated for 1 day. Attenuator Index = 8, Maximum Correlation Factor = 0.960. **(a):** Correlogram. **(b):** Size districation.

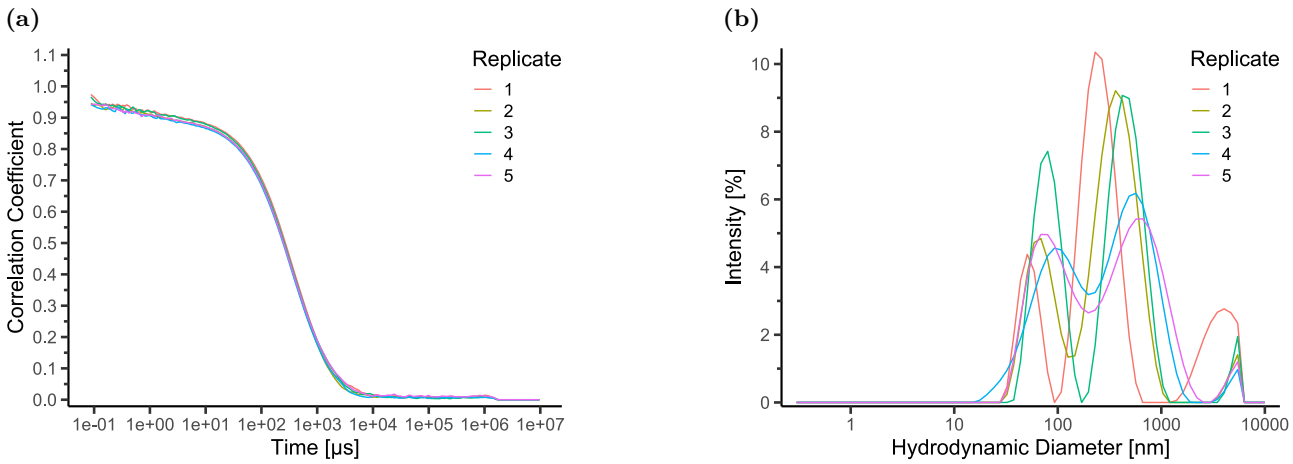

Figure 111: DLS Experiment 3: Measurement of a sample containing apo A4V and ligand APE **20**, incubated for 1 day. Replicate 1 was excluded from analysis. Attenuator Index = 8, Maximum Correlation Factor = 0.974. **(a):** Correlogram. **(b):** Size distriction.

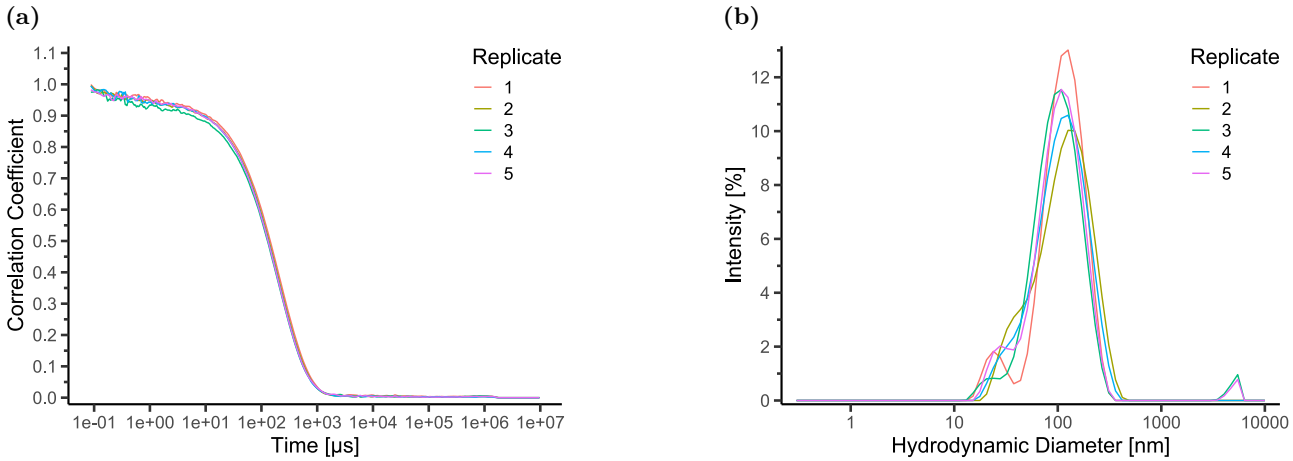

Figure 112: DLS Experiment 3: Measurement of a sample containing apo A4V and ligand AWE **38**, incubated for 1 day. Attenuator Index = 7, Maximum Correlation Factor = 0.999. **(a):** Correlogram. **(b):** Size distriction.

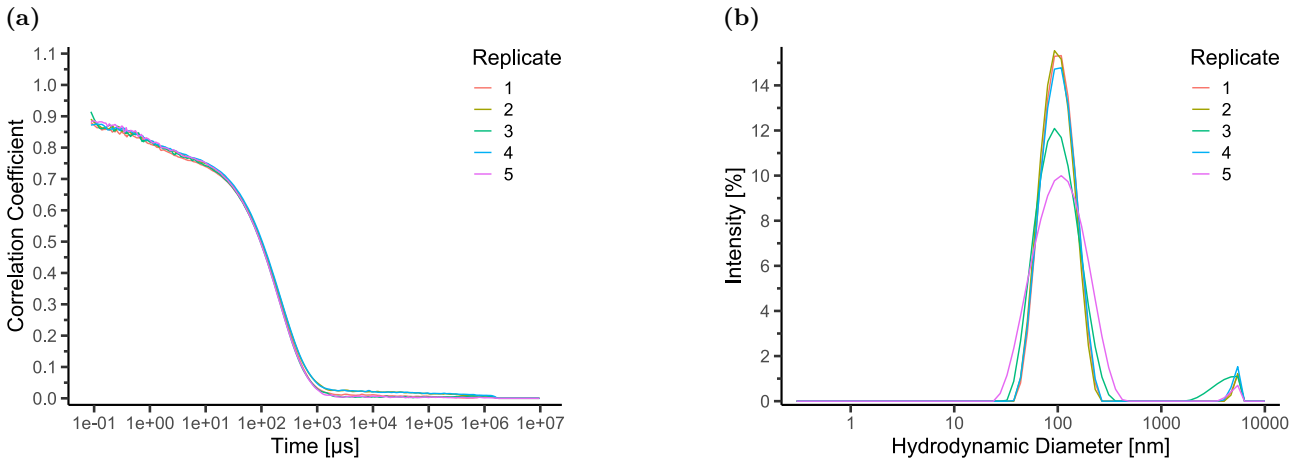

Figure 113: DLS Experiment 3: Measurement of a sample containing apo A4V and ligand ca-L **9**, incubated for 1 day. Attenuator Index = 9, Maximum Correlation Factor = 0.915. **(a):** Correlogram. **(b):** Size distriction.

10.5 Aggregation Assay

Table 35: Relative ThT fluorescence intensity for each sample of the aggregation assay. Relative intensities are provided as mean and standard deviation obtained from multiple experiments with multiple replicates each.

Ligand	Ligand Final Conc.	hSOD1 Variant	hSOD1 Final Conc.	ThT Final Conc.	Relative Intensity [%]
none	none	holo wt	20 µM	15 µM	−3.7 ± 2.1
AWE	1.0 mM	apo A4V	20 µM	15 µM	−0.5 ± 0.5
ALE	1.0 mM	apo A4V	20 µM	15 µM	5.7 ± 0.5
ALD	1.0 mM	apo A4V	20 µM	15 µM	20.8 ± 1.4
ca-L	1.0 mM	apo A4V	20 µM	15 µM	71.7 ± 2.1
APE	1.0 mM	apo A4V	20 µM	15 µM	87.3 ± 3.5
ABE	0.5 mM	apo A4V	20 µM	15 µM	89.5 ± 3.6
AOD	1.0 mM	apo A4V	20 µM	15 µM	90.3 ± 8.0
ABD	1.0 mM	apo A4V	20 µM	15 µM	90.6 ± 3.1
pyrimethamine	0.5 mM	apo A4V	20 µM	15 µM	91.0 ± 5.8
APD	1.0 mM	apo A4V	20 µM	15 µM	91.1 ± 5.3
AOE	0.2 mM	apo A4V	20 µM	15 µM	91.5 ± 6.4
AFE	1.0 mM	apo A4V	20 µM	15 µM	92.3 ± 3.9
APT	1.0 mM	apo A4V	20 µM	15 µM	96.8 ± 4.8
trehalose	20 mM	apo A4V	20 µM	15 µM	98.0 ± 5.4
trehalose	1.0 mM	apo A4V	20 µM	15 µM	98.4 ± 4.0
none	none	apo A4V	20 µM	15 µM	100.0 ± 3.3

10.6 NMR Spectra

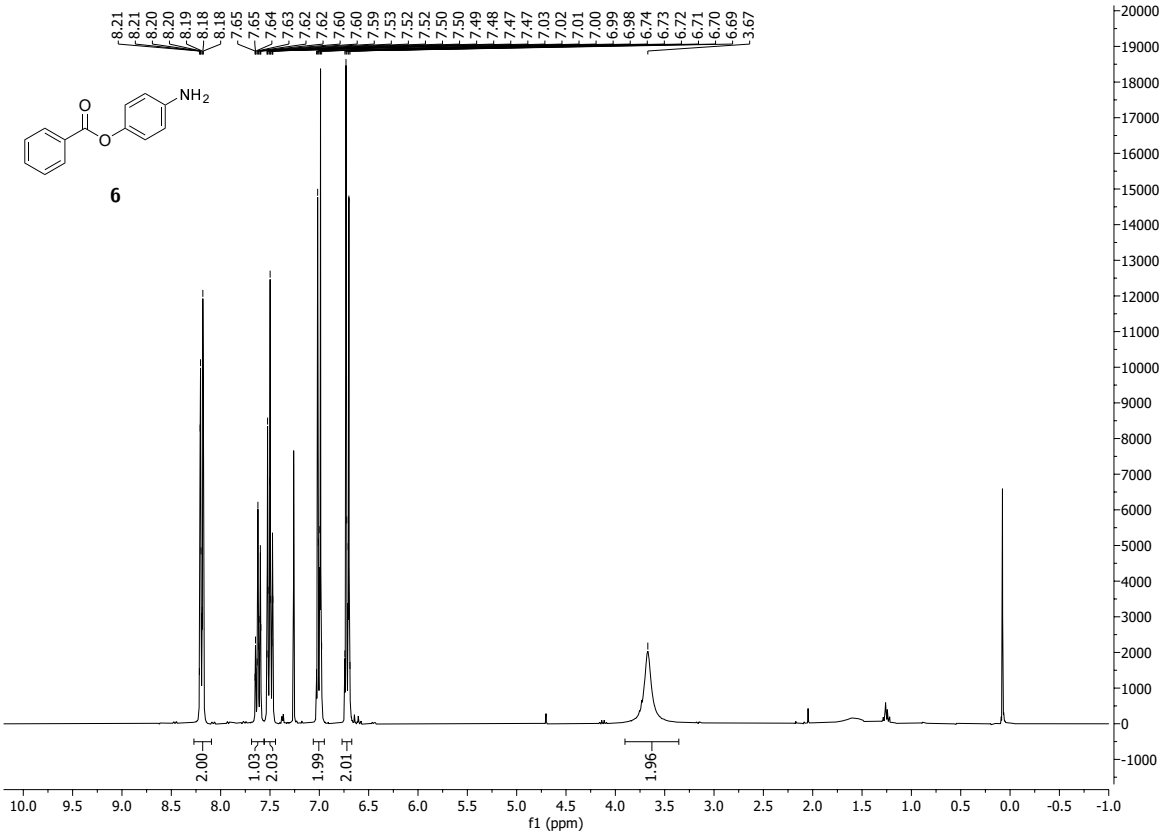

^{1}H NMR (300 MHz, $CDCl_3$) spectrum of 4-aminophenyl benzoate **6**.

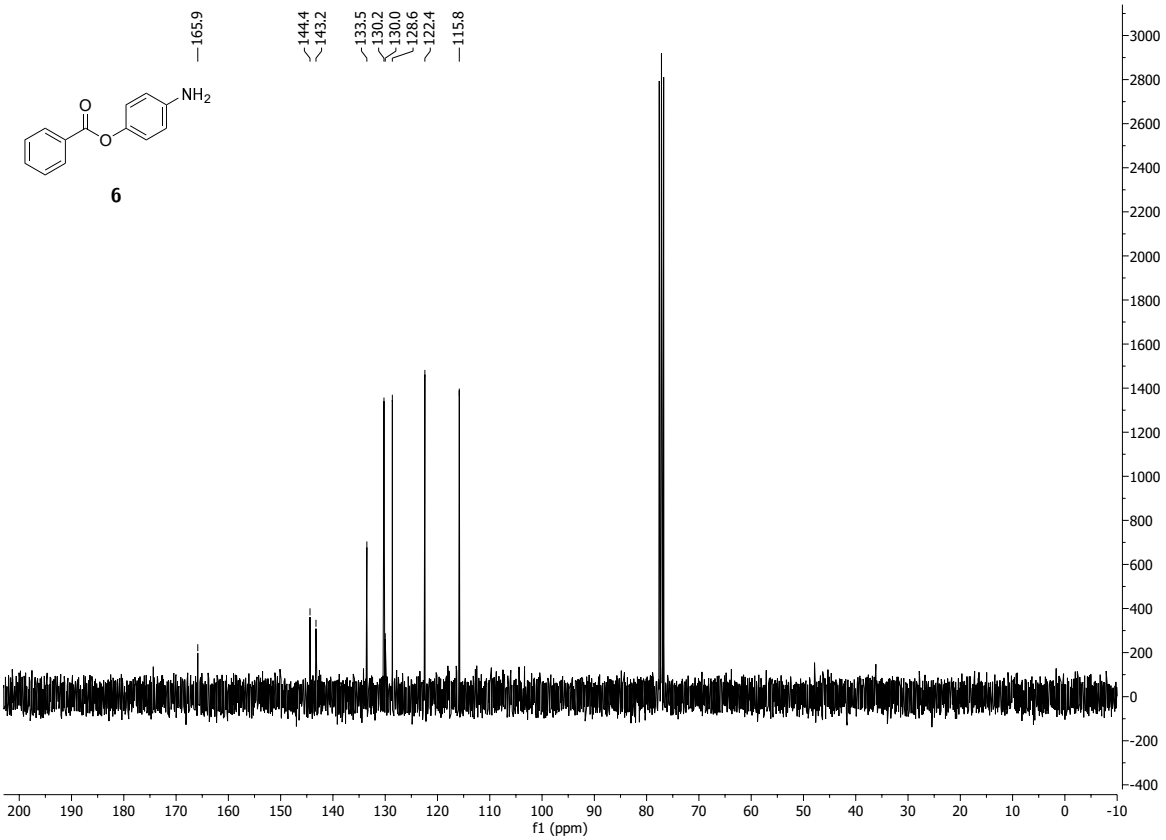

^{13}C NMR (75 MHz, $CDCl_3$) spectrum of 4-aminophenyl benzoate **6**.

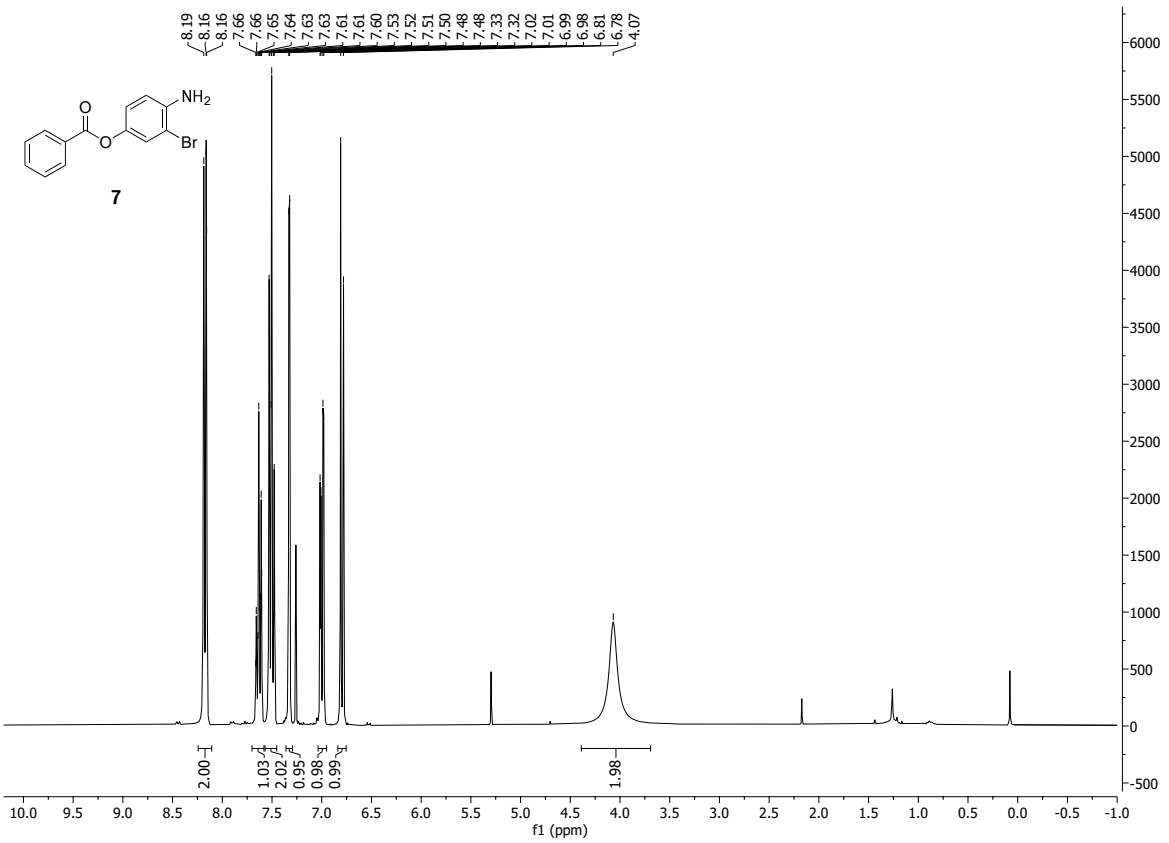

^{1}H NMR (300 MHz, $CDCl_3$) spectrum of
4-amino-3-bromophenyl benzoate **7**.

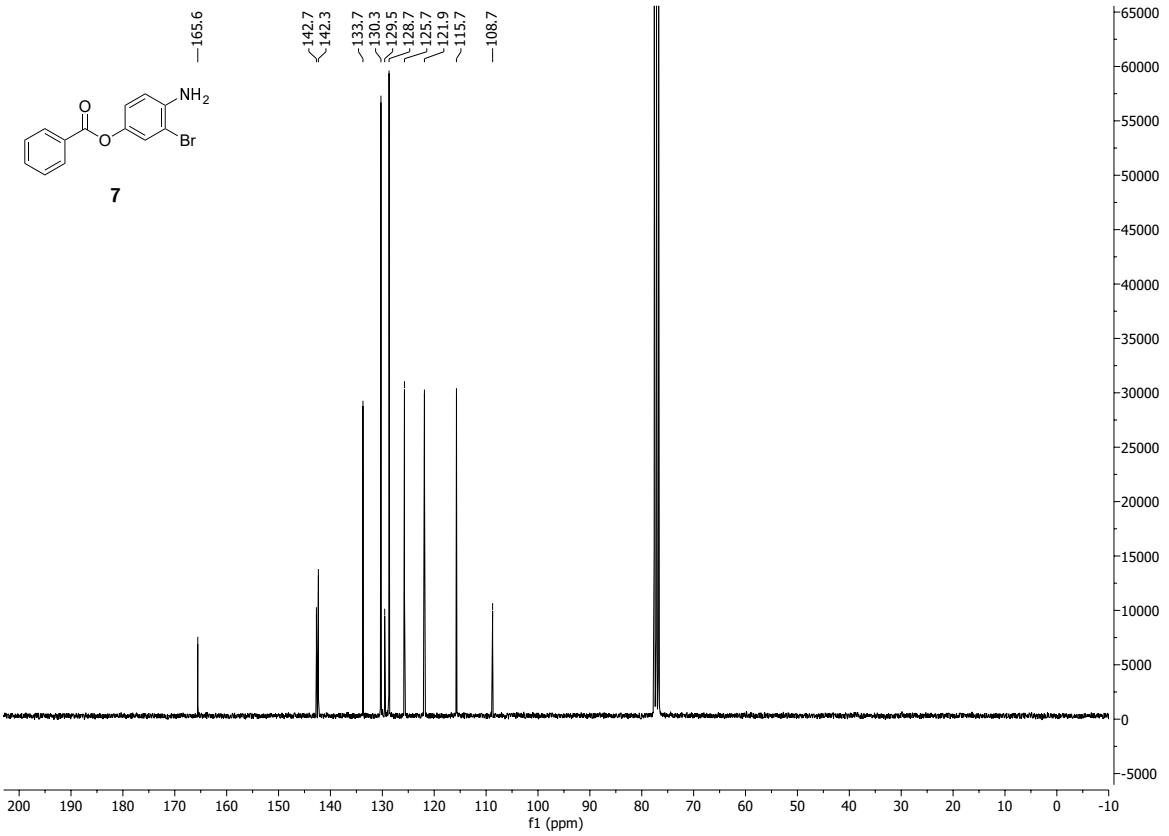

^{13}C NMR (75 MHz, $CDCl_3$) spectrum of
4-amino-3-bromophenyl benzoate **7**.

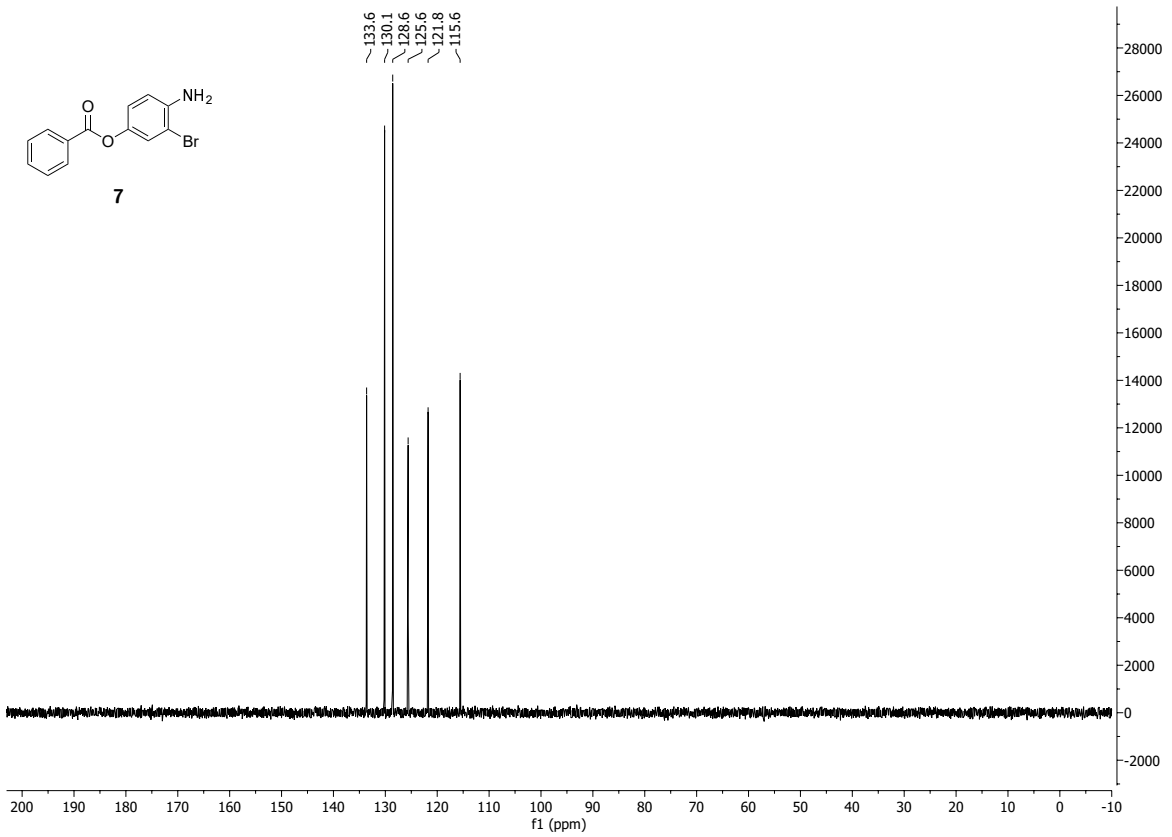

^{13}C DEPT 135 NMR (75 MHz, $CDCl_3$) spectrum of
4-amino-3-bromophenyl benzoate **7**.

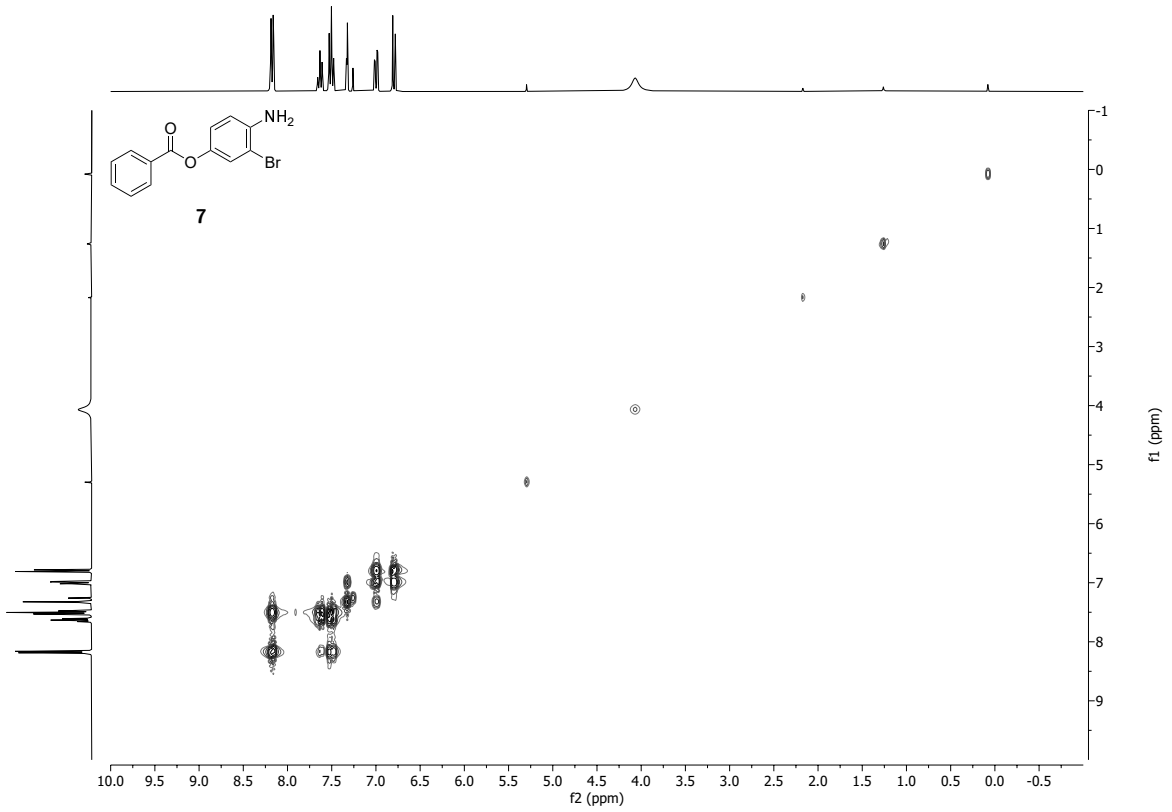

^{1}H ^{1}H COSY NMR (300 MHz, 300 MHz, $CDCl_3$) spectrum of
4-amino-3-bromophenyl benzoate **7**.

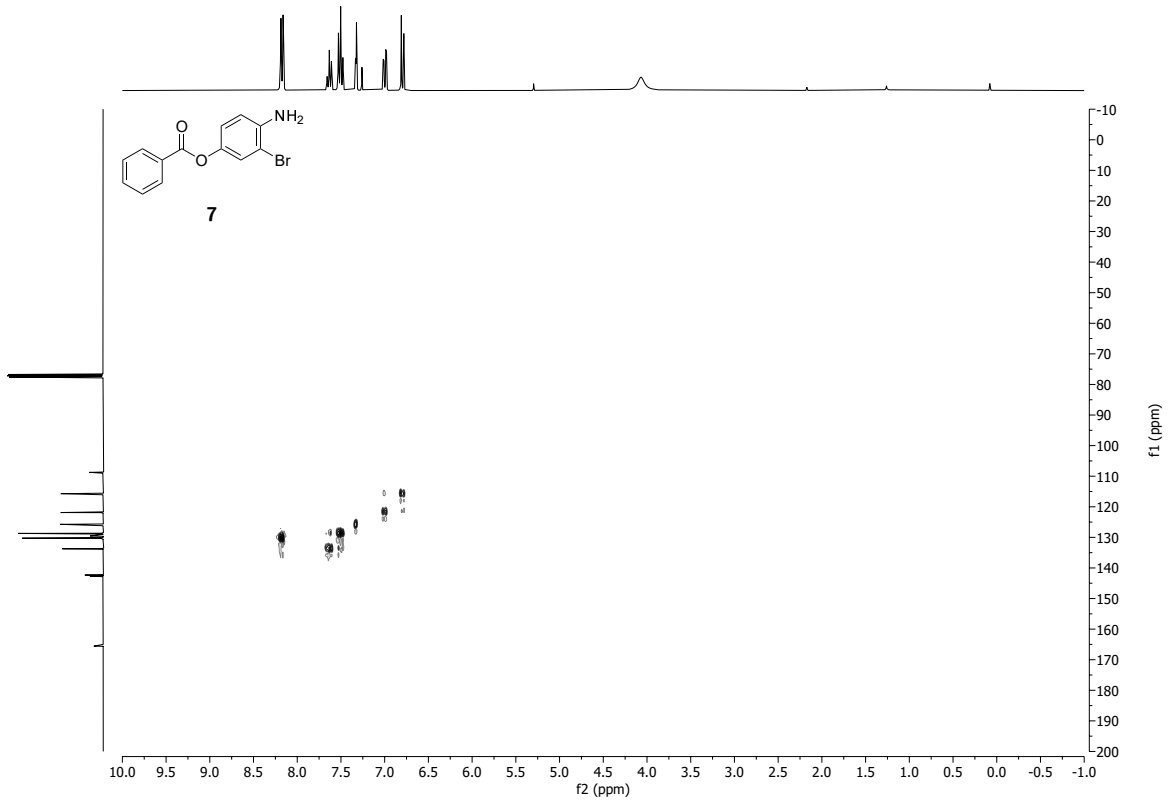

^{1}H ^{13}C HSQC NMR (300 MHz, 75 MHz, $CDCl_3$) spectrum of 4-amino-3-bromophenyl benzoate **7**.

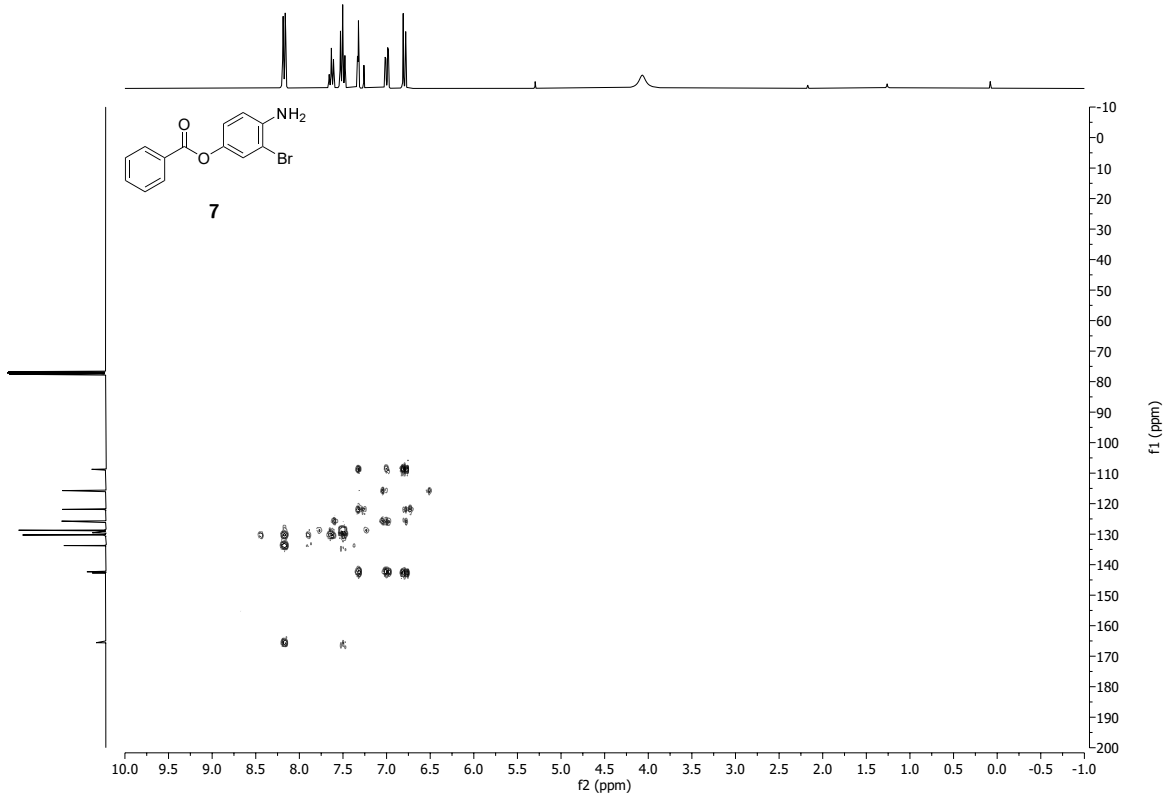

^{1}H ^{13}C HMBC NMR (300 MHz, 75 MHz, $CDCl_3$) spectrum of 4-amino-3-bromophenyl benzoate **7**.

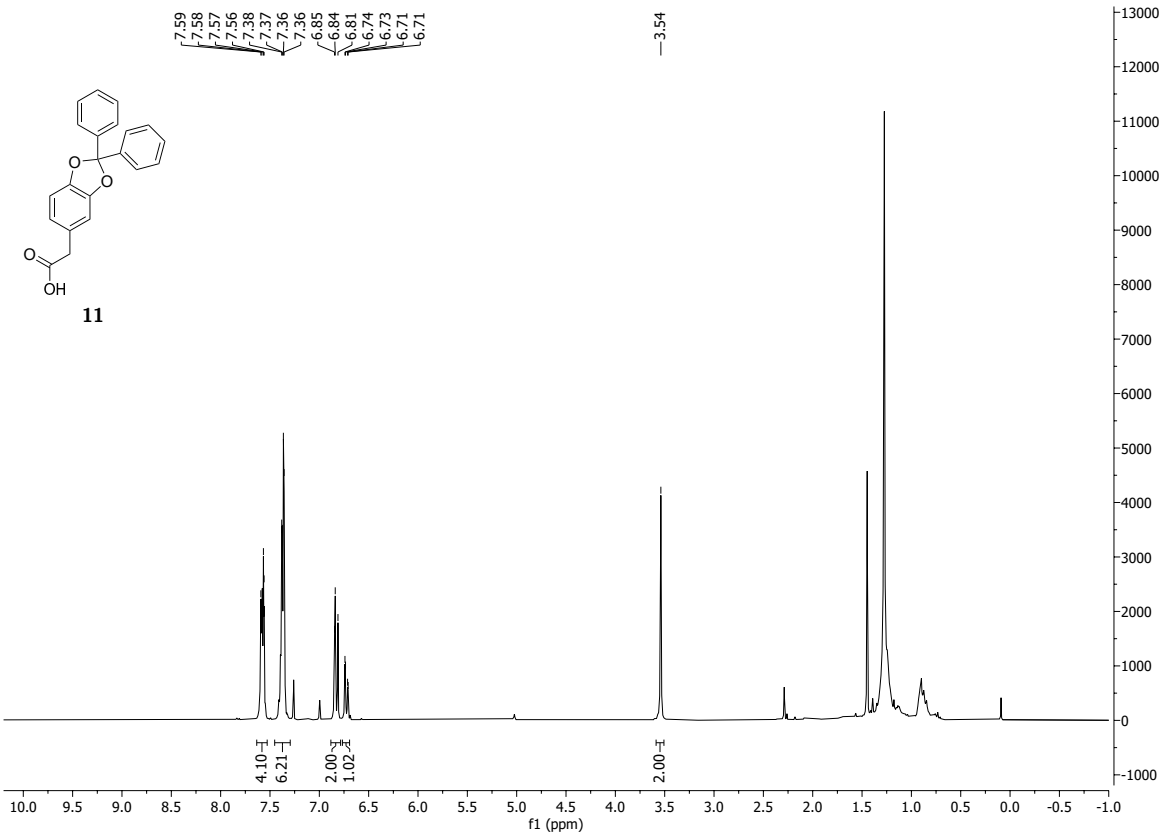

^{1}H NMR (300 MHz, $CDCl_3$) spectrum of
2-(2,2-diphenylbenzo[*d*][1,3]dioxol-5-yl)acetic acid **11**.

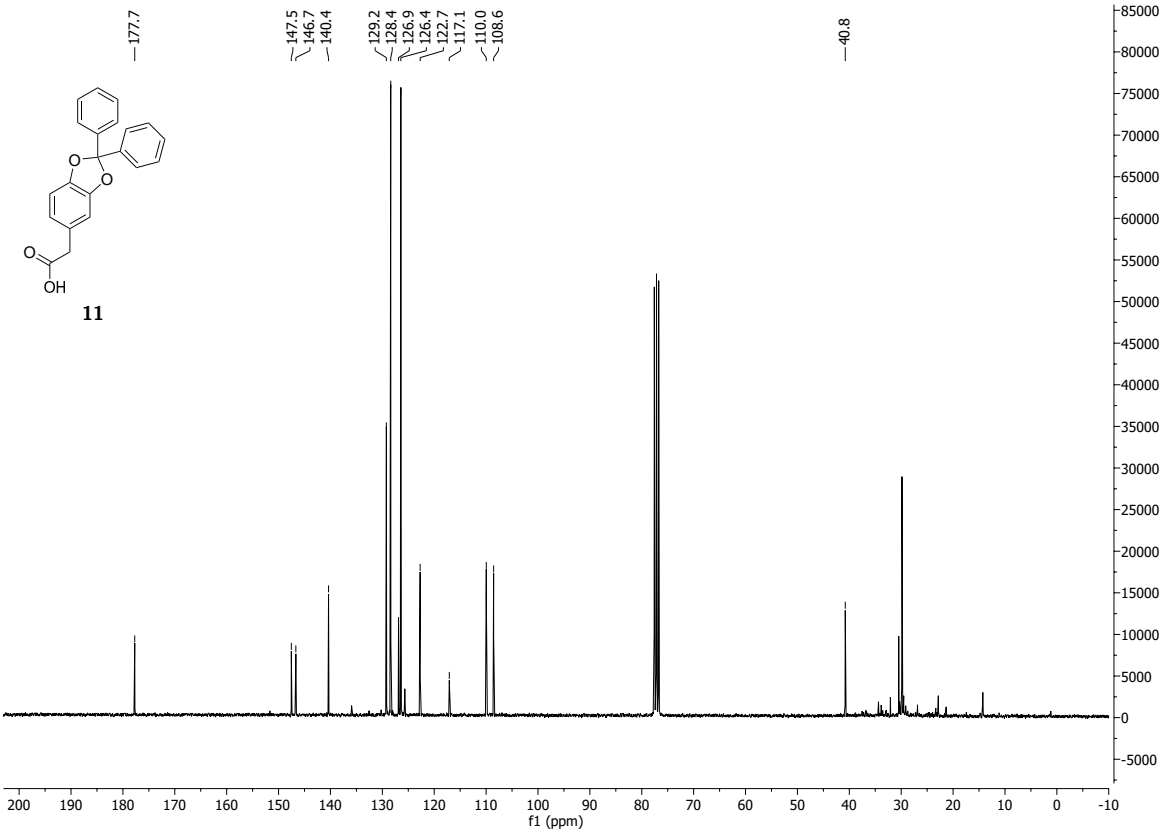

^{13}C NMR (75 MHz, $CDCl_3$) spectrum of
2-(2,2-diphenylbenzo[*d*][1,3]dioxol-5-yl)acetic acid **11**.

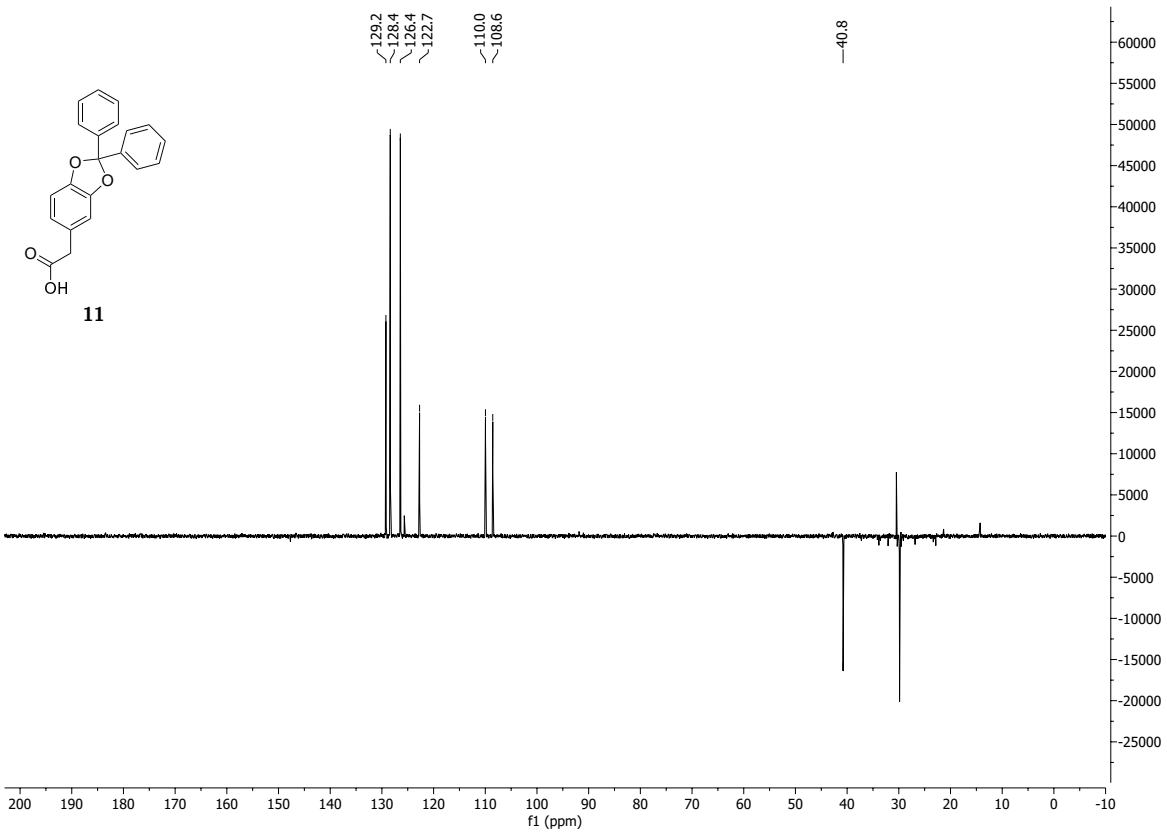

^{13}C DEPT 135 NMR (75 MHz, $CDCl_3$) spectrum of 2-(2,2-diphenylbenzo[*d*][1,3]dioxol-5-yl)acetic acid **11**.

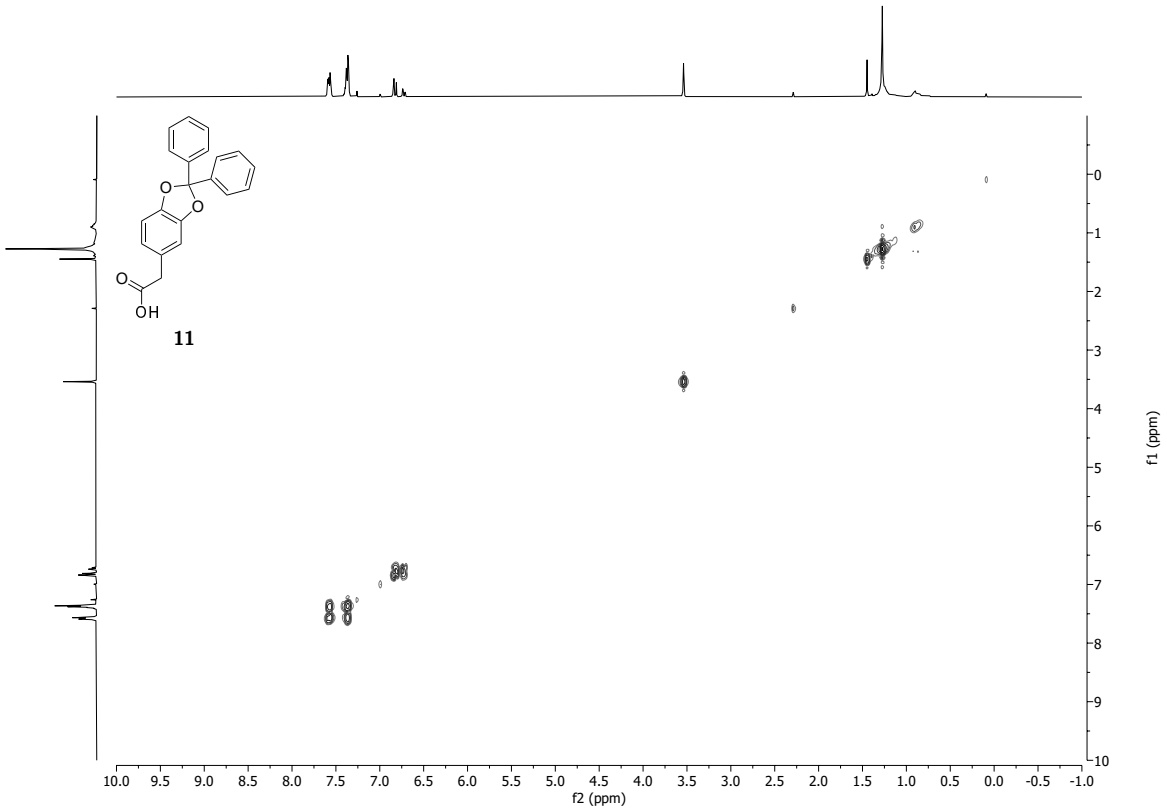

^{1}H ^{1}H COSY NMR (300 MHz, 300 MHz, $CDCl_3$) spectrum of 2-(2,2-diphenylbenzo[*d*][1,3]dioxol-5-yl)acetic acid **11**.

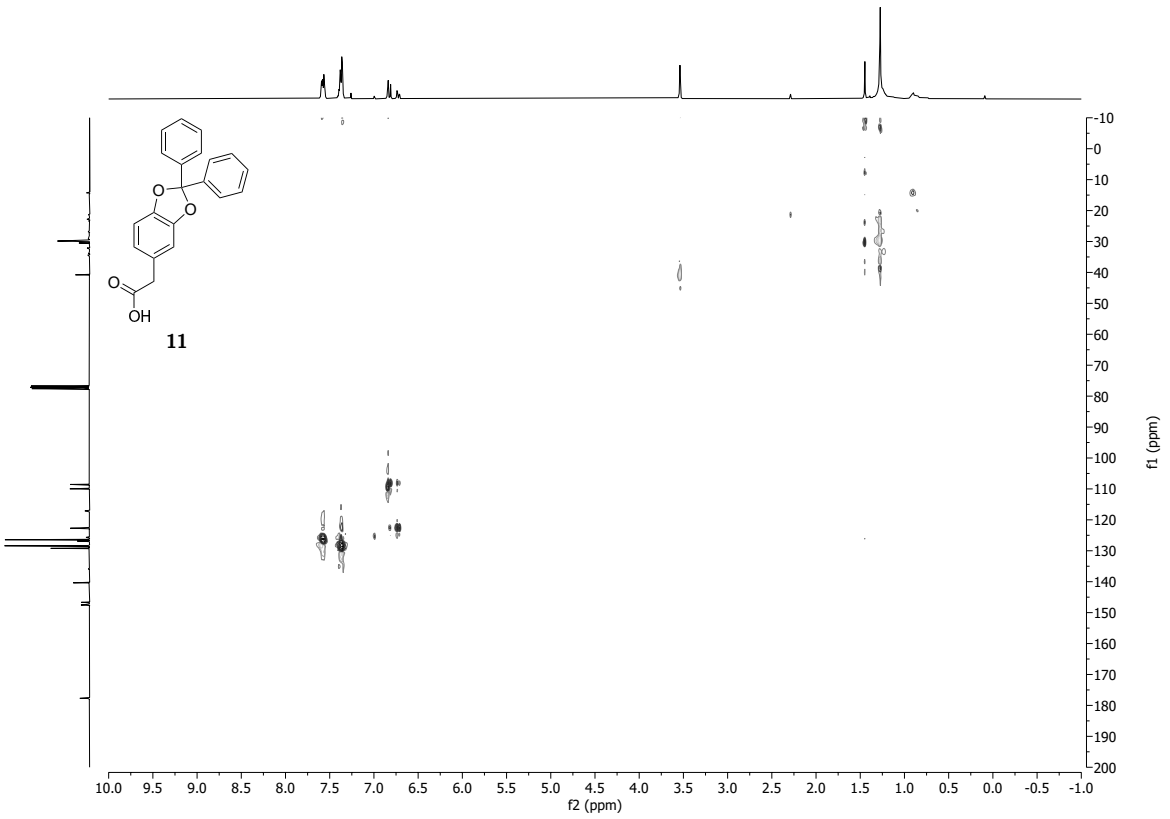

^{1}H ^{13}C HSQC NMR (300 MHz, 75 MHz, $CDCl_3$) spectrum of 2-(2,2-diphenylbenzo[*d*][1,3]dioxol-5-yl)acetic acid **11**.

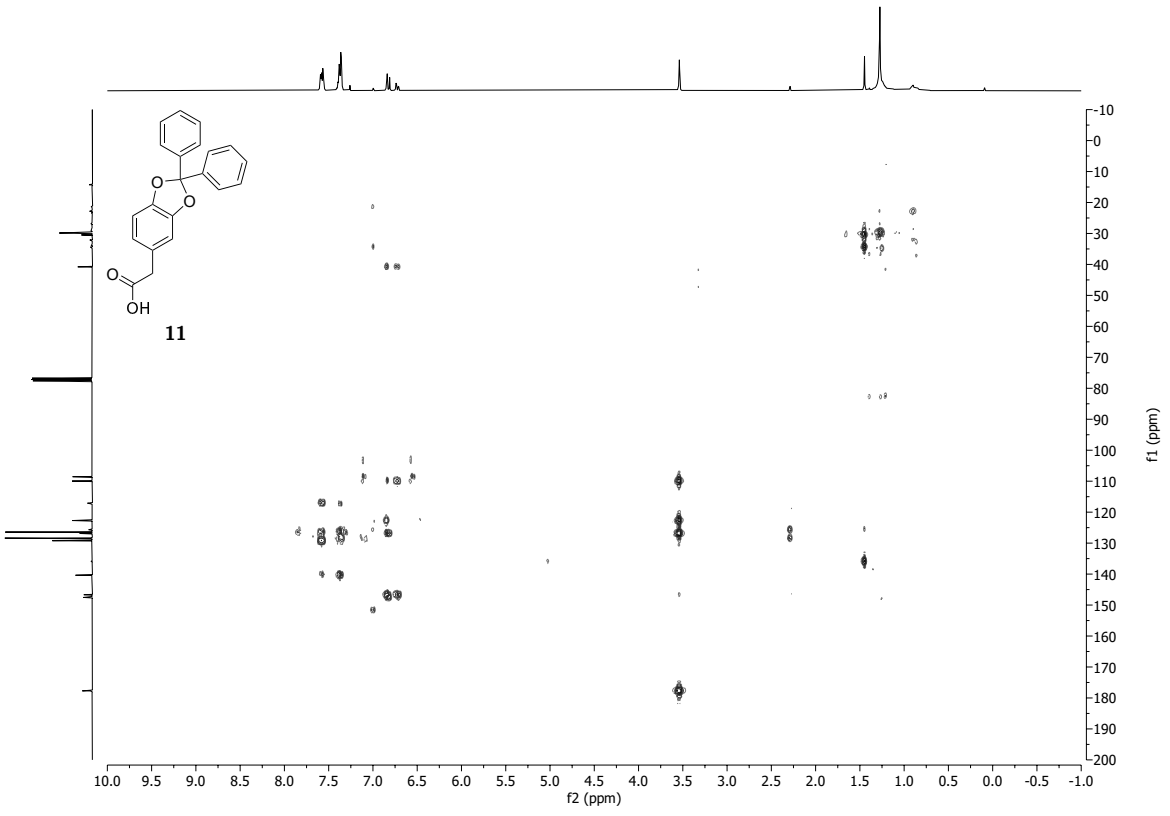

^{1}H ^{13}C HMBC NMR (300 MHz, 75 MHz, $CDCl_3$) spectrum of 2-(2,2-diphenylbenzo[*d*][1,3]dioxol-5-yl)acetic acid **11**.

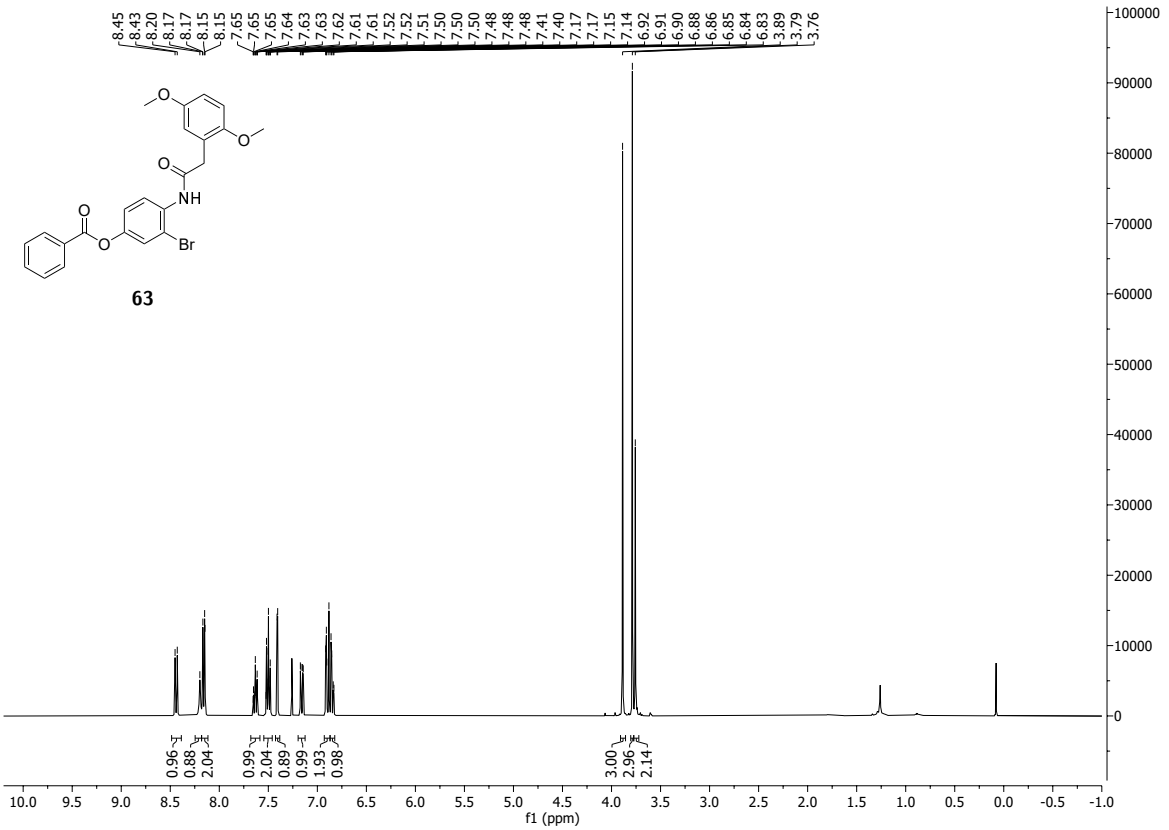

^{1}H NMR (400 MHz, $CDCl_3$) spectrum of
3-bromo-4-(2-(2,5-dimethoxyphenyl)acetamido)phenyl benzoate **63**.

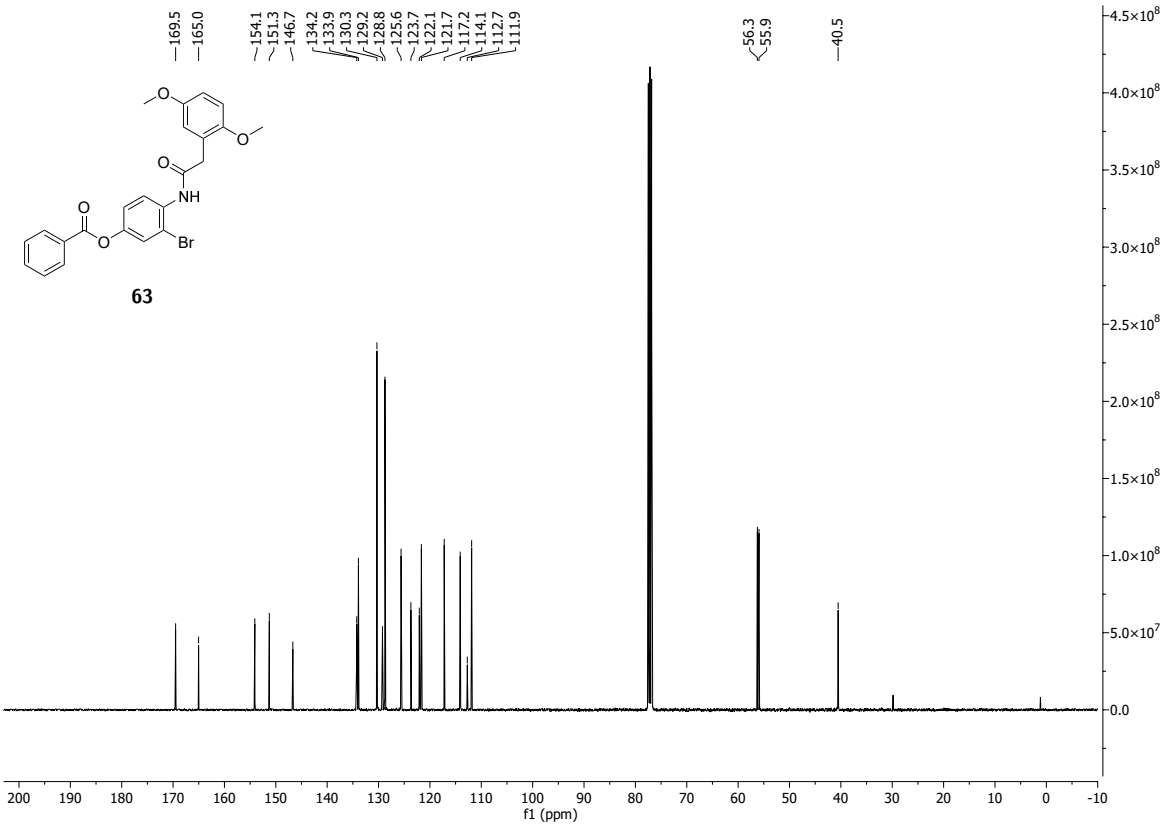

^{13}C NMR (100 MHz, $CDCl_3$) spectrum of
3-bromo-4-(2-(2,5-dimethoxyphenyl)acetamido)phenyl benzoate **63**.

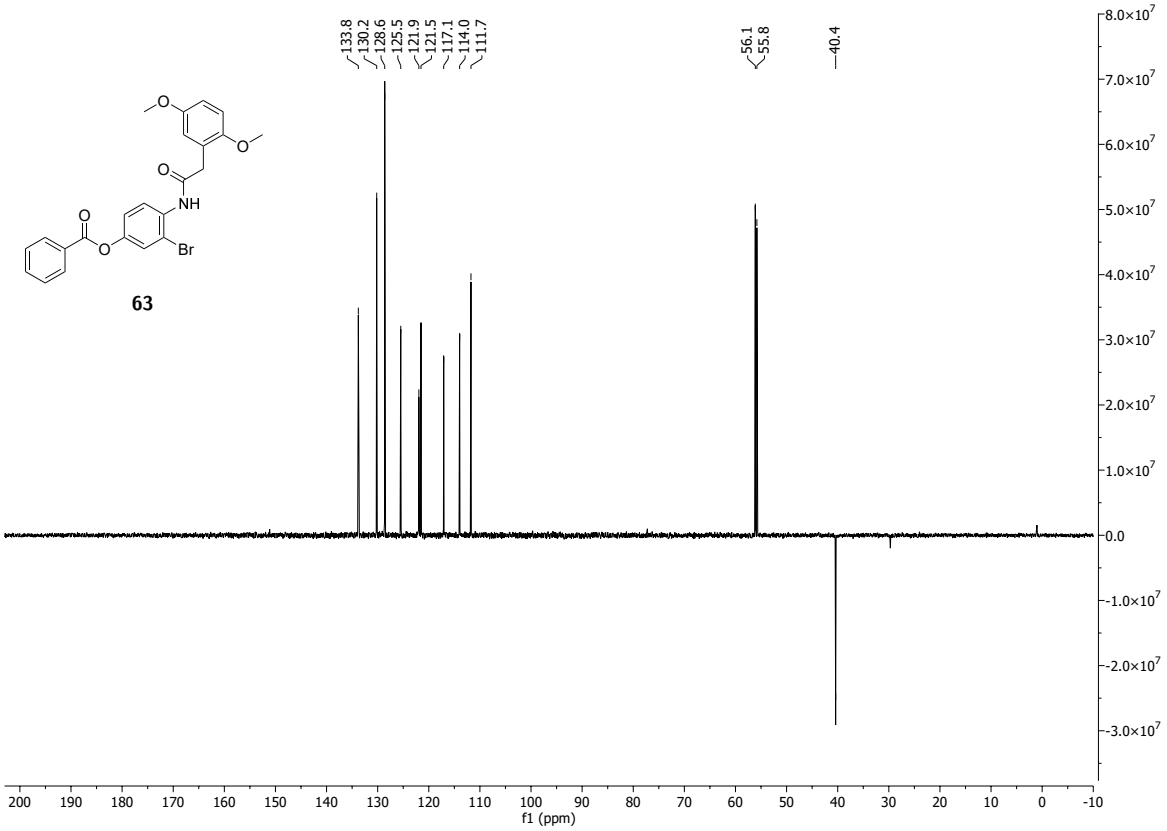

^{13}C DEPT 135 NMR (100 MHz, $CDCl_3$) spectrum of 3-bromo-4-(2-(2,5-dimethoxyphenyl)acetamido)phenyl benzoate **63**.

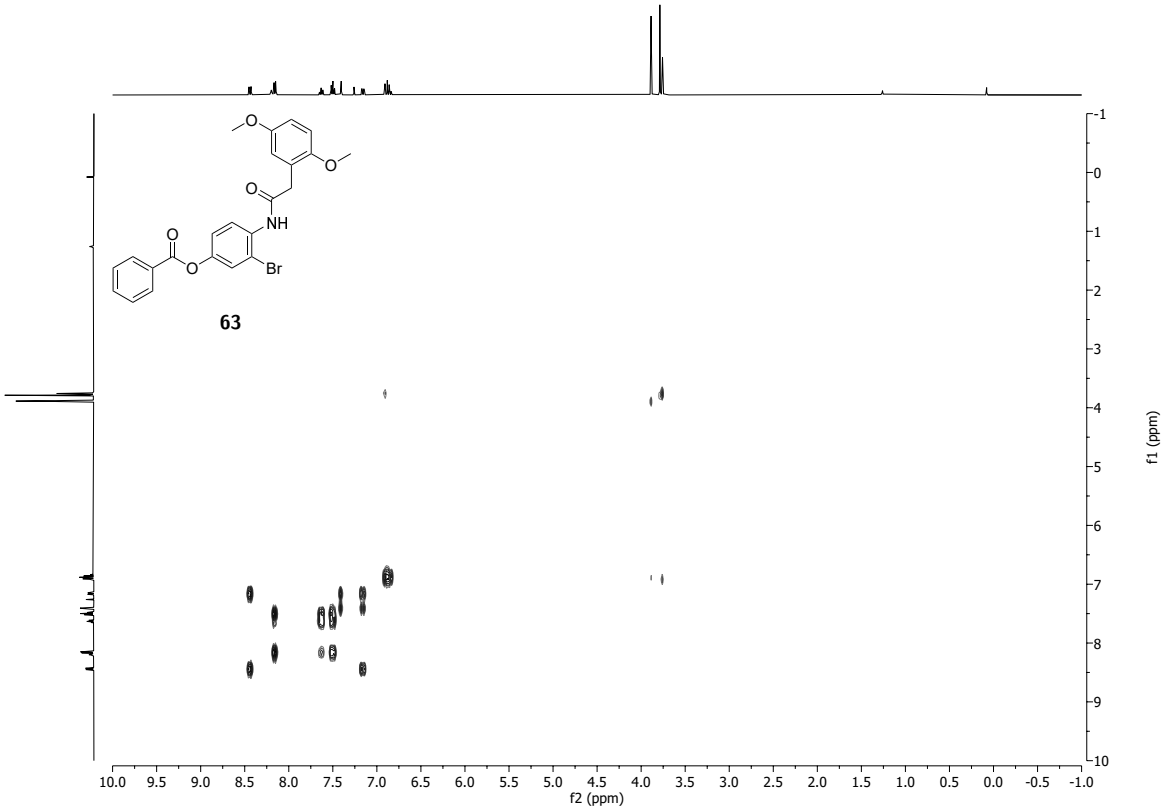

^{1}H ^{1}H COSY NMR (400 MHz, 400 MHz, $CDCl_3$) spectrum of 3-bromo-4-(2-(2,5-dimethoxyphenyl)acetamido)phenyl benzoate **63**.

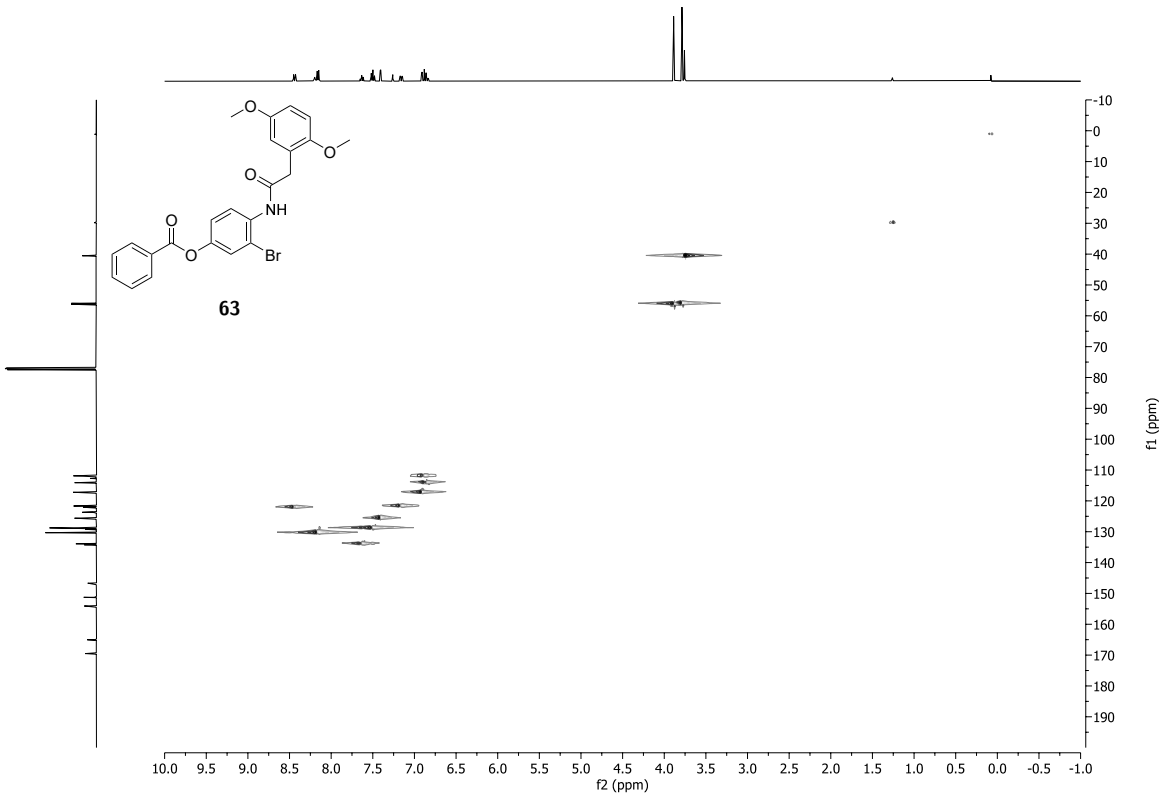

^{1}H ^{13}C HSQC NMR (400 MHz, 100 MHz, $CDCl_3$) spectrum of 3-bromo-4-(2-(2,5-dimethoxyphenyl)acetamido)phenyl benzoate **63**.

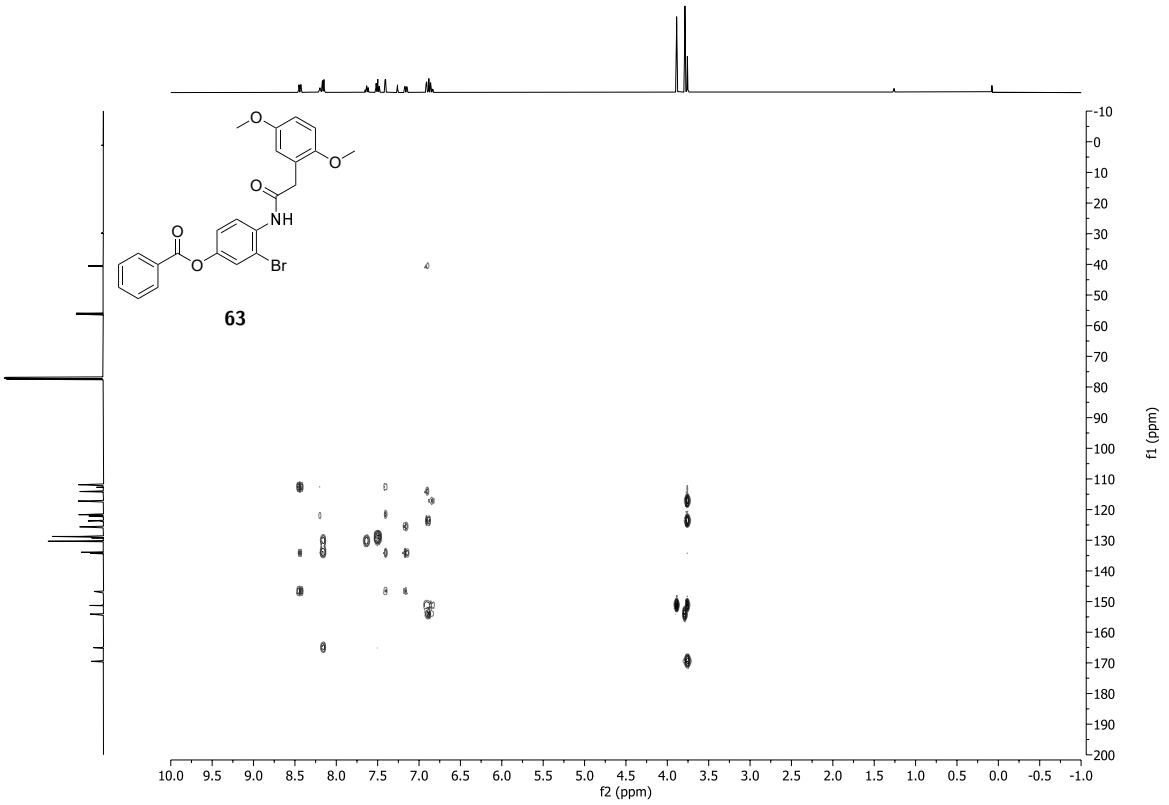

^{1}H ^{13}C HMBC NMR (400 MHz, 100 MHz, $CDCl_3$) spectrum of 3-bromo-4-(2-(2,5-dimethoxyphenyl)acetamido)phenyl benzoate **63**.

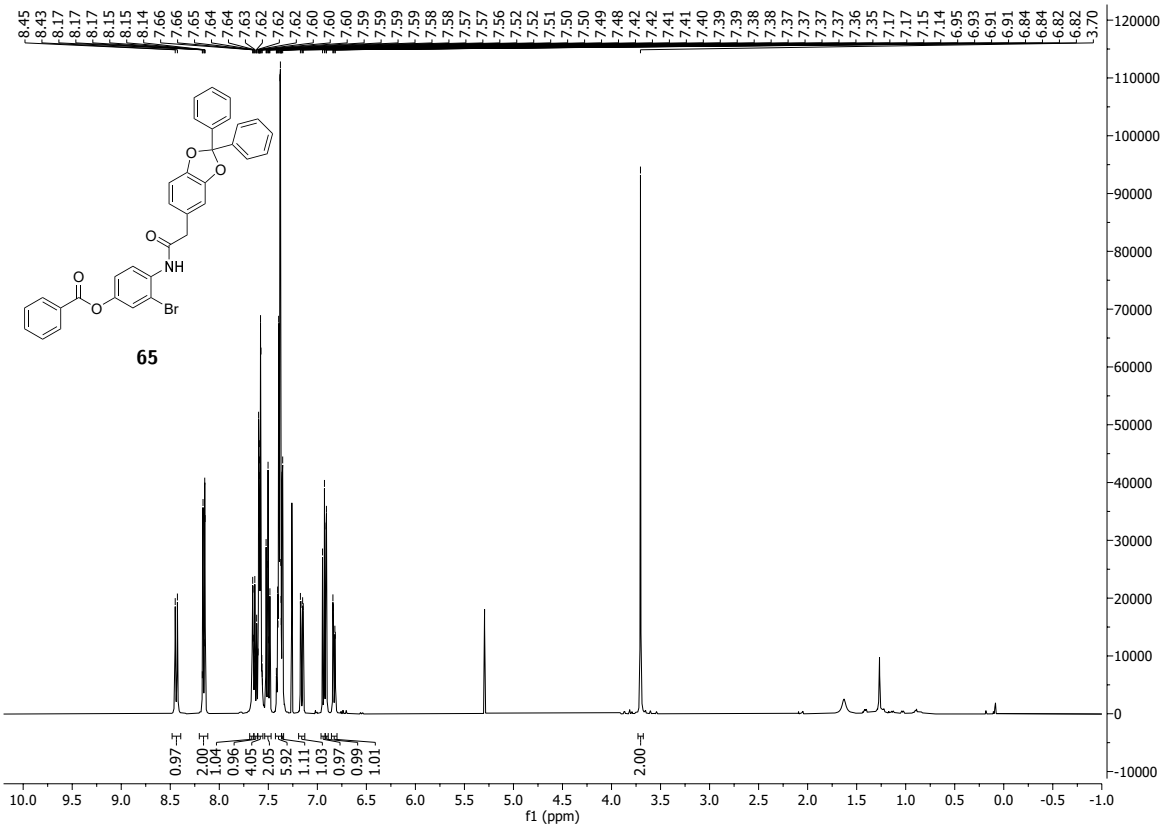

^{1}H NMR (400 MHz, $CDCl_3$) spectrum of
3-bromo-4-(2-(2,2-diphenylbenzo[*d*][1,3]dioxol-5-yl)acetamido)phenyl benzoate **65**.

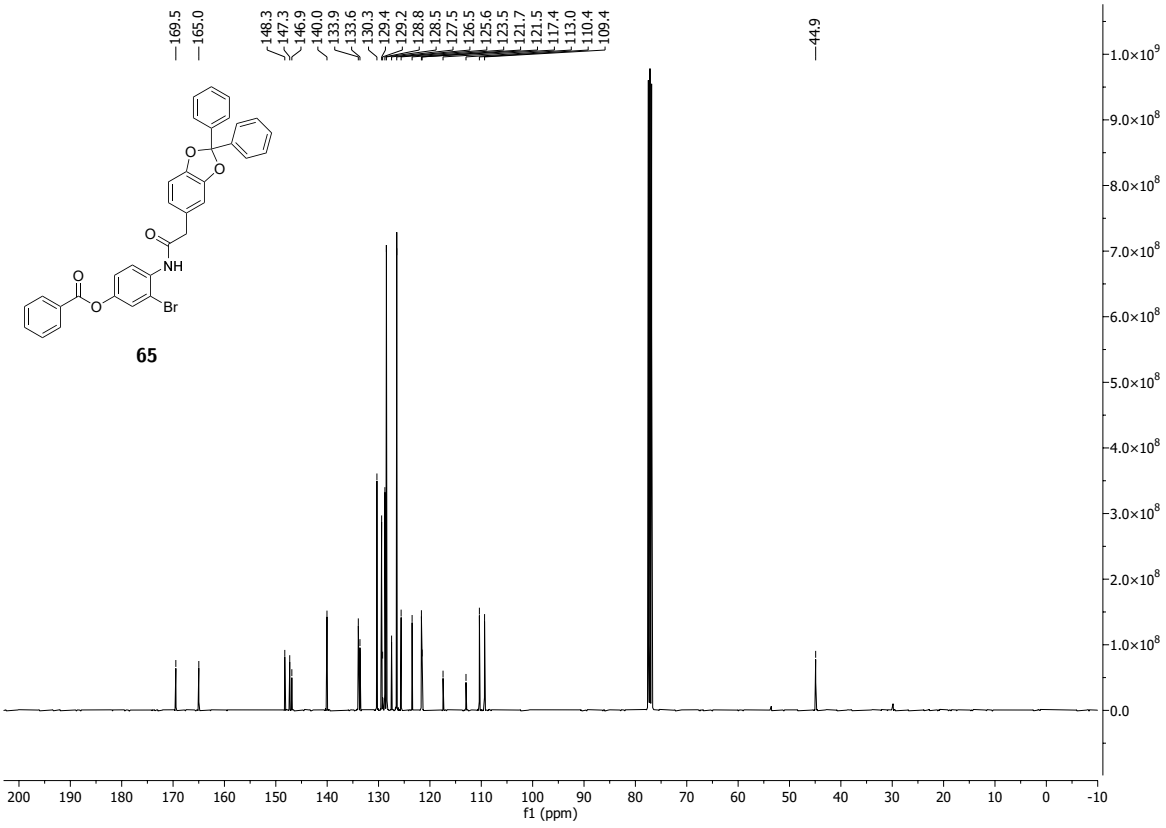

^{13}C NMR (100 MHz, $CDCl_3$) spectrum of
3-bromo-4-(2-(2,2-diphenylbenzo[*d*][1,3]dioxol-5-yl)acetamido)phenyl benzoate **65**.

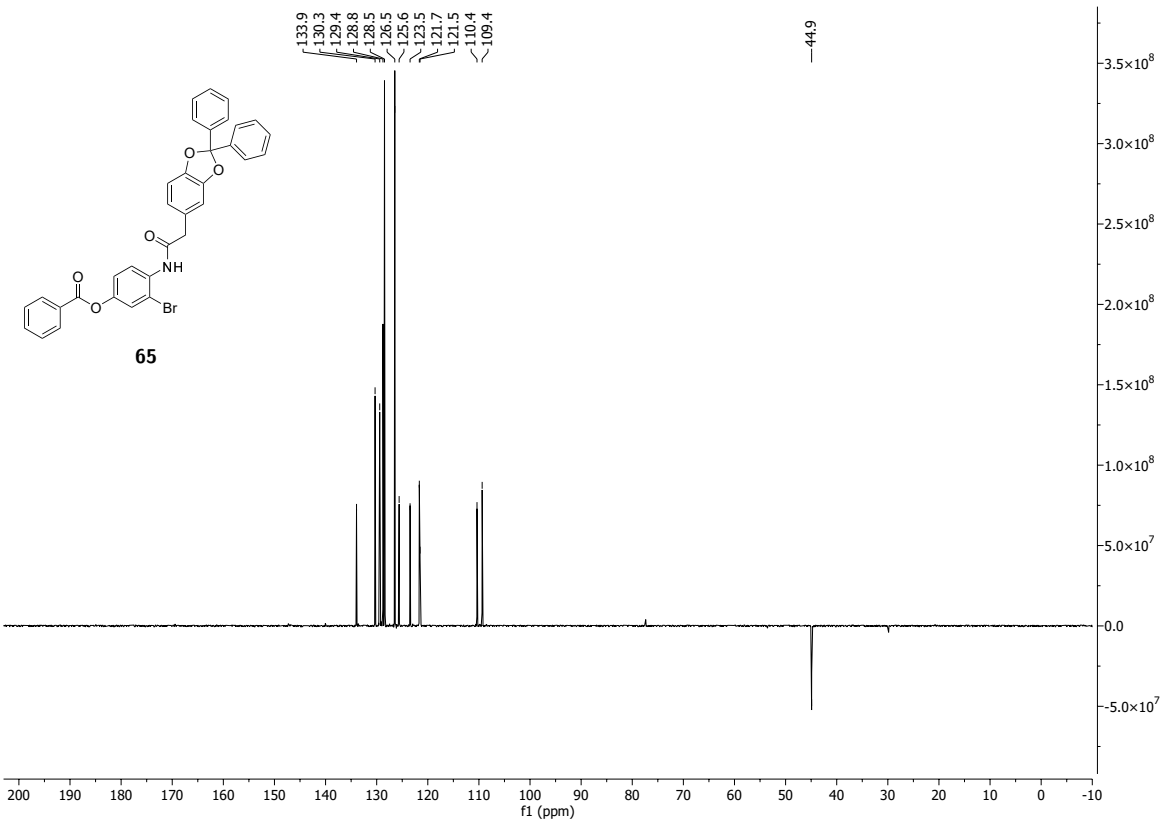

^{13}C DEPT 135 NMR (100 MHz, $CDCl_3$) spectrum of 3-bromo-4-(2-(2,2-diphenylbenzo[*d*][1,3]dioxol-5-yl)acetamido)phenyl benzoate **65**.

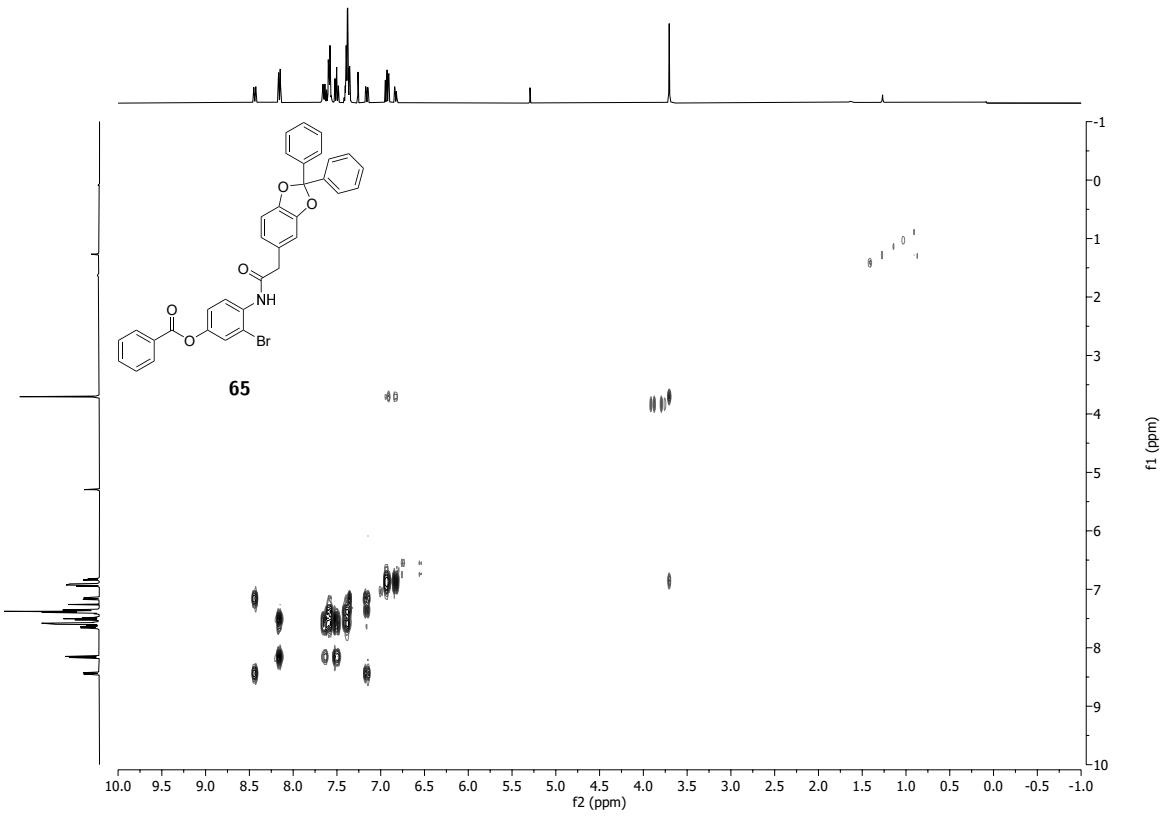

^{1}H ^{1}H COSY NMR (400 MHz, 400 MHz, $CDCl_3$) spectrum of 3-bromo-4-(2-(2,2-diphenylbenzo[*d*][1,3]dioxol-5-yl)acetamido)phenyl benzoate **65**.

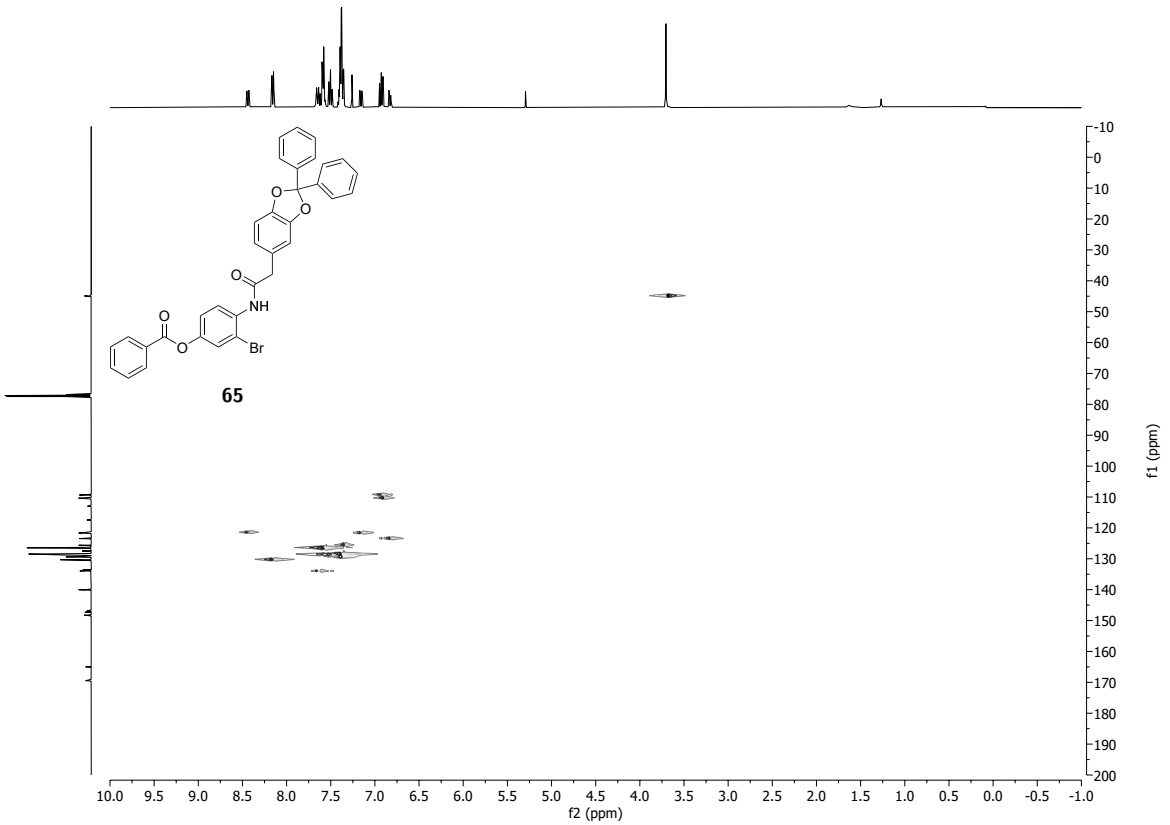

^{1}H ^{13}C HSQC NMR (400 MHz, 100 MHz, $CDCl_3$) spectrum of 3-bromo-4-(2-(2,2-diphenylbenzo[*d*][1,3]dioxol-5-yl)acetamido)phenyl benzoate **65**.

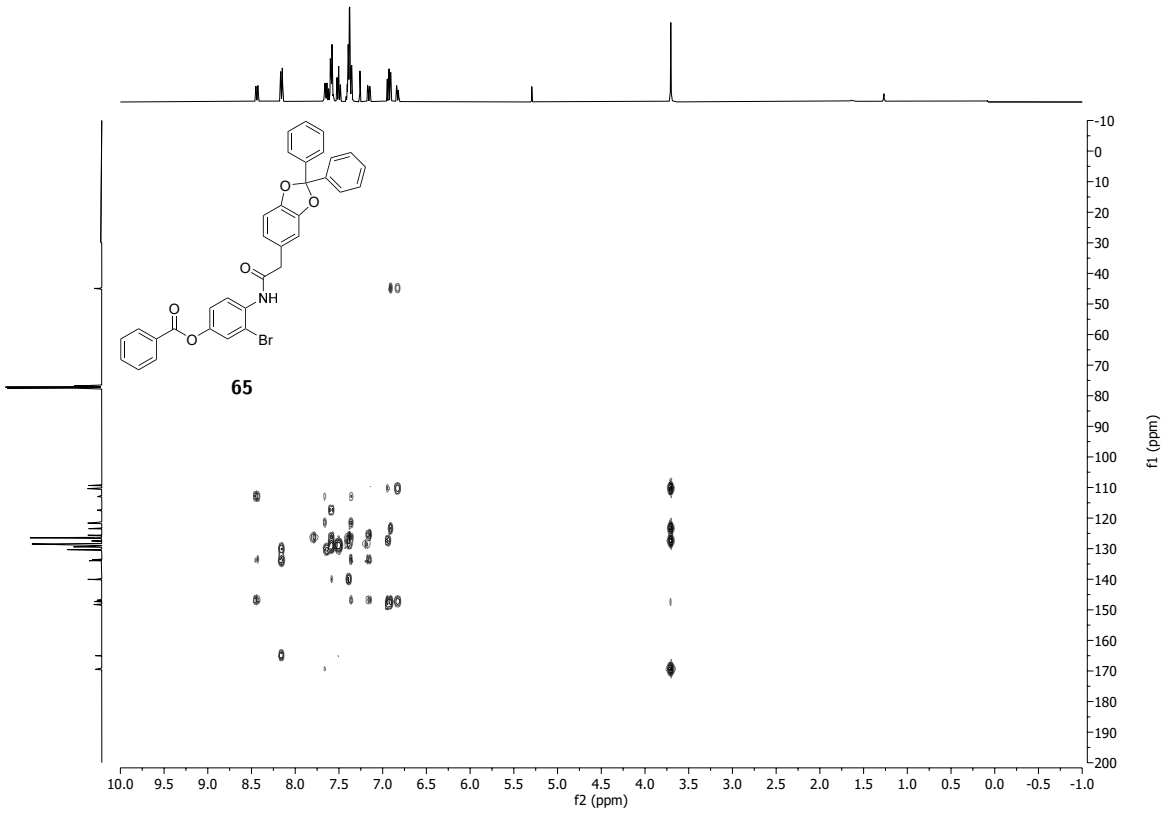

^{1}H ^{13}C HMBC NMR (400 MHz, 100 MHz, $CDCl_3$) spectrum of 3-bromo-4-(2-(2,2-diphenylbenzo[*d*][1,3]dioxol-5-yl)acetamido)phenyl benzoate **65**.

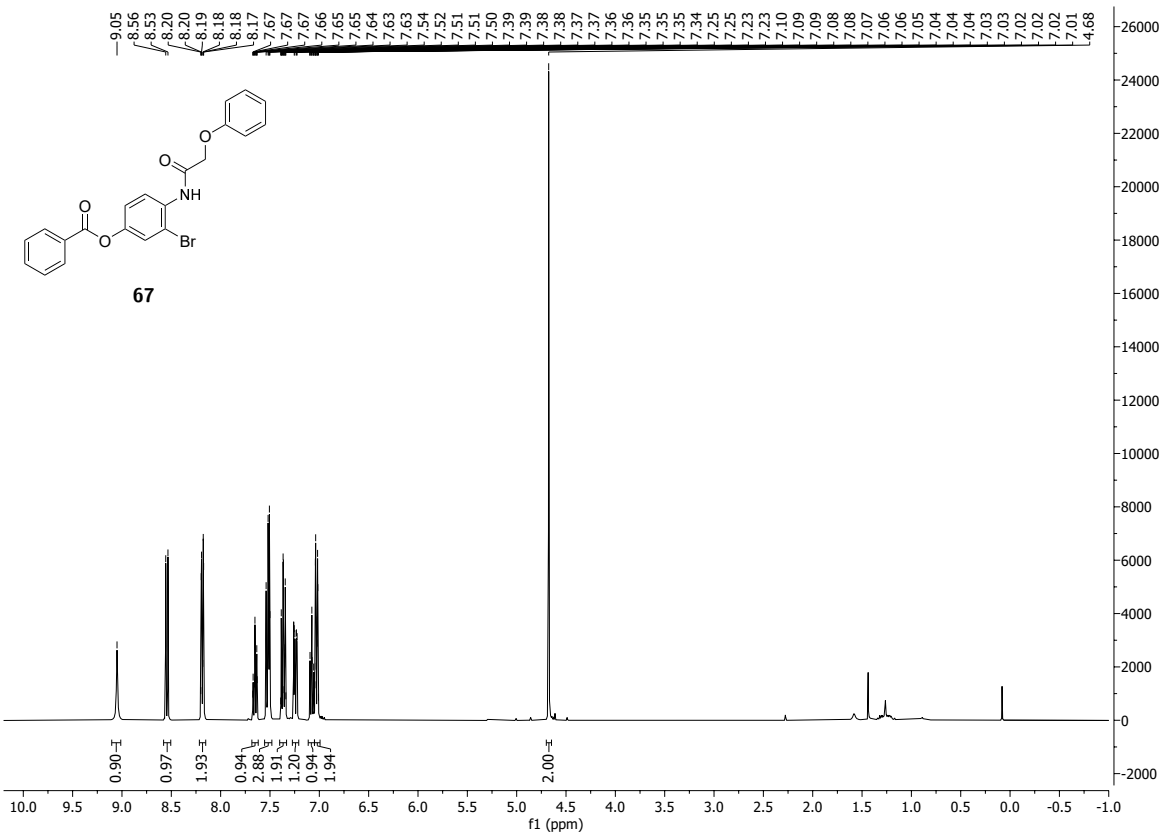

^{1}H NMR (400 MHz, $CDCl_3$) spectrum of
3-bromo-4-(2-phenoxyacetamido)phenyl benzoate **67**.

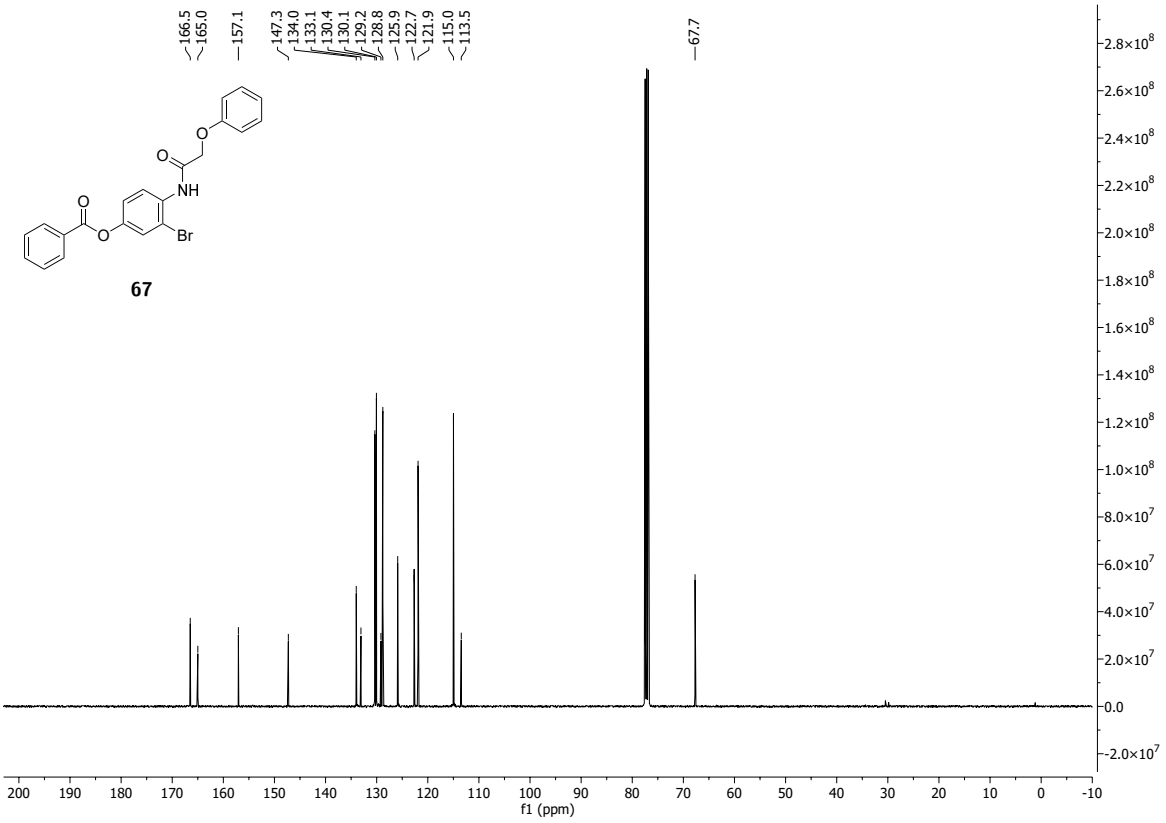

^{13}C NMR (100 MHz, $CDCl_3$) spectrum of
3-bromo-4-(2-phenoxyacetamido)phenyl benzoate **67**.

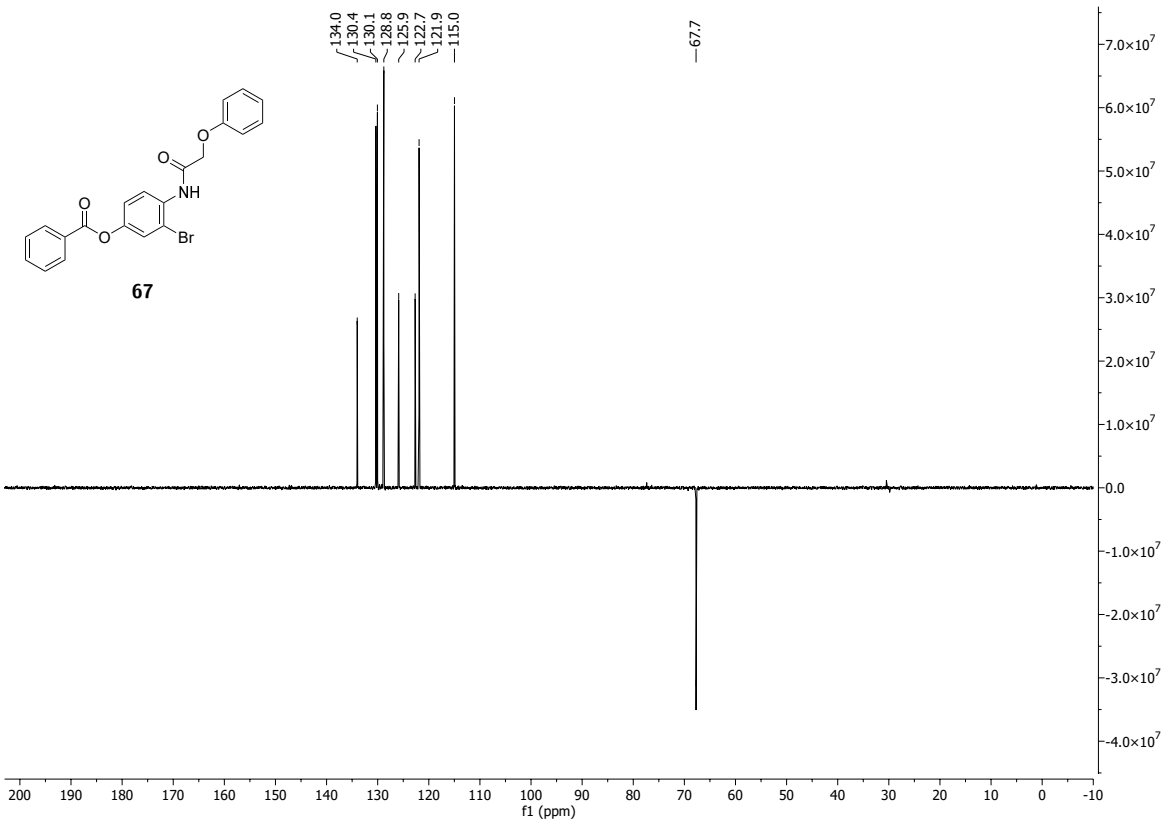

^{13}C DEPT 135 NMR (100 MHz, $CDCl_3$) spectrum of 3-bromo-4-(2-phenoxyacetamido)phenyl benzoate **67**.

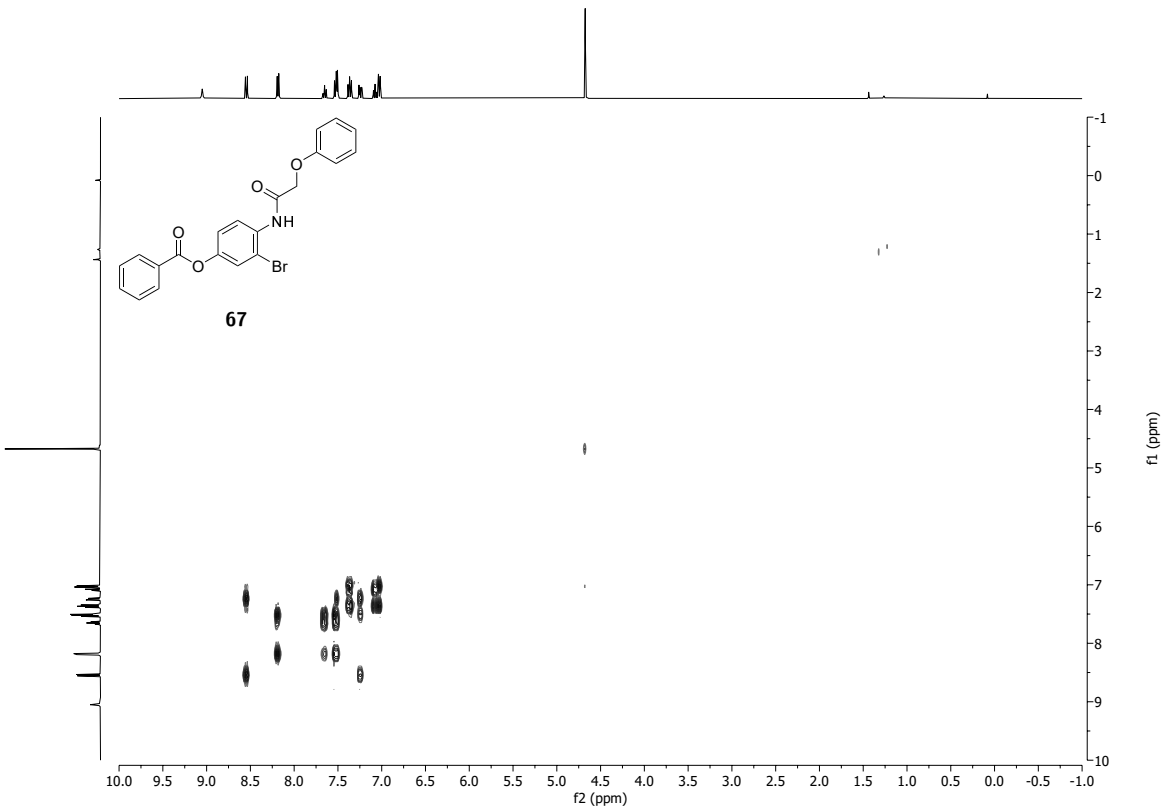

^{1}H ^{1}H COSY NMR (400 MHz, 400 MHz, $CDCl_3$) spectrum of 3-bromo-4-(2-phenoxyacetamido)phenyl benzoate **67**.

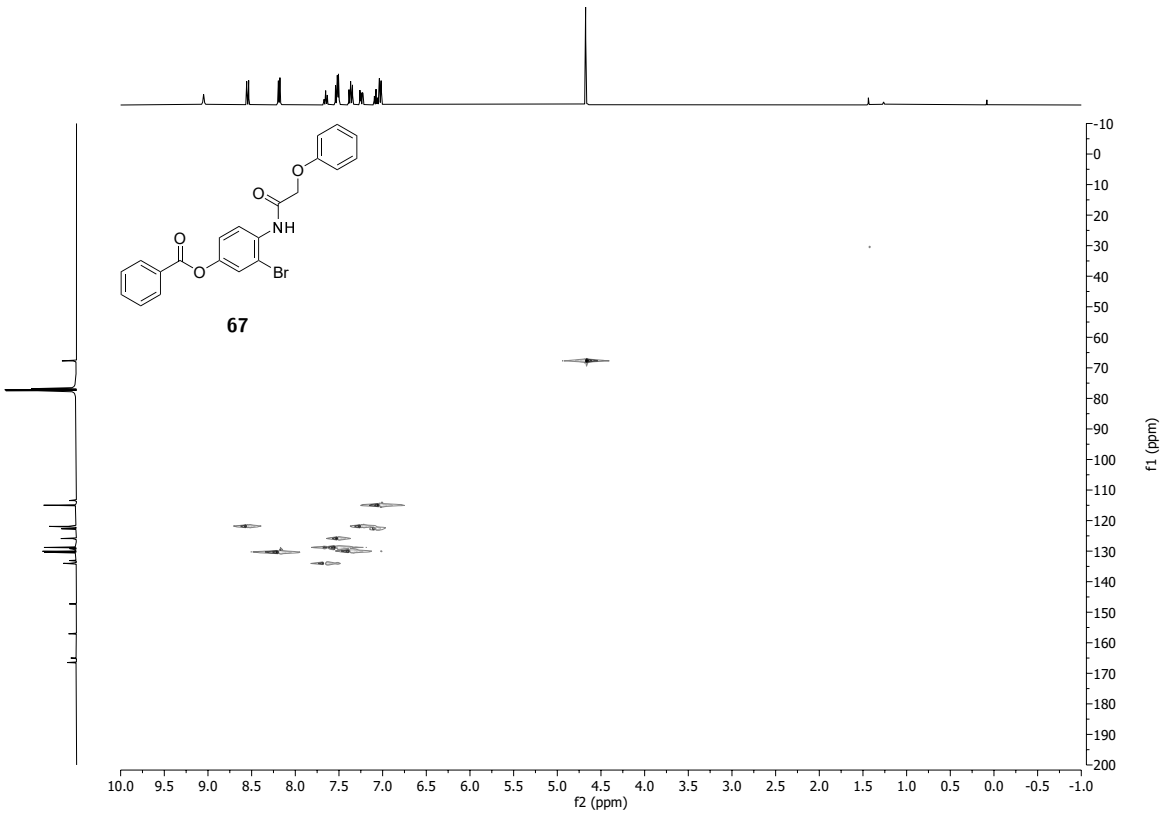

^{1}H ^{13}C HSQC NMR (400 MHz, 100 MHz, $CDCl_3$) spectrum of 3-bromo-4-(2-phenoxyacetamido)phenyl benzoate **67**.

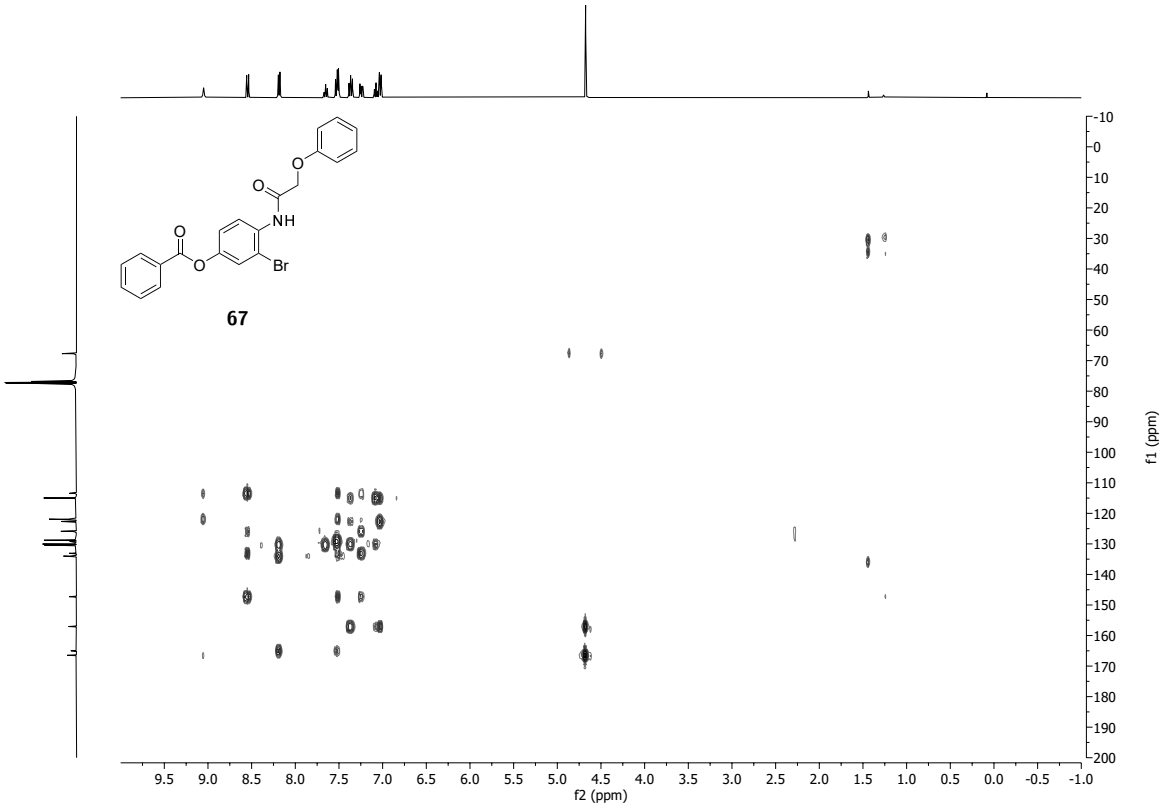

^{1}H ^{13}C HMBC NMR (400 MHz, 100 MHz, $CDCl_3$) spectrum of 3-bromo-4-(2-phenoxyacetamido)phenyl benzoate **67**.

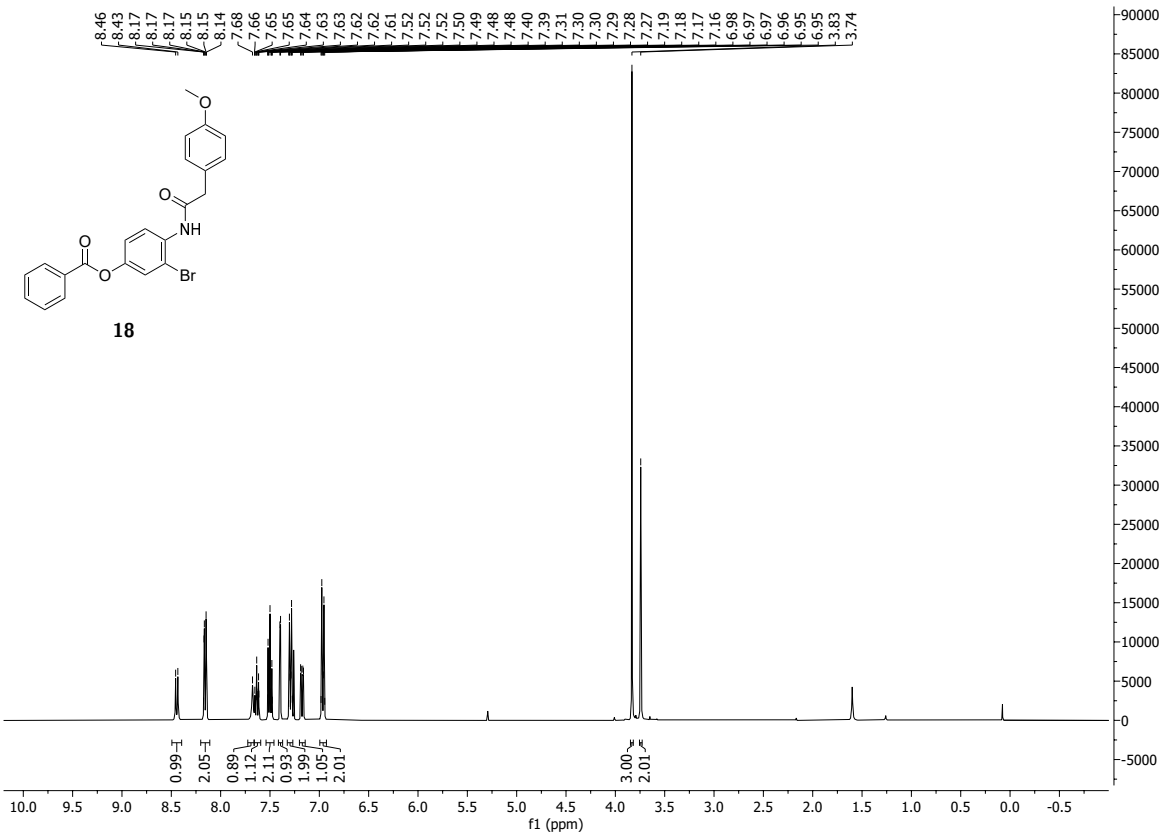

^{1}H NMR (400 MHz, $CDCl_3$) spectrum of
3-bromo-4-(2-(4-methoxyphenyl)acetamido)phenyl benzoate **18**.

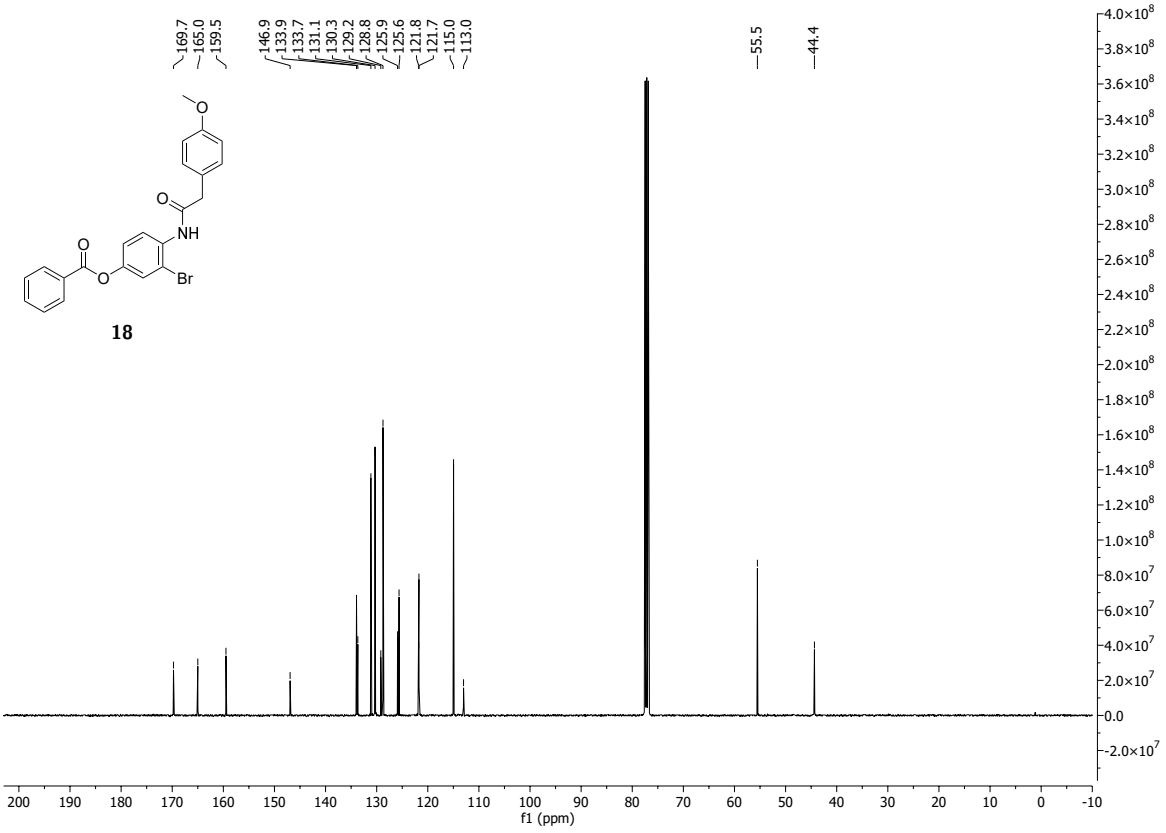

^{13}C NMR (100 MHz, $CDCl_3$) spectrum of
3-bromo-4-(2-(4-methoxyphenyl)acetamido)phenyl benzoate **18**.

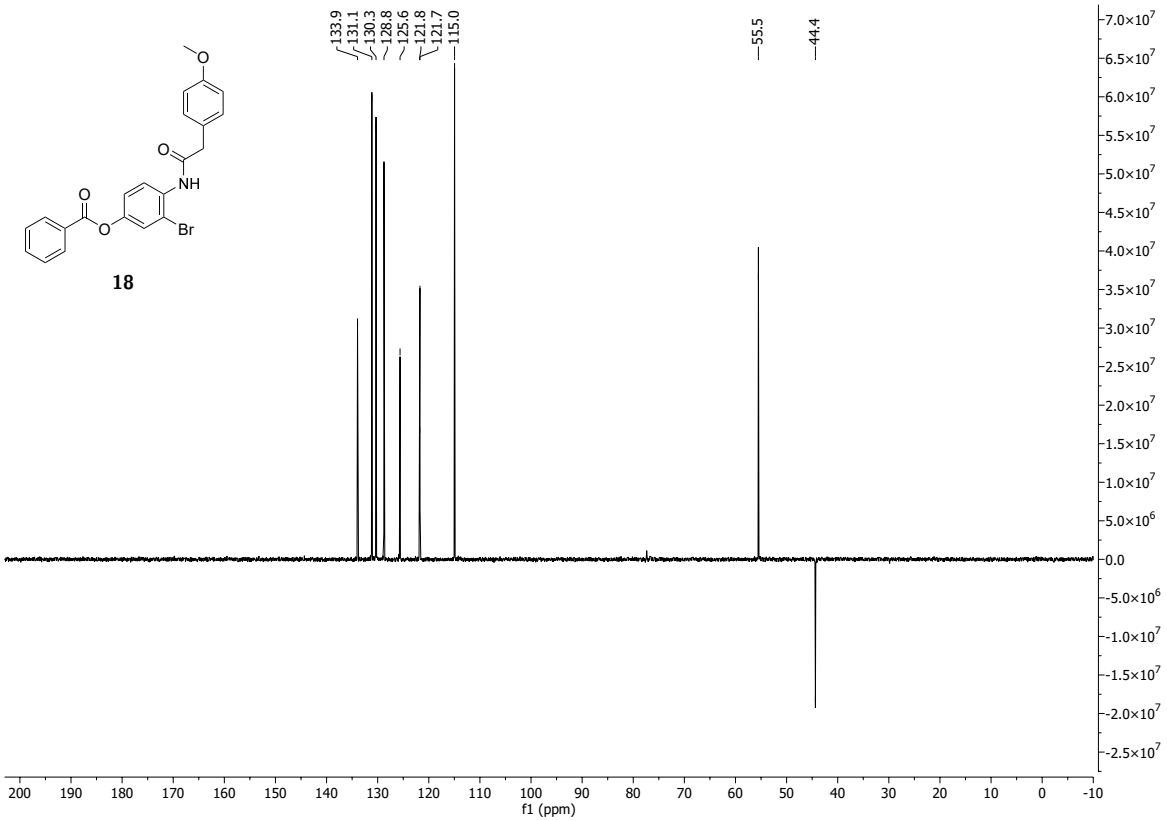

^{13}C DEPT 135 NMR (100 MHz, $CDCl_3$) spectrum of 3-bromo-4-(2-(4-methoxyphenyl)acetamido)phenyl benzoate **18**.

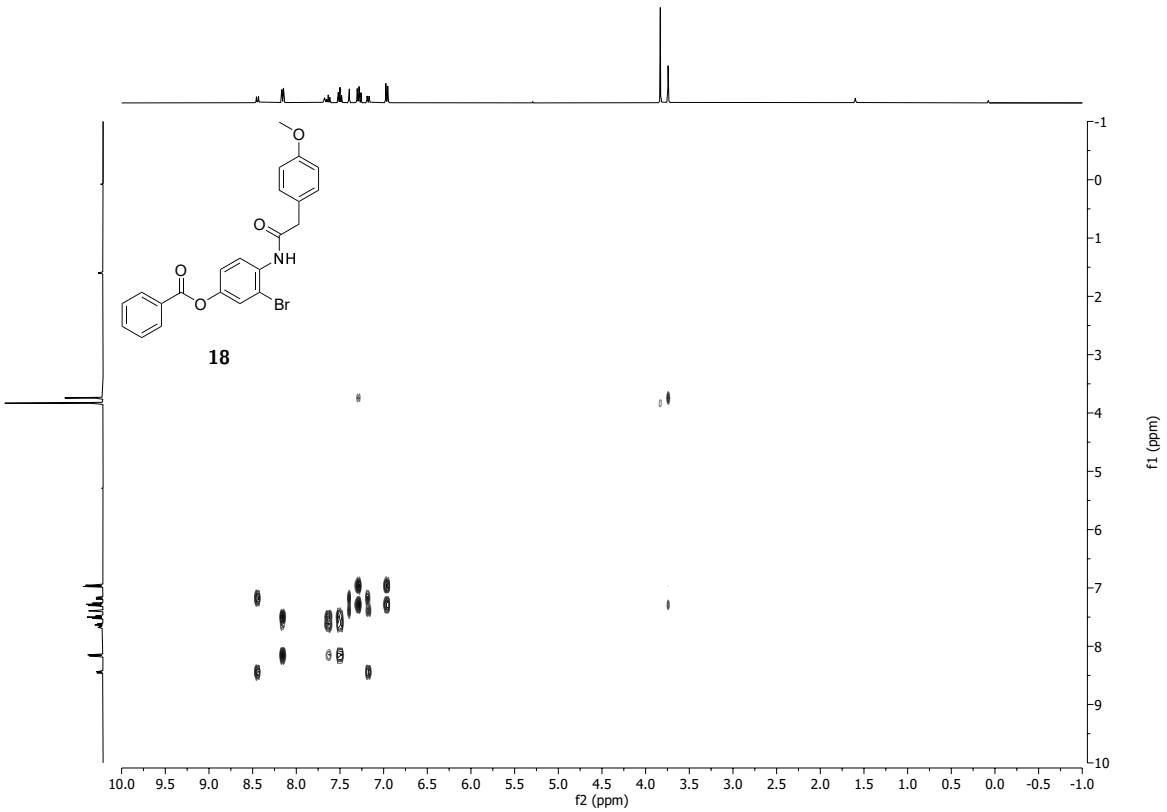

^{1}H ^{1}H COSY NMR (400 MHz, 400 MHz, $CDCl_3$) spectrum of 3-bromo-4-(2-(4-methoxyphenyl)acetamido)phenyl benzoate **18**.

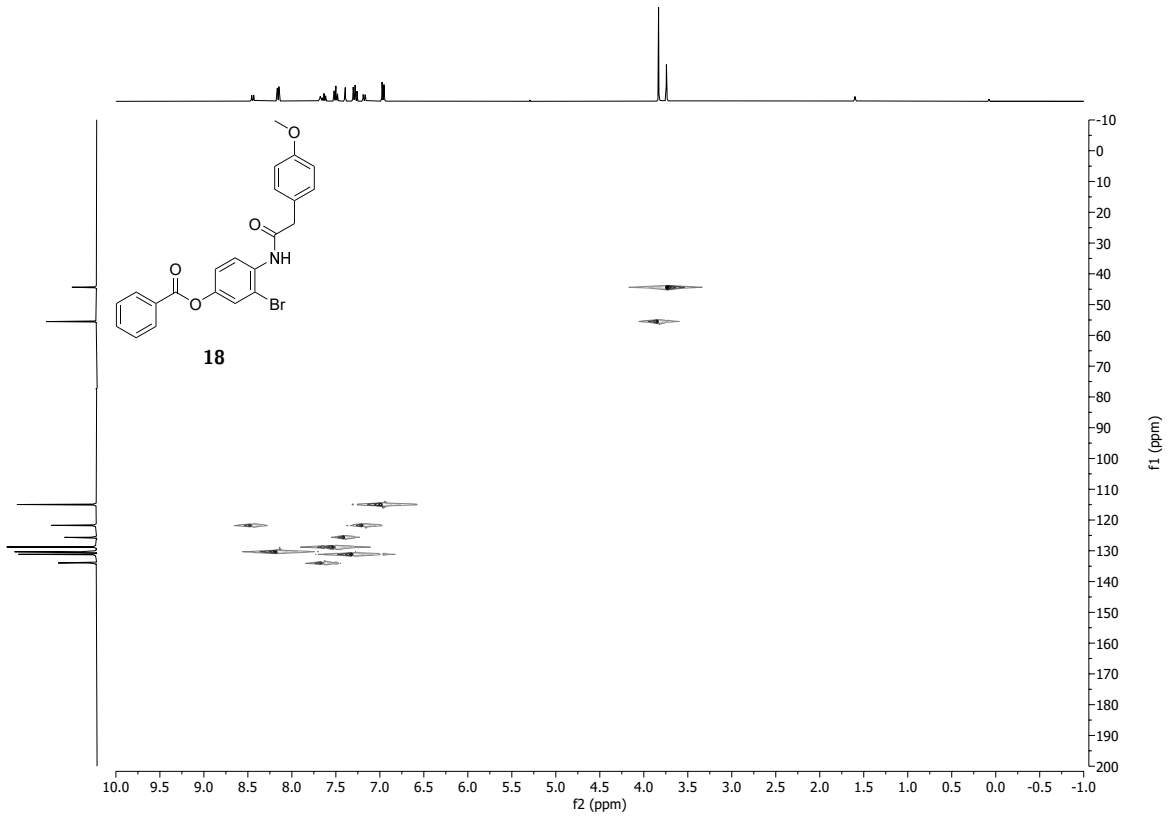

^{1}H ^{13}C HSQC NMR (400 MHz, 100 MHz, $CDCl_3$) spectrum of 3-bromo-4-(2-(4-methoxyphenyl)acetamido)phenyl benzoate **18**.

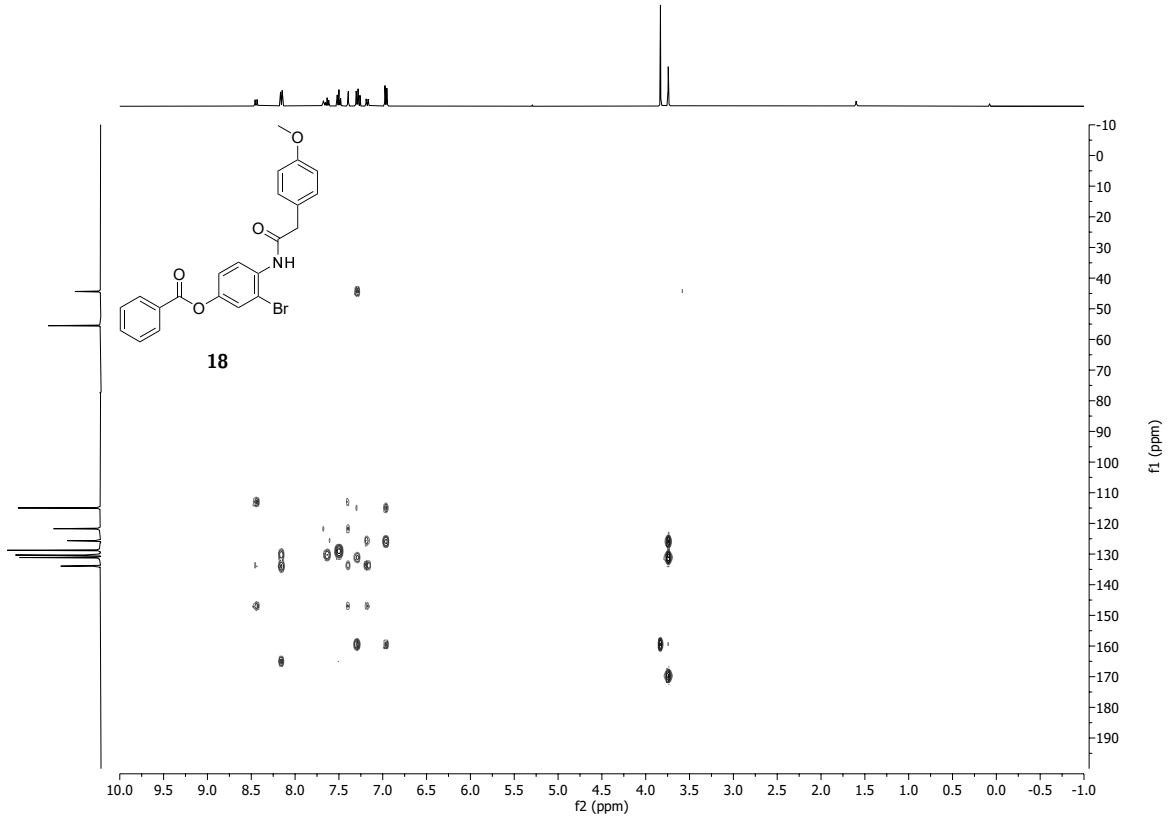

^{1}H ^{13}C HMBC NMR (400 MHz, 100 MHz, $CDCl_3$) spectrum of 3-bromo-4-(2-(4-methoxyphenyl)acetamido)phenyl benzoate **18**.

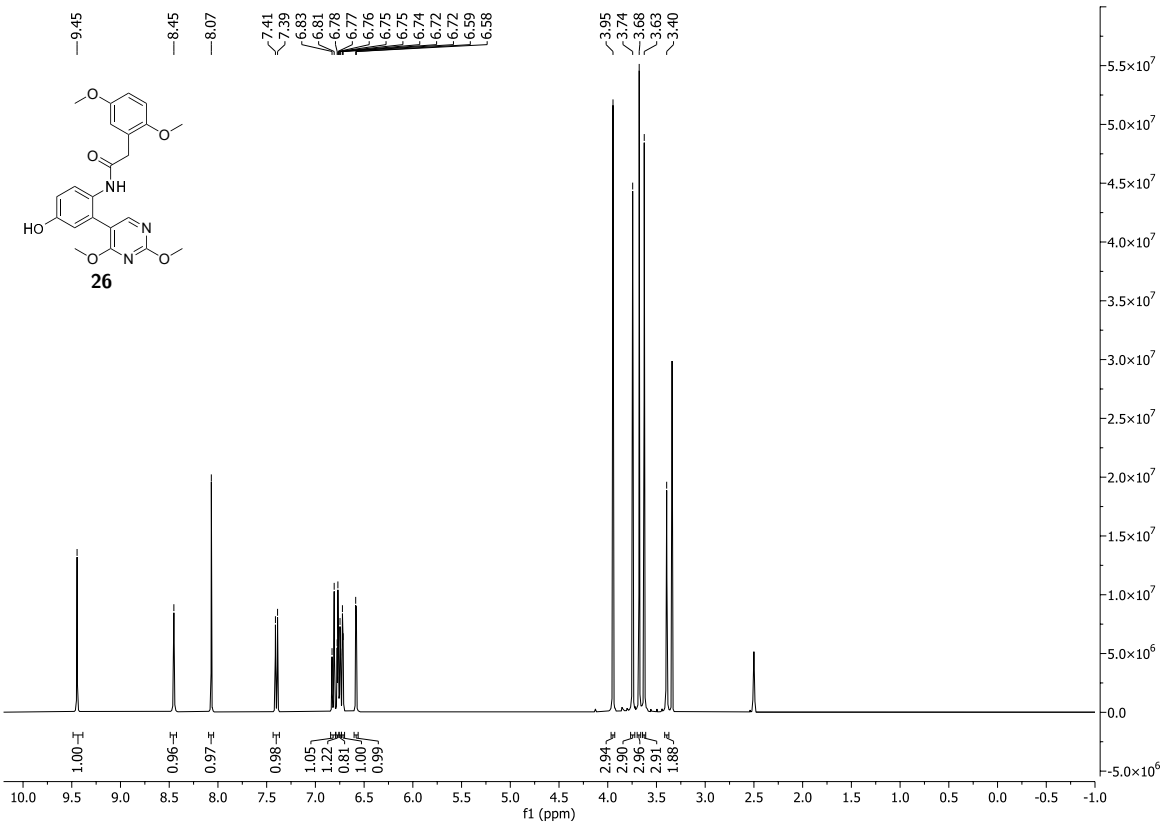

^{1}H NMR (400 MHz, DMSO – d_6) spectrum of
2-(2,5-dimethoxyphenyl)-*N*-(2-(2,4-dimethoxypyrimidin-5-yl)-4-hydroxyphenyl)acetamide **26**.

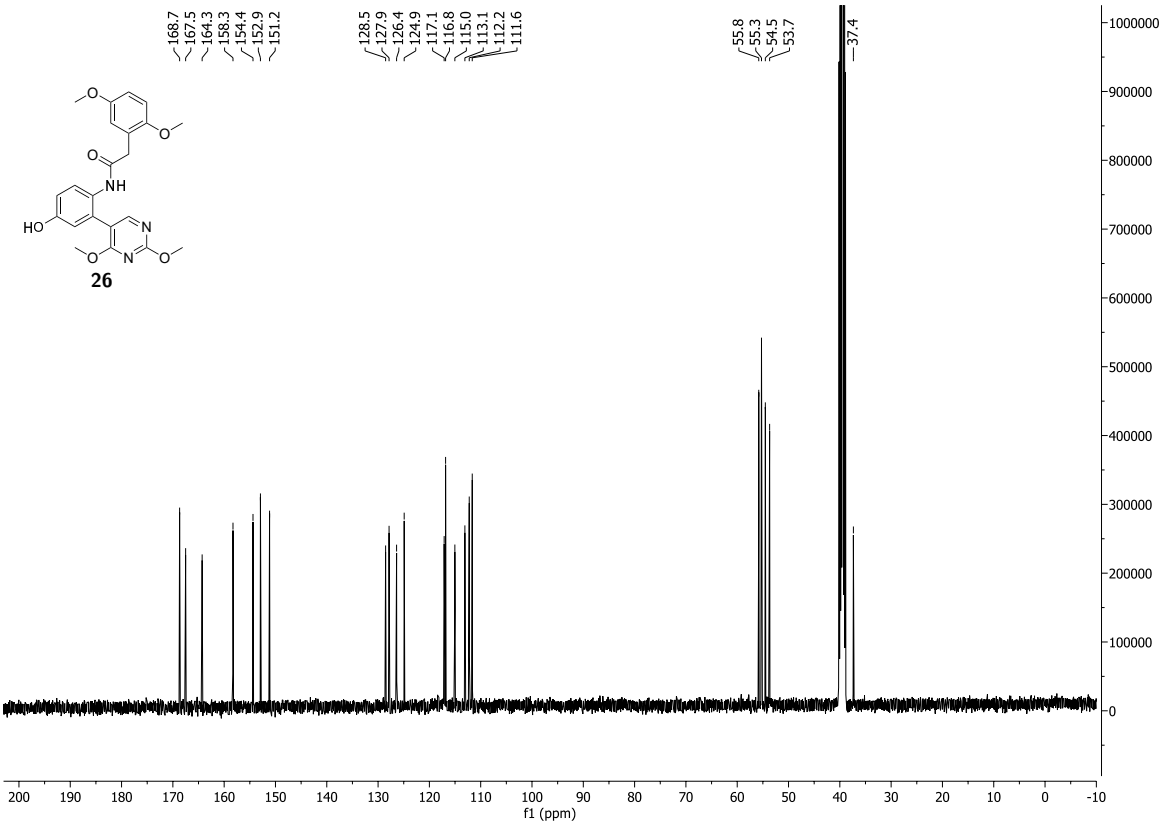

^{13}C NMR (100 MHz, DMSO – d_6) spectrum of
2-(2,5-dimethoxyphenyl)-*N*-(2-(2,4-dimethoxypyrimidin-5-yl)-4-hydroxyphenyl)acetamide **26**.

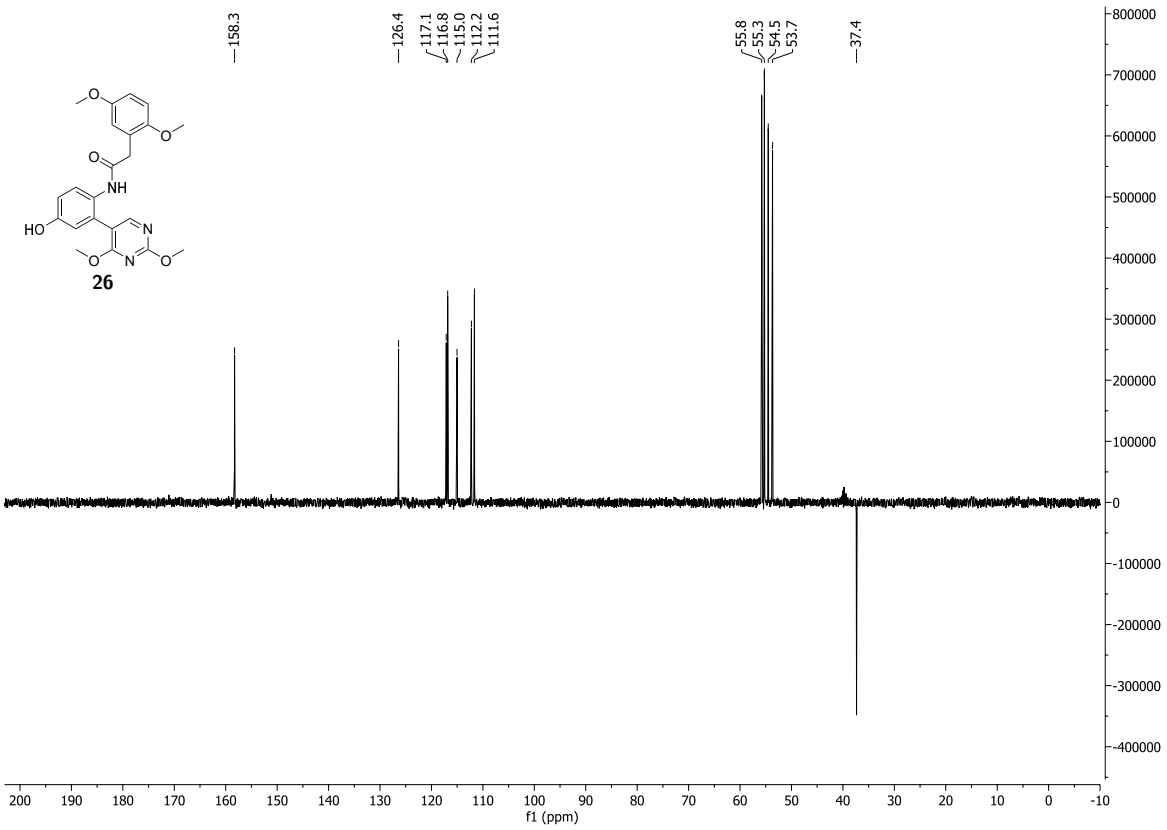

^{13}C DEPT 135 NMR (100 MHz, DMSO – d_6) spectrum of 2-(2,5-dimethoxyphenyl)-*N*-(2-(2,4-dimethoxypyrimidin-5-yl)-4-hydroxyphenyl)acetamide **26**.

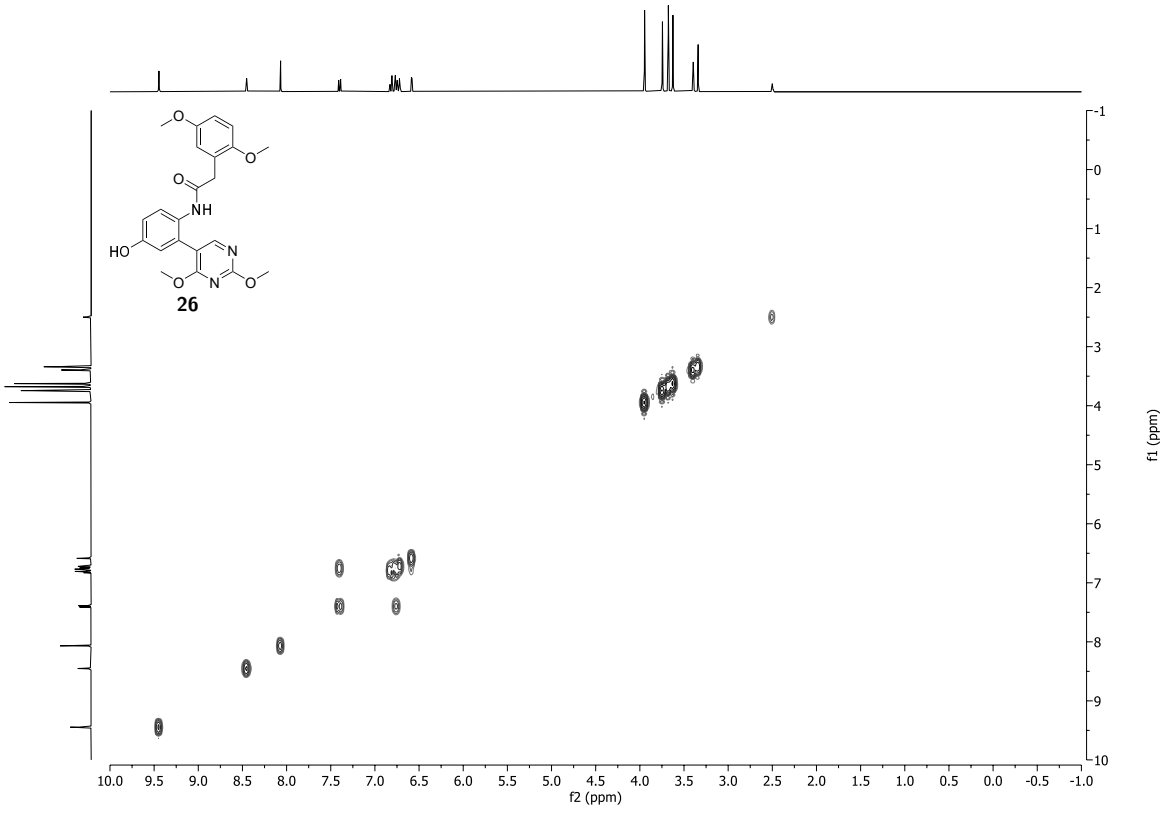

^{1}H ^{1}H COSY NMR (400 MHz, 400 MHz, DMSO – d_6) spectrum of 2-(2,5-dimethoxyphenyl)-*N*-(2-(2,4-dimethoxypyrimidin-5-yl)-4-hydroxyphenyl)acetamide **26**.

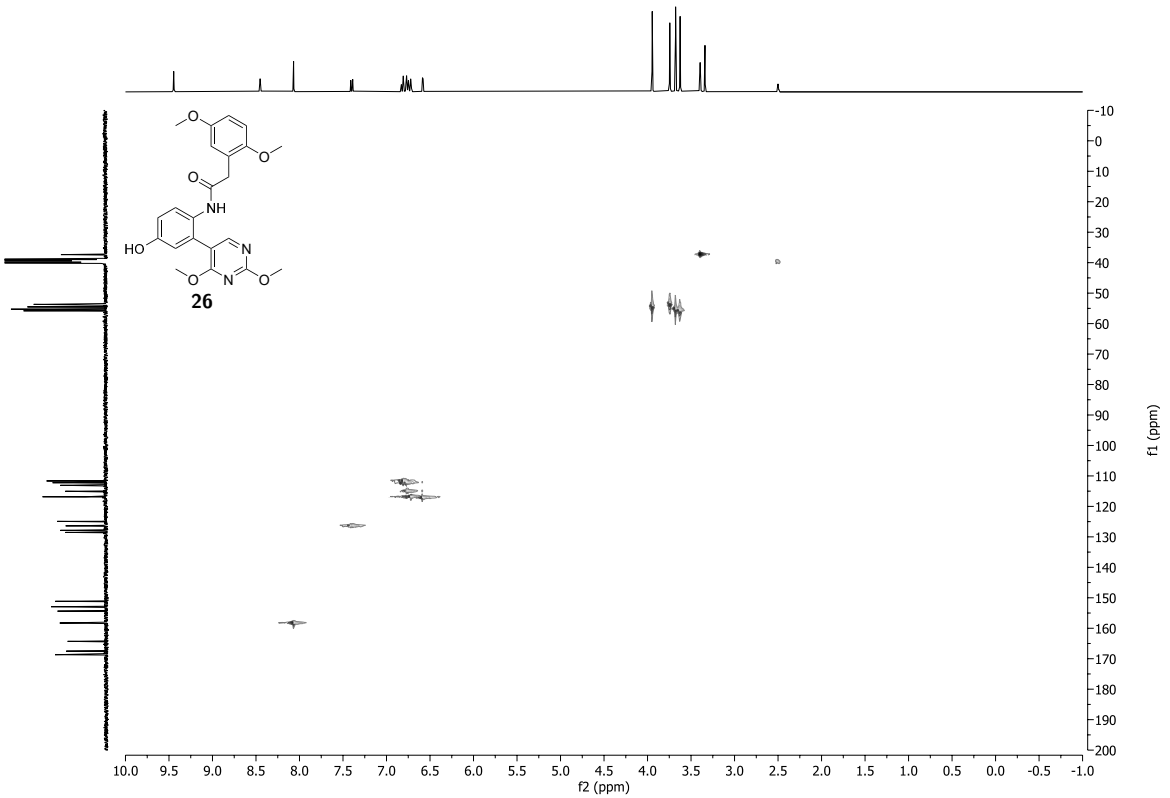

^{1}H ^{13}C HSQC NMR (400 MHz, 100 MHz, DMSO – d_6) spectrum of 2-(2,5-dimethoxyphenyl)-*N*-(2-(2,4-dimethoxypyrimidin-5-yl)-4-hydroxyphenyl)acetamide **26**.

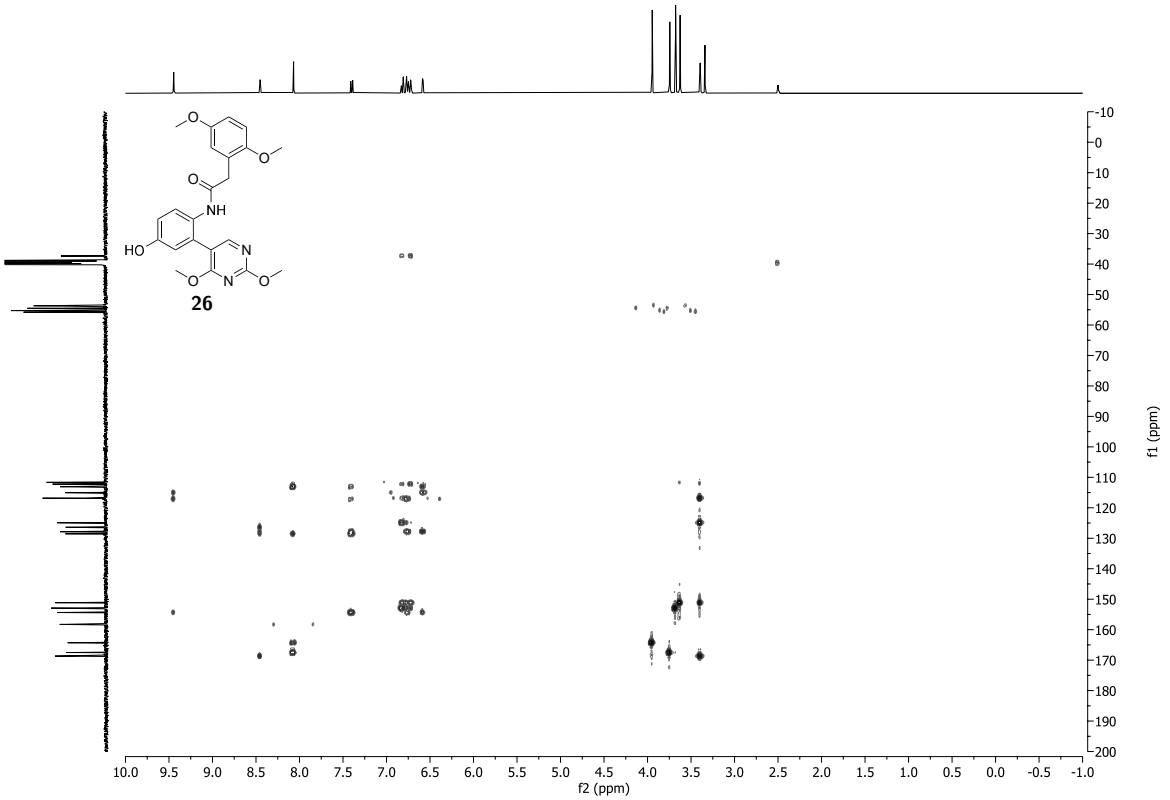

^{1}H ^{13}C HMBC NMR (400 MHz, 100 MHz, DMSO – d_6) spectrum of 2-(2,5-dimethoxyphenyl)-*N*-(2-(2,4-dimethoxypyrimidin-5-yl)-4-hydroxyphenyl)acetamide **26**.

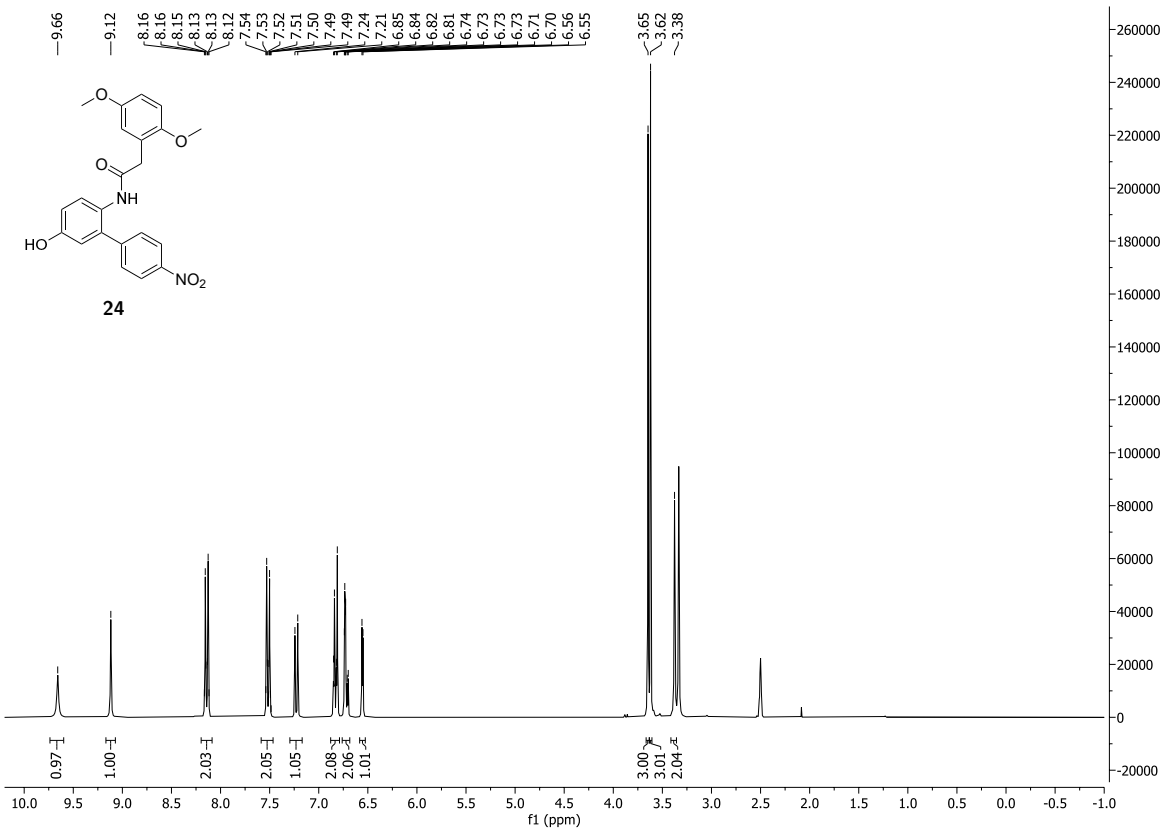

^{1}H NMR (300 MHz, DMSO – d_6) spectrum of
2-(2,5-dimethoxyphenyl)-*N*-(5-hydroxy-4'-nitro-[1,1'-biphenyl]-2-yl)acetamide **24**.

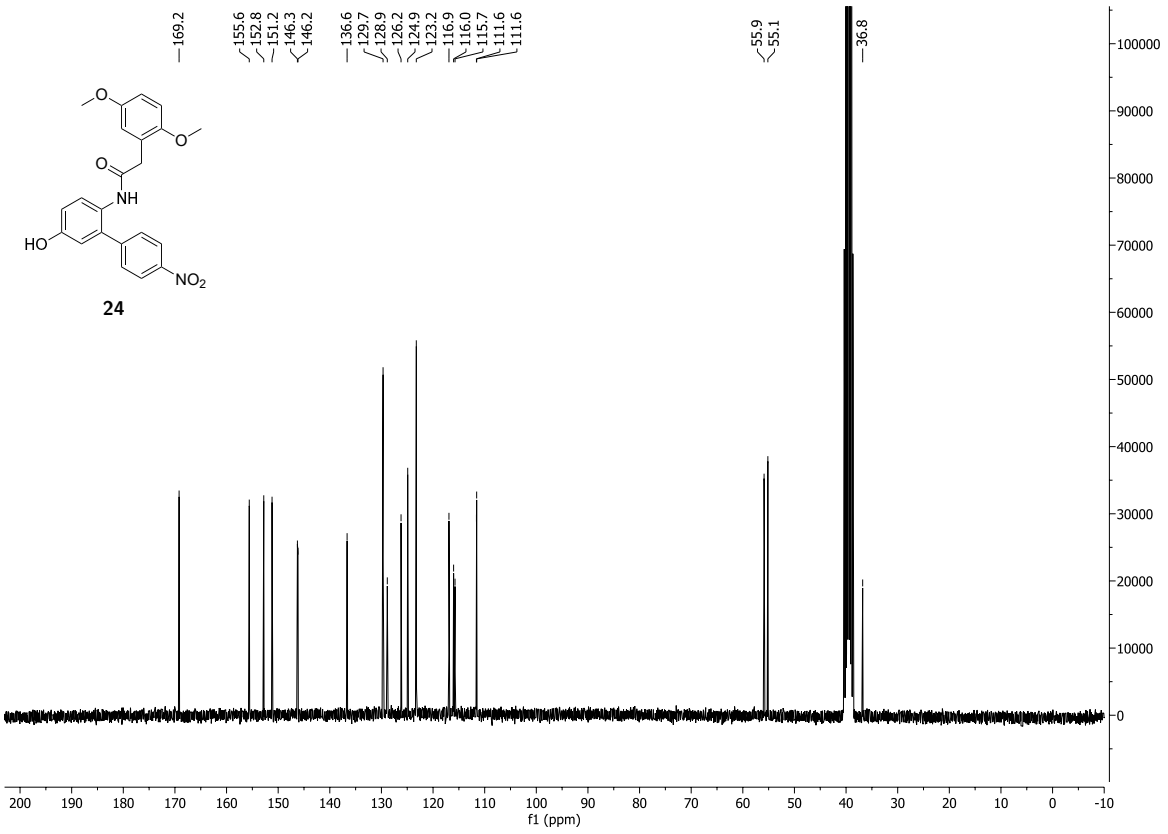

^{13}C NMR (75 MHz, DMSO – d_6) spectrum of
2-(2,5-dimethoxyphenyl)-*N*-(5-hydroxy-4'-nitro-[1,1'-biphenyl]-2-yl)acetamide **24**.

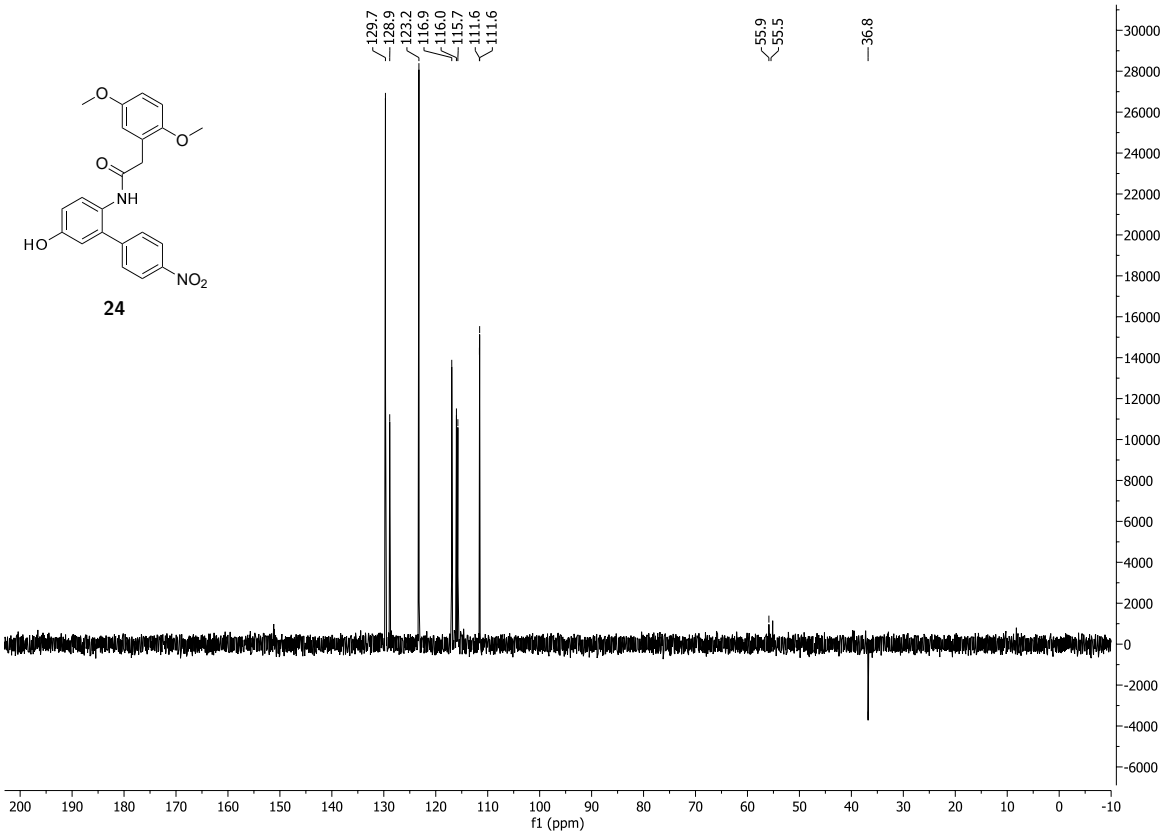

^{13}C DEPT 135 NMR (75 MHz, DMSO – d_6) spectrum of 2-(2,5-dimethoxyphenyl)-*N*-(5-hydroxy-4'-nitro-[1,1'-biphenyl]-2-yl)acetamide **24**.

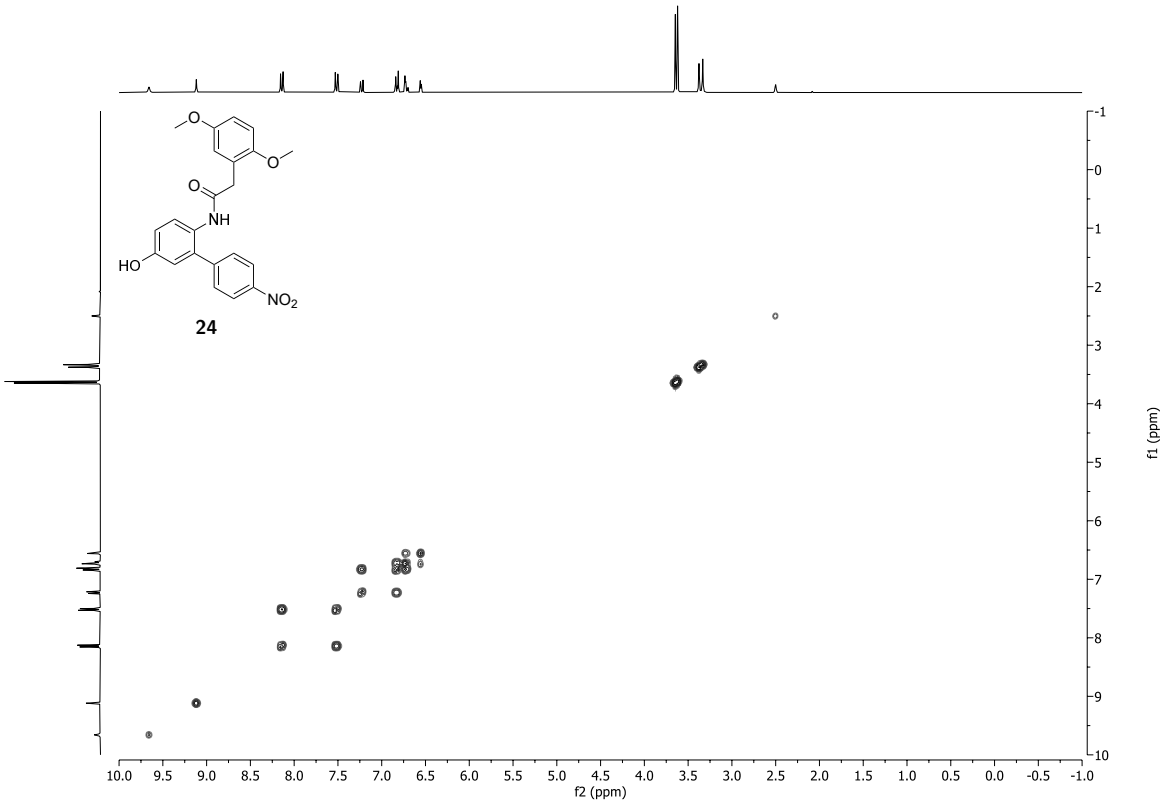

^{1}H ^{1}H COSY NMR (300 MHz, 300 MHz, DMSO – d_6) spectrum of 2-(2,5-dimethoxyphenyl)-*N*-(5-hydroxy-4'-nitro-[1,1'-biphenyl]-2-yl)acetamide **24**.

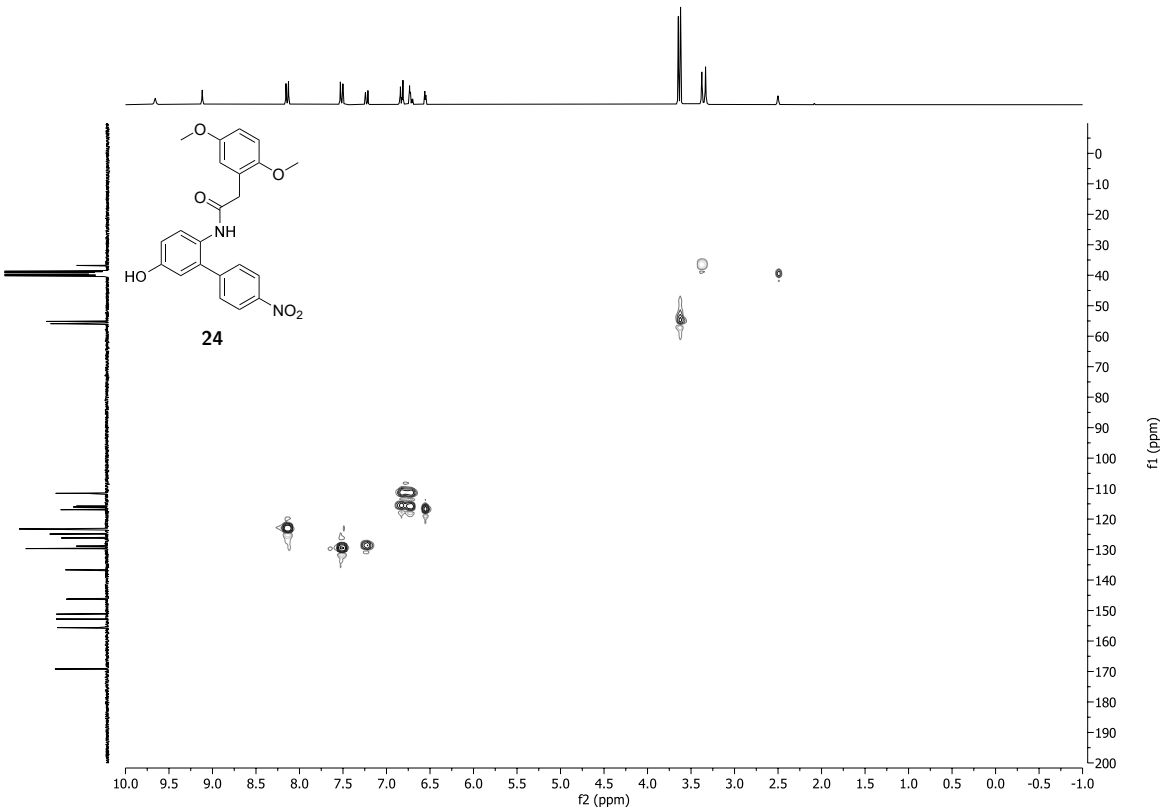

^{1}H ^{13}C HSQC NMR (300 MHz, 75 MHz, DMSO – d_6) spectrum of 2-(2,5-dimethoxyphenyl)-*N*-(5-hydroxy-4'-nitro-[1,1'-biphenyl]-2-yl)acetamide **24**.

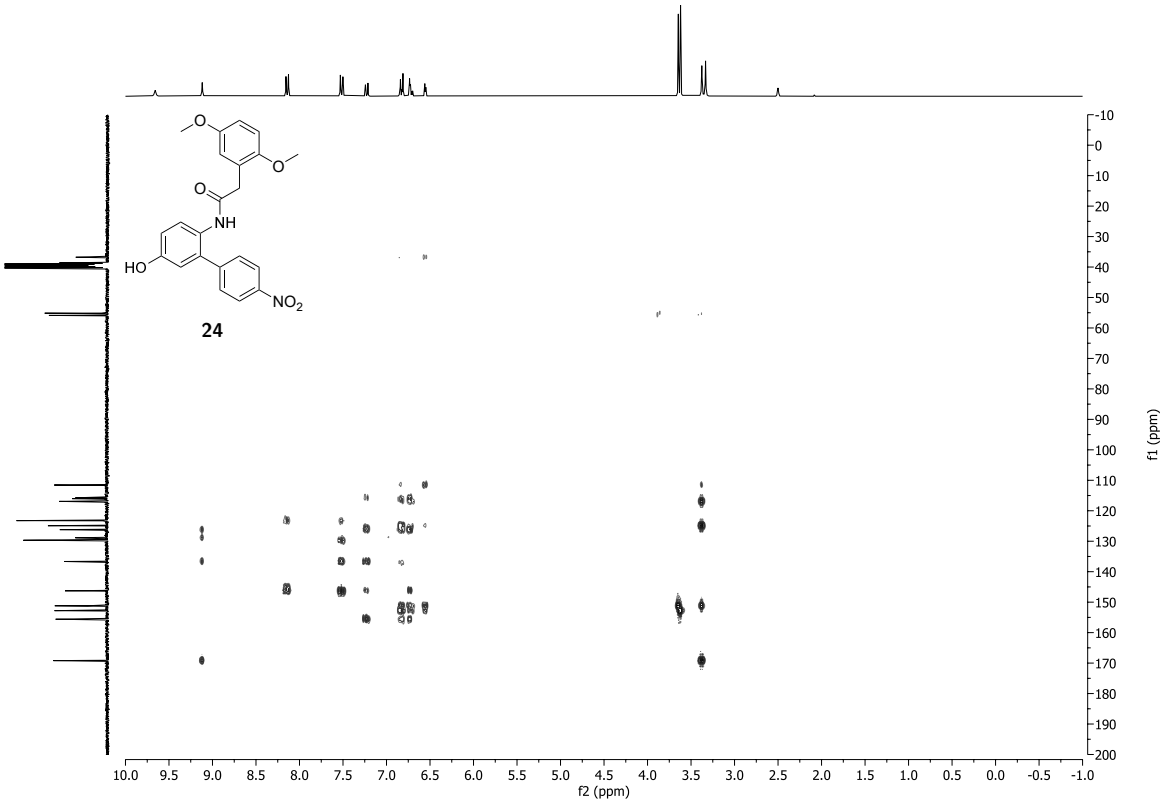

^{1}H ^{13}C HMBC NMR (300 MHz, 75 MHz, DMSO – d_6) spectrum of 2-(2,5-dimethoxyphenyl)-*N*-(5-hydroxy-4'-nitro-[1,1'-biphenyl]-2-yl)acetamide **24**.

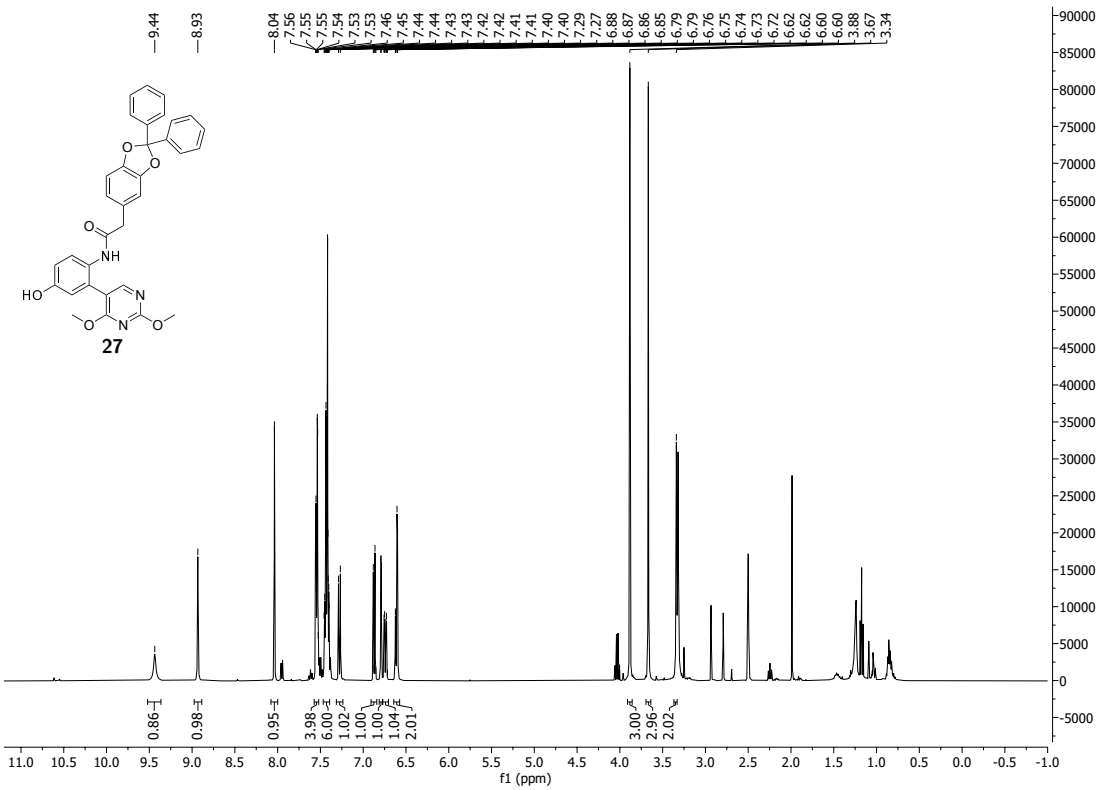

27

^{1}H NMR (400 MHz, DMSO – d_6) spectrum of *N*-(2-(2,4-dimethoxypyrimidin-5-yl)-4-hydroxyphenyl)-2-(2,2-diphenylbenzo[*d*][1,3]dioxol-5-yl) acetamide **27**.

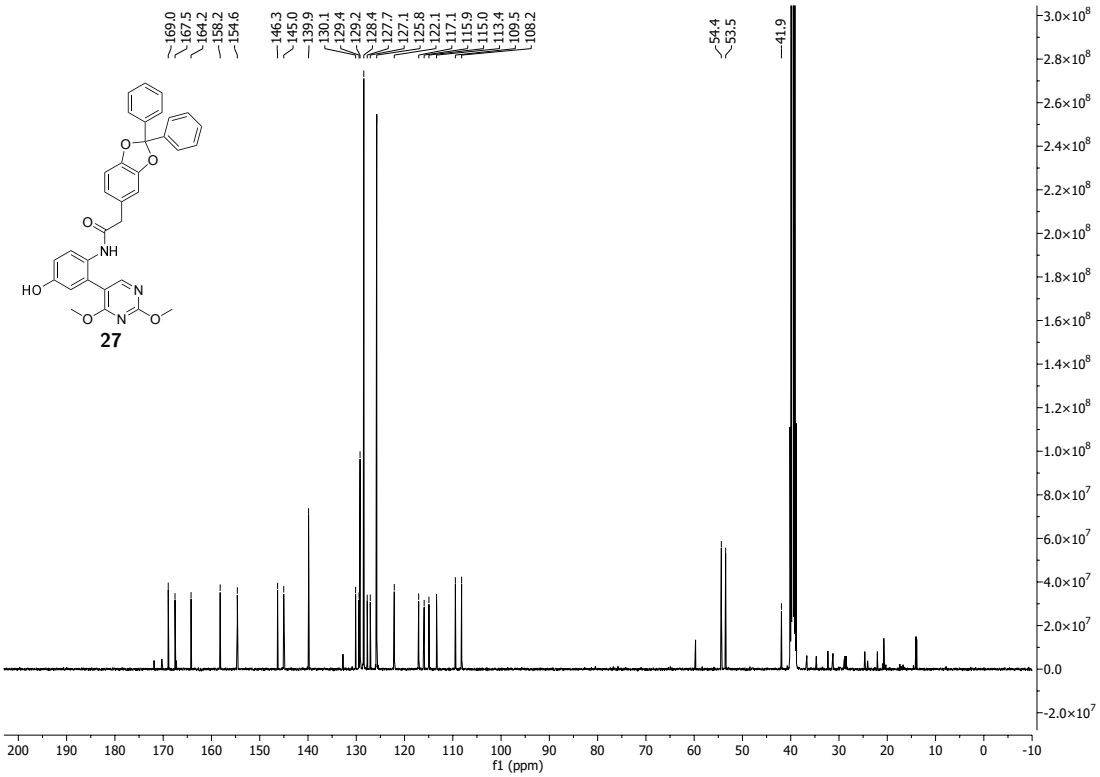

27

^{13}C NMR (100 MHz, DMSO – d_6) spectrum of *N*-(2-(2,4-dimethoxypyrimidin-5-yl)-4-hydroxyphenyl)-2-(2,2-diphenylbenzo[*d*][1,3]dioxol-5-yl) acetamide **27**.

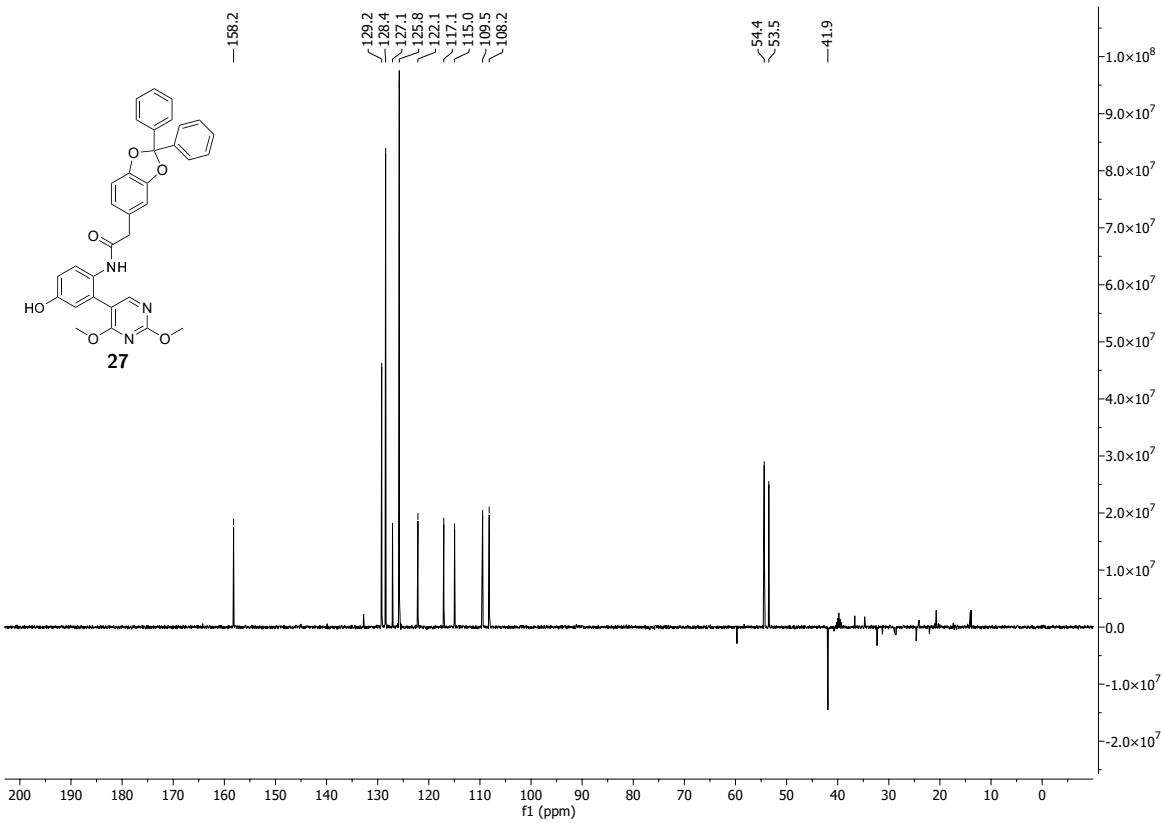

^{13}C DEPT 135 NMR (100 MHz, DMSO – d_6) spectrum of *N*-(2-(2,4-dimethoxypyrimidin-5-yl)-4-hydroxyphenyl)-2-(2,2-diphenylbenzo[*d*][1,3]dioxol-5-yl) acetamide **27**.

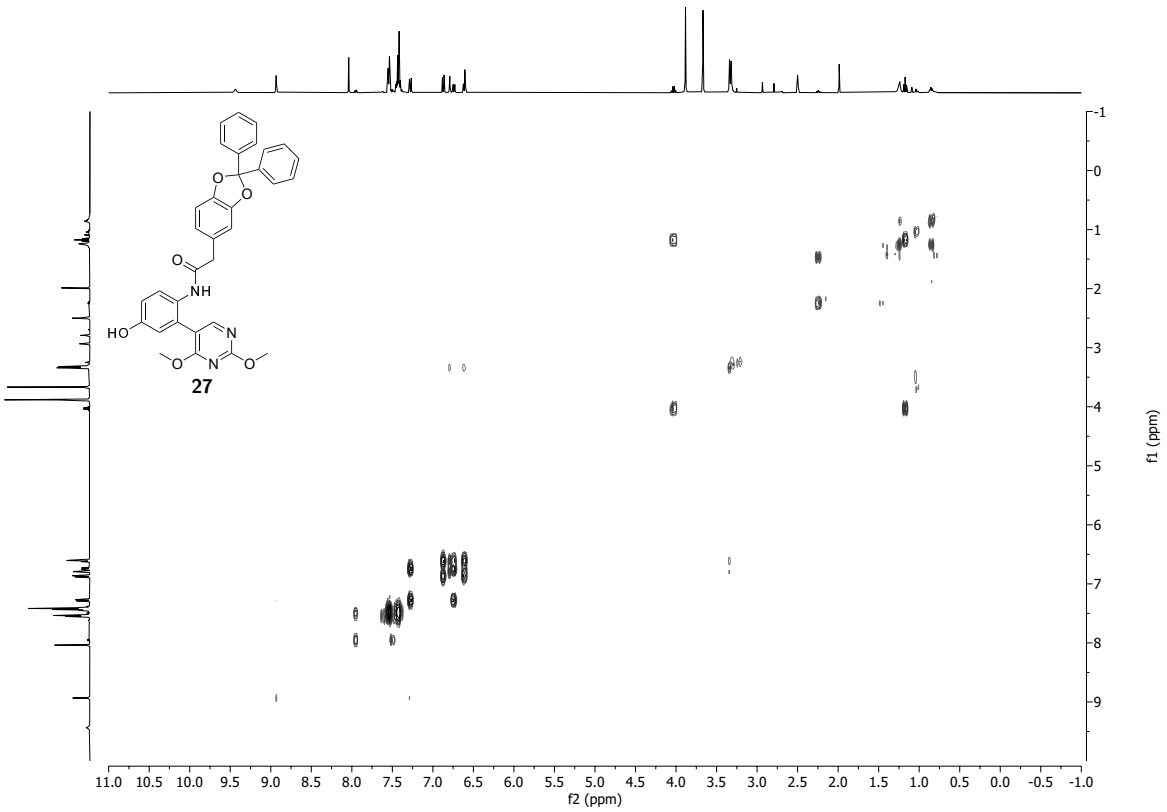

^{1}H ^{1}H COSY NMR (400 MHz, 400 MHz, DMSO – d_6) spectrum of *N*-(2-(2,4-dimethoxypyrimidin-5-yl)-4-hydroxyphenyl)-2-(2,2-diphenylbenzo[*d*][1,3]dioxol-5-yl) acetamide **27**.

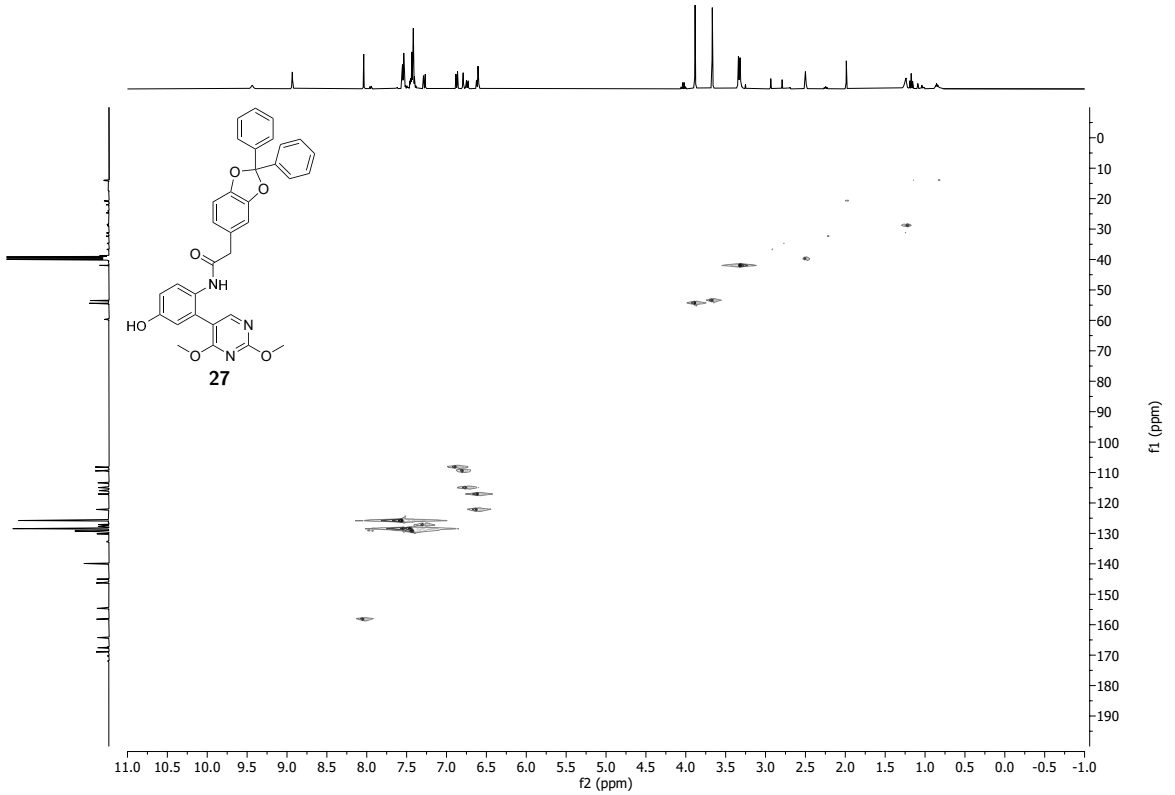

^{1}H ^{13}C HSQC NMR (400 MHz, 100 MHz, DMSO – d_6) spectrum of *N*-(2-(2,4-dimethoxypyrimidin-5-yl)-4-hydroxyphenyl)-2-(2,2-diphenylbenzo[*d*][1,3]dioxol-5-yl) acetamide **27**.

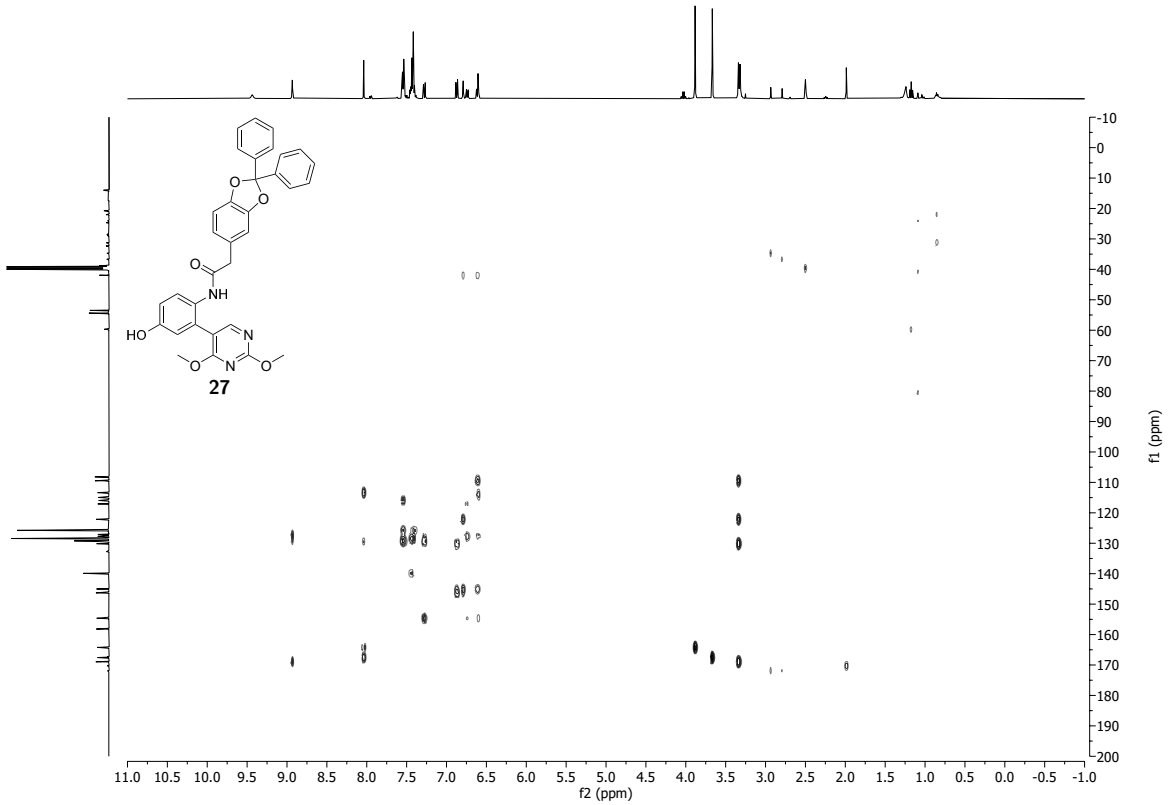

^{1}H ^{13}C HMBC NMR (400 MHz, 100 MHz, DMSO – d_6) spectrum of *N*-(2-(2,4-dimethoxypyrimidin-5-yl)-4-hydroxyphenyl)-2-(2,2-diphenylbenzo[*d*][1,3]dioxol-5-yl) acetamide **27**.

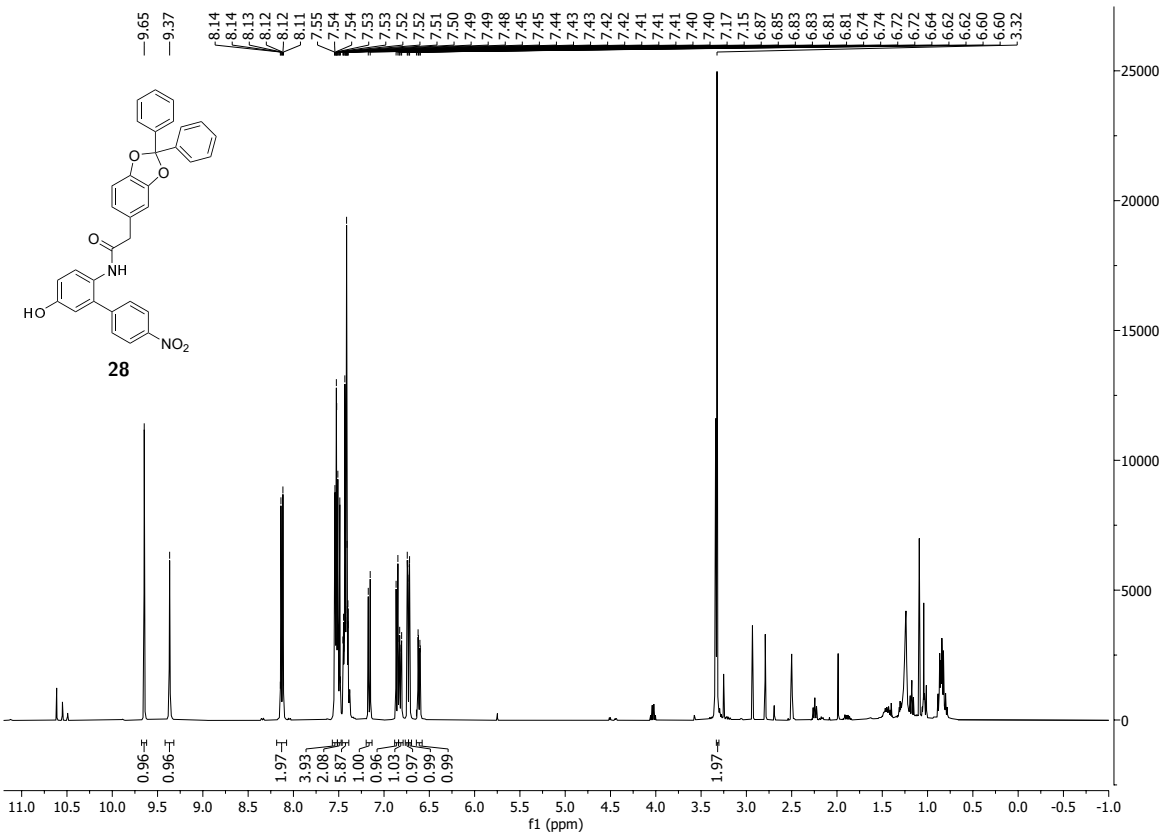

^{1}H NMR (400 MHz, DMSO – d_6) spectrum of
2-(2,2-diphenylbenzo[*d*][1,3]dioxol-5-yl)-*N*-(5-hydroxy-4'-nitro-[1,1'-biphenyl]-2-yl)acetamide **28**.

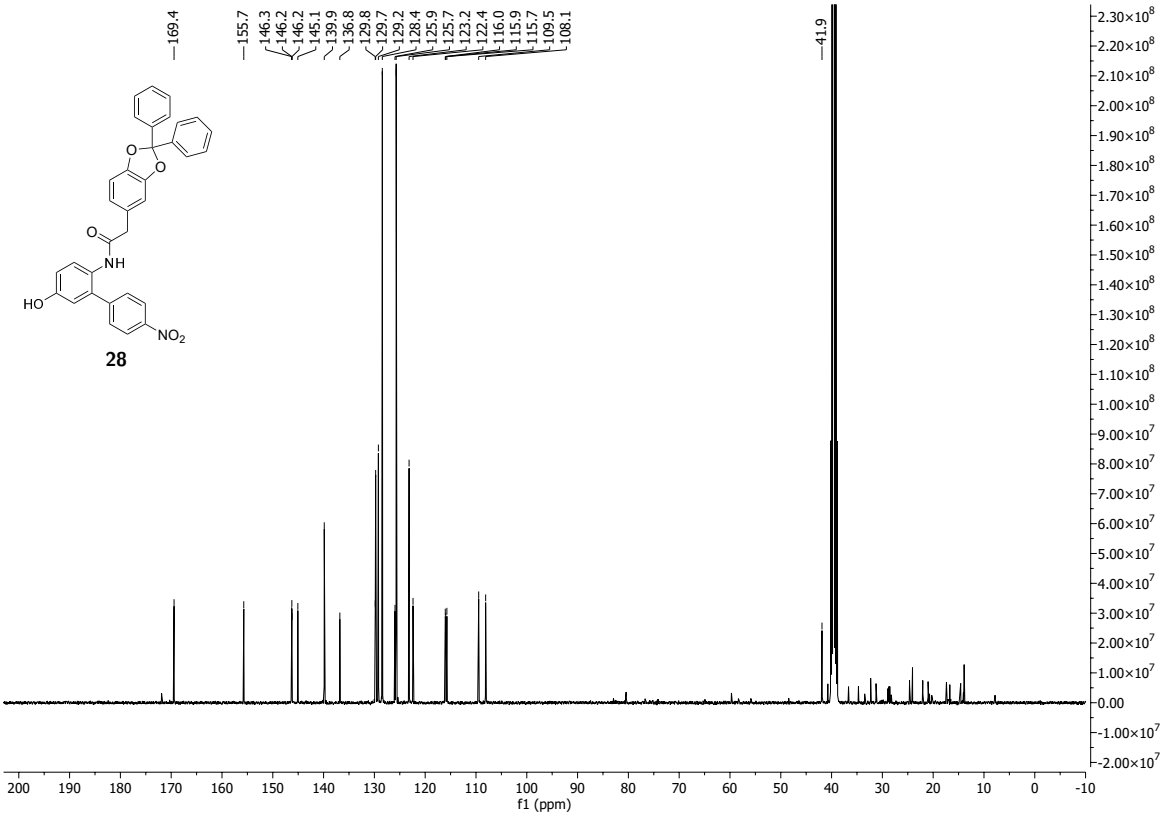

^{13}C NMR (100 MHz, DMSO – d_6) spectrum of
2-(2,2-diphenylbenzo[*d*][1,3]dioxol-5-yl)-*N*-(5-hydroxy-4'-nitro-[1,1'-biphenyl]-2-yl)acetamide **28**.

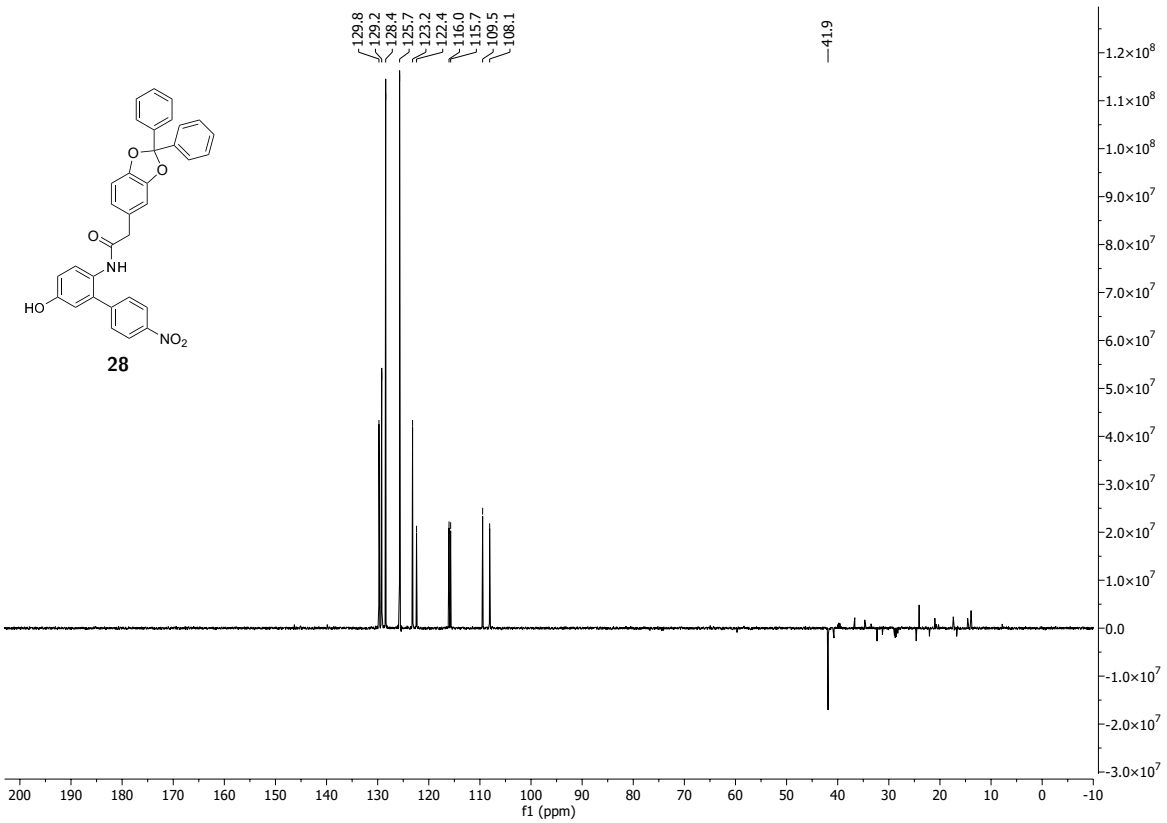

^{13}C DEPT 135 NMR (100 MHz, DMSO – d_6) spectrum of
2-(2,2-diphenylbenzo[*d*][1,3]dioxol-5-yl)-*N*-(5-hydroxy-4'-nitro-[1,1'-biphenyl]-2-yl)acetamide **28**.

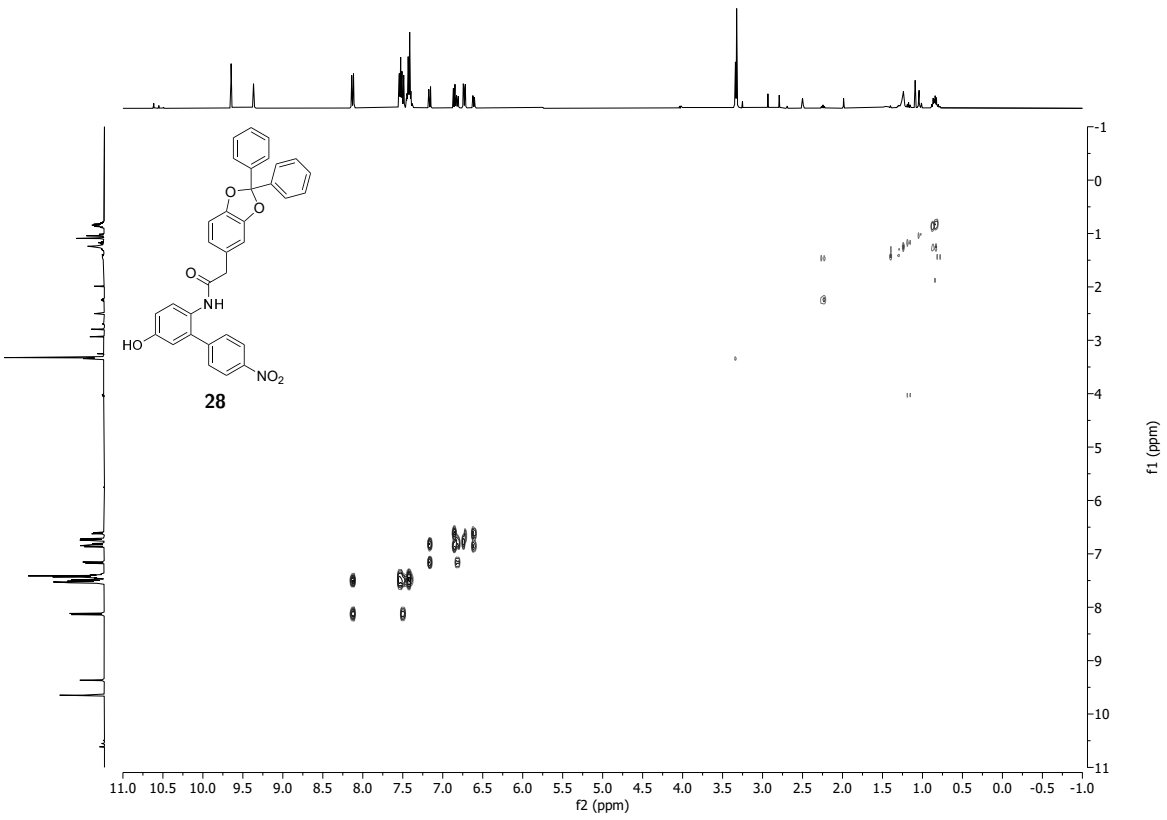

^{1}H ^{1}H COSY NMR (400 MHz, 400 MHz, DMSO – d_6) spectrum of
2-(2,2-diphenylbenzo[*d*][1,3]dioxol-5-yl)-*N*-(5-hydroxy-4'-nitro-[1,1'-biphenyl]-2-yl)acetamide **28**.

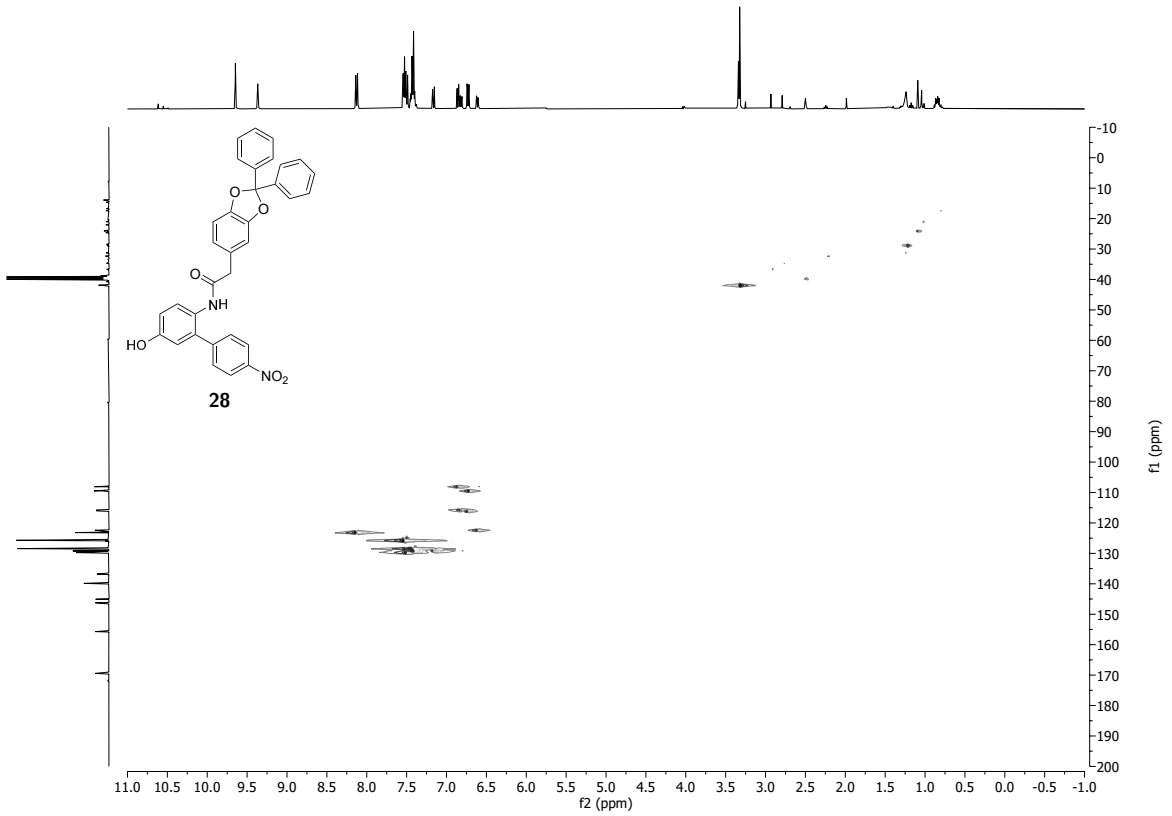

^{1}H ^{13}C HSQC NMR (400 MHz, 100 MHz, DMSO – d_6) spectrum of 2-(2,2-diphenylbenzo[*d*][1,3]dioxol-5-yl)-*N*-(5-hydroxy-4'-nitro-[1,1'-biphenyl]-2-yl)acetamide **28**.

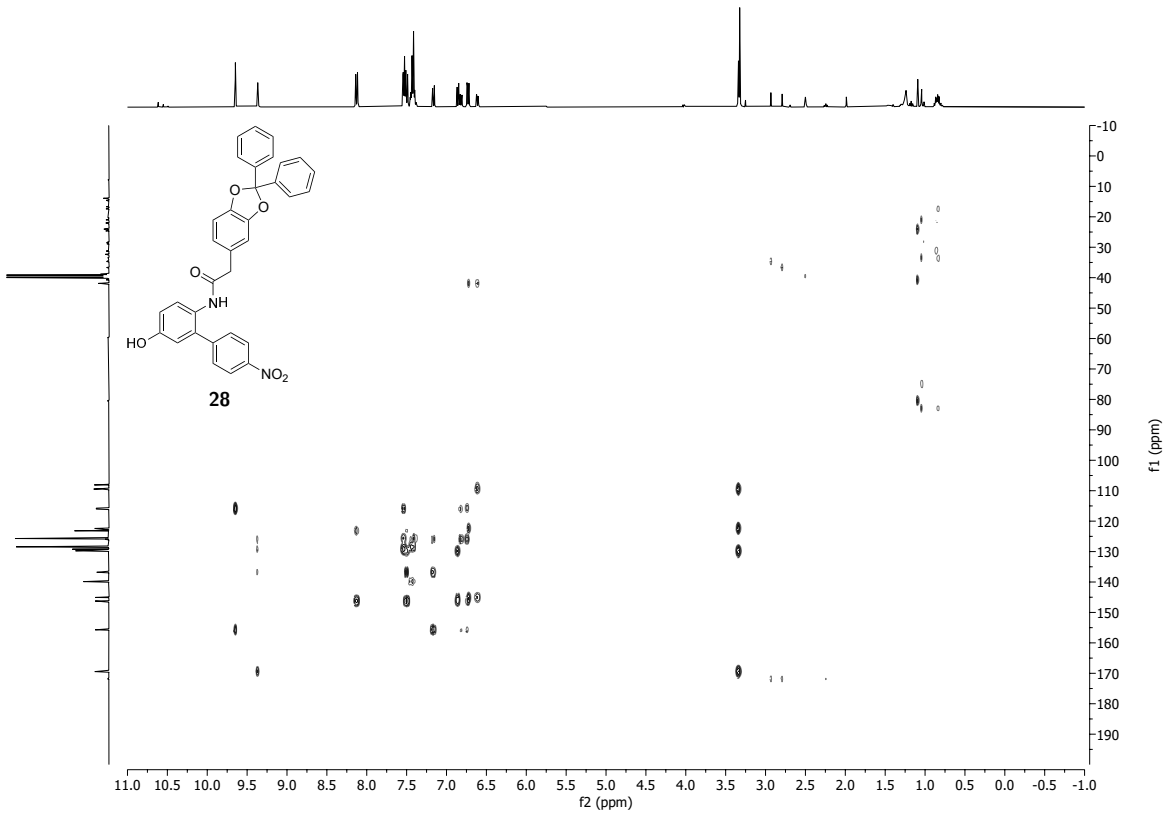

^{1}H ^{13}C HMBC NMR (400 MHz, 100 MHz, DMSO – d_6) spectrum of 2-(2,2-diphenylbenzo[*d*][1,3]dioxol-5-yl)-*N*-(5-hydroxy-4'-nitro-[1,1'-biphenyl]-2-yl)acetamide **28**.

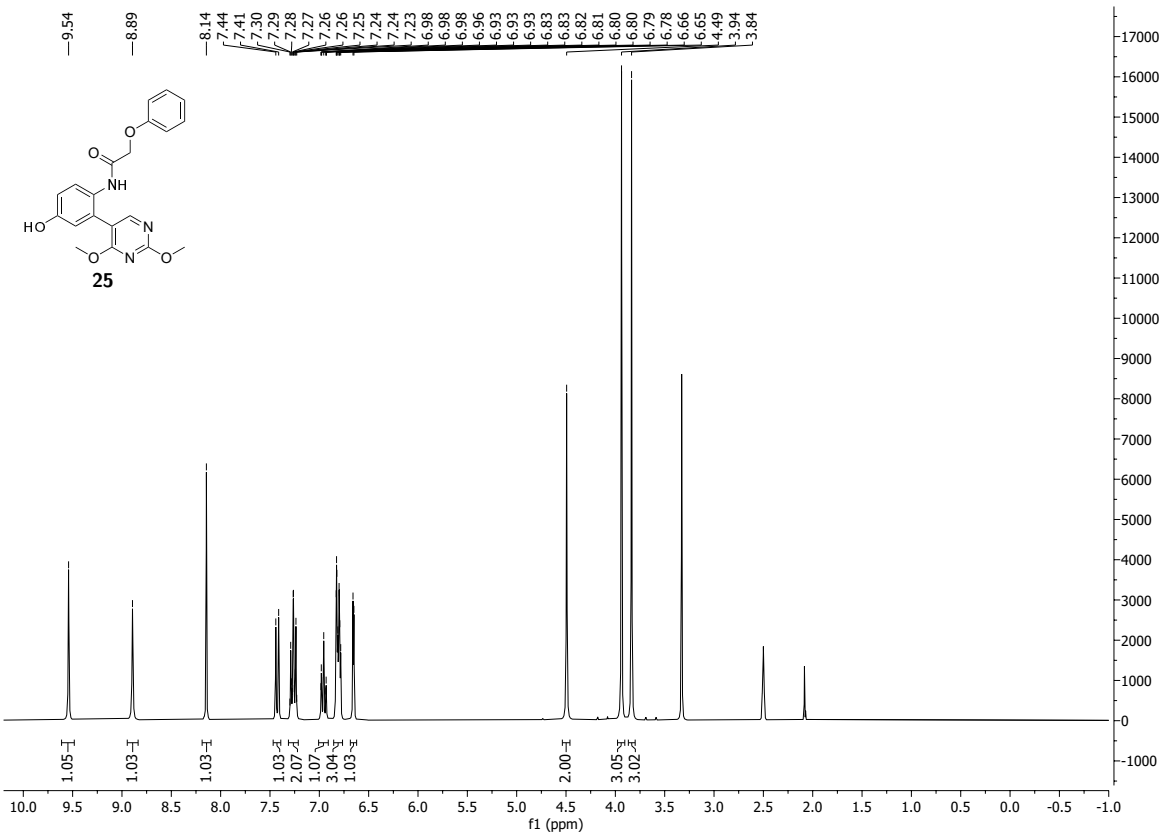

25

^{1}H NMR (300 MHz, DMSO – d_6) spectrum of
N-(2-(2,4-dimethoxypyrimidin-5-yl)-4-hydroxyphenyl)-2-phenoxyacetamide **25**.

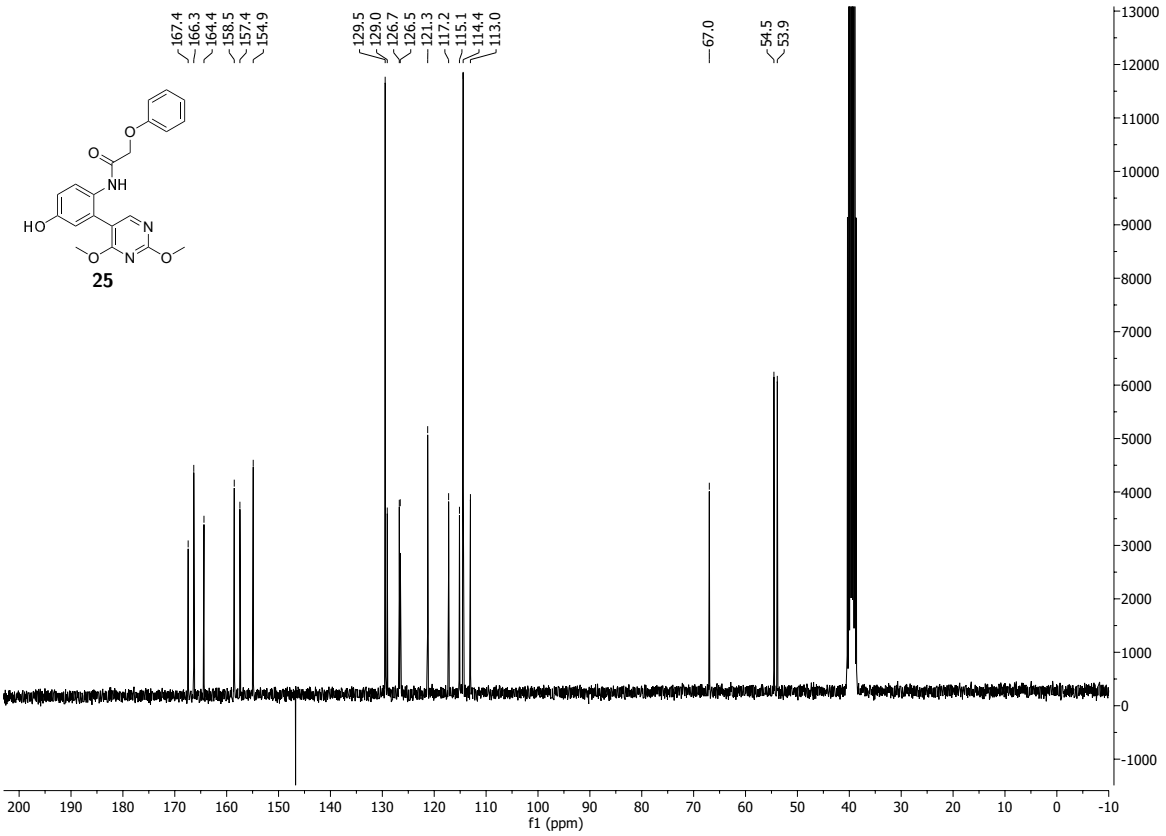

25

^{13}C NMR (75 MHz, DMSO – d_6) spectrum of
N-(2-(2,4-dimethoxypyrimidin-5-yl)-4-hydroxyphenyl)-2-phenoxyacetamide **25**.

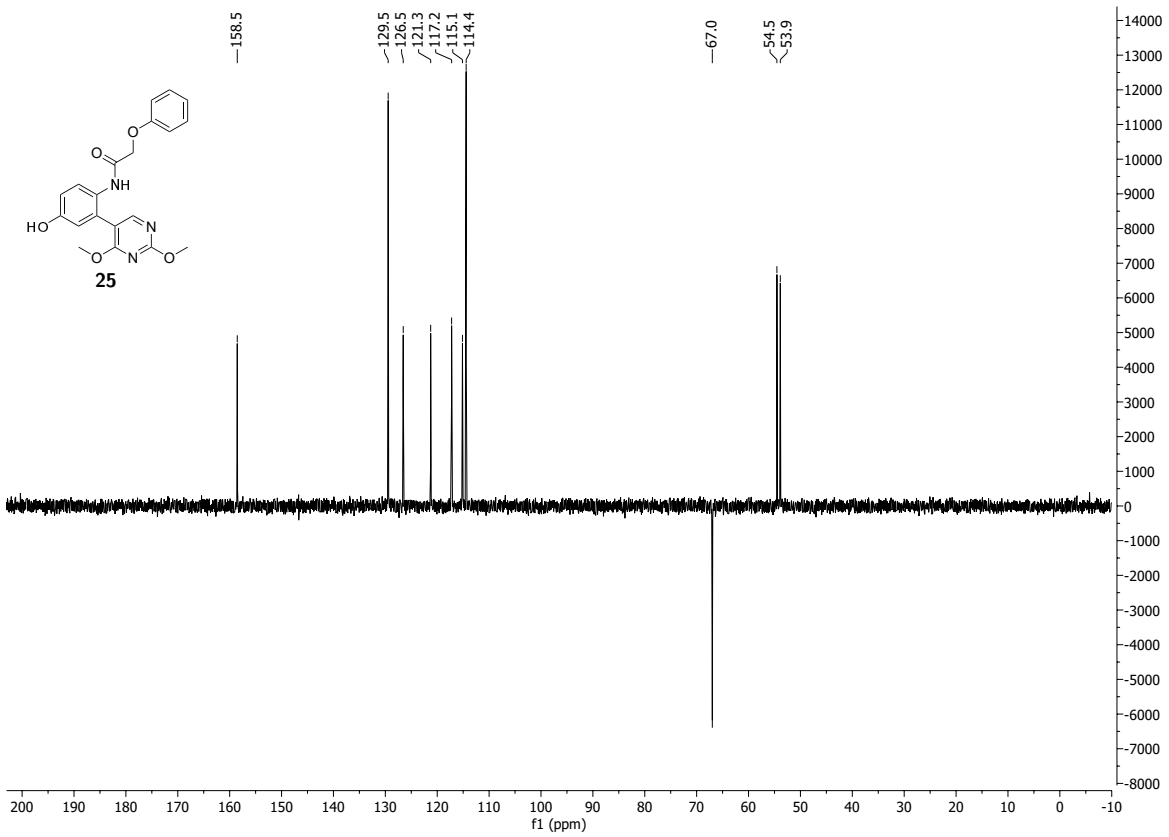

^{13}C DEPT 135 NMR (75 MHz, DMSO–d_6) spectrum of *N*-(2-(2,4-dimethoxypyrimidin-5-yl)-4-hydroxyphenyl)-2-phenoxyacetamide **25**.

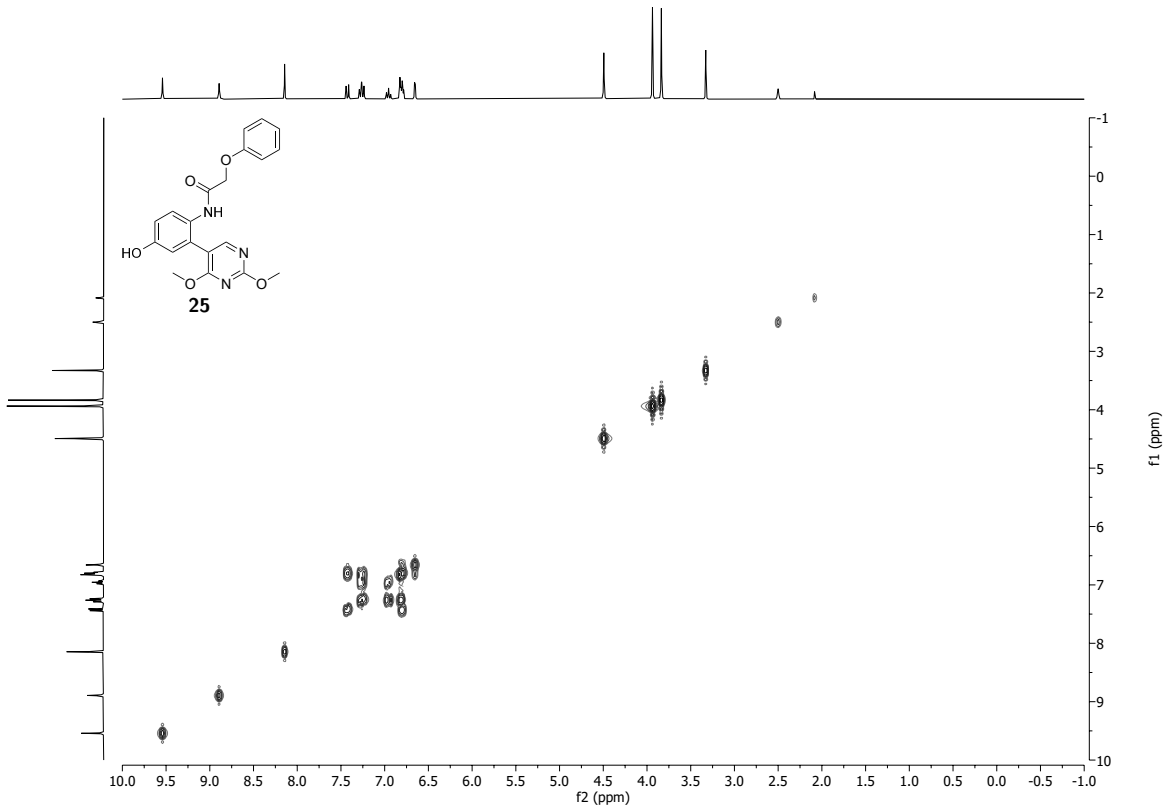

^{1}H ^{1}H COSY NMR (300 MHz, 300 MHz, DMSO–d_6) spectrum of *N*-(2-(2,4-dimethoxypyrimidin-5-yl)-4-hydroxyphenyl)-2-phenoxyacetamide **25**.

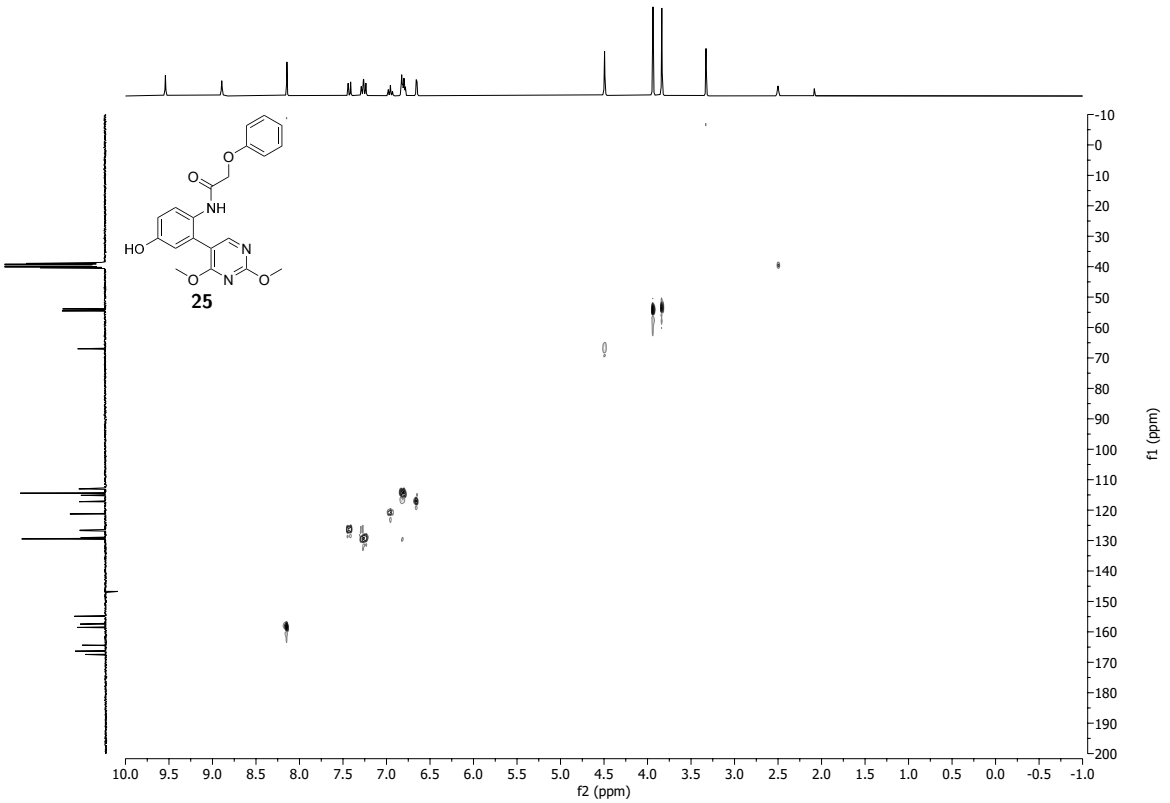

^{1}H ^{13}C HSQC NMR (300 MHz, 75 MHz, DMSO – d_6) spectrum of *N*-(2-(2,4-dimethoxypyrimidin-5-yl)-4-hydroxyphenyl)-2-phenoxyacetamide **25**.

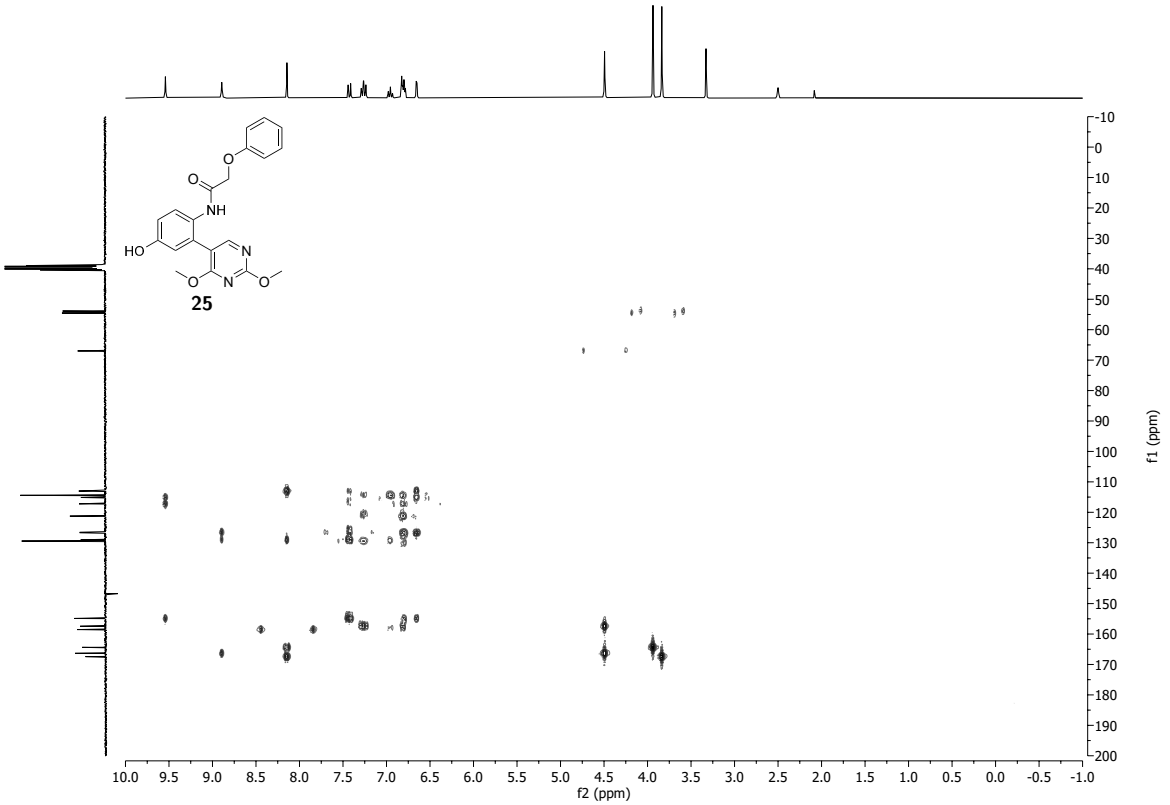

^{1}H ^{13}C HMBC NMR (300 MHz, 75 MHz, DMSO – d_6) spectrum of *N*-(2-(2,4-dimethoxypyrimidin-5-yl)-4-hydroxyphenyl)-2-phenoxyacetamide **25**.

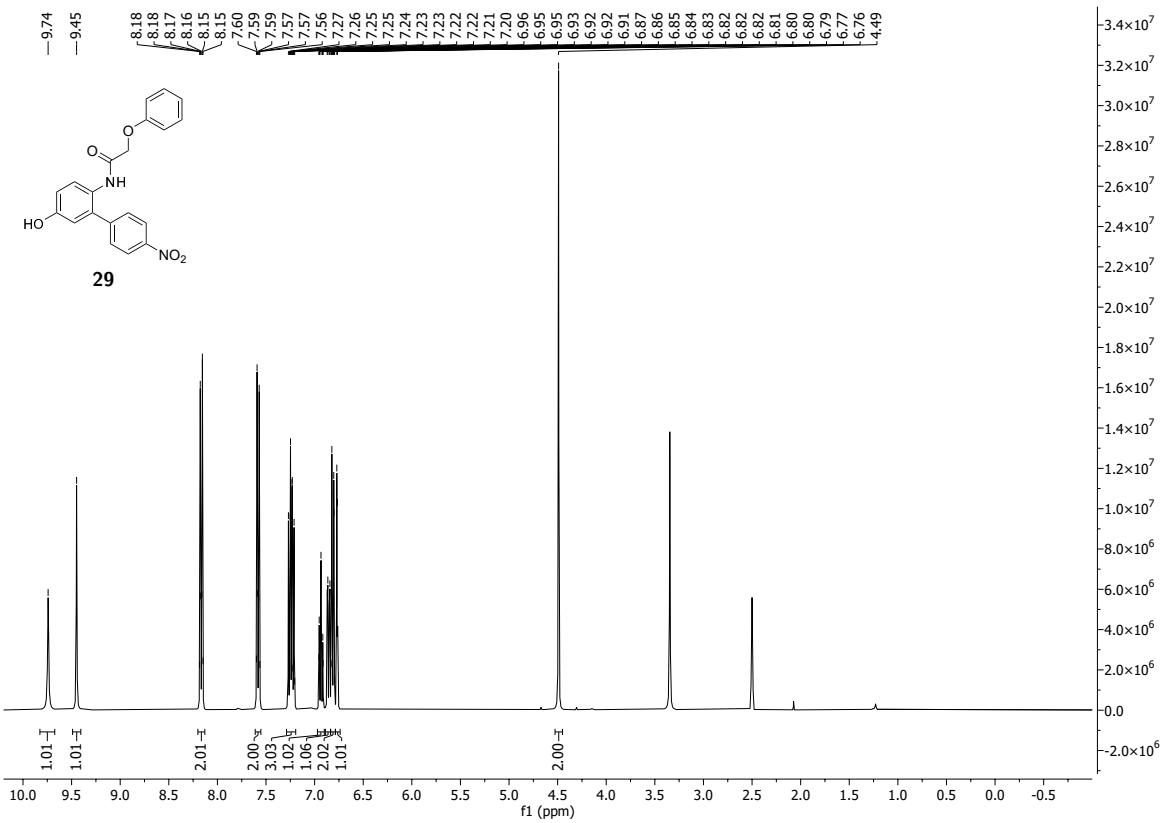

^{1}H NMR (400 MHz, DMSO – d_6) spectrum of
N-(5-hydroxy-4'-nitro-[1,1'-biphenyl]-2-yl)-2-phenoxyacetamide **29**.

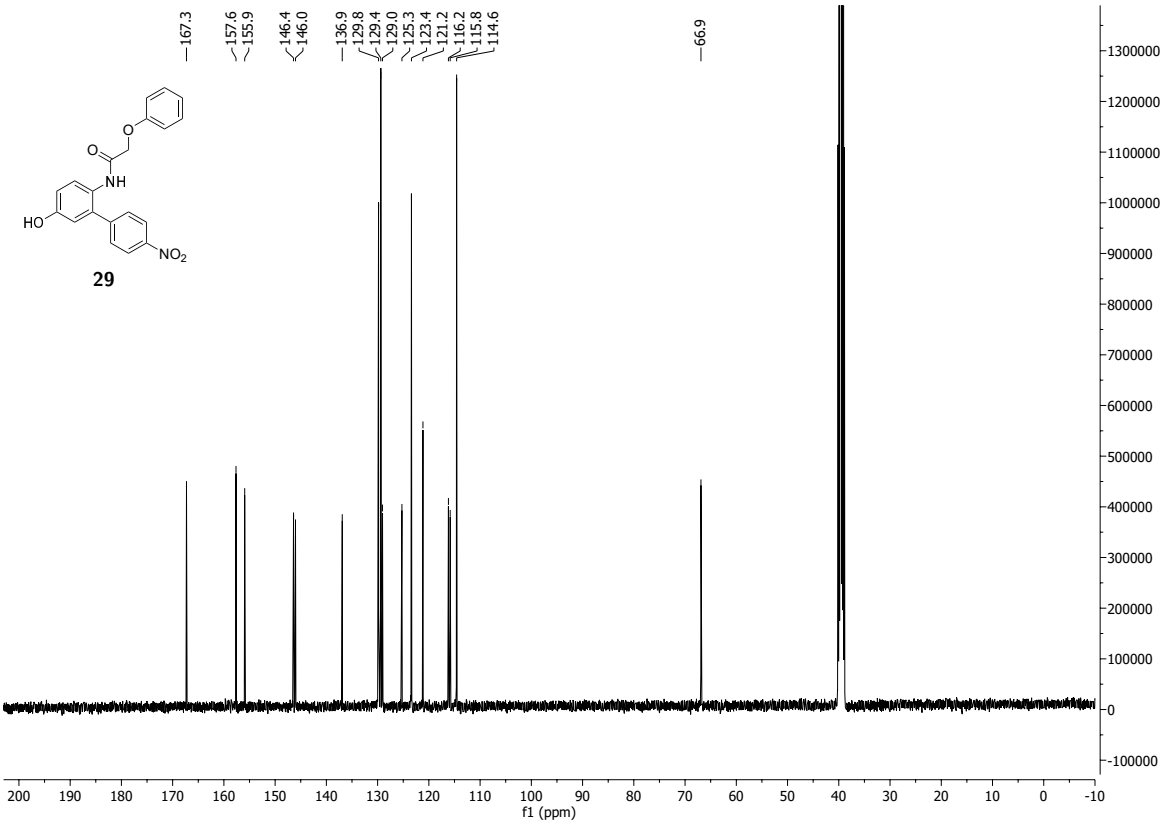

^{13}C NMR (100 MHz, DMSO – d_6) spectrum of
N-(5-hydroxy-4'-nitro-[1,1'-biphenyl]-2-yl)-2-phenoxyacetamide **29**.

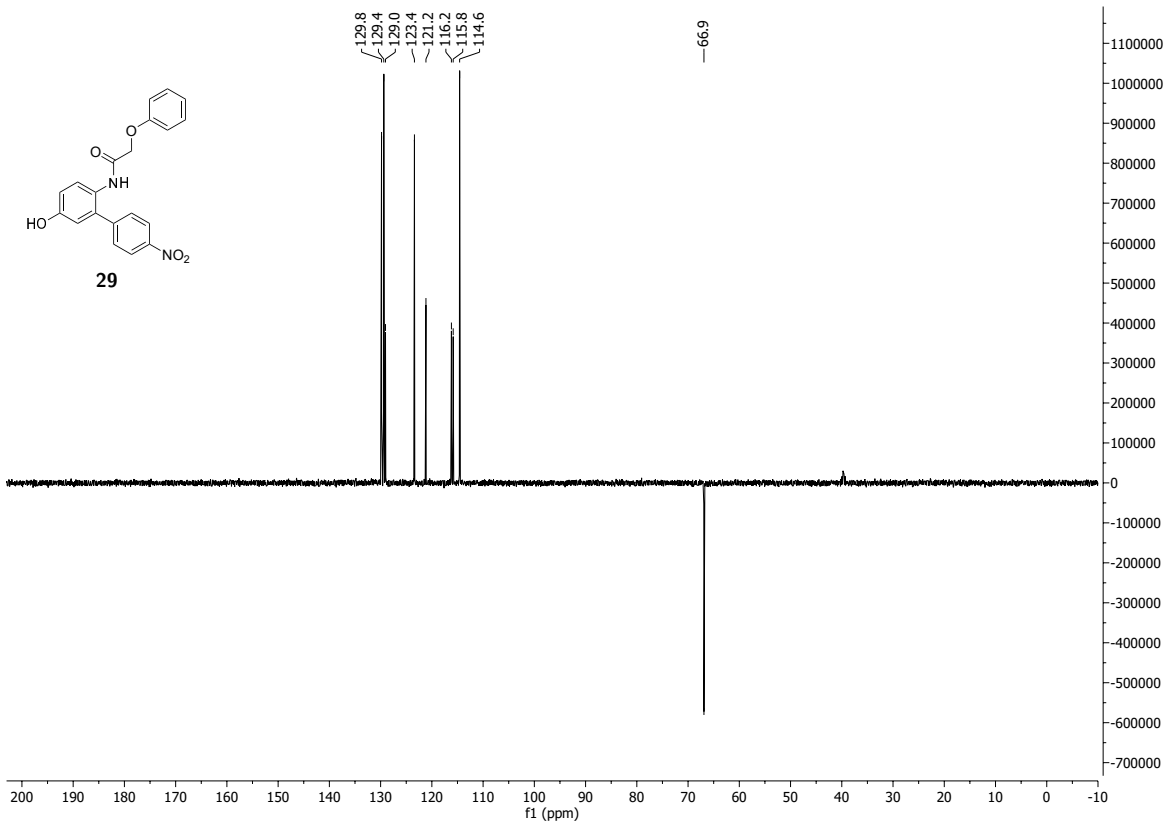

^{13}C DEPT 135 NMR (100 MHz, DMSO – d_6) spectrum of *N*-(5-hydroxy-4'-nitro-[1,1'-biphenyl]-2-yl)-2-phenoxyacetamide **29**.

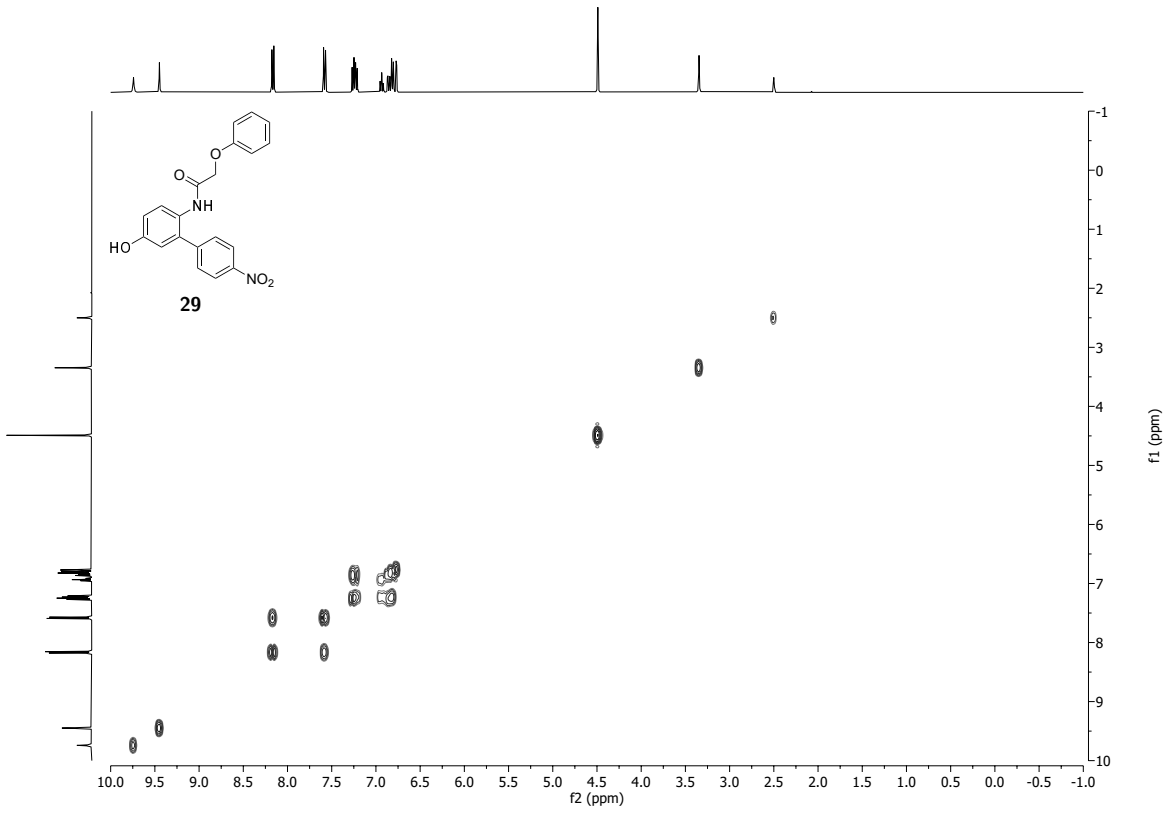

^{1}H ^{1}H COSY NMR (400 MHz, 400 MHz, DMSO – d_6) spectrum of *N*-(5-hydroxy-4'-nitro-[1,1'-biphenyl]-2-yl)-2-phenoxyacetamide **29**.

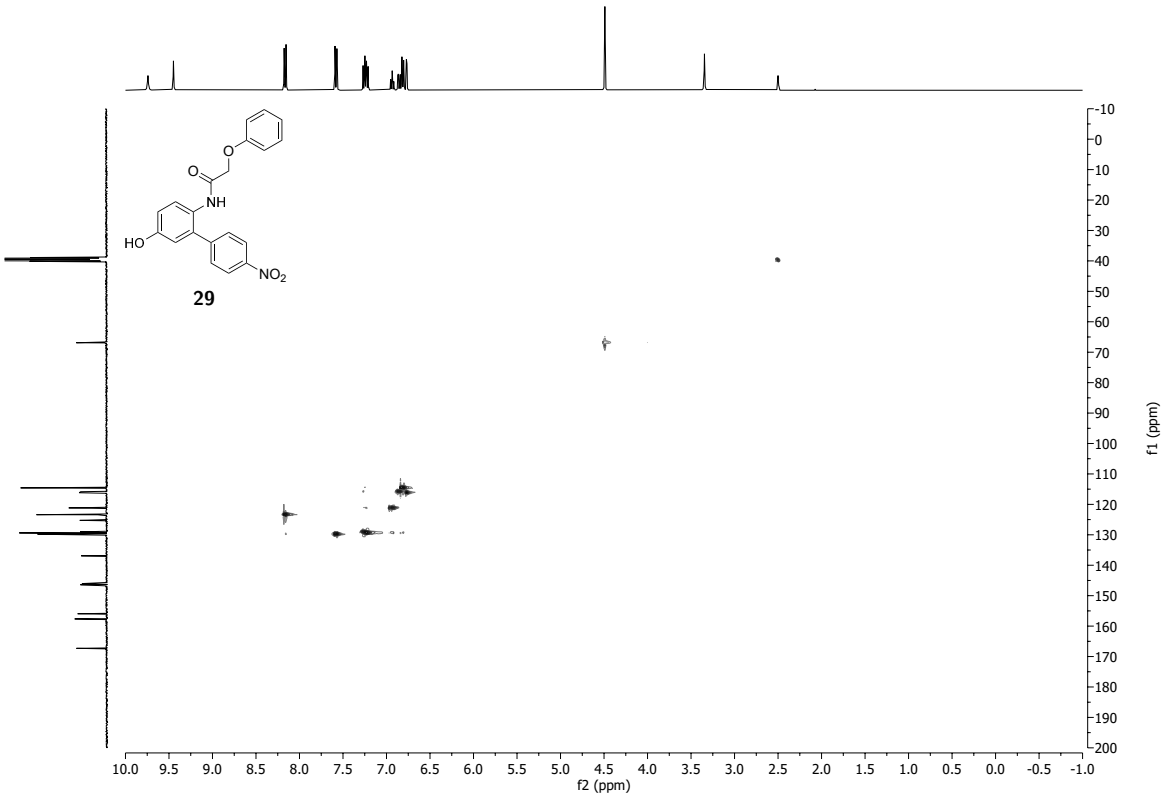

^{1}H ^{13}C HSQC NMR (400 MHz, 100 MHz, DMSO – d_6) spectrum of *N*-(5-hydroxy-4'-nitro-[1,1'-biphenyl]-2-yl)-2-phenoxyacetamide **29**.

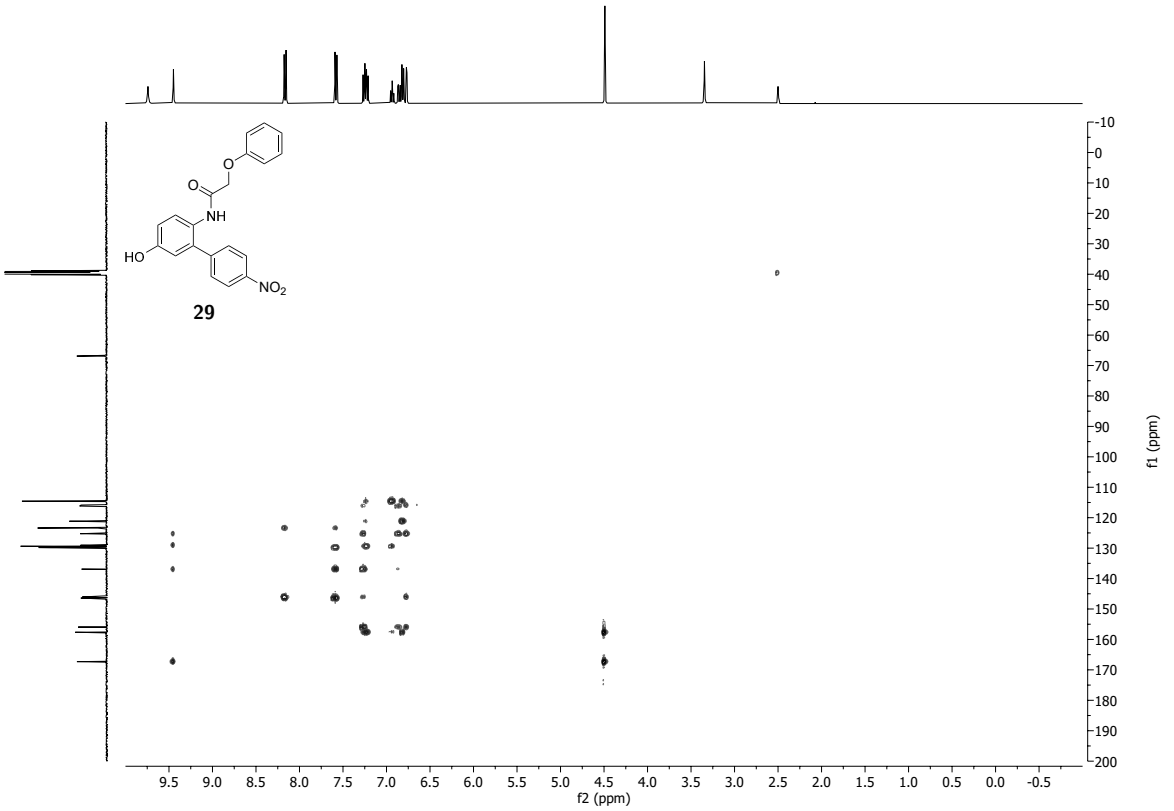

^{1}H ^{13}C HMBC NMR (400 MHz, 100 MHz, DMSO – d_6) spectrum of *N*-(5-hydroxy-4'-nitro-[1,1'-biphenyl]-2-yl)-2-phenoxyacetamide **29**.

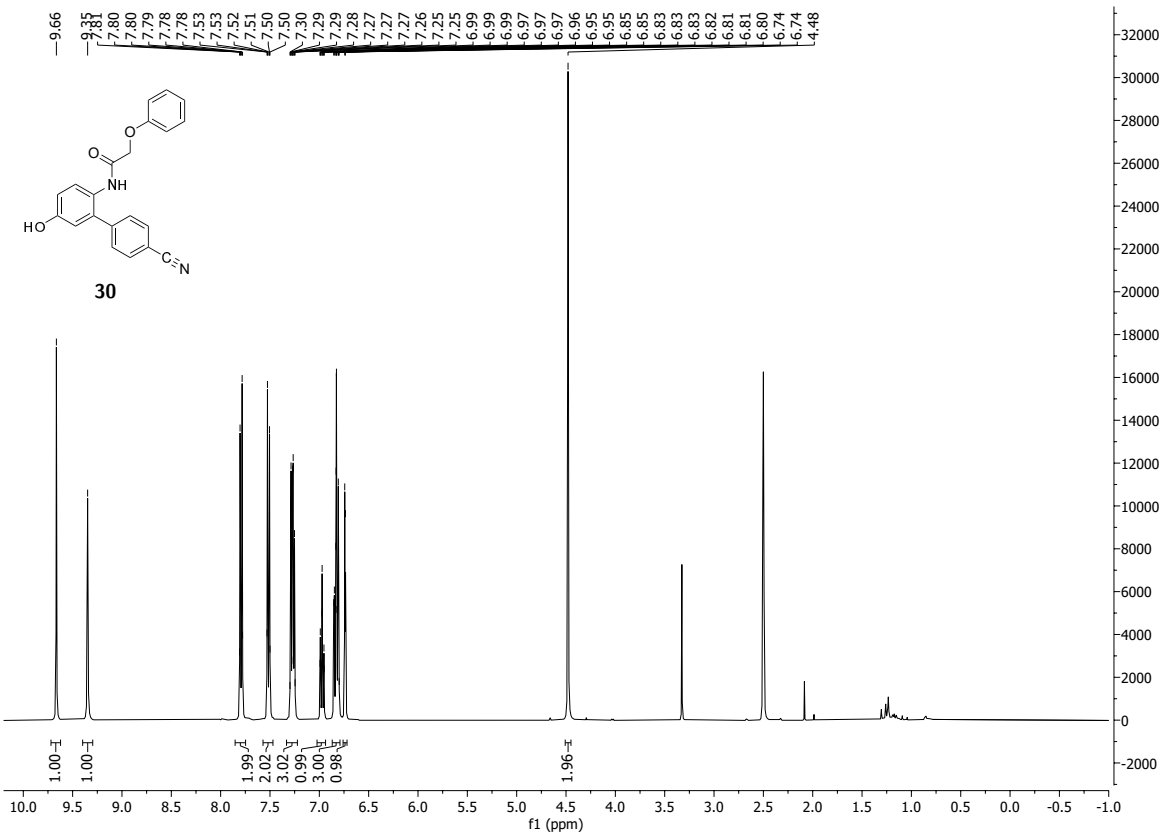

^{1}H NMR (400 MHz, DMSO – d_6) spectrum of
N-(4'-cyano-5-hydroxy-[1,1'-biphenyl]-2-yl)-2-phenoxyacetamide **30**.

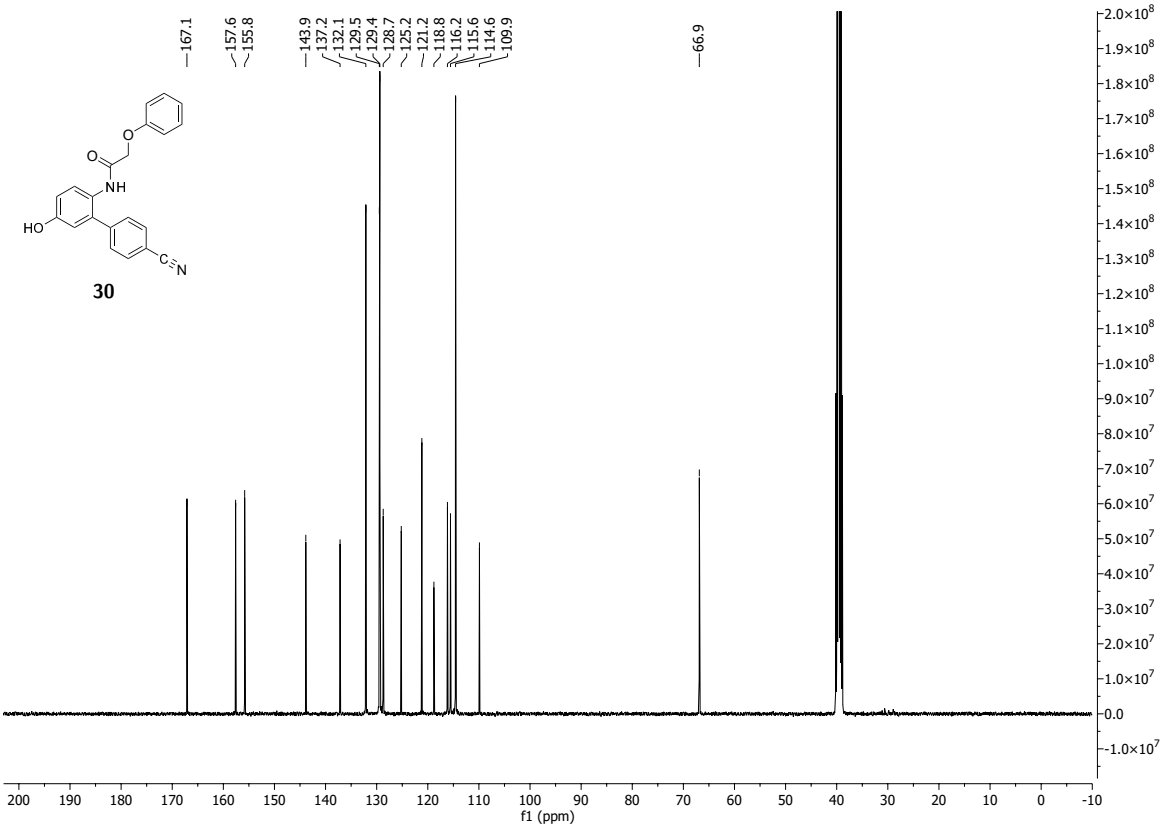

^{13}C NMR (100 MHz, DMSO – d_6) spectrum of
N-(4'-cyano-5-hydroxy-[1,1'-biphenyl]-2-yl)-2-phenoxyacetamide **30**.

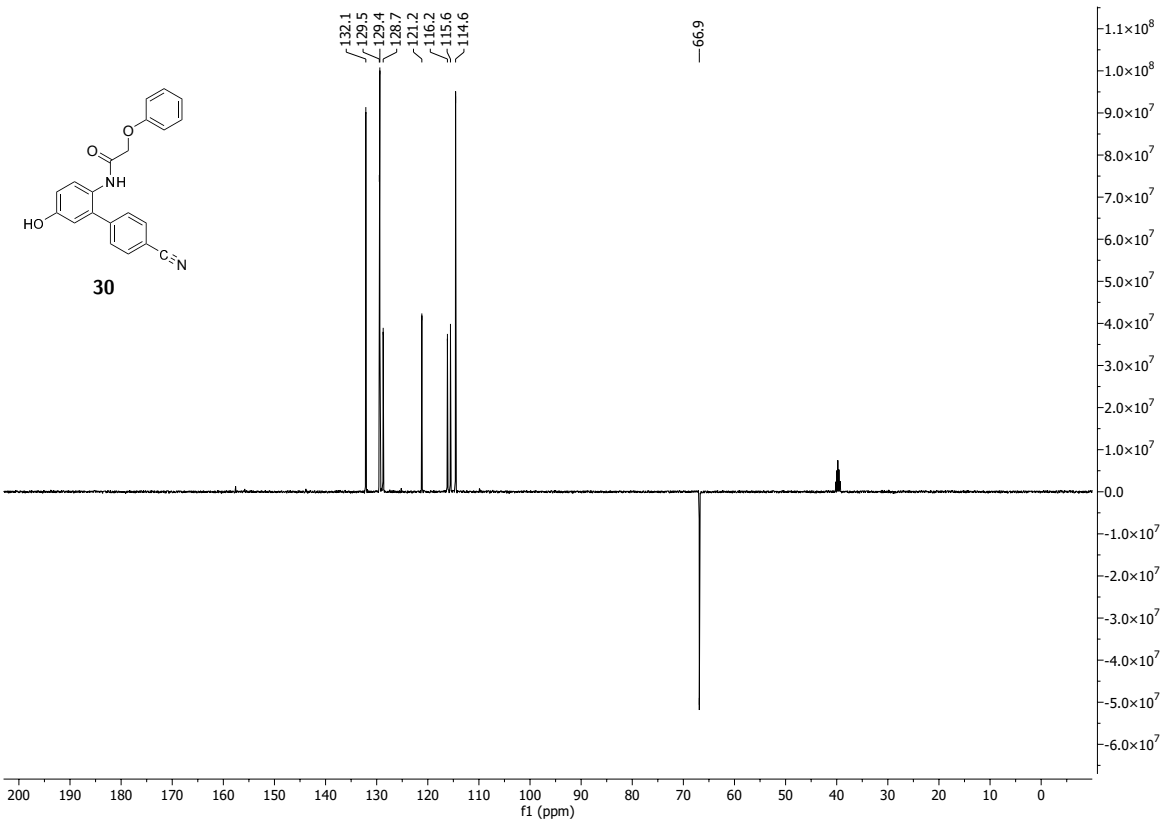

^{13}C DEPT 135 NMR (100 MHz, DMSO – d_6) spectrum of *N*-(4'-cyano-5-hydroxy-[1,1'-biphenyl]-2-yl)-2-phenoxyacetamide **30**.

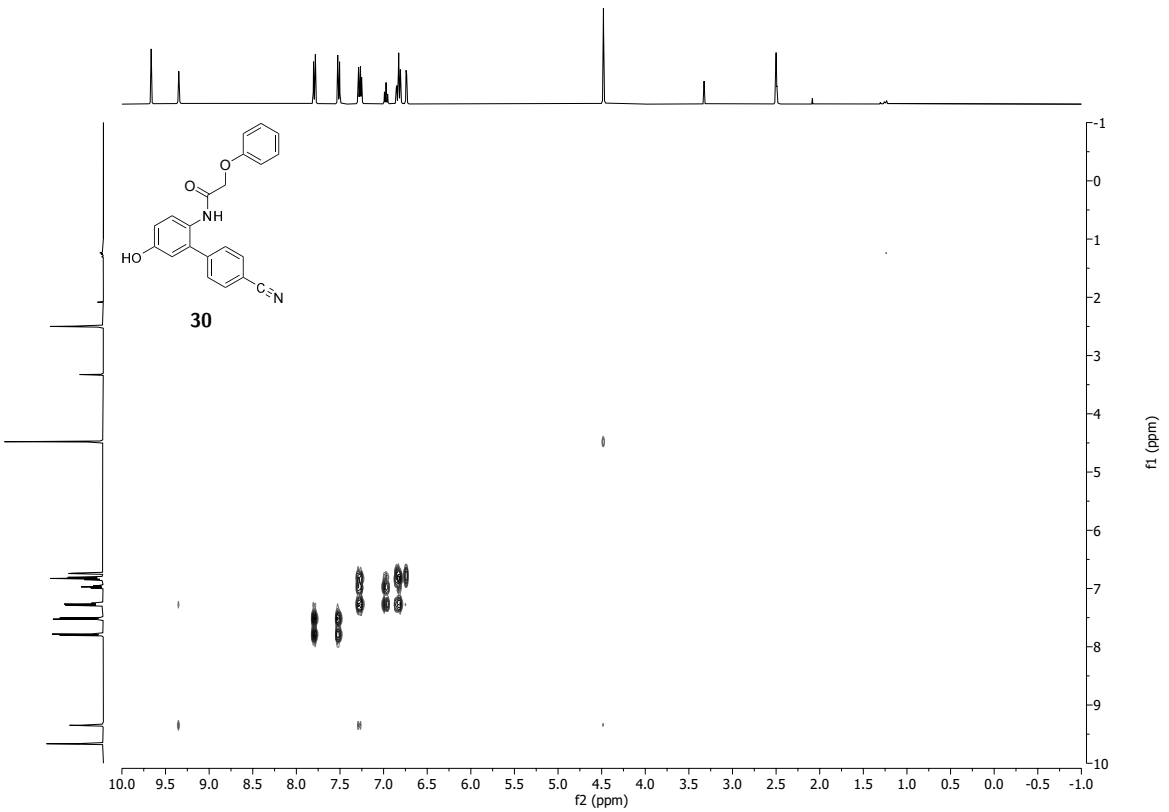

^{1}H ^{1}H COSY NMR (400 MHz, 400 MHz, DMSO – d_6) spectrum of *N*-(4'-cyano-5-hydroxy-[1,1'-biphenyl]-2-yl)-2-phenoxyacetamide **30**.

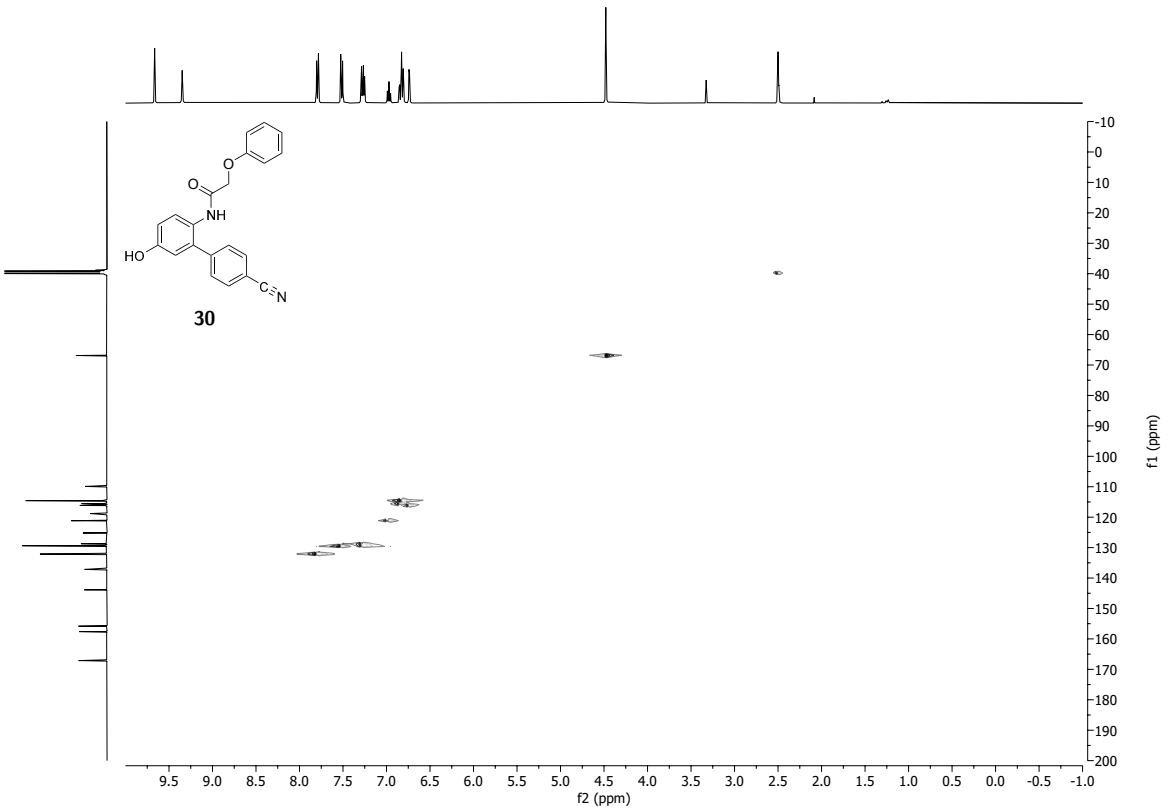

^{1}H ^{13}C HSQC NMR (400 MHz, 100 MHz, DMSO – d_6) spectrum of *N*-(4'-cyano-5-hydroxy-[1,1'-biphenyl]-2-yl)-2-phenoxyacetamide **30**.

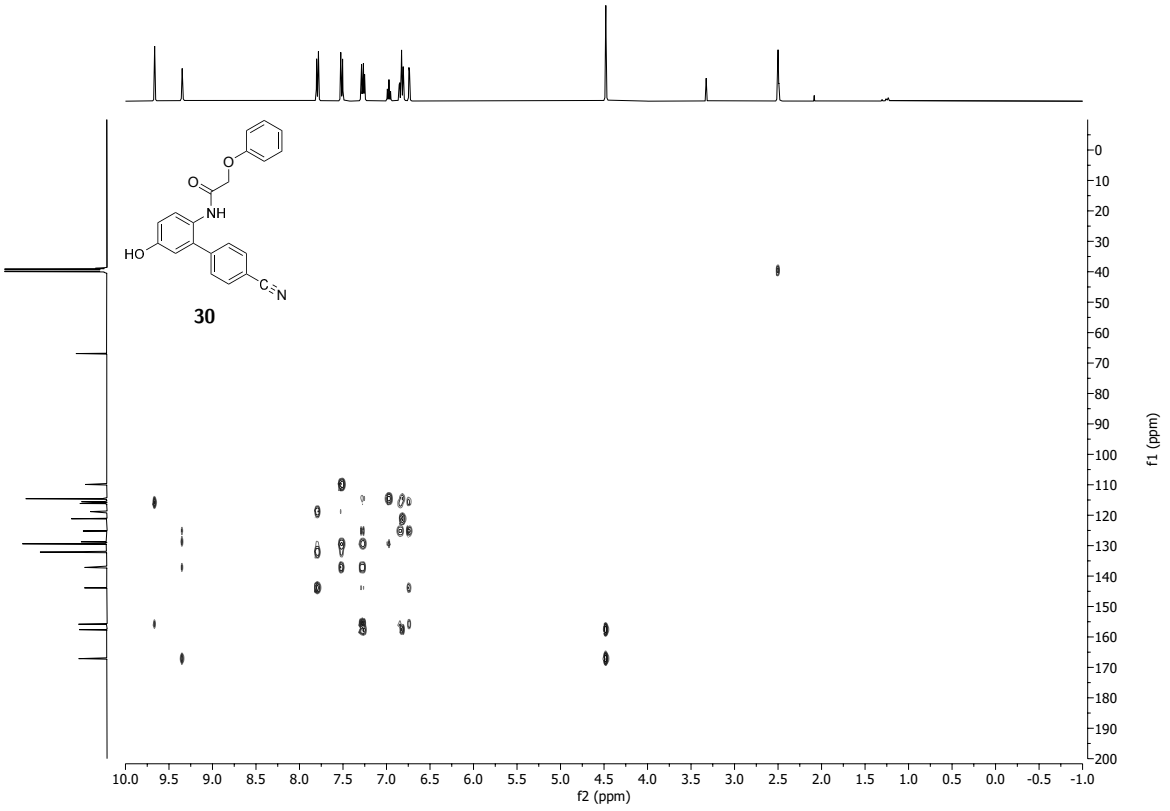

^{1}H ^{13}C HMBC NMR (400 MHz, 100 MHz, DMSO – d_6) spectrum of *N*-(4'-cyano-5-hydroxy-[1,1'-biphenyl]-2-yl)-2-phenoxyacetamide **30**.

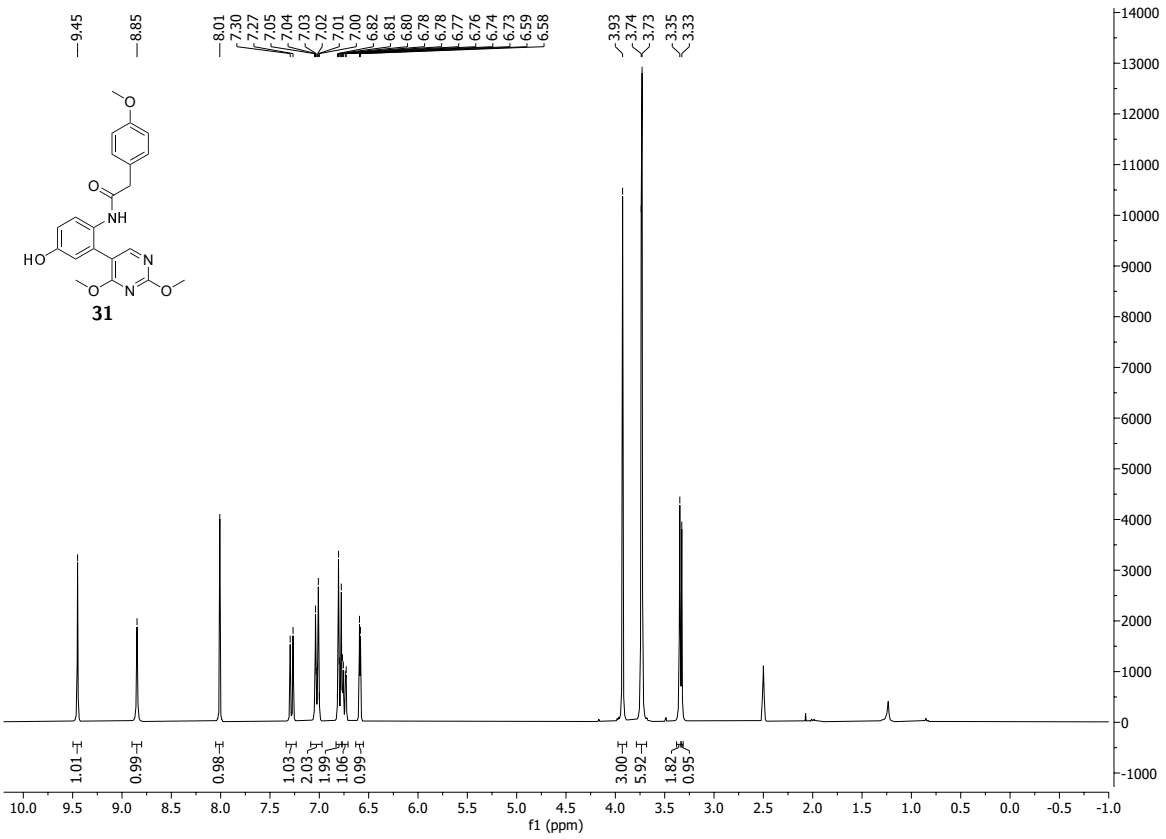

^{1}H NMR (300 MHz, DMSO – d_6) spectrum of *N*-(2-(2,4-dimethoxypyrimidin-5-yl)-4-hydroxyphenyl)-2-(4-methoxyphenyl)acetamide **31**.

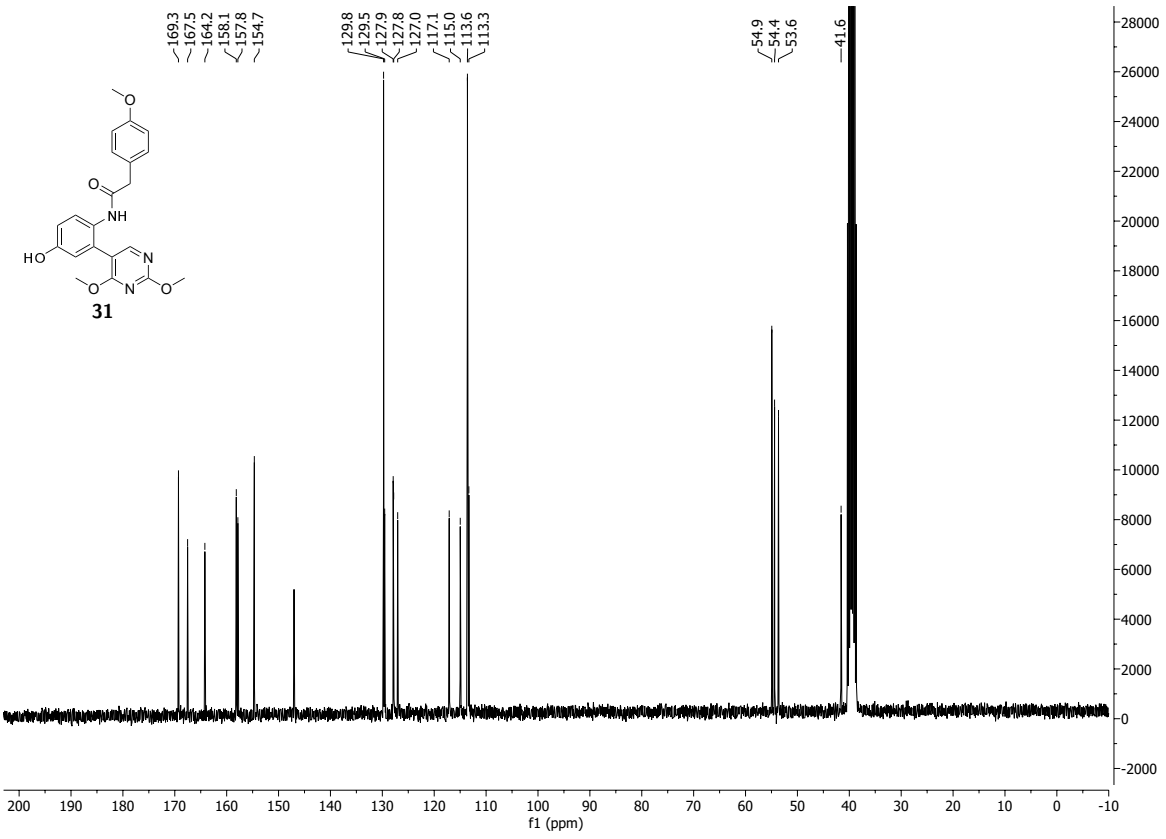

^{13}C NMR (75 MHz, DMSO – d_6) spectrum of *N*-(2-(2,4-dimethoxypyrimidin-5-yl)-4-hydroxyphenyl)-2-(4-methoxyphenyl)acetamide **31**.

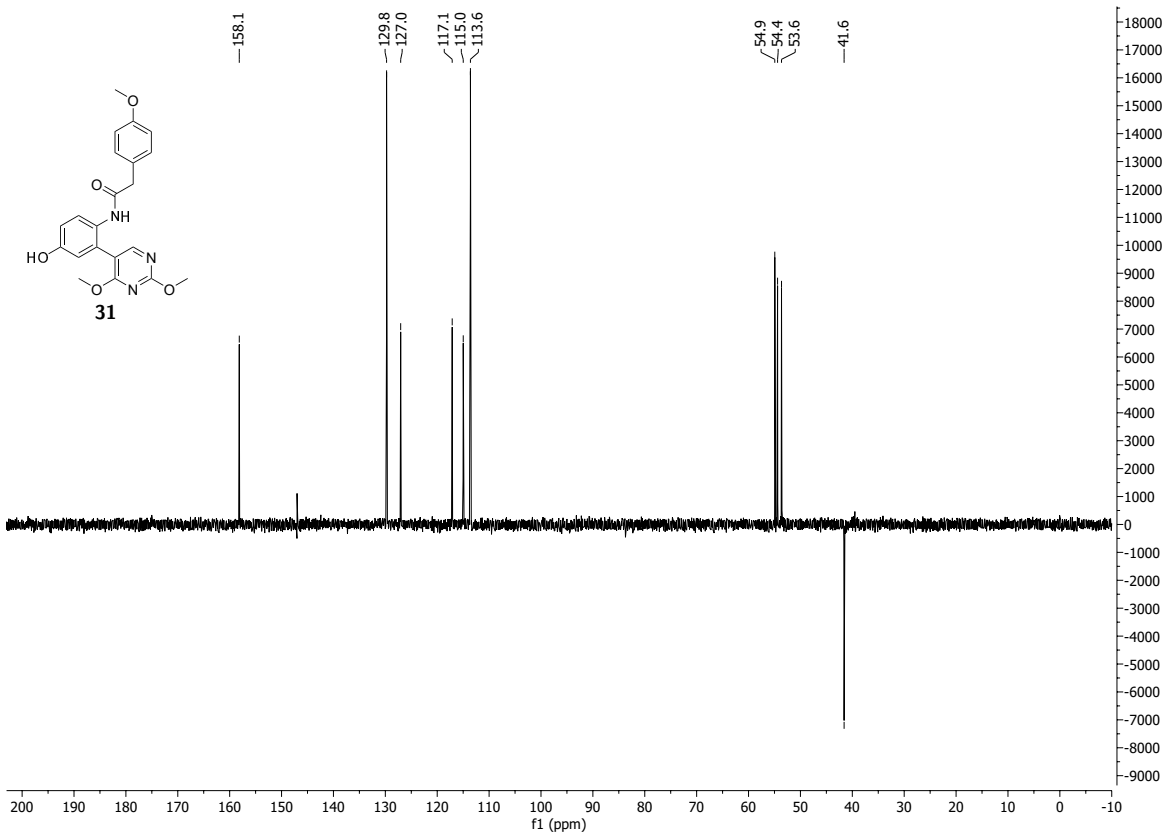

^{13}C DEPT 135 NMR (75 MHz, DMSO–d_6) spectrum of *N*-(2-(2,4-dimethoxypyrimidin-5-yl)-4-hydroxyphenyl)-2-(4-methoxyphenyl)acetamide **31**.

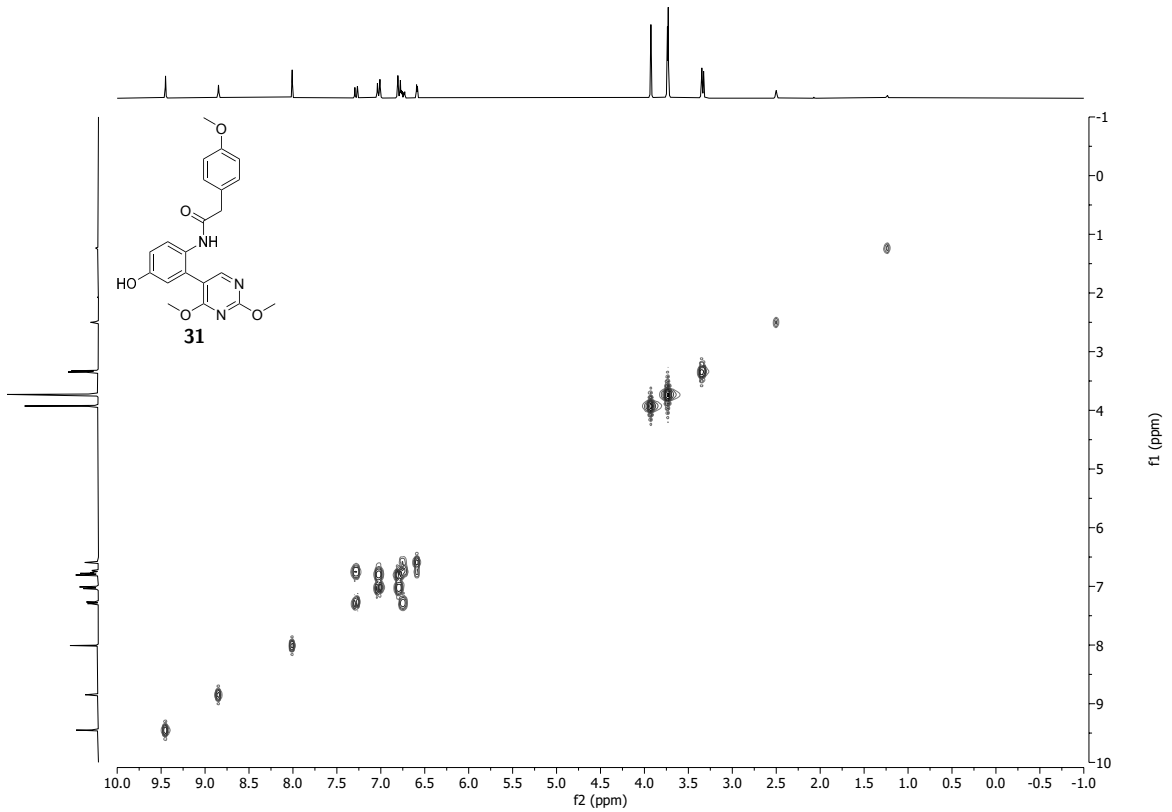

^{1}H ^{1}H COSY NMR (300 MHz, 300 MHz, DMSO–d_6) spectrum of *N*-(2-(2,4-dimethoxypyrimidin-5-yl)-4-hydroxyphenyl)-2-(4-methoxyphenyl)acetamide **31**.

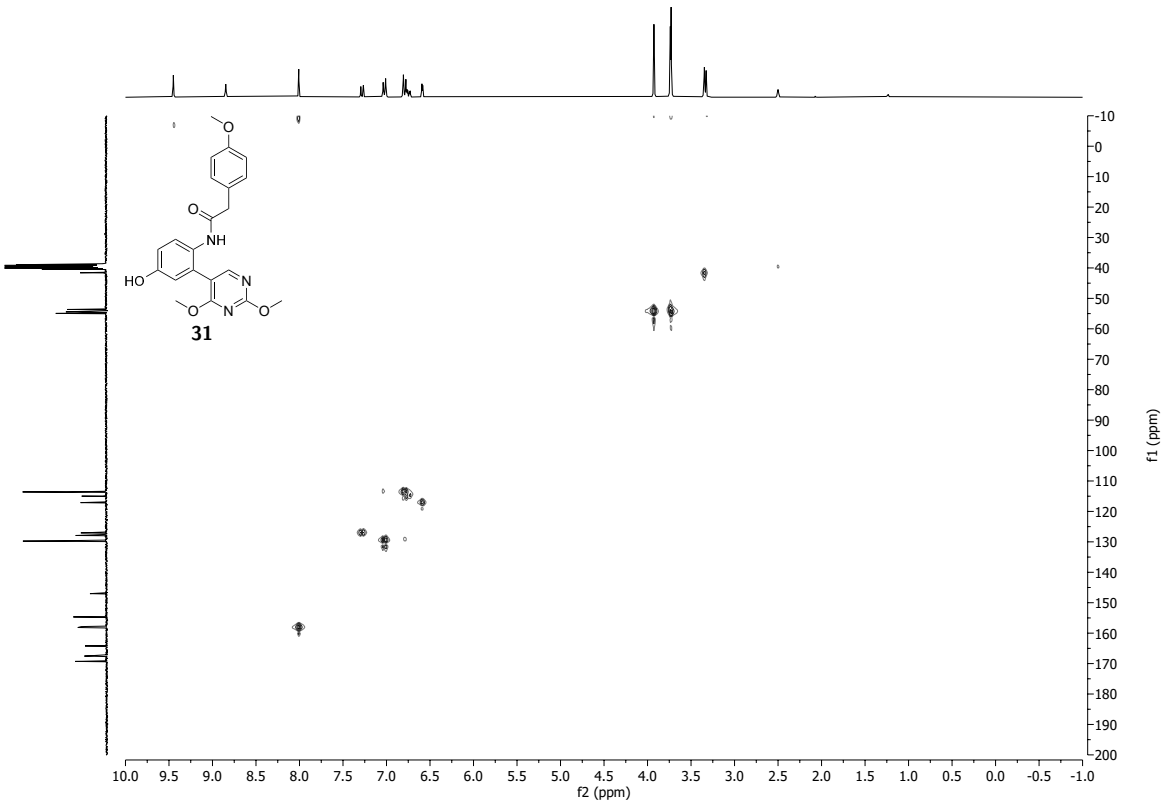

^{1}H ^{13}C HSQC NMR (300 MHz, 75 MHz, DMSO – d_6) spectrum of *N*-(2-(2,4-dimethoxypyrimidin-5-yl)-4-hydroxyphenyl)-2-(4-methoxyphenyl)acetamide **31**.

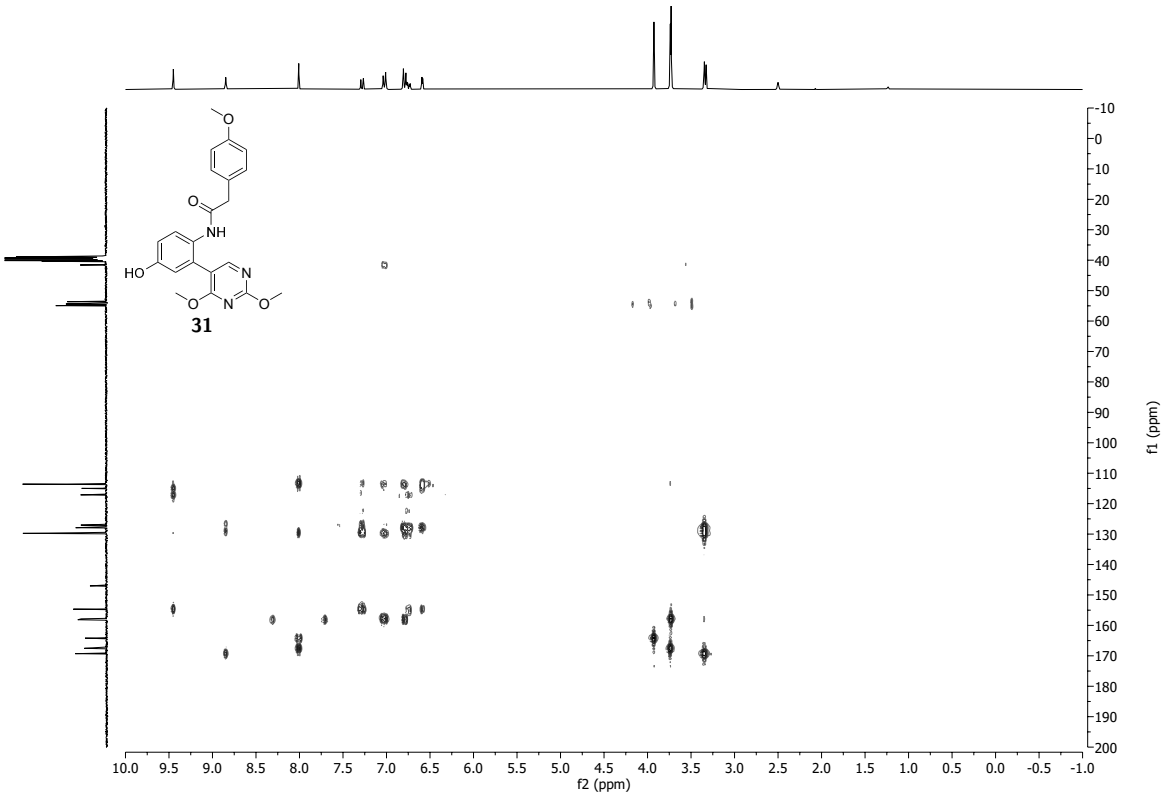

^{1}H ^{13}C HMBC NMR (300 MHz, 75 MHz, DMSO – d_6) spectrum of *N*-(2-(2,4-dimethoxypyrimidin-5-yl)-4-hydroxyphenyl)-2-(4-methoxyphenyl)acetamide **31**.

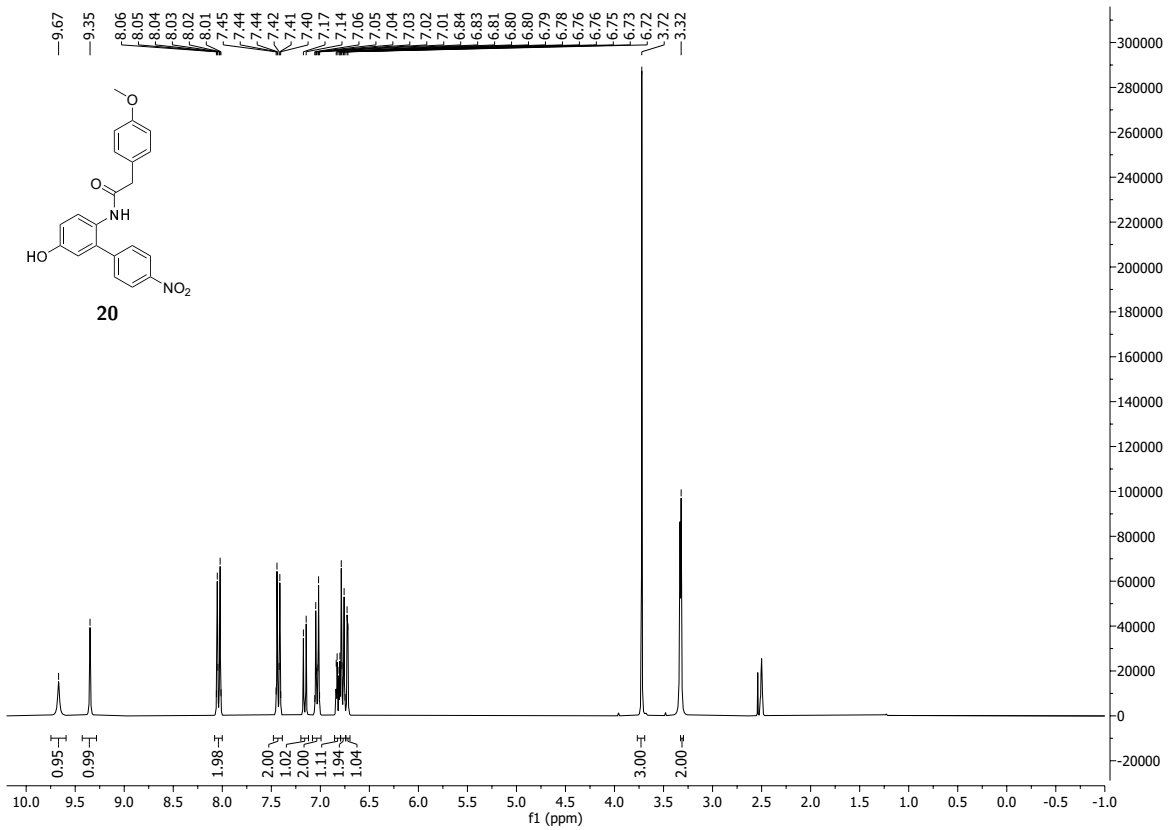

^{1}H NMR (300 MHz, DMSO – d_6) spectrum of
N-(5-hydroxy-4'-nitro-[1,1'-biphenyl]-2-yl)-2-(4-methoxyphenyl)acetamide **20**.

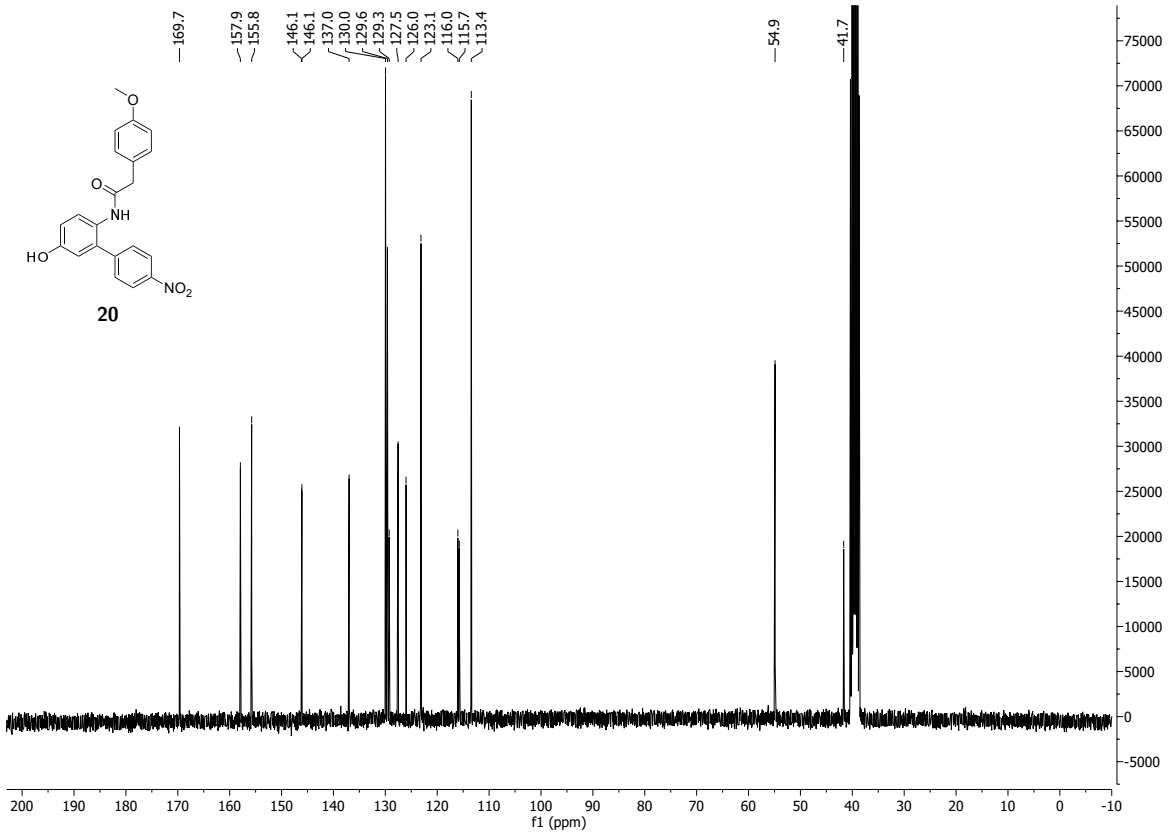

^{13}C NMR (75 MHz, DMSO – d_6) spectrum of
N-(5-hydroxy-4'-nitro-[1,1'-biphenyl]-2-yl)-2-(4-methoxyphenyl)acetamide **20**.

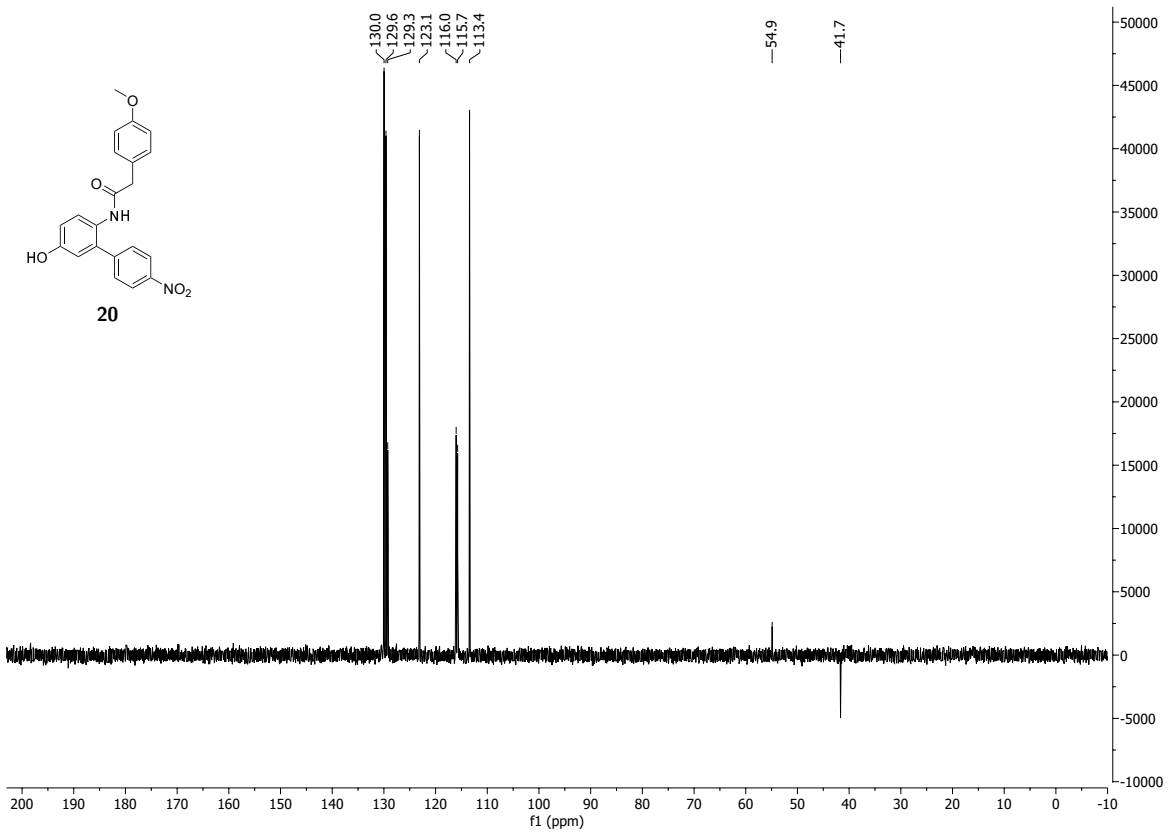

^{13}C DEPT 135 NMR (75 MHz, DMSO−d_6) spectrum of *N*-(5-hydroxy-4'-nitro-[1,1'-biphenyl]-2-yl)-2-(4-methoxyphenyl)acetamide **20**.

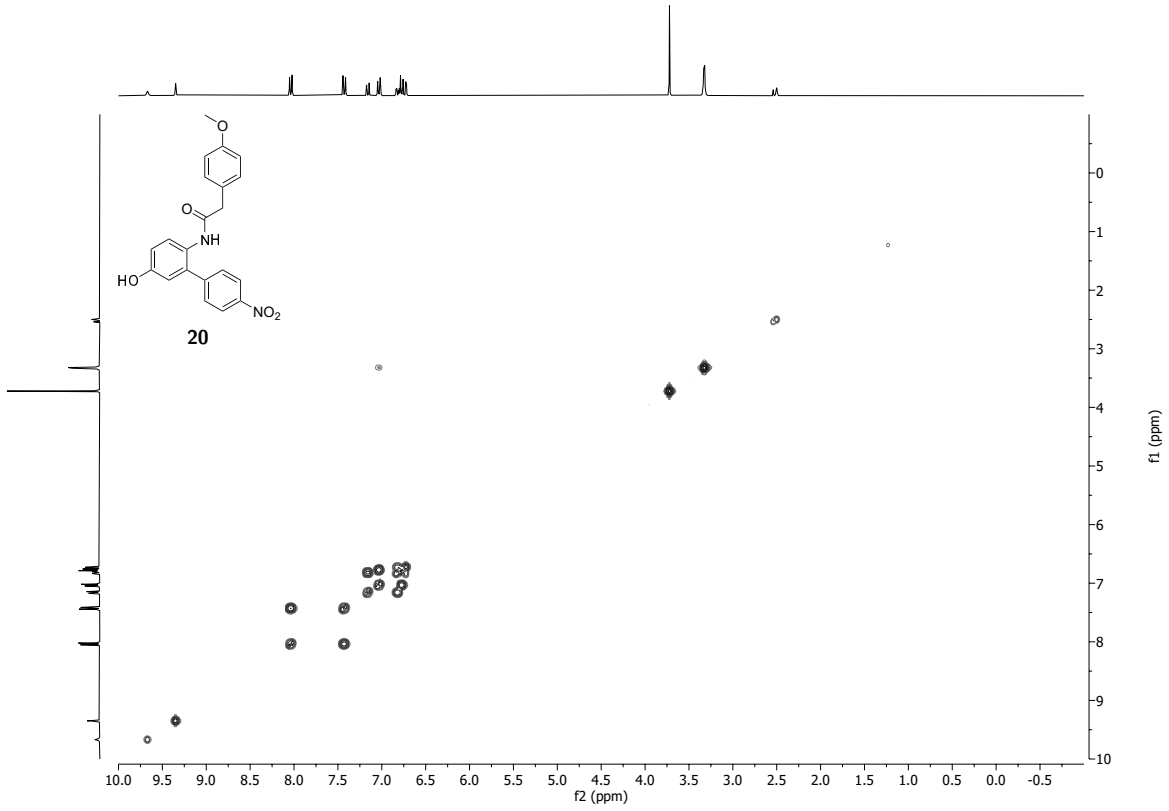

^{1}H ^{1}H COSY NMR (300 MHz, 300 MHz, DMSO−d_6) spectrum of *N*-(5-hydroxy-4'-nitro-[1,1'-biphenyl]-2-yl)-2-(4-methoxyphenyl)acetamide **20**.

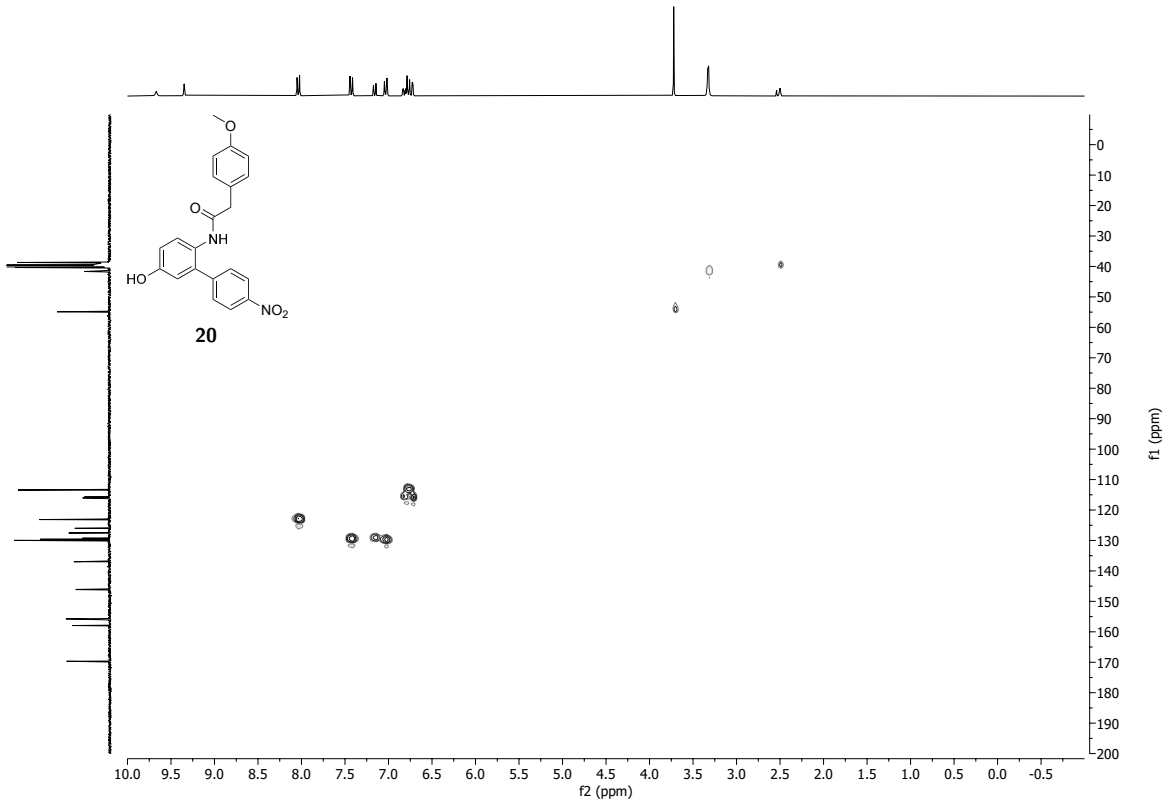

^{1}H ^{13}C HSQC NMR (300 MHz, 75 MHz, DMSO – d_6) spectrum of *N*-(5-hydroxy-4'-nitro-[1,1'-biphenyl]-2-yl)-2-(4-methoxyphenyl)acetamide **20**.

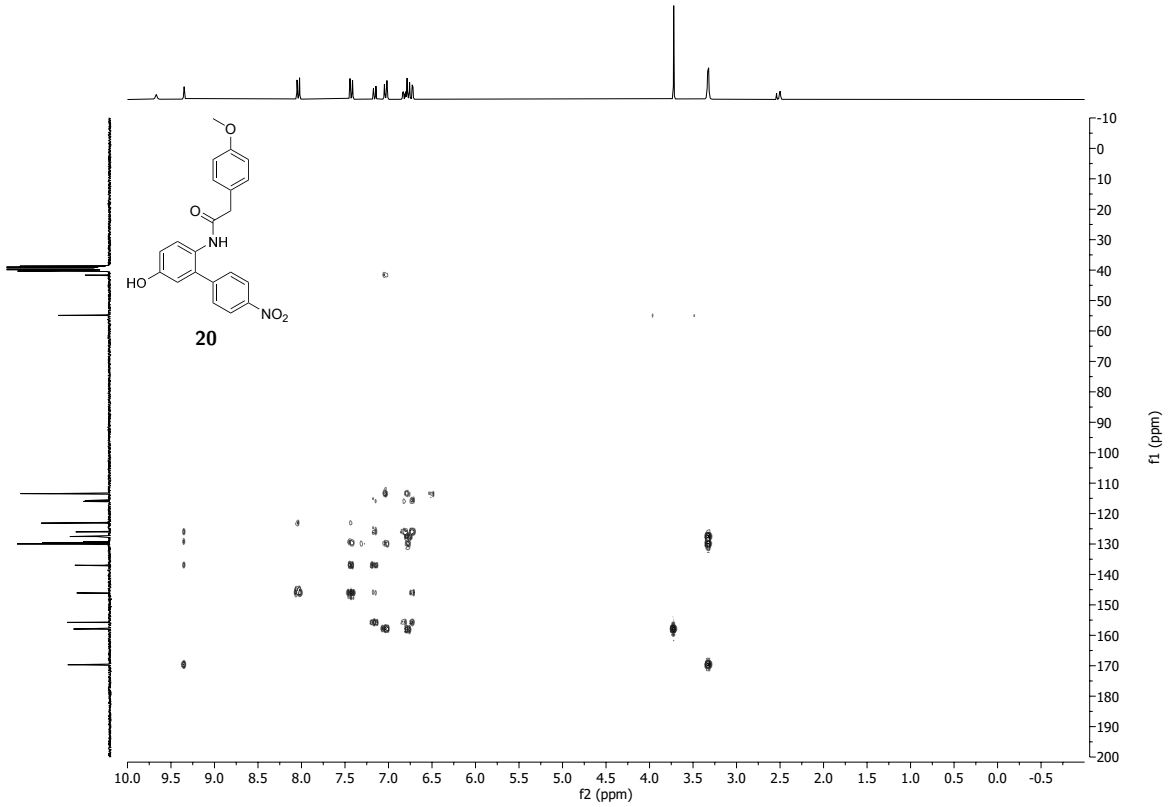

^{1}H ^{13}C HMBC NMR (300 MHz, 75 MHz, DMSO – d_6) spectrum of *N*-(5-hydroxy-4'-nitro-[1,1'-biphenyl]-2-yl)-2-(4-methoxyphenyl)acetamide **20**.

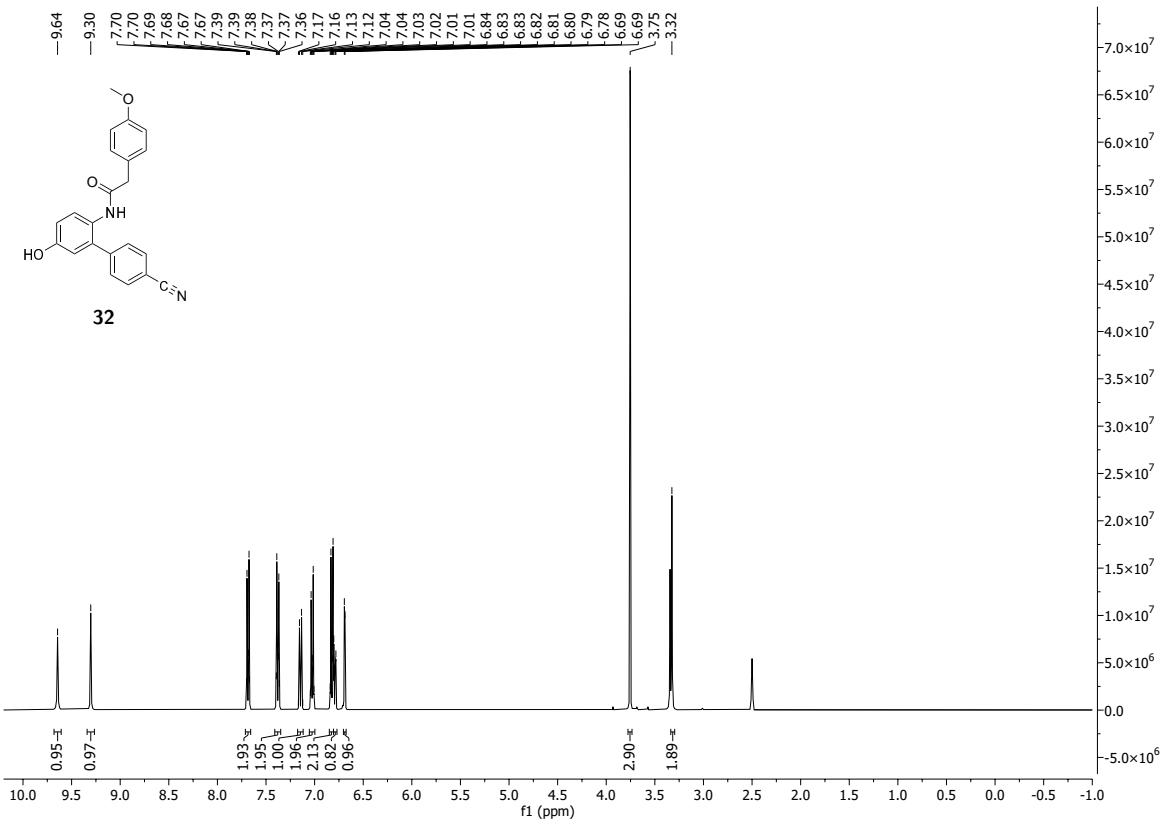

^{1}H NMR (400 MHz, DMSO – d_6) spectrum of
N-(4'-cyano-5-hydroxy-[1,1'-biphenyl]-2-yl)-2-(4-methoxyphenyl)acetamide **32**.

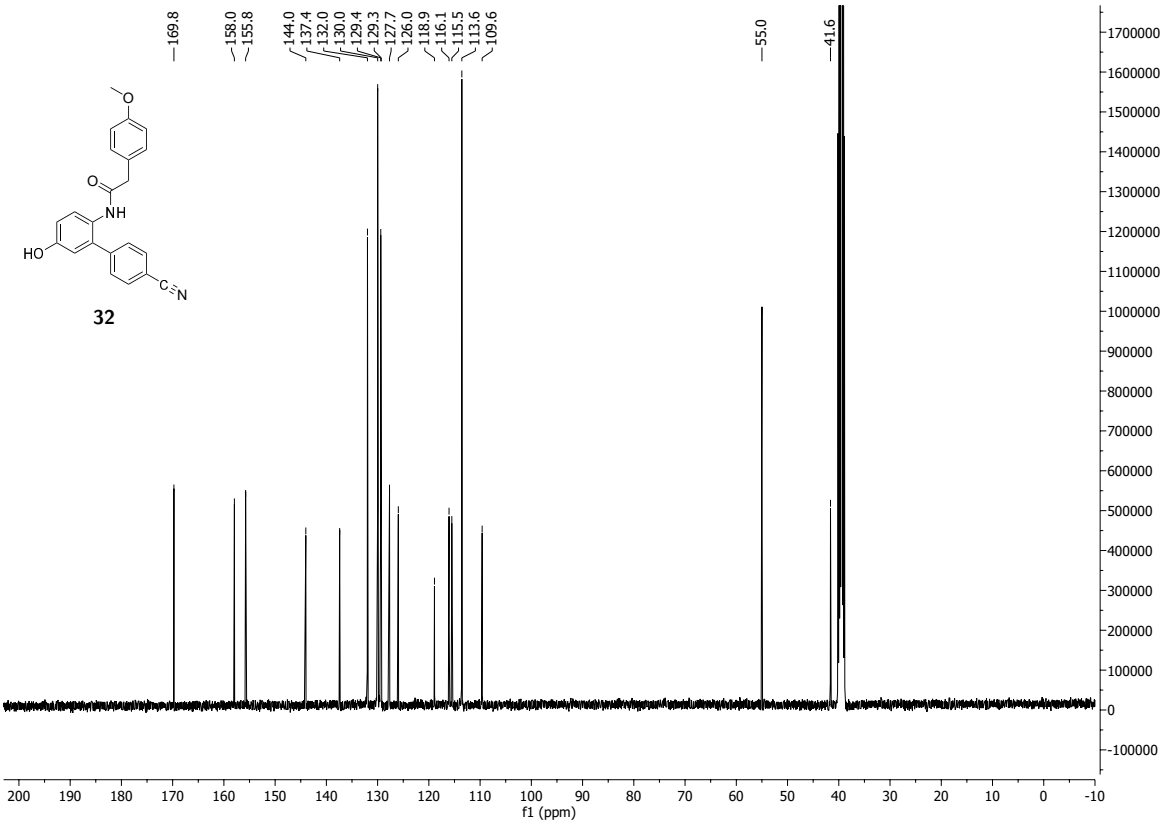

^{13}C NMR (100 MHz, DMSO – d_6) spectrum of
N-(4'-cyano-5-hydroxy-[1,1'-biphenyl]-2-yl)-2-(4-methoxyphenyl)acetamide **32**.

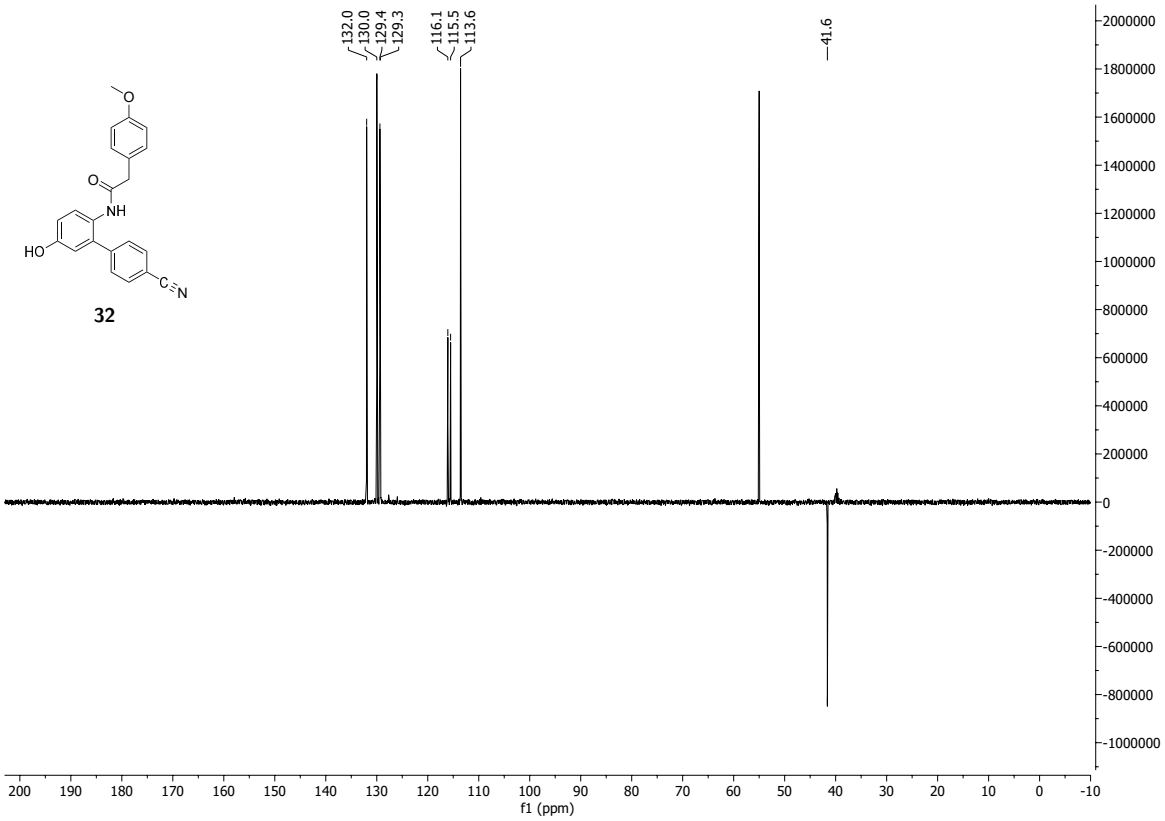

^{13}C DEPT 135 NMR (100 MHz, DMSO – d_6) spectrum of *N*-(4'-cyano-5-hydroxy-[1,1'-biphenyl]-2-yl)-2-(4-methoxyphenyl)acetamide **32**.

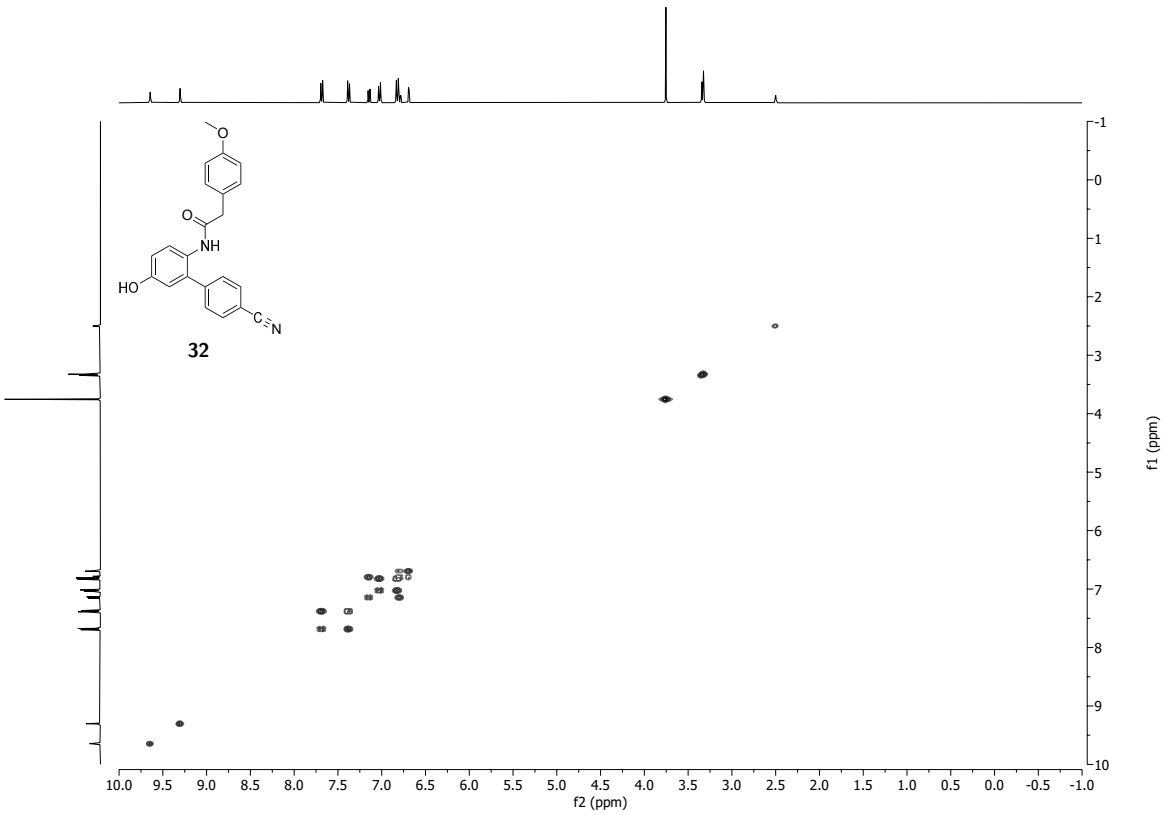

^{1}H ^{1}H COSY NMR (400 MHz, 400 MHz, DMSO – d_6) spectrum of *N*-(4'-cyano-5-hydroxy-[1,1'-biphenyl]-2-yl)-2-(4-methoxyphenyl)acetamide **32**.

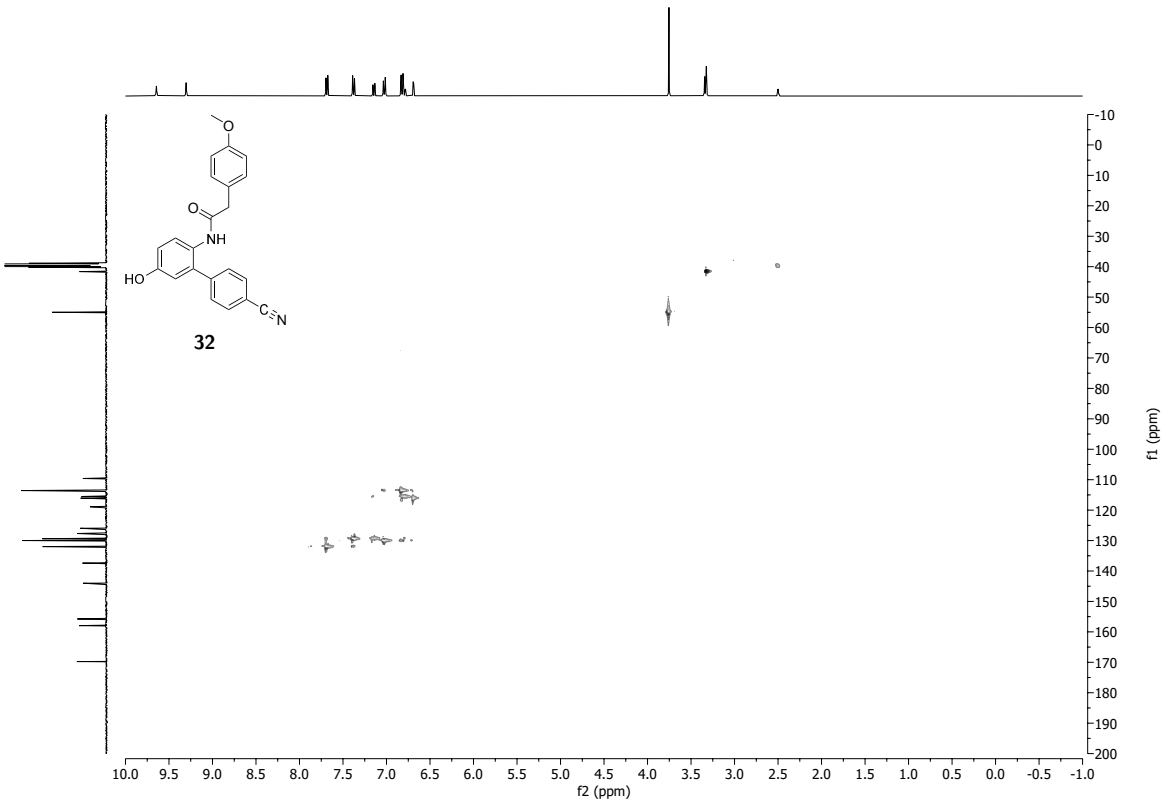

^{1}H ^{13}C HSQC NMR (400 MHz, 100 MHz, DMSO – d_6) spectrum of *N*-(4'-cyano-5-hydroxy-[1,1'-biphenyl]-2-yl)-2-(4-methoxyphenyl)acetamide **32**.

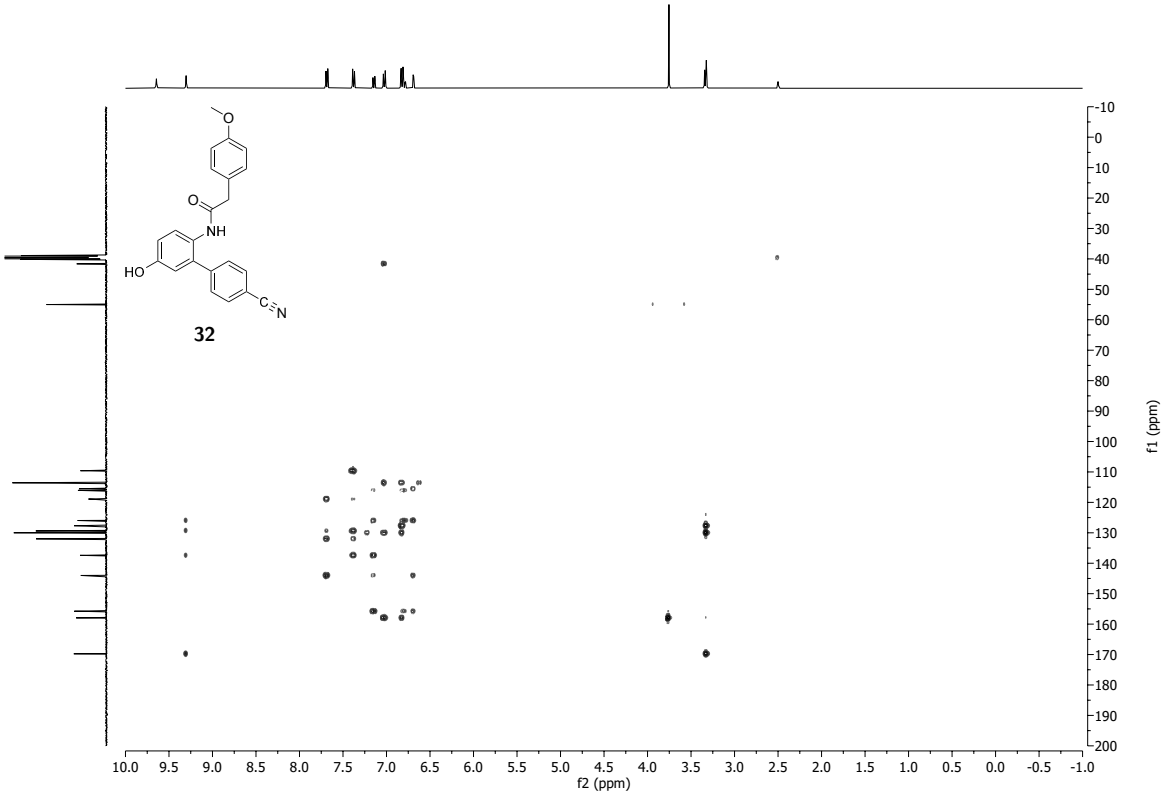

^{1}H ^{13}C HMBC NMR (400 MHz, 100 MHz, DMSO – d_6) spectrum of *N*-(4'-cyano-5-hydroxy-[1,1'-biphenyl]-2-yl)-2-(4-methoxyphenyl)acetamide **32**.

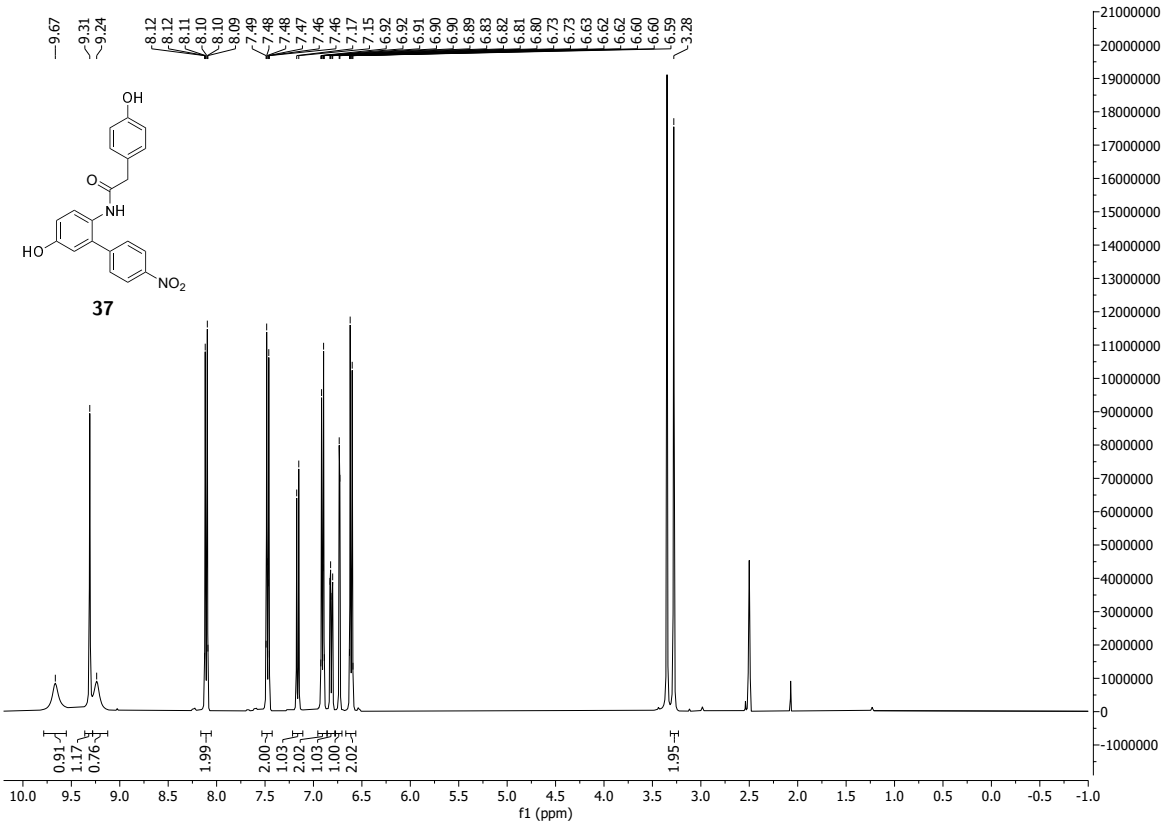

^{1}H NMR (400 MHz, DMSO – d_6) spectrum of
N-(5-hydroxy-4'-nitro-[1,1'-biphenyl]-2-yl)-2-(4-hydroxyphenyl)acetamide **37**.

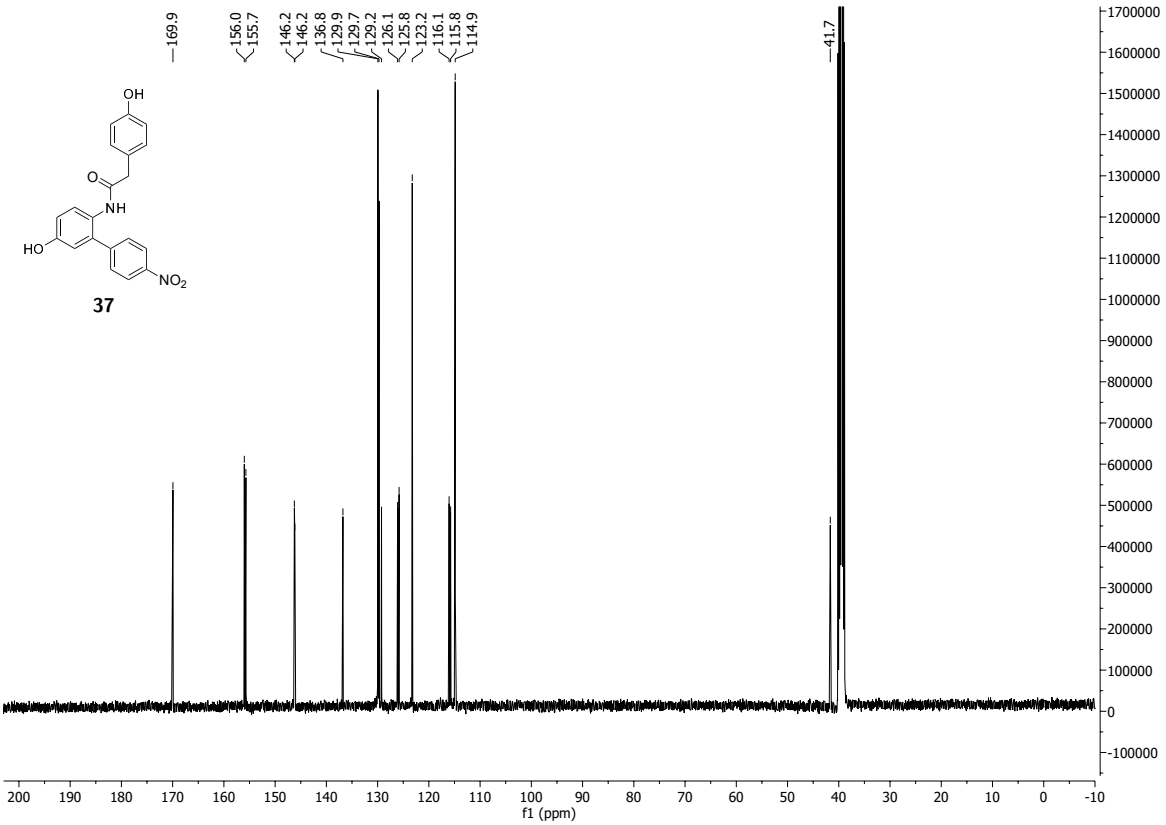

^{13}C NMR (100 MHz, DMSO – d_6) spectrum of
N-(5-hydroxy-4'-nitro-[1,1'-biphenyl]-2-yl)-2-(4-hydroxyphenyl)acetamide **37**.

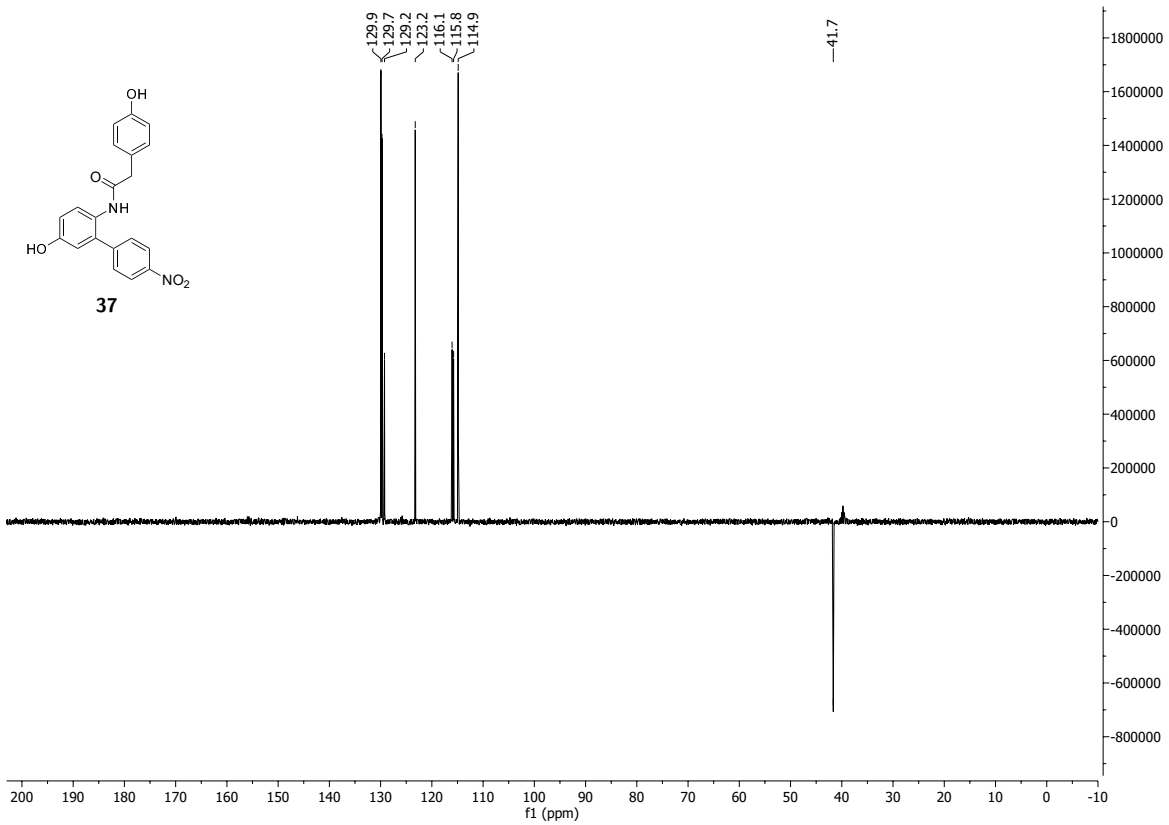

^{13}C DEPT 135 NMR (100 MHz, DMSO – d_6) spectrum of *N*-(5-hydroxy-4'-nitro-[1,1'-biphenyl]-2-yl)-2-(4-hydroxyphenyl)acetamide **37**.

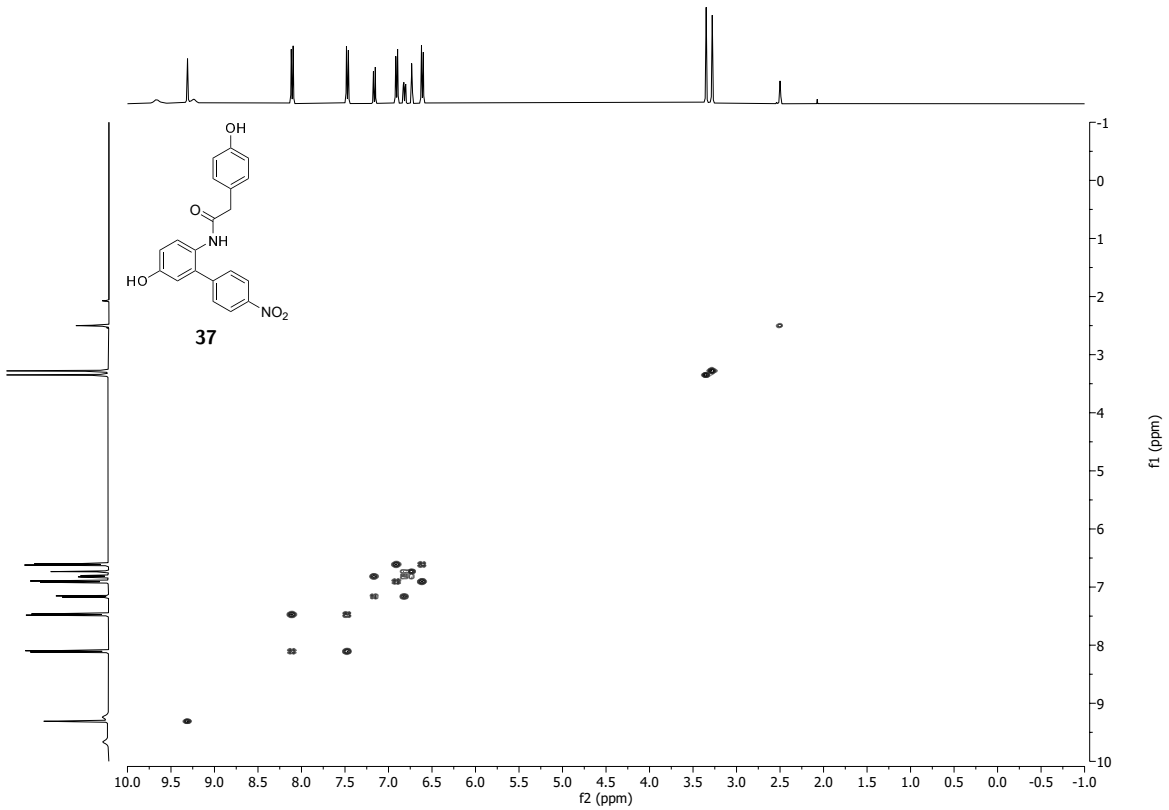

^{1}H ^{1}H COSY NMR (400 MHz, 400 MHz, DMSO – d_6) spectrum of *N*-(5-hydroxy-4'-nitro-[1,1'-biphenyl]-2-yl)-2-(4-hydroxyphenyl)acetamide **37**.

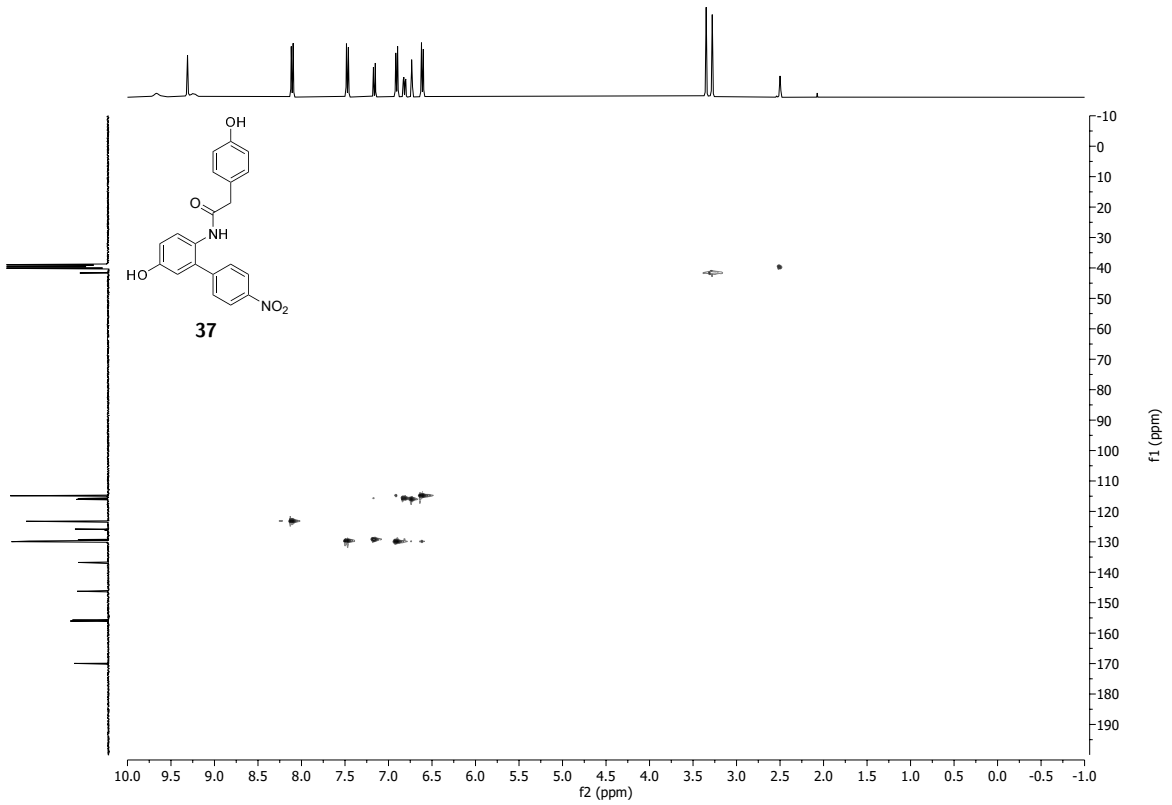

^{1}H ^{13}C HSQC NMR (400 MHz, 100 MHz, DMSO – d_6) spectrum of *N*-(5-hydroxy-4'-nitro-[1,1'-biphenyl]-2-yl)-2-(4-hydroxyphenyl)acetamide **37**.

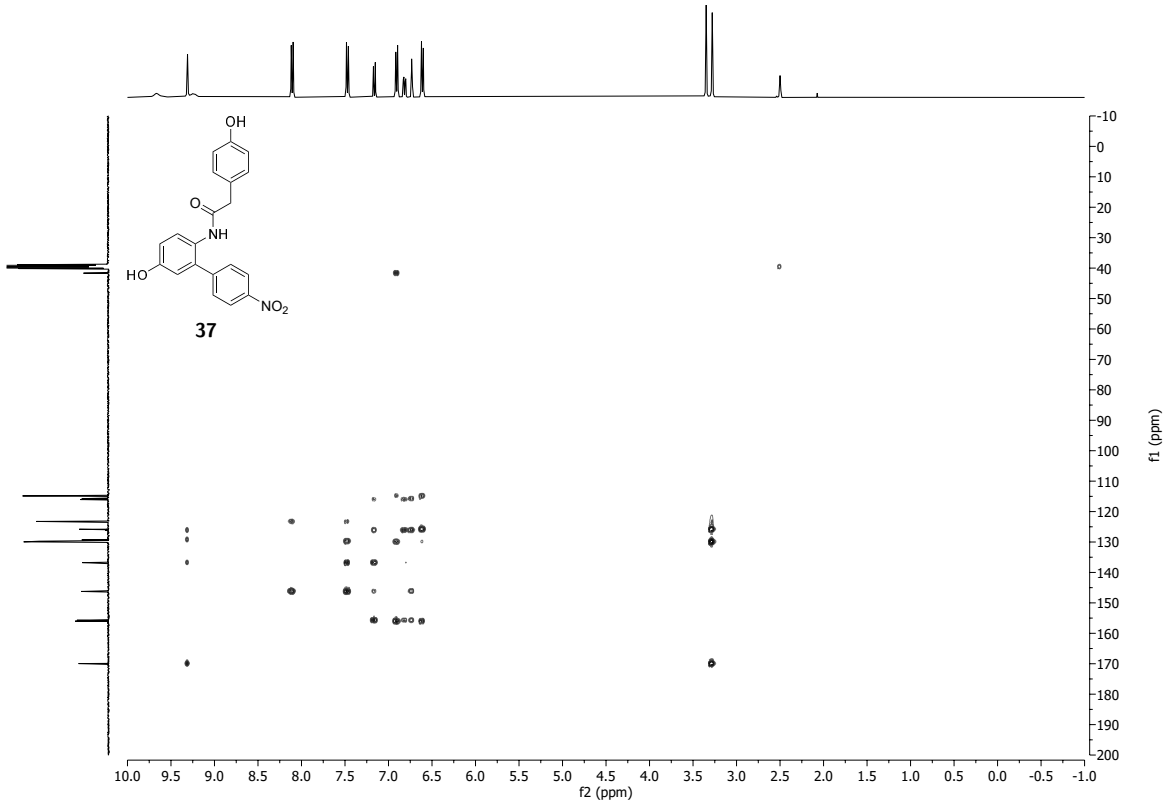

^{1}H ^{13}C HMBC NMR (400 MHz, 100 MHz, DMSO – d_6) spectrum of *N*-(5-hydroxy-4'-nitro-[1,1'-biphenyl]-2-yl)-2-(4-hydroxyphenyl)acetamide **37**.

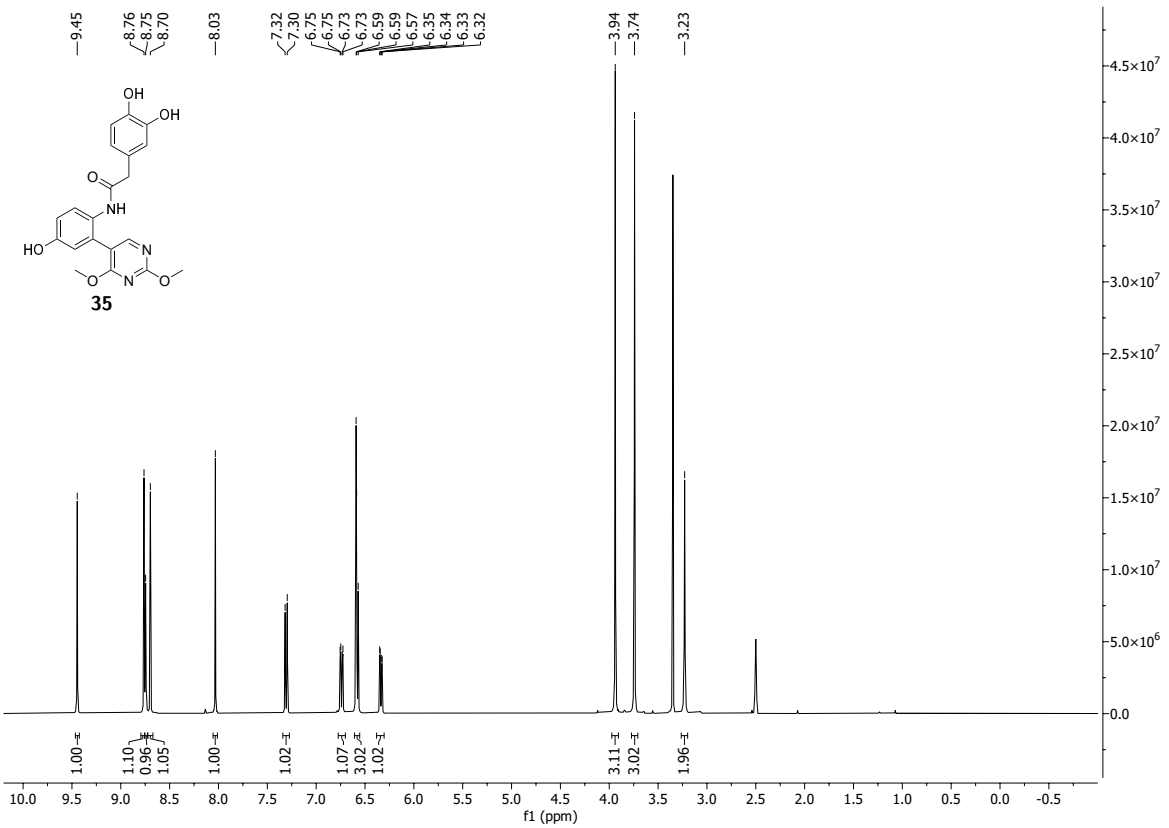

^{1}H NMR (400 MHz, DMSO – d_6) spectrum of
2-(3,4-dihydroxyphenyl)-*N*-(2-(2,4-dimethoxypyrimidin-5-yl)-4-hydroxyphenyl)acetamide **35**.

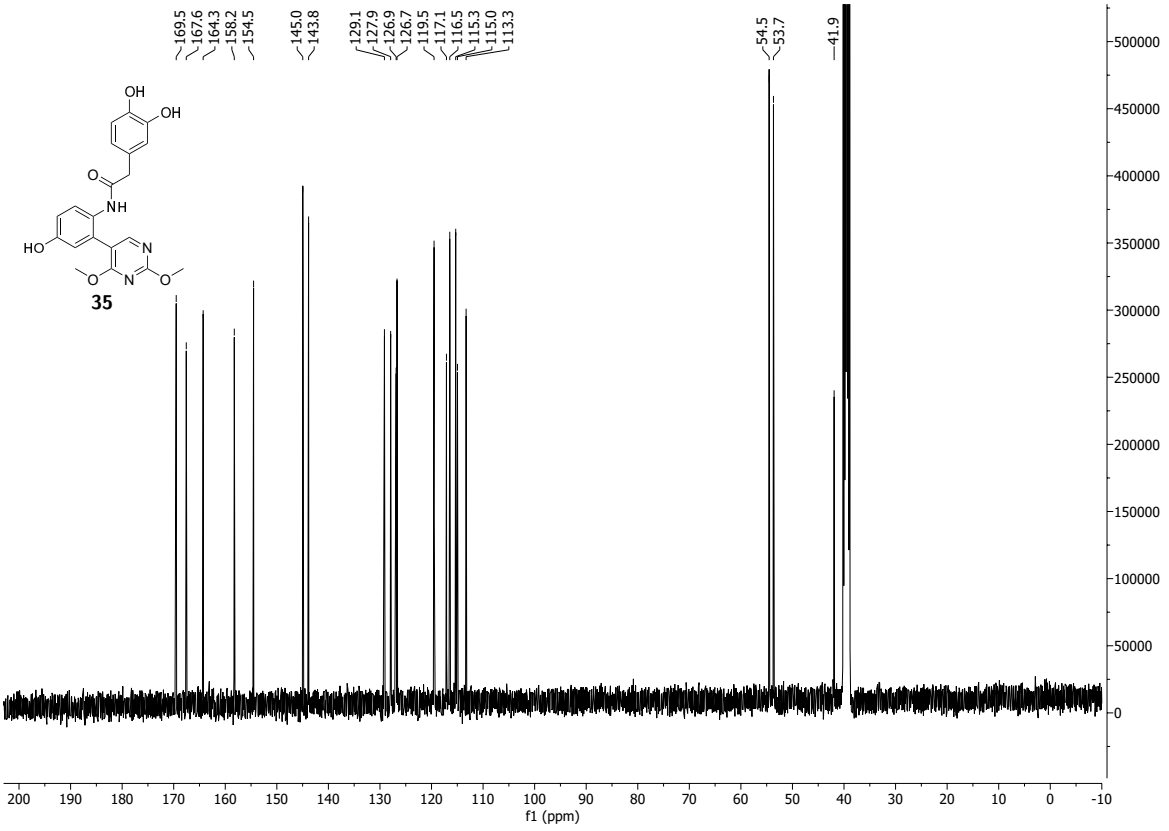

^{13}C NMR (100 MHz, DMSO – d_6) spectrum of
2-(3,4-dihydroxyphenyl)-*N*-(2-(2,4-dimethoxypyrimidin-5-yl)-4-hydroxyphenyl)acetamide **35**.

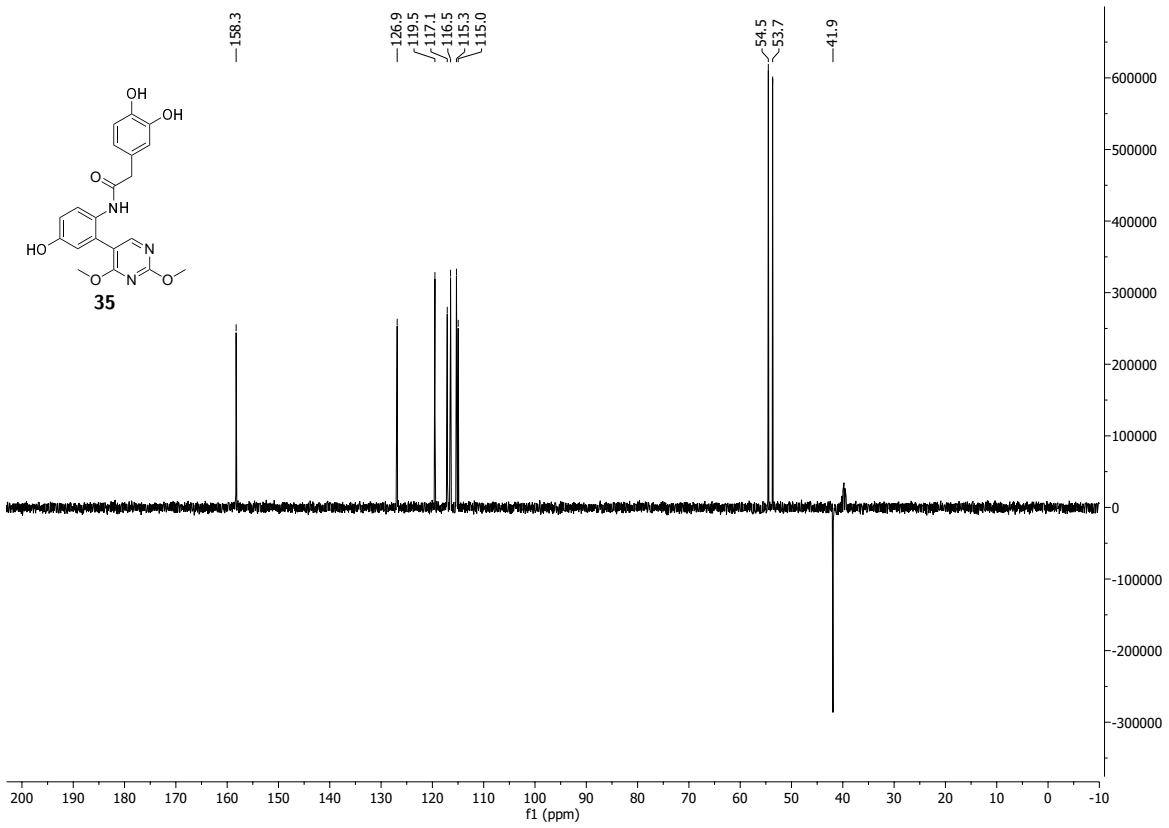

^{13}C DEPT 135 NMR (100 MHz, DMSO – d_6) spectrum of 2-(3,4-dihydroxyphenyl)-*N*-(2-(2,4-dimethoxypyrimidin-5-yl)-4-hydroxyphenyl)acetamide **35**.

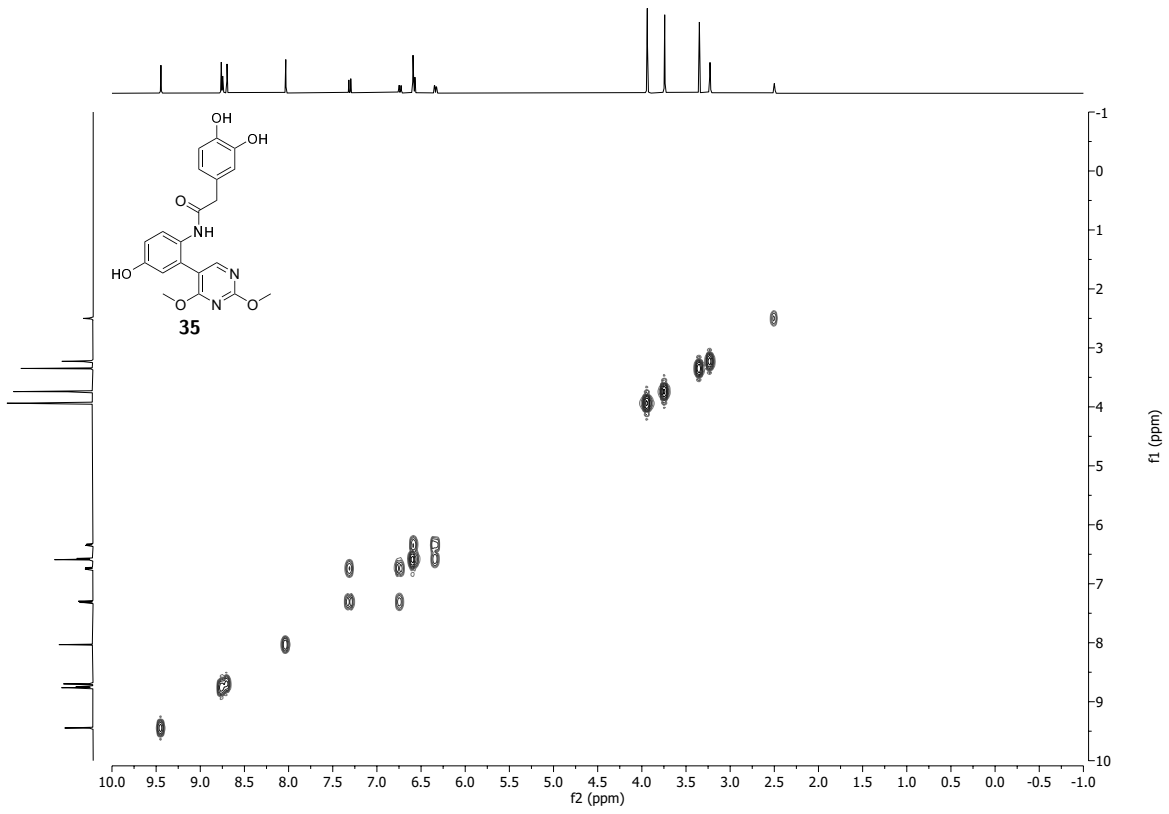

^{1}H ^{1}H COSY NMR (400 MHz, 400 MHz, DMSO – d_6) spectrum of 2-(3,4-dihydroxyphenyl)-*N*-(2-(2,4-dimethoxypyrimidin-5-yl)-4-hydroxyphenyl)acetamide **35**.

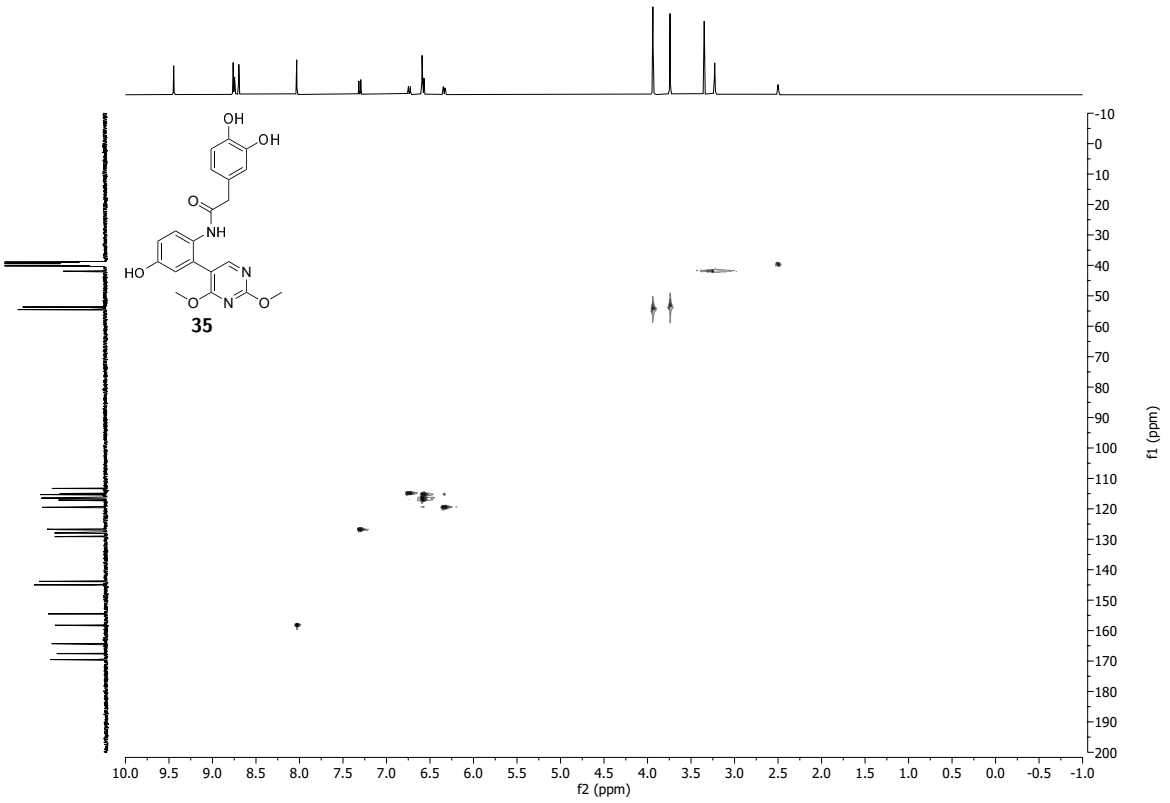

^{1}H ^{13}C HSQC NMR (400 MHz, 100 MHz, DMSO – d_6) spectrum of 2-(3,4-dihydroxyphenyl)-*N*-(2-(2,4-dimethoxypyrimidin-5-yl)-4-hydroxyphenyl)acetamide **35**.

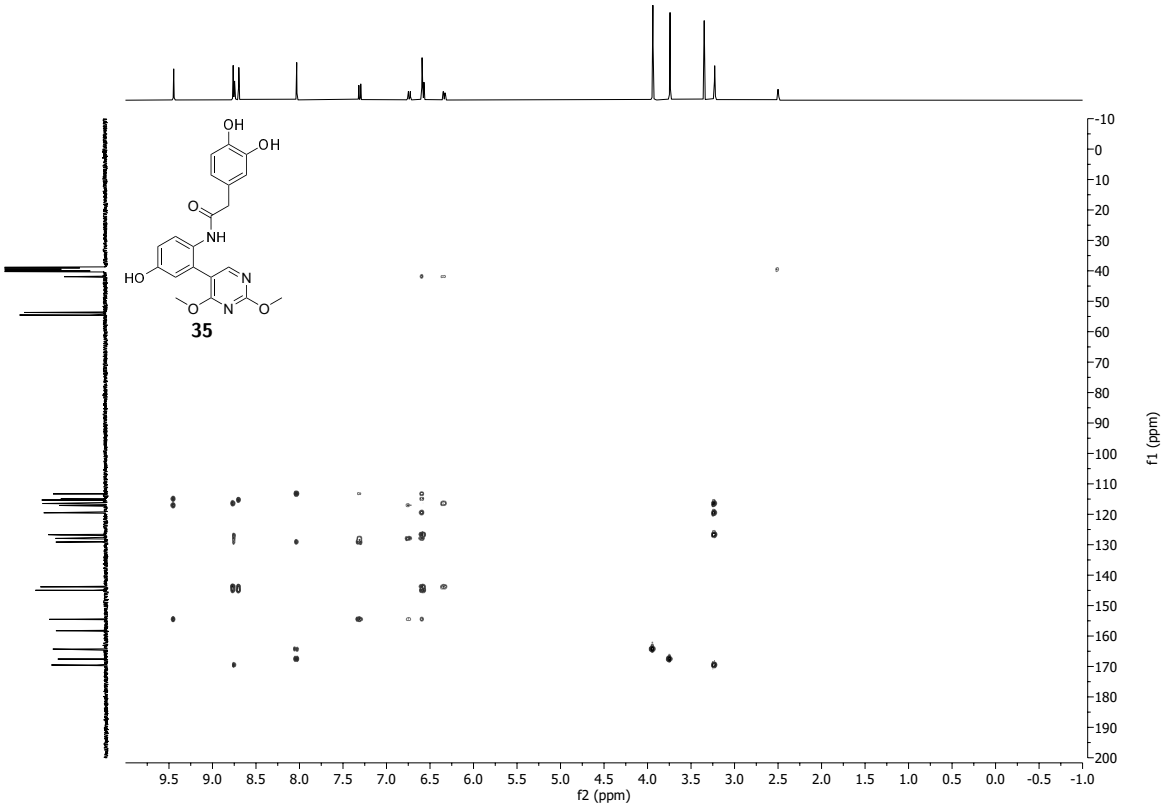

^{1}H ^{13}C HMBC NMR (400 MHz, 100 MHz, DMSO – d_6) spectrum of 2-(3,4-dihydroxyphenyl)-*N*-(2-(2,4-dimethoxypyrimidin-5-yl)-4-hydroxyphenyl)acetamide **35**.

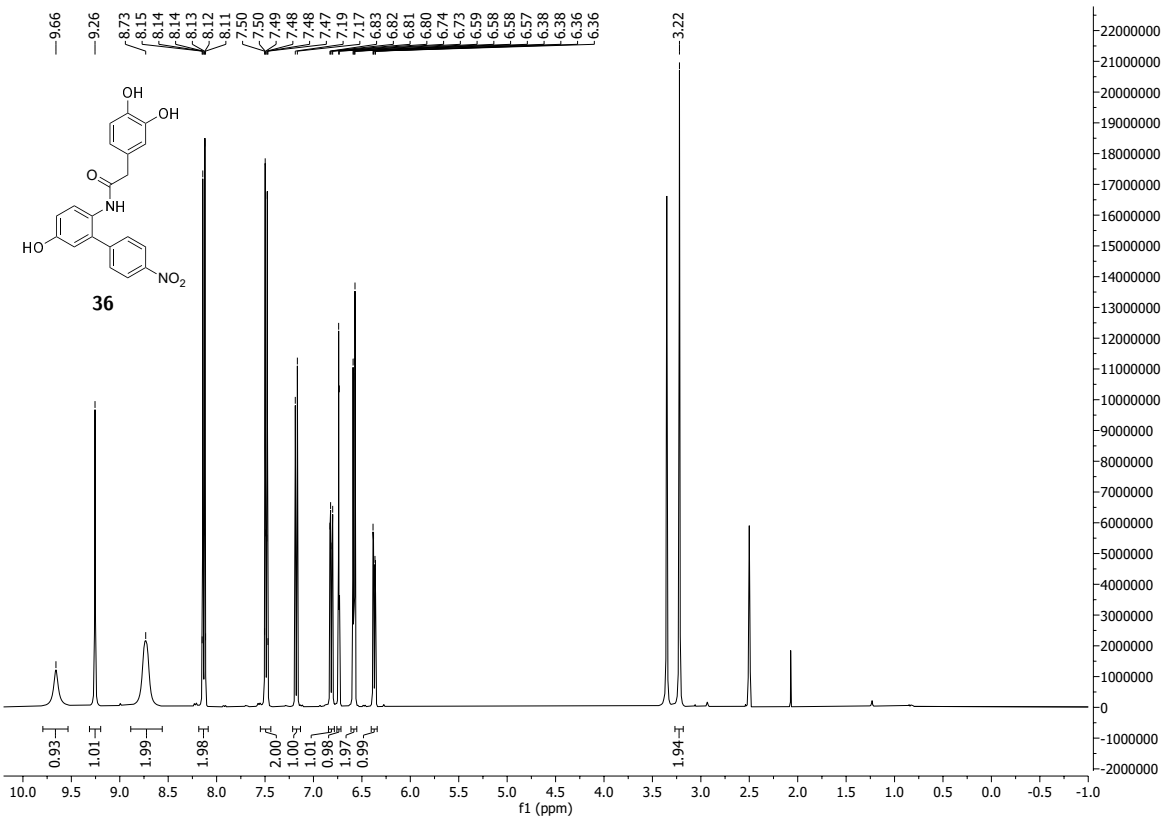

^{1}H NMR (400 MHz, DMSO – d_6) spectrum of
2-(3,4-dihydroxyphenyl)-*N*-(5-hydroxy-4'-nitro-[1,1'-biphenyl]-2-yl)acetamide **36**.

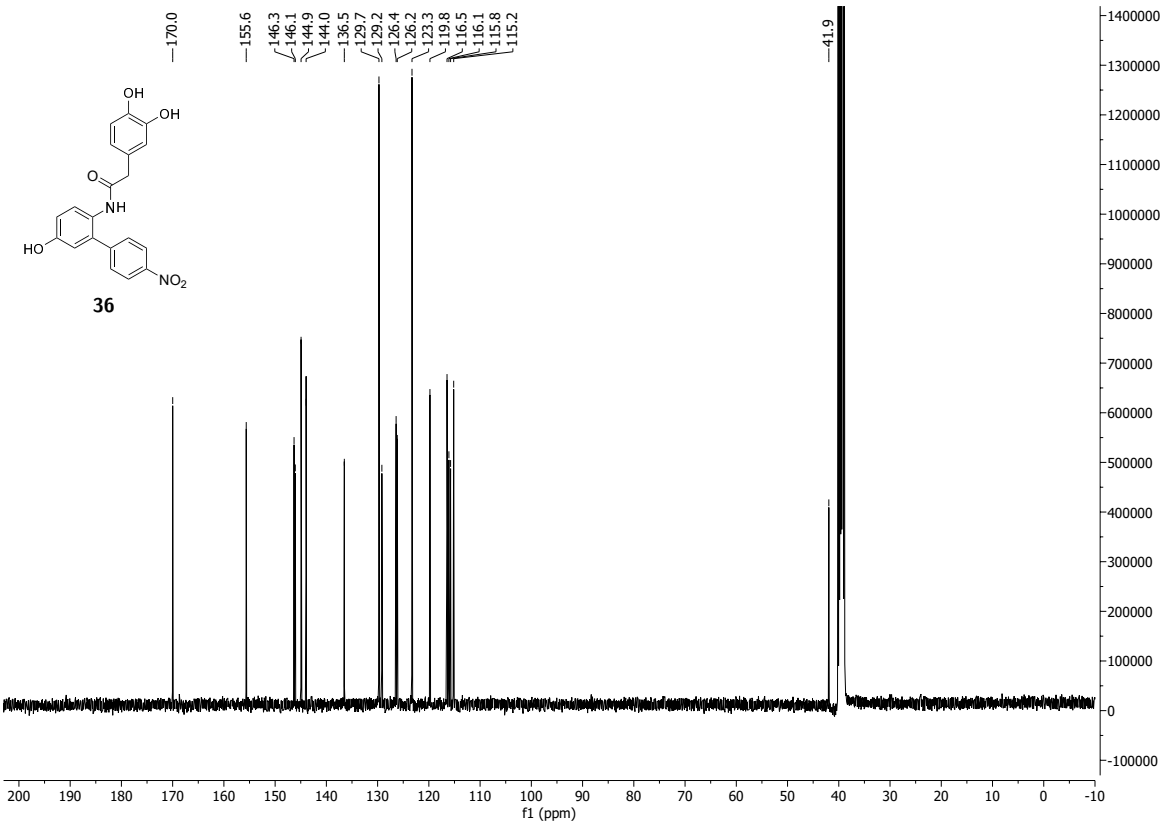

^{13}C NMR (100 MHz, DMSO – d_6) spectrum of
2-(3,4-dihydroxyphenyl)-*N*-(5-hydroxy-4'-nitro-[1,1'-biphenyl]-2-yl)acetamide **36**.

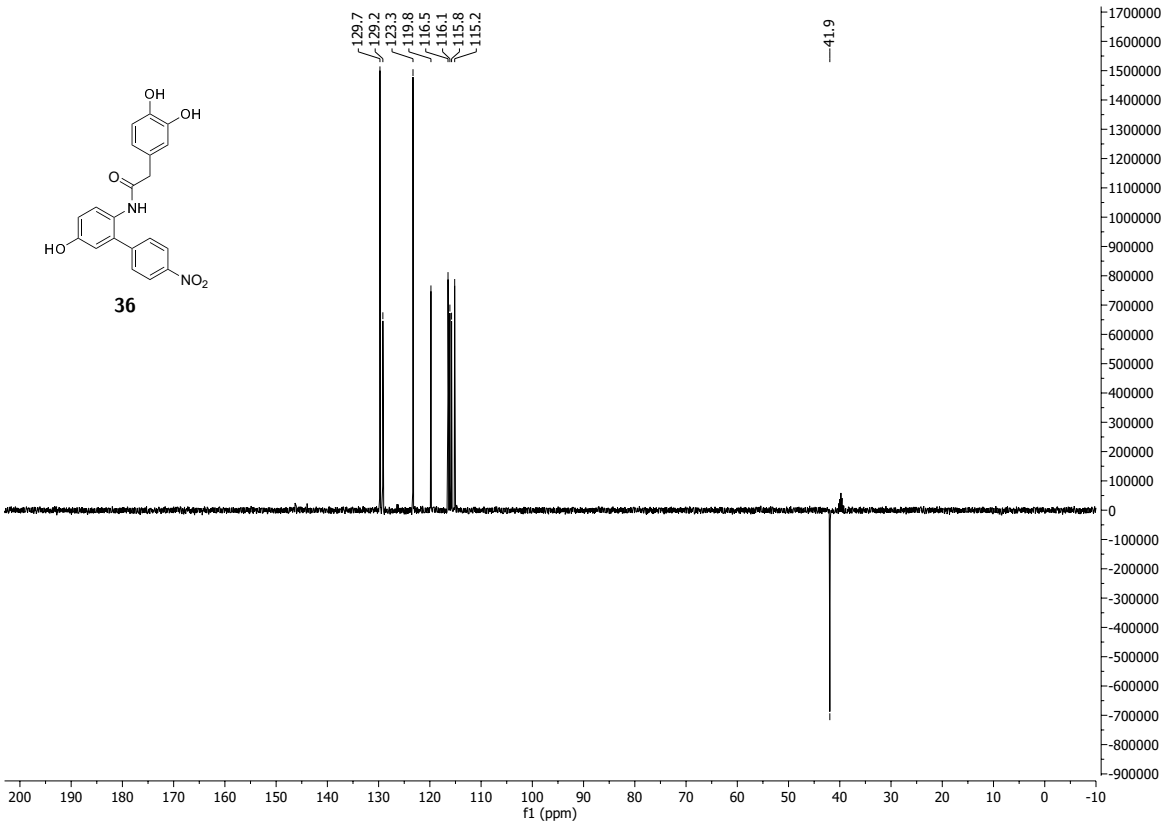

^{13}C DEPT 135 NMR (100 MHz, DMSO – d_6) spectrum of 2-(3,4-dihydroxyphenyl)-*N*-(5-hydroxy-4'-nitro-[1,1'-biphenyl]-2-yl)acetamide **36**.

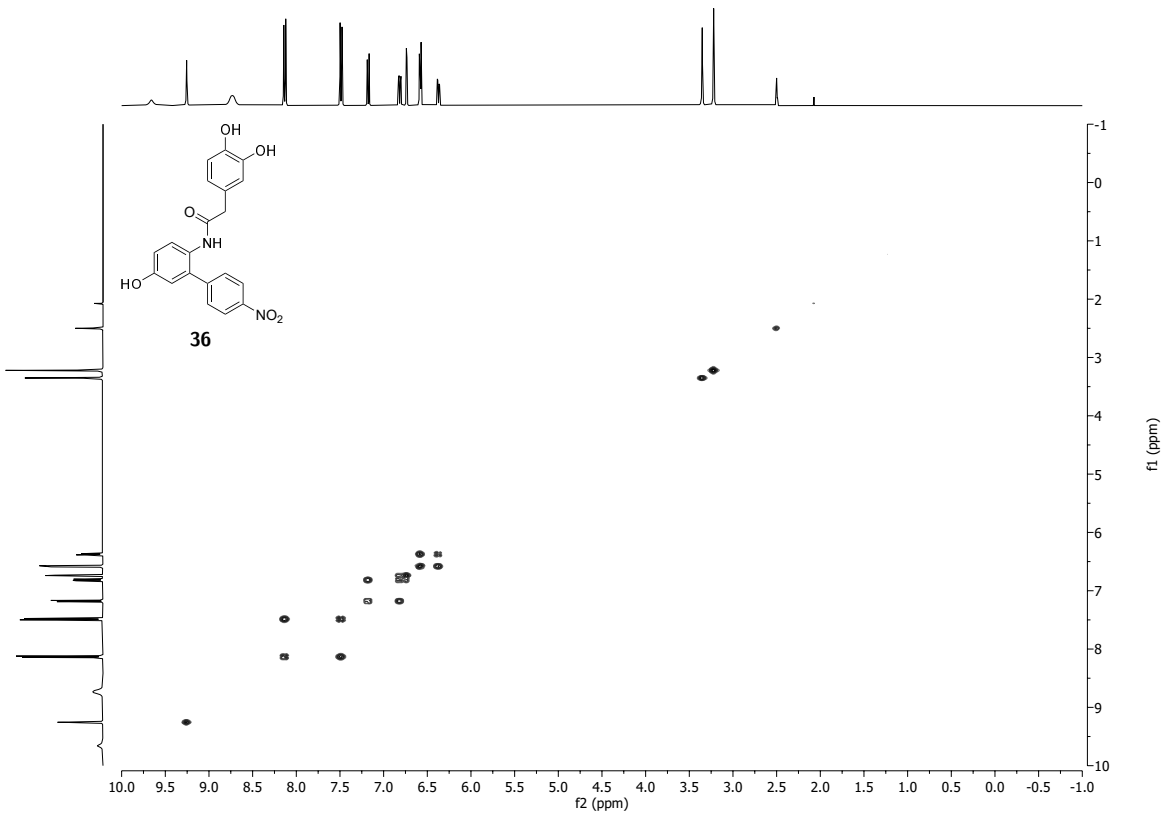

^{1}H ^{1}H COSY NMR (400 MHz, 400 MHz, DMSO – d_6) spectrum of 2-(3,4-dihydroxyphenyl)-*N*-(5-hydroxy-4'-nitro-[1,1'-biphenyl]-2-yl)acetamide **36**.

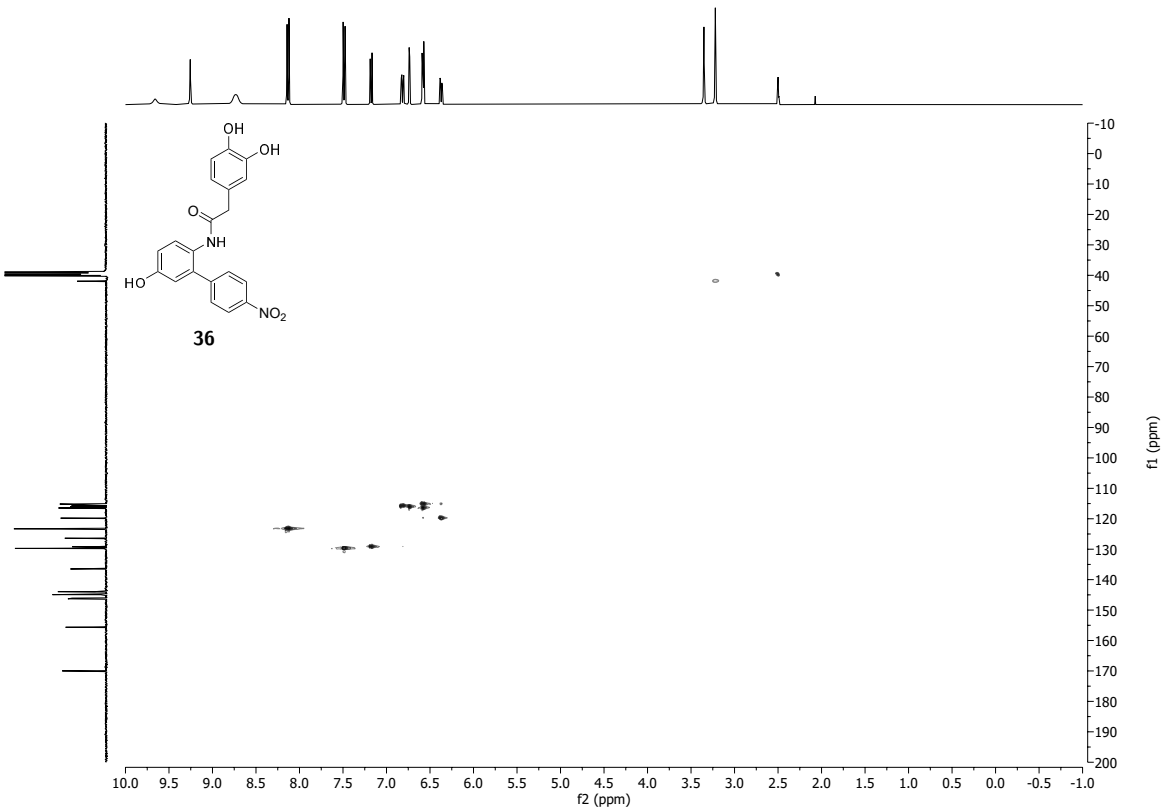

^{1}H ^{13}C HSQC NMR (400 MHz, 100 MHz, DMSO – d_6) spectrum of 2-(3,4-dihydroxyphenyl)-*N*-(5-hydroxy-4'-nitro-[1,1'-biphenyl]-2-yl)acetamide **36**.

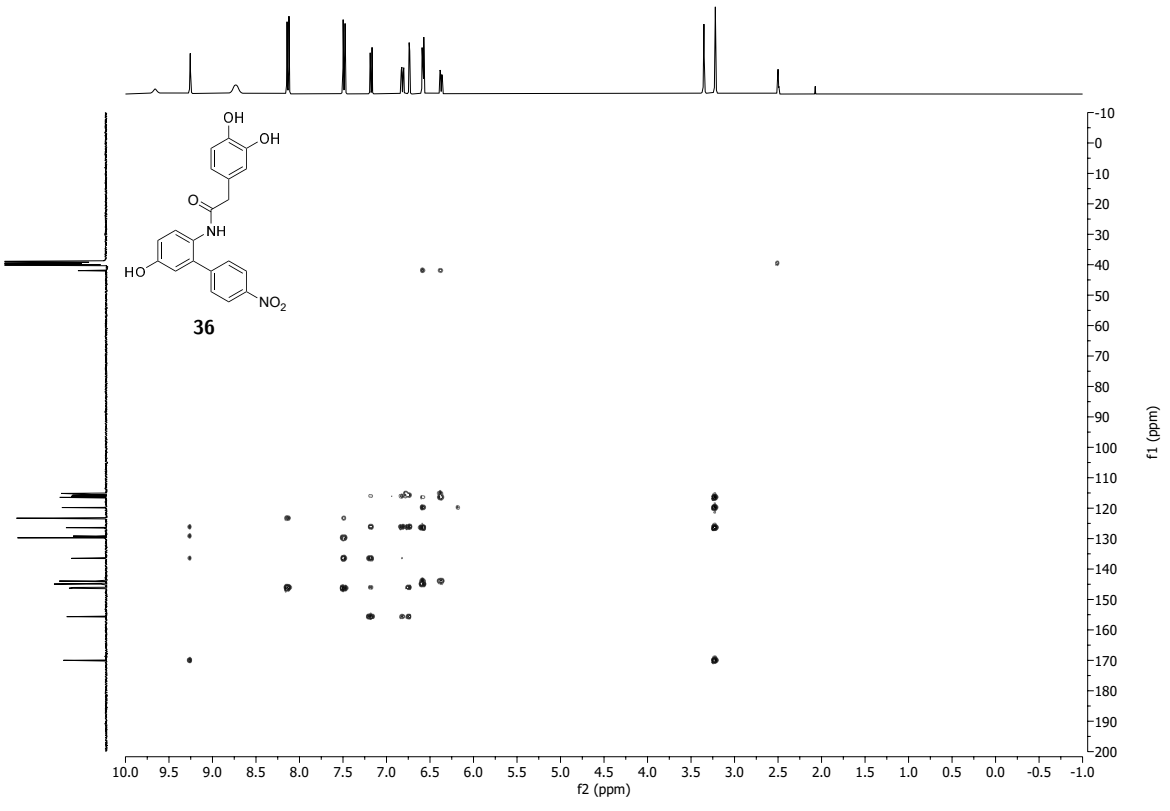

^{1}H ^{13}C HMBC NMR (400 MHz, 100 MHz, DMSO – d_6) spectrum of 2-(3,4-dihydroxyphenyl)-*N*-(5-hydroxy-4'-nitro-[1,1'-biphenyl]-2-yl)acetamide **36**.

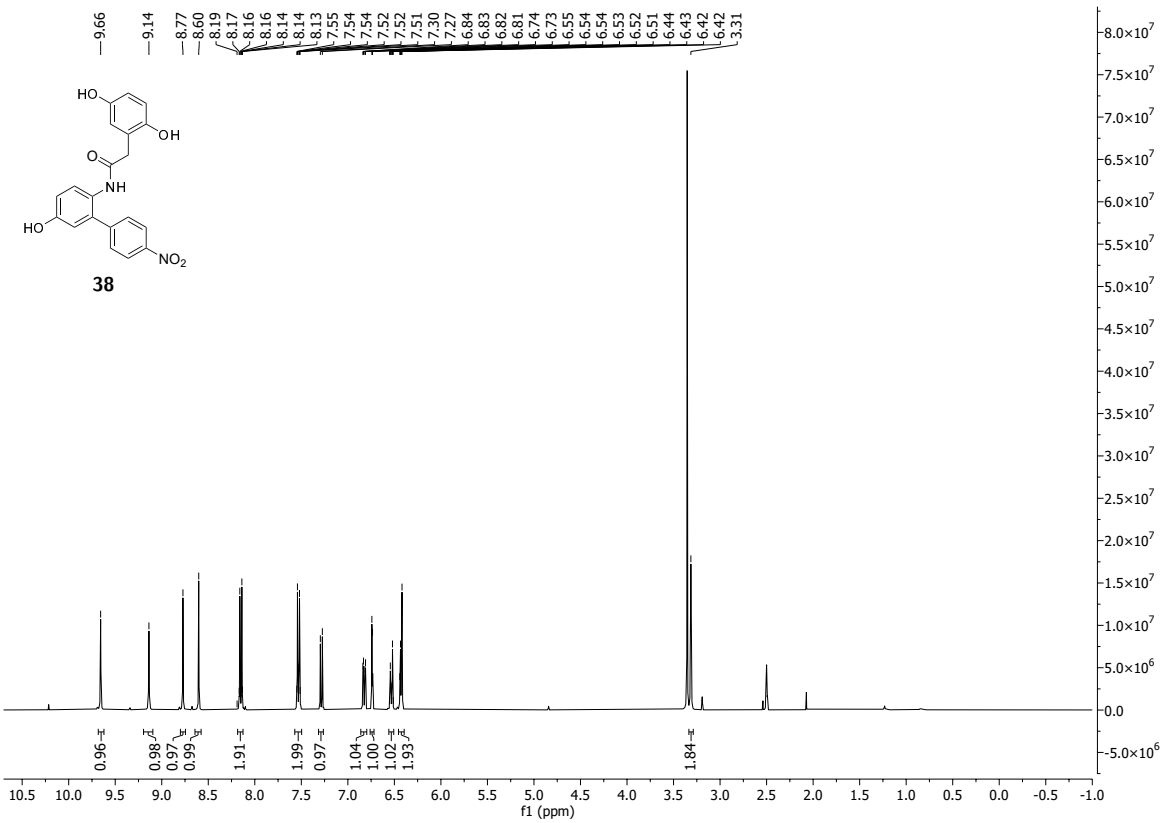

^{1}H NMR (400 MHz, DMSO – d_6) spectrum of
2-(2,5-dihydroxyphenyl)-*N*-(5-hydroxy-4'-nitro-[1,1'-biphenyl]-2-yl)acetamide **38**.

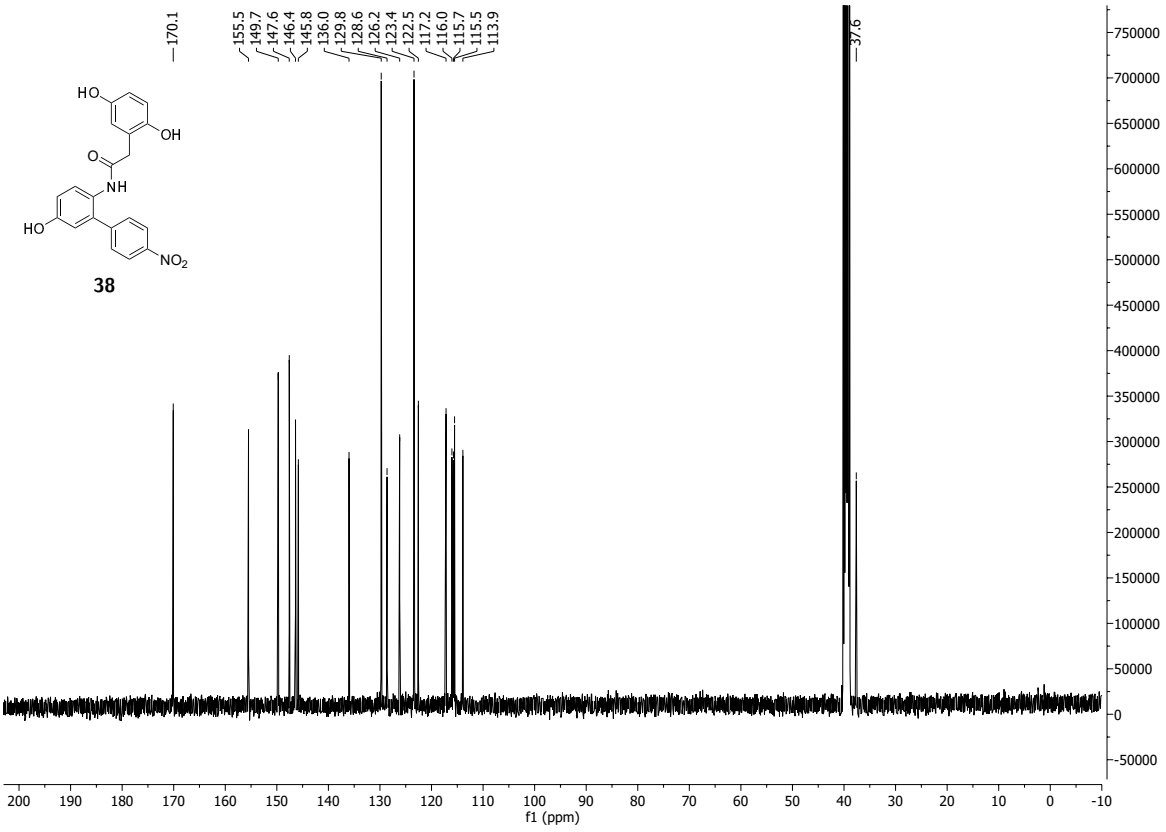

^{13}C NMR (100 MHz, DMSO – d_6) spectrum of
2-(2,5-dihydroxyphenyl)-*N*-(5-hydroxy-4'-nitro-[1,1'-biphenyl]-2-yl)acetamide **38**.

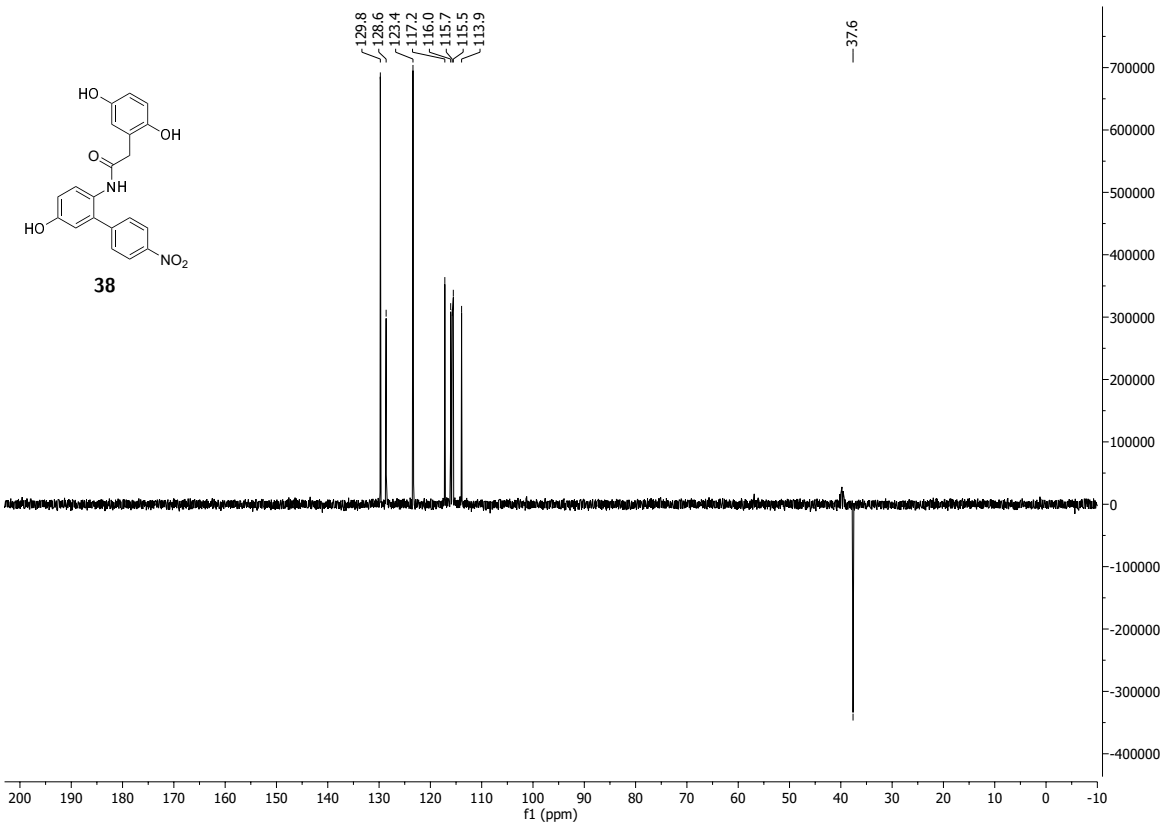

^{13}C DEPT 135 NMR (100 MHz, DMSO – d_6) spectrum of 2-(2,5-dihydroxyphenyl)-*N*-(5-hydroxy-4'-nitro-[1,1'-biphenyl]-2-yl)acetamide **38**.

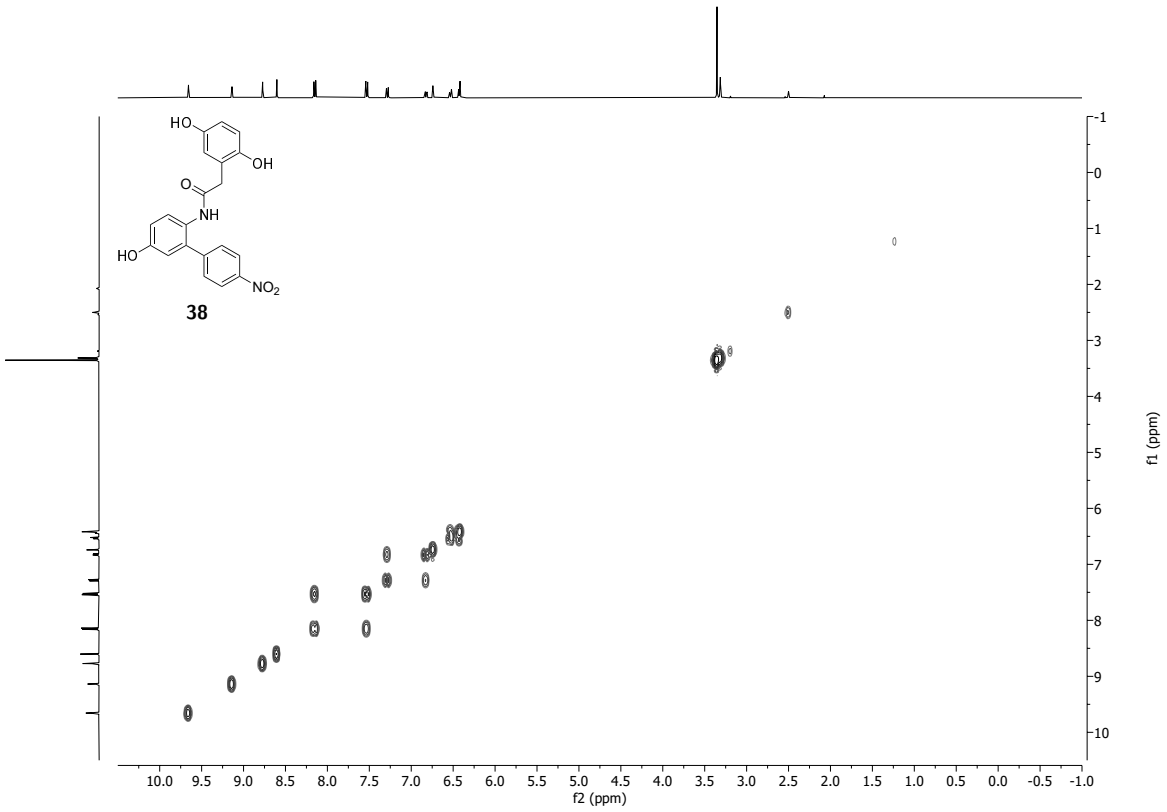

^{1}H ^{1}H COSY NMR (400 MHz, 400 MHz, DMSO – d_6) spectrum of 2-(2,5-dihydroxyphenyl)-*N*-(5-hydroxy-4'-nitro-[1,1'-biphenyl]-2-yl)acetamide **38**.

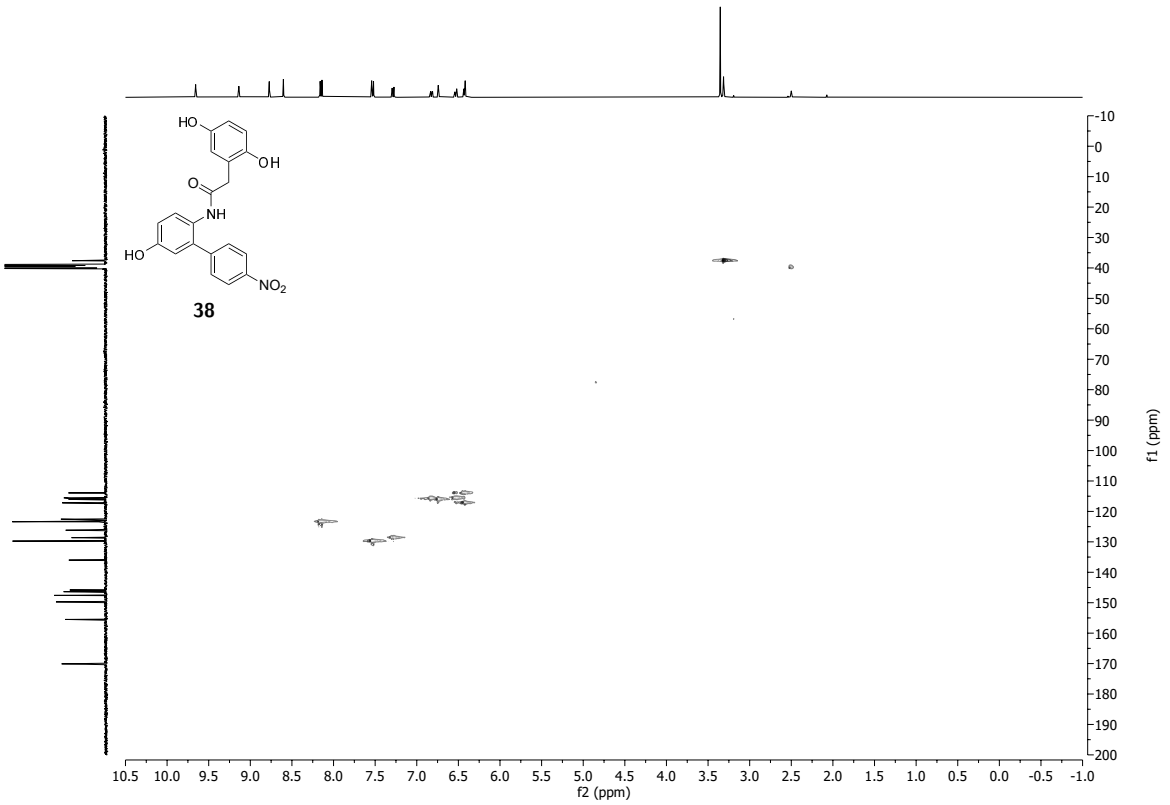

^{1}H ^{13}C HSQC NMR (400 MHz, 100 MHz, DMSO – d_6) spectrum of 2-(2,5-dihydroxyphenyl)-*N*-(5-hydroxy-4'-nitro-[1,1'-biphenyl]-2-yl)acetamide **38**.

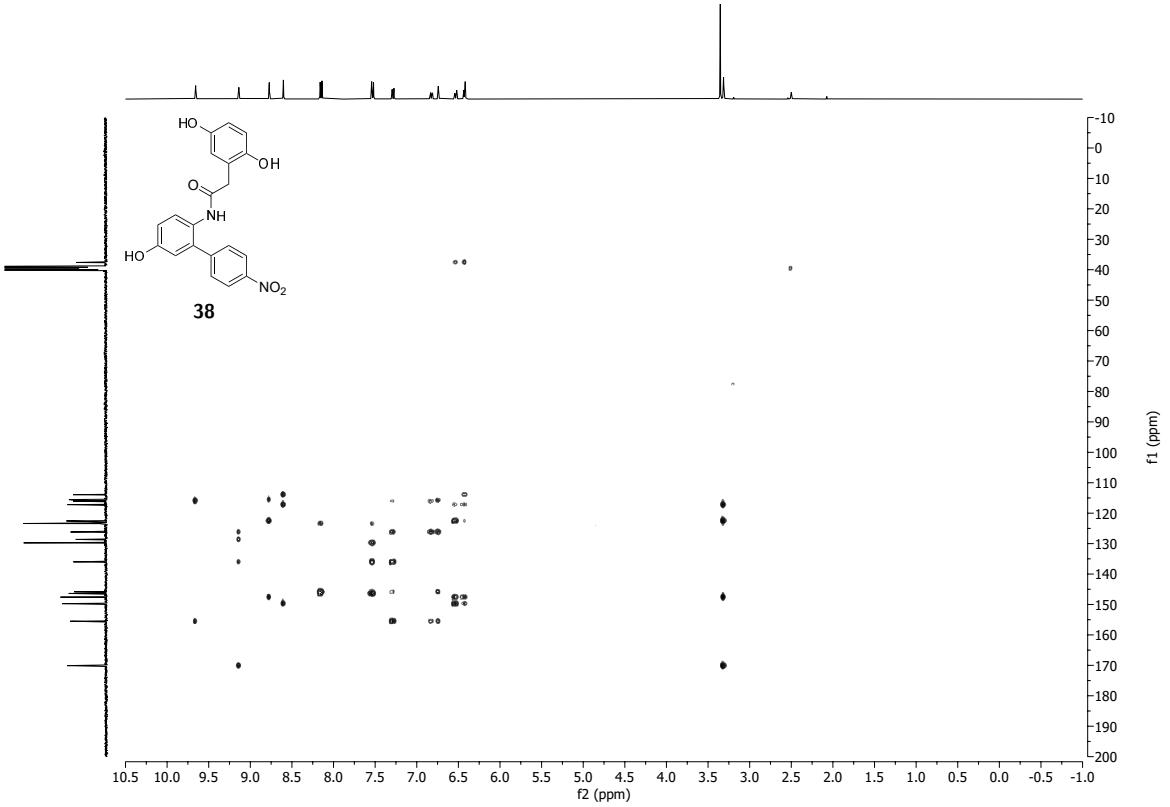

^{1}H ^{13}C HMBC NMR (400 MHz, 100 MHz, DMSO – d_6) spectrum of 2-(2,5-dihydroxyphenyl)-*N*-(5-hydroxy-4'-nitro-[1,1'-biphenyl]-2-yl)acetamide **38**.

10.7 HRMS Spectra

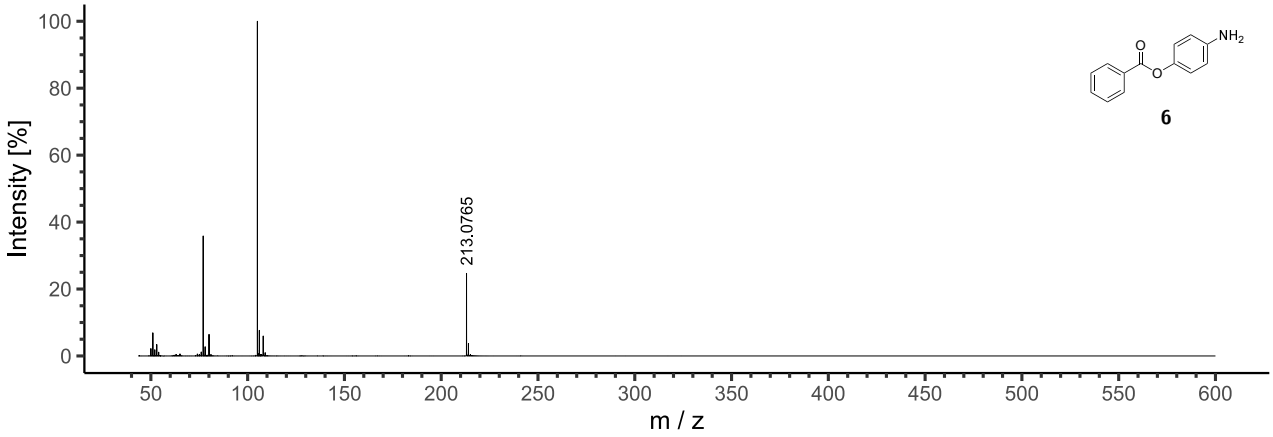

HRMS (EI^+) spectrum of
4-aminophenyl benzoate **6**.

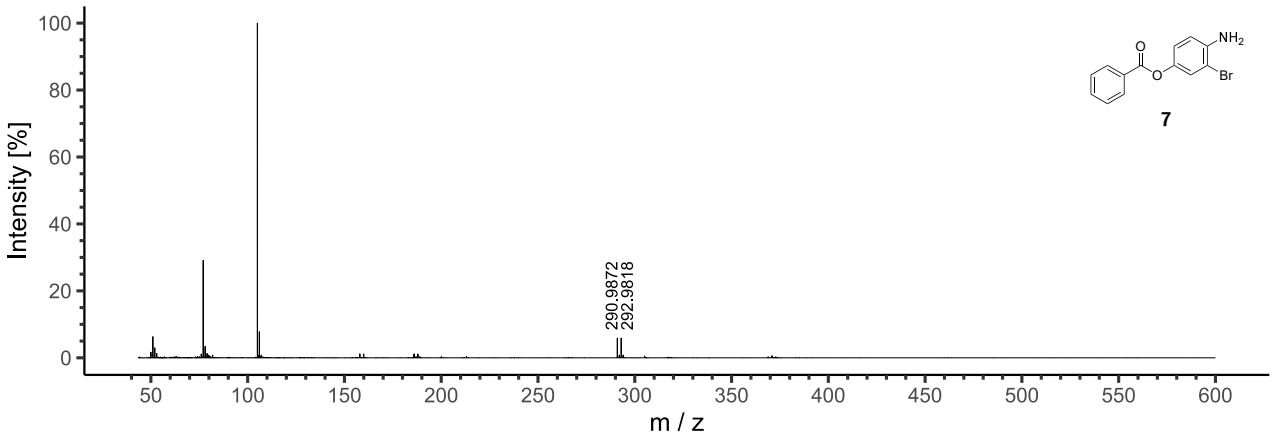

HRMS (EI^+) spectrum of
4-amino-3-bromophenyl benzoate **7**.

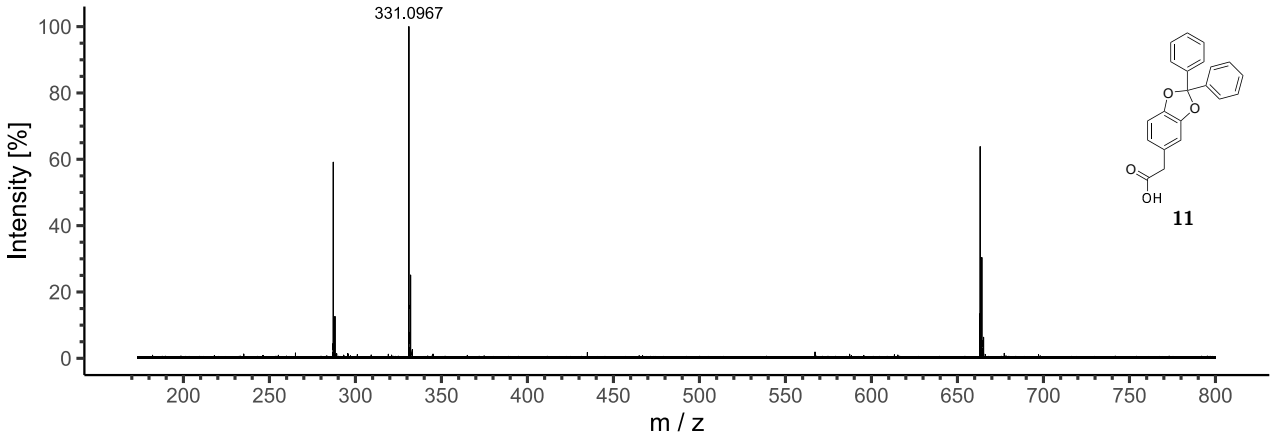

HRMS (ESI^-) spectrum of
2-(2,2-diphenylbenzo[*d*][1,3]dioxol-5-yl)acetic acid **11**.

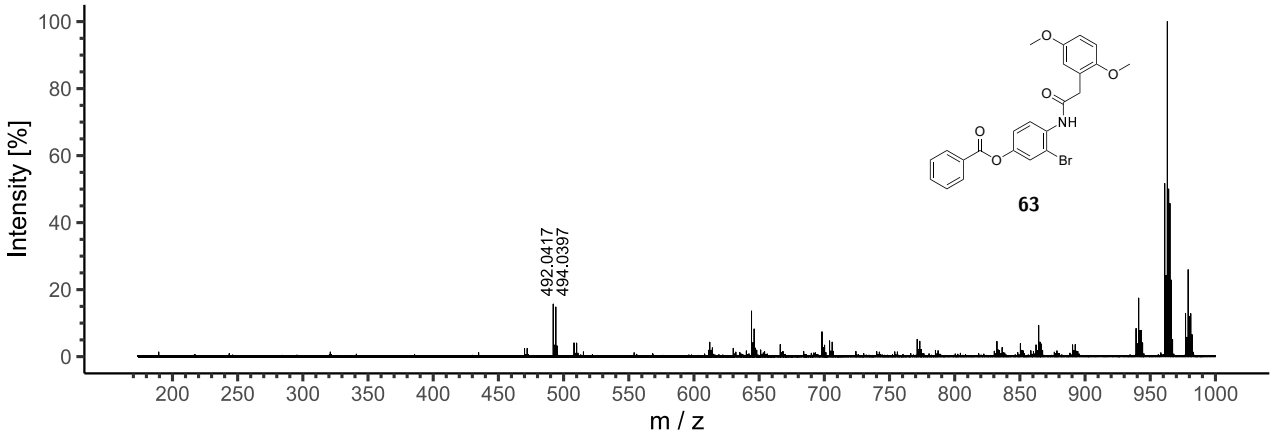

HRMS (ESI$^+$) spectrum of
3-bromo-4-(2-(2,5-dimethoxyphenyl)acetamido)phenyl benzoate **63**.

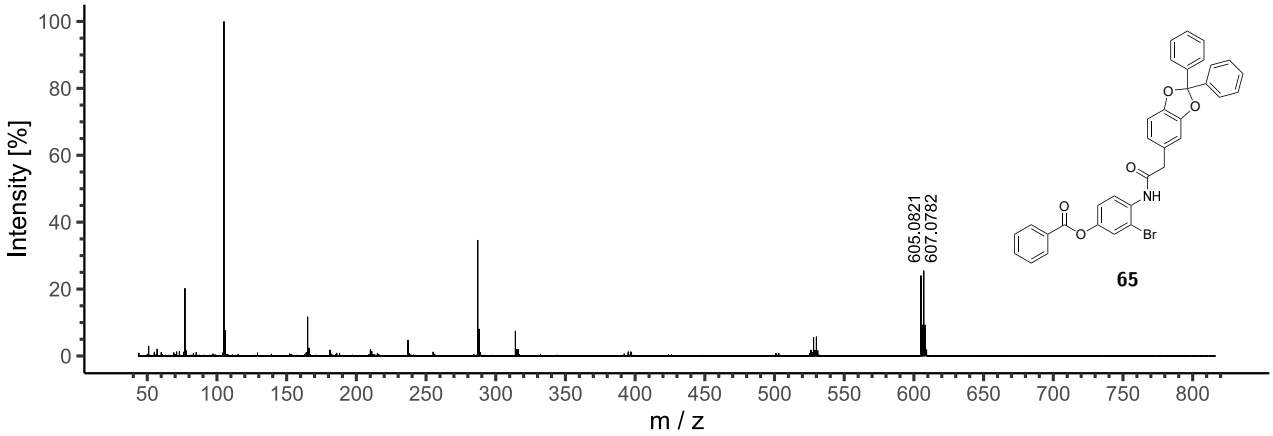

HRMS (EI$^+$) spectrum of
3-bromo-4-(2-(2,2-diphenylbenzo[*d*][1,3]dioxol-5-yl)acetamido)phenyl benzoate **65**.

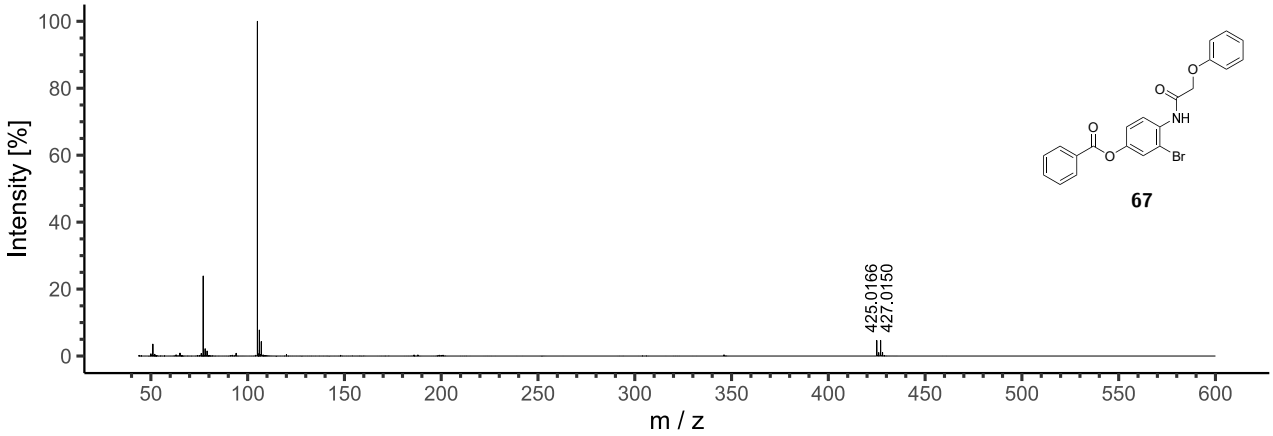

HRMS (EI$^+$) spectrum of
3-bromo-4-(2-phenoxyacetamido)phenyl benzoate **67**.

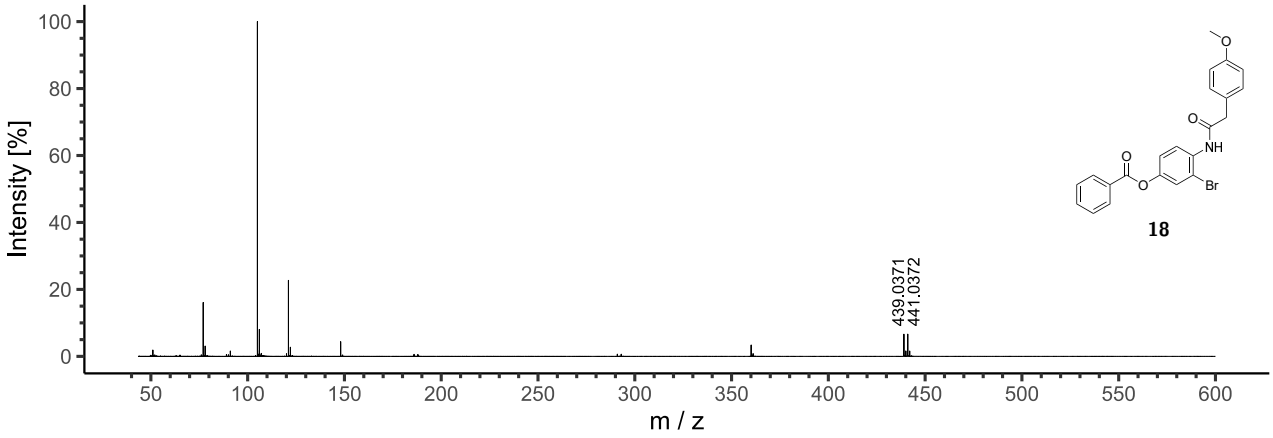

HRMS (EI$^+$) spectrum of
3-bromo-4-(2-(4-methoxyphenyl)acetamido)phenyl benzoate **18**.

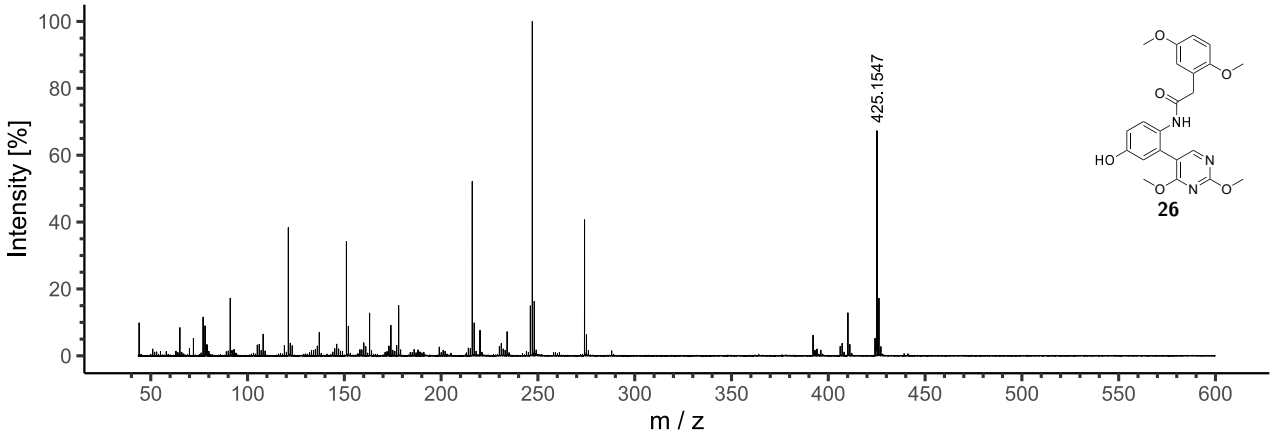

HRMS (EI$^+$) spectrum of
2-(2,5-dimethoxyphenyl)-*N*-(2-(2,4-dimethoxypyrimidin-5-yl)-4-hydroxyphenyl)acetamide **26**.

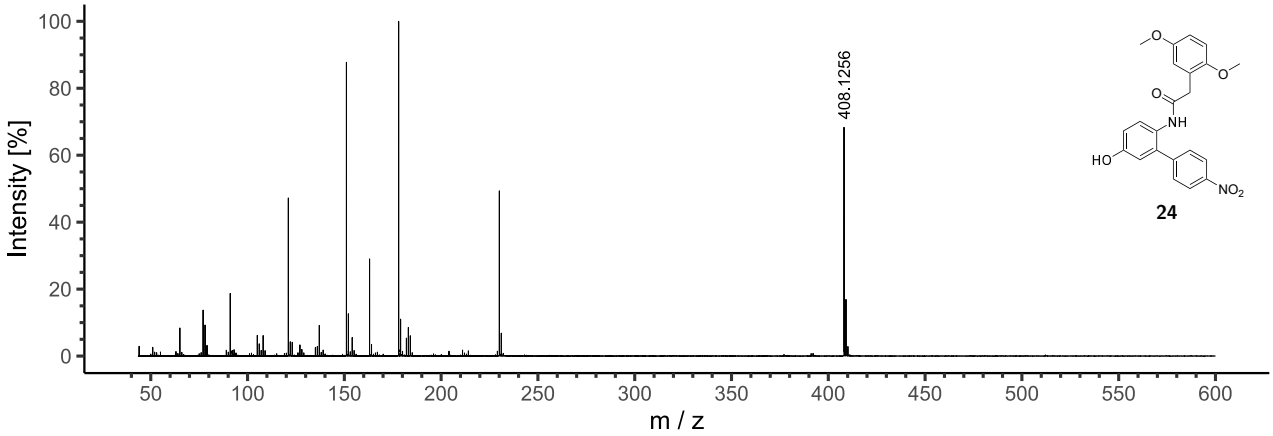

HRMS (EI$^+$) spectrum of
2-(2,5-dimethoxyphenyl)-*N*-(5-hydroxy-4'-nitro-[1,1'-biphenyl]-2-yl)acetamide **24**.

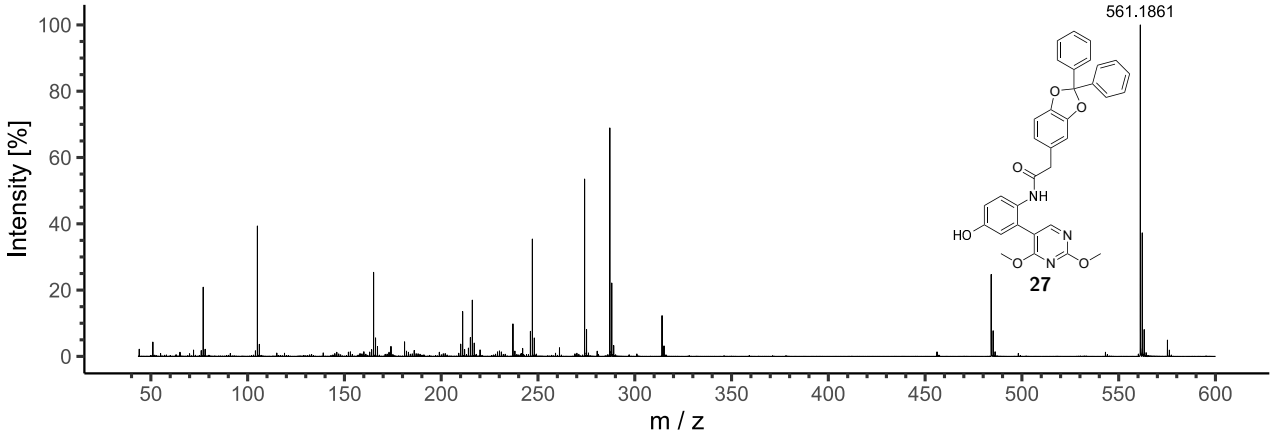

HRMS (EI$^+$) spectrum of
N-(2-(2,4-dimethoxypyrimidin-5-yl)-4-hydroxyphenyl)-2-(2,2-diphenylbenzo[*d*][1,3]dioxol-5-yl) acetamide **27**.

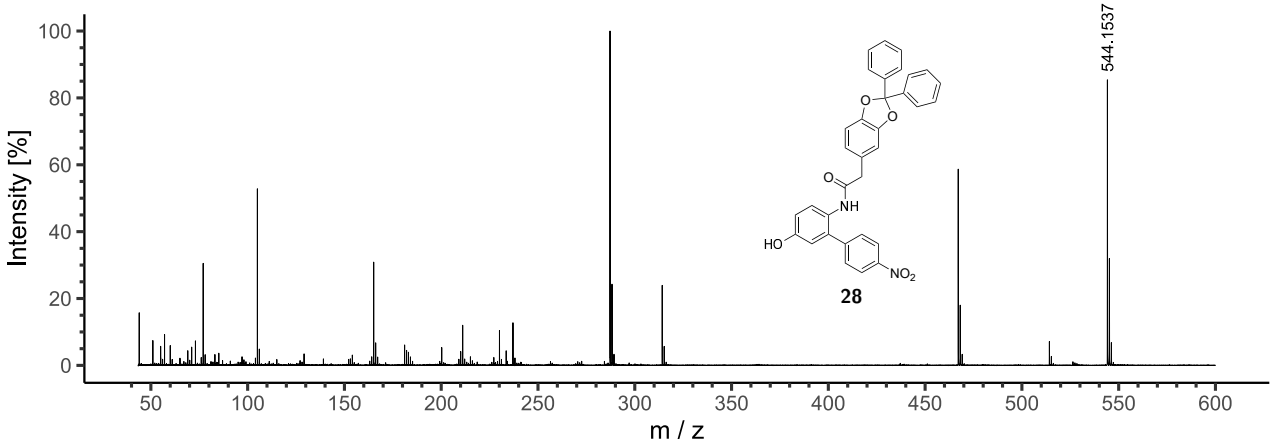

HRMS (EI$^+$) spectrum of
2-(2,2-diphenylbenzo[*d*][1,3]dioxol-5-yl)-*N*-(5-hydroxy-4'-nitro-[1,1'-biphenyl]-2-yl)acetamide **28**.

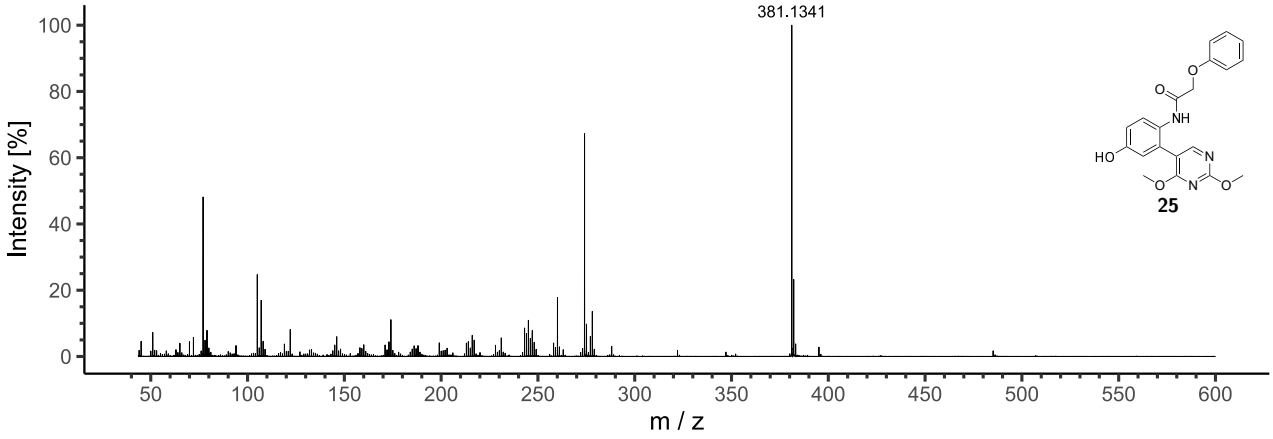

HRMS (EI$^+$) spectrum of
N-(2-(2,4-dimethoxypyrimidin-5-yl)-4-hydroxyphenyl)-2-phenoxyacetamide **25**.

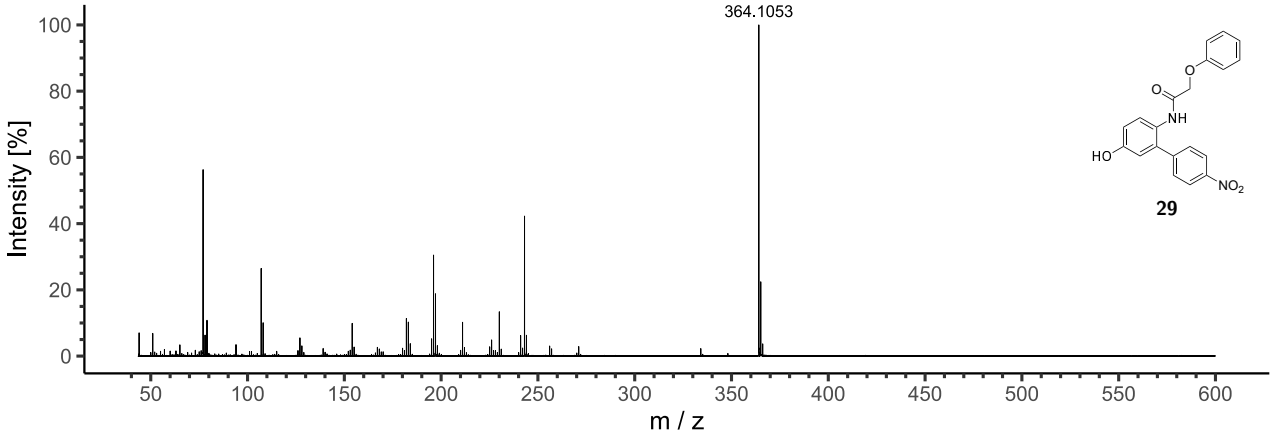

HRMS (EI$^+$) spectrum of
N-(5-hydroxy-4'-nitro-[1,1'-biphenyl]-2-yl)-2-phenoxyacetamide **29**.

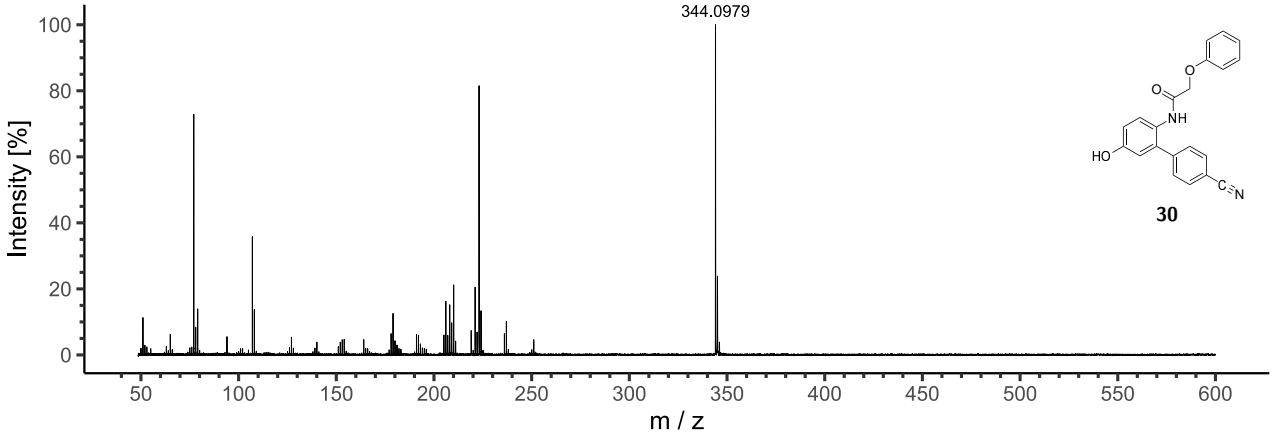

HRMS (EI$^+$) spectrum of
N-(4'-cyano-5-hydroxy-[1,1'-biphenyl]-2-yl)-2-phenoxyacetamide **30**.

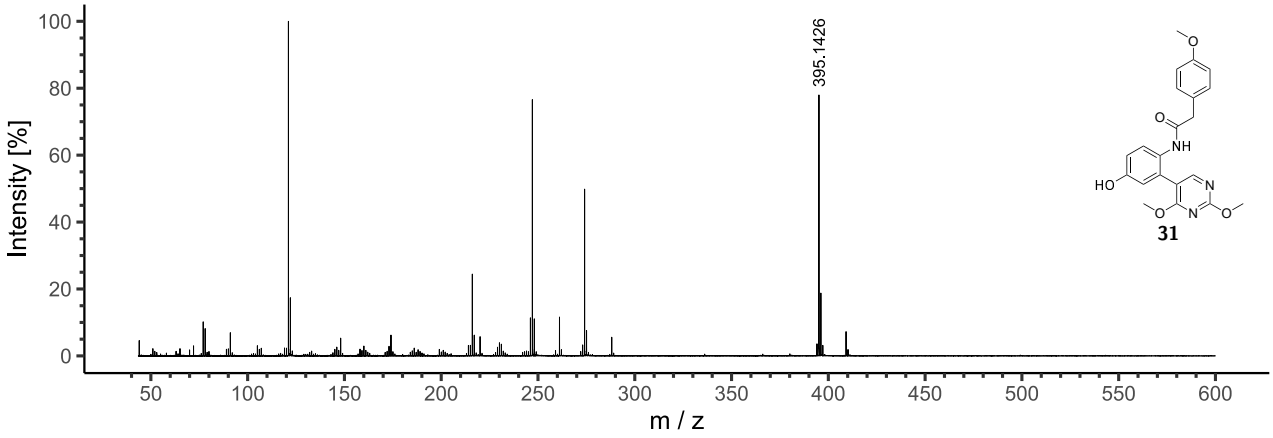

HRMS (EI$^+$) spectrum of
N-(2-(2,4-dimethoxypyrimidin-5-yl)-4-hydroxyphenyl)-2-(4-methoxyphenyl)acetamide **31**.

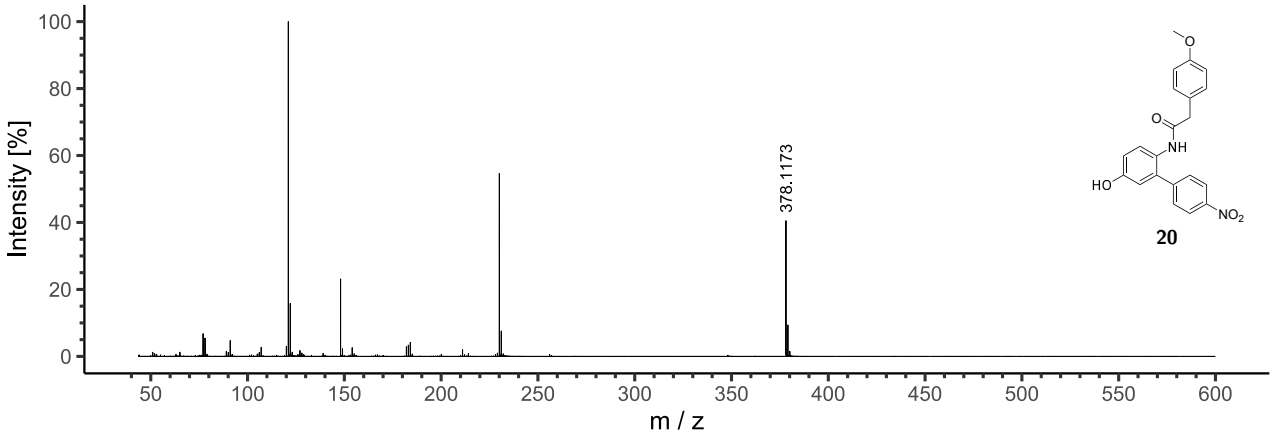

HRMS (EI$^+$) spectrum of
N-(5-hydroxy-4'-nitro-[1,1'-biphenyl]-2-yl)-2-(4-methoxyphenyl)acetamide **20**.

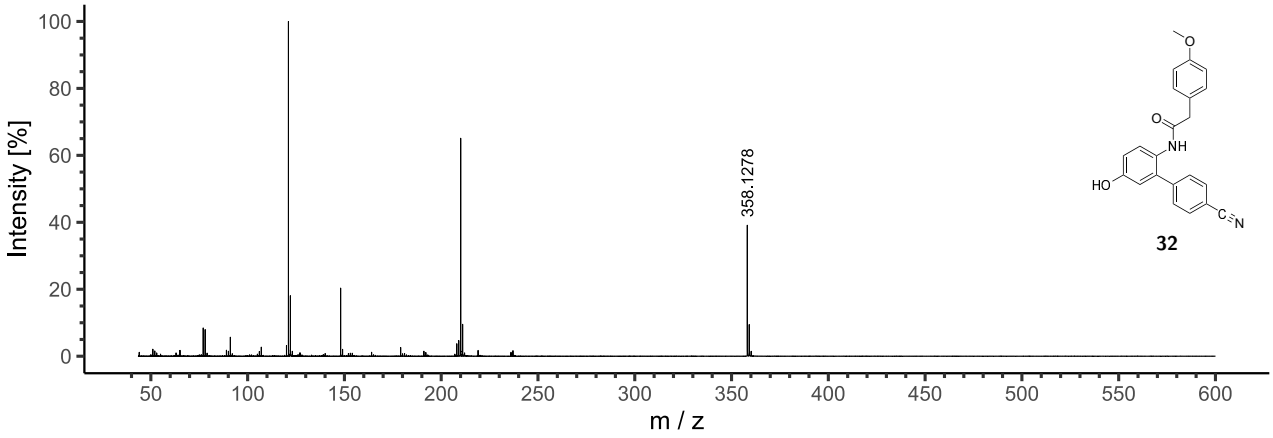

HRMS (EI$^+$) spectrum of
N-(4'-cyano-5-hydroxy-[1,1'-biphenyl]-2-yl)-2-(4-methoxyphenyl)acetamide **32**.

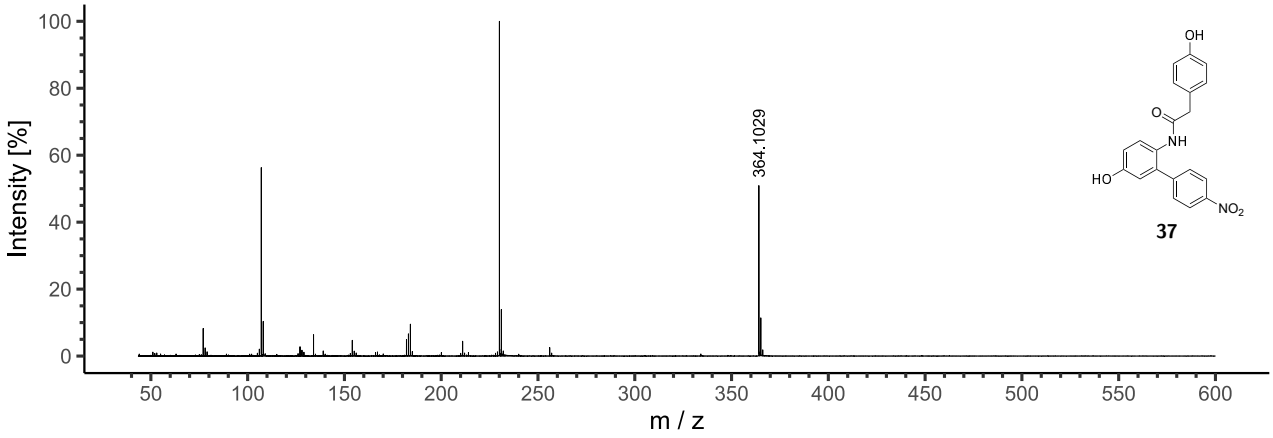

HRMS (EI$^+$) spectrum of
N-(5-hydroxy-4'-nitro-[1,1'-biphenyl]-2-yl)-2-(4-hydroxyphenyl)acetamide **37**.

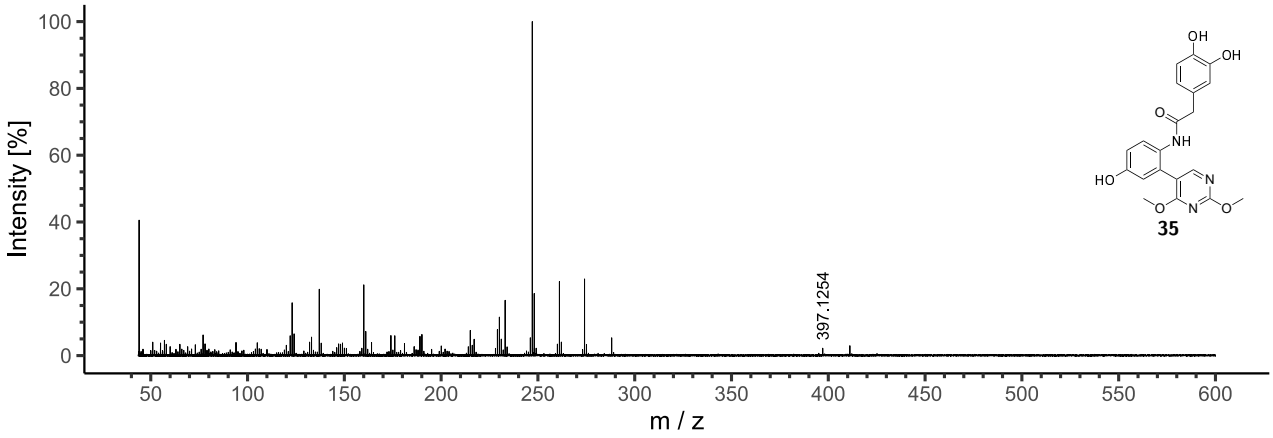

HRMS (EI$^+$) spectrum of
2-(3,4-dihydroxyphenyl)-*N*-(2-(2,4-dimethoxypyrimidin-5-yl)-4-hydroxyphenyl)acetamide **35**.

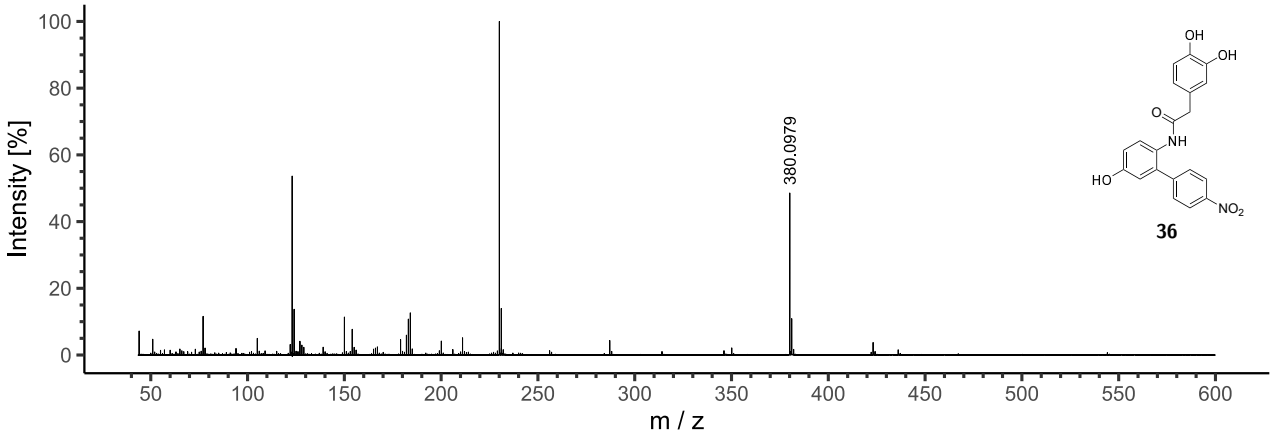

HRMS (EI$^+$) spectrum of
2-(3,4-dihydroxyphenyl)-*N*-(5-hydroxy-4'-nitro-[1,1'-biphenyl]-2-yl)acetamide **36**.

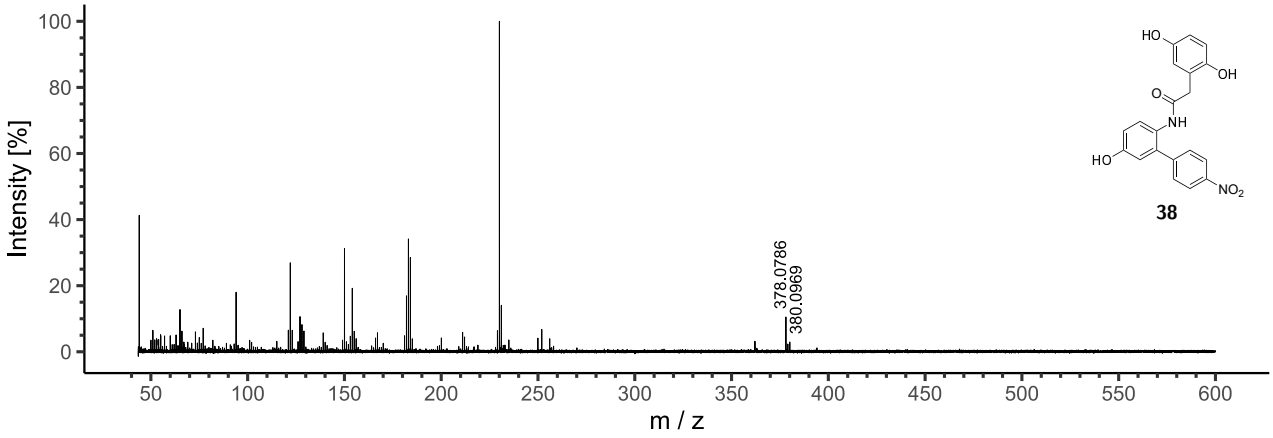

HRMS (EI$^+$) spectrum of
2-(2,5-dihydroxyphenyl)-*N*-(5-hydroxy-4'-nitro-[1,1'-biphenyl]-2-yl)acetamide **38**.

10.8 IR Spectra

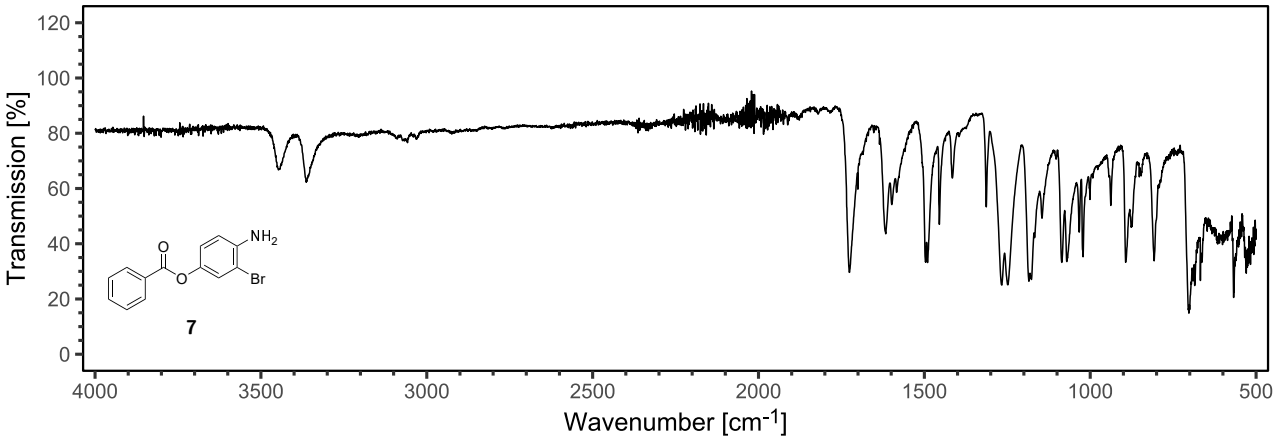

IR (solid, rt) spectrum of
4-amino-3-bromophenyl benzoate **7**.

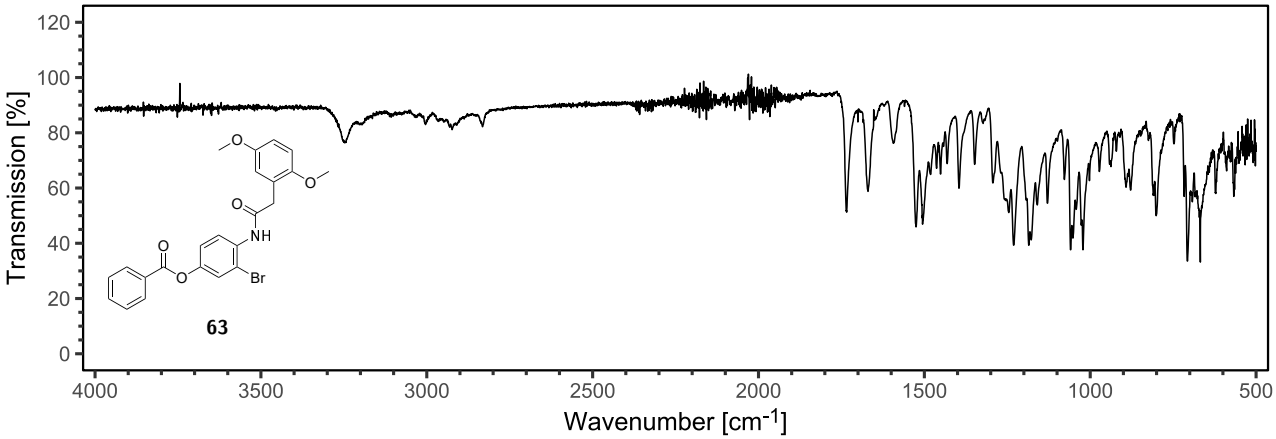

IR (solid, rt) spectrum of
3-bromo-4-(2-(2,5-dimethoxyphenyl)acetamido)phenyl benzoate **63**.

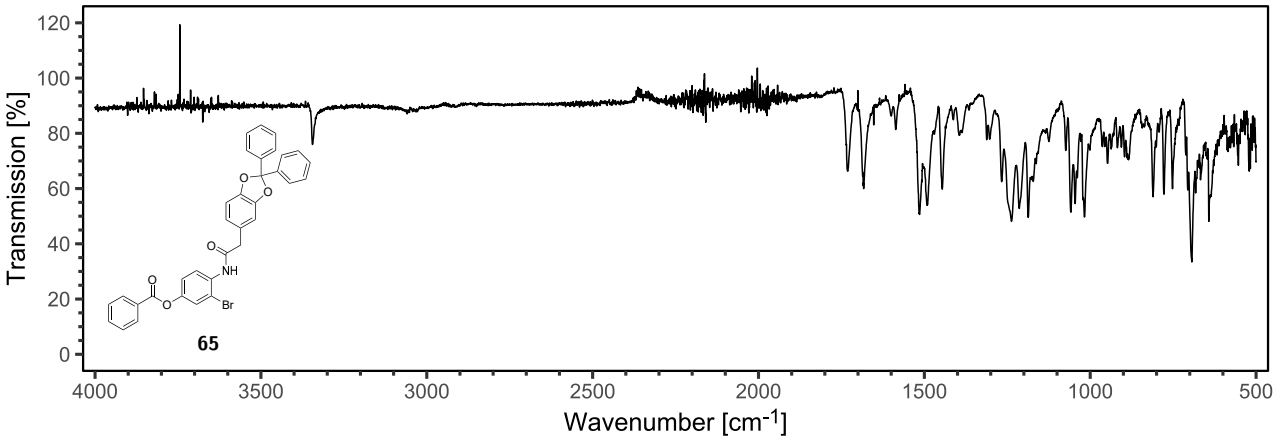

IR (solid, rt) spectrum of
3-bromo-4-(2-(2,2-diphenylbenzo[*d*][1,3]dioxol-5-yl)acetamido)phenyl benzoate **65**.

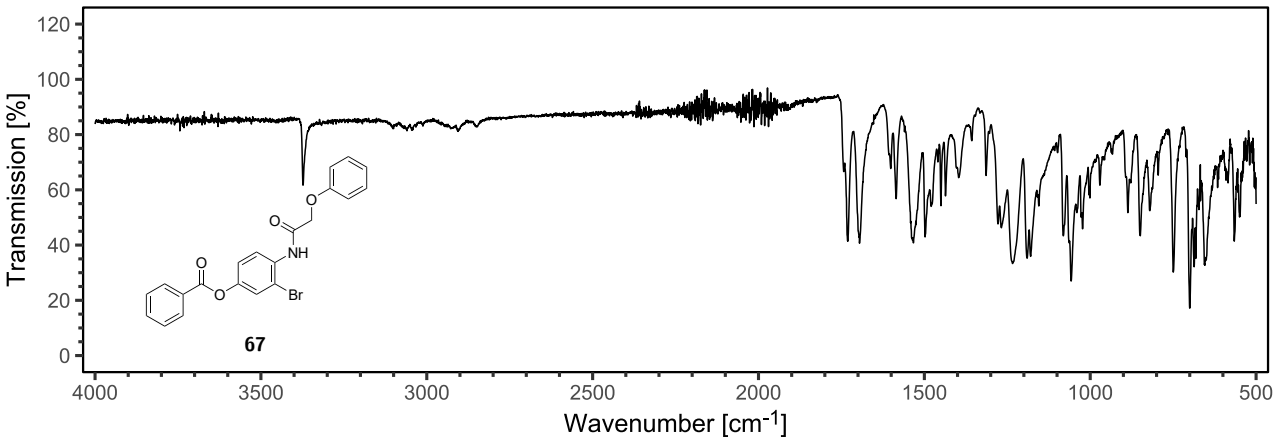

IR (solid, rt) spectrum of
3-bromo-4-(2-phenoxyacetamido)phenyl benzoate **67**.

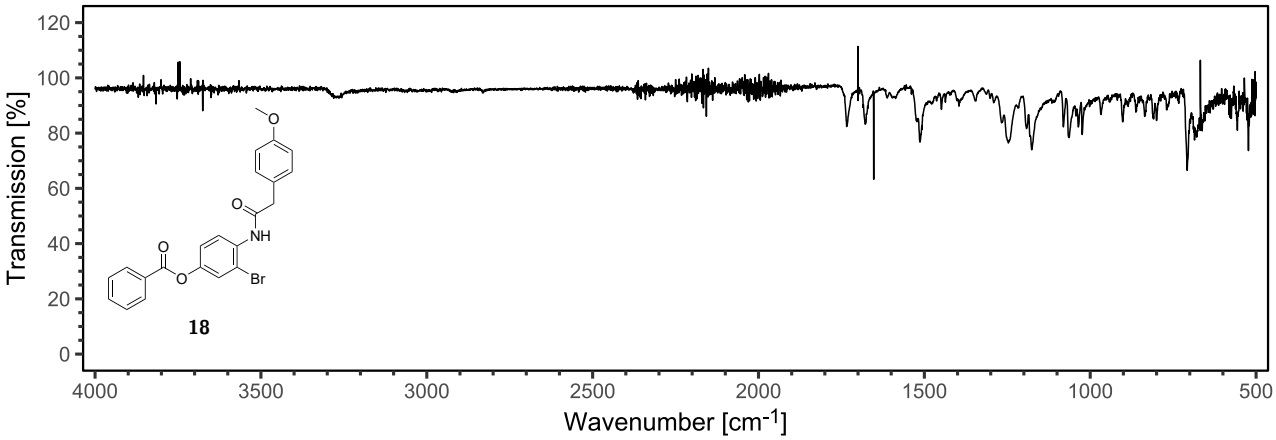

IR (solid, rt) spectrum of
3-bromo-4-(2-(4-methoxyphenyl)acetamido)phenyl benzoate **18**.

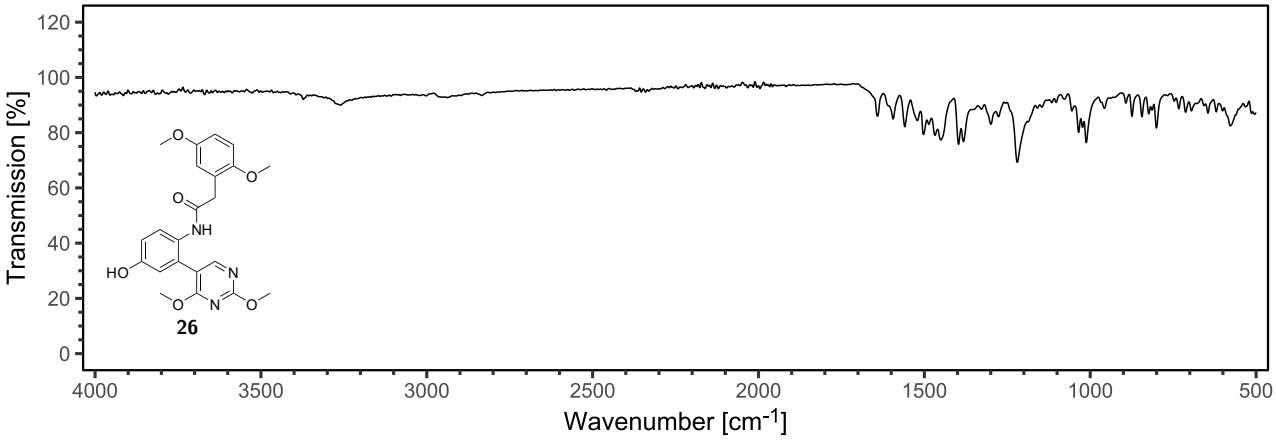

IR (solid, rt) spectrum of
2-(2,5-dimethoxyphenyl)-*N*-(2-(2,4-dimethoxypyrimidin-5-yl)-4-hydroxyphenyl)acetamide **26**.

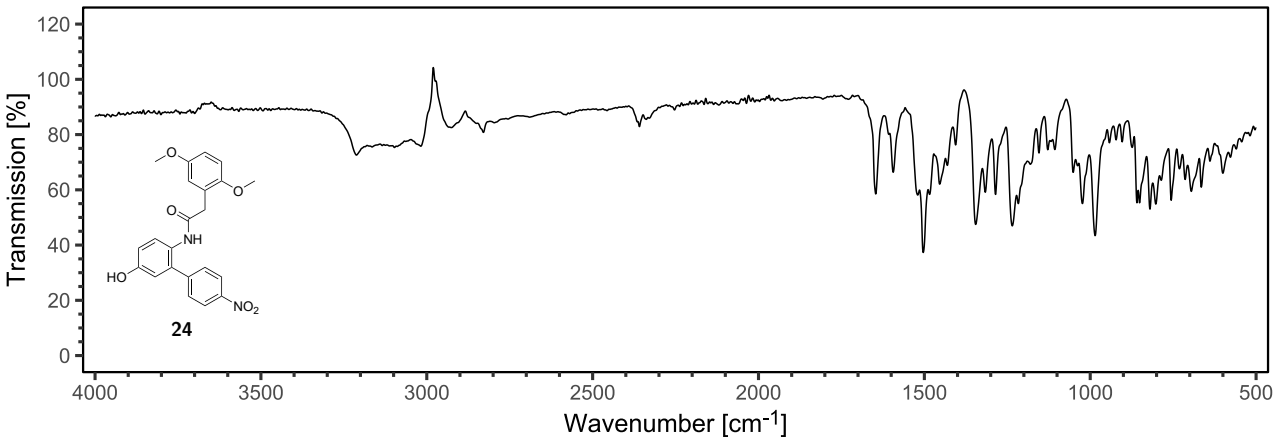

IR (solid, rt) spectrum of
2-(2,5-dimethoxyphenyl)-*N*-(5-hydroxy-4'-nitro-[1,1'-biphenyl]-2-yl)acetamide **24**.

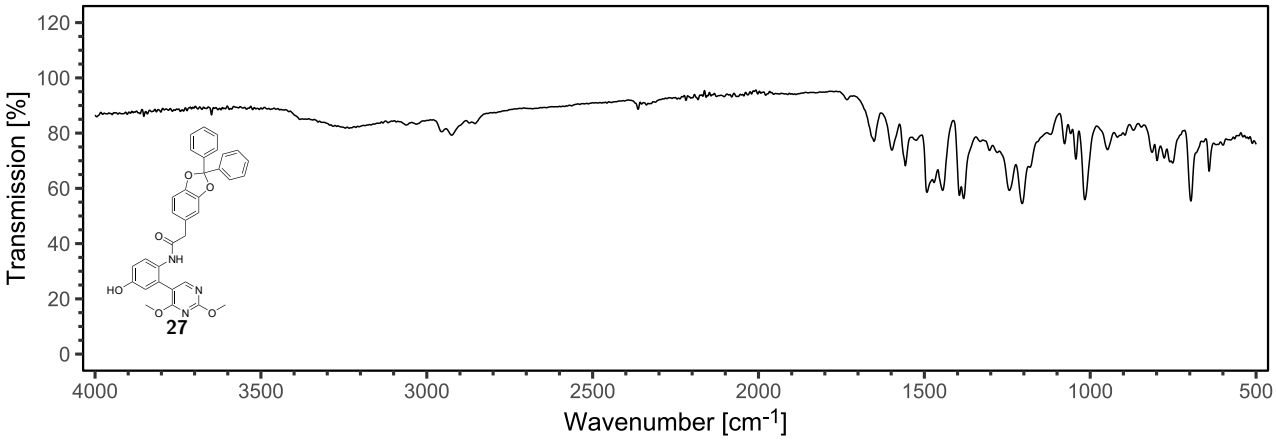

IR (solid, rt) spectrum of
N-(2-(2,4-dimethoxypyrimidin-5-yl)-4-hydroxyphenyl)-2-(2,2-diphenylbenzo[*d*][1,3]dioxol-5-yl)acetamide **27**.

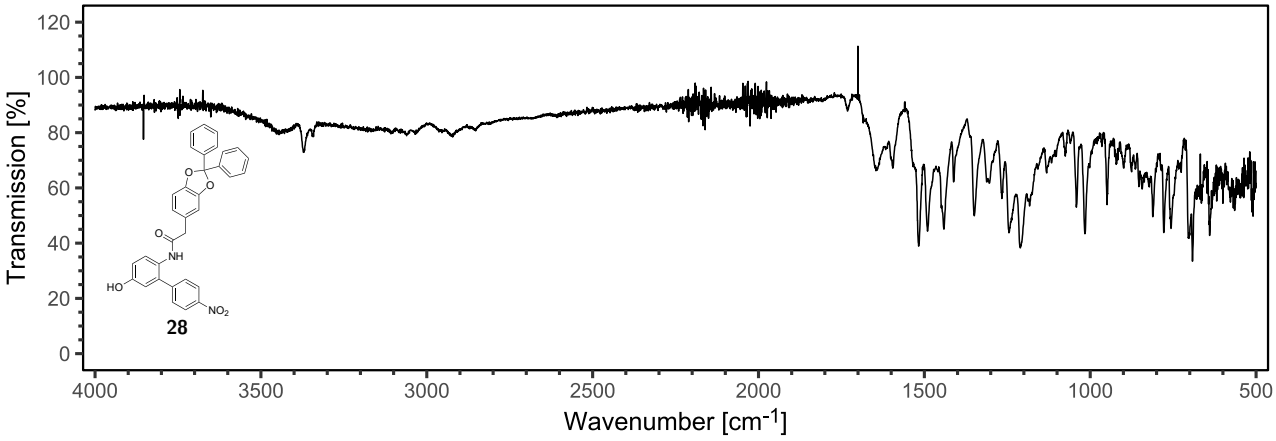

IR (solid, rt) spectrum of
2-(2,2-diphenylbenzo[*d*][1,3]dioxol-5-yl)-*N*-(5-hydroxy-4'-nitro-[1,1'-biphenyl]-2-yl)acetamide **28**.

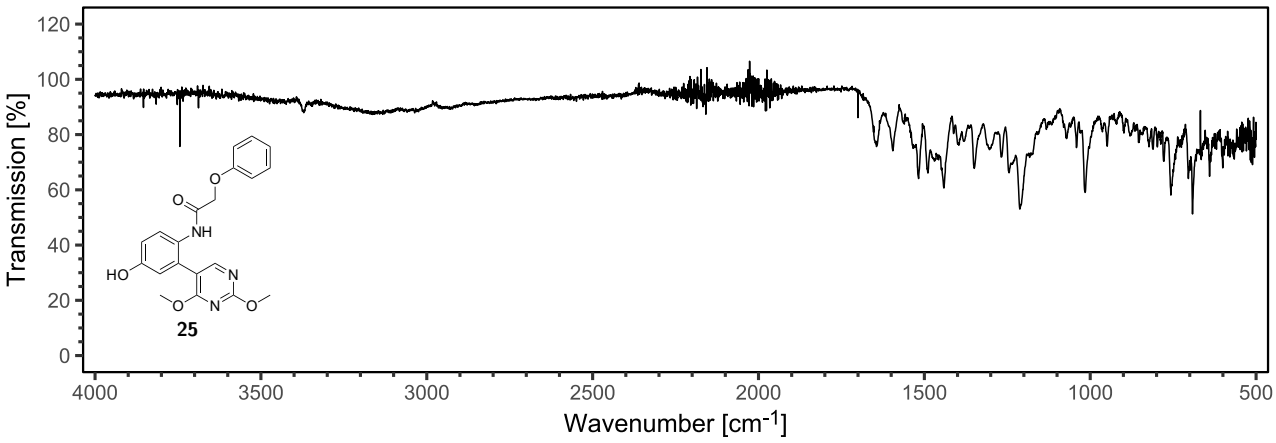

IR (solid, rt) spectrum of
N-(2-(2,4-dimethoxypyrimidin-5-yl)-4-hydroxyphenyl)-2-phenoxyacetamide **25**.

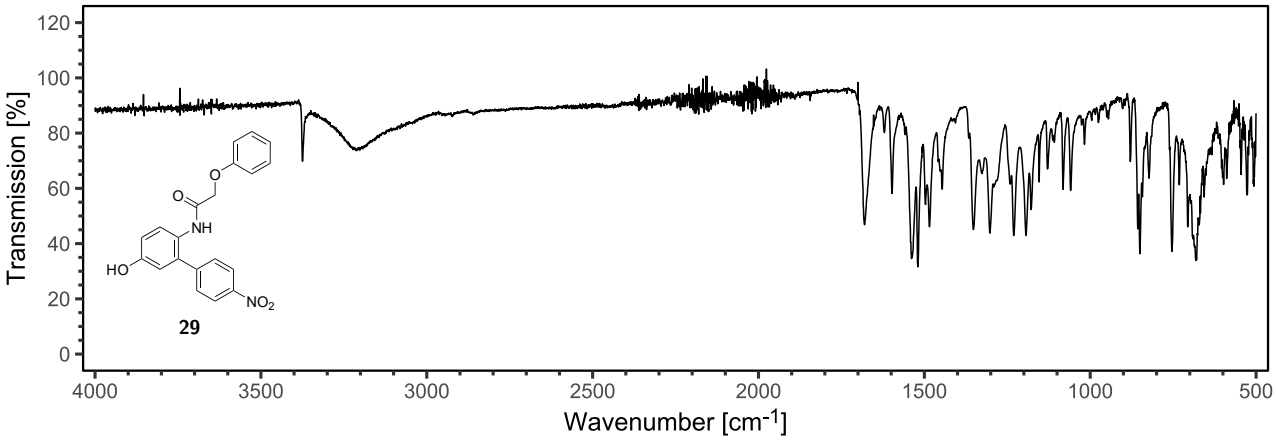

IR (solid, rt) spectrum of
N-(5-hydroxy-4'-nitro-[1,1'-biphenyl]-2-yl)-2-phenoxyacetamide **29**.

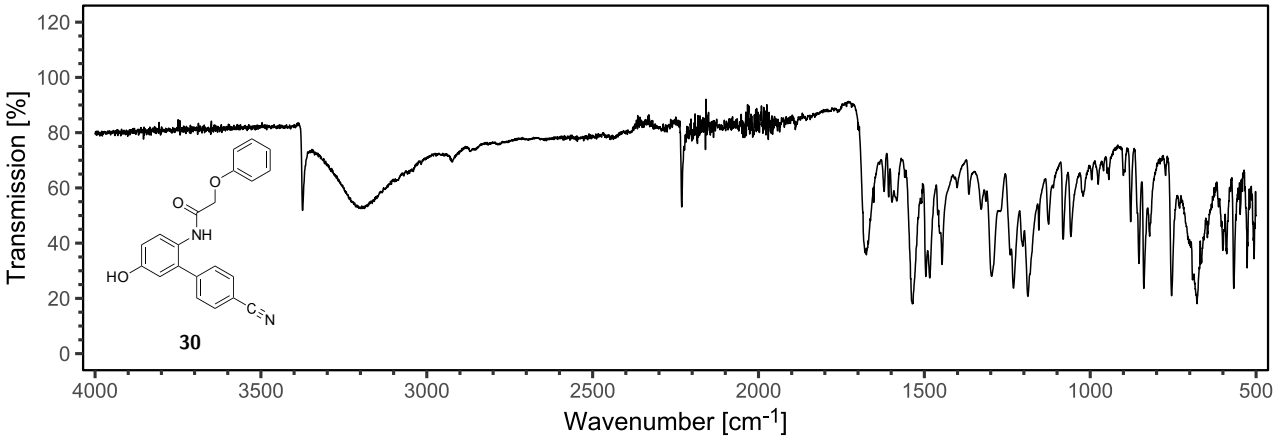

IR (solid, rt) spectrum of
N-(4'-cyano-5-hydroxy-[1,1'-biphenyl]-2-yl)-2-phenoxyacetamide **30**.

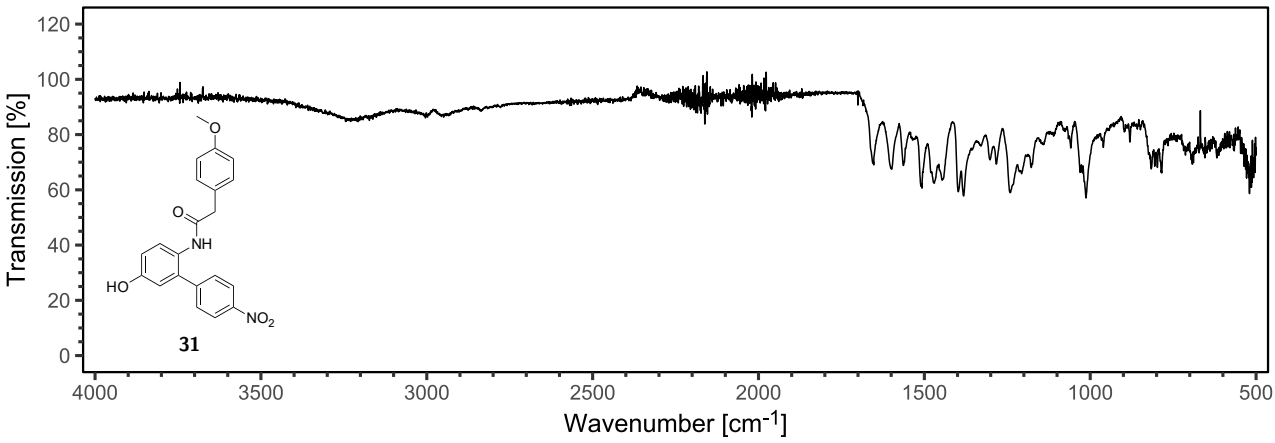

IR (solid, rt) spectrum of
N-(2-(2,4-dimethoxypyrimidin-5-yl)-4-hydroxyphenyl)-2-(4-methoxyphenyl)acetamide **31**.

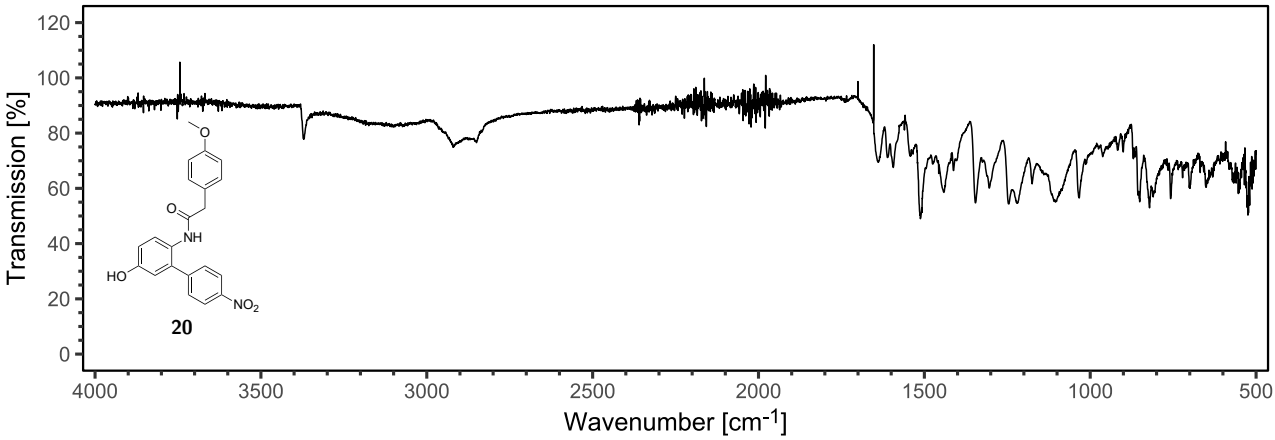

IR (solid, rt) spectrum of
N-(5-hydroxy-4'-nitro-[1,1'-biphenyl]-2-yl)-2-(4-methoxyphenyl)acetamide **20**.

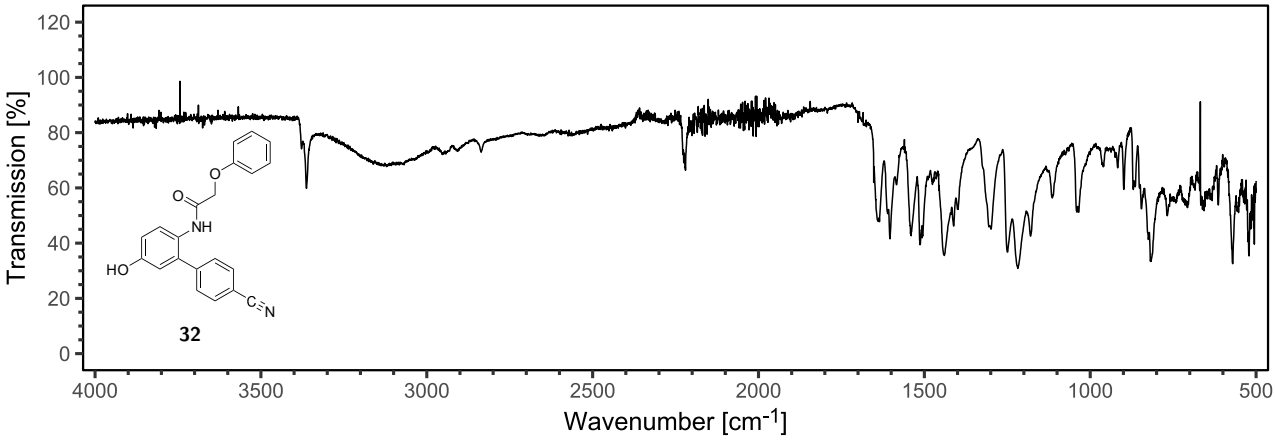

IR (solid, rt) spectrum of
N-(4'-cyano-5-hydroxy-[1,1'-biphenyl]-2-yl)-2-(4-methoxyphenyl)acetamide **32**.

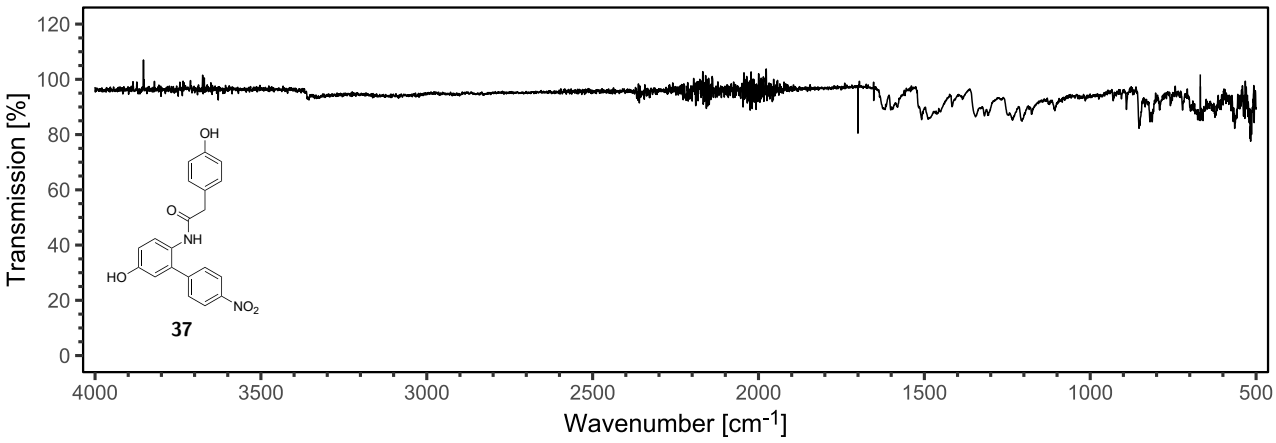

IR (solid, rt) spectrum of
N-(5-hydroxy-4'-nitro-[1,1'-biphenyl]-2-yl)-2-(4-hydroxyphenyl)acetamide **37**.

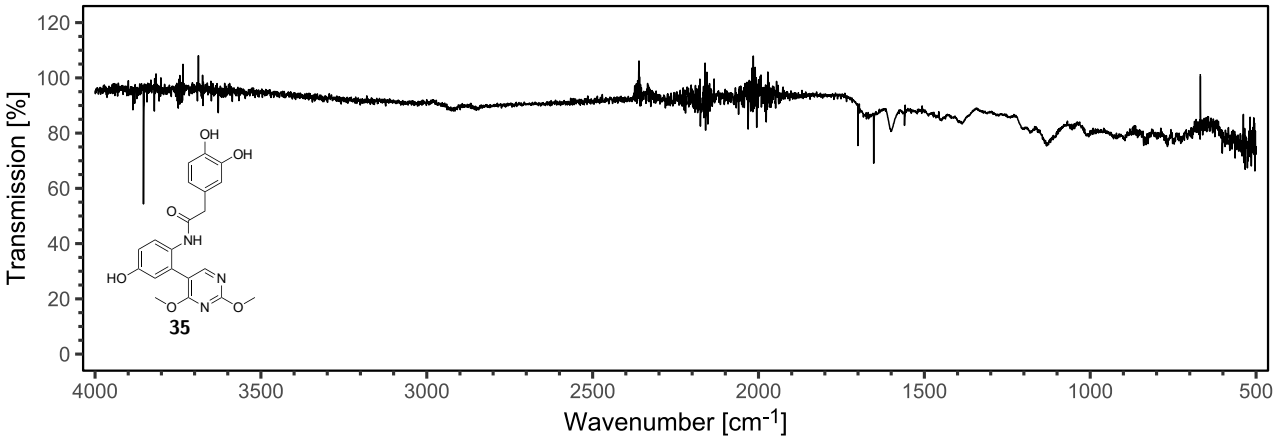

IR (solid, rt) spectrum of
2-(3,4-dihydroxyphenyl)-*N*-(2-(2,4-dimethoxypyrimidin-5-yl)-4-hydroxyphenyl)acetamide **35**.

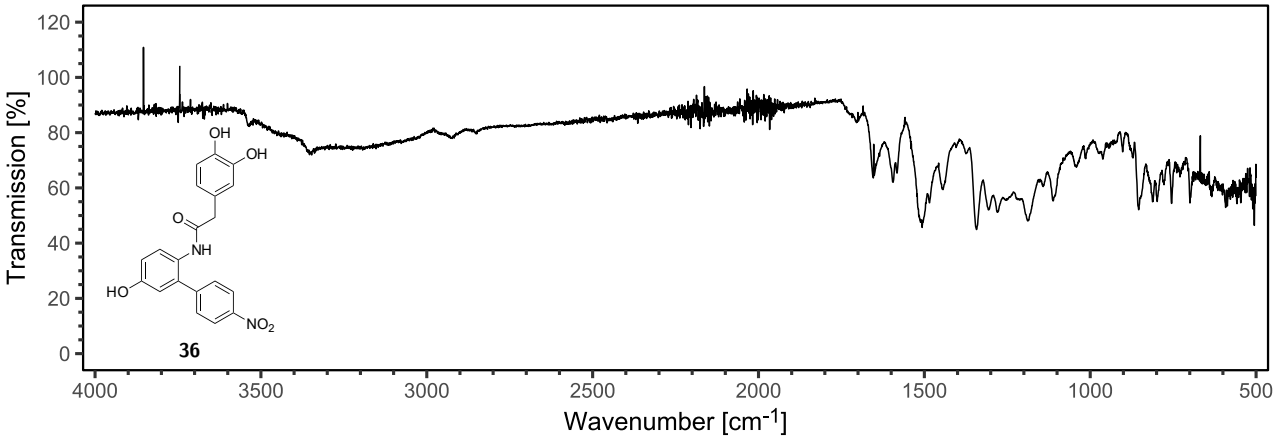

IR (solid, rt) spectrum of
2-(3,4-dihydroxyphenyl)-*N*-(5-hydroxy-4'-nitro-[1,1'-biphenyl]-2-yl)acetamide **36**.

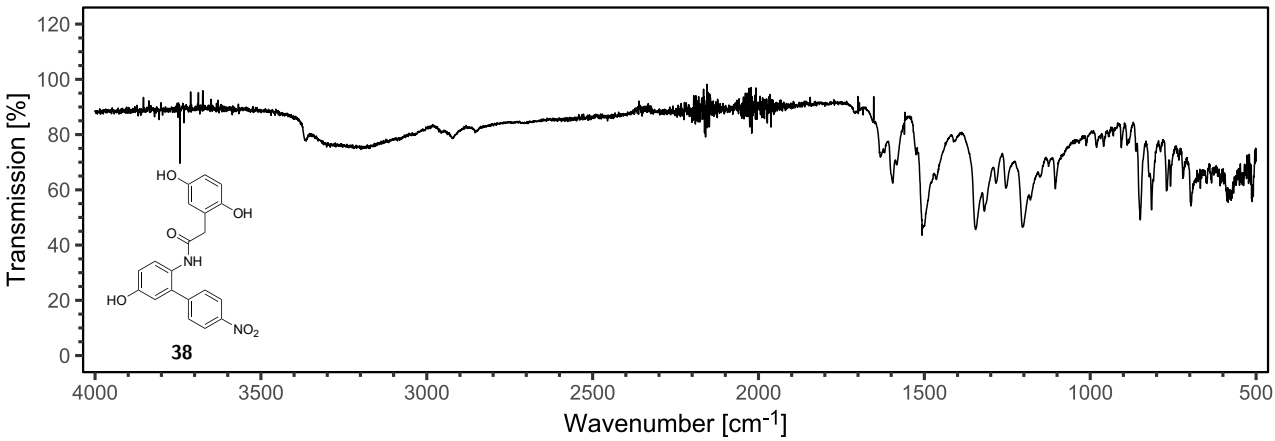

IR (solid, rt) spectrum of
2-(2,5-dihydroxyphenyl)-*N*-(5-hydroxy-4'-nitro-[1,1'-biphenyl]-2-yl)acetamide **38**.

10.9 Analytical HPLC Chromatograms

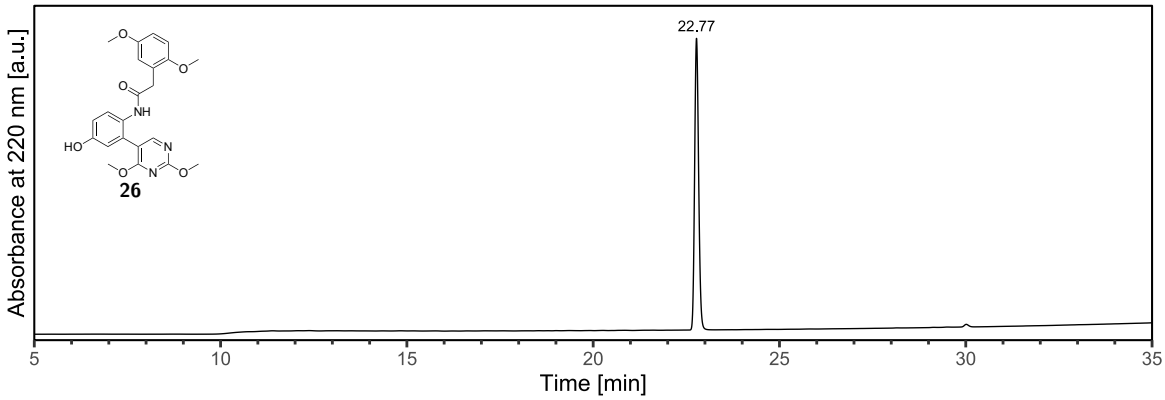

Analytical HPLC trace (gradient of 10–80% B in A over 30 min shown) of 2-(2,5-dimethoxyphenyl)-*N*-(2-(2,4-dimethoxypyrimidin-5-yl)-4-hydroxyphenyl)acetamide **26**

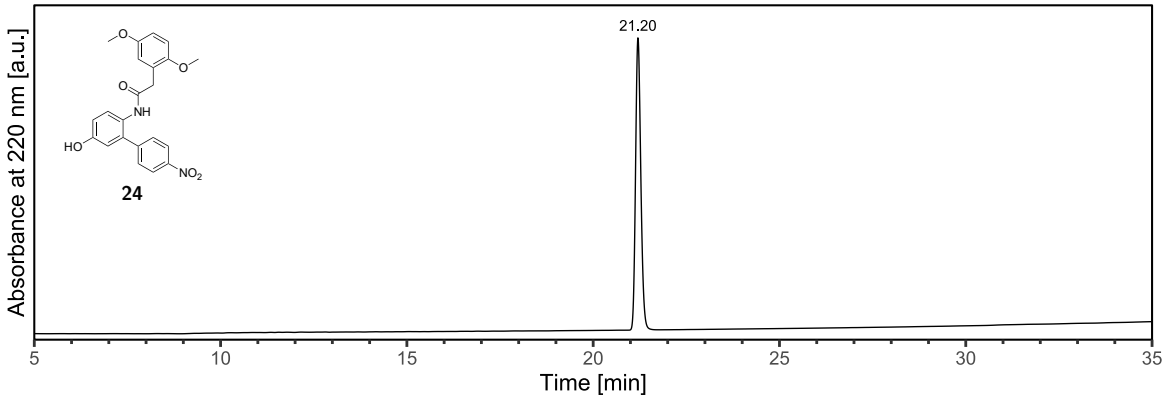

Analytical HPLC trace (gradient of 30–80% B in A over 30 min shown) of *N*-(2-(2,4-dimethoxypyrimidin-5-yl)-4-hydroxyphenyl)-2-(2,2-diphenylbenzo[*d*][1,3]dioxol-5-yl) acetamide **24**

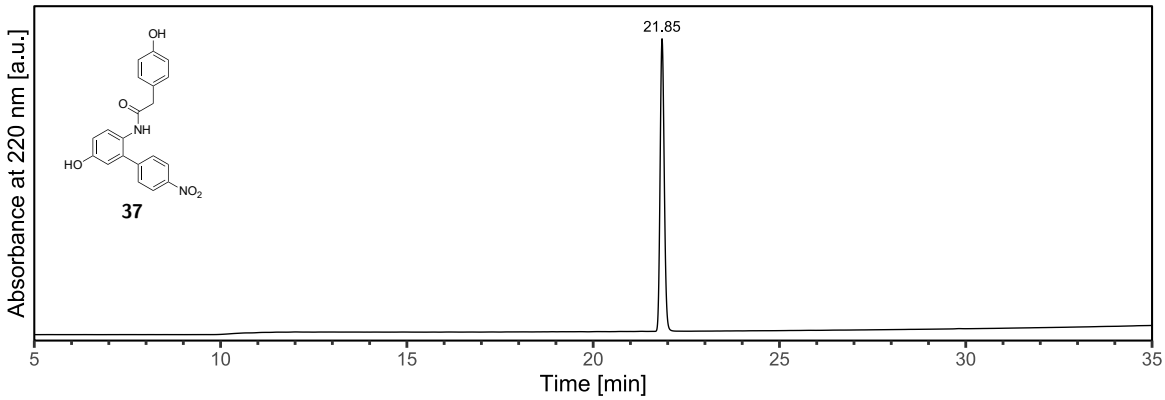

Analytical HPLC trace (gradient of 10–80% B in A over 30 min shown) of *N*-(5-hydroxy-4'-nitro-[1,1'-biphenyl]-2-yl)-2-(4-hydroxyphenyl)acetamide **37**

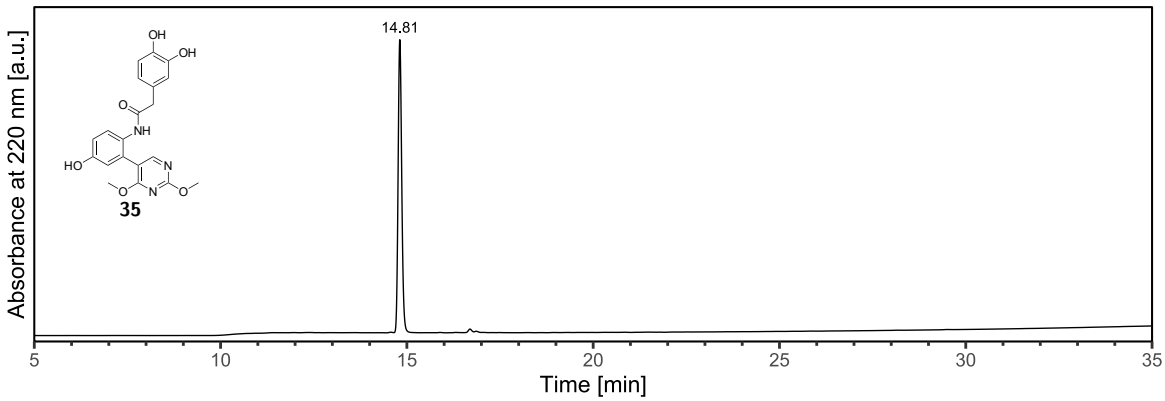

Analytical HPLC trace (gradient of 10–80% B in A over 30 min shown) of 2-(3,4-dihydroxyphenyl)-*N*-(2-(2,4-dimethoxypyrimidin-5-yl)-4-hydroxyphenyl)acetamide **35**

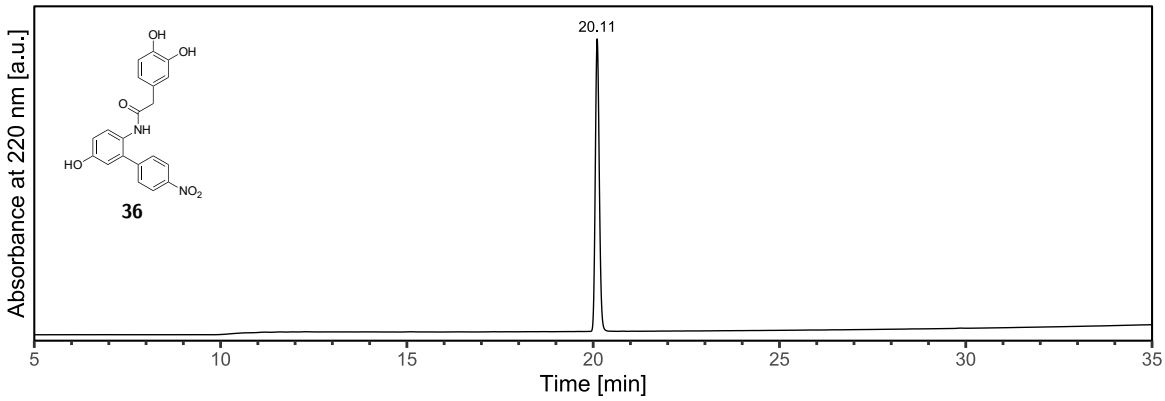

Analytical HPLC trace (gradient of 10–80% B in A over 30 min shown) of 2-(3,4-dihydroxyphenyl)-*N*-(5-hydroxy-4'-nitro-[1,1'-biphenyl]-2-yl)acetamide **36**

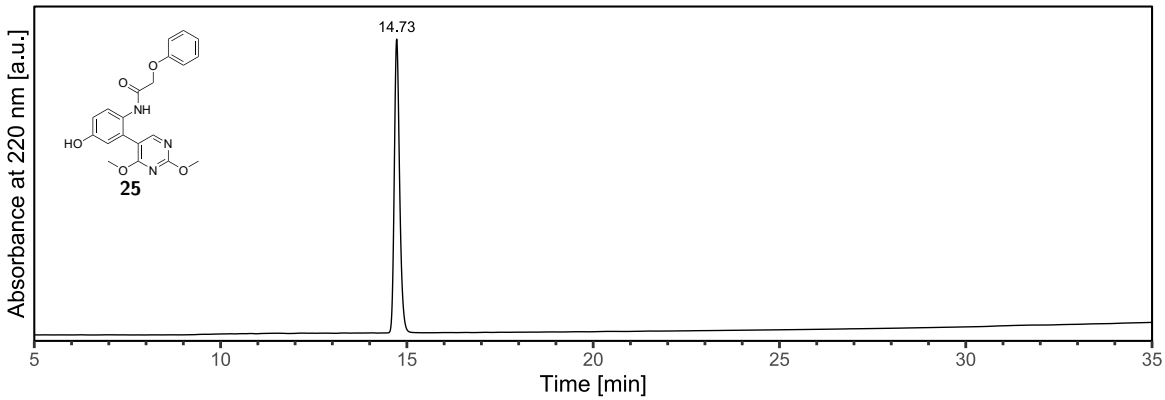

Analytical HPLC trace (gradient of 30–80% B in A over 30 min shown) of *N*-(2-(2,4-dimethoxypyrimidin-5-yl)-4-hydroxyphenyl)-2-phenoxyacetamide **25**

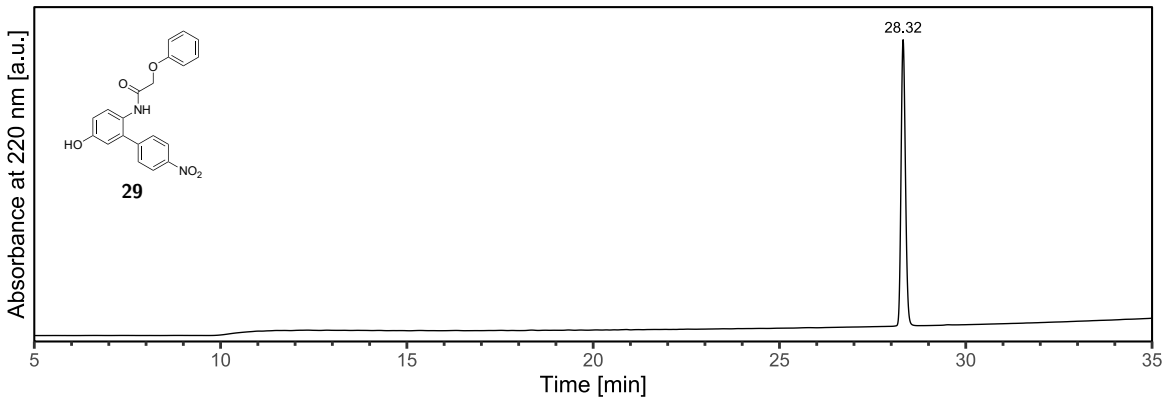

Analytical HPLC trace (gradient of 10–80% B in A over 30 min shown) of *N*-(5-hydroxy-4'-nitro-[1,1'-biphenyl]-2-yl)-2-phenoxyacetamide **29**

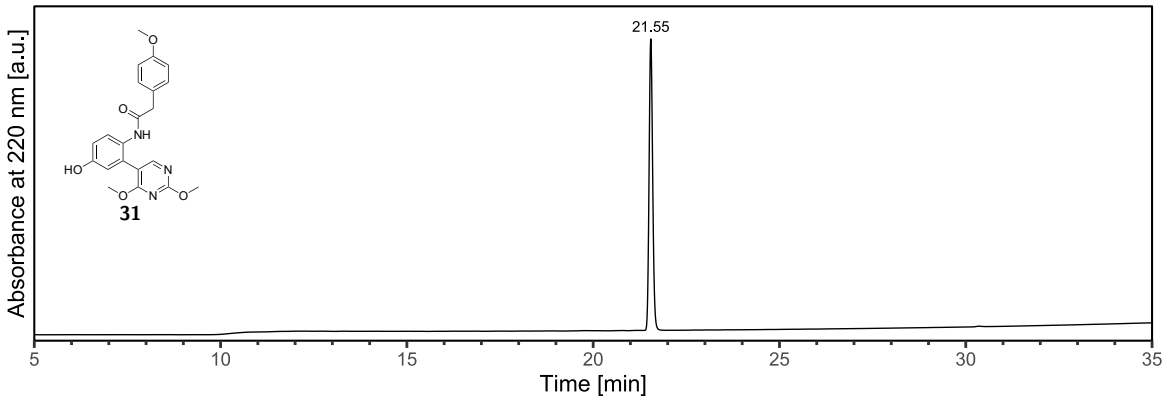

Analytical HPLC trace (gradient of 10–80% B in A over 30 min shown) of *N*-(2-(2,4-dimethoxypyrimidin-5-yl)-4-hydroxyphenyl)-2-(4-methoxyphenyl)acetamide **31**

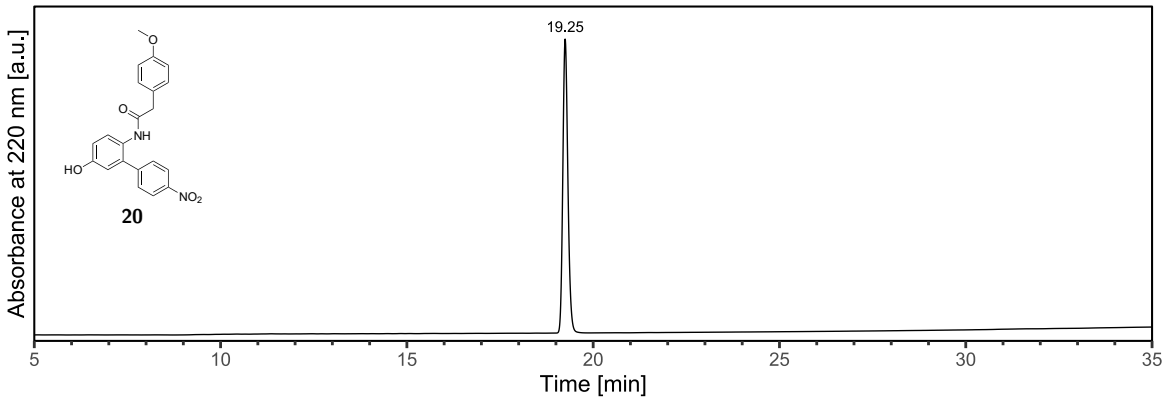

Analytical HPLC trace (gradient of 30–80% B in A over 30 min shown) of *N*-(5-hydroxy-4'-nitro-[1,1'-biphenyl]-2-yl)-2-(4-methoxyphenyl)acetamide **20**

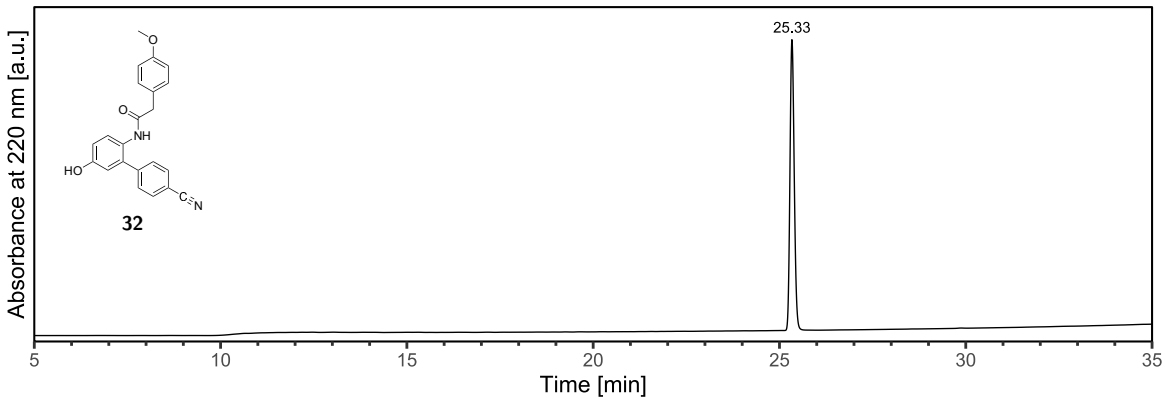

Analytical HPLC trace (gradient of 10–80% B in A over 30 min shown) of *N*-(4'-cyano-5-hydroxy-[1,1'-biphenyl]-2-yl)-2-(4-methoxyphenyl)acetamide **32**

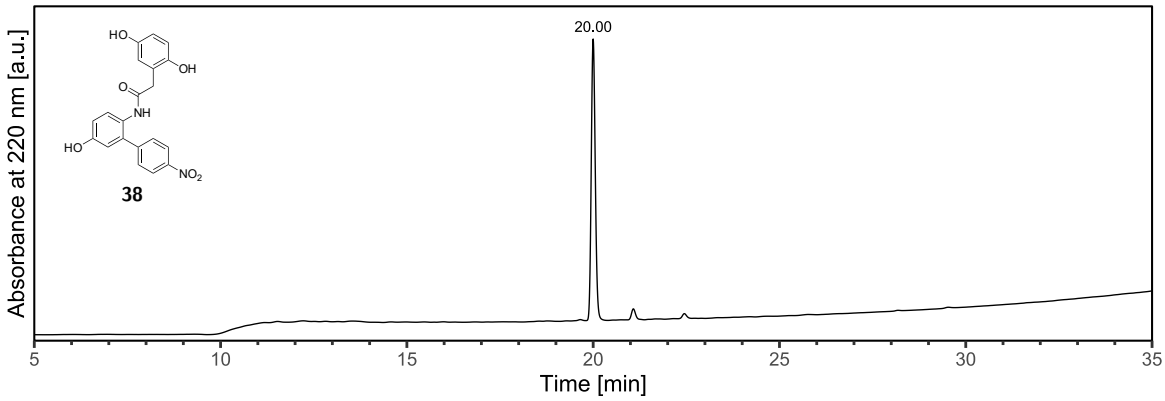

Analytical HPLC trace (gradient of 10–80% B in A over 30 min shown) of 2-(2,5-dihydroxyphenyl)-*N*-(5-hydroxy-4'-nitro-[1,1'-biphenyl]-2-yl)acetamide **38**

References

[1] E. L. Feldman et al., "Amyotrophic lateral sclerosis", *The Lancet* **2022**, *400*, 1363–1380.

[2] L. C. Wijesekera, P. Nigel Leigh, "Amyotrophic lateral sclerosis", *Orphanet Journal of Rare Diseases* **2009**, *4*.

[3] B. Marin et al., "Variation in worldwide incidence of amyotrophic lateral sclerosis: a meta-analysis", *International Journal of Epidemiology* **2017**, dyw061.

[4] E. Longinetti, F. Fang, "Epidemiology of amyotrophic lateral sclerosis: an update of recent literature", *Current Opinion in Neurology* **2019**, *32*, 771–776.

[5] L. Tzeplaeff et al., "Unraveling the Heterogeneity of ALS—A Call to Redefine Patient Stratification for Better Outcomes in Clinical Trials", *Cells* **2024**, *13*, 452.

[6] R. Mejzini et al., "ALS Genetics, Mechanisms, and Therapeutics: Where Are We Now?", *Frontiers in Neuroscience* **2019**, *13*.

[7] N. Riva et al., "Update on recent advances in amyotrophic lateral sclerosis", *Journal of Neurology* **2024**, *271*, 4693–4723.

[8] M. J. Strong et al., "Amyotrophic lateral sclerosis - frontotemporal spectrum disorder (ALS-FTSD): Revised diagnostic criteria", *Amyotrophic Lateral Sclerosis and Frontotemporal Degeneration* **2017**, *18*, 153–174.

[9] S. Abrahams, "Neuropsychological impairment in amyotrophic lateral sclerosis–frontotemporal spectrum disorder", *Nature Reviews Neurology* **2023**, *19*, 655–667.

[10] K. Talbot, "Familial versus sporadic amyotrophic lateral sclerosis–a false dichotomy?", *Brain* **2011**, *134*, 3429–3434.

[11] A. Al Sultan et al., "The genetics of amyotrophic lateral sclerosis: current insights", *Degenerative Neurological and Neuromuscular Disease* **2016**, 49.

[12] M. Huang et al., "Variability in SOD1-associated amyotrophic lateral sclerosis: geographic patterns, clinical heterogeneity, molecular alterations, and therapeutic implications", *Translational Neurodegeneration* **2024**, *13*.

[13] P. M. Andersen, A. Al-Chalabi, "Clinical genetics of amyotrophic lateral sclerosis: what do we really know?", *Nature Reviews Neurology* **2011**, *7*, 603–615.

[14] A. Chaouch et al., "The use of genetic testing in amyotrophic lateral sclerosis (ALS): a practical approach", *Amyotrophic Lateral Sclerosis and Frontotemporal Degeneration* **2025**, 1–7.

[15] E. Udine, A. Jain, M. van Blitterswijk, "Advances in sequencing technologies for amyotrophic lateral sclerosis research", *Molecular Neurodegeneration* **2023**, *18*.

[16] D. R. Rosen et al., "Mutations in Cu/Zn superoxide dismutase gene are associated with familial amyotrophic lateral sclerosis", *Nature* **1993**, *362*, 59–62.

[17] M. Neumann et al., "Ubiquitinated TDP-43 in Frontotemporal Lobar Degeneration and Amyotrophic Lateral Sclerosis", *Science* **2006**, *314*, 130–133.

[18] T. Arai et al., "TDP-43 is a component of ubiquitin-positive tau-negative inclusions in frontotemporal lobar degeneration and amyotrophic lateral sclerosis", *Biochemical and Biophysical Research Communications* **2006**, *351*, 602–611.

[19] M. Hasegawa et al., "Phosphorylated TDP-43 in frontotemporal lobar degeneration and amyotrophic lateral sclerosis", *Annals of Neurology* **2008**, *64*, 60–70.

[20] M. DeJesus-Hernandez et al., "Expanded GGGGCC Hexanucleotide Repeat in Noncoding Region of C9ORF72 Causes Chromosome 9p-Linked FTD and ALS", *Neuron* **2011**, *72*, 245–256.

[21] A. E. Renton et al., "A Hexanucleotide Repeat Expansion in C9ORF72 Is the Cause of Chromosome 9p21-Linked ALS-FTD", *Neuron* **2011**, *72*, 257–268.

[22] P. Heutink, I. E. Jansen, E. M. Lynes, "C9orf72; abnormal RNA expression is the key", *Experimental Neurology* **2014**, *262*, 102–110.

[23] T. J. Kwiatkowski et al., "Mutations in the FUS/TLS Gene on Chromosome 16 Cause Familial Amyotrophic Lateral Sclerosis", *Science* **2009**, *323*, 1205–1208.

[24] Z.-Y. Zou et al., "Genetic epidemiology of amyotrophic lateral sclerosis: a systematic review and meta-analysis", *Journal of Neurology Neurosurgery & Psychiatry* **2017**, *88*, 540–549.

[25] G. S. Jeon et al., "Pathological Modification of TDP-43 in Amyotrophic Lateral Sclerosis with SOD1 Mutations", *Molecular Neurobiology* **2019**, *56*, 2007–2021.

[26] M. Tsekrekou et al., "Protein aggregation and therapeutic strategies in SOD1- and TDP-43-linked ALS", *Frontiers in Molecular Biosciences* **2024**, *11*.

[27] I. R. A. Mackenzie et al., "Pathological TDP-43 distinguishes sporadic amyotrophic lateral sclerosis from amyotrophic lateral sclerosis with SOD1 mutations", *Annals of Neurology* **2007**, *61*, 427–434.

[28] B. Genç et al., "NU-9 improves health of hSOD1G93A mouse upper motor neurons in vitro, especially in combination with riluzole or edaravone", *Scientific Reports* **2022**, *12*.

[29] T. Domi et al., "Unveiling the SOD1-mediated ALS phenotype: insights from a comprehensive meta-analysis", *Journal of Neurology* **2024**, *271*, 1342–1354.

[30] C. G. Chung, H. Lee, S. B. Lee, "Mechanisms of protein toxicity in neurodegenerative diseases", *Cellular and Molecular Life Sciences* **2018**, *75*, 3159–3180.

[31] Y. Li, S. Li, H. Wu, "Ubiquitination-Proteasome System (UPS) and Autophagy Two Main Protein Degradation Machineries in Response to Cell Stress", *Cells* **2022**, *11*, 851.

[32] J. Keller, F. Huang, W. Markesbery, "Decreased levels of proteasome activity and proteasome expression in aging spinal cord", *Neuroscience* **2000**, *98*, 149–156.

[33] K. Puttaparthi et al., "Aggregate formation in the spinal cord of mutant SOD1 transgenic mice is reversible and mediated by proteasomes", *Journal of Neurochemistry* **2003**, *87*, 851–860.

[34] J. S. Elam et al., "Amyloid-like filaments and water-filled nanotubes formed by SOD1 mutant proteins linked to familial ALS", *Nature Structural & Molecular Biology* **2003**, *10*, 461–467.

[35] G. S. A. Wright, S. V. Antonyuk, S. S. Hasnain, "The biophysics of superoxide dismutase-1 and amyotrophic lateral sclerosis", *Quarterly Reviews of Biophysics* **2019**, *52*.

[36] L.-Q. Wang et al., "Cryo-EM structure of an amyloid fibril formed by full-length human SOD1 reveals its conformational conversion", *Nature Communications* **2022**, *13*.

[37] M. G. Savelieff et al., "Development of Multifunctional Molecules as Potential Therapeutic Candidates for Alzheimer's Disease, Parkinson's Disease, and Amyotrophic Lateral Sclerosis in the Last Decade", *Chemical Reviews* **2019**, *119*, 1221–1322.

[38] U. Nordström et al., "Mutant SOD1 aggregates formed in vitro and in cultured cells are polymorphic and differ from those arising in the CNS", *Journal of Neurochemistry* **2023**, *164*, 77–93.

[39] B. G. Trist et al., "Superoxide Dismutase 1 in Health and Disease: How a Frontline Antioxidant Becomes Neurotoxic", *Angewandte Chemie International Edition* **2021**, *60*, 9215–9246.

[40] C. Zhu et al., "Large SOD1 aggregates, unlike trimeric SOD1, do not impact cell viability in a model of amyotrophic lateral sclerosis", *Proceedings of the National Academy of Sciences* **2018**, *115*, 4661–4665.

[41] E. S. Choi, N. V. Dokholyan, "SOD1 oligomers in amyotrophic lateral sclerosis", *Current Opinion in Structural Biology* **2021**, *66*, 225–230.

[42] L. Tzeplaeff et al., "Current State and Future Directions in the Therapy of ALS", *Cells* **2023**, *12*, 1523.

[43] B. Paré et al., "Misfolded SOD1 pathology in sporadic Amyotrophic Lateral Sclerosis", *Scientific Reports* **2018**, *8*.

[44] A. Chiò et al., "Global Epidemiology of Amyotrophic Lateral Sclerosis: A Systematic Review of the Published Literature", *Neuroepidemiology* **2013**, *41*, 118–130.

[45] R. W. Strange et al., "Variable Metallation of Human Superoxide Dismutase: Atomic Resolution Crystal Structures of Cu–Zn, Zn–Zn and As-isolated Wild-type Enzymes", *Journal of Molecular Biology* **2006**, *356*, 1152–1162.

[46] M. DiDonato et al., "ALS Mutants of Human Superoxide Dismutase Form Fibrous Aggregates Via Framework Destabilization", *Journal of Molecular Biology* **2003**, *332*, 601–615.

[47] R. W. Strange et al., "Molecular dynamics using atomic-resolution structure reveal structural fluctuations that may lead to polymerization of human Cu–Zn superoxide dismutase", *Proceedings of the National Academy of Sciences* **2007**, *104*, 10040–10044.

[48] R. Graebner, "Design and Synthesis of Small Molecules for the Stabilization of the ALS-related SOD1 protein", *Master Thesis Heidelberg University* **2021**.

[49] Y. Sheng et al., "Superoxide Dismutases and Superoxide Reductases", *Chemical Reviews* **2014**, *114*, 3854–3918.

[50] E. C. A. Eleutherio et al., "SOD1, more than just an antioxidant", *Archives of Biochemistry and Biophysics* **2021**, *697*, 108701.

[51] E. D. Getzoff et al., "Electrostatic recognition between superoxide and copper, zinc superoxide dismutase", *Nature* **1983**, *306*, 287–290.

[52] S. Nedd et al., "Cu,Zn-Superoxide Dismutase without Zn Is Folded but Catalytically Inactive", *Journal of Molecular Biology* **2014**, *426*, 4112–4124.

[53] I. Bertini et al., "A spectroscopic characterization of a monomeric analog of copper, zinc superoxide dismutase", *European Biophysics Journal* **1994**, *23*, 167–176.

[54] A. Tiwari, L. J. Hayward, "Familial Amyotrophic Lateral Sclerosis Mutants of Copper/Zinc Superoxide Dismutase Are Susceptible to Disulfide Reduction", *Journal of Biological Chemistry* **2003**, *278*, 5984–5992.

[55] Y. Furukawa, T. V. O'Halloran, "Amyotrophic Lateral Sclerosis Mutations Have the Greatest Destabilizing Effect on the Apo- and Reduced Form of SOD1, Leading to Unfolding and Oxidative Aggregation", *Journal of Biological Chemistry* **2005**, *280*, 17266–17274.

[56] T. Bali et al., "Defining SOD1 ALS natural history to guide therapeutic clinical trial design", *Journal of Neurology Neurosurgery & Psychiatry* **2017**, *88*, 99–105.

[57] T. Philips, J. D. Rothstein, "Rodent Models of Amyotrophic Lateral Sclerosis", *Current Protocols in Pharmacology* **2015**, *69*.

[58] H.-X. Deng et al., "Conversion to the amyotrophic lateral sclerosis phenotype is associated with intermolecular linked insoluble aggregates of SOD1 in mitochondria", *Proceedings of the National Academy of Sciences* **2006**, *103*, 7142–7147.

[59] D. R. Rosen et al., "A frequent ala 4 to val superoxide dismutase-1 mutation is associated with a rapidly progressive familial amyotrophic lateral sclerosis", *Human Molecular Genetics* **1994**, *3*, 981–987.

[60] T. Juneja et al., "Prognosis in Familial Amyotrophic Lateral Sclerosis: Progression and Survival in Patients with Glu100gly and Ala4val Mutations in Cu,Zn Superoxide Dismutase", *Neurology* **1997**, *48*, 55–57.

[61] D. Petrov et al., "ALS Clinical Trials Review: 20 Years of Failure. Are We Any Closer to Registering a New Treatment?", *Frontiers in Aging Neuroscience* **2017**, *9*.

[62] R. J. Mead et al., "Amyotrophic lateral sclerosis: a neurodegenerative disorder poised for successful therapeutic translation", *Nature Reviews Drug Discovery* **2023**, *22*, 185–212.

[63] L. Van Den Bosch, "Genetic Rodent Models of Amyotrophic Lateral Sclerosis", *BioMed Research International* **2011**, *2011*, (Ed.: O. Gualillo).

[64] E. M. Fisher et al., "Opinion: more mouse models and more translation needed for ALS", *Molecular Neurodegeneration* **2023**, *18*.

[65] L. Zhou et al., "In Vitro Models of Amyotrophic Lateral Sclerosis", *Cellular and Molecular Neurobiology* **2023**, *43*, 3783–3799.

[66] https://www.clinicaltrials.gov.

[67] H. J. Wobst et al., "The clinical trial landscape in amyotrophic lateral sclerosis - Past, present, and future", *Medicinal Research Reviews* **2020**, *40*, 1352–1384.

[68] M. Boucher, M. Mierzwinski-Urban, "Emerging Drugs for Amyotrophic Lateral Sclerosis", *Canadian Journal of Health Technologies* **2022**, *2*.

[69] M. F. Elmansy et al., "Small molecules targeting different cellular pathologies for the treatment of amyotrophic lateral sclerosis", *Medicinal Research Reviews* **2023**, *43*, 2260–2302.

[70] X. Li, R. Bedlack, "Evaluating emerging drugs in phase II & III for the treatment of amyotrophic lateral sclerosis", *Expert Opinion on Emerging Drugs* **2024**, *29*, 93–102.

[71] A. G. Reaume et al., "Motor neurons in Cu/Zn superoxide dismutase-deficient mice develop normally but exhibit enhanced cell death after axonal injury", *Nature Genetics* **1996**, *13*, 43–47.

[72] R. A. Saccon et al., "Is SOD1 loss of function involved in amyotrophic lateral sclerosis?", *Brain* **2013**, *136*, 2342–2358.

[73] A. McCampbell et al., "Antisense oligonucleotides extend survival and reverse decrement in muscle response in ALS models", *Journal of Clinical Investigation* **2018**, *128*, 3558–3567.

[74] D. J. Lange, "Pyrimethamine as a therapy for SOD1 associated FALS: Early findings", *Amyotrophic Lateral Sclerosis* **2008**, *9*, 45–47.

[75] D. J. Lange et al., "Pyrimethamine decreases levels of SOD1 in leukocytes and cerebrospinal fluid of ALS patients: A phase I pilot study", *Amyotrophic Lateral Sclerosis and Frontotemporal Degeneration* **2013**, *14*, 199–204.

[76] D. J. Lange et al., "Pyrimethamine significantly lowers cerebrospinal fluid Cu/Zn superoxide dismutase in amyotrophic lateral sclerosis patients with SOD1 mutations", *Annals of Neurology* **2017**, *81*, 837–848.

[77] P. D. Wright et al., "Screening for inhibitors of the SOD1 gene promoter: Pyrimethamine does not reduce SOD1 levels in cell and animal models", *Neuroscience Letters* **2010**, *482*, 188–192.

[78] A. M. Quemener et al., "The powerful world of antisense oligonucleotides: From bench to bedside", *WIREs RNA* **2020**, *11*.

[79] M. C. Lauffer, W. van Roon-Mom, A. Aartsma-Rus, "Possibilities and limitations of antisense oligonucleotide therapies for the treatment of monogenic disorders", *Communications Medicine* **2024**, *4*.

[80] W. Filipowicz, S. N. Bhattacharyya, N. Sonenberg, "Mechanisms of post-transcriptional regulation by microRNAs: are the answers in sight?", *Nature Reviews Genetics* **2008**, *9*, 102–114.

[81] A. J. Pratt, I. J. MacRae, "The RNA-induced Silencing Complex: A Versatile Gene-silencing Machine", *Journal of Biological Chemistry* **2009**, *284*, 17897–17901.

[82] O. Khorkova et al., "Natural antisense transcripts as drug targets", *Frontiers in Molecular Biosciences* **2022**, *9*.

[83] S. H. Van Daele et al., "The sense of antisense therapies in ALS", *Trends in Molecular Medicine* **2024**, *30*, 252–262.

[84] S. S. Ray et al., "An Intersubunit Disulfide Bond Prevents in Vitro Aggregation of a Superoxide Dismutase-1 Mutant Linked to Familial Amytrophic Lateral Sclerosis", *Biochemistry* **2004**, *43*, 4899–4905.

[85] S. S. Ray, P. T. Lansbury, "A possible therapeutic target for Lou Gehrig's disease", *Proceedings of the National Academy of Sciences* **2004**, *101*, 5701–5702.

[86] S. S. Ray et al., "Small-molecule-mediated stabilization of familial amyotrophic lateral sclerosis-linked superoxide dismutase mutants against unfolding and aggregation", *Proceedings of the National Academy of Sciences* **2005**, *102*, 3639–3644.

[87] R. J. Nowak et al., "Improving Binding Specificity of Pharmacological Chaperones That Target Mutant Superoxide Dismutase-1 Linked to Familial Amyotrophic Lateral Sclerosis Using Computational Methods", *Journal of Medicinal Chemistry* **2010**, *53*, 2709–2718.

[88] S. Antonyuk, R. W. Strange, S. S. Hasnain, "Structural Discovery of Small Molecule Binding Sites in Cu–Zn Human Superoxide Dismutase Familial Amyotrophic Lateral Sclerosis Mutants Provides Insights for Lead Optimization", *Journal of Medicinal Chemistry* **2010**, *53*, 1402–1406.

[89] G. S. Wright et al., "Ligand binding and aggregation of pathogenic SOD1", *Nature Communications* **2013**, *4*.

[90] J. R. Auclair et al., "Strategies for stabilizing superoxide dismutase (SOD1), the protein destabilized in the most common form of familial amyotrophic lateral sclerosis", *Proceedings of the National Academy of Sciences* **2010**, *107*, 21394–21399.

[91] D. P. Donnelly et al., "Cyclic Thiosulfinates and Cyclic Disulfides Selectively Cross-Link Thiols While Avoiding Modification of Lone Thiols", *Journal of the American Chemical Society* **2018**, *140*, 7377–7380.

[92] M. A. Hossain et al., "Evaluating protein cross-linking as a therapeutic strategy to stabilize SOD1 variants in a mouse model of familial ALS", *PLOS Biology* **2024**, *22*, (Ed.: J. Dubnau), e3002462.

[93] G. S. A. Wright, S. V. Antonyuk, S. S. Hasnain, "A faulty interaction between SOD1 and hCCS in neurodegenerative disease", *Scientific Reports* **2016**, *6*.

[94] L. Banci et al., "Metal-free superoxide dismutase forms soluble oligomers under physiological conditions: A possible general mechanism for familial ALS", *Proceedings of the National Academy of Sciences* **2007**, *104*, 11263–11267.

[95] L. Banci et al., "Interaction of Cisplatin with Human Superoxide Dismutase", *Journal of the American Chemical Society* **2012**, *134*, 7009–7014.

[96] M. J. Capper et al., "The cysteine-reactive small molecule ebselen facilitates effective SOD1 maturation", *Nature Communications* **2018**, *9*.

[97] V. Chantadul et al., "Ebselen as template for stabilization of A4V mutant dimer for motor neuron disease therapy", *Communications Biology* **2020**, *3*.

[98] K. Amporndanai et al., "Novel Selenium-based compounds with therapeutic potential for SOD1-linked amyotrophic lateral sclerosis", *eBioMedicine* **2020**, *59*, 102980.

[99] S. Watanabe et al., "Ebselen analogues delay disease onset and its course in fALS by on-target SOD-1 engagement", *Scientific Reports* **2024**, *14*.

[100] B. Sever et al., "Comprehensive Research on Past and Future Therapeutic Strategies Devoted to Treatment of Amyotrophic Lateral Sclerosis", *International Journal of Molecular Sciences* **2022**, *23*, 2400.

[101] M. A. Singer, S. Lindquist, "Multiple Effects of Trehalose on Protein Folding In Vitro and In Vivo", *Molecular Cell* **1998**, *1*, 639–648.

[102] K. Römisch, "A Cure for Traffic Jams: Small Molecule Chaperones in the Endoplasmic Reticulum", *Traffic* **2004**, *5*, 815–820.

[103] P. Pinmanee et al., "Enhancing the Productivity and Stability of Superoxide Dismutase from Saccharomyces cerevisiae TBRC657 and Its Application as a Free Radical Scavenger", *Fermentation* **2022**, *8*, 169.

[104] C. Gomes, C. Escrevente, J. Costa, "Mutant superoxide dismutase 1 overexpression in NSC-34 cells: Effect of trehalose on aggregation, TDP-43 localization and levels of co-expressed glycoproteins", *Neuroscience Letters* **2010**, *475*, 145–149.

[105] R. S. S. Magalhães et al., "Trehalose Protects against Superoxide Dismutase 1 Proteinopathy in an Amyotrophic Lateral Sclerosis Model", *Antioxidants* **2024**, *13*, 807.

[106] K. Castillo et al., "Trehalose delays the progression of amyotrophic lateral sclerosis by enhancing autophagy in motoneurons", *Autophagy* **2013**, *9*, 1308–1320.

[107] Y. Li et al., "Trehalose decreases mutant SOD1 expression and alleviates motor deficiency in early but not end-stage amyotrophic lateral sclerosis in a SOD1-G93A mouse model", *Neuroscience* **2015**, *298*, 12–25.

[108] K. Hosseinpour-Moghaddam, M. Caraglia, A. Sahebkar, "Autophagy induction by trehalose: Molecular mechanisms and therapeutic impacts", *Journal of Cellular Physiology* **2018**, *233*, 6524–6543.

[109] S. Thams et al., "A Stem Cell-Based Screening Platform Identifies Compounds that Desensitize Motor Neurons to Endoplasmic Reticulum Stress", *Molecular Therapy* **2019**, *27*, 87–101.

[110] M. Lo Giudice et al., "Tauro-Urso-Deoxycholic Acid Trials in Amyotrophic Lateral Sclerosis: What is Achieved and What to Expect", *Clinical Drug Investigation* **2023**, *43*, 893–903.

[111] S. Vang et al., "The Unexpected Uses of Urso- and Tauroursodeoxycholic Acid in the Treatment of Non-liver Diseases", *Global Advances in Health and Medicine* **2014**, *3*, 58–69.

[112] U. Özcan et al., "Chemical Chaperones Reduce ER Stress and Restore Glucose Homeostasis in a Mouse Model of Type 2 Diabetes", *Science* **2006**, *313*, 1137–1140.

[113] J. K. Uppala, A. R. Gani, K. V. A. Ramaiah, "Chemical chaperone, TUDCA unlike PBA, mitigates protein aggregation efficiently and resists ER and non-ER stress induced HepG2 cell death", *Scientific Reports* **2017**, *7*.

[114] A. E. Elia et al., "Tauroursodeoxycholic acid in the treatment of patients with amyotrophic lateral sclerosis", *European Journal of Neurology* **2015**, *23*, 45–52.

[115] A. Albanese et al., "Tauroursodeoxycholic acid in patients with amyotrophic lateral sclerosis: The TUDCA-ALS trial protocol", *Frontiers in Neurology* **2022**, *13*.

[116] The TUDCA-ALS consortium announces top-line results from the Europeanphase 3 clinical trial of TUDCA in patients with amyotrophic lateral sclerosis(ALS). https://www.mndassociation.org/sites/default/files/2024-10/27.03.24-TUDCA-TOPLINE-RESULTS_0.pdf, **accessed 28.05.2025**.

[117] S. Paganoni et al., "Trial of Sodium Phenylbutyrate-Taurursodiol for Amyotrophic Lateral Sclerosis", *New England Journal of Medicine* **2020**, *383*, 919–930.

[118] S. Paganoni et al., "Long-term survival of participants in the CENTAUR trial of sodium phenylbutyrate-taurursodiol in amyotrophic lateral sclerosis", *Muscle & Nerve* **2020**, *63*, 31–39.

[119] S. Paganoni et al., "Effect of sodium phenylbutyrate/taurursodiol on tracheostomy/ventilation-free survival and hospitalisation in amyotrophic lateral sclerosis: long-term results from the CENTAUR trial", *Journal of Neurology Neurosurgery & Psychiatry* **2022**, *93*, 871–875.

[120] S. Paganoni et al., "Survival analyses from the CENTAUR trial in amyotrophic lateral sclerosis: Evaluating the impact of treatment crossover on outcomes", *Muscle & Nerve* **2022**, *66*, 136–141.

[121] S. Paganoni et al., "Analysis of sodium phenylbutyrate and taurursodiol survival effect in <scp>ALS</scp> using external controls", *Annals of Clinical and Translational Neurology* **2023**, *10*, 2297–2304.

[122] Amylyx Pharmaceuticals, Amylyx Pharmaceuticals Announces Topline Results From Global Phase 3 PHOENIX Trial of AMX0035 in ALS, https://www.amylyx.com/news/amylyx-pharmaceuticals-announces-topline-results-from-global-phase-3-phoenix-trial-of-amx0035-in-als, **accessed 27.05.2025**.

[123] Amylyx Pharmaceuticals, Amylyx Pharmaceuticals Announces Formal Intention to Remove RELYVRIO/ALBRIOZA from the Market; Provides Updates on Access to Therapy, Pipeline, Corporate Restructuring, and Strategy, https://www.amylyx.com/news/amylyx-pharmaceuticals-announces-formal-intention-to-remove-relyvrior/albriozatm-from-the-market-provides-updates-on-access-to-therapy-pipeline-corporate-restructuring-and-strategy, **accessed 23.08.2025**.

[124] E. Trias et al., "Post-paralysis tyrosine kinase inhibition with masitinib abrogates neuroinflammation and slows disease progression in inherited amyotrophic lateral sclerosis", *Journal of Neuroinflammation* **2016**, *13*.

[125] J. S. Mora et al., "Masitinib as an add-on therapy to riluzole in patients with amyotrophic lateral sclerosis: a randomized clinical trial", *Amyotrophic Lateral Sclerosis and Frontotemporal Degeneration* **2019**, *21*, 5–14.

[126] J. S. Mora et al., "Long-term survival analysis of masitinib in amyotrophic lateral sclerosis", *Therapeutic Advances in Neurological Disorders* **2021**, *14*.

[127] A. Ludolph, O. Hermine, "Masitinib Shows Prolonged Survival in Amyotrophic Lateral Sclerosis (ALS) Patients with Mild or Moderate Disease Severity at Baseline (S33.003)", *Neurology* **2023**, *100*.

[128] R. Benmohamed et al., "Identification of compounds protective against G93A-SOD1 toxicity for the treatment of amyotrophic lateral sclerosis", *Amyotrophic Lateral Sclerosis* **2010**, *12*, 87–96.

[129] G. Matsumoto et al., "Structural properties and neuronal toxicity of amyotrophic lateral sclerosis–associated Cu/Zn superoxide dismutase 1 aggregates", *The Journal of Cell Biology* **2005**, *171*, 75–85.

[130] T. Chen et al., "Arylsulfanyl pyrazolones block mutant SOD1-G93A aggregation. Potential application for the treatment of amyotrophic lateral sclerosis", *Bioorganic & Medicinal Chemistry* **2011**, *19*, 613–622.

[131] T. Chen et al., "ADME-Guided Design and Synthesis of Aryloxanyl Pyrazolone Derivatives To Block Mutant Superoxide Dismutase 1 (SOD1) Cytotoxicity and Protein Aggregation: Potential Application for the Treatment of Amyotrophic Lateral Sclerosis", *Journal of Medicinal Chemistry* **2011**, *55*, 515–527.

[132] Y. Zhang et al., "Arylazanylpyrazolone Derivatives as Inhibitors of Mutant Superoxide Dismutase 1 Dependent Protein Aggregation for the Treatment of Amyotrophic Lateral Sclerosis", *Journal of Medicinal Chemistry* **2013**, *56*, 2665–2675.

[133] P. C. Trippier et al., "Proteasome Activation is a Mechanism for Pyrazolone Small Molecules Displaying Therapeutic Potential in Amyotrophic Lateral Sclerosis", *ACS Chemical Neuroscience* **2014**, *5*, 823–829.

[134] Y. Zhang et al., "Tertiary Amine Pyrazolones and Their Salts as Inhibitors of Mutant Superoxide Dismutase 1-Dependent Protein Aggregation for the Treatment of Amyotrophic Lateral Sclerosis", *Journal of Medicinal Chemistry* **2015**, *58*, 5942–5949.

[135] W. Zhang et al., "Cyclohexane 1,3-diones and their inhibition of mutant SOD1-dependent protein aggregation and toxicity in PC12 cells", *Bioorganic & Medicinal Chemistry* **2012**, *20*, 1029–1045.

[136] Y. Zhang et al., "Chiral Cyclohexane 1,3-Diones as Inhibitors of Mutant SOD1-Dependent Protein Aggregation for the Treatment of ALS", *ACS Medicinal Chemistry Letters* **2012**, *3*, 584–587.

[137] B. Genç et al., "Improving mitochondria and ER stability helps eliminate upper motor neuron degeneration that occurs due to mSOD1 toxicity and TDP-43 pathology", *Clinical and Translational Medicine* **2021**, *11*.

[138] E. A. Johnson et al., "Inhibition of amyloid beta oligomer accumulation by NU-9: A unifying mechanism for the treatment of neurodegenerative diseases", *Proceedings of the National Academy of Sciences* **2025**, *122*.

[139] G. Xia et al., "Pyrimidine-2,4,6-trione Derivatives and Their Inhibition of Mutant SOD1-Dependent Protein Aggregation. Toward a Treatment for Amyotrophic Lateral Sclerosis", *Journal of Medicinal Chemistry* **2011**, *54*, 2409–2421.

[140] P. C. Trippier et al., "Substituted pyrazolones require N2 hydrogen bond donating ability to protect against cytotoxicity from protein aggregation of mutant superoxide dismutase 1", *Bioorganic & Medicinal Chemistry Letters* **2012**, *22*, 6647–6650.

[141] G. Xia et al., "Deuteration and fluorination of 1,3-bis(2-phenylethyl)pyrimidine-2,4,6(1H,3H,5H)-trione to improve its pharmacokinetic properties", *Bioorganic & Medicinal Chemistry Letters* **2014**, *24*, 5098–5101.

[142] M. S. Feiler et al., "TDP-43 is intercellularly transmitted across axon terminals", *Journal of Cell Biology* **2015**, *211*, 897–911.

[143] J. Vaquer-Alicea, M. I. Diamond, "Propagation of Protein Aggregation in Neurodegenerative Diseases", *Annual Review of Biochemistry* **2019**, *88*, 785–810.

[144] T. Nonaka, M. Hasegawa, "Prion-like properties of assembled TDP-43", *Current Opinion in Neurobiology* **2020**, *61*, 23–28.

[145] M. K. Jaiswal, "Riluzole and edaravone: A tale of two amyotrophic lateral sclerosis drugs", *Medicinal Research Reviews* **2018**, *39*, 733–748.

[146] A. Doble, "The pharmacology and mechanism of action of riluzole", *Neurology* **1996**, *47*.

[147] M. C. Bellingham, "A Review of the Neural Mechanisms of Action and Clinical Efficiency of Riluzole in Treating Amyotrophic Lateral Sclerosis: What have we Learned in the Last Decade?: Neural Mechanisms of Action and Clinical Efficiency of Riluzole in Treating ALS", *CNS Neuroscience & Therapeutics* **2011**, *17*, 4–31.

[148] M. Hinchcliffe, A. Smith, "Riluzole: real-world evidence supports significant extension of median survival times in patients with amyotrophic lateral sclerosis", *Degenerative Neurological and Neuromuscular Disease* **2017**, *Volume 7*, 61–70.

[149] K. Watanabe et al., "How is edaravone effective against acute ischemic stroke and amyotrophic lateral sclerosis?", *Journal of Clinical Biochemistry and Nutrition* **2018**, *62*, 20–38.

[150] S. Witzel et al., "Safety and Effectiveness of Long-term Intravenous Administration of Edaravone for Treatment of Patients With Amyotrophic Lateral Sclerosis", *JAMA Neurology* **2022**, *79*, 121.

[151] U.S. Food and Drug Administration, FDA Approves Oral Form for the treatment of adults with amyotrophic lateral sclerosis (ALS), https://www.fda.gov/drugs/news-events-human-drugs/fda-approves-oral-form-treatment-adults-amyotrophic-lateral-sclerosis-als, **accessed 20.08.2025**.

[152] Ferrer, Ferrer reports top-line results from Phase III ADORE study in ALS, https://www.ferrer.com/en/results-study-ADORE-ALS, **accessed 27.05.2025**.

[153] A. Saini, P. A. Chawla, "Breaking barriers with tofersen: Enhancing therapeutic opportunities in amyotrophic lateral sclerosis", *European Journal of Neurology* **2023**, *31*.

[154] R. A. Smith, "Antisense oligonucleotide therapy for neurodegenerative disease", *Journal of Clinical Investigation* **2006**, *116*, 2290–2296.

[155] T. Miller et al., "Phase 1–2 Trial of Antisense Oligonucleotide Tofersen for SOD1 ALS", *New England Journal of Medicine* **2020**, *383*, 109–119.

[156] M. J. Crisp et al., "In vivo kinetic approach reveals slow SOD1 turnover in the CNS", *Journal of Clinical Investigation* **2015**, *125*, 2772–2780.

[157] T. M. Miller et al., "Trial of Antisense Oligonucleotide Tofersen for SOD1 ALS", *New England Journal of Medicine* **2022**, *387*, 1099–1110.

[158] T. Meyer et al., "Neurofilament light-chain response during therapy with antisense oligonucleotide tofersen in SOD1-related ALS: Treatment experience in clinical practice", *Muscle & Nerve* **2023**, *67*, 515–521.

[159] V. Mrđen Debono, "Design and synthesis of multifunctional ligands to study and prevent aggregation processes in Amyotrophic Lateral Sclerosis proteins", *PhD Thesis University of Göttingen* **2020**.

[160] Cytiva, Ion Exchange Chromatography (IEX) Principles & Methods, CY13983-08Feb21-HB, **2021**.

[161] Cytiva, Size Exclusion Chromatography (SEC) Principles & Methods, CY12707-03Dec20-HB, **2020**.

[162] H. Ukeda et al., "Spectrophotometric Assay for Superoxide Dismutase Based on the Reduction of Highly Water-soluble Tetrazolium Salts by Xanthine-Xanthine Oxidase", *Bioscience Biotechnology and Biochemistry* **1999**, *63*, 485–488.

[163] A. V. Peskin, C. C. Winterbourn, "A microtiter plate assay for superoxide dismutase using a water-soluble tetrazolium salt (WST-1)", *Clinica Chimica Acta* **2000**, *293*, 157–166.

[164] A. V. Peskin, C. C. Winterbourn, "Assay of superoxide dismutase activity in a plate assay using WST-1", *Free Radical Biology and Medicine* **2017**, *103*, 188–191.

[165] J. M. McCord, I. Fridovich, "The Reduction of Cytochrome c by Milk Xanthine Oxidase", *Journal of Biological Chemistry* **1968**, *243*, 5753–5760.

[166] J. M. McCord, I. Fridovich, "Superoxide Dismutase: AN ENZYMIC FUNCTION FOR ERYTHROCUPREIN (HEMOCUPREIN)", *Journal of Biological Chemistry* **1969**, *244*, 6049–6055.

[167] I. Fridovich, "Quantitative Aspects of the Production of Superoxide Anion Radical by Milk Xanthine Oxidase", *Journal of Biological Chemistry* **1970**, *245*, 4053–4057.

[168] M. Ishiyama et al., "A New Sulfonated Tetrazolium Salt That Produces a Highly Water-Soluble Formazan Dye.", *Chemical and Pharmaceutical Bulletin* **1993**, *41*, 1118–1122.

[169] H. Naiki et al., "Fluorometric determination of amyloid fibrils in vitro using the fluorescent dye, thioflavine T", *Analytical Biochemistry* **1989**, *177*, 244–249.

[170] M. Biancalana, S. Koide, "Molecular mechanism of Thioflavin-T binding to amyloid fibrils", *Biochimica et Biophysica Acta (BBA) - Proteins and Proteomics* **2010**, *1804*, 1405–1412.

[171] D. M. Walsh et al., "Amyloid β-Protein Fibrillogenesis", *Journal of Biological Chemistry* **1999**, *274*, 25945–25952.

[172] A. A. Reinke, J. E. Gestwicki, "Insight into Amyloid Structure Using Chemical Probes", *Chemical Biology & Drug Design* **2011**, *77*, 399–411.

[173] I. Maezawa et al., "Congo red and thioflavin-T analogs detect Aβ oligomers", *Journal of Neurochemistry* **2007**, *104*, 457–468.

[174] L. Banci et al., "SOD1 and Amyotrophic Lateral Sclerosis: Mutations and Oligomerization", *PLoS ONE* **2008**, *3*, (Ed.: S. Koutsopoulos), e1677.

[175] Z. A. Oztug Durer et al., "Loss of Metal Ions, Disulfide Reduction and Mutations Related to Familial ALS Promote Formation of Amyloid-Like Aggregates from Superoxide Dismutase", *PLoS ONE* **2009**, *4*, (Ed.: A. I. Bush), e5004.

[176] K. Gade Malmos et al., "ThT 101: a primer on the use of thioflavin T to investigate amyloid formation", *Amyloid* **2017**, *24*, 1–16.

[177] R. Malik et al., "Examination of SOD1 aggregation modulators and their effect on SOD1 enzymatic activity as a proxy for potential toxicity", *The FASEB Journal* **2020**, *34*, 11957–11969.

[178] L. P. Jameson, N. W. Smith, S. V. Dzyuba, "Dye-Binding Assays for Evaluation of the Effects of Small Molecule Inhibitors on Amyloid (Aβ) Self-Assembly", *ACS Chemical Neuroscience* **2012**, *3*, 807–819.

[179] K. Mikalauskaite et al., "Effect of Ionic Strength on Thioflavin-T Affinity to Amyloid Fibrils and Its Fluorescence Intensity", *International Journal of Molecular Sciences* **2020**, *21*, 8916.

[180] S. A. Hudson et al., "The thioflavin T fluorescence assay for amyloid fibril detection can be biased by the presence of exogenous compounds", *The FEBS Journal* **2009**, *276*, 5960–5972.

[181] J. A. J. Housmans et al., "A guide to studying protein aggregation", *The FEBS Journal* **2021**, *290*, 554–583.

[182] V. Foderà et al., "Thioflavin T Hydroxylation at Basic pH and Its Effect on Amyloid Fibril Detection", *The Journal of Physical Chemistry B* **2008**, *112*, 15174–15181.

[183] Y.-M. Hwang et al., "Nonamyloid Aggregates Arising from Mature Copper/Zinc Superoxide Dismutases Resemble Those Observed in Amyotrophic Lateral Sclerosis", *Journal of Biological Chemistry* **2010**, *285*, 41701–41711.

[184] A. Abdolvahabi et al., "Stochastic Formation of Fibrillar and Amorphous Superoxide Dismutase Oligomers Linked to Amyotrophic Lateral Sclerosis", *ACS Chemical Neuroscience* **2016**, *7*, 799–810.

[185] M. A. I. Khan et al., "Cu/Zn Superoxide Dismutase Forms Amyloid Fibrils under Near-Physiological Quiescent Conditions: The Roles of Disulfide Bonds and Effects of Denaturant", *ACS Chemical Neuroscience* **2017**, *8*, 2019–2026.

[186] S. S. Leal et al., "Calcium Ions Promote Superoxide Dismutase 1 (SOD1) Aggregation into Non-fibrillar Amyloid", *Journal of Biological Chemistry* **2013**, *288*, 25219–25228.

[187] R. Malik et al., "The molecular tweezer CLR01 inhibits aberrant superoxide dismutase 1 (SOD1) self-assembly in vitro and in the G93A-SOD1 mouse model of ALS", *Journal of Biological Chemistry* **2019**, *294*, 3501–3513.

[188] T. P. J. Knowles et al., "An Analytical Solution to the Kinetics of Breakable Filament Assembly", *Science* **2009**, *326*, 1533–1537.

[189] L. Giehm, D. E. Otzen, "Strategies to increase the reproducibility of protein fibrillization in plate reader assays", *Analytical Biochemistry* **2010**, *400*, 270–281.

[190] Y. Li, V. Lubchenko, P. G. Vekilov, "The use of dynamic light scattering and Brownian microscopy to characterize protein aggregation", *Review of Scientific Instruments* **2011**, *82*.

[191] Malvern Panalytical, Particle Size Analysis - An Explanation, https://www.malvernpanalytical.com/products/measurement-type/particle-size, **accessed 02.09.2025**.

[192] W. Schärtl, *Light Scatteringfrom Polymer Solutions and NanoparticleDispersions*, Berlin, Heidelberg: Springer Berlin Heidelberg, **2007**.

[193] H. Voigt, S. Hess, "Comparison of the intensity correlation function and the intermediate scattering function of fluids: a molecular dynamics study of the Siegert relation", *Physica A: Statistical Mechanics and its Applications* **1994**, *202*, 145–164.

[194] B. J. Berne, R. Pecora, *Dynamic Light Scattering With Applications to Chemistry, Biology, and Physics*, Dover Publications, **2000**.

[195] Malvern Panalytics, Zetasizer Ultra/Pro User Guide, MAN0592-04-EN, **2019**.

[196] O. Trott, A. J. Olson, "AutoDock Vina: Improving the speed and accuracy of docking with a new scoring function, efficient optimization, and multithreading", *Journal of Computational Chemistry* **2010**, *31*, 455–461.

[197] J. Wendt, "Investigation of Protecting Group Strategies in the Synthesis of SOD1-stabilizing Molecules", *Bachelor Thesis Heidelberg University* **2021**.

[198] D. G. Brown, J. Boström, "Analysis of Past and Present Synthetic Methodologies on Medicinal Chemistry: Where Have All the New Reactions Gone?", *Journal of Medicinal Chemistry* **2016**, *59*, 4443–4458.

[199] J. Boström et al., "Expanding the medicinal chemistry synthetic toolbox", *Nature Reviews Drug Discovery* **2018**, *17*, 709–727.

[200] J. Blagg et al., "Indole derivative steroid 5-alpha-reductase inhibitors", WO9317014A1, **1993**.

[201] E. Blaise et al., "Access to 4-Alkylaminopyridazine Derivatives via Nitrogen-Assisted Regioselective Pd-Catalyzed Reactions", *The Journal of Organic Chemistry* **2014**, *79*, 10311–10322.

[202] C. J. O'Brien et al., "Easily Prepared Air- and Moisture-Stable Pd–NHC (NHC=N-Heterocyclic Carbene) Complexes: A Reliable, User-Friendly, Highly Active Palladium Precatalyst for the Suzuki–Miyaura Reaction", *Chemistry – A European Journal* **2006**, *12*, 4743–4748.

[203] P. G. Gildner, T. J. Colacot, "Reactions of the 21st Century: Two Decades of Innovative Catalyst Design for Palladium-Catalyzed Cross-Couplings", *Organometallics* **2015**, *34*, 5497–5508.

[204] N. Miyaura, A. Suzuki, "Palladium-Catalyzed Cross-Coupling Reactions of Organoboron Compounds", *Chemical Reviews* **1995**, *95*, 2457–2483.

[205] J. Sherwood et al., "Solvent effects in palladium catalysed cross-coupling reactions", *Green Chemistry* **2019**, *21*, 2164–2213.

[206] J. A. Molina de la Torre, P. Espinet, A. C. Albéniz, "Solvent-Induced Reduction of Palladium-Aryls, a Potential Interference in Pd Catalysis", *Organometallics* **2013**, *32*, 5428–5434.

[207] E. Tyrrell, P. Brookes, "The Synthesis and Applications of Heterocyclic Boronic Acids", *Synthesis* **2003**, *2003*, 0469–0483.

[208] K. L. Billingsley, K. W. Anderson, S. L. Buchwald, "A Highly Active Catalyst for Suzuki–Miyaura Cross-Coupling Reactions of Heteroaryl Compounds", *Angewandte Chemie International Edition* **2006**, *45*, 3484–3488.

[209] K. M. Clapham et al., "New Pyrimidylboronic Acids and Functionalized Heteroarylpyrimidines by Suzuki Cross-Coupling Reactions", *European Journal of Organic Chemistry* **2007**, *2007*, 5712–5716.

[210] P. Doig et al., "Rational design of inhibitors of the bacterial cell wall synthetic enzyme GlmU using virtual screening and lead-hopping", *Bioorganic & Medicinal Chemistry* **2014**, *22*, 6256–6269.

[211] K. L. Wilson et al., "Cyrene as a Bio-Based Solvent for the Suzuki–Miyaura Cross-Coupling", *Synlett* **2018**, *29*, 650–654.

[212] V. M. Kassel et al., "Heteroaryl–Heteroaryl, Suzuki–Miyaura, Anhydrous Cross-Coupling Reactions Enabled by Trimethyl Borate", *Journal of the American Chemical Society* **2021**, *143*, 13845–13853.

[213] A. J. J. Lennox, G. C. Lloyd-Jones, "Selection of boron reagents for Suzuki–Miyaura coupling", *Chem. Soc. Rev.* **2014**, *43*, 412–443.

[214] C. O. Kappe, "How to measure reaction temperature in microwave-heated transformations", *Chemical Society Reviews* **2013**, *42*, 4977.

[215] F. L. Benton, T. E. Dillon, "The Cleavage of Ethers with Boron Bromide. I. Some Common Ethers", *Journal of the American Chemical Society* **1942**, *64*, 1128–1129.

[216] J. McOmie, M. Watts, D. West, "Demethylation of aryl methyl ethers by boron tribromide", *Tetrahedron* **1968**, *24*, 2289–2292.

[217] M. V. Bhatt, S. U. Kulkarni, "Cleavage of Ethers", *Synthesis* **1983**, *1983*, 249–282.

[218] A. M. Felix, "Cleavage of protecting groups with boron tribromide", *The Journal of Organic Chemistry* **1974**, *39*, 1427–1429.

[219] S. Roy et al., "Design and development of benzoxazole derivatives with toll-like receptor 9 antagonism", *European Journal of Medicinal Chemistry* **2017**, *134*, 334–347.

[220] M. W. Dong, B. E. Boyes, "Modern trends and best practices in mobile-phase selection in reversed-phase chromatography", *LCGC North Am.* **2018**, *36*, 752–768.

[221] K. Sikora et al., "The Role of Counter-Ions in Peptides—An Overview", *Pharmaceuticals* **2020**, *13*.

[222] J. Lenčo, M. A. Khalikova, F. Švec, "Dissolving Peptides in 0.1% Formic Acid Brings Risk of Artificial Formylation", *Journal of Proteome Research* **2020**, *19*, 993–999.

[223] J. Alsenz, M. Kansy, "High throughput solubility measurement in drug discovery and development", *Advanced Drug Delivery Reviews* **2007**, *59*, 546–567.

[224] Expasy - ProtParam, https://web.expasy.org/protparam/, **accessed 12.10.2022**.

[225] ProtParam - Results for SODC_HUMAN (P00441), https://web.expasy.org/cgi-bin/protparam/protparam1?P00441@noft@, **accessed 12.10.2022**.

[226] Y. Yamazaki, T. Takao, "Metalation States versus Enzyme Activities of Cu, Zn-Superoxide Dismutase Probed by Electrospray Ionization Mass Spectrometry", *Analytical Chemistry* **2008**, *80*, 8246–8252.

[227] T. S. Choi, F. A. Tezcan, "Overcoming universal restrictions on metal selectivity by protein design", *Nature* **2022**, *603*, 522–527.

[228] M. Tajiri et al., "Metal distribution in Cu/Zn-superoxide dismutase revealed by native mass spectrometry", *Free Radical Biology and Medicine* **2022**, *183*, 60–68.

[229] M. W. Pantoliano, P. J. McDonnell, J. S. Valentine, "Reversible loss of metal ions from the zinc binding site of copper-zinc superoxide dismutase. The low pH transition", *Journal of the American Chemical Society* **1979**, *101*, 6454–6456.

[230] M. W. Pantoliano et al., "The pH dependence of metal ion binding to the native zinc site of bovine erythrocuprein (superoxide dismutase)", *Journal of the American Chemical Society* **1982**, *104*, 1717–1723.

[231] L. Banci et al., "Solution Structure of Reduced Monomeric Q133M2 Copper, Zinc Superoxide Dismutase (SOD). Why Is SOD a Dimeric Enzyme?", *Biochemistry* **1998**, *37*, 11780–11791.

[232] H.-X. Deng et al., "Amyotrophic Lateral Ssclerosis and Structural Defects in Cu,Zn Superoxide Dismutase", *Science* **1993**, *261*, 1047–1051.

[233] D. R. Borchelt et al., "Superoxide dismutase 1 with mutations linked to familial amyotrophic lateral sclerosis possesses significant activity.", *Proceedings of the National Academy of Sciences* **1994**, *91*, 8292–8296.

[234] A. C. Bowling et al., "Superoxide Dismutase Concentration and Activity in Familial Amyotrophic Lateral Sclerosis", *Journal of Neurochemistry* **1995**, *64*, 2366–2369.

[235] M. Jerabek-Willemsen et al., "Molecular Interaction Studies Using Microscale Thermophoresis", *ASSAY and Drug Development Technologies* **2011**, *9*, 342–353.

[236] M. Jerabek-Willemsen et al., "MicroScale Thermophoresis: Interaction analysis and beyond", *Journal of Molecular Structure* **2014**, *1077*, 101–113.

[237] M. Asmari et al., "Thermophoresis for characterizing biomolecular interaction", *Methods* **2018**, *146*, 107–119.

[238] R. Manjula et al., "Rational discovery of a SOD1 tryptophan oxidation inhibitor with therapeutic potential for amyotrophic lateral sclerosis", *Journal of Biomolecular Structure and Dynamics* **2019**, *37*, 3936–3946.

[239] S. Aouti, S. Padavattan, B. Padmanabhan, "Structure-based discovery of an antipsychotic drug, paliperidone, as a modulator of human superoxide dismutase 1: a potential therapeutic target in amyotrophic lateral sclerosis", *Acta Crystallographica Section D Structural Biology* **2023**, *79*, 531–544.

[240] S. Unni et al., "Structural insights into the modulation Of SOD1 aggregation By a fungal metabolite Phialomustin-B: Therapeutic potential in ALS", *PLOS ONE* **2024**, *19*, (Ed.: R. K. Kar), e0298196.

[241] S. A. Seidel et al., "Microscale thermophoresis quantifies biomolecular interactions under previously challenging conditions", *Methods* **2013**, *59*, 301–315.

[242] M. A. Hough et al., "Dimer destabilization in superoxide dismutase may result in disease-causing properties: Structures of motor neuron disease mutants", *Proceedings of the National Academy of Sciences* **2004**, *101*, 5976–5981.

[243] F. Arnesano et al., "The Unusually Stable Quaternary Structure of Human Cu,Zn-Superoxide Dismutase 1 Is Controlled by Both Metal Occupancy and Disulfide Status", *Journal of Biological Chemistry* **2004**, *279*, 47998–48003.

[244] P. A. Doucette et al., "Dissociation of Human Copper-Zinc Superoxide Dismutase Dimers Using Chaotrope and Reductant", *Journal of Biological Chemistry* **2004**, *279*, 54558–54566.

[245] I. Anzai et al., "Screening of Drugs Inhibiting In vitro Oligomerization of Cu/Zn-Superoxide Dismutase with a Mutation Causing Amyotrophic Lateral Sclerosis", *Frontiers in Molecular Biosciences* **2016**, *3*.

[246] N. K. Bhatia et al., "Curcumin binds to the pre-fibrillar aggregates of Cu/Zn superoxide dismutase (SOD1) and alters its amyloidogenic pathway resulting in reduced cytotoxicity", *Biochimica et Biophysica Acta (BBA) - Proteins and Proteomics* **2015**, *1854*, 426–436.

[247] N. K. Bhatia et al., "Quercetin and Baicalein Act as Potent Antiamyloidogenic and Fibril Destabilizing Agents for SOD1 Fibrils", *ACS Chemical Neuroscience* **2020**, *11*, 1129–1138.

[248] S. Sharma, V. R. Tomar, S. Deep, "Myricetin: A Potent Anti-Amyloidogenic Polyphenol against Superoxide Dismutase 1 Aggregation", *ACS Chemical Neuroscience* **2023**, *14*, 2461–2475.

[249] K. A. Vassall et al., "Decreased stability and increased formation of soluble aggregates by immature superoxide dismutase do not account for disease severity in ALS", *Proceedings of the National Academy of Sciences* **2011**, *108*, 2210–2215.

[250] C. Li et al., "Cupric Ions Induce the Oxidation and Trigger the Aggregation of Human Superoxide Dismutase 1", *PLoS ONE* **2013**, *8*, (Ed.: J. M. Sanchez-Ruiz), e65287.

[251] S. Famil Samavati et al., "Reduced thermodynamic stability as prerequisite for aggregation of SOD1 mutants: a path through the reduction in intramolecular disulfide bonds", *Journal of the Iranian Chemical Society* **2020**, *17*, 2053–2071.

[252] S. Gusain et al., "Development of carbazole-based molecules for inhibition of mutant hSOD1 protein aggregation in Amyotrophic Lateral Sclerosis", *Bioorganic & Medicinal Chemistry* **2025**, *120*, 118091.

[253] R. Chia et al., "Superoxide Dismutase 1 and tgSOD1G93A Mouse Spinal Cord Seed Fibrils, Suggesting a Propagative Cell Death Mechanism in Amyotrophic Lateral Sclerosis", *PLoS ONE* **2010**, *5*, (Ed.: M. B. Feany), e10627.

[254] C. Münch, J. O'Brien, A. Bertolotti, "Prion-like propagation of mutant superoxide dismutase-1 misfolding in neuronal cells", *Proceedings of the National Academy of Sciences* **2011**, *108*, 3548–3553.

[255] S. Lee, H.-J. Kim, "Prion-like Mechanism in Amyotrophic Lateral Sclerosis: are Protein Aggregates the Key?", *Experimental Neurobiology* **2015**, *24*, 1–7.

[256] E. Ekhtiari Bidhendi et al., "Mutant superoxide dismutase aggregates from human spinal cord transmit amyotrophic lateral sclerosis", *Acta Neuropathologica* **2018**, *136*, 939–953.

[257] R. G. Larson, "Twenty years of drying droplets", *Nature* **2017**, *550*, 466–467.

[258] A. Aronov et al., "Indazolinone compositions useful as kinase inhibitors", WO2004037814, **2004**.

[259] B. Zhao et al., "Effects of aprotic solvents on the stability of metal-free superoxide dismutase probed by native electrospray ionization–ion mobility–mass spectrometry", *Journal of Mass Spectrometry* **2019**, *54*, 351–358.

[260] D. Some et al., "Characterization of Proteins by Size-Exclusion Chromatography Coupled to Multi-Angle Light Scattering (SEC-MALS)", *Journal of Visualized Experiments* **2019**.

[261] M. Naiim et al., "Multiangle dynamic light scattering for the improvement of multimodal particle size distribution measurements", *Soft Matter* **2015**, *11*, 28–32.

[262] A. Sharma et al., "Evaluation and Screening of Biopharmaceuticals using Multi-Angle Dynamic Light Scattering", *AAPS PharmSciTech* **2023**, *24*.

[263] P. Ip et al., "Quercitrin and quercetin 3-β-d-glucoside as chemical chaperones for the A4V SOD1 ALS-causing mutant", *Protein Engineering Design and Selection* **2017**, *30*, 431–440.

[264] S. Forli et al., "Computational protein-ligand docking and virtual drug screening with the AutoDock suite", *Nature Protocols* **2016**, *11*, 905–919.

[265] Force a non-rotatable bond to be considered rotatable in ADT - AutoDock, http://autodock.scripps.edu/faqs-help/how-to/force-a-non-rotatable-bond-to-be-considered-rotatable-in-adt, Web Page, **accessed 18.10.2020**.

[266] M. M. Jaghoori, B. Bleijlevens, S. D. Olabarriaga, "1001 Ways to run AutoDock Vina for virtual screening", *Journal of Computer-Aided Molecular Design* **2016**, *30*, 237–249.

[267] AutoDock Vina - molecular docking and virtual screening program, http://vina.scripps.edu/manual.html, Web Page, **accessed 01.02.2021**.

[268] R Core Team, R: A Language and Environment for Statistical Computing, R Foundation for Statistical Computing, Vienna, Austria, **2024**.

[269] H. Wickham et al., "Welcome to the Tidyverse", *Journal of Open Source Software* **2019**, *4*, 1686.

[270] H. Wickham, *ggplot2: Elegant Graphics for Data Analysis*, Springer-Verlag New York, **2016**.

[271] G. R. Fulmer et al., "NMR Chemical Shifts of Trace Impurities: Common Laboratory Solvents, Organics, and Gases in Deuterated Solvents Relevant to the Organometallic Chemist", *Organometallics* **2010**, *29*, 2176–2179.

[272] M. Strohalm et al., "mMass 3: A Cross-Platform Software Environment for Precise Analysis of Mass Spectrometric Data", *Analytical Chemistry* **2010**, *82*, 4648–4651.

[273] S. Chun, Y. K. Chung, "Transition-Metal-Free Poly(thiazolium) Iodide/1,8-Diazabicyclo[5.4.0] undec-7-ene/Phenazine-Catalyzed Esterification of Aldehydes with Alcohols", *Org. Lett.* **2017**, *19*, 3787–3790.

[274] A. Aoyama et al., "Design, Synthesis, and Biological Evaluation of Novel Transrepression-Selective Liver X Receptor (LXR) Ligands with 5,11-Dihydro-5-methyl-11-methylene-6H-dibenz [b,e]azepin-6-one Skeleton", *J. Med. Chem.* **2012**, *55*, 7360–7377.

[275] Y. Xie et al., "Phenylsulfonylfuroxan NO-donor phenols: Synthesis and multifunctional activities evaluation", *Bioorg. Med. Chem.* **2017**, *25*, 4407–4413.

[276] C. J. Higginson et al., "Bioinspired Design Provides High-Strength Benzoxazine Structural Adhesives", *Angewandte Chemie International Edition* **2019**, *58*, 12271–12279.

[277] M. G. J. Baud et al., "New Synthetic Routes to Triazolo-benzodiazepine Analogues: Expanding the Scope of the Bump-and-Hole Approach for Selective Bromo and Extra-Terminal (BET) Bromodomain Inhibition", *Journal of Medicinal Chemistry* **2016**, *59*, 1492–1500.

[278] T. J. Collins, "ImageJ for Microscopy", *BioTechniques* **2007**, *43*.

[279] C. A. Schneider, W. S. Rasband, K. W. Eliceiri, "NIH Image to ImageJ: 25 years of image analysis", *Nature Methods* **2012**, *9*, 671–675.

[280] M. del Carmen Grande et al., "On the density and viscosity of (water+dimethylsulphoxide) binary mixtures", *The Journal of Chemical Thermodynamics* **2007**, *39*, 1049–1056.